frontiers | Research Topics

Biogeochemical processes of micro/trace elements and their impacts on marine ecosystems

Edited by
Wen Zhuang, Jinming Song
and Hermano Melo Queiroz

Published in
Frontiers in Marine Science

ISSN 1664-8714
ISBN 978-2-8325-4192-0
DOI 10.3389/978-2-8325-4192-0

About Frontiers

Frontiers is more than just an open access publisher of scholarly articles: it is a pioneering approach to the world of academia, radically improving the way scholarly research is managed. The grand vision of Frontiers is a world where all people have an equal opportunity to seek, share and generate knowledge. Frontiers provides immediate and permanent online open access to all its publications, but this alone is not enough to realize our grand goals.

Frontiers journal series

The Frontiers journal series is a multi-tier and interdisciplinary set of open-access, online journals, promising a paradigm shift from the current review, selection and dissemination processes in academic publishing. All Frontiers journals are driven by researchers for researchers; therefore, they constitute a service to the scholarly community. At the same time, the *Frontiers journal series* operates on a revolutionary invention, the tiered publishing system, initially addressing specific communities of scholars, and gradually climbing up to broader public understanding, thus serving the interests of the lay society, too.

Dedication to quality

Each Frontiers article is a landmark of the highest quality, thanks to genuinely collaborative interactions between authors and review editors, who include some of the world's best academicians. Research must be certified by peers before entering a stream of knowledge that may eventually reach the public - and shape society; therefore, Frontiers only applies the most rigorous and unbiased reviews. Frontiers revolutionizes research publishing by freely delivering the most outstanding research, evaluated with no bias from both the academic and social point of view. By applying the most advanced information technologies, Frontiers is catapulting scholarly publishing into a new generation.

What are Frontiers Research Topics?

Frontiers Research Topics are very popular trademarks of the *Frontiers journals series*: they are collections of at least ten articles, all centered on a particular subject. With their unique mix of varied contributions from Original Research to Review Articles, Frontiers Research Topics unify the most influential researchers, the latest key findings and historical advances in a hot research area.

Find out more on how to host your own Frontiers Research Topic or contribute to one as an author by contacting the Frontiers editorial office: frontiersin.org/about/contact

Biogeochemical processes of micro/trace elements and their impacts on marine ecosystems

Topic editors

Wen Zhuang — Shandong University, China

Jinming Song — Institute of Oceanology, Chinese Academy of Sciences (CAS), China

Hermano Melo Queiroz — University of São Paulo, Brazil

Citation

Zhuang, W., Song, J., Queiroz, H. M., eds. (2024). *Biogeochemical processes of micro/trace elements and their impacts on marine ecosystems*. Lausanne: Frontiers Media SA. doi: 10.3389/978-2-8325-4192-0

Table of contents

frontiers | Frontiers in Marine Science

TYPE Editorial
PUBLISHED 11 December 2023
DOI 10.3389/fmars.2023.1341214

OPEN ACCESS

EDITED AND REVIEWED BY
Eric 'Pieter Achterberg,
Helmholtz Association of German Research Centres (HZ), Germany

*CORRESPONDENCE
Jinming Song
jmsong@qdio.ac.cn
Wen Zhuang
wzhuang@sdu.edu.cn
Hermano Melo Queiroz
hermanomelo@usp.br

RECEIVED 20 November 2023
ACCEPTED 04 December 2023
PUBLISHED 11 December 2023

CITATION
Song J, Zhuang W and Queiroz HM (2023) Editorial: Biogeochemical processes of micro/trace elements and their impacts on marine ecosystems.
Front. Mar. Sci. 10:1341214.
doi: 10.3389/fmars.2023.1341214

Editorial: Biogeochemical processes of micro/trace elements and their impacts on marine ecosystems

Jinming Song[1]*, Wen Zhuang[2,3]* and Hermano Melo Queiroz[4]*

[1]Key Laboratory of Marine Ecology and Environmental Science, Institute of Oceanology, Chinese Academy of Sciences, Qingdao, China, [2]Institute of Eco-environmental Forensics, Shandong University, Qingdao, China, [3]School of Environmental Science and Engineering, Shandong University, Qingdao, China, [4]Department of Geography, University of São Paulo, São Paulo, SP, Brazil

KEYWORDS

microelements, trace elements, marine ecosystems, biogeochemistry and coastal-ocean transitional system, isotope

Editorial on the Research Topic
Biogeochemical processes of micro/trace elements and their impacts on marine ecosystems

The micro/trace elements (M/TEs) concentrations in marine ecosystems (e.g., estuaries, salt marshes, mangrove forests, coral reefs, the open ocean, and the deep-sea ocean) are mostly very low. However, they play a key role in the functioning of these ecosystems, contributing to various biological and chemical processes. For instance, M/TEs such as Fe, Mn, Zn, and Cu, are essential components of nutrient cycles in marine ecosystems affecting the growth of phytoplankton and bacteria, and an essential nutrient for plant species in coastal ecosystems. Thus, M/TEs often limit primary production in certain regions of the ocean and coastal zones. Additionally, M/TEs elements such as Fe plays a role in redox reactions, influencing the oxidation and reduction processes that occur in estuarine soils affecting the potential of C sequestration and contaminants immobilization.

The maintenance of a balanced distribution of M/TEs is crucial for the preservation of biological communities and chemical processes within marine ecosystems. Any disruption in this balance can lead to abnormal ecosystem functioning. Consequently, the intensification of human activities has led to the substantial input of M/TEs into the marine environment which has given rise to a new frontier of investigation focusing on ecological roles and functions of M/TEs in the marine environment. M/TEs can function as vital nutrients or hazardous substances crucial for sustaining life, while certain M/TEs can also serve as indicators of changes in ecological conditions or levels of pollution. The cycling of M/TEs in the ocean is a highly intricate process, with their concentration and influence on marine ecosystems contingent upon the overall chemical matrix. This complexity is further evident in their interactions with various inorganic and organic substances, suspended particles,

colloids, and seafloor sediments. Consequently, the investigation of M/TEs in the ocean has consistently remained a prominent subject of interest in marine research.

Within this particular context, the 12 articles featured in this Research Topic center their attention on the biogeochemical mechanisms governing M/TEs within the ocean and their effects on the ecological environment. The research endeavors to encompass the identification of sources, distribution across multiple mediums, biogeochemical cycles, and interconnections with biodiversity, structure, and species function of M/TEs (and/or their isotopes) within the ocean. These articles are further categorized into two distinct classifications.

1 Source, multimedium distribution, and control mechanism of micro/trace elements and/or their isotopes in the ocean

Wang Z. et al. studied the distribution characteristics of dissolved Mn (dMn) in the East China Sea. The comprehensive biogeochemical cycle of dMn was found to be significantly influenced by various factors, including the input from the Yangtze River, the redox cycle, water mass mixing, and cross continental shelf transportation. Ren et al. investigated the spatial variations, sources, and correlations of dissolved Fe, Mn, Cu, Zn, Cd, and Pb in the surface water of the Yellow River Estuary in China. The study unveiled the specific molecular weight colloids that possess the ability to govern the distribution patterns of these metals in colloidal form. Luan et al. studied the fractionation behavior of Pb in seven seaward rivers in the Yellow River Delta, and discovered that the predominant transport form of dissolved Pb in freshwater was truly dissolved Pb. However, in brackish water within estuaries, colloidal matter gradually assumed the role of the primary transport carrier. The increase in salinity resulted in the immobilization of truly dissolved Pb, yet the presence of colloidal matter hindered this deposition process. Yang et al. found that the spatial patterns of dissolved Al (dAl) and dMn in the Northeast Indian Ocean were influenced to varying extents by the desorption and/or dissolution release of constituents from sedimentary rocks carried by riverine inputs, re-emergence of lithogenic particles, and the remineralization of organic particles. Wang X. et al. conducted a study on the early diagenesis of various redox sensitive metals in sediments obtained from the Bohai Sea, Yellow Sea, and Yangtze River Estuary. Their findings revealed a strong association between the cycling processes of Mo and Mn, whereas the recycling of U and V exhibited a closer relationship with Fe oxides. Cao et al. examined the distribution patterns of dissolved rare-earth elements (REEs) in the Northwest Pacific, and reported a significant positive correlation between REEs and apparent oxygen utilization in subsurface water. This study provides useful proxy information for tracing regional water masses and estimating cross-shelf REE fluxes.

The isotopic composition of oxidation-reduction sensitive elements holds significant value in the field of paleoceanography and serves as a tool for distinguishing pollution sources originating from natural processes and human activities. Wang W. et al. conducted an investigation on the dissolution of Cr and δ^{53}Cr throughout the water column. This study also incorporated data on dissolved and colloidal Fe concentrations, turbidity, chlorophyll a, dissolved oxygen, and large nutrient concentrations. The aim was to evaluate the regulatory mechanisms governing the behavior of Cr and its isotopes. Matsuoka et al. analyzed the source, concentrations, and isotopic ratios of dissolved Mo and W in waters and estuarine systems of Japan, the ratios of $\delta^{186/184}$W and $\delta^{98/95}$Mo were used to reveal the proportion from human activities.

2 Chemical forms of micro/trace elements and their coupling with biogeochemical cycles and ecological processes of other biogenic elements in the ocean

Fan et al. observed a non-conservative pattern of dissolved Mo (dMo) in relation to salinity in both the surface and bottom seawater of the Bohai Sea and Yellow Sea. The distribution of dMo was primarily influenced by biological utilization, particle adsorption (particularly MnO_x), and freshwater dilution. They emphasized that the significance of dMo in nitrification reduction outweighed its role in N fixation. Qi et al. conducted a study on the distribution and correlation of Fe, P, and total organic C (TOC) contents in three sediment cores from a coastal aquaculture area of Jiangsu Province, China, providing a valuable theoretical basis for further understanding and regulating the input of Fe minerals and P components in coastal sediments; thus controlling the burial rate and storage of TOC. The investigation conducted by Chen et al. focused on examining the dissolved inorganic nutrients and hydrochemical parameters of the Yongle Blue Hole, the deepest blue hole. The findings revealed notable seasonal variations in nutrients, N/P, and Si/P, as well as their correlation with oxidative conditions, indicating the influence of redox conditions on nutrient cycling in hypoxic seawater.

Seagrass meadows (SMs) are recognized as highly valuable ecosystems due to their provision of various ecosystem services and functions. Nóbrega et al. examined the intensity of Fe and sulfate reduction within SMs across diverse geographical environments, and investigated the resulting effects on archaea and bacterial communities. The findings revealed that the specific plant species present in these meadows influence soil geochemistry and microbial communities, facilitate the retention of fine particles, promote oxidation in the rhizosphere, and induce hypoxic conditions to regulate the formation of Fe and S.

The systematic study of the ecological functions of marine M/TEs remains incomplete, and there is still limited understanding of the coupling relationships between M/TEs and ecological communities. It is imperative to investigate the macro-level marine environmental behavior characteristics of M/TEs, as well

as the micro-level exploration of nutrient supply and ecological toxicology, encompassing processes within biological and non-biological systems. The accurate and highly sensitive quantitative determination of M/TEs in seawater serves as the fundamental basis for studying marine M/TE environmental biogeochemical processes. M/TEs are poised to assume a growing significance within the domains of marine ecological environment evolution, ecological function disclosure, and ecological risk assessment. Furthermore, the information unveiled by these M/TEs is expected to exhibit enhanced precision and accuracy. Consequently, the investigation of marine M/TEs' biogeochemistry in the marine environment is anticipated to emerge as a pivotal focal point within geoenvironmental studies.

This Research Topic contributed with valuable insights into the biogeochemical cycle of M/TEs and their influence on the marine ecological environment. Moreover, it endeavors to inspire the scientific community to undertake comprehensive and in-depth research, building upon the findings presented in this Research Topic. By collaborating, we aspire to safeguard the well-being and resilience of our oceans, marine ecosystems.

Author contributions

JS: Conceptualization, Data curation, Funding acquisition, Investigation, Project administration, Resources, Supervision, Writing – original draft, Writing – review & editing. WZ: Conceptualization, Data curation, Formal Analysis, Funding acquisition, Investigation, Methodology, Project administration, Resources, Supervision, Validation, Writing – original draft, Writing – review & editing. HQ: Conceptualization, Data curation, Formal Analysis, Investigation, Methodology, Resources, Supervision, Validation, Writing – review & editing.

Funding

The author(s) declare financial support was received for the research, authorship, and/or publication of this article. Laoshan Laboratory Science and Technology Innovation Project (No. LSKJ202205003).

Acknowledgments

This Research Topic was possible and crucial to its success because of the knowledge, time, and effort of the authors and reviewers. Additionally, the editors would like to thank Frontiers in Marine Science's editorial team for providing an opportunity for this Research Topic to be organized and for providing strong support in its preparation and publication.

Conflict of interest

The authors declare that the research was conducted in the absence of any commercial or financial relationships that could be construed as a potential conflict of interest.

Publisher's note

frontiers | Frontiers in Marine Science

TYPE Original Research
PUBLISHED 24 November 2022
DOI 10.3389/fmars.2022.1074829

OPEN ACCESS

EDITED BY
Wen Zhuang,
Shandong University, China

REVIEWED BY
Kai Liu,
Dongying Research Institute for Oceanography Development, China
Fan Zhang,
Yunnan University of Traditional Chinese Medicine, China
Yuxuan Zhang,
Chinese Research Academy of Environmental Sciences, China

*CORRESPONDENCE
Yuxi Lu
yxlu@yic.ac.cn
Ning Wang
nwang@yic.ac.cn

SPECIALTY SECTION
This article was submitted to Marine Biogeochemistry, a section of the journal Frontiers in Marine Science

RECEIVED 20 October 2022
ACCEPTED 10 November 2022
PUBLISHED 24 November 2022

CITATION
Luan F, Yang T, Lu Y and Wang N (2022) Molecular size-fraction and seasonal characteristics of dissolved trace metals in river and estuarine waters of the Yellow River, China. *Front. Mar. Sci.* 9:1074829. doi: 10.3389/fmars.2022.1074829

Molecular size-fraction and seasonal characteristics of dissolved trace metals in river and estuarine waters of the Yellow River, China

Feng Luan[1], Tingting Yang[1], Yuxi Lu[2,3]* and Ning Wang[2,3]*

[1]College of Chemistry and Chemical Engineering, Yantai University, Yantai, China, [2]CAS Key Laboratory of Coastal Environmental Processes and Ecological Remediation, Research Center for Coastal Environment Engineering Technology of Shandong Province, Yantai Institute of Coastal Zone Research, Chinese Academy of Sciences, Yantai, China, [3]Shandong Key Laboratory of Coastal Environmental Processes, Yantai, China

The colloidal phase is an important metal storage form in the aquatic system. However, its biogeochemical behavior in the estuarine environment has been seldom studied. In this study, spatial variations, sources and correlations with seawater environmental factors of the dissolved Fe, Mn, Cu, Zn, Cd and Pb in the surface water of the Yellow River Estuary in China were investigated. The clean sampling system, centrifugal ultrafiltration technique, and ICP-MS were combined and used for the determination of the colloidal distribution of six metals in this region. Two stations of Zn in autumn had contamination factor values >1, which indicates lower contaminant levels of Cu, Zn, Cd and Pb. Dissolved target metal was divided into five fractions, i.e. <1 kDa, 1-3 kDa, 3-10 kDa, 10-100 kDa and 100 kDa-0.45 μm, while the average concentrations of each fraction were 60.17, 46.54, 47.73, 251.03, 1.44 and 1.08 nmol L^{-1} in spring and 62.30, 48.18, 15.35, 203.05, 1.20 and 1.70 nmol L^{-1} in autumn, respectively. The results showed that colloidal Mn, Cu, Zn, Cd and Pb might be dominated by high-molecular-weight fraction (100 kDa-0.45 μm). Additionally, the contribution of low-molecular-weight colloidal Fe (1-10 kDa) in this aquatic system was obvious. The addition in the colloidal and total dissolved fraction might be mainly related to particle-desorbed ligand, which was usually occurred in the middle salinity area. Dissolved organic carbon (DOC) and colloidal organic carbon (COC) concentration could not correlate with the behavior of Mn, Zn and Cd, which proved that the influence of inorganic ligands was higher than that of organic ligands or biological contributions, but the influence of salinity, dissolved oxygen (DO), pH and temperature should not be ignored. Overall, the results suggested that the occurrence of dynamic behaviors of colloidal metal in the YRE was highly associated with the salinity transition and formation of the organic matter-particle mixture system under complex hydrodynamic processes.

KEYWORDS

Yellow River Estuary, colloidal trace metal, centrifugal ultrafiltration, molecular size-fraction, geochemical feature

1 Introduction

The studies of the basic morphology of metals in the aquatic system are usually carried out by filtration through a 0.2 μm, 0.45 μm or 1 μm pore size filter, and the trace elements are simply divided into two parts, i.e. dissolved and particulate phases (Zhou et al., 2016; Lu et al., 2022). However, the part considered to be dissolved contains many colloidal particles that are easily overlooked, and it plays a significant biogeochemical role in the aquatic environment (Guo and Santschi, 2007; Xu et al., 2018a; Xu et al., 2018b; Xu et al., 2018c). In recent years, with the application of cross-flow ultrafiltration, centrifugal ultrafiltration (CFU) and other technologies, the research on the determination of colloidal trace elements in aquatic systems has been developed rapidly (Liu et al., 2013; Lu et al., 2019). Similarly, these studies found that most of the dissolved metals exist in the form of small-sized inorganic particles or macromolecular organic matter (ie, colloidal phase) in the aquatic environment, which largely participates in the operation of the water environment ecosystem (Cornu et al., 2018). For example, as the common and essential metal micronutrients, Fe, Cu and Zn play a significant role in plant metabolism by participating in electron transport, nitrate reduction, photosynthesis, respiration, chlorophyll synthesis, and so on (Han et al., 2021). Among them, Cu plays an important role in marine ecosystems (Peers and Price, 2006). For example, most phytoplankton requires Cu to perform some key redox effects, which has attracted more and more attention to its research (Illuminati et al., 2017; González-Álvarez et al., 2020). As an important biologically active metal, Cu has been proved in many studies to be easily adsorbed on inorganic/organic ligands in the water environment, thereby increasing its bioavailability, and maybe the important environmental factor for causing red tides, green tides and algal blooms in the nearshore area (Lu et al., 2021). Typical toxic heavy metals such as Cd and Pb may accumulate along the food chain, thereby threatening aquatic organisms and human health (Lu et al., 2019; Liang et al., 2022). Therefore, the study of the morphology of trace metals, especially the colloidal phase, is of great significance for understanding the morphological distribution and geochemical behavior of metals in the aquatic systems (Wen et al., 2011; Statham et al., 2012; Lu et al., 2020).

The Yellow River is the second-longest river in China with a basin area of ~ 7915 km^2 (Wang et al., 2016). It runs through northern China and brings a large number of pollutants from urban, agriculture and industrial pollutants into the Bohai Sea (Tang et al., 2010). The Yellow River Estuary (YRE) is an important fishing area in China and provides spawning sites for many aquatic organisms in the Bohai Sea and the Yellow Sea (Liu et al., 2018). In addition, it is adjacent to Shengli Oilfield (the second-largest oilfield of China) and the Yellow River Delta National Nature Reserve (Wang et al., 2011). The Yellow River flows through the world's largest loess deposit area, the Loess Plateau in north-central China, and carries a large number of suspended particulate matter (SPM) and freshwater, making it register as the world's most turbid river and the dominant land-based factor in the Bohai Sea (Zhang and Huang, 1993; Milliman and Ren, 1995; Bi et al., 2014). Therefore, great concern has been attracted in this area due to its unique environmental significance, ecological sensitivity and environmental conditions (Liu et al., 2016a and Liu et al., 2016b; Wang et al., 2018; Lu et al., 2021).

Previous studies of the YRE focused on the concentration, distribution, and environmental impact of trace elements in water and particulate matter (Qiao et al., 2007; Tang et al., 2010; Lin et al., 2016; Wang et al., 2018). However, minimal researches are available about the fate, migration and environmental behavior of the trace elements in this region, especially colloidal phases. Therefore, the dissolved metals in the YRE surface water were investigated through two sampling surveys in March and November 2021. The major objectives of our present research work were to: (1) introduce a self-made clean sampling technique and a fully enclosed pre-filtration system; (2) study the abundance and compositional variations of Fe, Mn, Cu, Zn, Cd and Pb in five molecular weight size ranges of dissolved phase in the river-sea mixing area; (3) reveal the specific molecular weight (MW) colloids that can regulate the behavior of colloidal Fe, Mn, Cu, Zn, Cd and Pb environmental conditions in this region; (4) explore the relationship between the dynamic behavior of target element and environmental factors in the five fraction of the dissolved phase. The basis for selecting these five dissolved fractions is that they cover the truly dissolved phase (<1 kDa), the low-molecular-weight (LMW) colloidal phase and the high-molecular-weight (HMW) colloidal phase, so as to facilitate the subsequent detailed evaluation of metal migration between each fraction. The results are the original report of colloidal Fe, Mn, Cu, Zn, Cd and Pb of the YRE and can provide some new insights into the geochemical feature and heterogeneity of micronutrient elements in the river-sea continuum and the aquatic system.

2 Material and methods

2.1 Sampling and pre-filtration

The internal-fluorinated high-density polyethylene (HDPE) bottles for sampling were pre-cleaned using a method reported by Lu et al. (2020 and Lu et al., 2021). Briefly, after being rinsed with Decon 90™ detergent (10%, v/v) 3 times, each bottle was stored in 1.5 M nitric acid (HNO_3) and 1.2 M hydrochloric acid (HCl) for 48 h, respectively, and finally rinsed with ultra-pure water (R = 18.2 MΩ-cm) which was produced by a Purelab Classic water purification system (ELGA Labwater, UK). The

HNO_3 and HCl used in the experiment were prepared by diluting high concentration, purchased from the Sinopharm Chemical Reagent Co., Ltd., China and processed by the sub-boiling distillation equipment before use. All labware in contact with samples or sub-samples must also be pre-cleaned using the above method and dried in a clean bench, and then double-packed until sampling.

The samples and field data used in this study were obtained through two cruises which were conducted in March (spring flood at peach-blossom time) and November (autumn, dry season of the Yellow River) 2021. 1 L of the surface water samples (1 m deep) were collected manually on a boat from 9 sites (Figure 1). The standard of water depth in this study referred to the study of Yang et al. (2020). The main body of the home-made pole-sampling equipment was equipped with a Teflon rod main body and the internal-fluorinated HDPE bottle was bound with disposable Nylon cable ties. The salinity, dissolved oxygen (DO), temperature and pH of the samples were measured by using the portable multi-parameter water quality analyzer (YSI ProPlus, USA). After the water sample was collected, put the sampling bottle in a polyethylene bag immediately and store it in a cooler box at about 4°C. After returning to the laboratory, the samples were pre-filtered immediately using a homemade fully enclosed filtration system. The system consists of a peristaltic pump, a diaphragm vacuum pump, pipes and a filter cover. The main working principle was as follows: first, unfiltered water samples were pumped along the C-flex® tubing into the upper part of the polysulfone vacuum filtration device by using a Masterflex® L/S peristaltic pump; secondly, the vacuum pump was turned on to perform fully enclosed real-time filtration of the sample; finally, the filtered water samples could be collected in another pre-cleaned HDPE bottles for further processing. The storage method of filtered samples was the same as that of unfiltered samples.

2.2 Centrifugal ultrafiltration

Four kinds of Macrosep® centrifugal ultrafiltration units (Pall Laboratory) with respective molecular weight cutoffs (MWCOs) of 1, 3, 10 and 100 kDa (Model: MAP010C38) were used with a Velocity 14R centrifuge (Dynamica Corporation, Australia). Before ultrafiltration, each unit was sequentially washed with 10 mL 0.05 M NaOH, 10 mL 0.02 M HCl and 10 mL ultra-pure water for 5-10 times to remove possible background (Lu et al., 2020). Each unit was then loaded with 15 mL of <0.45 μm pre-filtered samples, and centrifuged (4°C, 4200 × g, 50-70 min) to ≤0.5 mL to separate the ultrafiltrate (<1 kDa, <3 kDa, <10 kDa and <100 kDa) for the characterization of colloids with different molecular weight sizes (Lu et al., 2020). After CFU, 0.2 mL ultrafiltrate was pipetted and diluted to 10 mL with 0.5 M HNO_3. <0.45 μm total dissolved (TD) phase was treated in the same process. As for the concentrate, 3 mL 0.5 M HNO_3 was added in parallel for extracting metals. Then, 3 parallel extracts were well mixed and volume adjusted to 5 mL with 0.5 M HNO_3. All sub-samples were stable at room temperature (~25°C) for ≥48 h and then measured using an inductively coupled plasma mass spectrometer (ICP-MS). According to the concentration difference between the initial filtered sub-samples and the ultrafiltrate, the concentrations of colloidal metals in different size ranges were calculated (Lu et al., 2020). Finally, size fractions of colloidal metal can be defined as 1-3 kDa, 3-10 kDa, 10-100 kDa and 100 kDa-0.45 μm, and <1 kDa fraction was defined as the truly dissolved phase.

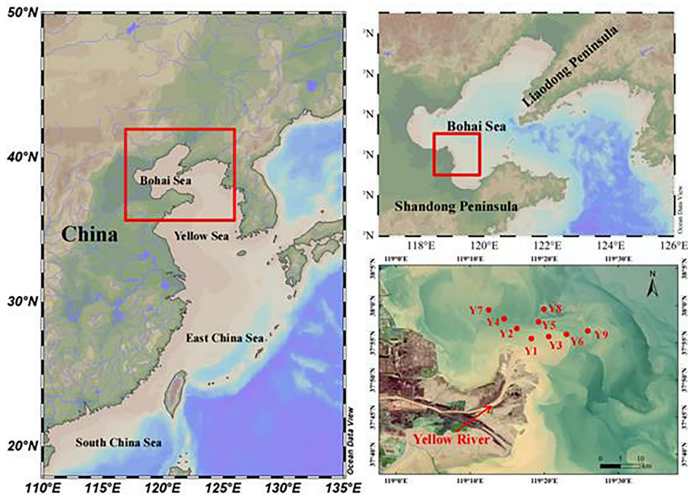

FIGURE 1
Location of sampling sites in the study area.

2.3 Analytical methods

2.3.1 Metal determination

For the water samples, metals in prefiltered waters, ultrafiltrate and concentrate were acid-extracted (using 0.5 M HNO_3) and directly determined by ELAN DRC II ICP-MS (USA), as described by Lu et al. (2020). The instrument was equipped with nickel sampler and skimmer cones, and internal standard (0.19 μM rhodium) was added to each sample. The plasma used in the ICP-MS analysis was 99.999% argon, and the optimized plasma gas flow rate (GFR), nebulizer GFR and auxiliary GFR were 15.0 L, 0.88 and 1.2 L min^{-1}, respectively. All calibration curves were obtained before analysis and each sample was measured in parallel 3 times. The baseline drift caused by instrument operation was eliminated by correcting the curves every 30 samples. The method blanks, parallel samples and spiked samples were sequentially analyzed, and the relative standard deviation (RSD) of parallel samples (n = 3) should < 10% (Wang et al., 2018).

2.3.2 Dissolved organic carbon determination

After pre-processing, saturated mercury chloride ($HgCl_2$) was added to the subsamples and then stored in pre-combusted borosilicate glass bottles (500°C, 5 h) for DOC analysis. Then, they were acidified with concentrated phosphoric acid (H_3PO_4) to pH ≤ 2 to remove all the dissolved inorganic carbon. Finally, all processed samples were analyzed using a total organic carbon analyzer (vario TOC select, Elementar, Germany) (Lu et al., 2021). The calibration curve was obtained before analysis and 3 parallel subsamples were measured for each CFU unit. As quality control, the entire detection system was checked after 7 consecutive sample injections using a reference material according to GSB07-1967-2005 developed by Institute for Environmental Reference Materials of Ministry of Environmental Protection (China), and the coefficient of variation on 5 repeated injections should be guaranteed to < 2% (Yang and Gao, 2019). The colloidal organic carbon (COC) data was obtained from the above-mentioned detection method after the water sample was processed by CFU.

2.4 Contamination factor of heavy metals

The CF was applied for the evaluation of water quality in our recent study (Lu et al., 2021). The corresponding value reflects the pollution level of a single heavy metal and overall trace metals in the matrix.

$$CF = \frac{C_{HM}}{C_{back\ ground}}$$

where $C_{background}$ is the quality standard background value of the corresponding metal in seawater, C_{HM} is total dissolved (TD) concentration of the corresponding metal. Due to the lack of background data on all the Heavy metals studied in YRE, the background concentrations were used the grade-one seawater quality standard issued by Administration of Quality Supervision, Inspection and Quarantine of China instead (i.e., 78.68 nmol L^{-1} Cu, 305.90 nmol L^{-1} Zn, 8.90 nmol L^{-1} Cd, 4.83 nmol L^{-1} Pb; GB 3097-1997) (AQSIQ, 1997). The CFs of seawater standards and the samples were summarized in Table 1.

2.5 Data and figure analysis

In this paper, the sampling site bitmap was drawn using CorelDRAW 12, Surfer, and Ocean Data View software, and the data map was drawn using Origin 2021 software. The statistical analysis of the data was carried out using Microsoft Excel 2010 and SPSS 19.0 software to determine the relationship between the relevant parameters. The statistical methods used in this paper mainly include linear regression and Pearson correlation analysis. Among them, Pearson correlation analysis was mainly used to determine the relationship between various

TABLE 1 The summary of the CF values of the sampling sites and seawater standard. Standard values were interpreted as recommended by Hakanson (1980) and Lü et al. (2015).

	Value				Contaminant level
	Cu	Zn	Cd	Pb	
Grade-one seawater quality standard (AQSIQ, 1997) (nmol L^{-1})	78.68	305.90	8.90	4.83	–
Grade-two seawater quality standard (AQSIQ, 1997) (nmol L^{-1})	157.37	764.76	44.48	24.13	–
Concentrations of YRE/(Average) (nmol L^{-1})	1.75-51.32 (31.54)	71.89-501.60(227.04)	0.89-1.87 (1.32)	0.85-2.29 (1.39)	–
CFs of YRE/(Average)	0.02-0.65(0.41)	0.24-1.64 (0.74)	0.10-0.21 (0.15)	0.18-0.47 (0.29)	–
CF standard	CF < 1	–	–	–	Low
	1 ≤ CF < 3	–	–	–	Moderate
	3 ≤ CF < 6	–	–	–	Considerable
	CF ≥ 6	–	–	–	Very high

environmental parameters involved. In the process of statistical analysis, when $p > 0.05$, the two sets of data were significantly correlated, on the contrary, if $p < 0.05$, the correlation was not significant.

3 Results

3.1 General environmental features

For the spatiotemporal characteristics of salinity, temperature, DO, pH and DOC during the investigations in the study area, their partial information has been previously reported (Lu et al., 2021). Overall, the water pH was relatively stable with the values from 7.52 to 8.41, while the salinity ranged widely from 0.52 to 33.04 (Table S1). It is evident that salinity reduction caused by strong mixing behavior occurred at most stations in autumn, while the mixing decreased from sea to land in spring (Table S1).

The DO values of surface water in the YRE ranged from 5.63 to 17.94 mg L^{-1}, and the temperature ranged from 3.3 to 15.8°C. In autumn, DO values dropped below 8.17 mg L^{-1} (Table S1), while DO concentration was > 15.26 mg L^{-1} in spring. Notably, the relatively lower DO concentration occurred in the mixing zone in autumn, indicating the important influence of mixing behavior on the DO dynamics.

3.2 Spatiotemporal variations in DOC

As for each dissolved fraction of DOC, the <1 kDa, 1-3 kDa, 3-10 kDa, 10-100 kDa and 100 kDa-0.45 μm fraction were 116.80-269.78, 0.04-162.59, 0.29-23.51, 0-30.87 and 3.96-94.03 μmol L^{-1} in spring, respectively, with averages of 200.16, 61.86, 8.45, 11.37 and 23.93 μmol L^{-1}, respectively (Figure 2A). In autumn, the corresponding values of DOC were 106.89-253.75 μmol L^{-1} in the <1 kDa fraction, 0.11-10.15 μmol L^{-11} in the 1-3 kDa fraction, 0.31-40.12 μmol L^{-1} in the 3-10 kDa fraction, 0.03-31.24 μmol L^{-1} in the 10-100 kDa fraction, and 0.39-6.18 μmol L^{-1} in the 100 kDa-0.45 μm fraction (Figure 2B). As for the percentages (Figure 3), truly dissolved DOC (<1 kDa) in spring was 35%-92% of their respective total dissolved pools (<0.45 μm), the 1-3 kDa fraction was 0.01%-49%, the 3-10 kDa fractions was 0.1%-7%, the 10-100 kDa fractions was 0%-9%, and the 100 kDa-0.45 μm fractions was 2%-23%; in autumn, the corresponding values of DOC in the five dissolved fractions were

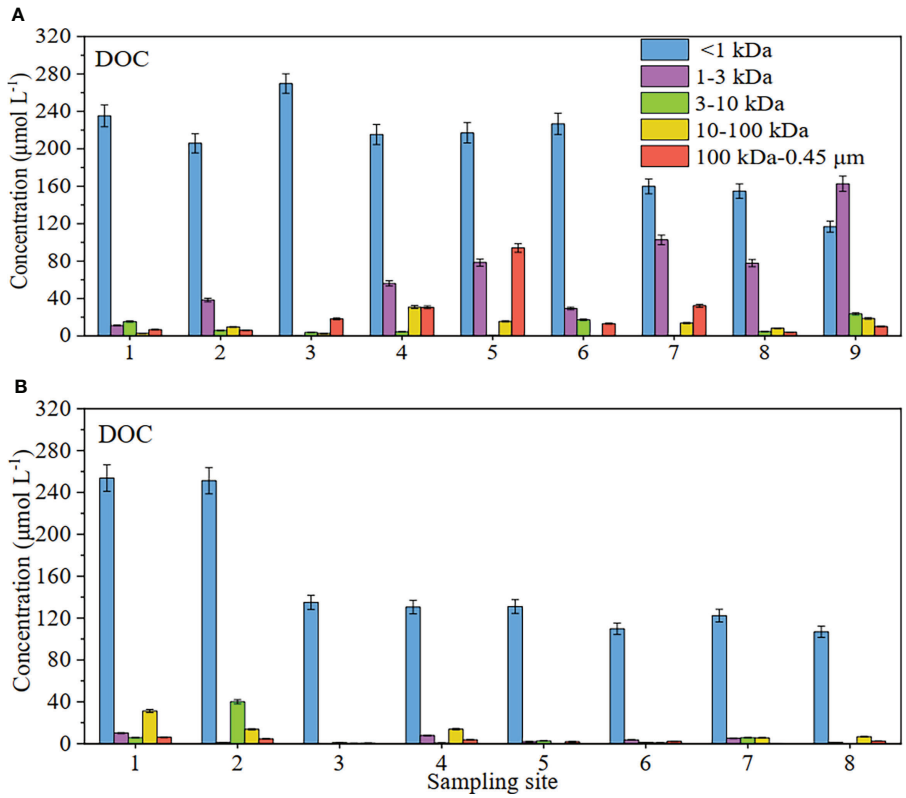

FIGURE 2
Concentration distribution of DOC at different sites in surface waters of the Yellow River Estuary in spring **(A)** and autumn **(B)**.

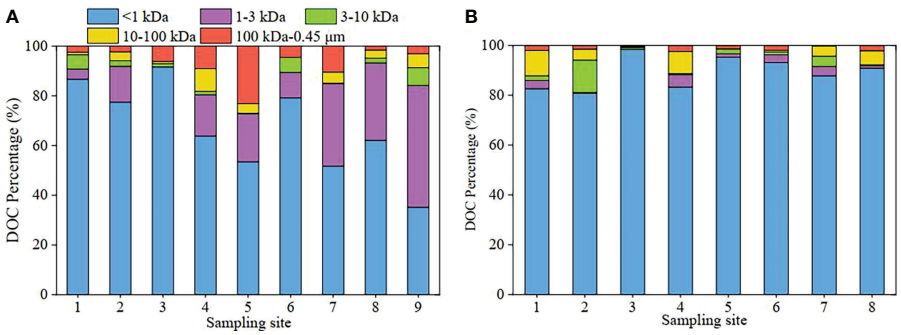

FIGURE 3
Percentage distribution of DOC at different sites in surface waters of the Yellow River Estuary in spring **(A)** and autumn **(B)**.

81%-98%, 0.1%-5%, 0.3%-13%, 0.03%-10% and 0.3%-2%, respectively. Obviously, the high values of DOC fractions were mainly distributed in the <1 kDa of both investigations in the surface water. As for 1 kDa-0.45 μm colloidal DOC, the high DOC values were mainly observed in the 1-3 kDa LMW fraction except for the autumn (Figures 2 and 3). In the autumntime, the colloidal DOC values were significantly lower than those in the <1 kDa fraction of the study area in the surface water, especially HMW (100 kDa-0.45 μm).

3.3 Dissolved metal concentrations

The distribution and CF of the heavy metals (Cu, Zn, Cd and Pb) in the YRE is presented in Figure 4. The concentrations of <0.45 μm TD fraction Fe, Mn, Cu, Zn, Cd and Pb during the two different seasons are presented in Table 2. In spring, six dissolved metal concentrations occurred in the following order: Zn > Fe > Cu > Mn > Cd > Pb. The TD Fe, Mn, Cu, Zn, Cd and Pb concentrations have ranges of 55.85-64.73 (60.17), 33.35-92.40 (46.54), 43.02-51.32 (47.73), 198.84-296.08 (251.03), 1.24-1.87 (1.44) and 0.85-1.43 (1.08) nmol L^{-1}, respectively (Table 2). The highest TD Fe concentration was found at site Y1, followed by that found in sites Y5 and Y4. The spatial pattern of nearshore concentration was higher than that of off shore concentration, reflecting the influence of river input in spring. The highest TD Mn concentration was found at Y1, followed by Y3 and Y6. Higher TD Zn concentrations were found in the eastern parts of the YRE. Similar distribution patterns were found in TD Cd and TD Pb. High concentrations of TD Cu and TD Zn were found in the middle parts of the study area, indicating the addition phenomenon in the middle salinity zone (or mixing zone) (Waeles et al., 2008). As for the autumn, the corresponding metal concentrations occurred in the following order: Zn > Fe > Mn > Cu > Pb > Cd. The concentrations of TD Fe, Mn, Cu, Zn, Cd and Pb ranged from 18.83 to 104.61, 23.18 to 83.30, 1.75 to 29.22, 71.89 to 501.6, 0.89 to 1.59 and 1.15 to 2.29 nmol L^{-1}, respectively, with averages of 62.30, 48.18, 15.35, 203.05, 1.20 and 1.70 nmol L^{-1}, respectively (Table 2). Significantly different from the spring, the highest concentration of TD Fe was found at Y3, followed by that found in Y5 and Y8. Similar distribution patterns were found in TD Mn, TD Cu and TD Zn, suggesting a clear contribution from the Yellow River input. Different from the above four elements, the higher concentrations of TD Pb appeared at Y1 and Y8 and showed dynamic fluctuations in the mixing area, which was similar to the distribution of TD Cd. In summary, the concentrations of TD Fe and Pb are elevated in autumn and have the lower values in spring, and the concentrations of TD Mn, Cu, Zn and Cd are elevated in spring and have the lower values in autumn.

We compared the corresponding results with other aquatic systems (Table 2) and found that the concentrations of TD Fe in the YRE were lower that of the Venice Lagoon (7.69-1124.92 nmol L^{-1}) in Martin and Dai (1995); TD Mn concentrations were higher than that of Venice Lagoon (11.12-44.26 nmol L^{-1}) (Martin and Dai, 1995), but lower than that of Port Jackson (5.95-1838.44 nmol L^{-1}) (Hatje et al., 2003); TD Cu levels were comparable with the similar area in Tang et al. (2010) (1.57-70.19 nmol L^{-1}) but higher than that in Pearl River Estuary (5.35-51.30 nmol L^{-1}) (Zhang et al., 2012), Venice Lagoon (3.15-8.85 nmol L^{-1}) (Martin and Dai, 1995) and Port Jackson (14.64-40.13 nmol L^{-1}) (Hatje et al., 2003); the concentrations of TD Zn, Cd and Pb were lower than that of the study by Tang et al. (2010) in similar area (183.54-1251.76 nmol L^{-1}, 0.89-28.64 nmol L^{-1} and 1.06-48.90 nmol L^{-1}, respectively); due to the application of the clean sampling method and the filter device, the TD Cd and TD Pb concentrations were relatively lower than the study of Wang et al. (2018) in the similar area (0.89-16.90 nmol L^{-1} Cd and 2.02-64.19 nmol L^{-1} Pb), but higher than Venice Lagoon (0.01-0.13 nmol L^{-1} Cd and 0.05-1.08 nmol L^{-1} Pb) and Port Jackson (0.03-0.50 nmol L^{-1} Pb).

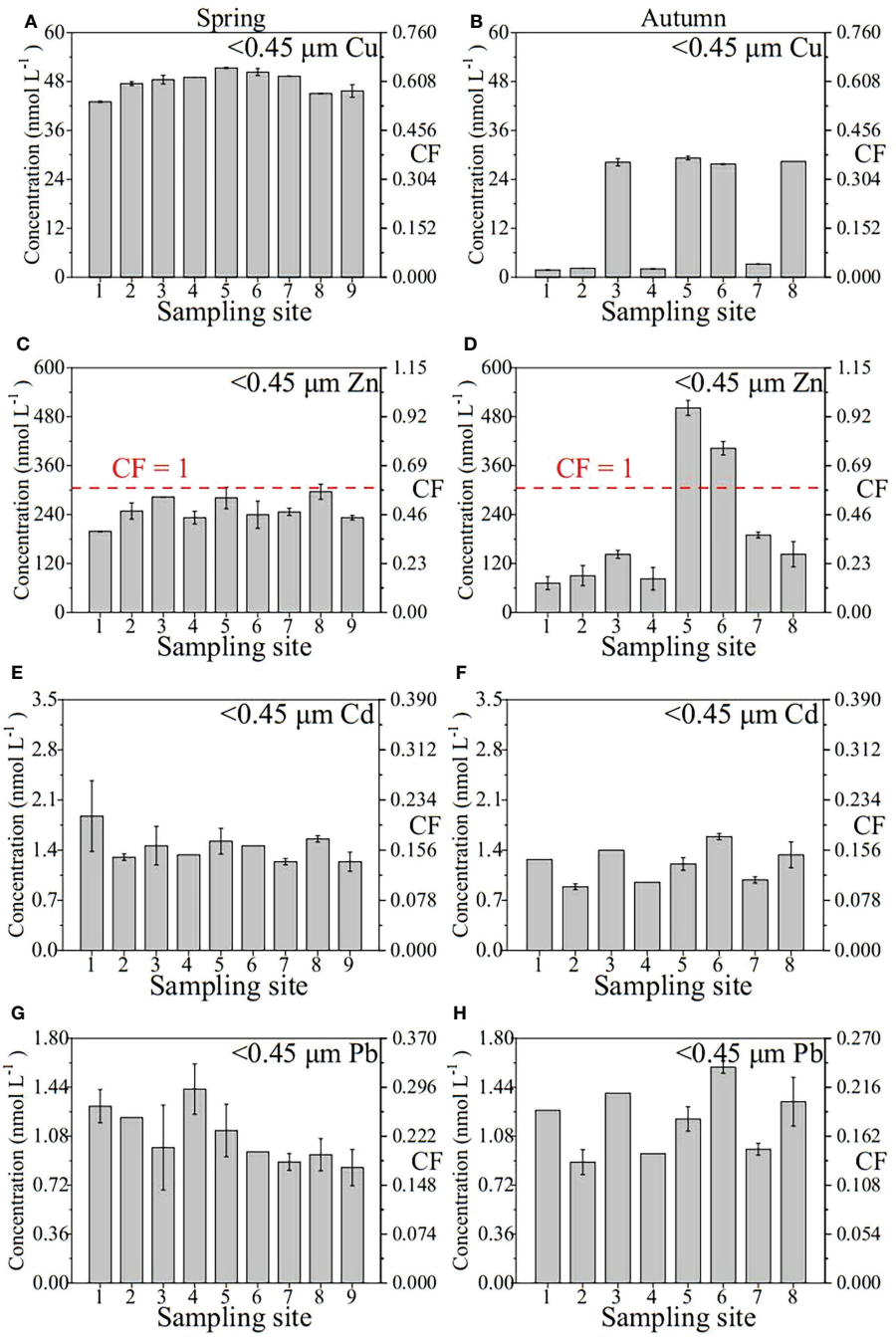

FIGURE 4
Concentration distribution and CF of Cu, Zn, Cd and Pb in the TD phase of the samples of the Yellow River Estuary in spring **(A, C, E** and **G)**; autumn **(B, D, F** and **H)**.

3.4 CF values of Cu, Zn, Cd and Pb

The concentrations of dissolved heavy metals (Cu, Zn, Cd and Pb) in YRE were assessed in accordance to the seawater quality standards of China (Table 1). The contamination levels were assessed according to the CF value standards (Table 1). The concentrations of TD Cu, Cd, and Pb at each site of the two voyages in spring and autumn were lower than the GB 3097-1997 (the grade-one standard), and the CFs ranged from 0.02-0.65 of Cu (average ~0.41), 0.10-0.21 of Cd (~0.15) and 0.18-0.47 of Pb (~0.29), respectively, which indicated low contaminant

TABLE 2 The summary of Fe, Mn, Cu, Zn, Cd and Pb) concentrations in the water of the Yellow River Estuary (YRE) and other estuarine systems in the world (nmol L^{-1}).

Region	Sample		Fe data	Mn data	Cu data	Zn data	Cd data	Pb data	Reference
YRE, China (spring)	Estuarine water	Range/ Mean	55.85-64.73 (60.17)	33.35-92.40 (46.54)	43.02-51.32 (47.73)	198.84-296.08 (251.03)	1.24-1.87 (1.44)	0.85-1.43 (1.08)	This study
YRE, China (autumn)	Estuarine water	Range/ Mean	18.83-104.61 (62.30)	23.18-80.30 (46.18)	1.75-29.22 (15.35)	71.89-501.60 (203.05)	0.89-1.59 (1.20)	1.15-2.29 (1.70)	This study
YRE, China	Estuarine water	Range/ Mean	- [a]	–	1.57-70.19 (41.70)	183.54-1251.76 (576.63)	0.89-28.64 (6.05)	1.06-48.90 (2.46)	Tang et al. (2010)
YRE, China	Estuarine water	Range/ Mean	–	–	0.63-487.84 (182.54)	30.13-645.46 (227.90)	0.89-16.90 (5.87)	2.02-64.19 (27.08)	Wang et al. (2018)
Pearl River Estuary, China	Estuarine water	Range/ Mean	–	–	5.35-51.30 (25.81)	207.10	0.01-2.67 (1.07)	0.92-22.10 (7.77)	Zhang et al. (2012)
Venice Lagoon, Italy	Coastal water	Range	7.69-1124.92	11.12-44.26	3.15-8.85	–	0.01-0.13	0.05-1.08	Martin and Dai (1995)
Port Jackson, Australia	Estuarine water	Range	–	5.95–1838.44	14.64-40.13	50.02-147.75	–	0.03-0.50	Hatje et al. (2003)

[a]"-" represents no relevant reference data.

level. For TD Zn, the CF value of site 5 and 6 in autumn exceeded moderate contaminant levels, while the CFs of the remaining sites were all < 1. In spring, the CF values of all sites showed low pollution levels. In fact, using the grade-one seawater quality standard as contamination background may rank the results differently, so realistic contamination levels may be higher than in our study.

3.5 Dissolved metals in various molecular weight fractions

The concentration and percentage results of the dissolved Fe, Mn, Cu, Zn, Cd and Pb for each fraction are shown in Figures 5 and Figure 6, respectively. A comparison of concentrations and percentages of each dissolved metal in Yellow River samples and other aquatic systems is shown in Table 3.

3.5.1 Concentration distribution

The results showed that the <1 kDa fraction of Fe, Mn, Cu, Zn, Cd and Pb in spring (Figures 5A, C, E, G, I and K) were 38.41-59.14, 23.34-76.13, 23.35-31.81, 140.15-200.73, 0.86-1.24 and 0.05-0.45 nmol L^{-1}, respectively, the 1-3 kDa fraction were 0.08-2.51, 0-2.76, 0.01-4.24, 1.97-55.02, 0-0.19 and 0-0.14 nmol L^{-1}, respectively, the 3-10 kDa fraction were 0.05-3.23, 0-1.77, 0.08-1.16, 0.76-63.48, 0-0.16 and 0-0.19 nmol L^{-1}, respectively, the 10-100 kDa fraction were 0.04-4.60, 0.05-3.27, 0.01-2.80, 0.40-83.12, 0-0.16 and 0-0.51 nmol L^{-1}, respectively, and the 100 kDa-0.45 µm fraction were 0.55-15.63, 7.49-14.99, 12.06-22.57, 4.23-84.61, 0.03-0.60 and 0.06-1.24 nmol L^{-1}, respectively. In autumn (Figures 5B, D, F, H, J and L5), the concentrations of Fe, Mn, Cu, Zn, Cd and Pb were 18.56-94.98 13.44-63.71, 0.77-15.32, 68.75-384.71, 0.64-1.24 and 0.66-1.51 nmol L^{-1} in the <1 kDa fraction, 0.04-5.72, 0.54-7.08, 0.03-2.64, 0.28-29.83, 0-0.22 and 0.03-0.32 nmol L^{-1} in the 1-3 kDa fraction, 0.03-4.45, 0-7.87, 0-2.09, 0.28-26.89, 0-0.22 and 0-0.50 nmol L^{-1} in the 3-10 kDa fraction, 0.04-0.80, 0-2.78, 0.03-1.52, 0.60-19.80, 0-0.13 and 0-0.23 nmol L^{-1} in the 10-100 kDa fraction, and 0.04-3.52, 0.43-53.27,0.87-14.46, 0.40-189.14, 0-0.38 and 0.03-1.01 nmol L^{-1} in the 100 kDa-0.45 µm fraction.

3.5.2 Percentage distribution

As for the percentages (Figure 6), truly dissolved Fe, Mn, Cu, Zn, Cd and Pb in spring (<1 kDa) in spring were 68%-97%, 59%-82%, 46%-65%, 47%-86%, 54%-95% and 5%-37% of their respective <0.45 µm total dissolved pools, respectively, the 1-3 kDa fraction were 0.1%-4%, 0%-7%, 0.01%-10%, 1%-24%, 0%-13% and 0%-14%, respectively, the 3-10 kDa fractions were 0.1%-5%, 0%-2%, 0.2%-2%, 0.3%-22%, 0%-8% and 0%-15%, respectively, the 10-100 kDa fractions were 0.1%-7%, 0.2%-9%, 0.03%-5%, 0.2%-30%, 0%-13% and 0%-60%, respectively, and the 100 kDa-0.45 µm fractions were 1%-27%, 14%-38%, 28%-45%, 2%-29%, 2%-37% and 8%-87%, respectively. In autumn, the corresponding values of Fe in the five fractions were 70%-99%, 0.2%-12%, 0.1%-10%, 0.2%-2% and 0.2%-9%, respectively, the percentages of Mn in the Five fractions were 17%-86%, 1%-31%, 0%-12%, 0%-4% and 1%-66%, respectively, the percentages of Cu were 31%-54%, 0.2%-9%, 0%-7%, 0.2%-5% and 46%-51%, respectively, the percentages of Zn were 42%-97%, 0.1%-6%, 0.4%-9%, 1%-16% and 1%-56%, respectively, the percentages of Cd were 65%-89%, 0%-23%, 0%-18%, 0%-13% and 0%-30%, respectively, and the percentages of Pb were 44%-84%, 2%-18%, 0%-32%, 0%-10% and 2%-46%, respectively.

Obviously, for the four colloidal fractions (1-3 kDa, 3-10 kDa, 10-100 kDa and 100 kDa-0.45 µm fraction), six target metals were more likely to bind to the colloid with a molecular

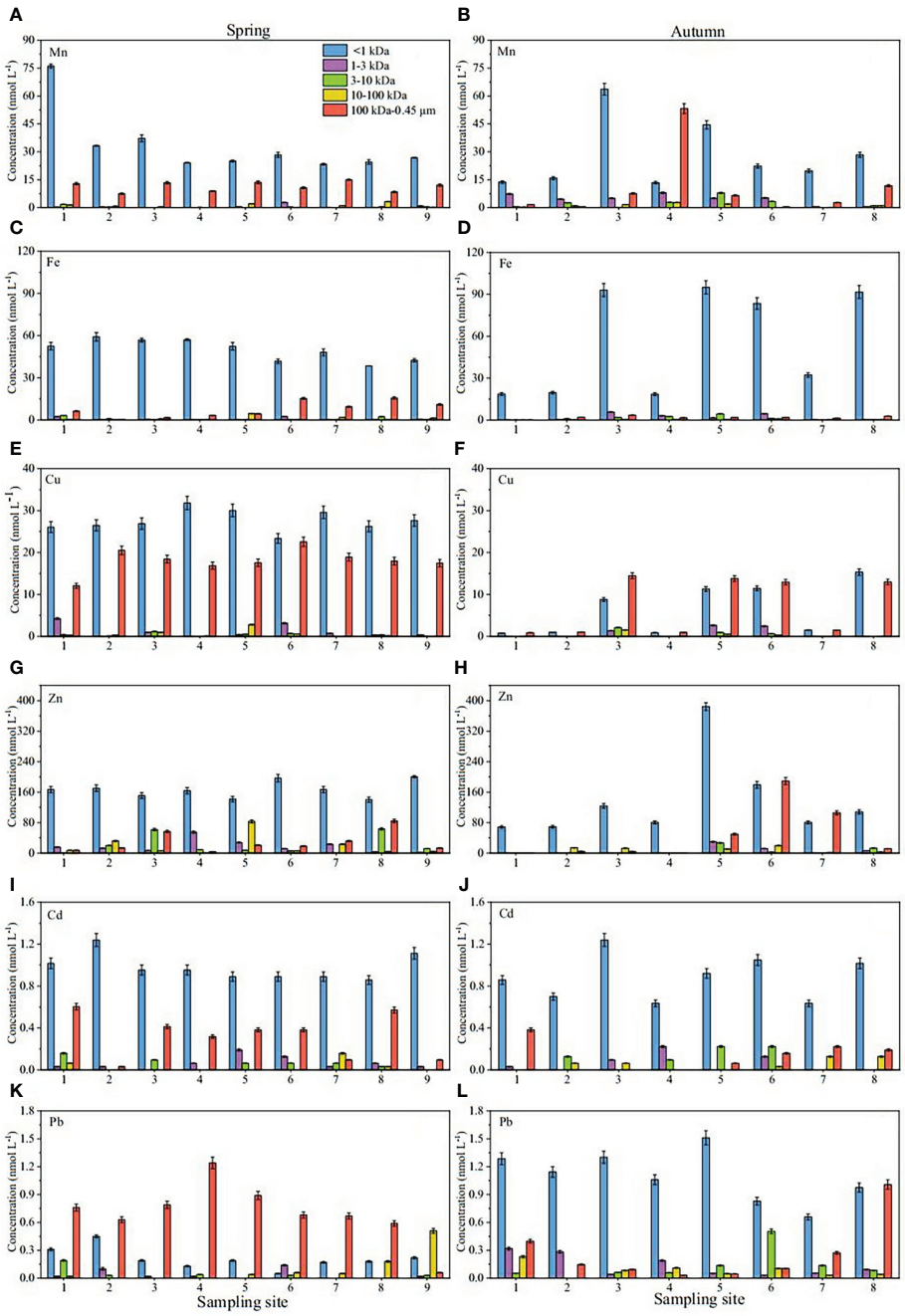

FIGURE 5
Concentration distribution of Mn, Fe, Cu, Zn, Cd and Pb at different sites in surface waters of the Yellow River Estuary in spring **(A, C, E, G, I** and **K)**; autumn **(B, D, F, H, J** and **L)**.

weight of 100 kDa-0.45 μm in spring, indicating that the colloidal matter of this size range may play a significant role in its biogeochemical cycle in this season, which is similar to the previous report data by Wen et al. (1999). In autumn, the difference was that Fe was more inclined to combine with small molecular colloids (1-3 and 3-10 kDa), while other metals were still dominated by HMW (100 kDa-0.45 μm) colloids. In general, the proportion of colloidal metals in their respective total dissolved pools was significantly higher in spring than in autumn.

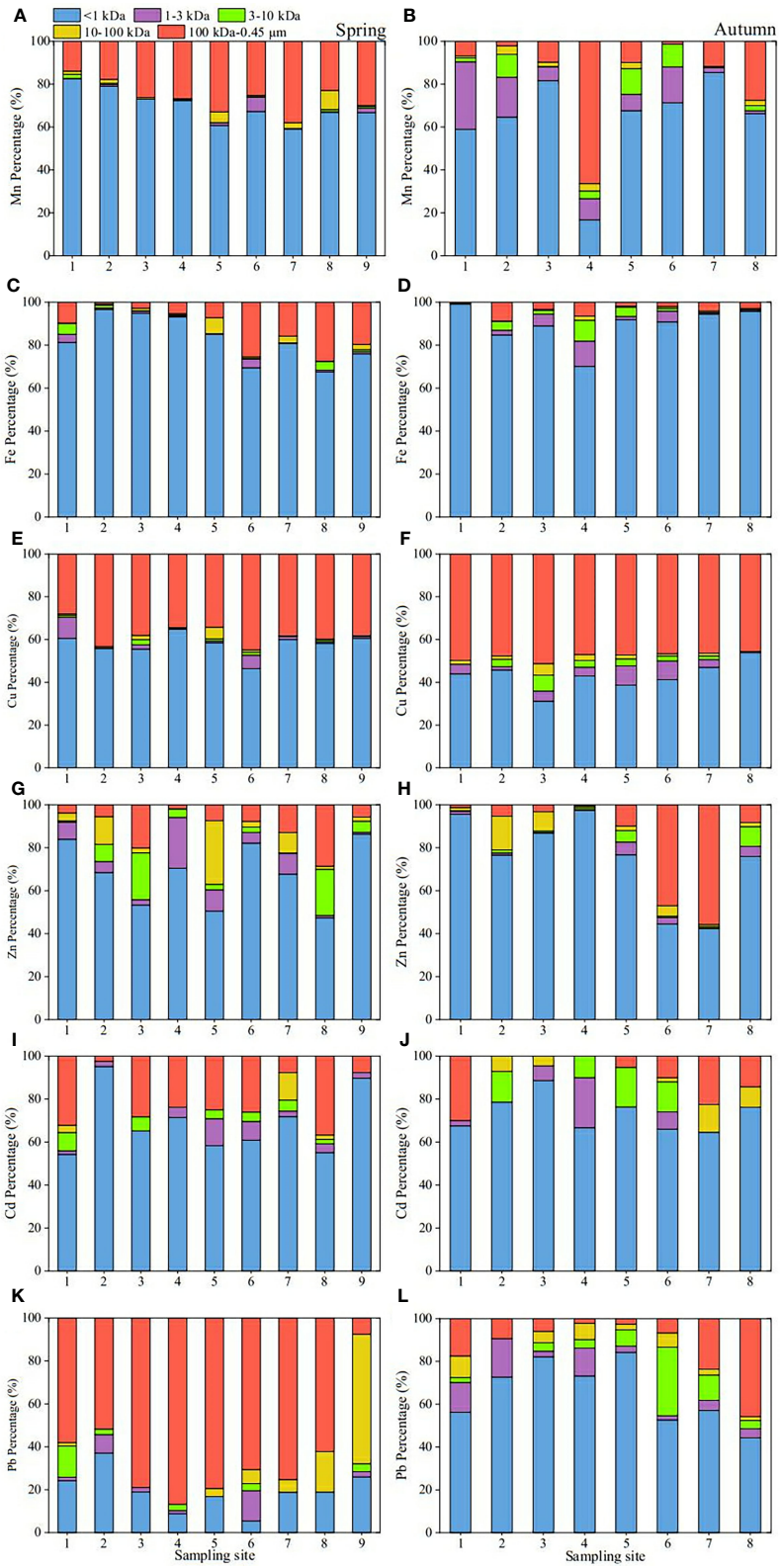

FIGURE 6
Percentage distribution of Mn, Fe, Cu, Zn, Cd and Pb at different sites in surface waters of the Yellow River Estuary in spring **(A, C, E, G, I** and **K)**; autumn **(B, D, F, H, J** and **L)**.

TABLE 3 A comparison of the colloidal metal data in this study and the other literature. C_C and $C_T$represent the concentrations of the colloidal phase and TD phase, respectively.

Region	C_C (nmol L^{-1})						C_C/C_T (%)						Reference
	Fe	Mn	Cu	Zn	Cd	Pb	Fe	Mn	Cu	Zn	Cd	Pb	
YRE, China	0.16-18.47	3.37-66.86	0.98-26.97	2.17-223.43	0.06-0.86	0.28-1.30	1-32	15-83	35-69	3-58	5-46	16-95	This study
Venice Lagoon, Italy	5.21-1121.67	4.50-26.42	1.18-8.34	- [a]	0.001-0.04	0.002-0.98	68-100	24-77	21-59	–	1-63	3-95	Martin and Dai (1995)
Lake Taihu, China	62.72-444.09	5.64-29.49	7.24-13.53	31.51-126.03	0.06-0.16	12.64-17.86	32-81	16-75	13-32	7-54	38-86	11-27	Lu et al. 2020, Lu et al. 2021
Penzé estuary, France	–	–	2.14-2.86	–	0.07-0.30	0.03-0.27	–	–	93-95	–	82	91	Waeles et al. (2008)
North Yellow Sea, China	–	–	5.35 and 5.19	–	0.04 and 0.10	2.75 and 8.20	–	–	31 and 51	–	47 and 50	31 and 50	Lu et al. (2019)
Urban riverine and estuarine waters, China	–	–	0.24-6.88	–	0.02-0.05	0.23-1.11	–	–	17-24	–	10-20	10-42	Lu et al. (2020)

[a]"-" represents no relevant reference data.

4 Discussion

4.1 Effect of salinity on the metal dynamics

Changes in the concentration of chloride irons may significantly affect the behaviors of many trace metals in the aquatic environment (Colombo et al., 2008; Sanders et al., 2015). This phenomenon has been found in many previous studies, which is particularly obvious in the river-sea continuum (or estuary area) (Byrne and Yao, 2000). In this study, limited significant correlations were found in spring for six metals, with only colloid Pb with >10 kDa size fraction showing significant relationships with salinity (Figure 7). Among them, 10-100 kDa was negatively correlated with salinity ($P < 0.05$), while 100 kDa -0.45 µm showed a significant positive correlation ($P < 0.05$), indicating that colloidal Pb tended to form a stable HMW state in this season (Lu et al., 2020). In autumn, however, intriguing correlations between salinity and metal dynamics were discovered. For each dissolved fraction, <1 kDa truly dissolved Fe, Mn, Cu and Cd concentrations positively correlated with salinity, and the 1-3 kDa Pb concentrations negatively correlated with the salinity (P < 0.05) (Figure 7). The positive relations between each corresponding concentration suggest that they may have a common origin (Duan et al., 2010), while the negative correlation may be attributed to the coagulation/flocculation of LMW colloids to the HMW forms (Lu et al., 2021). It is noteworthy that TD Fe, Cu and Cd all showed significant positive correlations with salinity, and there was no significant correlation for TD Mn, Zn and Pb. The data reported by Sanders et al. (2015) in the Korogoro Creek of New South Wales (Australia) proved that the behavior of TD Fe in the estuary with a wide range of salinity (5-35) conformed to the characteristic of gradually decreasing with increasing salinity,

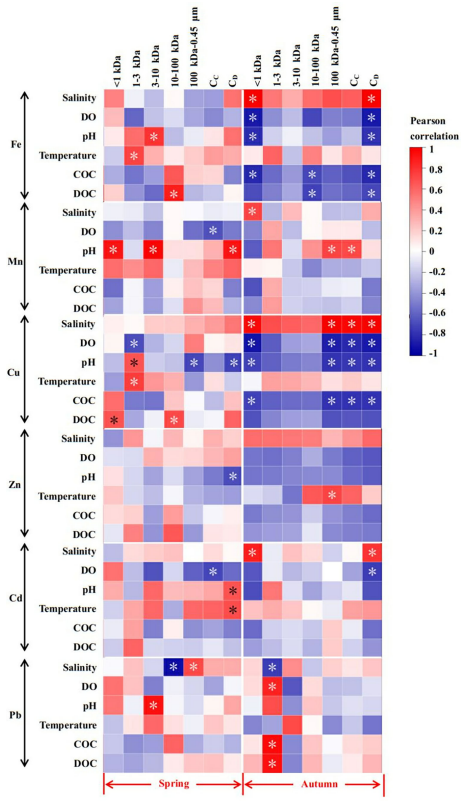

FIGURE 7
Pearson correlation matrix for the concentrations of dissolved Mn, Fe, Cu, Zn, Cd and Pb and the physicochemical parameters in different seasons of YRE. * represents significant (P < 0.05).

but results herein indicate that the dominant total dissolved Fe, Cu and Cd in the mixing zone may not be input from the river but the organic colloid addition on the particle surface, which is similar to the report by Waeles et al. (2008) in the France riverine water. For other colloidal fractions, only 100 kDa-0.45 μm Cu and the whole colloidal Cu were significantly positively correlated with salinity. Since the medium salinity region (salinity 20-30) of the estuarine area often has the phenomenon of metal desorption from the surface of the particulate matter into the water body, although Lu et al. (2020) investigation in the river water of Yantai City (China) found that this situation was more likely to occur in winter, but obviously, this behavior may not be ignored in autumn.

4.2 Effect of DO, pH and temperature on the metal dynamics

Studies have shown that factors such as DO, pH and temperature may affect the migration of elements in the particulate matter-organic matter mixed system (Lu et al., 2021). In addition, Fe, Mn, Cu, and Zn have long been thought to be closely related to phytoplankton growth (Huang et al., 2014; Han et al., 2021), while colloids Cd and Pb have been shown to possess seasonal variation characteristics (Lu et al., 2020; Lu et al., 2022). However, DO, an important biological indicator, did not show a significant correlation with each dissolved fraction of Fe, Zn and Pb in spring (Figure 7). As for other metals, only 1-3 kDa Cu was significantly negatively correlated with DO. Generally, <10 kDa colloids in the aquatic system were primarily considered to be fresh peptides or humic/fulvic compounds (Lu et al., 2020). However, 1 kDa-0.45μm Mn and Cd were significantly negatively correlated with DO, and the increase of DO concentration easily promoted the growth of phytoplankton and further promoted the formation of organic colloid ligands (Lu et al., 2021). Therefore, the behavior of colloid Mn and Cd in spring may be related to the behavior of inorganic colloidal ligands. For pH and temperature, a similar situation occurred for <10 kDa Fe, Mn, Cu and Pb, that is, there were significant positive correlations with pH, which proved the higher activity of colloid of this size fraction. Different from spring, HMW colloids in autumn, especially >10 kDa Mn and Zn, were significantly related to the dynamic changes of DO, pH and temperature. In addition, the truly dissolved Fe, Cu and other <1 kDa biotrophic metal elements showed high activity (Figure 7). Compared to spring (March), the increase of temperature in autumn (November) may promote the growth of plankton in the water, and the released substances such as peptidoglycans, proteins and extracellular polysaccharides may promote the overall increase of HMW organic ligand concentrations, which may be an important factor in increasing the HMW colloidal trace metal percentages (Kaplan et al., 1987; Lee et al., 1996; Hung et al., 2001; Lead and Wilkinson, 2006). However, the significant downward trend of the relationship between 1-100 kDa fraction and environmental parameters (except Pb) proves that the flocculation or coagulation of LMW colloids in autumn was considerable. Generally, LMW organics in aquatic environments were considered to be newly released polypeptides or humus/fulvic compounds (Lu et al., 2020).

4.3 Effect of COC/DOC on the metal dynamics

DOC, as an important component in dissolved organic matter (DOM), is a key carbon source for the growth and metabolism of planktonic bacteria, and its bioavailability has always been the focus and hotspot of ecosystem research (Li et al., 2008). In addition, DOC is an important indicator to explore the relationship between elemental behavior and organic matter (Lu et al., 2021). In spring, only the concentrations of 10-100 kDa fraction colloidal Fe and Cu were closely related to the DOC concentration ($p < 0.05$) (Figure 7), suggesting that they may have a common organic origin (Duan et al., 2010; Lu et al., 2021). On the contrary, the result in autumn indicated that negative relations of 10-100 kDa Fe vs. COC and DOC ($p < 0.05$) and 100 kDa-0.45 μm and 1 kDa-0.45 μm Cu vs. COC ($p < 0.05$), which suggested that the main source of HMW colloidal Fe and Cu in this season may be the inorganic sources rather than organic matter or the decomposition of organic ligands on the surface of particles (Mavrocordatos et al., 2000; Stolpe et al., 2013). However, 1-3 kDa Pb showed significant positive correlation with COC and DOC ($p < 0.05$), indicating that Pb behavior was still mainly affected by organic ligands in this season. These intriguing phenomena may prove the heterogeneity of colloids in the YRE. First, the concentration of DOC in the TRE is much lower than the average level of DOC in the world's rivers of ~416.67 μmol L^{-1} (0.5 mg L^{-1}) (Meybeck, 1982; Lu et al., 2021). Also, the lower light transmittance brought by the turbid water body limits the effective growth of phytoplankton to a certain extent (Pakulski et al., 2000). The combined effect of the above two may lead to an insignificant relationship between the colloidal metal and the organic ligands in the YRE. Secondly, the disturbance of sediment caused by strong hydrodynamics and the river-sea mixing behavior make the trace elements, particulate matter and organic matter may undergo violent migration and transformation in a limited area (Skrabal et al., 1997; Sun et al., 2007; Santos-Echeandia et al., 2008; Janot et al., 2012; Bao et al., 2019). Dai and Martin (1995) and Dai et al. (1995) assumed that the colloidal matter consisted of at least two parts: one part was stable in physicochemical properties (ie: the conserved part) and the other part was removed at the river-sea interface. Among them, unlike proteins containing multiple amino acid residues and humic acid (as a mixture), carbohydrates usually possess stable

structures. Among them, many studies have shown that the behavior of carbohydrates, an important carbon source, may significantly affect the behavior of colloidal metals in aquatic environments (Xu et al., 2018a). In addition, carbohydrate tends to form a colloidal system with network structures in saline systems, which could result in a stable behavior of the colloidal phase after flocculation (Guo et al., 2009). Obviously, in the YRE mixing area, the non-conservative part may dominate the geochemical behavior of colloidal metals in the spring and autumn. However, the contribution of inorganic colloidal ligands should not be ignored.

4.4 Effect of organic matter-particle mixture system on the metal dynamics

However, a single influencing factor is difficult to exist. In other words in the natural aquatic environment, the migration of dissolved metal may be affected by the organic matter-particle mixture system. First, the organic matter and particulate matter compete with the free metals in the water environment (Wood, 1996; Sures and Zimmermann, 2007), and then causing the metals to migrate between the organic (or colloidal) and particulate phases, mainly determined by the physical and chemical properties of particulate matter and organic matter. Secondly, trace elements can inhibit their adsorption on the particulate matter when they are considered to be stable complexes with small organic ligands and inorganic ligands in water systems (Zakharova, 1987; Wood, 1996; Cobelo-García, 2013; Liu et al., 2019). In addition, the presence of organic matter in the water may change the surface properties of the particles, and the adhesion of different organic matter to the surface of different particles may cause the surface area and potential of the particles to change together, which may directly affect the migration of the elements between the two (Liu and Gao, 2019). Hence, more comprehensive demonstration of the metal migration process in complex aquatic systems may not be allowed to proceed based on limited data. However, the results obtained can still provide some insights into the heterogeneity of colloidal metals in the aquatic environment of this region.

5 Conclusions

Over this study, clean sampling technology and modified CFU method have proved their high efficiency to separate and determine the various dissolved fractions of Fe, Mn, Cu, Zn, Cd and Pb in the YRE. All the CF values were <1 except TD Zn at station 5 and 6 in autumn (CF = 1.64 and 1.32), indicating lower contaminant levels of the YRE. Our results have shown that the concentration and percentage of 100 kDa-0.45 μm HMW metals were dominant in the YRE drainage system except for 1-10 kDa Fe in autumn. The size-fractionation variations of six colloidal metals along the environmental parameters were examined and some insights affecting the migration of the dissolved fraction from the river to seawater in this system were provided: (a) the TD Fe, Mn, Cu, Zn, Cd and Pb concentration exhibits non-conservative behavior from the river to sea; (b) the addition of colloidal metals in the middle salinity region should be attributed to the contribution of the colloidal ligand, especially colloidal Fe, Cu and Cd; (c) strong ligand, mixing process and desorption from the surface of the particles co-regulate colloidal metals of the YRE; (d) the distributions of Fe, Cu and Pb are affected by the characteristics of DOC or COC to a certain extent, but this is limited to the >10 kDa HMW colloidal Pb and <10 kDa LMW colloidal Fe and Cu. However, whether the lower and stable DOC level in the YRE region has a stronger effect on colloidal metals than suspended particles or sediments remains to be further studied. In addition, the quantitative effect of phytoplankton on dissolved metals or each dissolved fraction should also be studied further. In summary, although the factors affecting the migration of colloidal metals are comprehensive and complex, the results obtained in this paper may still enrich the existing knowledge of colloids and biogeochemical cycling for better understanding of the dynamic behaviors of trace metals in aquatic systems.

Data availability statement

The datasets presented in this study can be found in online repositories. The names of the repository/repositories and accession number(s) can be found in the article/Supplementary Material.

Author contributions

FL and TY: Investigation, formal analysis, conceptualization, methodology, validation, writing - original draft. YL and NW: Funding acquisition, resources, conceptualization, methodology, validation, supervision, writing - review & editing. All authors contributed to the article and approved the submitted version.

Funding

This work was financially supported by the National Natural Science Foundation of China (No. 42207520 and 51903247), the Natural Science Foundation of Shandong Province (ZR2022QD127) and the Fundamental Research Projects of Science & Technology Innovation and Development Plan in Yantai City (No. 2022MSGY063). The assistance of Prof. Dawei Pan in voyage and the sample collection is greatly appreciated.

Conflict of interest

The authors declare that the research was conducted in the absence of any commercial or financial relationships that could be construed as a potential conflict of interest.

Publisher's note

All claims expressed in this article are solely those of the authors and do not necessarily represent those of their affiliated organizations, or those of the publisher, the editors and the reviewers. Any product that may be evaluated in this article, or claim that may be made by its manufacturer, is not guaranteed or endorsed by the publisher.

Supplementary material

The Supplementary Material for this article can be found online at: https://www.frontiersin.org/articles/10.3389/fmars.2022.1074829/full#supplementary-material

References

AQSIQ (1997). "Sea Water quality standard (GB 3097-1997)," in *Administration of quality supervision, inspection and quarantine* (Beijing: Standard Press of China).

Bao, T. L., Wang, P. F., Hu, B., and Shi, Y. (2019). Investigation on the effects of sediment resuspension on the binding of colloidal organic matter to copper using fluorescence techniques. *Chemosphere* 236, 124312. doi: 10.1016/j.chemosphere.2019.07.043

Bi, N. S., Yang, Z. S., Wang, H. J., Xu, C. L., and Guo, Z. G. (2014). Impact of artificial water and sediment discharge regulation in the huanghe (Yellow river) on the transport of particulate heavy metals to the sea. *Catena* 121, 232–240. doi: 10.1016/j.catena.2014.05.006

Byrne, R. H., and Yao, W. S. (2000). Formation of palladium(II) hydroxychloride complexes and precipitates in sodium chloride solutions and seawater. *Geochim. Cosmochim. Ac.* 64, 4153–4156. doi: 10.1016/S0016-7037(00)00501-9

Cobelo-García, A. (2013). Kinetic effects on the interactions of Rh(III) with humic acids as determined using size-exclusion chromatography (SEC). *Environ. Sci. pollut. Res.* 20 (4), 2330–2339. doi: 10.1007/s11356-012-1113-8

Colombo, C., Oates, C. J., Monhemius, A. J., and Plant, J. A. (2008). Complexation of platinum, palladium and rhodium with inorganic ligands in the environment. *Geochem.-Explor. Env. A.* 8, 91–101. doi: 10.1144/1467-7873/07-151

Cornu, S., Samouëlian, A., Ayzac, A., and Montagne, D. (2018). Soluble and colloidal translocation of Al, fe, Si and Mn in an artificially drained French retisol. *Geoderma* 330, 193–203. doi: 10.1016/j.geoderma.2018.05.032

Dai, M. H., and Martin, J. M. (1995). First data on trace metal level and behaviour in two major Arctic river-estuarine systems (Ob and yenisey) and in the adjacent kara Sea, Russia. *Earth. Planet. Sc. Lett.* 131, 127–141. doi: 10.1016/0012-821X(95)00021-4

Dai, M. H., Martin, J. M., and Cauwet, G. (1995). The significant role of colloids in the transport and transformation of organic carbon and associated trace metals (Cd, Cu and Ni) in the Rhone delta (France). *Mar. Chem.* 51, 159–175. doi: 10.1016/0012-821X(95)00021-4

Duan, L. Q., Song, J. M., Li, X. G., Yuan, H. M., and Xu, S. S. (2010). Distribution of selenium and its relationship to the eco-environment in bohai bay seawater. *Mar. Chem.* 121, 87–99. doi: 10.1016/j.marchem.2010.03.007

González-Álvarez, R. J., Bellido-Millab, D., Pinto, J. J., and Moreno, C. (2020). A handling-free methodology for rapid determination of Cu species in seawater based on direct solid micro-samplers analysis by high-resolution continuum source graphite furnace atomic absorption spectrometry. *Talanta* 206, 120249. doi: 10.1016/j.talanta.2019.120249

Guo, L. D., and Santschi, P. H. (2007). "Ultrafiltration and its applications to sampling and characterisation of aquatic colloids," in *Environmental colloids and particles: Behavior, separation and characterisation*. Eds. K. Wilkinson and J. Lead (Chichester: John Wiley & Sons Ltd.), 159–221.

Guo, L., Sun, C. M., Li, G. Y., Liu, C. P., and Ji, C. N. (2009). Thermodynamics and kinetics of Zn(II) adsorption on crosslinked starch phosphates. *J. Hazard. Mater.* 161 (1), 510–515. doi: 10.3724/SP.J.1095.2014.40065

Hakanson, L. (1980). An ecological risk index for aquatic pollution control. A sedimentological approach. *Water Res.* 14, 975–1001. doi: 10.1016/0043-1354(80)90143-8

Han, H. T., Pan, D. W., Pan, F., Hu, X. P., and Zhu, R. L. (2021). A functional micro-needle sensor for voltammetric determination of iron in coastal waters. *Sensor. Actuat. B-Chem.* 327, 128883. doi: 10.1016/j.snb.2020.128883

Hatje, V., Apte, S. C., Hales, L. T., and Birch, G. F. (2003). Dissolved trace metal distributions in port Jackson estuary (Sydney harbour). *Aust. Mar. pollut. Bull.* 46, 719–730. doi: 10.1016/j.csr.2013.11.014

Huang, P., Li, T. G., Li, A. C., Yu, X. K., and Hu, N. J. (2014). Distribution, enrichment and sources of heavy metals in surface sediments of the north yellow Sea. *Cont. Shelf Res.* 73, 1–13. doi: 10.1016/j.csr.2013.11.014. Yu.

Hung, C. C., Tang, D., Warnken, K. W., and Santschi, P. H. (2001). Distributions of carbohydrates, including uronic acids, in estuarine waters of Galveston bay. *Mar. Chem.* 73 (3-4), 305–318. doi: 10.1016/S0304-4203(00)00114-6

Illuminati, S., Annibaldi, A., Romagnoli, T., Libani, G., Antonucci, M., Scarponi, G., et al. (2017). Distribution of cd, Pb and Cu between dissolved fraction, inorganic particulate and phytoplankton in seawater of Terra Nova bay (Ross Sea, Antarctica) during austral summer 2011-12. *Chemosphere* 185, 1122–1135. doi: 10.1016/j.chemosphere.2017.07.087

Janot, N., Reiller, P. E., Zheng, X., Croue, J. P., and Benedetti, M. F. (2012). Characterization of humic acid reactivity modifications due to adsorption onto a-Al_2O_3. *Water Res.* 46 (3), 731–740. doi: 10.1016/j.watres.2011.11.042

Kaplan, D., Christiaen, D., and Arad (Malis), S. (1987). Chelating properties of extracellular polysaccharides from chlorella spp. *Appl. Environ. Microb.* 53, 2953–2956. doi: 10.1128/aem.53.12.2953-2956.1987

Lead, J. R., and Wilkinson, K. J. (2006). Natural aquatic colloids: current knowledge and future trends. *Environ. Chem.* 3, 159–171. doi: 10.1071/EN06025

Lee, J. G., Ahner, B. A., and Morel, F. M. M. (1996). Export of cadmium and phytochelatin by the marine diatom thalassiosira weissflogii. *Environ. Sci. Technol.* 30, 1814–1821. doi: 10.1021/es950331p

Liang, Y., Pan, D. W., Wang, C. C., Lu, Y. X., and Fan, X. (2022). Distribution and ecological health risk assessment of dissolved trace metals in surface and bottom seawater of yantai offshore, China. *Front. Mar. Sci.* 9. doi: 10.3389/fmars.2022.993965

Lin, H. Y., Sun, T., Xue, S. F., and Jiang, X. L. (2016). Heavy metal spatial variation, bioaccumulation, and risk assessment of *Zostera japonica* habitat in the YRE, China. *Sci. Total Environ.* 541, 435–443. doi: 10.1016/j.scitotenv.2015.09.050

Liu, K., and Gao, X. L. (2019). Adsorption and fractionation of pt, pd and Rh onto inorganic microparticles and the effects of macromolecular organic compounds in seawater. *Environ. pollut.* 255, 113192. doi: 10.1016/j.envpol.2019.113192

Liu, K., Gao, X. L., Li, L., Chen, C. T. A., and Xing, Q. G. (2018). Determination of ultra-trace pt, pd and Rh in seawater using an offline pre-concentration method and inductively coupled plasma mass spectrometry. *Chemosphere* 212, 429–437. doi: 10.1016/j.chemosphere.2018.08.098

Liu, K., Gao, X. L., Xing, Q. G., and Chen, F. S. (2019). Adsorption kinetics of platinum group elements onto macromolecular organic matter in seawater. *Acta Oceanol. Sin.* 38 (8), 8–16. doi: 10.1007/s13131-019-1433-3

Liu, R. X., Lead, J. R., and Zhang, H. (2013). Combining cross flow ultrafiltration and diffusion gradients in thin-films approaches to determine trace metal speciation in freshwaters. *Geochim. Cosmochim. Ac.* 109, 14–26. doi: 10.1016/j.gca.2013.01.030

Liu, H. Q., Liu, G. J., Wang, J., Yang, Z. J., and Da, C. N. (2016a). Fractional distribution and risk assessment of heavy metals in sediments collected from the yellow river, China. *Environ. Sci. pollut. Res.* 23, 11076–11084. doi: 10.1007/s11356-016-6291-3

Liu, H. Q., Liu, G. J., Wang, S. S., Zhou, C. C., Yuan, Z. J., and Da, C. N. (2016b). Distribution of heavy metals, stable isotope ratios (^{d}13C and ^{d}15N) and risk assessment of fish from the YRE, China. *Chemosphere* 208, 731–739. doi: 10.1016/j.chemosphere.2018.06.028

Li, W., Wu, F. C., Liu, C. Q., Fu, P. Q., Wang, J., Mei, Y., et al. (2008). Temporal and spatial distributions of dissolved organic carbon and nitrogen in two small lakes on the southwestern China plateau. *Limnology* 9 (2), 163–171. doi: 10.1007/s10201-008-0241-9

Lu, Y. X., Gao, X. L., and Chen, C. T. A. (2019). Separation and determination of colloidal trace metals in seawater by cross-flow ultrafiltration, liquid-liquid extraction and ICP-MS. *Mar. Chem.* 215, 103685. doi: 10.1016/j.marchem.2019.103685

Lu, Y. X., Gao, X. L., Song, J. M., Chen, C. T. A., and Chu, J. L. (2020). Colloidal toxic trace metals in urban riverine and estuarine waters of yantai city, southern coast of north yellow Sea. *Sci. Total Environ.* 717, 135265. doi: 10.1016/j.scitotenv.2019.135265

Lu, Y. X., Pan, D. W., Yang, T. T., and Wang, C. C. (2021). Spatial and environmental characteristics of colloidal trace Cu in the surface water of the yellow river estuary, China. *Mar. pollut. Bull.* 168, 112401. doi: 10.1016/j.marpolbul.2021.112401

Lu, Y. X., Pan, D. W., Yang, T. T., and Wang, C. C. (2022). Distribution characteristics and controlling factors of typical heavy metals in yellow river estuary of China. *J. Oceanol. Limnol.* doi: 10.1007/s00343-021-1320-6

Lü, D., Zheng, B., Fang, Y., Shen, G., and Liu, H. J. (2015). Distribution and pollution assessment of trace metals in seawater and sediment in Laizhou Bay. *China. J. Oceanol. Limnol.* 33, 1053–61. doi: 10.1007/s00343-015-4226-3

Martin, J. M., and Dai, M. H. (1995). Significance of colloids in the biogeochemical cycling of organic carbon and trace metals in the Venice lagoon (Italy). *Limnol. Oceanogr.* 40 (1), 119–131. doi: 10.4319/lo.1995.40.1.0119

Mavrocordatos, D., Mondi-Couture, C., Atteia, O., Leppard, G. G., and Perret, D. (2000). Formation of a distinct class of fe-Ca(-C_{org})-rich particles in a complex peat-karst system. *J. Hydrol.* 237, 234–247. doi: 10.1016/S0022-1694(00)00309-7

Meybeck, M. (1982). Carbon, nitrogen and phosphorus transport by world rivers. *Am. J. Sci.* 282, 401–450. doi: 10.1016/j.crte.2004.09.016

Milliman, J. D., and Ren, M.-E. (1995). *Climate change: Impact on coastal habitation*. Ed. E. Eisma (Boca Raton, Florida: CRC Press), 57–83.

Pakulski, J., Benner, R., Whitledge, T., Amon, R., Eadie, B., Cifuentes, L., et al. (2000). Microbial metabolism and nutrient cycling in the Mississippi and atchafalaya river plumes. *Estuar. Coast. Shelf Sci.* 50 (2), 173–184. doi: 10.1006/ecss.1999.0561

Peers, G., and Price, N. M. (2006). Copper-containing plastocyanin used for electron transport by an oceanic diatom. *Nature* 441(7091), 341–344. doi: 10.1038/nature04630

Qiao, S. Q., Yang, Z. S., Pan, Y. J., and Guo, Z. G. (2007). Metals in suspended sediments from the changjiang (Yangtze river) and huanghe (Yellow river) to the sea, and their comparison. *Estuar. Coast. Shelf Sci.* 74, 539–548. doi: 10.1016/j.ecss.2007.05.042

Sanders, C. J., Santos, I. R., Maher, D. T., Sadat-Noori, M., Schnetger, B., and Brumsack, H. (2015). Dissolved iron exports from an estuary surrounded by coastal wetlands: Can small estuaries be a significant source of fe to the ocean? *Mar. Chem.* 176, 75–82. doi: 10.1016/j.marchem.2015.07.009

Santos-Echeandia, J., Laglera, L. M., Prego, R., and van den Berg, C. M. G. (2008). Dissolved copper speciation behavior during estuarine mixing in the San Simon inlet (wet season, galicia). influence of perticulate matter. *Estuar. Coast. Shelf S.* 76, 447–453. doi: 10.1016/j.ecss.2007.07.007

Skrabal, S. A., Donat, J. R., and Burdige, D. J. (1997). Fluxes of copper-complexing ligands from estuarine sediments. *Limnol. Oceanogr.* 42, 992–996. doi: 10.2307/2838904

Statham, P. J., Jacobson, Y., and van den Berg, C. M. G. (2012). The measurement of organically complexed Fe^{II} in natural waters using competitive ligand reverse titration. *Anal. Chim. Acta* 743, 111–116. doi: 10.1016/j.aca.2012.07.014

Stolpe, B., Guo, L. D., Shiller, A. M., and Aiken, G. R. (2013). Abundance, size distributions and trace-element binding of organic and iron-rich nanocolloids in alaskan rivers, as revealed by field-flow fractionation and ICP-MS. *Geochim. Cosmochim. Ac.* 105, 221–239. doi: 10.1016/j.gca.2012.11.018

Sun, X. J., Qin, B. Q., Zhu, G. W., and Zhang, Z. P. (2007). Effect of wind-induced wave on concentration of colloidal nutrient and phytoplankton in lake taihu. *Environ. Sci.* 28 (3), 506–511. doi: 10.13227/j.hjkx.2007.03.011

Sures, B., and Zimmermann, S. (2007). Impact of humic substances on the aqueous solubility, uptake and bioaccumulation of platinum, palladium and rhodium in exposure studies with dreissena polymorpha. *Environ. pollut.* 146 (2), 444–451. doi: 10.1016/j.envpol.2006.07.004

Tang, A., Liu, R., Ling, M., Xu, L., and Wang, J. (2010). Distribution characteristics and controlling factors of soluble heavy metals in the YRE and adjacent sea. *Proc. Environ. Sci.* 2, 1193–1198. doi: 10.1016/j.proenv.2010.10.129

Waeles, M., Tanguy, V., Lespes, G., and Riso, R. D. (2008). Behavior of colloidal trace metals (Cu, Pb and cd) in estuarine waters: An approach using frontal ultrafiltration (UF) and stripping chronopotentiometric methods (SCP). *Estuar. Coast. Shelf S.* 80, 538–544. doi: 10.1016/j.ecss.2008.09.010

Wang, Y., Liu, R. H., Zhang, Y. Q., Cui, X. Q., Tang, A. K., and Zhang, L. J. (2016). Transport of heavy metals in the huanghe river estuary, China. *Environ. Earth Sci.* 75, 288. doi: 10.1007/s12665-015-4908-3

Wang, C., Wang, W., He, S., Du, J., and Sun, Z. (2011). Sources and distribution of aliphatic and polycyclic aromatic hydrocarbons in yellow river delta nature reserve, China. *Appl. Geochem.* 26, 1330–1336. doi: 10.1016/j.apgeochem.2011.05.006

Wang, X. Y., Zhao, L. L., Xu, H. Z., and Zhang, X. M. (2018). Spatial and seasonal characteristics of dissolved heavy metals in the surface seawater of the YRE, China. *Mar. pollut. Bull.* 137, 465–473. doi: 10.1016/j.marpolbul.2018.10.052

Wen, L. S., Santschi, P. H., Gill, G., and Paternostro, C. (1999). Estuarine trace metal distributions in Galveston bay: Importance of colloidal forms in the speciation of the dissolved phase. *Mar. Chem.* 63, 185–212. doi: 10.1016/S0304-4203(98)00062-0

Wen, L. S., Santschi, P. H., Warnken, K. W., Davison, W., Zhang, H., Li, H. P., et al. (2011). Molecular weight and chemical reactivity of dissolved trace metals (Cd, Cu, Ni) in surface waters from the Mississippi river to gulf of Mexico. *Estuar. Coast. Shelf S.* 92, 649–658. doi: 10.1016/j.ecss.2011.03.009

Wood, S. A. (1996). The role of humic substances in the transport and fixation of metals of economic interest (Au, pt, pd, U, V). *Ore Geol. Rev.* 11 (95), 1–31. doi: 10.1016/0169-1368(95)00013-5

Xu, H. C., Houghton, E. M., Houghton, C. J., and Guo, L. D. (2018a). Variations in size and composition of colloidal organic matter in a negative freshwater estuary. *Sci. Total Environ.* 615, 931–941. doi: 10.1016/j.scitotenv.2017.10.019

Xu, H. C., Lin, H., Jiang, H. L., and Guo, L. D. (2018b). Dynamic molecular size transformation of aquatic colloidal organic matter as a function of pH and cations. *Water Res.* 144, 543–552. doi: 10.1016/j.watres.2018.07.075

Xu, H. C., Xu, M. W., Li, Y. N., Liu, X., Guo, L. D., and Jiang, H. L. (2018c). Characterization, origin and aggregation behavior of colloids in eutrophic shallow lake. *Water Res.* 142, 176–186. doi: 10.1016/j.watres.2018.05.059

Yang, B., and Gao, X. L. (2019). Chromophoric dissolved organic matter in summer in a coastal mariculture region of northern Shandong peninsula, north yellow Sea. *Cont. Shelf Res.* 176, 19–35. doi: 10.1016/j.csr.2019.02.006

Yang, B., Gao, X. L., Zhao, J. M., Lu, Y. X., and Gao, T. C. (2020). Biogeochemistry of dissolved inorganic nutrients in an oligotrophic coastal mariculture region of the northern Shandong peninsula, north yellow Sea. *Mar. pollut. Bull.* 150, 110693. doi: 10.1016/j.marpolbul.2019.110693

Zakharova, I. A. (1987). Coordination compounds of Pd(II) and Pt(II) with thiodiacetic acid. *Polyhedron* 6 (5), 1065–1070. doi: 10.1016/S0277-5387(00)80956-0

Zhang, J., and Huang, W. W. (1993). Dissolved trace metals in the huanghe: the most turbid large river in the world. *Water Res.* 27 (1), 1–8. doi: 10.1016/0043-1354(93)90188-N

Zhang, D., Zhang, X., Tian, L., Ye, F., Huang, X., Zeng, Y., et al. (2012). Seasonal and spatial dynamics of trace elements in water and sediment from pearl river estuary, south China. *Environ. Earth Sci.* 68, 1053–1063. doi: 10.1007/s12665-012-1807-8

Zhou, Z. Z., Stolpe, B., Guo, L. D., and Shiller, A. M. (2016). Colloidal size spectra, composition and estuarine mixing behavior of DOM in river and estuarine waters of the northern gulf of Mexico. *Geochim. Cosmochim. Ac.* 181, 1–17. doi: 10.1016/j.gca.2016.02.032

frontiers | Frontiers in Marine Science

TYPE Original Research
PUBLISHED 14 December 2022
DOI 10.3389/fmars.2022.1094846

OPEN ACCESS

EDITED BY
Wen Zhuang,
Shandong University, China

REVIEWED BY
Xiangbin Ran,
Ministry of Natural Resources, China
Qingzhen Yao,
Ocean University of China, China

*CORRESPONDENCE
Liqin Duan
duanliqin@qdio.ac.cn

SPECIALTY SECTION
This article was submitted to Marine Biogeochemistry, a section of the journal Frontiers in Marine Science

RECEIVED 10 November 2022
ACCEPTED 30 November 2022
PUBLISHED 14 December 2022

CITATION
Fan J, Duan L, Yin M, Yuan H and Li X (2022) Nonconservative behavior of dissolved molybdenum and its potential role in nitrogen cycling in the Bohai and Yellow Seas. *Front. Mar. Sci.* 9:1094846. doi: 10.3389/fmars.2022.1094846

Nonconservative behavior of dissolved molybdenum and its potential role in nitrogen cycling in the Bohai and Yellow Seas

Jinqi Fan[1,2,3,4], Liqin Duan[1,2,3,4]*, Meiling Yin[1,2,3,4], Huamao Yuan[1,2,3,4] and Xuegang Li[1,2,3,4]

[1]CAS Key Laboratory of Marine Ecology and Environmental Sciences, Institute of Oceanology, Chinese Academy of Sciences, Qingdao, China, [2]University of Chinese Academy of Sciences, Beijing, China, [3]Laboratory for Marine Ecology and Environmental Sciences, Qingdao National Laboratory for Marine Science and Technology, Qingdao, China, [4]Center for Ocean Mega-Science, Chinese Academy of Sciences, Qingdao, China

Molybdenum plays an important role in marine biological activity, especially in nitrogen cycling as a cofactor for N_2 fixation and nitrate reductase. However, the dissolved Mo (dMo) behavior and its interaction with N cycling in the coastal waters is still unclear. In this study, the dMo concentrations and parameters related to Mo distribution and N cycling in surface and bottom seawaters of the Bohai (BS) and Yellow Seas (YS) were examined. The results showed that dMo concentrations ranged from 36.4 nmol L^{-1} to 125.0 nmol L^{-1}, most of which deviated significantly from the conservative line, indicating nonconservative behavior of Mo relative to salinity. The highest dMo concentrations occurring in 36°N section of north of the South YS (SYS), were close to conservative value (105 nmol L^{-1}). Significant depletion up to 40-50 nmol L^{-1} of dMo mainly appeared in the BS, NYS and south of the SYS, suggesting the possible removal of dMo by biological utilization and particle adsorption. Particularly, the increasing dMo concentrations away the Yellow River estuary indicated that freshwater dilution was one of reasons for dMo distributions in the BS. The similar spatial distribution of dMo and dissolved Mn concentrations suggested the possible scavenging by MnO_x phases for Mo removal. The negative correlation between dMo and chlorophyll-*a* (Chl-*a*) concentrations in surface seawaters suggested that biological uptake was involved in dMo removal. The depleted dMo in most of sites corresponded with the higher nitrite concentrations, implying the possible involvement of nitrate reduction process. Although the highest N_2 fixation rates and relative abundances of cyanobacteria appeared in 36°N section, corresponding with the conservative dMo, suggesting that Mo may play a minor role in N_2 fixation process there. The ten-folds of relative abundance of bacteria with nitrate reduction function than that with N_2 fixation function suggested that dMo seems to play more important role in nitration reduction than nitrogen fixation in the BS and YS.

KEYWORDS

dissolved molybdenum, nonconservative behavior, biological uptake, N_2 fixation, nitrate reduction

1 Introduction

As the most abundant transition metal, molybdenum (Mo) exists mainly as in the dissolved forms (MoO_4^{2-}, $HMoO_4^-$) in the oxygenated ocean. Dissolved Mo (dMo) concentrations are stable in the open ocean, with reported concentrations between 105 and 107 nmol L^{-1} (Collier, 1985; Smedley and Kinniburgh, 2017). DMo shows a conservative characteristic in the open ocean (Audry et al., 2007; Beck et al., 2012; Valdivieso-Ojeda et al., 2020). The constant stable isotope ratio of Mo in the ocean also suggests the relative unreactivity of oceanic Mo (Nakagawa et al., 2012; Ho et al., 2018). However, dMo in several estuaries and coastal areas showed non-conservative behavior (Dellwig et al., 2007; Wang et al., 2016; Ho et al., 2018). Various dMo concentrations in different costal and estuarine waters were found, with most of dMo depleted. For example, dMo in Mississippi Estuary (Mohajerin et al., 2016), Itchen Estuary (Archer and Vance, 2008), multiple estuaries in India (Rahaman et al., 2010), Wadden Sea (Dellwig et al., 2007), and Taiwan Strait (Wang et al., 2016) displayed depletion and nonconservative behavior. The reasons for Mo depletion are varied and likely related to biological processes, scavenging by particles (e.g., Fe/Mn oxides), and sedimentary interactions (Reitz et al., 2007; Ho et al., 2018). The Mo excess in some studies is attributed to extra sources, e.g., porewater diffusion at sediment-water interface (Dellwig et al., 2007; Strady et al., 2009; Waeles et al., 2013), submarine groundwater discharge (Dalai et al., 2005), and industrial discharge (Rahaman et al., 2010; Wang et al., 2016).

The main abiotic processes affecting dMo distribution in the coastal waters are riverine input and particle adsorption. Molybdenum entering into the oceans mainly by riverine input after oxidative weathering on the land (Zerkle et al., 2011). Rivers have supplied ~22,000 t a^{-1} of Mo to the oceans (Smedley and Kinniburgh, 2017), accounting to~90% of total dMo (Morford and Emerson, 1999; Wang et al., 2016). Riverine Mo concentrations are low, with the estimated values of ~4.38 nmol L^{-1} (Chen et al., 2014) and 1.15-89.9 nmol L^{-1} (Linnik et al., 2015) in the world rivers. Thus, dMo generally displays an increase with the increasing salinity of estuaries due to the freshwater dilution. A non-biotic adsorption onto MnO_x phases has been proved one reason for Mo depletion (Dellwig et al., 2007). It has been found that dMo had a positive correlation with dissolved Mn (Wang et al., 2016) and a negative correlation with particle Mn (Dellwig et al., 2007), suggesting the scavenging of dMo by MnO_x phase. The scavenging and deposition of dMo with ferromanganese oxides accounts for ~35% of removal of modern marine Mo (Scott et al., 2008; Zerkle et al., 2011).

Molybdenum is an essential element for N_2 and nitrate assimilation due to it is a cofactor for some N_2 fixation and nitrate reductase (Wolfe, 1954; Fay and Fogg, 1962; Robson et al., 1986; Fischer et al., 2005). Thus, Mo depletion is more related to biotic processes. Extremely low dMo concentration (<3 nmol L^{-1}) can limit heterotroph growth in freshwater and seawater (Glass et al., 2012; Wang et al., 2016). Mo scarcity (0.6-4 nmol L^{-1}) in some lakes also can limit phytoplankton growth (Goldman, 1960; Glass et al., 2010; Glass et al., 2012). However, the influence of biological uptake on Mo removal in the coastal waters is still unclear. The higher cellular Mo concentrations in phytoplankton (~5.3 μmol L^{-1}; Ho et al., 2003) and bacteria (53 μmol L^{-1}; Barton et al., 2007) than in seawater suggest that marine algae and heterotrophs could consume dMo and contribute to the dMo depletion in water column (Wang et al., 2016). The negative correlation between Chl-*a* and dMo were observed in both the coastal waters (Wang et al., 2016) and open sea (Ho et al., 2018), further suggesting the involvement of biological uptake in removing dMo out of the water column.

The Mo removal by utilization of nitrogen fixation organisms were observed in cultures. For example, the addition of Mo and NO_3^- in the hypolimnion of Castle Lake could promote nitrogen assimilation protein activity increase when NH_4^+ was scarce (Glass et al., 2012). However, the limitation of Mo on nitrogen fixation in the ocean has not been found or not been studied. Positive and negative Mo concentration anomalies were found in N_2 fixation in the Eastern Equatorial Pacific (+5 nmol L^{-1}, -3 nmol L^{-1}; Tuit and Ravizza, 2003), presumably related to biological nitrogen fixation processes (Dellwig et al., 2007). In addition, the Mo removal also is related to the utilization by marine algae and/or cyanobacteria with nitrate reductase. Ho et al. (2018) has found that some depleted dMo corresponded with the nitrite maximum in the oxygen deficient zone (ODZ) off the Peru margin, suggesting that Mo likely involved in nitrate reduction.

Marine nitrogen fixation and denitrification are two important processes in the nitrogen cycle, which play a key role in understanding marine nitrogen fixation, nitrogen loss and nitrogen budget balance (Fowler et al., 2013). In particular, the recent studies have found that the marginal seas may be a potential hotspot for nitrogen fixing organisms (Zehr and Capone, 2020; Qu et al., 2022). However, the dMo behavior and its interaction with N cycling in the coastal waters is still unclear. The Bohai Sea (BS) and Yellow Sea (YS) are one of main marginal seas in China, receiving a large amount of inorganic nutrients from terrestrial sources. The DIN concentration in the BS and YS underwent a 6-7-fold increase from the late 1990s to the 2010s (Xin et al., 2019; Zheng and Zhai, 2021), inducing a DIN/DIP ratio increase and DSi/DIN ratio decline (Liu et al., 2011; Guo et al., 2014). Their biological activities also are frequent. In this study, dMo concentrations and parameters related to Mo distribution and N cycling in surface and bottom seawaters of the BS and YS were examined. The aim is to identify dMo behavior and its potential regulatory role in nitrogen cycling of the BS and YS.

2 Materials and methods

2.1 Study area

The BS and YS are typical semi-enclosed continental shelf seas, located in the western Pacific Ocean between mainland China and the Korean Peninsula. The BS has the area of 77×10^3 km^2 and average depth of 18 m with the maximum depth of 83 m in the Bohai Strait. The YS has the area of 380×10^3 km^2 and average depth of 44 m with a maximum depth of 140 m. The Yellow River (YR) is the main river entering the BS, with the freshwater influx of ~200×10^8 m^3 a^{-1} (Xu et al., 2013). The main current in the BS is the Bohai Sea Coastal Current (BSCC), which can carry low-temperature, low-salinity and high nutrients into the YS under the influence of northwest monsoon (Chen, 2009). However, the currents in the YS are complex. The interaction among monsoon, bottom topography, river discharge and the Kuroshio intrusion leads to various circulation regimes and different water masses. The seasonal circulation is mainly reflected in the Yellow Sea Warm Current (YSWW). In summer and autumn, the YSWW moves northward under the influence of southeast monsoon. In winter, the YSWW forms a circulation in the SYS region affected by northeast monsoon (Chen, 2009). This study focused on autumn, when there are the Yellow Sea Coastal Current (YSCC) in the west, the South Korean Coastal Current (WKCC) in the east, and the YSWW in the middle of the SYS, which can move northward through the Bohai Strait into the BS. In addition, there is a typical seasonal cold water mass in the YS, namely the Yellow Sea Cold Water (YSCW). The YSCW (<12°C) mainly appears in summer and autumn when the southwest monsoon prevails. The YSCW exhibits low temperature and high salinity characteristics (Wang et al., 2014). In addition, the low DO and pH values also are found in the YSCW (Zhai, 2018; Guo et al., 2020).

The sample collection in the BS and YS was conducted aboard the R/V *Lan Hai 101* in 18 October and 4 November 2021 (Figure 1). Seawater samples at surface (2 m) and bottom (2 m above seafloor) layers were collected at 38 stations using 12-L Niskin bottles for dMo, nutrients, chlorophyll-*a* (Chl-*a*), dissolved oxygen (DO) and pH. The water sampler was installed on a rosette with a Seabird conductivity, temperature, depth (CTD) sensor to determine *in situ* temperature, salinity and depth. Seawater samples for DO and pH measurement were collected firstly. Seawater samples for dMo and nutrients were filtered through 0.45 μm Nuclepore® polycarbonate membrane filters previously cleaned with 5% HCl. Samples were filtered into pre-cleaned HDPE bottles and immediately acidified with ultrapure HCl to pH<2. Another part of filtered seawaters was collected in acid-clean, 60 ml HDPE bottles and stored at -20°C for nutrient analysis. Samples for Chl-*a* were filtered through cellulose acetate fiber filters (0.45μm pore size; Whatman) and

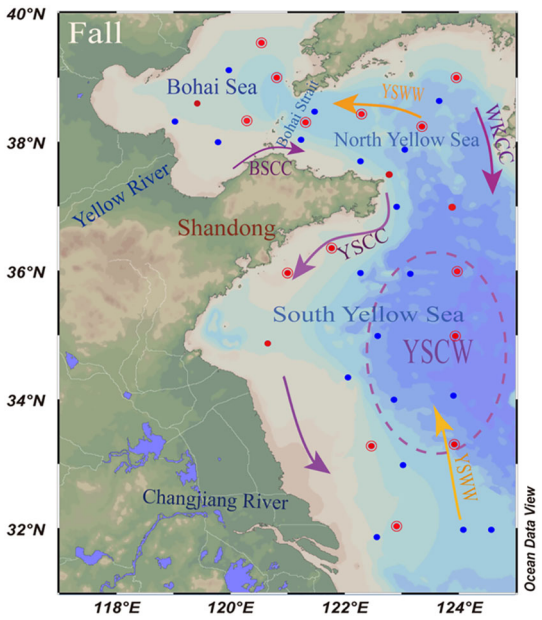

FIGURE 1
Study area and sampling sites in the Bohai Sea (BS) and Yellow Sea (YS) between 18 October and 4 November 2021. Temperature, salinity, DO, inorganic nutrients, Chl-*a* and dMo concentrations in surface and bottom seawater at all stations (blue + red) were determined. N_2-fixation rates at 14 stations (red hollow circles) and 16s rRNA at 18 stations (red solid dots) were measured in surface seawaters. In autumn, the circulation schematic includes the Bohai Sea Coastal Current (BSCC), Yellow Sea Coastal Current (YSCC), Western Korean Coastal Current (WKCC) and Yellow Sea Warm Water mass (YSWW). The Yellow Sea cold water (YSCW) is located in the dashed circles.

stored in dark at -20°C until further analysis in the laboratory. Microbial samples at 18 stations were collected by filtering 1 L of seawater through a 0.2 μm polycarbonate membrane. After filtration, the samples were kept in cryovials and stored at -80°C.

Surface seawaters at 14 stations were collected for nitrogen fixation incubations. 1 L surface seawater was collected and filtered immediately before the incubation period for determining the particulate ^{15}N abundance in original seawater. The N_2 fixation rates (NFRs) were determined using the $^{15}N_2$ gas dissolution method described in Mohr et al. (2010). The $^{15}N_2$-enrich seawater was prepared using $^{15}N_2$ gas at each station. Briefly, the filtered seawater was degassed and 1 ml of 99 atom% pure $^{15}N_2$ gas was injected into 100 ml of degassed seawater using the method described by Mohr et al. (2010). Unfiltered Seawater was added to duplicate acid-cleaned 600 ml polycarbonate bottles slowly to avoid air bubbles. Before incubation, 45 ml of seawater was removed from bottle. Then, 45 ml of $^{15}N_2$-enrich seawater was injected into incubation bottles. Each incubation bottle was shaken 5 times to ensure that water was fully mixed. Incubation was performed in incubator with continuous *in situ* seawater flow under natural

light for 24 h. After incubation, seawater was filtered (<100 mm Hg) *via* pre-combusted (450°C, 5 h) Whatman GF/F filter and stored at -20°C for determining the particulate ^{15}N abundance.

2.3 Sample analysis

2.3.1 DO and pH

The DO concentration and pH were determined using a Seven Excellence Multiparameter (Mettler Toledo, US) equipped with the DO and pH probes. The DO values were calibrated by the Winkler titration method (Bryan et al., 1976). The pH was calibrated to the *in situ* value by seawater temperature.

2.3.2 Dissolved Mo and Mn

Dissolved Mo and Mn concentrations were determined by inductively coupled plasma mass spectrometry (ICP-MS, Thermo iCAP Q) after 10-fold dilution with 0.4 M ultrapure HNO_3. Helium and KED were used as collision gas and mode of interference elimination. Internal standards Y for Mo and Sc for Mn were chosen. Certified reference material NASS-6 was used to ensure accuracy of the analytical procedure with accuracy of 98.0% for Mo and 96.2% for Mn. Replicate measurement was conducted on NASS-6 and samples with the relative standard deviations (RSD) of 4.5% for Mo and 7.6% for Mn. Procedural acid blanks for diluting samples were determined every 10 samples. The acid blanks are lower than the detection limits.

2.3.3 Nutrients and Chl-*a*

Nutrients including nitrate (NO_3-N), nitrite (NO_2-N), ammonium (NH_4-N), phosphate (PO_4-P) and silicate (SiO_3-Si) were determined photometrically using a continuous segmented flow analyzer (QuAAtro, Bran-Luebbe Inc., Germany). Their detection limits were 0.02 μmol L^{-1}, 0.02 μmol L^{-1}, 0.03 μmol L^{-1}, 0.01 μmol L^{-1} and 0.04 μmol L^{-1}, respectively. The standard deviation (SD) of three measurements was< 3%. Dissolved inorganic nitrogen (DIN) includes NO_3-N, NO_2-N and NH_4-N.

The filters for Chl-*a* were extracted with N, N-dimethylformamide for 12 h at 4°C. The extracts were measured using a fluorescence spectrophotometer (F-4500, Hitachi Co, Japan). Its detection limit was 1.5 μg L^{-1} with SD of<1% for 11 parallel determinations.

2.3.4 Bacteria abundance

The DNA was extracted by QIAquick Gel Extraction Kit (Qiagen, Germany). The PCR amplifications were conducted with the 515f/806r primer set that amplifies the V4 region of the 16S rRNA gene. High-throughput sequencing was carried out on the Illumina HiSeq 2500 platform (Illumana, San Diego, USA) by Novogene Technology Co., Ltd. (Beijing, China). The sequences with 96% similarity were classified into the identical operational taxonomic units (OTUs). Taxonomic data were assigned by Ribosomal Database Project (RDP) classifiers. The relative abundance of cyanobacteria at the phylum-level was used in this study.

2.3.5 N_2 fixation rate

Filters were freeze-dried and then determined by an Elemental Analyzer (Thermo Flash 2000)-Isotope Ratio Mass Spectrometer (Thermo-MAT253) to determine the natural and tracer-enriched ^{15}N abundances. The calculation formula of NFR is as follows (Mohr et al., 2010):

$$NFR = \frac{(A_{PN}^{final} - A_{PN}^{t=0})}{(A_{N_2} - A_{PN}^{t=0})} \times \frac{1}{\Delta t}\left(\frac{PN_f + PN_0}{2}\right)$$

where A = atom% ^{15}N in the particulate organic nitrogen (PN) or dissolved N_2 at the final or beginning (t = 0) of incubation, Δt is the incubation time (d), A_{N2} represents the nitrogen substrate in the system at the beginning of the culture. The formula is as follows:

$$A_{N_2}(\%) = \left(\frac{A_S \times V_S + A_{atm} \times C \times V_b}{V_s + C \times V_b}\right) \times 100$$

where A_{atm} and A_S are the atomic percentages of ^{15}N in atmospheric N_2 (0.366%) and in the added ^{15}N tracer (98%), V_b and V_S are the volumes of the culture system (L) and the ^{15}N tracer (mL), C is the N_2 concentration in the culture water.

2.4 Statistical analysis

Pearson correlation analysis using SPSS 16.0 was used to determine the relationships among the dMo, dMn, Chl-*a*, nutrients, NFR, relative abundance of cyanobacterial, N_2 fixation functional bacteria and nitrate reduction functional bacteria in the BS and YS. P< 0.05 (two-tailed) values were considered significant correlations. Origin 2021 and Ocean Date View 2021 ware used to plot the data.

3 Results

3.1 Dissolved Mo and Mn

The dMo had similar concentration ranges between surface (76.4 ± 19.2 nmol L^{-1}) and bottom (74.6 ± 22.4 nmol L^{-1}) seawaters in the BS and YS. The lowest dMo values (68.9 ± 17.0 nmol L^{-1} in surface and 64.5 ± 19.1 nmol L^{-1} in bottom) were in the BS, while the highest dMo concentrations (95.9 ± 21.0 nmol L^{-1} in surface, and 94.9 ± 19.2 nmol L^{-1} in bottom) appeared in north of the SYS (near 36°N; Figure 2A). In the YSCW, the dMo concentrations in surface seawaters were slightly higher than that in bottom ones, but it showed the opposite trend in the other areas (Table S1).

The dissolved Mn (dMn) concentrations in surface seawaters (1.06 ± 1.87 μmol L^{-1}) were higher than that in bottom seawaters (0.52 ± 0.89 μmol L^{-1}; Figure 2B). In surface seawaters, the highest dMn values appeared at surface above the YSCW (2.45 ± 2.32 μmol L^{-1}) and station (1.50 ± 2.36 μmol L^{-1}) in 36°N section, followed by the nearshore station. In bottom seawaters, the higher dMn values occurred at nearshore of the SYS.

3.2 Hydrochemical characteristics

The temperature in surface seawaters (19.1 ± 2.1°C) was higher than that in bottom seawaters (16.7 ± 4.1°C) in the BS and YS in autumn. However, the temperature in bottom seawaters showed abnormally low values (10.4 ± 1.0°C) in the YSCW (Figure 3A). The salinity in surface seawaters (30.62 ± 1.65) was lower than that in bottom seawaters (31.16 ± 0.90) in the BS and YS. There were abnormally high salinity values (32.37 ± 0.41) in bottom seawaters of the YSCW (Figure 3B). The pH in surface seawaters (8.12 ± 0.11) was higher than that in bottom seawaters (8.05 ± 0.06) in the BS and YS. The relatively high pH in surface seawaters appeared at nearshore and above the YSCW (Figure 3C). The DO concentrations in surface seawaters (7.5 ± 0. 7 mg L^{-1}) was higher than that in bottom seawaters (7.0 ± 0.6 mg L^{-1}) in the BS and YS (Figure 3D). There were abnormally low pH (8.07 ± 0.05) and DO values (6.3 ± 0.3 mg L^{-1}) in bottom seawaters of the YSCW. The Chl-*a* concentrations in surface seawaters (2.10 ± 4.00 μg L^{-1}) was higher than that in bottom seawaters (0.98 ± 0.86 μg L^{-1}) in the BS and YS. The Chl-*a* concentrations decreased from the BS to the NYS and to the SYS and from nearshore to the outer seas (Figure 3E; Table S2).

3.3 Inorganic nutrients

The nutrient concentrations in surface and bottom seawaters of the BS and YS were examined (Figure 4). Concentrations of DIN, PO_4-P and SiO_3-Si in surface seawaters (DIN: 3.12-23.0 μmol L^{-1}; PO_4-P: 0.08-0.61 μmol L^{-1}; SiO_3-Si: 1.29-12.7 μmol L^{-1}) were lower than that in bottom seawaters (DIN: 3.15-24.8 μmol L^{-1}; PO_4-P: 0.04-1.81 μmol L^{-1}; SiO_3-Si: 1.12-15.6 μmol L^{-1}) in the BS and YS in autumn (Table S1). NH_4-N and NO_3-N were the main forms of DIN, accounting for 55% and 41%. PO_4-P, DIN and SiO_3-Si concentrations generally presented the highest values in the BS, followed by the NYS and the SYS. Besides, they also displayed higher values in the YSCW. Outside the YSCW region, nutrients displayed negative correlations with salinity in the SYS, but only PO_4-P presented a relatively conservative behavior ($r=-0.546$, $p<0.01$).

3.4 N_2 fixation rates and cyanobacteria abundances

The NFRs and relative abundances of cyanobacteria in surface seawaters of the BS and YS were determined. The NFRs were 0.11-1.05 nmol N L^{-1} d^{-1}. The highest NFRs were in the SYS (0.55 ± 0.27 nmol N L^{-1} d^{-1}), followed by the NYS (0.42 ± 0.09 nmol N L^{-1} d^{-1}) and the BS (0.13 ± 0.17 nmol N L^{-1} d^{-1}; Figure 5A). The highest NFR appeared in north of the SYS (near 36°N). Similarly, the highest relative abundances of cyanobacteria were in the SYS (27.0 ± 19.3%), followed by the NYS (18.7 ± 10.1%) and BS (7.0 ± 10.2%), with the highest values in north of the SYS (near 36°N; Figure 5B).

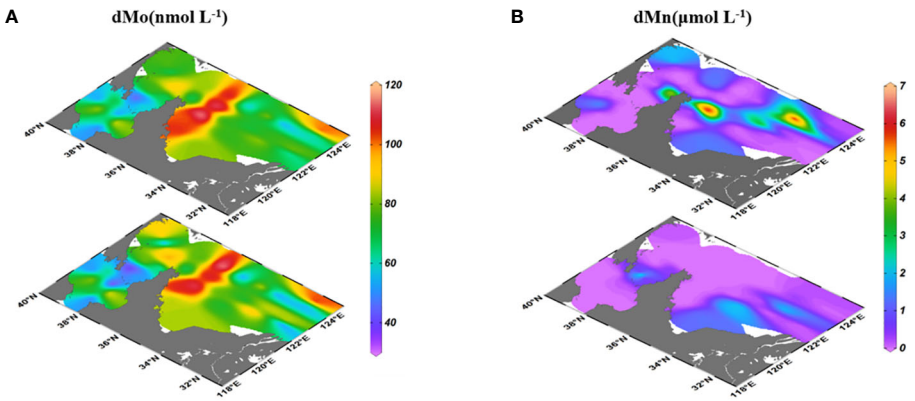

FIGURE 2
Distributions of dMo **(A)** and dMn **(B)** in surface and bottom seawaters of the BS and YS.

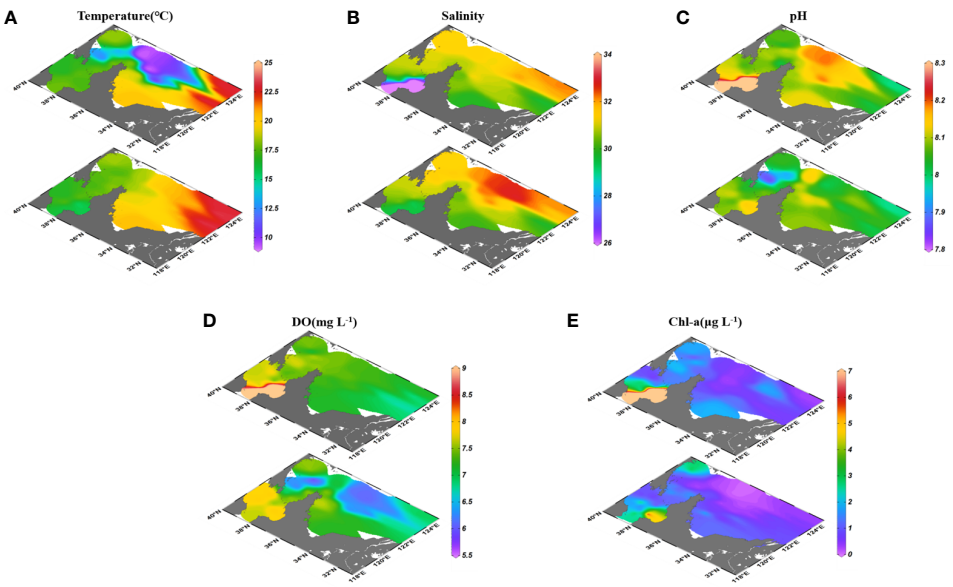

FIGURE 3
Distributions of hydrochemical parameters temperature **(A)**, salinity **(B)**, pH **(C)**, DO **(D)** and Chl-*a* **(E)** in surface and bottom seawaters of the BS and YS.

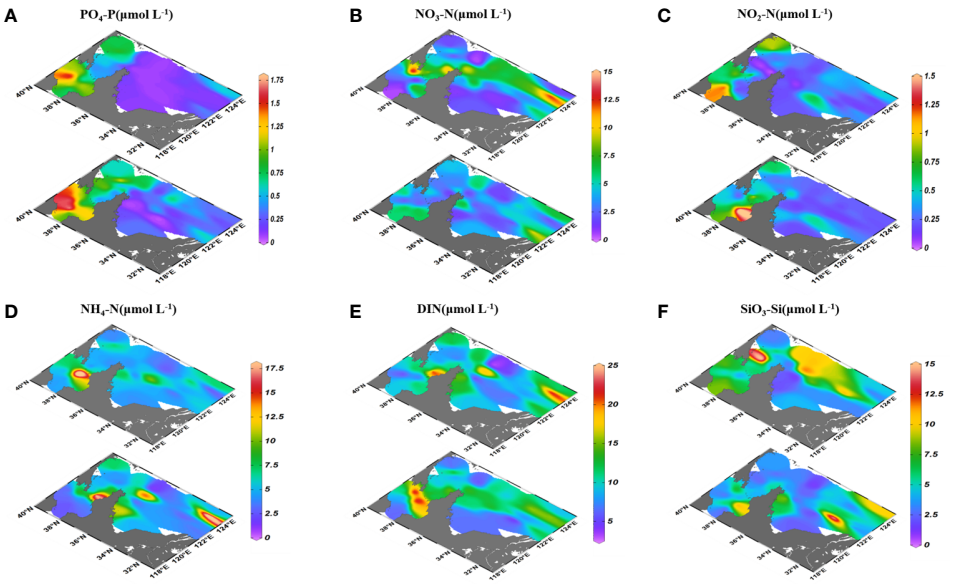

FIGURE 4
Distributions of PO_4-P **(A)**, NO_3-N **(B)**, NO_2-N **(C)**, NH_4-N **(D)**, DIN **(E)** and SiO_3-Si **(F)** in surface and bottom seawaters of the BS and YS.

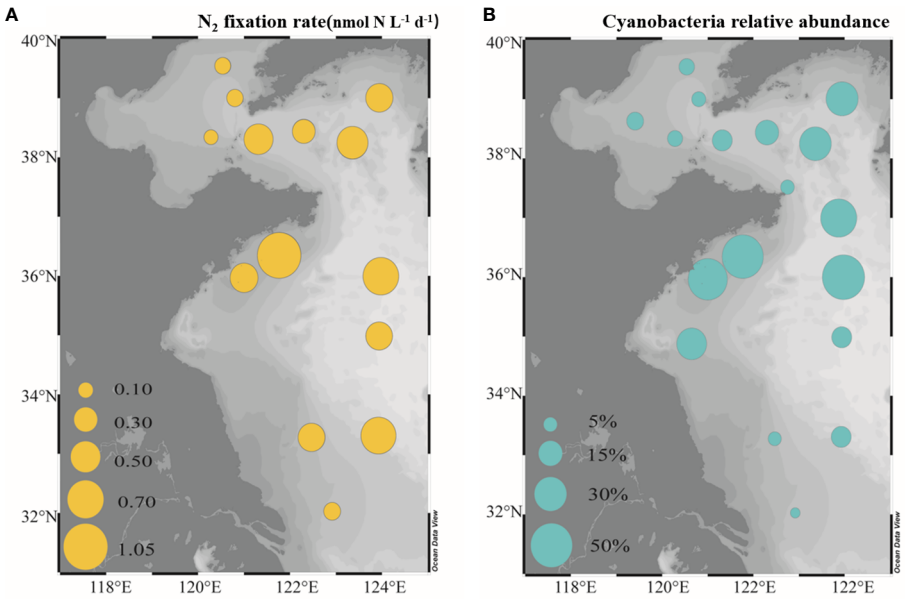

FIGURE 5
Distribution of N_2 fixation rates **(A)** and the relative abundance of cyanobacteria **(B)** in surface seawaters of the BS and YS.

4 Discussion

4.1 Nonconservative behavior of dMo

Despite its biological requirement, Mo generally shows a conservative behavior independent of marine biological activities (Collier, 1985; Prange and Kremling, 1985). The conservative behavior of dMo in some estuaries also were found (Strady et al., 2009; Waeles et al., 2013). In these estuaries, dMo concentrations showed a closely liner relationship with salinity due to the dilution of Mo-rich seawaters by river waters with lower biological activity (Howarth and Cole, 1985; Strady et al., 2009). Differently, dMo concentrations in our study area had no correlation with salinity (Figure 6), indicating that conservative mixing with river waters was not the dominating process and thus the nonconservative property of dMo in the BS and YS. Most of dMo concentrations in the BS and YS were below a conservative mixing and were depleted by more than ~30%. Significant depletion up to 40-50 nmol L^{-1} of dMo was even seen in the BS and NYS regions. The dMo removal was attributed to scavenging by abiogenic and/or biogenic particles in the mixing process (Prange and Kremling, 1985). The lowest dMo concentration (49.1 nmol L^{-1}) occurred in station (S=23.6) near the Yellow River in the BS, which was lower than its concentration in conservative estuaries with the same salinity (Rahaman et al., 2010; Waeles et al., 2013). This seems to suggest that although the riverine input played an important role in dMo distribution there, there still was other reasons for dMo depletion. For example, the biological uptake and complexation with organic matter or incorporation into sediment aggregates could contribute to the dMo removal (Head and Burton, 1970; Dellwig et al., 2007).

In contrary, some dMo concentrations in the BS and YS were higher than those expected for a conservative mixing. The

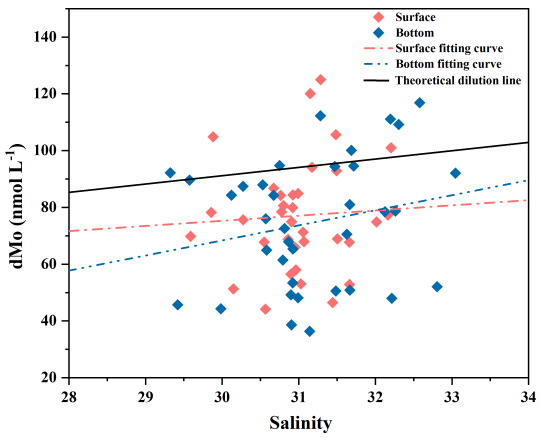

FIGURE 6
The plot of dMo against salinity in the BS and YS. Blue and red dots respect values in surface and bottom seawaters, respectively. The black line represents the theoretical mixing line between river water (dMo = 1 nmol L^{-1}) and ocean water (dMo = 105 nmol L^{-1}) at salinity of 35.

addition of dMo mainly appeared at 36 °N section and bottom seawaters in south of the SYS. It has been suggested that the addition of Mo resulted from its desorption from particles or release from bottom sediments when bottom redox condition changed from reducing to oxic (Dalai et al., 2005; Morford et al., 2007; Smedley and Kinniburgh, 2017). Due to the significant differences in the hydrochemistry and biological activities among the BS, NYS and SYS, the main control factors of nonconservative Mo behavior in these three sea areas were different. This will be discussed in the below section.

Compared with horizontal distribution, vertical difference of dMo concentrations was small, suggesting the influencing factors at different depth of same station was more similar than regional differences due to the relatively shallow depths of the study area. Compared with other sea areas in the world (Table 1), dMo concentrations in the BS and YS (36.4-125.0 nmo L^{-1}) were similar to the nonconservative dMo in other estuaries (Khan and Van Den Berg, 1989; Dalai et al., 2005; Dellwig et al., 2007; Archer and Vance, 2008; Rahaman et al., 2010; Mohajerin et al., 2016; Schneider et al., 2016; Smedley and Kinniburgh, 2017), but lower than the open ocean (Firdaus et al., 2008; Ho et al., 2018) and higher than the euxinic seas (Neal and Robson, 2000; Rahaman et al., 2010; Chen et al., 2014).

4.2 The physics and chemistry processes involved into Mo cycling

4.2.1 The riverine dilution and particle adsorption of dMo

The increase of dMo from the coast toward offshore was mainly observed in the BS, especially off the Yellow River estuary. The area off the estuary was characterized by low dMo concentrations mainly due to the river discharge from the Yellow River with low Mo concentration. Previous study had also attributed the occurrence of dMo depletion in estuary to the dilution effect of freshwater (Waeles et al., 2013). Although we did not determine dMo concentrations in the Yellow River, it has been suggested that average dMo concentration in world rivers was ~12.6 nmol L^{-1} (Linnik et al., 2015). Besides, in autumn, under the influence of the northwest monsoon, a large amount of the BS water flows into the NYS through the Bohai Strait (Zhang et al., 2018), resulting in the lower dMo in the Bohai Strait.

The horizontal and vertical differences of dMo could not be attributed solely to the freshwater dilution effect. The importance of Mn cycling to Mo behavior has been found. It has been suggested that the removal of MoO_4^{2-} from surface seawaters was associated with Mn oxidation and adsorption by freshly formed MnO_x phases, which would settle on the sediments (Dellwig et al., 2007). In this study, both dMo and dMn presented the highest values in the SYS, followed by the NYS, and the lowest in the BS. This distribution was opposite to DO concentrations, likely suggesting that high DO level might favor the formation of Mn oxides and associated Mo adsorption. There was a significant positive correlation ($r=0.55$, $p<0.01$; Figure 7A) between dMo and dMn in the BS and YS except for the area with extremely high dMn values. The more significant correlation was found in the BS ($r=0.89$, $p<0.01$; Figure 7B), suggesting that the role of the adsorption to inorganic particles to remove dMo in the BS was more important than in the YS.

4.2.2 Effect of seasonal YSCW on dMo

The YSCW is an important current, supplying abundant nutrients to upper seawaters and stimulating the algal blooms (Guo et al., 2020). Thus, it is necessary to discuss the influence of the YSCW on dMo depletion. The dMo concentrations in both surface and bottom seawaters displayed low values in the YSCW. However, the slightly higher dMn values in surface seawaters than bottom seawaters, indicating that the adsorption by inorganic particles with MnO_x may be not the main reason for Mo depletion there.

The YSCW is a seasonal current, which usually appears in summer and autumn. It has low DO, low temperature and high salinity (Wang et al., 2014). The same phenomenon was observed in this study (Figure 8). Mo as a redox-sensitive element, seasonal DO change has an important influence on the dynamics of dMo. Particularly, the relatively low DO in the YSCW contributed to the Mo removal from bottom seawaters to sediments. Morford et al. (2007) has found that Mo could be sequestered into sediments along

TABLE 1 Dissolved molybdenum concentrations in estuaries and open seas in the world.

Sea area	dMo (nmo L^{-1})	References
Tamar Estuary, England	15.0-89.9	(Khan and Van Den Berg, 1989)
Chao Phraya Estuary, Thailand	3.20-117	(Dalai et al., 2005)
Estuary of Wadden Sea, Germany	82.3-156	(Dellwig et al., 2007)
Itchen Estuary, England	4.79-117	(Archer and Vance, 2008)
Multiple estuaries, India	1.00-89.6	(Rahaman et al., 2010)
Mississippi Estuary, United States	9.10-55.9	(Mohajerin et al., 2016)
Elbe, Rhine and Weser estuaries	20.0-125	(Schneider et al., 2016)
Oxic open water,	96.9-108	(Firdaus et al., 2008; Ho et al., 2018)
Euxinic Black Sea	7.00-39.0	(Neal and Robson, 2000;Nagler et al., 2011)

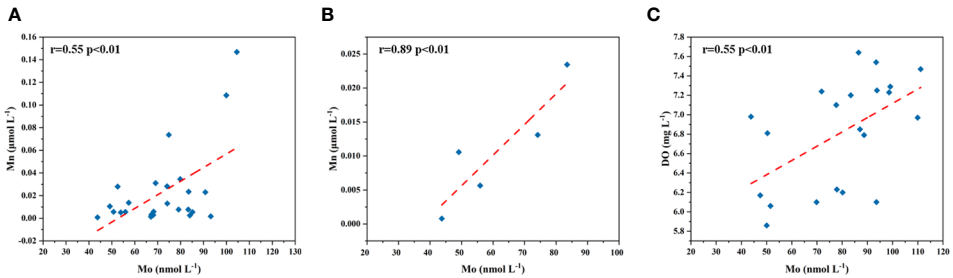

FIGURE 7
Correlations between dMo and dMn concentrations in surface seawaters of the BS and YS **(A)** and that of the BS **(B)**, and correlation between DO and dMo concentrations in bottom seawaters of the YS **(C)**.

the western Indian continental shelf when seasonal oxygen minimum zone appeared. However, sedimentary Mo can be later released to bottom seawater when oxic condition appeared. The strong upwelling in this region can carry bottom Mo to the surface (Smedley and Kinniburgh, 2017). Sulu-Gambari et al. (2017) found a clear Mo enrichment in the upper sediment layer in anoxic summer and autumn, whereas small Mo enrichment in oxic winter and spring. Our results showed that the lower bottom dMo concentrations in the YSCW was consistent with the lower DO concentrations, suggesting that dMo in bottom seawaters moved into sediments or the release of dMo from porewater was restricted under low DO levels in autumn. Within sediments, MoO_4^{2-} can be fixed by thiol and buried as sulfide in high sulfide sedimentary environment, resulting in Mo enrichments in marine sediments (Brumsack, 2006). The upward transport of dMo was also prevented due to the water stratification in the YSCW. This part of oxidative Mo (MoO_4^{2-}) may be released into seawaters *via* the sediment/water interface when the YSCW disappeared in winter and spring. This speculation requires further confirmation. There was a significant correlation between DO and dMo concentrations in bottom seawaters of the YS (except for stations near 36°N and the Bohai Strait) (r=0.55, p<0.01; Figure 7C), further suggesting that the higher DO level favored the dMo release from sediment while lower DO attenuated this process.

4.3 The biological processes involved into Mo cycling

4.3.1 Phytoplankton utilization of dMo

Mo exists in >60 enzyme cofactors (Stiefel, 1996) and involved in catalyzing key processes in the global carbon, sulfur and nitrogen cycles (Mendel, 2009). Both phytoplankton

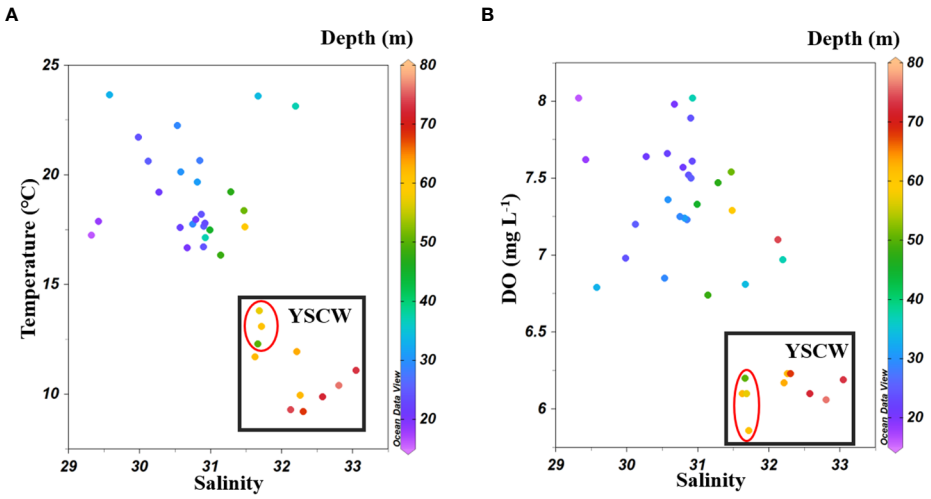

FIGURE 8
Scatter plots of bottom sea water salinity and temperature **(A)**, and salinity and DO **(B)** in the BS and YS. The Yellow Sea Cold Water (YSCW) was boxed in black rectangle and stations in the NYS affected by YSCW circled in red oval.

and heterotrophs require Mo participating in metabolic activities (Glass et al., 2012). It has been found that the Mo concentrations in phytoplankton (Ho et al., 2003) and bacterial (Barton et al., 2007) cells were far higher than in seawater, suggesting that the high abundances of phytoplankton and bacteria may consume a large amount of dMo, and may cause the dMo removal in seawater (Wang et al., 2016). Especially, the more depleted dMo can occur in phytoplankton blooms (Kowalski et al., 2009). Our results showed that more depleted dMo concentrations appeared in the BS and the NYS, where Chl-*a* concentrations were higher. The negative correlation of dMo with Chl-*a* (except for two extremely high Chl-*a* in the BS) (r= -0.45, p<0.01; Figure 9A) in the BS and YS indicated that high primary productivity likely played an important role in the dMo removal. Their correlations were most significant in the BS (r= -0.97, p<0.01; Figure 9B), followed by the NYS (r=-0.60, p<0.01; Figure 9C) and the SYS (r= -0.42, p<0.01; Figure 9D), suggesting that the uptake of phytoplankton was more important removal mechanism for dMo in the BS than the YS. The dMo removal by phytoplankton utilization also has been found in other sea areas, such as the Southampton estuary (Head and Burton, 1970), the Taiwan Strait (Wang et al., 2016), and East Pacific Zonal Transect (Ho et al., 2018). However, Chl-*a* and nutrients (especially PO_4-P and SiO_3-Si) might have the obvious low values in 36 °N section, corresponding to the conservative dMo concentrations, suggesting that low biological activity had little effect on the Mo removal there.

According to the estimation method of Wang et al. (2016), Chl-*a* level of 5 μmol L^{-1} as 5 × 10^6 cells mL^{-1} and cellular Mo of 5.3 μmol L^{-1} in phytoplankton (Ho et al., 2003) were used to estimate the depletion of dMo by phytoplankton. The whole BS and YS was assumed to be an enclosed system in autumn, and Chl-*a* values in the BS and YS and were used. The depletion of dMo and biological removal amount of Mo were estimated to be up to 50 nmol L^{-1} with an average of 20 nmol L^{-1} and 8.9×10^7 mol if a bloom continued for 1 month. The biological removal amount was obtained by multiplying the depleted Mo concentration with the water volume (457×10^{10} m^3) in the upper layer of the BS and YS (from surface to 10 m).

4.3.2 Coupling of dMo to nitrogen cycling

Mo is key for microbial N_2 and nitrate assimilation due to its presence in nitrogenase and nitrate reductase (the first step in NO_3^- assimilation). Marine and freshwater diazotrophic cyanobacteria

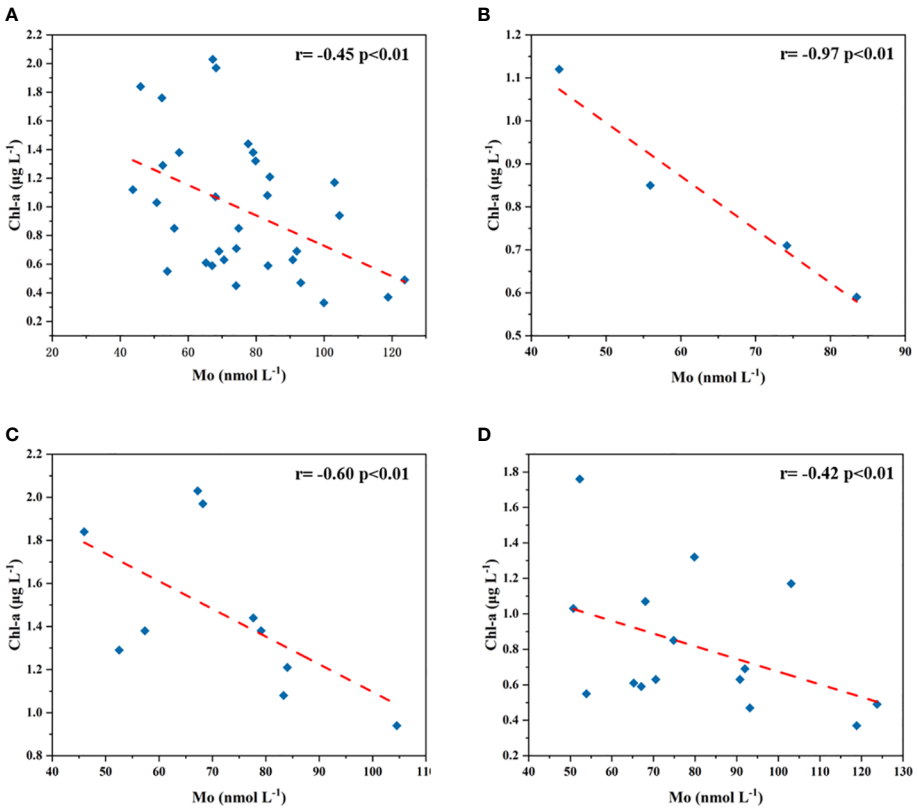

FIGURE 9
Correlations of dMo with Chl-*a* in the BS and YS **(A)**, the BS **(B)**, the NYS **(C)** and the SYS **(D)**.

use a Mo-dependent enzyme, nitrogenase (*Nif*) for N_2 fixation. The study on Mo limitation to N_2 fixation focuses on freshwaters, due to its low dMo concentrations (<20 nmol L^{-1}) and oligotrophic levels. It has been suggested that *Anabaena* had optimal growth at 50-2000 nmol L^{-1} of dMo concentrations (Wolfe, 1954; Tersteeg et al., 1986; Attridge and Rowell, 1997). Mo at 1-5 nmol L^{-1} could limit N_2 fixation (Vasconcelos and Fay, 1974; Zerkle et al., 2006; Glass et al., 2012). However, Mo has long been considered as a potential limiting factor for marine N_2 fixation due to its high seawater value. Several Mo addition experiments in conservative seawaters showed that N_2 fixation rate did not change significantly (Paulsen et al., 1991; Marino et al., 2003). Sulfate inhibition has been considered as an important reason for N_2 fixation role of Mo due to their similar size and stereochemistry (Howarth et al., 1988). In this study, dMo concentrations in seawaters were higher than that in freshwaters, even higher than the Mo limitation in pure cultures, but they were lower than the conservative concentration (~105 nmol L^{-1}). It is unclear about the Mo effect on N_2 fixation in the depleted Mo coastal waters. N_2 fixating and nitrate assimilating cyanobacteria dependent on Mo have been found in the coastal and marine waters, such as *Nostoc* sp. CCMP 2511 (Glass et al., 2010), *Aphanizomenon* sp. (Walve and Larsson, 2007), *Nodularia spumigena* (Walve and Larsson, 2007), *Trichodesmium erythraeum* strain IMS101 (Tuit et al., 2004), *Trichodesmium* (Tuit et al., 2004; Nuester et al., 2012), *Crocosphaera watsonii* strain WH8501 (Tuit et al., 2004). They have Mo:C of 0.2-132, with the highest in *Nostoc* sp. CCMP 2511 (0.2-132) and *Trichodesmium* (9-54). In order to understand the interaction between Mo and N_2 fixation, the NFRs and the relative abundances of cyanobacteria were determined in this study. NFRs and the relative abundances of cyanobacteria presented opposite distributions to Chl-*a*, hinting the competitive growth between phytoplankton and cyanobacteria. The NFRs had a positive correlation with the relative abundance of cyanobacteria (r=0.77, p<0.01; Figure 10A), suggesting that heterocystous cyanobacteria (HC) may be the dominant species of cyanobacteria. The growth of HC likely was more dependent on the availability of Mo than non-HC due to the role of HC in inorganic nitrogen assimilation (Glass et al., 2012). The higher NFRs and relative abundances of cyanobacteria appeared in the SYS with the relatively low nutrient. Particularly, NH_4-N had an opposite distribution to NFRs (r= -0.57, p<0.01; Figure 10B), suggesting that lower NH_4-N was more conducive to N_2 fixation. The depleted dMo concentrations (<90 nmol L^{-1}, except for the BS) negatively correlated with NFRs (r=-0.47, p<0.05; Figure 10C), indicating that the potential effect of Mo on N_2 fixation in the most stations of the YS with the depleted dMo. The relatively conservative dMo in 36 °N section corresponded to higher NFRs and lower Chl-*a*, indicating that phytoplankton uptake is the main removal mechanism of dMo with HC nitrogenase utilization playing a minor role.

Mo is also required for reduction of NO_3^- to NO_2^- through protein nitrate reductase. It has been found that low freshwater Mo concentrations may limit the function of Mo-based nitrogenase and nitrate reductase, thus slowing the growth of cyanobacteria (Glass et al., 2010). In our study, the lower dMo in surface seawaters corresponding to NO_2-N maxima within the BS, and while the dMo maxima corresponding to the lower NO_2-N in 36°N of the YS.

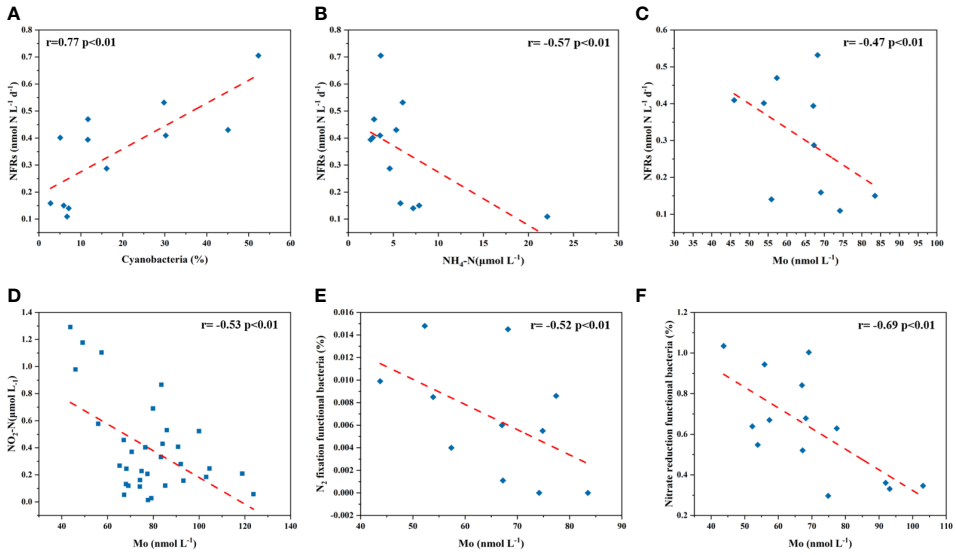

FIGURE 10
Correlations of the relative abundance of cyanobacteria with NFRs **(A)**, NH_4-N with NFRs **(B)** in the BS and YS, dMo (<90 nmol L^{-1}) with NFRs in the YS **(C)**, dMo with NO_2-N **(D)**, dMo with N_2 fixation functional bacteria **(E)** and dMo with nitrate reduction functional bacteria **(F)** in the BS and YS.

NO_2-N concentrations negatively correlated with dMo concentrations (r= -0.53, p<0.01; Figure 10D). These correlations suggested that dMo was involved in nitrate reduction in the study area.

The function prediction of N_2 fixation and nitrate reduction among 16s rRNA data was performed by the FAPROTAX software, which maintains a functional classification database based on species information (Louca et al., 2016). Prediction results showed that the relative abundances of bacteria with N_2 fixation and nitrate reduction genes were small, accounting for 0.001-0.01% and 0.2-1.1% of total bacterial, respectively. The highest N_2 fixation bacteria abundance occurred in south of the SYS (Figure 11), corresponding to the lower dMo and Chl-*a* and higher NFRs. The highest nitrate reduction bacteria abundance occurred in the BS (Figure 11), corresponding to the lower dMo and highest NO_2-N. The dMo concentrations negatively correlated with the relative abundances of bacteria with N_2 fixation (r= -0.52, p<0.01; Figure 10E) and nitrate reduction function (r= -0.69, p<0.01; Figure 10F), suggesting the involving of Mo in N cycling in the BS and SYS. Based on Chl-*a*, nutrients, NFR, function prediction and dMo data, it can be suggested that both the utilization of phytoplankton and nitrate reductase were the main biological pathways of dMo removal in the BS, the utilization of phytoplankton, nitrate reductase and HC nitrogenase were the main biological approaches of dMo removal in the NYS, nitrogenase utilization was the main biological pathway of dMo removal in south of the SYS, whereas dMo in north of the SYS (near 36 °N section) was not affected by biological activity. According to biological abundance, the contribution of biological activities to depleted dMo in the sea area affected by two to three biological activities was in the order of phytoplankton uptake, nitrate reductase and nitrogenase utilization. It has been shown that N_2 fixation required more Mo than NO_3-N assimilation in freshwater (Attridge and Rowell, 1997; Glass et al., 2010; Glass et al., 2012). The contrary phenomenon was found in our study. It seems that although depleted dMo in the BS and YS, its concentration was still higher than freshwater, resulting in the less limitation on N_2 fixation.

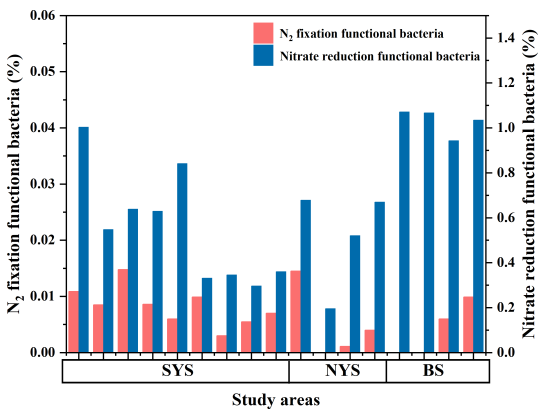

FIGURE 11
The relative abundances of bacteria with N_2 fixation and nitrate reduction function. The function prediction was performed by the FAPROTAX software based on 16s rRNA data.

5 Conclusions

Molybdenum behavior and it involving into nitrogen cycling in the BS and YS were studied. DMo concentrations in the BS and YS (except for 36 °N section) were significantly below those expected for a conservative mixing, indicating nonconservative behavior of dMo. The removal pathways of dMo in the BS and YS included scavenging by Mn-oxides, upward transport block due to water stratification and sediment Mo enrichment in low DO level of the YSCW, phytoplankton uptake and involving in N cycling. Based on the hydrochemical and biological data, it can be concluded that the combined effect of inorganic particle adsorption and biological utilization, especially phytoplankton and nitrate reductase utilization, was the removal mechanism of dMo in the BS and NYS. Biological uptake, especially nitrogenase utilization, was the main removal pathway of dMo in south of the SYS. These removal mechanisms induced the depleted dMo in the BS and YS (except for north of the SYS near 36°N section). The relatively conservative Mo in the 36°N section corresponding to the higher dMn and NFRs, and the lower Chl-*a* and NO_2-N, suggesting it involving in N_2 fixation. However, the nitrogenase utilization of dMo was small due to low cyanobacteria abundance.

Data availability statement

The datasets presented in this study are available in the NCBI SRA repositories. The names of the repository/repositories and accession number(s) can be found below: SRR22378289–SRR22378306.

Author contributions

JF, methodology, conceptualization, formal analysis, investigation, and writing original draft. LD, methodology, conceptualization, resources, writing original draft, review and editing, and supervision. MY, formal analysis, and investigation. HY and XL, formal analysis. All authors contributed to the article and approved the submitted version.

Funding

This work was supported by the National Natural Science Foundation of China (No. 41976037), Shandong Provincial

Natural Science Foundation (ZR2020YQ28), the Taishan Scholars Program, Wenhai Program of QNLM (NO. 2021WHZZB0903), Yantai "Double Hundred Plan" funding project, and National Natural Science Foundation of China (No. 41906035). Samples were collected onboard of R/V *Lan Hai 101* implementing the open research cruise NORC2021-01 supported by NSFC Shiptime Sharing Project (No. 42049901).

Conflict of interest

The authors declare that the research was conducted in the absence of any commercial or financial relationships that could be construed as a potential conflict of interest.

Publisher's note

Supplementary material

The Supplementary Material for this article can be found online at: https://www.frontiersin.org/articles/10.3389/fmars.2022.1094846/full#supplementary-material

References

Archer, C., and Vance, D. (2008). The isotopic signature of the global riverine molybdenum flux and anoxia in the ancient oceans. *Nat. Geosci.* 1, 597–600. doi: 10.1038/ngeo282

Attridge, E. M., and Rowell, P. (1997). Growth, heterocyst differentiation and nitrogenase activity in the cyanobacteria *Anabaena variabilis* and *Anabaena cylindrica* in response to molybdenum and vanadium. *New Phytol.* 135, 517–526. doi: 10.1046/j.1469-8137.1997.00666.x

Audry, S., Blanc, G., Schafer, J., Guerin, F., Masson, M., and Robert, S. (2007). Budgets of Mn, cd and Cu in the macrotidal gironde estuary (SW France). *Mar. Chem.* 107, 433–448. doi: 10.1016/j.marchem.2007.09.008

Barton, L. L., Goulhen, F., Bruschi, M., Woodards, N. A., Plunkett, R. M., and Rietmeijer, F. J. M. (2007). The bacterial metallome: Composition and stability with specific reference to the anaerobic bacterium *Desulfovibrio desulfuricans*. *Biometals* 20, 291–302. doi: 10.1007/s10534-006-9059-2

Beck, M., Dellwig, O., Fischer, S., Schnetger, B., and Brumsack, H. J. (2012). Trace metal geochemistry of organic carbon-rich watercourses draining the NW German coast. *Estuar. Coast. Shelf Sci.* 104, 66–79. doi: 10.1016/j.ecss.2012.03.025

Brumsack, H. J. (2006). The trace metal content of recent organic carbon-rich sediments: Implications for Cretaceous black shale formation. *Palaeogeogr. Palaeoclimatol. Palaeoecol.* 232, 344–336. doi: 10.1016/j.palaeo.2005.05.011

Bryan, J. R., Riley, J. P., and Williams, P. J. L. (1976). Winkler procedure for making precise measurements of oxygen concentration for productivity and related studies. *J. Exp. Mar. Biol. Ecol.* 21, 191–197. doi: 10.1016/0022-0981(76)90114-3

Chen, C. T. A. (2009). Chemical and physical fronts in the bohai, yellow and East China seas. *J. Mar. Syst.* 78, 394–410. doi: 10.1016/j.jmarsys.2008.11.016

Chen, J. B., Gaillardet, J., Bouchez, J., Louvat, P., and Wang, Y. N. (2014). Anthropophile elements in river sediments: Overview from the seine river, France. *Geochem. Geophys. Geosyst.* 15, 4526–4546. doi: 10.1002/2014gc005516

Collier, R. W. (1985). Molybdenum in the northeast pacific ocean. *Limnol. Oceanogr.* 30, 1351–1354. doi: 10.4319/lo.1985.30.6.1351

Dalai, T. K., Nishimura, K., and Nozaki, Y. (2005). Geochemistry of molybdenum in the chao phraya river estuary, Thailand: Role of suboxic diagenesis and porewater transport. *Chem. Geol.* 218, 189–202. doi: 10.1016/j.chemgeo.2005.01.002

Dellwig, O., Beck, M., Lemke, A., Lunau, M., Kolditz, K., Schnetger, B., et al. (2007). Non-conservative behaviour of molybdenum in coastal waters: Coupling geochemical, biological, and sedimentological processes. *Geochim. Cosmochim. Acta*71, 2745–2761. doi: 10.1016/j.gca.2007.03.014

Fay, P., and Fogg, G. E. (1962). Studies on nitrogen fixation by blue-green algae III. growth and nitrogen fixation in chlorogloea fritschii mitra. *Arch. Mikrobiol.* 42, 310–321. doi: 10.1007/bf00422048

Firdaus, M. L., Norisuye, K., Nakagawa, Y., Nakatsuka, S., and Sohrin, Y. (2008). Dissolved and labile particulate zr, hf, Nb, Ta, Mo and W in the western north pacific ocean. *J. Oceanogr.* 64, 247–257. doi: 10.1007/s10872-008-0019-z

Fischer, K., Barbier, G. G., Hecht, H. J., Mendel, R. R., Campbell, W. H., and Schwarz, G. (2005). Structural basis of eukaryotic nitrate reduction: Crystal structures of the nitrate reductase active site. *Plant Cell* 17, 1167–1179. doi: 10.1105/tpc.104.029694

Fowler, D., Pyle, J. A., Raven, J. A., and Sutton, M. A. (2013). The global nitrogen cycle in the twenty-first century: Introduction. *Philos. Trans. R. Soc B Biol. Sci.* 368, 20130165. doi: 10.1098/rstb.2013.0165

Glass, J. B., Axler, R. P., Chandra, S., and Goldman, C. R. (2012). Molybdenum limitation of microbial nitrogen assimilation in aquatic ecosystems and pure cultures. *Front. Microbiol.* 3, 1–11. doi: 10.3389/fmicb.2012.00331

Glass, J. B., Wolfe-Simon, F., Elser, J. J., and Anbar, A. D. (2010). Molybdenum-nitrogen co-limitation in freshwater and coastal heterocystous cyanobacteria. *L* 55, 667–676. doi: 10.4319/lo.2009.55.2.0667

Goldman, C. R. (1960). Molybdenum as a factor limiting primary productivity in castle lake, California. *Science* 132, 1016–1017. doi: 10.1126/science.132.3433.1016

Guo, S. J., Li, Y. Q., Zhang, C. X., Zhai, W. D., Huang, T., Wang, L. F., et al. (2014). Phytoplankton community in the bohai Sea and its relationship with environmental factors. *Mar. Sci. Bull.* 33, 95–105 doi: 10.11840/j.issn.1001-6392.2014.01.013

Guo, J. Q., Yuan, H. M., Song, J. M., Li, X. G., and Duan, L. Q. (2020). Hypoxia, acidification and nutrient accumulation in the yellow Sea cold water of the south yellow Sea. *Sci. Total Environ.* 745, 141050. doi: 10.1016/j.scitotenv.2020.141050

Head, P. C., and Burton, J. D. (1970). Molybdenum in some ocean and estuarine waters. *J. Mar. Biol. Assoc. U. K.* 50, 439–448. doi: 10.1017/s002531540000463x

Ho, P., Lee, J. M., Heller, M. I., Lam, P. J., and Shiller, A. M. (2018). The distribution of dissolved and particulate Mo and V along the US GEOTRACES East pacific zonal transect (GP16): The roles of oxides and biogenic particles in their distributions in the oxygen deficient zone and the hydrothermal plume. *Mar. Chem.* 201, 242–255. doi: 10.1016/j.marchem.2017.12.003

Ho, T. Y., Quigg, A., Finkel, Z. V., Milligan, A. J., Wyman, K., Falkowski, P. G., et al. (2003). The elemental composition of some marine phytoplankton. *J. Phycol.* 39, 1145–1159. doi: 10.1111/j.0022-3646.2003.03-090.x

Howarth, R. W., and Cole, J. J. (1985). Molybdenum availability, nitrogen limitation, and phytoplankton growth in natural waters. *Science* 229, 653–655. doi: 10.1126/science.229.4714.653

Howarth, R. W., Marino, R., Lane, J., and Cole, J. J. (1988). Nitrogen-fixation in fresh-water, estuarine, and marine ecosystems I.rates and importance. *Limnol. Oceanogr.* 33, 669–687. doi: 10.4319/lo.1988.33.4_part_2.0669

Khan, S. H., and Van Den Berg, C. M. G. (1989). The determination of molybdenum in estuarine waters using cathodic stripping voltammetry. *Mar. Chem.* 27, 31–42. doi: 10.1016/0304-4203(89)90026-1

Kowalski, N., Dellwig, O., Beck, M., Grunwald, M., Fischer, S., Piepho, M., et al. (2009). Trace metal dynamics in the water column and pore waters in a temperate tidal system: Response to the fate of algae-derived organic matter. *Ocean Dynami.* 59, 333–350. doi: 10.1007/s10236-009-0192-7

Linnik, P. N., Zhezherya, V. A., Linnik, R. P., Ignatenko, I. I., and Zubenko, I. B. (2015). Metals in surface water of Ukraine: The migration forms, features of distribution between the abiotic components of aquatic ecosystems, and potential bioavailability. *Russ. J. Gen. Chem.* 85, 2965–2984. doi: 10.1134/s1070363215130162

Liu, S. M., Li, L. W., and Zhang, Z. N. (2011). Inventory of nutrients in the bohai. *Continent. Shelf Res.* 31, 1790–1797. doi: 10.1016/j.csr.2011.08.004

Louca, S., Parfrey, L. W., and Doebeli, M. (2016). Decoupling function and taxonomy in the global ocean microbiome. *Science* 353, 1272–1277. doi: 10.1126/science.aaf4507

Marino, R., Howarth, R. W., Chan, F., Cole, J. J., and Likens, G. E. (2003). Sulfate inhibition of molybdenum-dependent nitrogen fixation by planktonic cyanobacteria under seawater conditions: A non-reversible effect. *Hydrobiologia* 500, 277–293. doi: 10.1023/a:1024641904568

Mendel, R. R. (2009). Cell biology of molybdenum. *Biofactors* 35, 429–434. doi: 10.1002/biof.55

Mohajerin, T. J., Helz, G. R., and Johannesson, K. H. (2016). Tungsten-molybdenum fractionation in estuarine environments. *Geochim. Cosmochim. Acta* 177, 105–119. doi: 10.1016/j.gca.2015.12.030

Mohr, W., Grosskopf, T., Wallace, D. W. R., and LaRoche, J. (2010). Methodological underestimation of oceanic nitrogen fixation rates. *PloS One* 5, 7. doi: 10.1371/journal.pone.0012583

Morford, J. L., and Emerson, S. (1999). The geochemistry of redox sensitive trace metals in sediments. *Geochim. Cosmochim. Acta* 63, 1735–1750. doi: 10.1016/s0016-7037(99)00126-x

Morford, J. L., Martin, W. R., Kalnejais, L. H., Francois, R., Bothner, M., Karle, I. M., et al. (2007). Insights on geochemical cycling of U, re and Mo from seasonal sampling in Boston harbor. *Geochim. Cosmochim. Acta* 71, 895–917. doi: 10.1016/j.gca.2006.10.016

Nagler, T.F., Neubert, N., Bottcher, M. E., Dellwig, O., and Schnetger, B. (2011). Molybdenum isotope fractionation in pelagic euxinia: Evidence from the modern Black and Baltic Seas. *Chem. Geol.* 289, 1–11. doi: 10.1016/j.chemgeo.2011.07.001

Nakagawa, Y., Takano, S., Firdaus, M. L., Norisuye, K., Hirata, T., Vance, D., et al. (2012). The molybdenum isotopic composition of the modern ocean. *Geochem. J.* 46, 131–141. doi: 10.2343/geochemj.1.0158

Neal, C., and Robson, A. J. (2000). A summary of river water quality data collected within the land-ocean interaction study: Core data for eastern UK rivers draining to the north Sea. *Sci. Total Environ.* 251, 585–665. doi: 10.1016/s0048-9697(00)00397-1

Nuester, J., Vogt, S., Newville, M., Kustka, A. B., and Twining, B. S. (2012). The unique biogeochemical signature of the marine diazotroph *Trichodesmium*. *Front. Microbiol.* 3. doi: 10.3389/fmicb.2012.00150

Paulsen, D. M., Paerl, H. W., and Bishop, P. E. (1991). Evidence that molybdenum-dependent nitrogen fixation is not limited by high sulfate concentrations in marine environments. *Limnol. Oceanogr.* 36, 1325–1334. doi: 10.4319/lo.1991.36.7.1325

Prange, A., and Kremling, K. (1985). Distribution of dissolved molybdenum, uranium and vanadium in baltic sea waters. *Mar. Chem.* 16, 259–274. doi: 10.1016/0304-4203(85)90066-0

Qu, P. P., Fu, F. X., Wang, X. W., Kling, J. D., Elghazzawy, M., Huh, M., et al. (2022). Two co-dominant nitrogen-fixing cyanobacteria demonstrate distinct acclimation and adaptation responses to cope with ocean warming. *Environ. Microbiol. Rep.* 14, 203–217. doi: 10.1111/1758-2229.13041

Rahaman, W., Singh, S. K., and Raghav, S. (2010). Dissolved Mo and U in rivers and estuaries of India: Implication to geochemistry of redox sensitive elements and their marine budgets. *Chem. Geol.* 278, 160–172. doi: 10.1016/j.chemgeo.2010.09.009

Reitz, A., Wille, M., Nagler, T. F., and de Lange, G. J. (2007). Atypical Mo isotope signatures in eastern Mediterranean sediments. *Chem. Geolo.* 245, 1–8. doi: 10.1016/j.chemgeo.2007.06.018

Robson, R. L., Eady, R. R., Richardson, T. H., Miller, R. W., Hawkins, M., and Postgate, J. R. (1986). The alternative nitrogenase of *Azotobacter chroococcum* is a vanadium enzyme. *Nature* 322, 388–390. doi: 10.1038/322388a0

Schneider, A. B., Koschinsky, A., Kiprotich, J., Poehle, S., and do Nascimento, P. C. (2016). An experimental study on the mixing behavior of Ti, zr, V and Mo in the Elbe, Rhine and weser estuaries. *Estuar. Coast. Shelf Sci.* 170, 34–44. doi: 10.1016/j.ecss.2015.12.002

Scott, C., Lyons, T. W., Bekker, A., Shen, Y., Poulton, S. W., Chu, X., et al. (2008). Tracing the stepwise oxygenation of the proterozoic ocean. *Nature* 452, 456–459. doi: 10.1038/nature06811

Smedley, P. L., and Kinniburgh, D. G. (2017). Molybdenum in natural waters: A review of occurence, distributions and controls. *Appl. Geochem.* 84, 387–432. doi: 10.1016/j.apgeochem.2017.05.008

Stiefel, E. I. (1996). Molybdenum bolsters the bioinorganic brigade. *Science* 272, 1599–1600. doi: 10.1126/science.272.5268.1599

Strady, E., Blanc, G., Schafer, J., Coynel, A., and Dabrin, A. (2009). Dissolved uranium, vanadium and molybdenum behaviours during contrasting freshwater discharges in the gironde estuary (SW France). *Estuar. Coast. Shelf Sci.* 8, 550–560. doi: 10.1016/j.ecss.2009.05.006

Sulu-Gambari, F., Roepert, A., Jilbert, T., Hagens, M., Meysman, F. J. R., and Slomp, C. P. (2017). Molybdenum dynamics in sediments of a seasonally-hypoxic coastal marine basin. *Chem. Geol.* 466, 627–640. doi: 10.1016/j.chemgeo.2017.07.015

Tersteeg, P. F., Hanson, P. J., and Paerl, H. W. (1986). Growth-limiting quantities and accumulation of molybdenum in *Anabaena oscillarioides* (Cyanobacteria). *Hydrobiologia* 140, 143–147. doi: 10.1007/bf00007567

Tuit, C. B., and Ravizza, G. (2003). The marine distribution of molybdenum. *Geochim. Cosmochim. Acta* 67, A495–A495.

Tuit, C., Waterbury, J., and Ravizza, G. (2004). Diel variation of molybdenum and iron in marine diazotrophic cyanobacteria. *Limnol. Oceanogr.* 49, 978–990. doi: 10.4319/lo.2004.49.4.0978

Valdivieso-Ojeda, J. A., Huerta-Diaz, M. A., and Delgadillo-Hinojosa, F. (2020). Non-conservative behavior of dissolved molybdenum in hypersaline waters of the Guerrero Negro saltern, Mexico. *Appl. Geochem.* 115, 104565. doi: 10.1016/j.apgeochem.2020.104565

Vasconcelos, L. D., and Fay, P. (1974). Nitrogen metabolism and ultrastructure in *Anabaena cylindrica* I. the effect of nitrogen starvation. *Arch. Microbiol.* 96, 271–279. doi: 10.1007/bf00590183

Waeles, M., Dulaquais, G., Jolivet, A., Thebault, J., and Riso, R. D. (2013). Systematic non-conservative behavior of molybdenum in a macrotidal estuarine system (Aulne-bay of Brest, France). *Estuar. Coast. Shelf Sci.* 131, 310–318. doi: 10.1016/j.ecss.2013.06.018

Walve, J., and Larsson, U. (2007). Blooms of Baltic Sea *Aphanizomenon* sp. (Cyanobacteria) collapse after internal phosphorus depletion. *Aquat. Microb. Ecol. Proc. Conf.* 49, 57–69. doi: 10.3354/ame01130

Wang, B., Hirose, N., Kang, B., and Takayama, K. (2014). Seasonal migration of the yellow Sea bottom cold water. *J. Geophys. Res-Oceans* 119, 4430–4443. doi: 10.1002/2014jc009873

Wang, D. L., Xia, W. W., Lu, S. M., Wang, G. Z., Liu, Q., Moore, W. S., et al. (2016). The nonconservative property of dissolved molybdenum in the western Taiwan strait: Relevance of submarine groundwater discharges and biological utilization. *Geochem. Geophys. Geosyst.* 17, 28–43. doi: 10.1002/2014gc005708

Wolfe, M. (1954). The effect of molybdenum upon the nitrogen metabolism of *Anabaena cylindrica* I. a study of the molybdenum requirement for nitrogen fixation and for nitrate and ammonia assimilation. *Ann. Bot.* 18, 299–308. doi: 10.1093/oxfordjournals.aob.a083396

Xin, M., Wang, B. D., Xie, L. P., Sun, X., Wei, Q. S., Mang, S. K., et al. (2019). Long-term changes in nutrient regimes and their ecological effects in the bohai Sea, China. *Mar. pollut. Bull.* 146, 562–573. doi: 10.1016/j.marpolbul.2019.07.011

Xu, B. C., Burnett, W., Dimova, N., Diao, S. B., Mi, T. Z., Jiang, X. Y., et al. (2013). Hydrodynamics in the yellow river estuary via radium isotopes: Ecological perspectives. *Cont. Shelf Res.* 66, 19–28. doi: 10.1016/j.csr.2013.06.018

Zehr, J. P., and Capone, D. G. (2020). Changing perspectives in marine nitrogen fixation. *Science* 368, eaay9514. doi: 10.1126/science.aay9514

Zerkle, A. L., House, C. H., Cox, R. P., and Canfield, D. E. (2006). Metal limitation of cyanobacterial N_2 fixation and implications for the precambrian nitrogen cycle. *Geobiology* 4, 285–297. doi: 10.1111/j.1472-4669.2006.00082.x

Zerkle, A. L., Scheiderich, K., Maresca, J. A., Liermann, L. J., and Brantley, S. L. (2011). Molybdenum isotope fractionation by cyanobacterial assimilation during nitrate utilization and N_2 fixation. *Geobiology* 9, 94–106. doi: 10.1111/j.1472-4669.2010.00262.x

Zhai, W. D. (2018). Exploring seasonal acidification in the yellow Sea. *Sci. China-Earth Sci.* 61, 647–658. doi: 10.1007/s11430-017-9151-4

Zhang, Z. X., Qiao, F. L., Guo, J. S., and Guo, B. H. (2018). Seasonal changes and driving forces of inflow and outflow through the bohai strait. *Cont. Shelf Res.* 154, 1–8. doi: 10.1016/j.csr.2017.12.012

Zheng, L. W., and Zhai, W. D. (2021). Excess nitrogen in the bohai and yellow seas, China: Distribution, trends, and source apportionment. *Sci. Total Environ.* 794, 148702. doi: 10.1016/j.scitotenv.2021.148702

frontiers | Frontiers in Marine Science

TYPE Original Research
PUBLISHED 18 January 2023
DOI 10.3389/fmars.2022.1110913

OPEN ACCESS

EDITED BY
Wen Zhuang,
Shandong University, China

REVIEWED BY
Ruifeng Zhang,
Shanghai Jiao Tong University, China
Qunqun Liu,
Yantai Institute of Coastal Zone Research (CAS), China

*CORRESPONDENCE
Jingling Ren
renjingl@ouc.edu.cn

SPECIALTY SECTION
This article was submitted to Marine Biogeochemistry, a section of the journal Frontiers in Marine Science

RECEIVED 29 November 2022
ACCEPTED 30 December 2022
PUBLISHED 18 January 2023

CITATION
Wang Z, Ren J, Xuan J, Liu S and Zhang J (2023) Distribution and off–shelf transport of dissolved manganese in the East China Sea. *Front. Mar. Sci.* 9:1110913. doi: 10.3389/fmars.2022.1110913

Distribution and off–shelf transport of dissolved manganese in the East China Sea

Zhaowei Wang[1], Jingling Ren[2,3]*, Jiliang Xuan[4], Sumei Liu[2] and Jing Zhang[5]

[1]College of Environmental Science and Engineering, Dalian Maritime University, Dalian, China, [2]Frontiers Science Center for Deep Ocean Multispheres and Earth System, and Key Laboratory of Marine Chemistry Theory and Technology, Ministry of Education, Ocean University of China, Qingdao, China, [3]Laboratory for Marine Ecology and Environmental Science, Qingdao National Laboratory for Marine Science and Technology, Qingdao, China, [4]State Key Laboratory of Satellite Ocean Environment Dynamics, Second Institute of Oceanography, Ministry of Natural Resources, Hangzhou, China, [5]State Key Laboratory of Estuarine and Coastal Research, East China Normal University, Shanghai, China

To gain a better understanding of the geochemical behavior of dissolved manganese (Mn) in the marginal seas with respect to distribution and exchange fluxes, more than 200 water samples were collected in the East China Sea (ECS) in May, August, and October of 2013. The concentration of dissolved Mn in the ECS ranged from 1.1 to 81.5 nM, with a gradual decrease with distance from the shore. Seasonal distribution of dissolved Mn varies significantly in the Changjiang estuary, mainly regulated by freshwater input from the Changjiang (Yangtze River) and redox variations. The ECS continental shelf is an important source of Mn for adjacent waters, and the export of Mn–rich coastal waters had an important effect on its re-distribution and internal cycling. The dynamic variation fluxes of water and dissolved Mn across the 100– and 200–m isobaths in the ECS were calculated with an aid of the Finite–Volume Coastal Ocean Model (FVCOM). The ECS continental shelf exported (5.69 $\pm$ 1.14) $\times$ 10^8 mol/yr of Mn into the East/Japan Sea from the Tsushima Strait. The Kuroshio surface waters receive an additional (1.02 $\pm$ 3.12) $\times$ 10^8 mol/yr of Mn from the ECS continental shelf through a cross–shelf exchange process, which could potentially affect dissolved Mn in the Northwest Pacific. Our data suggest that off-shelf transport from the ECS continental shelf is essential for understanding the biogeochemical cycles of trace metals in the Northwest Pacific Ocean and the East/Japan Sea.

KEYWORDS

dissolved manganese, transport, flux, East China Sea, redox

1 Introduction

Manganese (Mn) is an important tracer in the transport of terrestrial materials, yet it exists at micromolar levels in the ocean. Considerable data regarding the distribution of dissolved Mn has been obtained during the last 40 years, including in the Pacific Ocean (Landing and Bruland, 1987; Resing et al., 2015; Zheng et al., 2019), Indian Ocean (Saager

et al., 1989), Southern Ocean (Middag et al., 2011), Atlantic Ocean (Shiller, 1997; Wu et al., 2014; Middag et al., 2015), and Arctic Ocean (Colombo et al., 2020). Its distribution reflects external sources, scavenging removal away from these sources, as well as internal cycling in the ocean (Van Hulten et al., 2016). External sources, such as riverine input and eolian dust, are responsible for elevated concentrations of dissolved Mn in coastal waters and the surface layer (Sim and Orians, 2019). Mn can also enter the water column by reductive dissolution from anoxic or suboxic sediments (Heiser et al., 2001), lateral transportation from marginal sediments, or hydrothermal input (Middag et al., 2011). However, most of the existing Mn data comes from studies conducted in open waters and knowledge on the internal cycling and transport from marginal seas remains limited. Understanding the processes controlling the distribution of dissolved Mn in the marginal seas is therefore important for studying the cycle of trace metals in the ocean.

Marginal seas are located between continents and open oceans. Concentrations of dissolved Mn typically increase in marginal seas where waters receive abundant continental materials from rivers and coastlines (Aguilar-Islas and Bruland, 2006; Roy et al., 2013). The East China Sea (ECS) is one of important marginal seas in the North Pacific and has the largest continental shelf (Sherman and Tang, 1999). It is connected to the mainland China and linked with the Yellow Sea and the South China Sea. The Changjiang (Yangtze River) flows into the ECS from mainland China, forming an enormous plume of freshwater into the ECS (10^{12} m^3/yr, Zhang et al., 2007). The western boundary current (Kuroshio Waters, KW) flows along the ECS shelf edge, playing an important role in the exchange of material and heat energy in the China marginal seas (Guo et al., 2012). The ECS continental shelf has complex circulation systems under the effect of monsoons and is simultaneously influenced by both fluvial input and the Kuroshio incursion. The exchange between the ECS and the KW is an important process controlling the geochemical cycle of biogenic elements (Liu, 2000; Wang et al., 2021; Zhang et al., 2021a), which has received increased attention in the past decade. Therefore, a better understanding of the transport processes in the present study is important to the overall knowledge of marine biogeochemical cycles of Mn in the ECS.

On-shelf and off-shelf transport are crucial for marine processes, which have generated interest involving the geochemical budgets of biogenic elements (Ren et al., 2015; Ding et al., 2019; Zhang et al., 2021b). In this study, we examined the distribution and seasonal variations of dissolved Mn across the ECS from the eutrophic coastal waters to the oligotrophic KW. By using numerical simulations and tracer experiments, we calculated the dynamic exchange flux of dissolved Mn across the 100– and 200–m isobaths in the ECS to improve our understanding of the impact of off-shelf transport of terrestrial materials from the ECS to the western Pacific.

2 Materials and methods

2.1 Field sampling

Seawater samples from the ECS were collected at different seasons in 2013 from the *R/V* "Dongfanghong 2" (August 2013) and the *R/V* "Bei Dou" (May 2013 and October 2013) (Figure 1A). Restricted by ship time and logistical problems, a limited number of stations were monitored in May 2013 and October 2013. A CTD-rosette assembly with Niskin bottles (Model: Sea-Bird 911^{plus}) was used to measure the profiles of temperature, salinity, and dissolved oxygen (DO) in the water column at grid stations. The internal black rubber springs and "O" rings were replaced by silicon springs and silicon "O" rings. The silicon springs and silicon "O" rings were strictly cleaned with Milli-Q water before the cruise. All Niskin bottles were thoroughly cleaned by soaking in diluted acid (0.1 M HCl) at least one week, then filled with Milli-Q water and sealed by plastic bags before sampling. We conducted inter–calibration of different water sampling systems (MITLESS from MIT, newly designed X–Vane, and the Niskin bottle) during the August cruise of 2013 to insure the quality of our sampling data. MITLESS samplers were demonstrated as suitable for trace metal sampling (Zhang et al., 2015). Considering we found no significant differences between final Mn concentrations using MITLESS and Niskin bottle, we consider our sampling using Niskin bottle free from contamination and adapted for trace metal sampling in the ECS continental shelf (Zhang et al., 2015). After collection, all samples were filtered through pre-cleaned Whatman polycarbonate filters (pore size: 0.4 μm) in a class-100 clean bench. Prior to use, the filters were immersed in an ultrapure HCl solution (pH = 2; Merck) for 24 h and then rinsed with Milli–Q water until a neutral pH was obtained. The filtrates were kept in 250 mL LDPE bottles (Nalgene), double-bagged in zipper-seal polyethylene bags, and stored at –18°C until analyzed in the laboratory. Blanks were prepared at sea by filtering a known volume of Milli-Q water with methods identical to the bulk sample sets. The amount of suspended particulate matter (SPM) was measured by determining the weight of particles retained on the filters. During the summer cruise, additional samples were collected at 0.5m depth for dMn concentrations using a modified "towed fish" to characterize dissolved Mn in the inner Changjiang Estuary. Those samples were pumped into the laboratory clean unit on the ship through Teflon-lined plastic tubing using a pneumatic diaphragm pump.

2.2 Analytical methods

Dissolved Mn samples were analyzed in the lab after the cruise by using the flow injection analysis method developed by Aguilar-Islas and Bruland (2006). Briefly, this is a sensitive flow injection analysis method based on spectrophotometric determination from the reaction between leucomalachite green and sodium periodate using nitrilotriacetic acid as an activator. One minor modification of our system is that we changed the buffer solution in-line before column loading with ammonium acetate buffer instead of borate buffer. The procedural blanks, detection limits and precisions of the above-described method are shown in Supplementary Material. The total procedural blank in this study was 0.95 ± 0.07 nM, and the detection limit was 0.21 nM. As an independent comparison, the certification samples collected from the North Atlantic GEOTRACES reference samples as of 2008 (GS) and the certified reference material NASS-6 (National Research Council, Canada) were analyzed for dissolved Mn. The results of our group were consistent with the consensus values and those of other laboratories (all differences were within 10%).

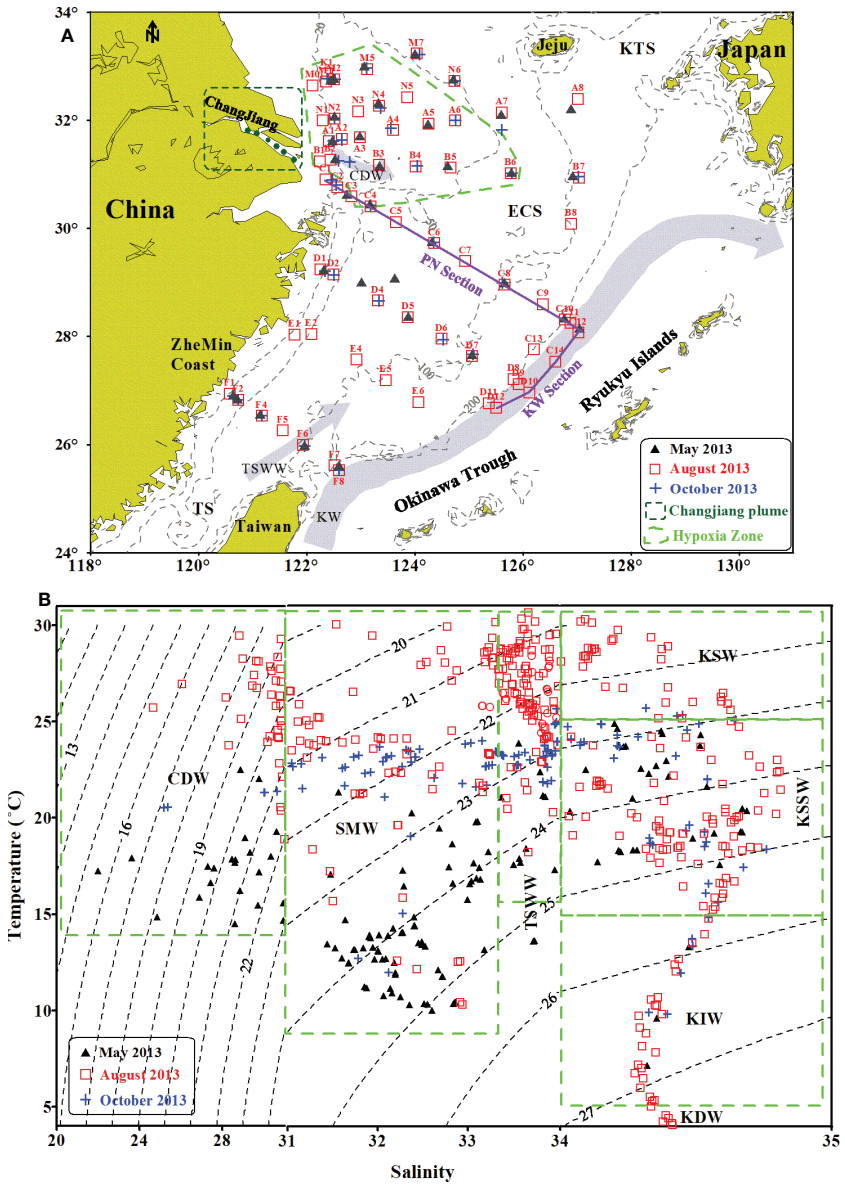

FIGURE 1
(A) Sampling stations of three cruises across the East China Sea in 2013 (▲: May, □: August, +: October), with illustrations of circulation regimes, including the Changjiang Diluted Water (CDW), Kuroshio Water (KW) and Taiwan Strait Warm Water (TSWW). Sampling stations in the Changjiang plume are indicated with a rectangle. The PN Section (from the Changjiang Estuary to the Ryukyu Islands) and KW Section (along the KW in the ECS edge) are highlighted by purple solid lines. The green dashed area represents the Hypoxia Zone that occurred in near-bottom waters outside the Changjiang Estuary (DO < 100 μM) in summer 2013. **(B)** A plot of salinity-temperature data for the ECS, which includes the Changjiang Diluted Water (CDW), Shelf Mixed Water (SMW), Taiwan Strait Warm Water (TSWW), Kuroshio Surface Water (KSW), Kuroshio Subsurface Water (KSSW), Kuroshio Intermediate Water (KIW), and Kuroshio Deep Water (KDW) (Su, 1998; Qi et al., 2014). (ECS, East China Sea; TS, Taiwan Strait; KTS, Korea/Tsushima Strait).

2.3 Numerical simulations

The Finite–Volume Coastal Ocean Model (FVCOM) with a large domain of Bohai Sea, Yellow Sea, ECS and part of the Pacific Ocean was used for a high-resolution (10 km) simulation of the currents in the ECS. Detailed information including bathymetric, driving forces, boundary conditions, and model results can be found in (Xuan et al., 2016; Xuan et al., 2017; Xuan et al., 2019) and Wang et al. (2021). The 100–m isobath was usually chosen as the cut-offs to study the contribution of ECS continental shelf transport, while the 200–m isobath was a reference line where Kuroshio flows along with it (Guo et al., 2006). Therefore, the Taiwan Strait (TS), 100– and 200–m isobaths, sections of East of Cheju (EC) and the Cheju Strait (CS) were selected as the exchange boundaries to calculate the water budgets across the ECS (Figure 2). The off–shelf transport flux of dissolved Mn across the 100–m isobath was assumed to be the total Mn export from the ECS continental shelf, then the transport flux on the 200–m isobath enters into the Kuroshio current. The volume transport and water mass balance in the ECS were compared with published results to validate the simulation results (Xuan et al., 2019). To improve our understanding of the on–shelf and off-shelf transport of dissolved Mn across the ECS continental shelf, we focused on the current velocities and flow directions on the 100– and 200–m isobaths in the ECS at each grid points. The grid points of the 100– and 200–m isobaths

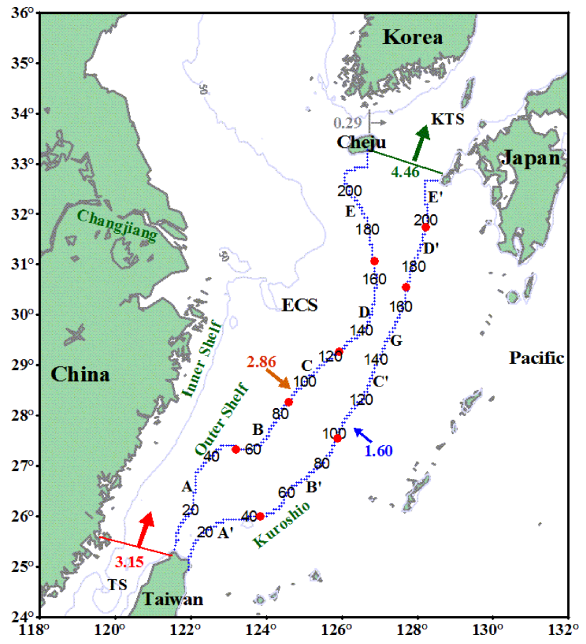

FIGURE 2
Water budgets through the Taiwan Strait (TS), the 100– and 200–m isobaths, East of Cheju (EC), and the Cheju Strait (CS) in the ECS. The blue dots along the 100– and 200–m isobaths indicate the grid number used for the water budget calculation. The number by each arrow indicates volume transport (Sv) through that section and the arrow indicates the direction of transport. The 100– and 200–m isobaths are separated into different sections (A to E along the 100–m isobaths and A' to E' along the 200–m isobath) according to the reversal of current.

generally follow their water depths. A depth–stretched coordinate system was used to specify 40 vertical layers with a vertical resolution of approximately 1–5 m in the mixed layer (Wang et al., 2021).

3 Results

3.1 Hydrographic setting of the study area

Basic hydrographic regimes in the ECS can be identified based on the characteristics of potential temperature and salinity (Figure 1B), including 1) Changjiang Diluted Water (CDW); 2) Taiwan Strait Warm Water (TSWW); 3) Kuroshio Waters (KW, including Kuroshio Surface Water [KSW], Kuroshio Subsurface Water [KSSW] and Kuroshio Intermediate Water [KIW]) and 4) Shelf Mixed Water (SMW). The distributions of temperature, salinity, SPM, and DO in the surface and bottom waters of the ECS are shown in Figures 3–5. Lower salinity (S < 31) was associated with higher SPM, indicating the influence of CDW in the coastal area of Changjiang Estuary. In spring and summer, the Changjiang plume extended predominantly toward the east and northeast (the direction from the Changjiang mouth to Jeju Island), while the trend of CDW spreading southward was strengthened in autumn. Characterized by a high temperature and high salinity (T > 22°C, S > 33), the TSWW reflects the northward movement of warm water off the Min-Zhe coasts of China. It occurs in the middle of the ECS continental shelf at depths of 50–100 m. With the aid of southwest monsoons, the TSWW becomes more obvious in summer (Jan et al., 2002). Upwelling conditions are sustained by the incursion of the KW on the outer shelf area of the ECS where the highest salinity (> 34) and lowest SPM concentrations occurred. The nearshore KW branch current in the ECS is impeded by the enhanced CDW during the summer. A water mass with salinity lower than 33 is defined as Shelf Mixed Water (SMW), which is a mixture of CDW, TSWW, and KW. Remarkably, a hypoxic zone (DO < 3 mg/L) occurs in near-bottom waters of the Changjiang Estuary in summer.

3.2 Distributions of dissolved Mn across the ECS and seasonal variations

Distributions of dissolved Mn in the ECS in spring, summer, and autumn are depicted in Figures 3–5. The distribution of dissolved Mn in the ECS showed a trend of gradually decreasing from the nearshore to the sea, reflecting impacts from terrestrial input. The intrusion of the KW with relatively low dissolved Mn concentrations resulted in low concentrations of dissolved Mn occurring along the ECS shelf edge. Concentrations of dissolved Mn in the ECS ranged from 2.5 to 29.1 nM in spring (7.0 ± 4.1 nM, n=138), 1.1 to 81.5 nM in summer (13.2 ± 15.4 nM nM, n=349), and 1.1 to 15.2 nM in autumn (5.0 ± 2.3 nM, n=133) in 2013. Higher concentrations of dissolved Mn were found mainly in the shelf regions (> 10 nM) while low levels of dissolved Mn were found in the shelf break (< 5 nM). Dissolved Mn concentrations in the ECS were higher in summer than in other seasons. There was no significant difference in the distribution of dissolved Mn in spring and autumn except for nearshore areas with special inputs (*t*-test, $P < 0.05$). Only a small number of stations had higher concentrations in the bottom layer during spring and autumn, which may be a result of the re-suspension of bottom sediments. It is worth noting that the distribution of dissolved Mn in the ECS changed significantly in summer. Dissolved Mn concentration were at their maximum (up to 81.5 nM) in the near-bottom low-oxygen region in the coastal area adjacent to the Changjiang Estuary.

3.3 Vertical distribution of dissolved Mn in the East China Sea

Data obtained from the deep waters of section KW (Figure 1A, D12→D10→C14→C12) during the summer cruise were used to investigate the vertical distribution of dissolved Mn in the ECS (Figure 6). The KSW, KSSW, and KIW can be clearly distinguished from one another. The highest salinity water (> 34.5) occurred in the KSSW between 50 and 400 m. Vertical profiles of dissolved Mn in the KW generally exhibited a surface maximum, a mid-depth minimum in the KSSW, and a gradual increase near the bottom. These results indicated that the vertical distribution of dissolved manganese in the out shelf of the ECS presents a characteristic of surface enrichment and depletion at depth. The concentrations of dissolved Mn in the KSW ranged from 3.4 to 6.5 nM while it remained at relatively lower concentrations in the KSSW (< 2 nM). Interestingly, the concentration of dissolved Mn in the KSW was much higher at *St.* C14 than *St.* D12, which had relatively low salinity (33.7-34.0).

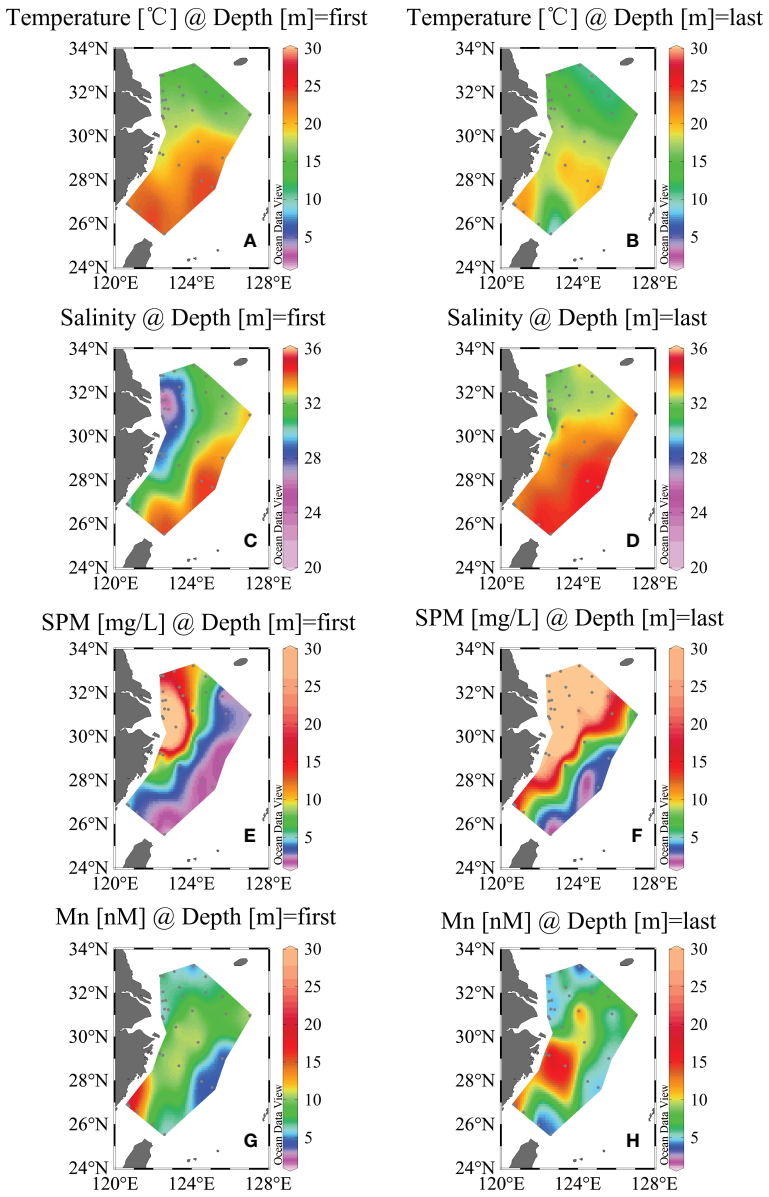

FIGURE 3
Horizontal distributions of temperature (°C), salinity, SPM (mg/L), and dissolved Mn (nM) in the surface **(A, C, E, G)** and the bottom layers **(B, D, F, H)** in the East China Sea in May 2013.

4 Discussion

4.1 Seasonal variations of dissolved Mn in ECS and its level in marginal seas

Although the biogeochemical cycle of dissolved Mn in the open ocean has been studied for more than half a century, relatively little research had been done in the marginal seas, especially in China. By conducting 3 cruises at different seasons, we aim to address seasonal variations of dissolved Mn in the ECS. The highest concentrations of dissolved Mn occurred in summer, while the range and average concentration in spring and autumn were almost the same (Figure 7). In spring and autumn, the concentration of dissolved Mn was slightly higher in surface waters than in the bottom waters, presumably because of the freshwater input and/or dust input (Tan et al., 2012). In summer, the concentration of dissolved Mn was significantly higher in the bottom waters than in the surface waters (*t*-test, $P < 0.05$). Large increases of dissolved Mn in bottom waters in summer were associated with the onset of hypoxia in ECS (Wang et al., 2016). Inter-annual variations of dissolved Mn in the ECS are not easily noticeable. Interesting features revealed that dissolved Mn undergoes significant seasonal variations in the ECS, and that changes in the redox environment played an important role in controlling the source of dissolved Mn.

Comparisons of dissolved Mn among the ECS and other global marginal seas are shown in Table 2. Since dissolved Mn is highly influenced by regional environmental differences, the concentration ranges of dissolved Mn differ greatly among marginal seas. For example, in the anoxic environments of the Black Sea, Baltic Sea, and the Dead Sea, the dissolved Mn concentration is maintained at a

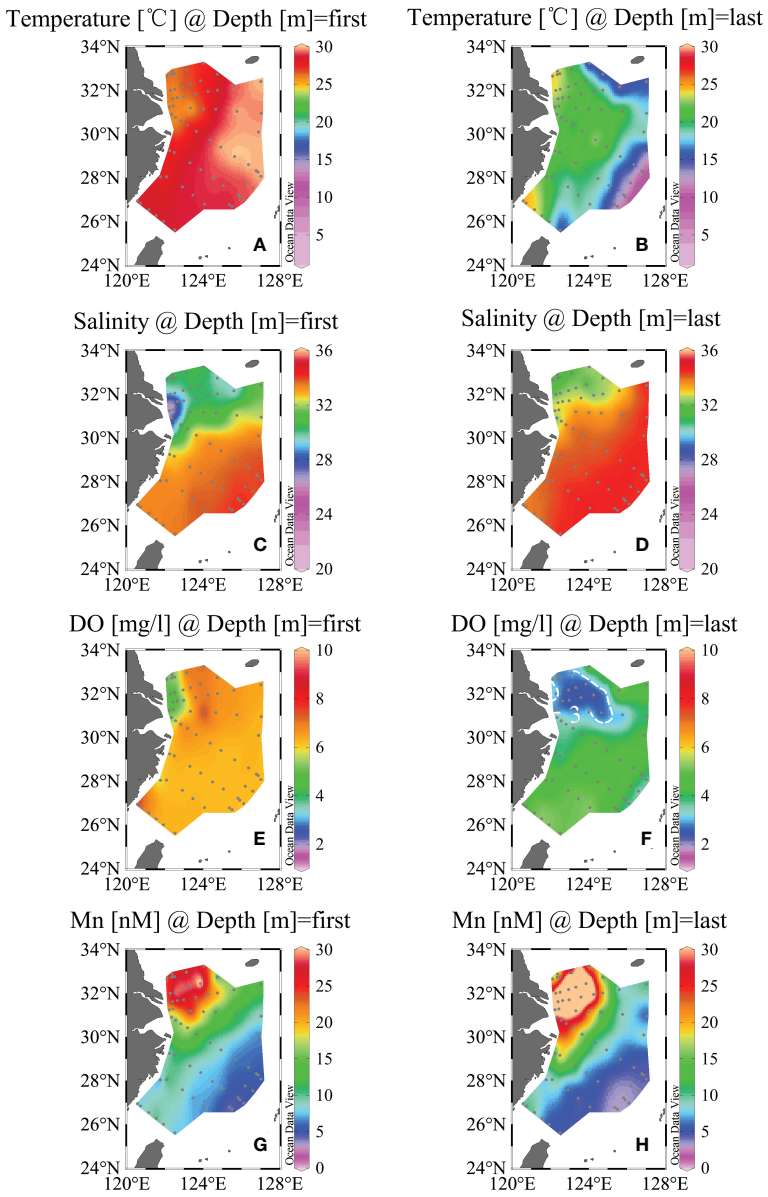

FIGURE 4
Horizontal distributions of temperature (°C), salinity, dissolved oxygen (DO, mg/L), and dissolved Mn (nM) in the surface **(A, C, E, G)** and the bottom layers **(B, D, F, H)** in the East China Sea in August 2013.

high level (μM rather than nM), especially in the oxygen minimum zone (OMZ) (Table 1). Elevated concentrations of dissolved Mn in water bodies have consistently been found under low oxygen conditions (if oxygen drops below 120 mM, Lewis and Luther, 2000; Yemenicioglu et al., 2006; Yakushev et al., 2009), which may be due to reduction of Mn oxides and degradation of organic materials (Wang et al., 2016). Marginal seas receiving large inputs from land runoff, such as the East China Sea, South China Sea, Columbia Estuary, and Coastal Red Sea also have high dissolved Mn concentrations (usually dozens of nM). However, in relatively open areas such as the Weddell Sea, Philippine Sea, and the Sargasso Sea the concentration of dissolved Mn is quite low (below 1 nM, although the surface layer can reach 4–5 nM) because they are far from land and receive little terrestrial input. Using previously reported data we can estimate that the world average dissolved Mn concentration in marginal seas ranges from 7–38 nM and that dissolved Mn has a relatively short residence time ranging from 5–19 yr (Jickells, 1999; de Jong et al., 2007).

4.2 Processes controlling the distribution of dissolved Mn in the ECS

The behavior of dissolved Mn acts as a sensitive proxy for different terrestrial input and redox cycling in marine environments. The major source and space-time variations of dissolved Mn in the ECS are relatively complex. This study may be helpful to deepen understanding of these issues in the marginal seas.

Water masses mixing: Changjiang serves as the main source of terrestrial materials for the ECS as it supplies over 90% of the total

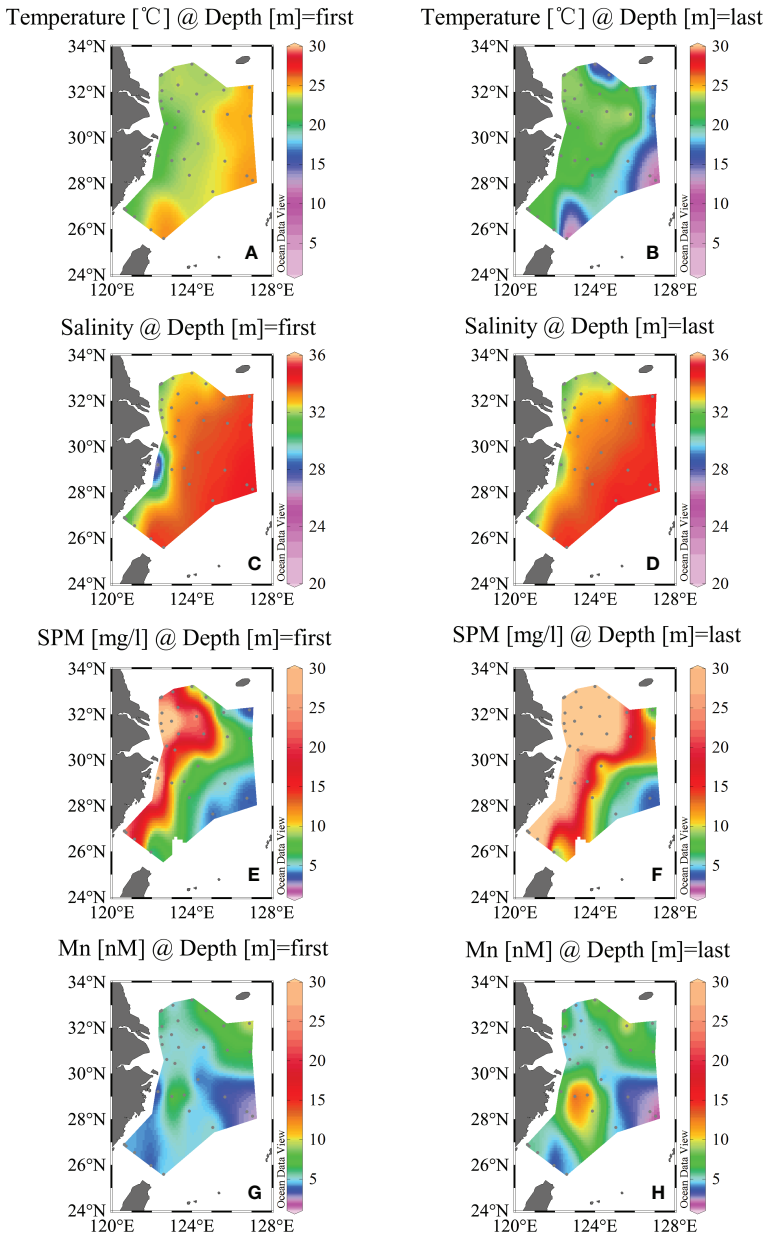

FIGURE 5
Horizontal distributions of temperature (°C), salinity, SPM (mg/L), and dissolved Mn (nM) in the surface **(A, C, E, G)** and the bottom layers **(B, D, F, H)** in the East China Sea in October 2013.

discharge of freshwater (Zhang et al., 2007). All samples during these cruises were divided into four subareas based on geographic locations (Figure 8): samples in the Changjiang plume, which show the Changjiang input into the ECS; samples in the inner shelf (depth < 50 m), which was strongly influenced by terrestrial/bottom boundary inputs; samples in the outer shelf (50 m < depth < 200 m), which was influenced by different water masses mixing; and samples in the Kuroshio mainstream water (depth > 200 m). The average concentrations of dissolved Mn in the Changjiang plume, inner shelf, outer shelf, and Kuroshio were (32.9 ± 25 nM), (15.4 ± 20 nM), (6.4 ± 2 nM) and (3.1 ± 1 nM), respectively. The highest concentrations of dissolved Mn were found in the Changjiang plume. The gradual decrease of dissolved Mn with distance reflects the contribution from the terrestrial input (Wang et al., 2016). The PN section from the Changjiang Estuary to the Ryukyu Islands crosses the whole ECS continental shelf to Kuroshio (Figure 1), and it has become one of the most representative sections to study the distribution of dissolved metals under the effect of water masses mixing. We compared the vertical profiles of dissolved Mn in the PN section at different seasons (Figure 9). The Changjiang estuary (within 150 km of the Changjiang mouth in the PN section) has the highest concentration of dissolved Mn in summer affected by the CDW, followed by spring and the smallest in autumn, especially for the surface waters. Away from the Changjiang Estuary in relatively open waters, a low-Mn plume intruded into the ECS continental shelf, reflecting the influence of the KW (Yang et al., 2018). Seasonal variation of dissolved Mn in the PN section indicates that mixing of different water masses plays an important role in redistribution of dissolved Mn in the ECS.

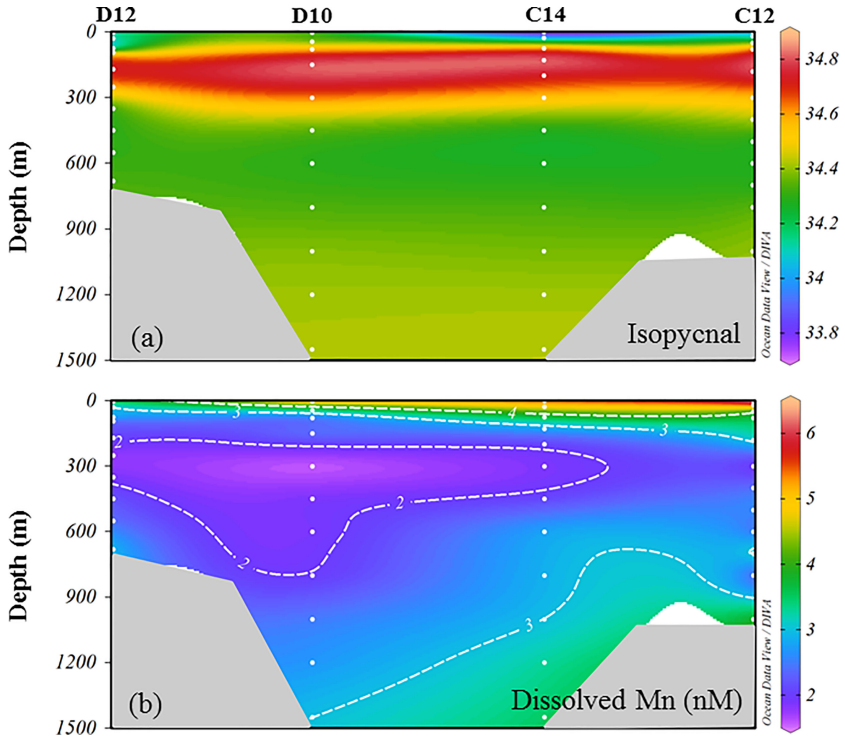

FIGURE 6
Vertical distributions of salinity **(A)** and dissolved Mn **(B)** across the KW section.

Redox cycling: Increasing concern has recently developed regarding hypoxia in the Changjiang Estuary (Zhu et al., 2016). Mn is a redox-sensitive element. The behavior of dissolved Mn in the Changjiang Estuary needs to be considered if the redox environment changes. We first compared vertical profiles of dissolved oxygen (DO) and dissolved Mn at *st.* N4 (123.4°E, 32.2°N) in different seasons (Figure 10A). In May, the concentration of dissolved Mn at *st.* N4 was less than 10 nM. In August, it increased to more than 60 nM in near-bottom waters experiencing hypoxia (DO < 3 mg/L). By October, the dissolved Mn concentration had returned to the level seen in May. Organic matter decomposition plays an important role in the process of oxygen depletion in the Changjiang Estuary. Data on the ratio of dissolved organic nitrogen and dissolved inorganic nitrogen (DON/DIN) is used here as a simple proxy to indicate the degree of the organic matter decomposition processes. The lower the ratio of DON/DIN, the higher the degree of organic matter decomposition (Zhu et al., 2016). The near-bottom data of apparent oxygen utilization (AOU), nutrients data of DON/DIN, and dissolved Mn were used to further investigate the internal mechanism of regeneration of dissolved Mn under hypoxia conditions (Figures 10B, C). Dissolved Mn concentration was positively correlated with the bottom AOU (r = 0.72, n = 24), indicating that the regeneration of dissolved Mn is related to the degree of oxygen consumption. Dissolved Mn is negatively correlated with DON/DIN, which confirms that the high value of dissolved Mn is largely caused by organic matter decomposition in the hypoxic zone. We can conclude that dissolved Mn in near-bottom waters is substantially controlled by the redox environment in summer, and the form of Mn in seawaters changes rapidly in reduction environments.

Shelf export: The ECS continental shelf continues to receive terrestrial inputs (Changjiang) and shelf benthic inputs, causing the continental shelf to be rich in terrigenous materials. The off-shelf transport of terrestrial materials from continental shelf waters to out shelf waters in the ECS is recognized as one of the important processes for the biogeochemical cycle of biogenic elements (Yool and Fasham, 2001; Ya et al., 2017). The KW is an important carrier for receiving those terrestrial materials from the ECS continental shelf. An important clue to this lateral transportation of dissolved Mn in the ECS is that the vertical profiles of dissolved Mn in the KW varies significantly with different geographic locations and hydrographic regimes (Figure 11). It is noteworthy that the background concentration of dissolved Mn in KSW was approximately 1.0 nM. It increased to 3–4 nM at F8 and D12, then further increased to above 6 nM at St. C12 as the KW flows across the ECS shelf edge. Those signals can be ignored in deep waters. The enrichment of dissolved Mn in the KSW can be attributed to the off-shelf transport of Mn-rich continental shelf waters. Previous report also suggested that the influence of aerosol Mn inputs could not result in such a large increment of dissolved Mn in the KSW (Hsu et al., 2010; Jiang et al., 2018).

4.3 Quantitative estimation of exchange fluxes of dissolved Mn across the 100– and 200–m isobaths

Water exchange between the ECS continental shelf and the KW result in mesoscale dynamic processes, leading to both on-shelf and

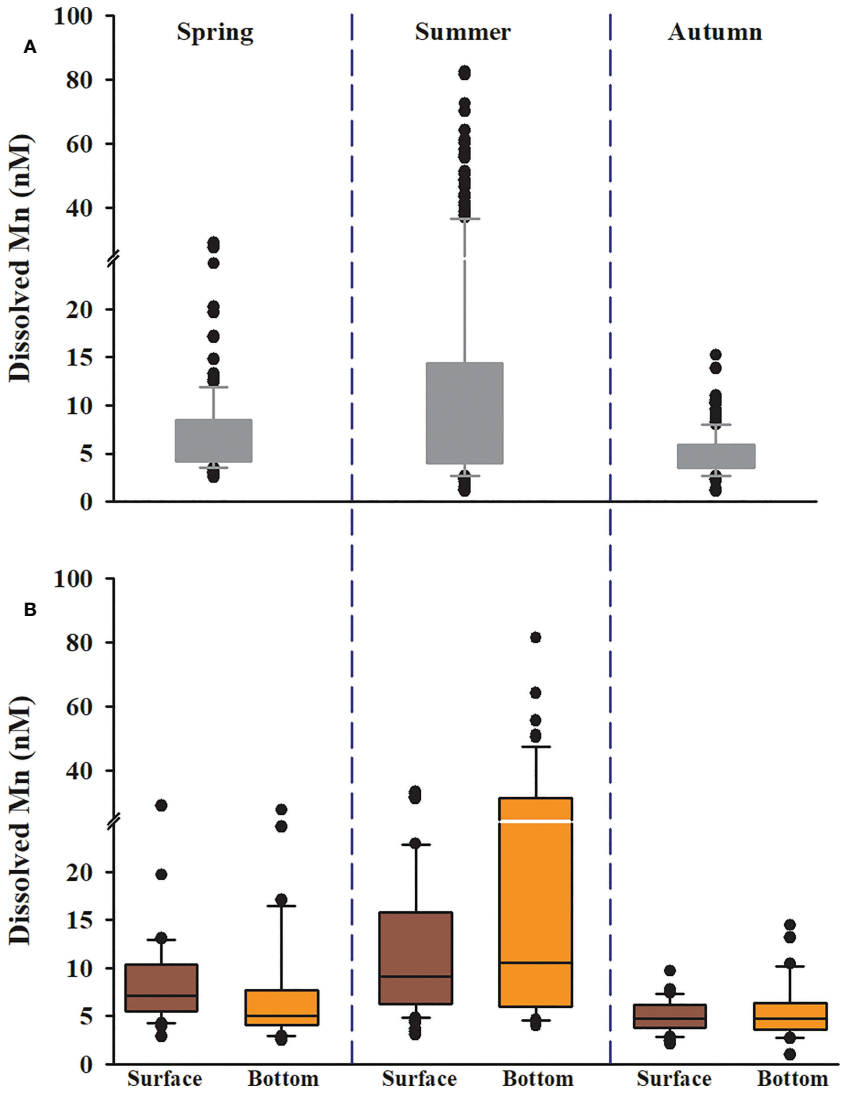

FIGURE 7
Statistical distribution of seasonal changes **(A)**, surface and bottom data **(B)** of dissolved Mn in the East China Sea.

TABLE 1 Comparison of dissolved manganese concentrations in ECS with global marginal seas.

Region	Sampling time(year)	Mn concentration(nM)	Reference
East China Sea	2013	1.1 – 20.5	Present study
		Hypoxia Zone: 9.1 – 81.5	
	2011	0.9 – 21.8	Wang et al., 2016; Zhang et al., 2021b
		Hypoxia Zone: 8.5 – 140.7	
South China Sea	2011, 2015	0.5 – 29.9	Wang et al., 2018
Weddell Sea	2008	≤ 0.2 – 1.5	Middag et al., 2013
Baltic Sea	2008	> 1000	Yakushev et al., 2009
Philippine Sea	2002	< 0.4 – 4.5	Obata et al., 2007
Wadden Sea	2002–2003	60 – 700	Dellwig et al., 2007
Black Sea	2001	> 1000	Yemenicioglu et al., 2006

(Continued)

TABLE 1 Continued

Region	Sampling time(year)	Mn concentration(nM)	Reference
Arabian Sea	1995	≤ 0.6 – 8	Lewis and Luther, 2000
Columbia Estuary	1994	12–40	Klinkhammer et al., 1997
Sargasso Sea	1986	0.7 – 4.3	Sunda and Huntsman, 1988
Coastal Red Sea	1980–1981	5.3 – 46	Saad and Kandeel, 1988
Dead Sea	1977–1979	> 1000	Nishri, 1984

TABLE 2 Fluxes of water and dissolved Mn across the 100−m isobath in the ECS (+: off−shelf, -: on−shelf).

Region	Total Water Flux (Sv)	Total Mn Flux(× 10^8 mol/yr)	Depth (m)	Water Flux (Sv)	Mn concentration (nM)	Mn Flux(× 10^8 mol/yr)
A	−0.25	−0.01 ± 0.20	0–10	0.12	4.4 ± 0.9	0.17 ± 0.03
			10–65	0.23	3.1 ± 0.8	0.22 ± 0.06
			65–100	−0.60	2.1 ± 0.6	−0.40 ± 0.11
B	1.14	1.52 ± 0.17	0–10	0.18	6.5 ± 1.1	0.37 ± 0.06
			10–65	0.71	4.1 ± 0.4	0.92 ± 0.09
			65–100	0.25	2.9 ± 0.3	0.23 ± 0.02
C	−0.15	−0.02 ± 0.08	0–10	0.08	3.8 ± 1.1	0.10 ± 0.03
			10–65	0.05	3.7 ± 0.8	0.06 ± 0.01
			65–100	−0.28	2.1 ± 0.4	−0.18 ± 0.04
D	1.39	3.06 ± 0.48	0–10	0.25	8.2 ± 1.3	0.65 ± 0.10
			10–65	0.90	6.8 ± 1.1	1.93 ± 0.31
			65–100	0.24	6.1 ± 0.9	0.48 ± 0.07
E	0.73	1.14 ± 0.21	0–10	0.25	5.2 ± 1.0	0.41 ± 0.08
			10–65	0.66	4.2 ± 0.5	0.87 ± 0.10
			65–100	−0.18	2.4 ± 0.6	−0.14 ± 0.03
Total	2.86	5.69 ± 1.14				

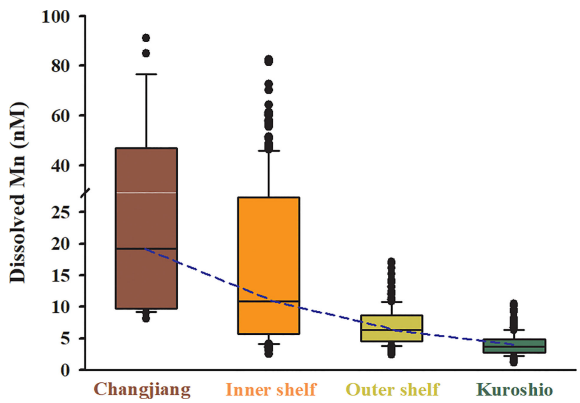

FIGURE 8
Dissolved Mn concentration distribution throughout the East China Sea. All samples were divided into four groups: the Changjiang plume, Inner shelf, Outer shelf, and Kuroshio waters.

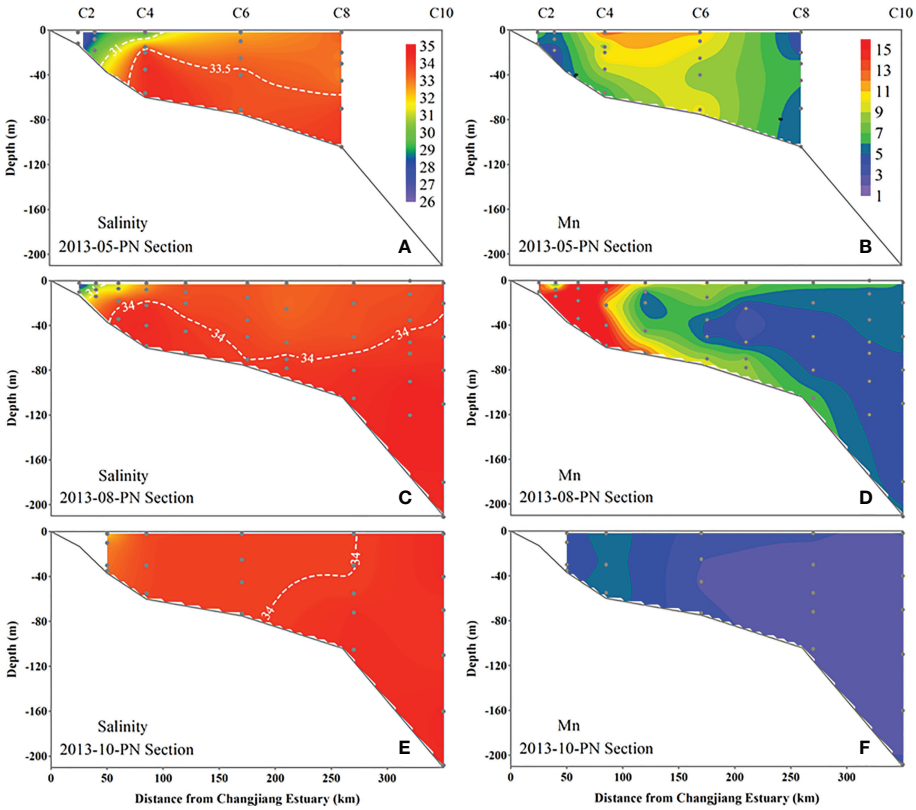

FIGURE 9
Seasonal variations of salinity **(A, C ,E)** and dissolved Mn **(**nM, **B ,D, F)** (nM) across the PN section.

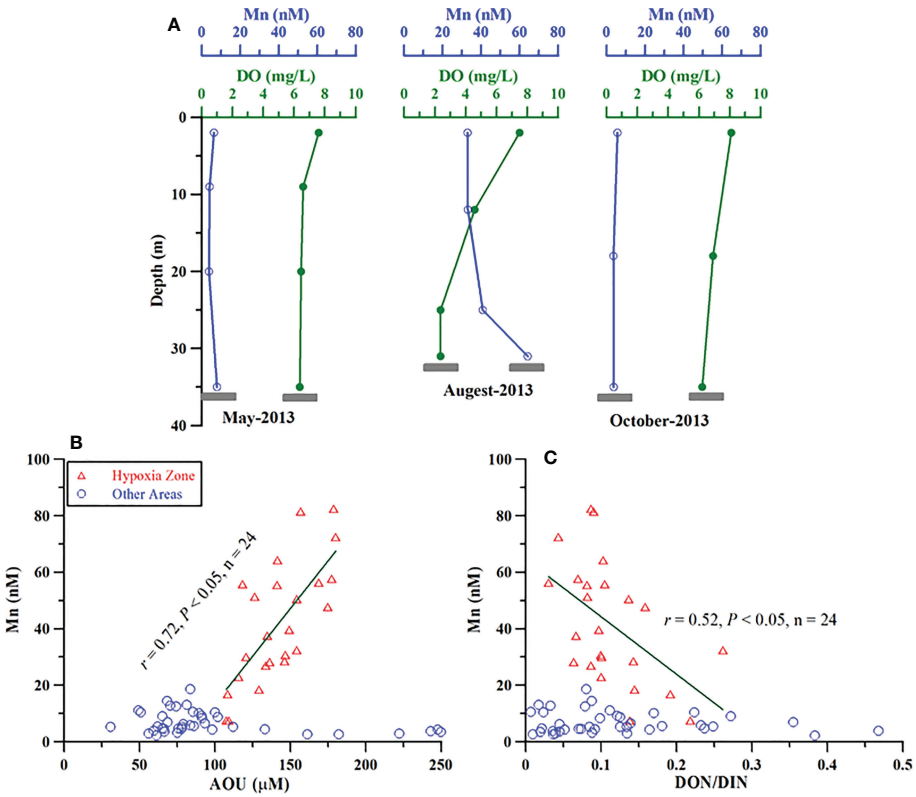

FIGURE 10
Comparison of seasonal profiles of dissolved oxygen and dissolved Mn at station N4 in the Changjiang Estuary **(A)**. Bottom dissolved Mn concentration plotted as a function of AOU **(B)** and DON/DIN **(C)**. The hypoxic zone is emphasized with a red triangle.

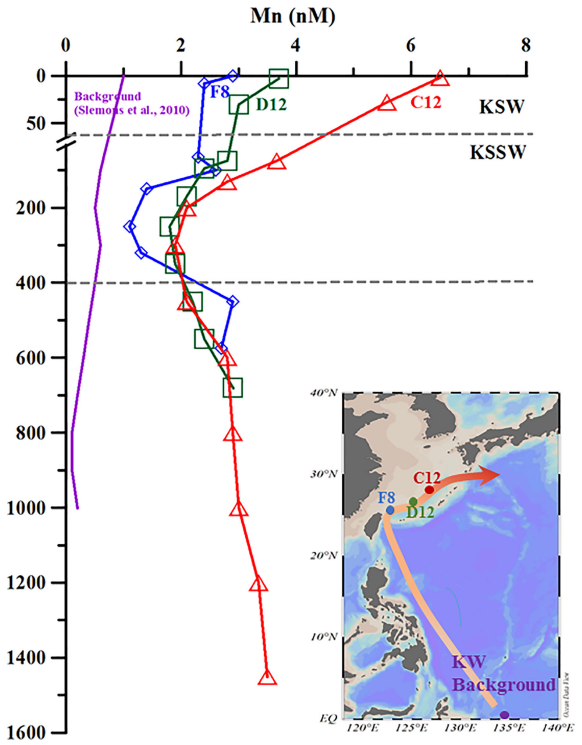

FIGURE 11
Vertical profiles of dissolved Mn at stations F8, D12, and C12 along the Kuroshio flow through the ECS edge. The positions of the stations are marked on the map. The background data of dissolved Mn in the KW is cited from (Slemons et al., 2010).

off-shelf transport (Guo et al., 2006; Zhou et al., 2015; Che and Zhang, 2018). This dynamic exchange driven by the physical mixing process not only modifies the properties of water masses but also pumps dissolved Mn transport in the ECS, which is recognized as an important issue for quantifying biogeochemical cycling in the ocean (Guo et al., 2012). To further confirm the dynamic variation of water and dissolved Mn exchanges across the ECS, the 100– and 200–m isobaths were selected as boundaries between the ECS continental shelf and the KW. We compared vertical distributions of current velocity and dissolved Mn at each grid point along the 100– and 200–m isobaths (Figure 12). The dynamic variations of on–shelf and off-shelf water exchanges across the 100– and 200–m isobaths were significant (t-test, $P < 0.05$). The KW with low concentrations of dissolved Mn intruded into the ECS continental shelf from the northeast of Taiwan, and the on–shelf intrusion of KW water across the 100–m isobath occurred at 27.2°N, 122.7°E (between grid numbers 30 and 60, Figure 2). The off-shelf transport of ECS continental shelf water across the 100–m isobath occurred at 28°N, 124°E (between grid numbers 60 and 80), and 30°N, 127°E (between grid numbers 150 and 170). The results fitted our prediction of lateral transport of dissolved Mn due to water masses mixing, and that the location of high concentrations of dissolved Mn is consistent with the off-shelf flow fields. A similar phenomenon can be found across the 100– and 200–m isobaths. Off–shelf transport of dissolved Mn across the 100–m isobath is more significant than across the 200–m isobath. The cross-shelf transport pattern in the ECS has also been well-validated by observational studies and numerical models (Ding et al., 2019; Zhang et al., 2019; Wang et al., 2021).

The exchange fluxes of dissolved Mn can be defined as the product of volume transport of water and representative Mn concentrations. The 100– and 200–m isobaths were divided into five horizontal sections based on flow direction and intensity (Figure 2). Each section was also divided into three layers based on the seawater density (σ_θ; kg/m^3, Wang et al., 2021): the upper layer ($\sigma_\theta < 21.5$), the middle layer ($21.5 < \sigma_\theta < 24.5$), and the deep layer ($\sigma_\theta > 24.5$). We used the average concentrations of dissolved Mn at ~5–10 km around each section across the 100– and 200–m isobaths as the representative concentrations of inflow and outflow transport to calculate the on–shelf and off–shelf fluxes of dissolved Mn, respectively. Details of the exchange fluxes of dissolved Mn across the 100– and 200–m isobaths are provided in Tables 2, 3. The ECS continental shelf is a net source of dissolved Mn for the adjacent waters. The net dissolved Mn transport flux across the 100– and 200–m isobaths is $(5.69 \pm 1.14) \times 10^8$ mol/yr and $(1.02 \pm 3.12) \times 10^8$ mol/yr, respectively. The difference in dissolved Mn flux between the 100– and 200–m isobaths [$(4.67 \pm 4.26) \times 10^8$ mol/yr] indicates that most of the dissolved Mn from the ECS continental shelf is transported north to the East/Japan Sea through the Tsushima Strait. The dissolved Mn flux across the 200–m isobath enters into the KW [$(1.02 \pm 3.12) \times 10^8$ mol/yr], which could potentially affect the distribution of dissolved Mn in the Northwest Pacific. The contribution of off-shelf transport of dissolved Mn in the ECS obtained here is comparable to previously published results for dissolved aluminum and neodymium (Ren et al., 2015; Che and Zhang, 2018). These results indicate the important contribution of cross-shelf transport to the geographical distribution of biogenic elements and their biogeochemical cycles in marginal seas.

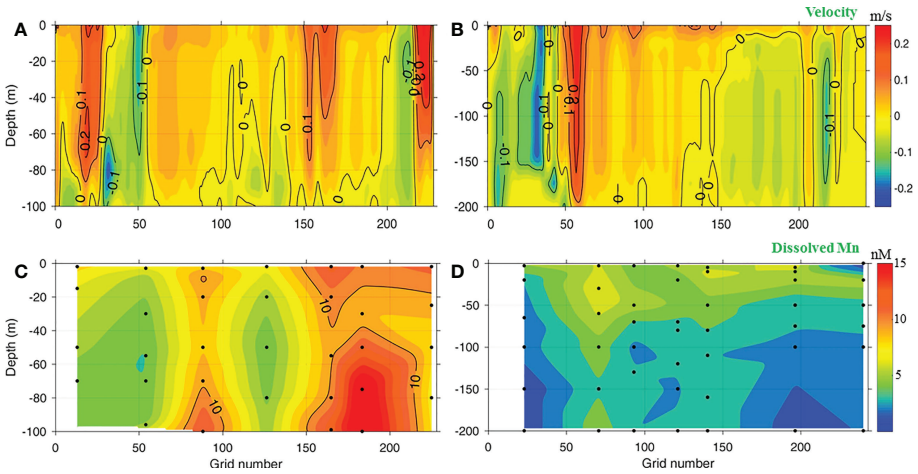

FIGURE 12
Current velocity distributions (m/s, **A, B**) and dissolved Mn distributions (nM, **C, D**) along the 100– and 200–m isobaths originating from Taiwan (+: off–shelf, –: on–shelf). Grid numbers represent locations used for the water budget calculation along the 100– and 200–m isobaths. Detailed information can be found in Figure 2. Part of the dissolved Mn data (Grid number > 180) comes from unpublished data from other cruises.

5 Summary and conclusions

In this study, we investigated the distribution of dissolved Mn in the ECS on three cruises in various seasons. There was a clear seasonality in dissolved Mn concentrations in the ECS, with the highest concentrations occurring in summer. The internal biogeochemical cycle of dissolved Mn in the ECS was influenced by a combination of Changjiang input, redox cycling, water masses mixing and cross-shelf transport. We demonstrated that the waters adjacent to the ECS receive a significant amount of Mn through cross–shelf transport processes. This off–shelf transport flux of dissolved Mn across the 100– and 200–m isobaths through the ECS continental shelf was further quantitatively estimated. The total Mn export from the ECS continental shelf was (5.69 ± 1.14) × 10^8 mol/yr across the 100–m isobath. Nearly 82% of the total output enters into the East/Japan Sea, while the remaining 18% enters into the Kuroshio current. Our findings contribute to a better understanding of the behaviors influencing Mn biogeochemical cycles as well as defining the role of cross–shelf transport processes in the ECS. Future research needs to be focused on the physical mechanisms controlling shelf

TABLE 3 Fluxes of water and dissolved Mn across the 200–m isobath in the ECS (+: off–shelf, -: on–shelf).

Region	Total Water Flux (Sv)	Total Mn Flux(× 10^8 mol/yr)	Depth (m)	Water Flux (Sv)	Mn concentration (nM)	Mn Flux(× 10^8 mol/yr)
A’	–3.19	–2.56 ± 0.80	0–65	–1.12	3.5 ± 1.1	–1.23 ± 0.39
			65–100	–1.36	2.1 ± 0.7	–0.90 ± 0.30
			100–200	–0.71	1.9 ± 0.5	–0.43 ± 0.11
B’	3.03	4.77 ± 1.27	0–65	1.77	5.8 ± 1.5	3.24 ± 0.84
			65–100	0.96	4.2 ± 1.2	1.27 ± 0.36
			100–200	0.30	2.7 ± 0.7	0.26 ± 0.07
C’	1.26	1.90 ± 0.43	0–65	1.00	5.2 ± 1.1	1.64 ± 0.35
			65–100	0.22	3.3 ± 1.0	0.23 ± 0.07
			100–200	0.04	2.4 ± 0.8	0.03 ± 0.01
D’	–1.85	–2.02 ± 0.46	0–65	–0.46	4.9 ± 1.7	–0.71 ± 0.25
			65–100	–0.79	3.4 ± 0.5	–0.84 ± 0.12
			100–200	–0.60	2.5 ± 0.5	–0.47 ± 0.09
E’	–0.85	–1.07 ± 0.16	0–65	–0.22	5.4 ± 1.2	–0.37 ± 0.08
			65–100	–0.29	4.7 ± 0.6	–0.42 ± 0.05
			100–200	–0.34	2.6 ± 0.3	–0.28 ± 0.03
Total	–1.60	1.02 ± 3.12				

transport and migration behavior through field observations and numerical simulations, as well as the significant contribution of using dissolved Mn as a tracer to track the output of terrestrial pollutants such as nutrients in the ocean.

Data availability statement

The raw data supporting the conclusions of this article will be made available by the authors, without undue reservation.

Author contributions

ZW and JX: Investigation, formal analysis, conceptualization, methodology, validation, writing - original draft. SL: conceptualization, supervision, review & editing. JR and JZ: Funding acquisition, resources, conceptualization, methodology, validation, writing - review & editing. All authors contributed to the article and approved the submitted version.

Funding

This study was funded by the National Science Foundation of China (42176042) and the National Basic Research Program of China (973 project, 2014CB441502). High-end users Program of "Kexue" (No. KEXUE2019GZ01), Taishan Scholars Programme of Shandong Province (No. ts 201511014), Innovation and Entrepreneurship Projects for High-Level Talents of Dalian (2020RQ015) and Research Projects supported by State Key Laboratory of Tropical Oceanography, South China Sea Institute of Oceanology, Chinese Academy of Sciences (Project No. LTO2016) are also acknowledged.

Acknowledgments

R. Schlitzer and colleagues from the Alfred-Wegener-Institute for Polar and Marine Research (AWI) provided free use of the software Ocean Data View (ODV), which was used for data processing.

Conflict of interest

The authors declare that the research was conducted in the absence of any commercial or financial relationships that could be construed as a potential conflict of interest.

Publisher's note

All claims expressed in this article are solely those of the authors and do not necessarily represent those of their affiliated organizations, or those of the publisher, the editors and the reviewers. Any product that may be evaluated in this article, or claim that may be made by its manufacturer, is not guaranteed or endorsed by the publisher.

Supplementary material

The Supplementary Material for this article can be found online at: https://www.frontiersin.org/articles/10.3389/fmars.2022.1110913/full#supplementary-material

References

Aguilar-Islas, A. M., and Bruland, K. W. (2006). Dissolved manganese and silicic acid in the Columbia river plume: A major source to the California current and coastal waters off Washington and Oregon. *Mar. Chem.* 101 (3), 233–247. doi: 10.1016/j.marchem.2006.03.005

Che, H., and Zhang, J. (2018). Water mass analysis and end-member mixing contribution using coupled radiogenic Nd isotopes and Nd concentrations: interaction between marginal seas and the northwestern pacific. *Geophys. Res. Lett.* 45 (5), 2388–2395. doi: 10.1002/2017GL076978

Colombo, M., Jackson, S. L., Cullen, J. T., and Orians, K. J. (2020). Dissolved iron and manganese in the Canadian Arctic ocean: on the biogeochemical processes controlling their distributions. *Geochim. Cosmochim. Ac.* 227, 150–174. doi: 10.1016/j.gca.2020.03.012

de Jong, J., Boye, M., Gelado-Caballero, M. D., Timmermans, K. R., Veldhuis, M. J. W., Nolting, R. F., et al. (2007). Inputs of iron, manganese and aluminum to surface waters of the northeast Atlantic ocean and the European continental shelf. *Mar. Chem.* 107 (2), 120–142. doi: 10.1016/j.marchem.2007.05.007

Dellwig, O., Bosselmann, K., Kölsch, S., Hentscher, M., Hinrichs, J., Böttcher, M. E., et al. (2007). Sources and fate of manganese in a tidal basin of the German wadden Sea. *J. Sea. Res.* 57 (1), 1–18. doi: 10.1016/j.seares.2006.07.006

Ding, R. B., Huang, D. J., Xuan, J. L., Zhou, F., and Pohlmann, T. (2019). Temporal and spatial variations of cross-shelf nutrient exchange in the East China Sea, as estimated by satellite altimetry and *in situ* measurements. *J. Geophys. Res-Oceans.* 124 (2), 1331–1356. doi: 10.1029/2018JC014496

Guo, X. Y., Miyazawa, Y., and Yamagata, T. (2006). The kuroshio onshore intrusion along the shelf break of the East China Sea: The origin of the tsushima warm current. *J. Phys. Oceanogr.* 36 (12), 2205–2231. doi: 10.1175/JPO2976.1

Guo, X. Y., Zhu, X. H., Wu, Q. S., and Huang, D. J. (2012). The kuroshio nutrient stream and its temporal variation in the East China Sea. *J. Geophys. Res-Oceans.* 117 (C1), 01026. doi: 10.1029/2011JC007292

Heiser, U., Neumann, T., Scholten, J., and Stüben, D. (2001). Recycling of manganese from anoxic sediments in stagnant basins by seawater inflow: a study of surface sediments from the gotland basin, Baltic Sea. *Mar. Geol.* 177 (1), 151–166. doi: 10.1016/S0025-3227(01)00129-3

Hsu, S. C., Wong, G. T. F., Gong, G. C., Shiah, F. K., Huang, Y. T., Kao, S. J., et al. (2010). Sources, solubility, and dry deposition of aerosol trace elements over the East China Sea. *Mar. Chem.* 120 (1), 116–127. doi: 10.1016/j.marchem.2008.10.003

Jan, S., Wang, J., Chern, C. S., and Chao, S. Y. (2002). Seasonal variation of the circulation in the Taiwan strait. *J. Mar. Syst.* 35 (3), 249–268. doi: 10.1016/S0924-7963(02)00130-6

Jiang, S., Zhang, J., Zhang, R. F., Xue., Y., and Zheng, W. (2018). Dissolved lead in the East China Sea with implications for impacts of marginal seas on the open ocean through cross-shelf exchange. *J. Geophys. Res-Oceans.* 123 (8), 6004–6018. doi: 10.1029/2018JC013955

Jickells, T. D. (1999). The inputs of dust derived elements to the Sargasso Sea: A synthesis. *Mar. Chem.* 68 (1), 5–14. doi: 10.1016/S0304-4203(99)00061-4

Klinkhammer, G. P., Chin, C. S., Wilson, C., Rudnicki, M. D., and German, C. R. (1997). Distributions of dissolved manganese and fluorescent dissolved organic matter in the Columbia river estuary and plume as determined by *in situ* measurement. *Mar. Chem.* 56 (1-2), 1–14. doi: 10.1016/S0304-4203(96)00079-5

Landing, W. M., and Bruland, K. W. (1987). The contrasting biogeochemistry of iron and manganese in the pacific ocean. *Geochim. Cosmochim. Ac.* 51 (1), 29–43. doi: 10.1016/0016-7037(87)90004-4

Lewis, B. L., and Luther, G. W.III (2000). Processes controlling the distribution and cycling of manganese in the oxygen minimum zone of the Arabian Sea. *Deep-Sea. Res. Pt. II.* 47 (7), 1541–1561. doi: 10.1016/S0967-0645(99)00153-8

Liu, K. K. (2000). Cross-shelf and along-shelf nutrient fluxes derived from flow fields and chemical hydrography observed in the southern East China Sea off northern Taiwan. *Cont. Shelf Res.* 20 (4), 493–523. doi: 10.1016/S0278-4343(99)00083-7

Middag, R., De Baar, H. J. W., Klunder, M. B., and Laan, P. (2013). Fluxes of dissolved aluminum and manganese to the weddell Sea and indications for manganese co-limitation. *Limnol. Oceanogr.* 58 (1), 287–300. doi: 10.4319/lo.2013.58.1.0287

Middag, R., De Baar, H. J. W., Laan, P., Cai, P. H., and van Ooijen, J. C. (2011). Dissolved manganese in the Atlantic sector of the southern ocean. *Deep-Sea. Res. Pt. II.* 58 (25), 2661–2677. doi: 10.1016/j.dsr2.2010.10.043

Middag, R., Séférian, R., Conway, T. M., John, S. G., Bruland, K. W., and De Baar, H. J. W. (2015). Intercomparison of dissolved trace elements at the Bermuda Atlantic time series station. *Mar. Chem.* 177, 476–489. doi: 10.1016/j.marchem.2015.06.014

Nishri, A. (1984). The geochemistry of manganese in the dead Sea. *Earth Planet. Sc. Lett.* 71 (2), 415–426. doi: 10.1016/0012-821X(84)90107-9

Obata, H., Doi, T., Hongo, Y., Alibo, D. S., Minami, H., Kato, Y., et al. (2007). Manganese, cerium and iron in the sulu, celebes and Philippine seas. *Deep-Sea. Res. Pt. II.* 54 (1), 38–49. doi: 10.1016/j.dsr2.2006.09.004

Qi, J. F., Yin, B. S., Zhang, Q. L., Yang, D. Z., and Xu, Z. H. (2014). Analysis of seasonal variation of water masses in East China Sea. *Chin. J. Oceanol. Limn.* 32 (4), 958–971. doi: 10.1007/s00343-014-3269-1

Ren, J. L., Xuan, J. L., Wang, Z. W., Huang, D. J., and Zhang, J. (2015). Cross-shelf transport of terrestrial Al enhanced by the transition of northeasterly to southwesterly monsoon wind over the East China Sea. *J. Geophys. Res-Oceans.* 120 (7), 5054–5073. doi: 10.1002/2014JC010655

Resing, J. A., Sedwick, P. N., German, C. R., Jenkins, W. J., Moffett, J. W., Sohst, B. M., et al. (2015). Basin-scale transport of hydrothermal dissolved metals across the south pacific ocean. *Nature* 523 (7559), 200–203. doi: 10.1038/nature14577

Roy, M., McManus, J., Goñi, M. A., Chase, Z., Borgeld, J. C., Wheatcroft, R. A., et al. (2013). Reactive iron and manganese distributions in seabed sediments near small mountainous rivers off Oregon and California (USA). *Cont. Shelf Res.* 54, 67–79. doi: 10.1016/j.csr.2012.12.012

Saad, M. A. H., and Kandeel, M. M. (1988). Distribution of copper, iron and manganese in the coastal red Sea waters in front of Al-ghardaqa. *Proc. Indian Natn. Sci. Acad.* 54 (4), 642–652.

Saager, P. M., De Baar, H. J. W., and Burkill, P. H. (1989). Manganese and iron in Indian ocean waters. *Geochim. Cosmochim. Ac.* 53 (9), 2259–2267. doi: 10.1016/0016-7037(89)90348-7

Sherman, K., and Tang, Q. (1999). Large Marine ecosystems of the pacific rim [M]. *Blackwell Sci.* 57-101:57-60. doi: 10.1016/0016-7037(89)90348-7

Shiller, A. M. (1997). Dissolved trace elements in the Mississippi river: seasonal, interannual, and decadal variability. *Geochim. Cosmochim. Ac.* 61 (20), 4321–4330. doi: 10.1016/S0016-7037(97)00245-7

Sim, N., and Orians, K. J. (2019). Annual variability of dissolved manganese in northeast pacific along line-p: 2010–2013. *Mar. Chem.* 216, 103702. doi: 10.1016/j.marchem.2019.103702

Slemons, L. O., Murray, J. W., Resing, J., Paul, B., and Dutrieux, P. (2010). Western Pacific coastal sources of iron, manganese, and aluminum to the equatorial undercurrent. *Global Biogeochem. Cy.* 24 (3), 1–16. doi: 10.1029/2009GB003693

Su, J. L. (1998). Circulation dynamics of the China seas north of 18o n. *Sea.* 11, 483–505.

Sunda, W. G., and Huntsman, S. A. (1988). Effect of sunlight on redox cycles of manganese in the southwestern Sargasso Sea. *Deep-Sea. Res. Pt. I.* 35 (8), 1297–1317. doi: 10.1016/0198-0149(88)90084-2

Tan, S. C., Shi, G. Y., and Wang, H. (2012). Long-range transport of spring dust storms in inner Mongolia and impact on the China seas. *Atmos. Environ.* 46, 299–308. doi: 10.1016/j.atmosenv.2011.09.058

Van Hulten, M. M. P., Dutay, J. C., Middag, R., De Baar, H. J. W., Roy-Barman, M., Gehlen, M., et al. (2016). Manganese in the world ocean: a first global model. *Biogeosci. Discussions.* 14 (5), 1123–1152. doi: 10.5194/bg-2016-282

Wang, Z. W., Ren, J. L., Jiang, S., Liu, S. M., Xuan, J. L., and Zhang, J. (2016). Geochemical behavior of dissolved manganese in the East China Sea: Seasonal variation, estuarine removal, and regeneration under suboxic conditions. *Geochem. Geophy. Geosy.* 17 (2), 282–299. doi: 10.1002/2015GC006128

Wang, Z. W., Ren, J. L., Xuan, J. L., Li, F. M., Yang, T. T., and Guo, Y. (2018). Processes controlling the distribution and cycling of dissolved manganese in the northern south China Sea. *Mar. Chem.* 204, 152–162. doi: 10.1016/j.marchem.2018.07.003

Wang, Z. W., Xuan, J. L., Li, F. M., Ren, J. L., Huang, D. J., and Zhang, J. (2021). Monsoon-facilitated off-shelf tansport of dissolved aluminum across the East China Sea during summer. *J. Geophys. Res-Oceans.* 126 (6), 1–20. doi: 10.1029/2020JC016953

Wu, J. F., Roshan, S., and Chen, G. (2014). The distribution of dissolved manganese in the tropical–subtropical north Atlantic during US GEOTRACES 2010 and 2011 cruises. *Mar. Chem.* 166, 9–24. doi: 10.1016/j.marchem.2014.08.007

Xuan, J. L., Huang, D. J., Pohlmann, T., Su, J., Mayer, B., Ding, R. B., et al. (2017). Synoptic fluctuation of the Taiwan warm current in winter on the East China Sea shelf. *Ocean Sci.* 13 (1), 105–122. doi: 10.5194/os-13-105-2017

Xuan, J. L., Su, J., Wang, H., Huang, D. J., Ding, R. B., Zhou, F., et al. (2019). Improving low-resolution models *via* parameterisation of the effect of submesoscale vertical advection on temperature: A case study in the East China Sea. *Ocean Model.* 136, 51–65. doi: 10.1016/j.ocemod.2019.03.002

Xuan, J. L., Yang, Z. Q., Huang, D. J., Wang, T. P., and Zhou, F. (2016). Tidal residual current and its role in the mean flow on the changjiang bank. *J. Mar. Syst.* 154, 66–81. doi: 10.1016/j.jmarsys.2015.04.005

Yakushev, E., Pakhomova, S., Sørenson, K., and Skei, J. (2009). Importance of the different manganese species in the formation of water column redox zones: Observations and modeling. *Mar. Chem.* 117 (1), 59–70. doi: 10.1016/j.marchem.2009.09.007

Yang, S. C., Zhang, J., Sohrin, Y., and Ho, T. Y. (2018). Cadmium cycling in the water column of the kuroshio-oyashio extension region: Insights from dissolved and particulate isotopic composition. *Geochim. Cosmochim. Ac.* 233, 66–80. doi: 10.1016/j.gca.2018.05.001

Ya, M., Wang, X., Wu, Y., Li, Y., Yang, J., Fang, C., et al. (2017). Seasonal variation of terrigenous polycyclic aromatic hydrocarbons along the marginal seas of China: input, phase partitioning, and ocean-current transport. *Environ. Sci. Technol.* 51 (16), 9072–9079. doi: 10.1021/acs.est.7b02755

Yemenicioglu, S., Erdogan, S., and Tugrul., S. (2006). Distribution of dissolved forms of iron and manganese in the black Sea. *Deep-Sea. Res. Pt. II.* 53 (17), 1842–1855. doi: 10.1016/j.dsr2.2006.03.014

Yool, A., and Fasham, M. J. (2001). An examination of the "continental shelf pump" in an open ocean general circulation model. *Global Biogeochem. Cy.* 15 (4), 831–844. doi: 10.1029/2000GB001359

Zhang, J., Guo, X. Y., and Zhao, L. (2021a). Budget of riverine nitrogen over the East China Sea shelf. *Environ. pollut.* 289, 117915. doi: 10.1016/j.envpol.2021.117915

Zhang, K., Li, A., Huang, P., Lu, J., Liu, X., and Zhang, J. (2019). Sedimentary responses to the cross-shelf transport of terrigenous material on the East China Sea continental shelf. *Sediment. Geol.* 384, 50–59. doi: 10.1016/j.sedgeo.2019.03.006

Zhang, Y., Li, L., Ren, J. L., He, H. J., Zhang, R. F., Zhao, L., et al. (2021b). Distribution and influencing factors of dissolved manganese in the yellow Sea and the East China Sea. *Mar. Chem.* 234, 104002. doi: 10.1016/j.marchem.2021.104002

Zhang, J., Liu, S. M., Ren, J. L., Wu, Y., and Zhang, G. L. (2007). Nutrient gradients from the eutrophic changjiang (Yangtze river) estuary to the oligotrophic kuroshio waters and re-evaluation of budgets for the east china sea shelf. *Prog. Oceanogr.* 74 (4), 449–478. doi: 10.1016/j.pocean.2007.04.019

Zhang, R. F., Zhang, J., Ren, J. L., Li, J., Li, F. M., and Zhu, X. C. (2015). X-Vane: A sampling assembly combining a niskin-X bottle and titanium frame vane for trace metal analysis of sea water. *Mar. Chem.* 177, 653–661. doi: 10.1016/j.marchem.2015.10.006

Zheng, L., Minami, T., Konagaya, W., Chan, C. Y., Tsujisaka, M., Takano, S., et al. (2019). Distinct basin-scale-distributions of aluminum, manganese, cobalt, and lead in the north pacific ocean. *Geochim. Cosmochim. Ac.* 254, 102–121. doi: 10.1016/j.gca.2019.03.038

Zhou, F., Xue, H. J., Huang, D. J., Xuan, J. L., Ni, X. B., Xiu, P., et al. (2015). Cross-shelf exchange in the shelf of the East China Sea. *J. Geophys. Res-Oceans.* 120, 1545–1572. doi: 10.1002/2014JC010567

Zhu, J. R., Zhu, Z. Y., Lin, J., Wu, H., and Zhang, J. (2016). Distribution of hypoxia and pycnocline off the changjiang estuary, China. *J. Mar. Syst.* 154, 28–40. doi: 10.1016/j.jmarsys.2015.05.002

frontiers | Frontiers in Marine Science

TYPE Original Research
PUBLISHED 08 February 2023
DOI 10.3389/fmars.2022.1085142

OPEN ACCESS

EDITED BY
Wen Zhuang,
Shandong University, China

REVIEWED BY
Chuanbo Guo,
Institute of Hydrobiology (CAS), China
Fajin Chen,
Guangdong Ocean University, China

*CORRESPONDENCE
Kai Liu
kliu@yic.ac.cn

SPECIALTY SECTION
This article was submitted to Marine Biogeochemistry, a section of the journal Frontiers in Marine Science

RECEIVED 31 October 2022
ACCEPTED 13 December 2022
PUBLISHED 08 February 2023

CITATION
Ren P, Schmidt BV, Liu Q, Wang S, Liu X, Liu K and Shi D (2023) Fractionation of toxic metal Pb from truly dissolved and colloidal phases of seaward rivers in a coastal delta. *Front. Mar. Sci.* 9:1085142. doi: 10.3389/fmars.2022.1085142

Fractionation of toxic metal Pb from truly dissolved and colloidal phases of seaward rivers in a coastal delta

Peng Ren[1], Bjorn V. Schmidt[2], Qun Liu[3], Shuzhen Wang[4], Xinyan Liu[5], Kai Liu[1,6*] and Dalei Shi[1]

[1]Dongying Research Institute for Oceanography Development, Dongying, Shandong, China, [2]Department of Biological and Environmental Sciences, Texas A&M University-Commerce, Commerce, TX, United States, [3]Bureau of Agriculture and Rural Affairs of GuangRao, Dongying, Shandong, China, [4]Dongying Real Estate Registration Center Dongying Branch, Dongying, Shandong, China, [5]Natural Resources and Planning Bureau of Lijin, Dongying, Shandong, China, [6]China University of Petroleum, National University Science and Technology Park Postdoctoral Workstation, Dongying, Shandong, China

Colloids of natural river water is a key intermediate carrier of lead (Pb). It is important to monitor the transport–transformation behavior of Pb in the colloidal phase of seaward water because this behavior is related to the levels of pollution input and environmental risks posed to the sea, especially in coastal delta areas. In this study, the fractionation behavior and distribution of toxic Pb from the truly dissolved phase and the different colloidal phases in seven seaward rivers in the Yellow River Delta were investigated. The concentrations of total dissolved Pb, truly dissolved Pb, and colloidal Pb were 0.99–40.09 μg L^{-1}, 0.40–8.10 μg L^{-1}, and 0.60–35.88 μg L^{-1}, respectively. In freshwater rivers, the main component of total dissolved Pb (about > 50%) is truly dissolved Pb but the main component of total dissolved Pb in the seawater environment is colloidal Pb (> 80%). A dramatic increase in salinity causes the deposition (about ≈94%) of all forms of Pb to sediment from estuarine water in winter. However, this sedimentation behavior of colloidal Pb gradually decreases (in the Shenxiangou River) when the river salinity approaches seawater salinity (S = ≈29). In the industrial port (Xiaoqinghe River) and mariculture (Yongfenghe River) estuarine areas, which have extensive seawater, the deposition behavior of colloidal Pb (<15%) is less affected by the change in salinity. This suggests that human activity contributes to the spread of Pb in the offshore environment. The concentration of 100 kDa–0.22 μm Pb has a postive correlation with total colloidal Pb. Its variation is minimally affected by salinity compared with other colloidal components. In addition, the correlation between the molecular weight and aromaticity of chromophoric dissolved organic matter (CDOM) and colloidal Pb suggests that macromolecules in seawater will be important transport carriers of Pb. In all, truly dissolved Pb is the main transport form of dissolved Pb in river freshwater; however, in brackish water in estuaries, colloidal matter gradually becomes the

main transport carrier. Surging salinity immobilizes truly dissolved Pb in the estuarine region, but colloidal matter inhibits this deposition. Colloidal phase is the important conversion for land–sea transport of Pb by seaward rivers.

KEYWORDS

metal fractionation, colloidal components, salinity deposition, truly dissolved, migration behavior

1 Introduction

Heavy metals pose a very serious health risk for humans and wildlife because of their biological toxicity, carcinogenic effects, and ability to bioaccumulate in food chains (Huang et al., 2011; Latosinska and Czapik, 2020; Men et al., 2020; Xiang et al., 2021). These risks are mainly dominated by metal speciation and existence in the environment (Weng et al., 2014). Previous studies have shown that free heavy metal ions have significantly higher toxicity and form deposits more easily because of their higher redox potential (Dallas et al., 2013). However, macromolecular organic compounds (>1 kDa, kilodalton), including natural colloidal organic matter, could complex the structure of the free metal ions, and their ability to form deposits (Fytianos, 2001). Natural aqueous environments, such as rivers, seas, and lakes, could supply abundant natural macromolecular organic matter (the main components of natural organic matter) to complex the free metal ions' structure, and their ability to form deposits (Fytianos, 2001). Furthermore, colloidal organic matter (COM) rich in hydroxyl functional groups, tends to make the bound metal more lipid-soluble, which enhances its bioavailability for metals such as lead (Pb), mercury (Hg_3), and antimony (Sb_{51}) (Hargreaves et al., 2018). This could have a profound impact on the migration and conversion behaviors of heavy metals in river environments (He et al., 2016). However, emphasizing the diverse effects of these factors, colloidal organic matter, which is mainly composed of humic acid, often also plays a role in reducing metal toxicity. In addition, colloidal organic matter can modify the surface properties of particles to facilitate or hinder their adsorption of metal ions (Liu and Gao, 2019). Therefore, it is necessary to investigate the geochemical behavior between heavy metals with natural colloidal organic matter in natural water systems.

Lead (Pb), is widely used in natural water environments and, therefore, is a reliable indicator of human activity in these environments, and is a compound that has a unique geochemical behavior (Zhang et al., 2008). Pb ions typically have high exhibit biotoxicity, they easily form sediments, and are difficult to release from mineral and particulate states (Savenko and Savenko, 2019). However, natural organic matter (mainly colloidal organic matter) has a strong complexing effect on Pb ions and facilitates Pb migration and release. It has been demonstrated that colloidal organic matter can prevent the formation of low-solubility mineral lead, such as cerussite and hydrocerussite crystals, and enhance the formation of soluble lead ions (Abdelrady et al., 2021). The chromophoric dissolved organic matter (CDOM), which is an important component of colloidal matter, could be the key factor to influence the geochemical behavior of Pb (Stolpe and Hassellov, 2010). The CDOM-complex-Pb could directly contact plasma membranes of organisms by adsorption and express a higher biological risk than free ions, ultimately (Nadella et al., 2013; Worms et al., 2015). However, environmental conditions, such as the pH value of seawater (i.e., seawater acidification), are important factors that affect the distribution of heavy metals in different phases (Lao et al., 2019; Ma et al., 2019; Lao et al., 2022). Under the influence of salinity and pH, the binding ability of different components of CDOM to Pb varies greatly (Wood et al., 2011). Furthermore, the change of physicochemical factors also affects the molecular structure of the CDOM (Guzman et al., 2014), which in turn affects the formation of complex bonds between CDOM and metal ions (Liu et al., 2019). This biogeochemical process is key factor to affect the environment risk of Pb in the environment which salinity and pH changed dramaticly (Marcinek et al., 2022). In all, the transformation to the colloidal phase is a very important aspect of the geochemical cycle of Pb in natural water systems.

River water flowing into the sea is the most important transportation and conversion channel for Pb in the natural environment, especially in coastal deltas. Pb enters offshore waters as part of the river flow, in turn having toxicological effects on marine organisms such as plankton, urchin and fish (Cao et al., 2018). Meanwhile, these rivers tend to vary drastically in salinity, which could have a profound effect on the interaction between CDOM and Pb (Marcinek et al., 2022). It is important to monitor the concentration, distribution, and sources of Pb in rivers flowing into sea. The Yellow River Delta is a typical wetland ecosystem in a warm, temperate zone of the world. Unlike the Pearl River and the Yangtze River deltas, which have highly developed industries, there are several unique features

pertaining to the industrial and economic development in this region. This region comprises a highly developed chemical industry in a narrowly confined space, an undeveloped nature reserve, and regions with primarily agricultural and maricultural developments (Zhi et al., 2020). These areas are closely linked through a dense network of rivers in the delta. Some rivers also serve at the same time as a source of water and a sewage ditch (Cheng et al., 2021). These rivers are the primary transportation and conversion channels through which Pb enters Laizhou Bay. As the fastest hydrodynamic exchange (0.52a) area within the Bohai Sea, Laizhou Bay could potentially spread Pb to the Bohai Sea and even to the Yellow Sea (Lin et al., 2019). Recently, the pollution control required in the Yellow River Delta and the Bohai Sea has received unprecedented attention from the Chinese government (Ma et al., 2019). It is essential to monitor the ecological risk speciation of Pb in the rivers flowing into sea in these deltas. Analysis of colloidal Pb in the rivers would provide essential evidence for evaluating the environmental risks posed by pollution in the Bohai Sea and the Yellow River Delta.

In this study, the distribution and fractionation of Pb at different stages of the colloidal phase (<1 kDa, 1–3 kDa, 3–10 kDa, 10–100 kDa and 100 kDa–0.22 μm) in six seaward rivers of the Yellow River Delta in winter were investigated. The six rivers pass through urban, industrial, mariculture, and agricultural areas located in the south and northeast region of the Yellow River Delta. There are two main rivers (the Yellow River and Xiaoqinghe River), and four canals driven by the Yellow River: Yongfenghe River, Guangli River, Xiaodaohe River and Shenxiangou River. We selected winter as the period to study the fractionation of the toxic metal Pb in the colloids. In this season, the change of colloidal properties is slow because of the lower winter temperatures, which could prolong the interaction time between Pb and colloidal matter (Wu et al, 2020; Mudge et al., 2021).

2 Materials and methods

2.1 Reagents and labware preparation

In this study, the maximum experimental safe gap must be minimized because there are trace levels of Pb in the Yellow River (Gao et al., 2015). All reagents used in this study were guaranteed reagent (GR) grade. The concentrated form of nitric acid (HNO_3) (Fisher®) used in this study was distilled by an acid purification system (DST-4000, Savillex™). The stock solution of 1 mg L^{-1} Pb was prepared in 10% HNO_3 (v/v) by multistage dilution. The 1000 mg L^{-1} standard solution was prepared in 500 mL of polytetrafluoroethylene bottles (Asone®). The Pb standard solution was Cl-forms (+2) and was supplied by the National Center of Analysis and Testing for Nonferrous Metals and Electronic Materials, China. Ultrapure water (>18 MΩ-cm) was obtained by a water purification system (Milli-Q®).

The labware, including sampling bottles and tubes, had to be made from Teflon materials (Teflon®) and cleaned according to a strict trace metal cleaning process (Liu et al., 2018). First, a pre-cleaning process was conducted to wash away obvious dirt from the labware, with tap water, 10% cleaning solution (v/v) (Decon90®), and ultrapure water (>18 MΩ-cm), being used successively. Second, the pre-cleaned labware was soaked in 10% hydrochloric acid (HCL) (v/v) (Fisher®) and 3% HNO_3 (v/v) for 48 h, respectively. Ultrapure water was used to rinse residual acid off the soaked labware; this was performed five times. Finally, labware were dried in the ultra-clean bench (Class 100) at room temperature (i.e., 20–25°C). After drying, each piece of labware was double-bagged in polyethylene Ziploc (Ziploc®) bags and stored in a sealed container at a consistent temperature range of 20–25°C.

2.2 Sampling collection

The study areas were in the Yellow River Delta, which is a typical wetland ecosystem in a warm, temperate zone of the world (Figure 1). Sampling stations were selected according to the locations of cities, villages, farmlands, industrial areas, breeding areas, and salt fields that the seaward rivers passed through during January 2020 (Figure 1). Surface water samples (10–20 cm) were collected and the clean sampling system was used according to the trace metal rule to avoid contamination at all stations. The clean sampling system is composed of a desktop ultra-clean workbench, peristaltic pump, water intake system, syringe filter, and a sampling bottle (Li et al., 2015; Liu et al., 2018). All sample components were connected by C-Flex tubes. The sample process is briefly described below (Figure 2A). First, the water intake system was washed five times with ultrapure water before sampling. Second, the pre-washed water intake system was placed 10–20 cm below the surface at the sample water station. Third, the peristaltic pump (Masterflex®) was turned on so that the water sample passed through the syringe filter (Swinnex®) with the pre-installed membrane (0.22 μm; Pall®). The first 10 mL of sample was discarded to prevent interference from the membrane. A total volume of 1 L of the water sample was collected into the fluorinated high-density polyethylene sample bottle (Nalgene®), after which 1 mL of concentrated HNO_3 was added and the sample stored at room temperature. The other 1 L of water was collected in the fluorinated high-density polyethylene sample bottle and metal was separated by ultrafiltration as soon as possible in the laboratory (<48 h). A total of 70 mL of water sample was taken in a brown glass bottle for DOC and CDOM analysis (<48 h). Further steps were required. The water intake system

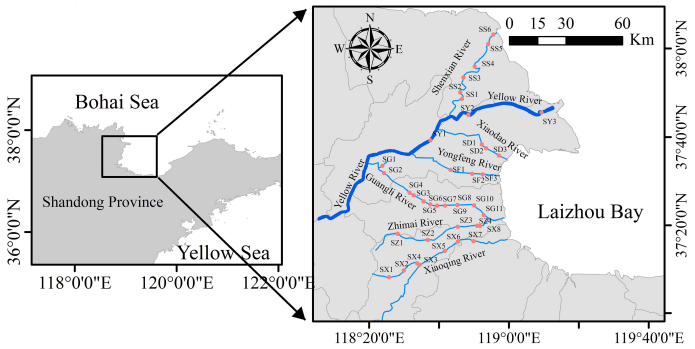

FIGURE 1
Location map of sampling stations in seaward rivers in the Yellow River Delta. The blue dots indicate sampling sites, and the blue line represents the river.

should be soaked in 3% HNO_3 (v/v) until just before use. The filter membrane should be replaced after the filtration of every sample. The basic hydrological data, such as salinity, pH, and temperature, were measured by the multiparameter water quality analyzer (YSI®).

2.3 Colloidal Pb fractionation

The different sizes of colloidal Pb were separated according to centrifugal ultrafiltration (CUF) units (Amicon® Ultra-15) using a fixed-rotor centrifuge (Cence®). Four cut-off values (i.e., <1 kDa,<3 kDa,<10 kDa,<100 kDa) of CUF units were used. The ultrafiltration process is as follows (Figure 2B). First, the CUF units were sequentially washed 6–8 times with 0.1% sodium hydroxide (NaOH) (g/g), 0.06% HCl (v/v), and ultrapure water to remove possible contaminants (Lu et al., 2020). Second, 15 mL of sample was loaded to the obtain the different cut-off values and centrifuged for 50–70 min at 4800×g in the rotor centrifuge. Approximately 0.5 mL of ultrafiltrate was obtained from the inner ultrafiltration tube and transferred to the pre-cleaned 10-mL polypropylene sample centrifuge tube (Falcon™). After CUF, 1 mL of 3% HNO_3 (v/v) was added to the inner tube and soaked for 2 h to extract the residual colloidal metal. The extraction was performed three times and mixed in the sample tube. The volume of colloidal sample was adjusted to 5 mL with 3% HNO_3 (v/v). Before measuring, colloidal Pb samples were stored in an ultra-clean bench (Class 100; at 25°C) for more than 1 week to ensure that the colloidal organic matter was fully decomposed. Finally, 0.2 mL of the decomposed solution was diluted to 10 mL with 3% HNO_3 (v/v); this solution was then used for detecting colloidal Pb.

A method blank and solvent blank of the ultrafiltration were used simultaneously with samples to assess errors. It should be noted that the actual cut-off values of the CUF used in this experiment were generally higher than those stated by the

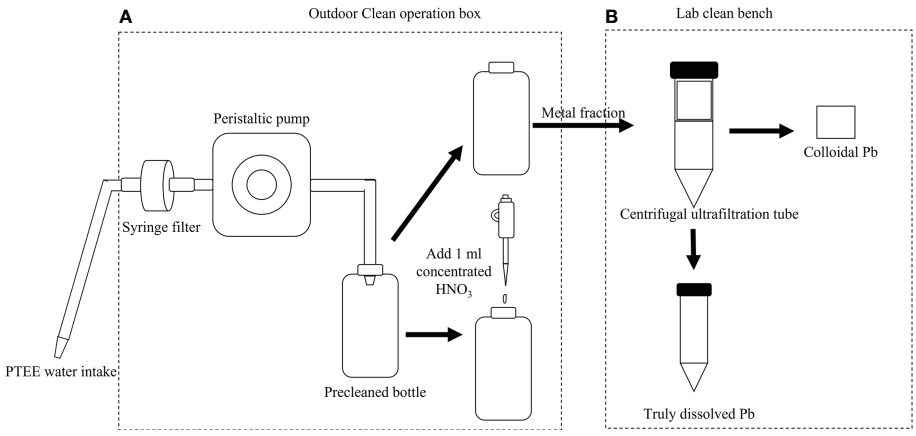

FIGURE 2
The diagram of clean sampling and metal fractionation. **(A)** The clean sampling process; and **(B)** the metal fractionation process.

manufacturer (Xu et al., 2018; Lu et al., 2020). This can usually lead to biased perceptions of the colloidal trace element concentration in the ultrafiltrate by researchers. We used standard macromolecules, including vitamin B_{12} and standard fluorescent-tagged dextrans, to calibrate the CUF units according to previous studies (Lu et al., 2019; Lu et al., 2020).

2.4 Fractionation factor

The fractionation factor (F) was defined as the ratio of the concentration of truly dissolved Pb and colloidal Pb to evaluate the fractionation behavior of Pb by the colloids present in the system (Liu et al., 2019):

$$Fclt = \frac{C_{Pb,c}}{C_{Pb,t}}$$

where $C_{Pb3,c}$ and $C_{Pb3,t}$ are the concentrations of Pb in colloids, respectively. $F_{c/t}$ is the fractionation factor between colloidal Pb and truly dissolved Pb. When the $F_{c/t} > 1$ or< 1, the Pb preferentially migrated to colloidal matter or the truly dissolved phase.

2.5 Chromophoric dissolved organic matter

The UV absorption spectrum of CDOM was measured using a UV–Vis spectrophotometer (TU-1950, Persee®). Ultrapure water was used as a blank and for baseline scanning. The samples were spectrally scanned in the range of 200–800 nm, and the scanning interval was 1 nm. All absorbance values were deducted by the mean value of the 680–700 nm range to eliminate the refractive index differences and baseline drift.

The absorption coefficient $a(355)$ was selected as the parameter represent the concentration of CDOM and was calculated from the following equation (Peuravuori and Pihlaja, 1997; Wu et al., 2022):

$$a(\lambda) = 2.303xA(\lambda)/L$$

where $a(\lambda)$ (m^{-1}) is the absorption spectrum at the wavelength of λ nm; $A(\lambda)$ is the absorbance at the wavelength of λ nm; and L is the length of cuvette.

The specific ultraviolet absorbance ($SUVA_{254}$) was defined as the ratio of the absorption coefficient at the wavelength of 254 nm to the concentration of dissolved organic matter (DOC) of the sample. This parameter could represent the aromaticity of CDOM in the aquatic system. It was calculated from the following equation (Peuravuori and Pihlaja, 1997; Wu et al., 2022):

$$SUVA_{254} = \frac{a(254)}{C_{DOC}}$$

where $SUVA_{254}$ (l (mg m)$^{-1}$) is the specific ultraviolet absorbance; $a(254)$ is the absorption spectrum at the wavelength of 254 nm; and C_{DOC} is the concentration of dissolved organic matter.

The ratio of the absorption coefficient (E2 : E3) at a specific wavelength was used to represent the change of the relative molecular weight of CDOM and was calculated using the following equation (Peuravuori and Pihlaja, 1997; Wu et al., 2022):

$$\frac{E_2}{E_3} = \frac{a(250)}{a(365)}$$

where E_2/E_3 is the ratio of the absorption coefficient of the water sample at the wavelength of 250 and 365 nm; $a(250)$ is the absorption coefficient at the wavelength of 250 nm; and $a(365)$ is the absorption coefficient at the wavelength of 365 nm.

2.6 Instruments and analysis

In this study, the concentration of different sized colloidal Pb was determined by using an inductively coupled plasma mass spectrometer (ICP-MS, iCAP RQ, Thermo Fisher Scientific Inc). The internal standard [indium (In_{49}), 10.00 μg^{-1}] was spiked in every sample. To maintain the stability of the instrument, we used 1.00 μg L^{-1} tune solution [lithium (Li_3), cerium (Ce_{58}), barium (Ba_{56}), In_{49}, and uranium (U_{92})] to monitor the oxide formation (BaO/Ba< 3%). The isobaric interference on Pb was corrected by monitoring ^{200}Hg and ^{111}Cd (Cd_{48}). The data of ^{108}Pb, ^{65}Cu (Cu_{29}), ^{68}Zn (Zn_{30}), ^{85}Sr (Sr_{38}), ^{89}Y (Y_{39}), and ^{95}Mo (Mo_{42}) were used to monitor the potential polyatomic interference. ICP-MS analysis was conducted with 99.999% argon at the optimized plasma gas flow rate (GFR) of 15.0 L min^{-1}, an auxiliary GFR of 1.2 L min^{-1} and at a nebulizer GFR of 0.88 L min^{-1}.

To ensure the accuracy of the method, we measured the method blanks to verify and control the reliability of the analysis data. The method blanks were determined by using an ultrapure water sample. The method blank followed the same process as sample preparation as follows: 3% HNO_3 extraction, 3% HNO_3 dilution, and ICP-MS parallel determination (n = 11) (Lu et al., 2020). The quantification limits [i.e., limit of quantification (LOQ)] for Pb were 10 times that of the standard deviation (σ) of the blanks, and the detection limits [i.e., limit of detection (LOD)] were 3σ (Table 1). To verify LOQ and LOD, we used the GBW08608 and GSB07–1183 reference materials to test the linear correlations (R^2) of the method. The linear ranges were 0.2 μg L^{-1}, 0.5 μg L^{-1}, 1 μg L^{-1}, and 2 μg L^{-1}. The performance was shown in Table 1. 0.50 μg L^{-1} of Pb standard sample was determined every 12 samples to measure the stability of the ICP-MS.

ICP–MS, inductively coupled plasma mass spectrometer; LOD, limit of detection; LOQ, limit of quantification.

TABLE 1 Performance of the inductively coupled plasma mass spectrometer (ICP-MS) and the analysis method.

	LOD (μg L^{-1})	LOQ (μg L^{-1})	Linear ranges (μg L^{-1})	Linear correlations (R^2)
Analysis method	0.14	0.43	–	–
GBW08608	–	–	0.2–2	0.9999
GSB07–1183	–	–	0.2–2	0.9999

–, represents no data.

3 Results

3.1 Mass balance, the actual cutoff of centrifugal ultrafiltration

The fractionation method, solvent used, and detection error will determine the result of Pb in the different samples. We used the mass balance (M) to monitor the precision of the result. The mass balance was defined as the ratio between the dissolved concentration of Pb of the non-fractionated sample and the summary of the different fractionation concentrations of Pb. Once the difference value between M and 100% was less than 10%, we believe that there on loss during the experiment. Moreover, once the value reached greater than 10%, we believed that the loss of Pb affects the result of the experiment (Liu and Gao, 2019). The mass balance ratio results of the different stations are shown in Figure 3. The mass balance ratio difference between M and 100% was 9%–10%. This means that the level of error introduced by the method, solvent and detection was overlooked in this study. Notably, the recovery ratio varied with the location of the sample station. Higher recovery ratios were observed in stations influenced by human activities. It is shown that there is an inference relationship between human activities and Pb. Intense human activity often leads to a stronger release of Pb into the environment (Zang et al., 2020). It will lead to the introduction of Pb contamination during field sampling or pre-treatment, ultimately causing high recovery rates (Chen et al., 2022).

The actual cut-off value for CUF was consistent with previous work because we used the same batch of products in this study (Liu et al., 2018; Lu et al., 2019; Lu et al., 2020). The actual MWCO of the 1, 3, 10 and 100 kDa CUF units were estimated to be 2, 7, 32 and 393 kDa, respectively. This indicated an overestimation of the colloidal trace element concentration in the ultrafiltrate of this study. However, the ultrafiltration performance of the CUF could still precisely fractionate the Pb into different sized colloids. Therefore, the experimental results could reflect the migration behavior of Pb from truly dissolved to colloidal phases in rivers flowing into sea.

3.2 Hydrographic parameters

Hydrographic parameters such as water temperature, salinity and pH of the rivers are described in Table 2. Water temperature of all the stations fluctuated in the range of 1.6°C to 7.8°C, with gradual decreases toward the direction of input sea. In addition, more than 80% stations were lower than 5°C, which

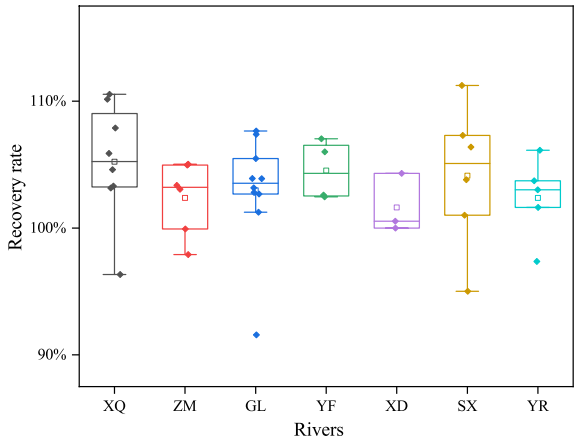

FIGURE 3
The mass balance of lead (Pb) in different rivers. XQ represents the Xiaoqinghe River; ZM represents the Zhimaihe River; GL represents the Guanglihe River; YF represents the Yongfenghe River; XD represents the Xiaodaohe River; SX represents the Shenxiangou River; and YR represents the Yellow River.

10.3389/fmars.2022.1085142

TABLE 2 Hydrographic parameters, such as water temperature, salinity, and pH of the rivers.

Sample station	Temperature (°C)	pH	Salinity (S)
Yellow River			
SY1	2.7	8.71	0.42
SY2	2.4	8.71	0.42
SY3	1.8	8.84	0.42
Xiaoqinghe River			
SX1	6.0	8.29	1.2
SX2	5.8	8.28	1.21
SX3	7.8	8.17	2.67
SX4	6.8	8.32	2.08
SX5	5.5	8.43	1.88
SX6	5.3	8.36	2.13
SX7	4.8	8.42	2.10
SX8	3.7	8.30	7.70
Yongfenghe River			
SF1	1.6	8.62	9.42
SF2	2.6	8.52	9.09
SF3	2.2	8.44	15.38
Xiaodaohe River			
SD1	2.3	8.49	21.45
SD2	3.2	8.43	21.86
SD3	2.4	8.47	26.42
Zhimaihe River			
SZ1	3.5	8.32	4.33
SZ2	3.1	4.18	8.71
SZ3	3.9	7.83	8.57
SZ4	2.5	8.21	14.25
SZ5	2.4	8.29	17.20
Guanglihe River			
SG1	3.9	8.24	2.83
SG2	3.3	8.96	1.75
SG3	4.1	8.59	4.93
SG4	5.5	8.16	4.86
SG5	3.9	8.81	3.29
SG6	3.7	9.08	2.68
SG7	3.5	9.08	2.44
SG8	3.6	9.08	2.51

(Continued)

TABLE 2 Continued

Sample station	Temperature (°C)	pH	Salinity (S)
SG9	3.5	9.12	3.77
SG10	3.2	8.51	10.87
SG11	2.7	8.38	18.33
Shenxiangou River			
SS1	3.7	8.37	1.48
SS2	4.1	8.55	0.99
SS3	4.1	8.59	1.11
SS4	3.7	9.25	5.76
SS5	2.0	8.70	21.03
SS6	1.5	8.28	29.46

means that the biogeochemical effects between microorganisms and the metals were very small and could be negligible (Cao et al., 2018; Marcinek et al., 2022). A notable phenomenon was that the water temperature of the Zihe-Xiaoqinghe river system was significantly higher (i.e., ≈1°C) than that of other rivers in this study. Higher water temperatures (i.e., >5°C) were recorded at the station near the village and the highway. The pH of most rivers was above 8.10, and the highest value appeared at the station of Shenxiangou River, with a value of about 9.25 (Table 2). There is an obvious high pH (>9.00) area in the Guanglihe River section passing through the urban area of Dongying City (Figure 3). This higher pH may be related to the weak flow of the river and the salinization of the land. To prevent sea tide intrusion, the flow of the Guangli River into the sea is controlled by a dam with fixed opening and closing times. The damming of the river by humans leads to a weaker flow of the Guangli River. A weak Guanglihe River flow is susceptible to saline seepage from salinized sediment, which often increases the pH of the water (Xie et al., 2019). In addition, in the reach of the Zihe River (which merges into the Xiaoqinghe River), there are stations with pH lower than 8.00, with values around 7.70–7.90. The station with the lowest pH (≈4.18) appears in the Zhimaihe River section, close to an industrial area, and the low pH river section continues for about 15 kilometers. From the potential results, all rivers are reducing environments under alkaline conditions, with the river pH >7.00 (Table 2). Significant differences were found in the salinity of the rivers. For the main rivers, such as Yellow River and Xiaoqinghe River, changes of salinity were not detected owing to the impact of the strong supply of upstream fresh water. There is no significant change of the salinity at the stations of the Yellow River, which remained at 0.42. In the Xiaoqing River, whose hydrodynamic force is weaker than that of the Yellow River, the salinity only reaches 7.00 at the station near the estuary and did not exceed 3.00 at other stations. For the trunk channels, the salinity changed drastically. A pronounced increase of salinity was found along the direction of the seaward river output into the sea. Some sample stations with a salinity greater than 20.00 appeared in the Xiaodaohe River and Shenxiangou River. The salinity changes observed in the Guanglihe River and Yongfenghe River were relatively slow, but the salinity exceeds 15.00 at the stations near the estuary.

3.3 The concentration of Pb in the seaward river

The seaward rivers could be classified into three categories according to the discussion in Section 3.1. The Xiaoqinghe River and the Yellow River are natural rivers (NR). Trunk canals of the Yellow River are divided into two categories according to the influence of tidal seawater. The Yongfenghe River and Xiaodaohe River are rivers strongly influenced by seawater (SFR), whereas the Zhimaihe River, Guanglihe River, and Shenxiangou River are weakly influenced by seawater (WFR).

3.3.1 Total dissolved Pb

Total dissolved Pb is the sum of colloidal and dissolved lead, which reflects the level of transportable Pb in water. It is an important indicator for measuring Pb pollution in the river. The distribution of dissolved Pb in the different rivers was described in Figure 4. The concentration of total dissolved Pb in all rivers ranged from 0.99 to 40.09 μg L^{-1}. The concentration gradually decreased as the location approached the estuary and did not exceed the surface water standard for China (i.e., 100.00 μg L^{-1}) for more than 95% of the stations. Only three stations, SZ1, SX1, and SZ5, were observed with values over and above the standard. SZ1 had a concentration of 19.73 μg L^{-1} and was in the upstream sample area of the Xiaoqing River. SZ1 and SZ5 were all in the Zhimaihe rivers, with the concentrations of 40.09 μg L^{-1} and 12.94 μg L^{-1}, respectively. Among these sites, SX1 and SZ1 are

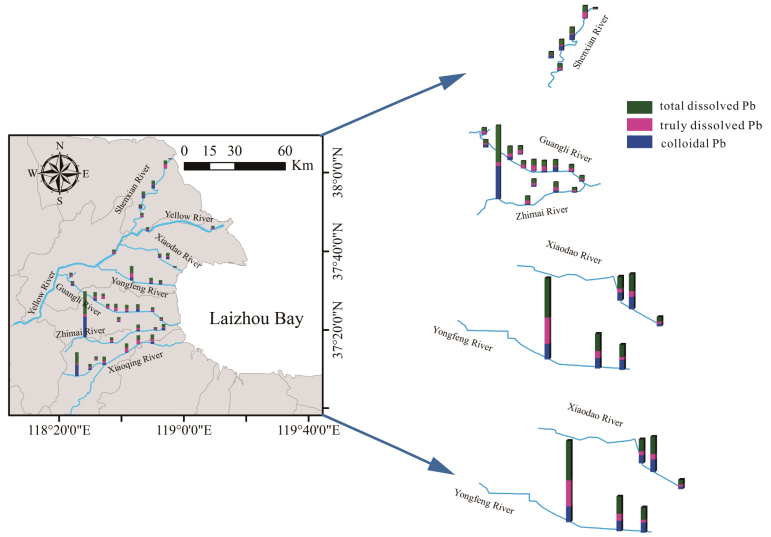

FIGURE 4
The distribution of total dissolved lead (Pb), truly dissolved Pb, and colloidal Pb in different seaward rivers.

the highest concentration points regarding concentrations of Pb and were also the farthest from the estuary along the river where they are located. However, SZ5 is near the estuary. The minimum concentration of total dissolved Pb occurred near the Shenxiangou estuary and was about 0.99 μg L^{-1}.

Obvious variations were found in the distribution trend of total dissolved Pb in different rivers. Among the five trunk canals of the Yellow River, the concentration of Pb decreased gradually with the increase of salinity in rivers, which was strongly influenced by seawater. But in other trunk canals, the distribution of Pb is relatively complex. A trough-like distribution trend of Pb was observed along the direction of the Zhimai River flowing into the sea. The highest fluctuation of about 35.00 μg L^{-1} Pb and a significant increment of about 10.50 μg L^{-1} of Pb was observed at the Zhimaihe estuary. In Shenxiangou and Guangli River, the distribution of Pb showed more frequent and smaller fluctuation changes (i.e., 0.20–5.70 μg L^{-1}). Those differences may be related to the river basin. The sampling areas of the Yongfenghe River and Xiaodaohe River are mostly surrounded by mariculture and salt-drying farms, the Guangli River and Shenxiangou flow through urban areas and townships, and the Zhimaihe River flows through farmland, industrial areas, and salt farms. The concentration of Pb in urban areas was higher than areas of farmland and salt farms. It should be noted that the hydrodynamic forces of these rivers are weaker than natural rivers. For the natural rivers, the distribution of Pb was also different. The concentration of Pb in the Xiaoqing River was significantly higher than that of the Yellow River, and with an average concentration difference of about 5.00 μg L^{-1}. In the Yellow River, the concentration variations in the different stations are lower, with a range of 0.50–1.5 μg L^{-1}. However, it could reach 16 concentration units in the stations of the Xiaoqinghe River. A gradual decrease of Pb concentration was observed as the location approached the estuary in the Yellow River. However, the Pb concentration increased significantly at the SY3. In the Xiaoqing River, the distribution trend of Pb was a mechanical wave like that observed in the Guangli River. A sharp decrease in Pb concentration was recorded at the upstream position of the sampling area (SX1→SX2). In addition, the Pb concentration increased at the junction area of the Zihe River with the Xiaoqinghe River. After the mixture, Pb concentration increased to 7.28 μg L^{-1} at SX3 station.

3.3.2 Truly dissolved Pb

Metal ions in true solution are very mobile and bioavailable Therefore, it is necessary to give a further explanation for the investigation of the geochemical behavior of Pb in the river. Truly dissolved Pb concentrations in the rivers varied with the location of the sample station (Figure 4). For all rivers, the concentration of truly dissolved Pb ranged from 0.25 to 7.37 μg L^{-1}. The highest concentration of truly dissolved Pb appeared at SF1 in the Yongfenghe River and the lowest appeared at SX1 in the Xiaoqing River. In the two natural rivers, truly dissolved Pb was the dominant fractionation (i.e., >60%) of the total dissolved Pb and ranged from 1.57 to 2.99 μg L^{-1}. For both rivers, following a downstream, seaward direction, truly dissolved Pb of the samples increased then declined. The average concentration of truly dissolved Pb in the Xiaoqing River was significantly higher than that in the Yellow River. In some river reaches of the Xiaoqing River, the truly dissolved Pb increased significantly to about 2.22 μg L^{-1}, especially for those sample

stations located in urban or farmland areas. The distribution trend of truly dissolved Pb varied across the trunk canals. A decrease of truly dissolved Pb was found in the SFR river as stations neared the estuary, with a sharp decline to about 4.68 μg L^{-1} observed in the Yongfenghe River. However, truly dissolved Pb demonstrated significant fluctuations in the TFR river. A pronounced increase in truly dissolved Pb was found in the Zhimai River estuary, which was a different pattern from that observed for most other rivers. In the Guangli River, the distribution fluctuation was stronger than that in other TFR rivers. Reaches that flowed through urban areas had significantly higher truly dissolved Pb than reaches in the estuary and canal source. Low levels of truly dissolved Pb (less than 1.00 μg L^{-1}) were observed in the Shenxiangou River, except for SS5 (about 5.98 μg L^{-1}) at the estuary area. However, a sharp decrease (of about 5.60 μg L^{-1}) of truly dissolved Pb occurred with a salinity increase from ≈21.00 to ≈30.00. In general, truly dissolved Pb followed an obvious input and migration process in some areas. Furthermore, these processes are greatly disturbed by human activity.

3.3.3 Colloidal Pb

Colloidal Pb (>1 kDa) is Pb ions complexed with or adsorbed to colloidal matter, which has a relatively stronger bioavailability and chemical activity than other forms of dissolved lead. It is an important reservoir for Pb in natural water. The data of different sizes of colloidal Pb are detailed in Figure 5. As illustrated in the figure, colloidal Pb (>1 kDa) is the major constituent of the total dissolved Pb in the seaward rivers in the Yellow River Delta. A total of 46% of sample stations recorded high percentages (≈50.00%) of colloidal Pb. At the SX1 (on the Xiaoqinghe River), the percentage of the colloidal Pb even accounted for more than 95.00% of the total dissolved metal. Furthermore, there were only three stations that recorded low colloidal fractions below or around 10%: SX6, SG6, and SS5. In the sample stations near the estuary, colloidal Pb was higher, ranging from 41.52% to 86.94%.

In the natural river, the percentage of colloidal lead expressed a different distribution trend. In the Yellow River, most colloidal Pb was close to 40%. As shown in Figure 5A, the metal was mainly bound by the 1–3 kDa and 100 kDa–0.22μm colloidal matter, with values of ≈30.00% and ≈50.00%, in most of stations, respectively. Obvious changes occurred in low MWCO (1–100 kDa). At SY1, 1–3 kDa Pb (≈25.00% decrease) migrated into the 10–100kDa colloidal matter (≈23.00% increase). But at SY3, the percentage of 10–100 kDa Pb decreased to 0% and 3–10 kDa Pb increased from 0.74% to 23.78%, respectively. In the Xiaoqing River, those changes are much more complicated with the input of another river and salinity. As shown in Figure 5B, 1–3 kDa Pb was the main component (> 70.00%) before the input from the Zihe River in the Xiaoqing River. At the mixture station (SX4), the percentage of 1–3kDa Pb decreased to 5.74%, but 100 kDa–0.22 μm Pb and 3–10 kDa Pb increased from 9.71% to 40.16% and 14.39% to 36.07%, respectively. After the mixture, 10–100 kDa Pb was found in a low percentage (of about< 10.00%) and the distribution of colloidal Pb mainly occurred in 3 kDa–0.22 μm colloidal matter. Furthermore, Pb ions prefer to distribute to 3–10 kDa and 100 kDa–0.22 μm colloidal matter near the estuary.

An opposite distribution characteristic of colloidal lead was found in the trunk canals strongly influenced by seawater (SFR). The percentage of colloidal Pb in the Yongfenghe River increased continuously from 39.34% to 80.99% with the increase of salinity, but it gradually decreases from 71.85% to 52.45% in the Xiaodaohe River. There was no obvious relationship between the distribution of Pb in the different sizes of colloidal matter and salinity. Pb ions were still mainly bound by the 1–100 kDa colloidal matter, similar to its distribution characteristic in natural rivers (Figure 5C). In the Xiaodaohe River, which is more affected by seawater, colloidal Pb with a size of 100 kDa–0.22 μm was stable at about 41.00% ± 1.30% (Figure 5D). However, the percentage of 100 kDa–0.22 μm Pb changed significantly in the Yongfenghe River, which is weakly affected by seawater. This shows the obvious migration behaviors of Pb ions in different sizes of colloidal matter.

In the trunk canals weakly influenced by seawater (WFR), colloidal Pb presents various distribution characteristics with different rivers reaches. In the Zhimaihe River, the percentage of colloidal Pb exhibited a fluctuating reduction trend from 89.50% to 56.18% as the stations approached the estuary. A sharp decrease in concentration (from 35.88 μg L^{-1} to 1.28 μg L^{-1}) and the percentage (from 89.50% to 26.83%) of colloidal Pb was observed at the station where the seawater began to interact with freshwater (Figure 5E). The distribution of Pb in different sizes of colloidal matter changed from the 3–10 kDa fraction to the 10–100 kDa and 100k–0.22 μm fractions. Never the less, a significant increase in concentration (i.e., from 1.25 μg L^{-1} to 7.27 μg L^{-1}) and percentage (from 47.71% to 56.18%) of colloidal Pb occurred near the estuary (SZ5). The colloidal Pb mainly was in the 1–3 kDa fractionation at about 47.04% for this station. Differing from the Zhimai River, the Guangli River has a longer section that is not affected by salinity and that also passes through an urban area. The hydrodynamic force of this part of the river is relatively slow, and the interaction between colloidal matter and Pb is more sufficient. The concentration and percentage of colloidal Pb ranged from 0.68 μg L^{-1} to 5.46 μg L^{-1} and from 10.63% to 88.86%, respectively. The distribution of colloidal Pb changed from the 3–100 kDa fraction to the 100 kDa–0.22 μm fraction. Notably, in the station near the estuary, the salinity makes the distribution of Pb more uniform in the different sizes of colloidal matter (Figure 5F). Similar to the Guangli River, the Shenxiangou River also has a reach (SS1→SS4) less affected by seawater (Figure 5G). The concentration and percentage of colloidal Pb ranged from 0.99 μg L^{-1} to 5.88 μg L^{-1} and from 20.77% to 88.99%, respectively, in this area. In this area, colloidal Pb was also mainly distributed in fractions of 3–100 kDa to 100 kDa–0.22 μm. However, the percentage of colloidal Pb decreased to ≈10.00% with a significant increase in salinity. It should be noted that the percentage of colloidal Pb in the total

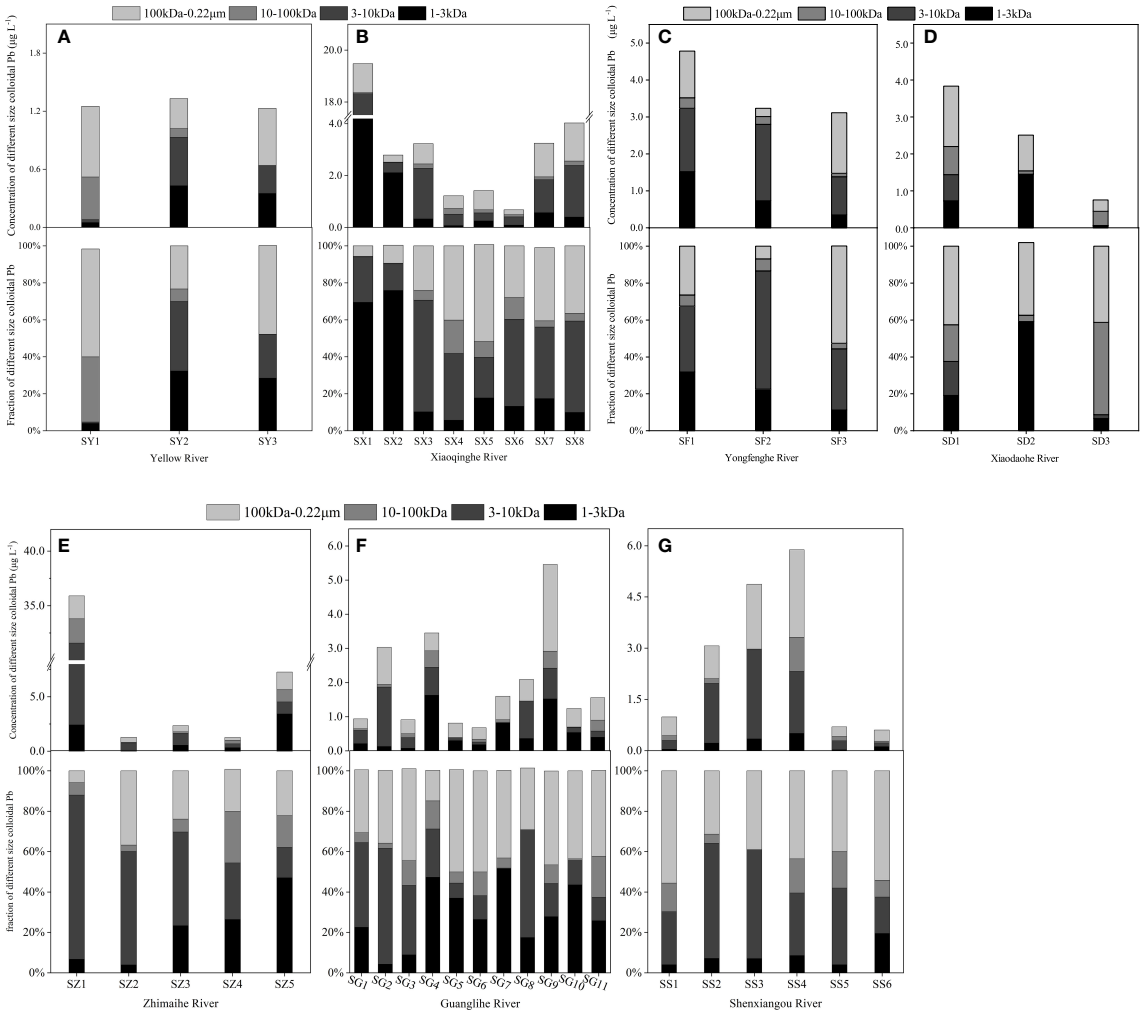

FIGURE 5
The concentration and fractionation of different sizes of colloidal lead (Pb). **(A)** The concentration and fractionation of different sizes of colloidal Pb in the Yellow River; **(B)** the concentration and fractionation of different sizes of colloidal Pb in the Xiaoqinghe River; **(C)** the concentration and fractionation of different sizes of colloidal Pb in the Yongfenghe River; **(D)** the concentration and fractionation of different sizes of colloidal Pb in the Xiaodaohe River; **(E)** the concentration and fractionation of different sizes of colloidal Pb in the Zhimaihe River; **(F)** the concentration and fractionation of different sizes of colloidal Pb in the Guanglihe River; and **(G)** the concentration and fractionation of different sizes of colloidal Pb in the Shenxiangou River.

dissolved metal increased significantly, but the actual concentration decreased. In all, salinity is an important factor that promotes the partitioning of Pb ions into 1–3 kDa and 100 kDa–0.22 μm fractions.

4 Discussion

4.1 The migration behavior of Pb

In this study, the migration behavior of Pb in the Yellow River was used as a reference location. This sample reach is not affected by industrial and domestic wastewater outfalls and agricultural activities in the winter. In addition, the concentration parameters showed that colloidal Pb (1.27 ± 0.06 μg L^{-1}) is basically stable in the Yellow River. This means that the Pb migration mainly occurs between the truly dissolved and particulate or sediment phase related to the weakened hydrodynamics. As the Yellow River flows into the sea, the main channel gradually becomes wider with a reduction in flow (Du et al., 2022). Low hydrodynamic action increases the chance of truly dissolved Pb entering the sediment with particle settlement (Moore et al., 1996). However, anthropogenic activities significantly influenced the Pb concentration behavior regarding partition patterns between colloid and truly dissolved Pb in other rivers. The change trend of the

fractionation factor (F) of Pb in the different phases is shown in Figure 6. The Xiaoqing River sampling area consisted of three reaches, the upper reach (SX1), the middle reach (SX2→SX6) and the estuary (SX7→SX8) (Figure 1). The upper reach and the estuary are greatly affected by chemical industry, salt industry, and port activities, whereas the middle reach is less affected by human activities because there is little agricultural activity in winter. Sewage discharge from the refining and chemical industry likely led to the surge of colloidal Pb (to 19.60 μg L^{-1}) at the SX1 station. Downstream in SX2, the colloidal Pb decreased sharply and truly dissolved Pb was stable. This phenomenon might be due to the unstable upstream chemical source of colloidal Pb, and input sources disappeared in this region (Teien et al., 2004). In addition, the colloidal Pb and truly dissolved Pb in the Xiaoqing River increased significantly after passing through some large residential areas (SX4). This phenomenon is related to the direct discharge of sewage from this area (Gu et al., 2022). Domestic wastewater produced by residential areas often contains large amounts of Pb and organic matter (Deng et al., 2020; Silva et al., 2020). In addition, this residential area is also home to petrochemical factories. The factories could produce wastewater containing high levels of Pb and organic matter (Wang et al., 2017; Dong et al., 2022). Hence, the domestic mixed factory discharge is likely to be an important source and disturbance factor of Pb in the Xiaoqing River. Notably, total dissolved Pb changed little after flowing through the area with less human influence (SX4→SX6). Furthermore, the dissolved Pb mainly migrated from the colloid phase to the truly dissolved phase (Figures 5, 6). This phenomenon is the opposite of the behavior of dissolved Pb in the Yellow River. It may be related to a difference of types of colloidal organic matter that are present in the Yellow River and the Xiaoqing River (Lu et al., 2021). An increase in colloidal Pb was observed after passing through the Yangkou port with its intensive human activities (SX8). The significant reduction of truly dissolved Pb in this region may be related to the rapid increase in salinity. Similar phenomena as were observed in the Xiaoqing River was also observed in the Zhimaihe River, the Yongfenghe River, and the Xiaodaohe River. Both the concentration and the fractionation of colloidal Pb significantly increased after those rivers passed through ports or residential areas (Figure 5). However, the migration of Pb was more complex in the Guanglihe River and Shenxiangou River because of the lower hydrodynamic force combined with the higher flow through urban areas. Previous studies have shown higher levels of Pb and more variable biogeochemical parameters, such as DOC and CDOM, in rivers flowing through urban areas (Liang et al., 2018; Liu et al., 2022). Overall, domestic and industrial sewage were the dominant factor regarding partitioning between truly dissolved Pb and colloidal Pb in the rivers flowing into the sea in the Yellow River Delta in the winter.

4.2 The roles of salinity, pH, and temperature

As shown in Figure 7, total dissolved Pb sharply decreased with salinity gradient, expect for the Zhimaihe River. It previously demonstrated that salinity could induce the flocculation of Pb in river water and this behavior was non-conservative (Wu et al., 2015). However, Pb in different phase express different behavior. Truly dissolved Pb gradually decreased with the salinity gradient and expresses a non-conservative behavior (Figure 7). But for colloidal Pb, both non-conservative and conservative behavior can be observed. The removal behavior of Pb mainly occurs in the truly dissolved

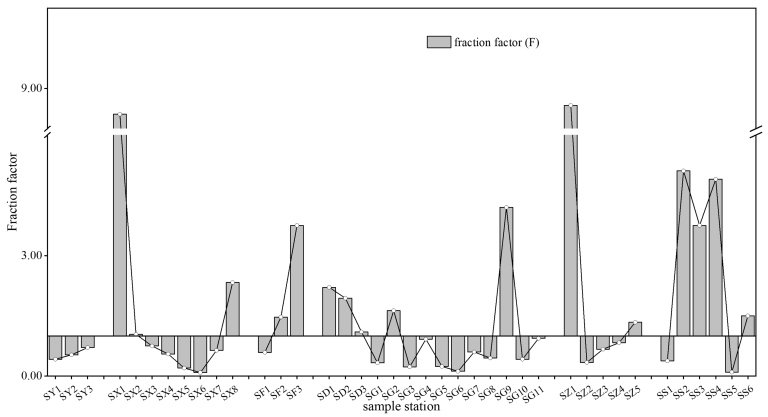

FIGURE 6
The fractionation factor (F) of lead (Pb_3) between the colloidal and truly dissolved phases. SY represents the Yellow River; SX represents the Xiaoqinghe River; SF represents the Yongfenghe River; SD represents the Xiaodaohe River; SZ represents the Zhimaihe River; SG represents the Guanglihe River; and SS represents the Shenxiangou River.

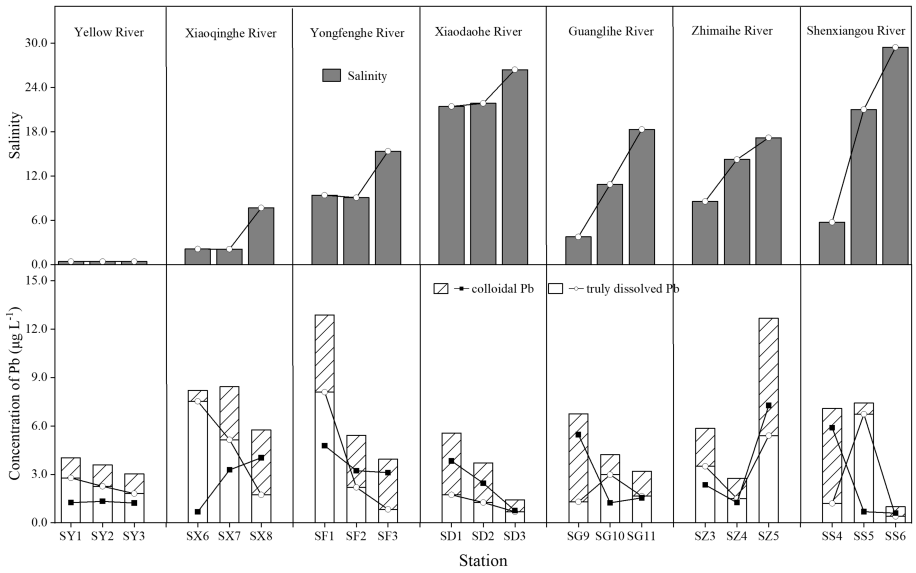

FIGURE 7
Changes in the trend of total dissolved lead (Pb) with the increase of salinity in different rivers.

state. This phenomenon may be the result of the combined effect of the speciation of Pb ions and the flocculation effect of salinity on low molecular organic matter (Xu et al., 2020; Nghiem et al., 2022). At elevated pH (>8.00), Pb ions easily transform to $PbCO_3$ precipitate with increasing of salinity (Powell et al., 2009). Some studies had demonstrated that organic Pb chelates was the dominate species in the truly dissolved Pb in natural water (Raudina et al., 2021). Therefore, the gradual increase in salinity and higher pH promotes the precipitation of truly dissolved Pb (Table 2). To clarify this combined effect, we performed principal component analysis of the pH and salinity variables with different state Pb and shown in Figure 8. From the figure we could found, pH values and salinity of the river water have similar negative correction with the dissolved Pb, especially for the truly dissolved Pb. But for colloidal Pb, pH expresses a positive correlation (Figure 8B). Meanwhile, pH had more intense effect than salinity for all state Pb (Figure 8). This behavior may dominate by the interaction between salinity, pH, and the accumulation of colloid matter (Cantwell and Burgess, 2001). Salt may induce organic matter to aggregate with each other for flocculation (Lasareva et al., 2019), but not completely flocculate the large sized colloidal matter (Herzog et al., 2019). The colloidal material can be stable under high pH and high salinity such as humic acid (Liu and Gao, 2019; Furukawa et al., 2014). The coagulation of inorganic colloids would reduce while above a certain salinity range, especially in presence of organic matter (Wang et al., 2015; Zhang et al., 2015). Therefore, temperature might another factor to affect the migration of Pb. It had demonstrated that temperature tended maintain the stabilization COC in the winter river (Gong et al., 2022). The principal component analysis between the temperature with different dissolved state Pb also performance (Figure 8). Low temperature had a positive correction with the state of dissolved Pb (Figure 8). It means temperature might an important factor to maintain the dissolve state of Pb. However, pH had a significant negative correction with the truly dissolved Pb (Figure 8C). It means truly dissolved Pb removal from the water in the estuary area where the salinity increasing rapidly, higher pH values, and especially in the low temperature. These results suggested that low temperature, high pH, and increased salinity have a combined or together effect on the removal of Pb form river water. These three biogeochemical factors associated reduced 33.3%≈95.4% of Pb entering to the sea with the seaward river.

4.3 The role of colloidal matter

Colloidal Pb was stable, and the colloidal organic carbon (COC, represented by the concentration of DOC) decreased with the direction toward the sea in the Yellow River (Figure S1). However, 10–100kDa colloidal Pb demonstrates a significant correlation with the change of COC (Table S1; Figure S1). This phenomenon might be related to the components of colloidal matter. It has demonstrated that different colloidal components could strongly bind the Pb_3 ions in water, and this binding ability varies with the character of the colloidal matter (Stolpe and Hassellov, 2010; Feng et al., 2022). However, it is difficult to clarify this effect because of the lack of analysis techniques that exactly separate and

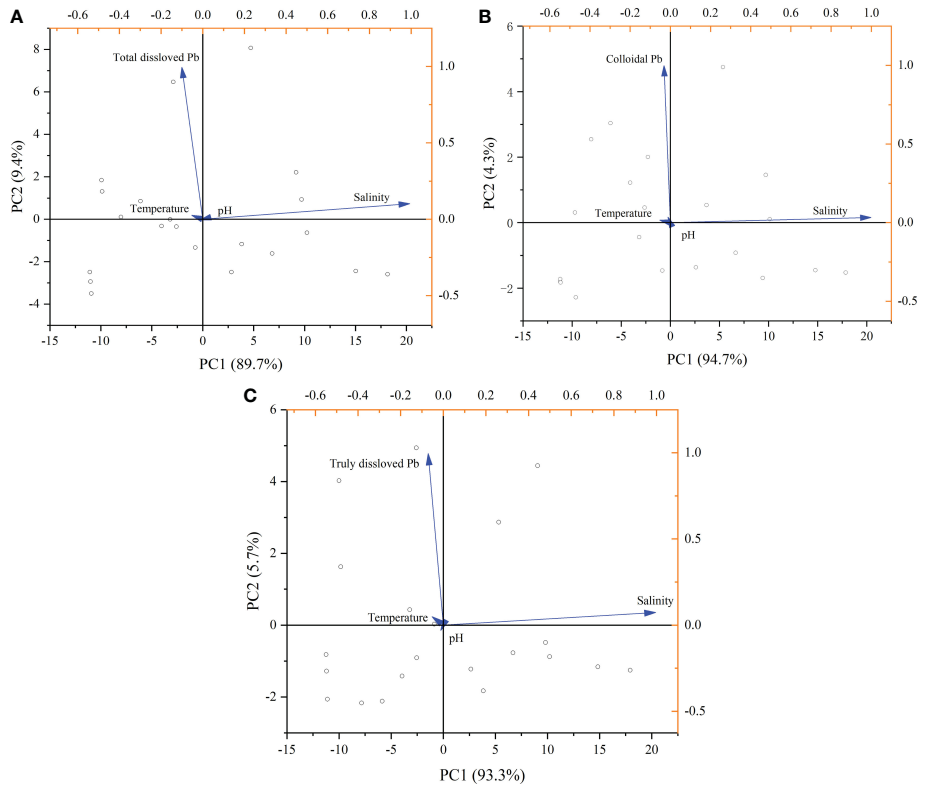

FIGURE 8
The principal component analysis of temperature, pH, and salinity with lead (Pb) at different dissolved states. **(A)** For total dissolved Pb; **(B)** for colloidal Pb; and **(C)** for truly dissolved Pb.

quantify colloidal matter components (Klun et al., 2019). Fortunately, some studies have discovered a significant relationship between CDOM of colloidal matter and Pb ions (Javed et al., 2017). Hence, we discussed the correlation between the molecular weight and components of CDOM and the colloidal Pb to explore this effect (Stolpe and Hassellov, 2010). The CDOM-UV parameter in different stations was shown in Table 3. We used the absorption constant at 355 nm to represent the concentration of CDOM, $SUVA_{254}$ represents the aromaticity of CDOM, and *a*250/*a*365 represents the molecular of CDOM.

In the Yellow River, the concentration of CDOM and COC was decreased but $SUVA_{254}$ was enhanced. Meanwhile, the *a*250/*a*365 value (10.09–14.45) showed that the molecular weight of CDOM was higher (Table 2). However, the concentration and the aromaticity of CDOM had a poor correlation with the different sizes of colloidal Pb (Figure S2). This shows that non-aromatic organic matter exhibited obvious aggregation or elimination, and inert soluble organic matter increased in concentration (Lu et al., 2019). In addition, Pb ions tend to partition in high-molecular-weight colloidal organic matter (Figure 5). Hence, the stable colloidal Pb in the Yellow River indicates a likely close relationship with this metal to the high-molecular-weight aromatic-like matter. Therefore, results suggest that the migration of colloidal Pb may be related to aromatic CDOM in areas with less disturbance from human activities and freshwater areas. In the Xiaoqing River, which is also a natural river, the changes of CDOM and colloidal Pb were more complicated. Except for the Zihe input station (SX4), the aromaticity and molecular weight of CDOM in the Xiaoqing River were lower (Table 2 and Figure S3). This illustrates that the distribution of Pb_3 in different sizes of colloidal matter have a close relationship with the high-molecular-weight aromatic matter. However, in the trunk channels which are greatly affected by the tide, the salinity induced the aromatic components of CDOM to gradually aggregate and promote agglomeration of colloidal Pb. Meanwhile, the trend in change of the CDOM abundance was conformation for all sizes of colloidal Pb (Figures S4–S8). Human activity mainly causes input of low-molecular-weight CDOM, which is also an important migration destination of Pb ions (Figure 5). The CDOMs are not stable and have relative ease of decomposition, inducing a complex distribution of Pb in different sizes of colloidal matter (Table 2). Overall, the highest concentration of colloidal Pb_3 was observed in the station that has stronger aromaticity of present CDOM

10.3389/fmars.2022.1085142

TABLE 3 The chromophoric dissolved organic matter (CDOM)-UV parameter in different sample stations.

Sample station	$a(355)$ (m^{-1})	$SUVA_{254}$	$a(250)/a(365)$
Yellow River			
SY1	0.47	3.11	10.09
SY2	0.52	4.04	14.45
SY3	0.23	8.46	10.32
Xiaoqinghe River			
SX1	0.93	0.3	3.98
SX2	3.47	0.25	1.43
SX3	5.41	3.13	3.37
SX4	1.9	3.82	9.45
SX5	4.67	1.2	2.51
SX6	4.06	1.42	0.78
SX7	2	2.38	1.6
SX8	3.95	1.36	4.75
Yongfenghe River			
SF1	3.77	0.92	5.12
SF2	1.72	5.28	9.66
SF3	0.86	3.87	2.89
Xiaodaohe River			
SD1	2.67	2.33	1.42
SD2	3.35	6	0.84
SD3	1.12	33.28	16.1
Zhimaihe River			
SZ1	4.35	10.01	0.79
SZ2	4.42	1.72	4.21
SZ3	3.89	1.88	0.93
SZ4	2.84	13.01	1.19
SZ5	4.67	15.29	0.63
Guanglihe River			
SG1	4.9	6.94	0.62
SG2	7.99	0.21	1
SG3	4.13	3.67	0.78
SG4	5.34	3.42	0.69
SG5	3.01	2.9	1.1
SG6	3.53	1.92	5.21
SG7	2.95	3.4	0.91
SG8	3.34	5.27	1.09

(Continued)

TABLE 3 Continued

Sample station	$a(355)$ (m^{-1})	$SUVA_{254}$	$a(250)/a(365)$
SG9	3.3	6.65	0.76
SG10	3.06	3.28	0.91
SG11	0.62	4.45	22.03
Shenxiangou River			
SS1	1.98	2.31	1.76
SS2	2.35	14.42	7.68
SS3	2.33	6.76	6.13
SS4	5.06	10.49	3.1
SS5	2.67	1.39	0.27
SS6	0.43	5.9	6.79

(Table 2 and Figure 5). Furthermore, Pb was also more inclined to be found in the large-sized colloidal matter. However, in winter, the distribution of Pb in large-sized colloids is relatively stable because of the low decomposition effect of the low temperature.

To further verify those findings, we compared the fractionation behavior between Pb in the truly dissolved phase and colloidal organic matter phase in other rivers into the sea. Table 4 shows the concentration of Pb in the truly dissolved phase and colloidal phase in different areas. It can be observed from Table 4 that the truly dissolved Pb was the main components in the freshwater (Javed et al., 2017; Gandois et al., 2020; Lu et al., 2020; Zhang et al., 2022). However, with the enhancement of salinity, the colloidal Pb became the main components of the dissolved Pb in the brackish water environment (Illuminati et al., 2019; Lu et al., 2020; Pavoni et al., 2020; Feng et al., 2022; Nasrabadi et al., 2022). Many studies have demonstrated that Pb is prone to sedimentation in estuary where salt water and freshwater are mixed (Pavoni et al, 2020; Nasrabadi et al., 2022). This phenomenon of migration distribution is more pronounced in the estuarine area. For example, colloidal Pb exceeded 50% of the total dissolved Pb in most estuarine areas (Illuminati et al., 2019; Lu et al., 2020; Pavoni et al., 2020; Feng et al., 2022; Nasrabadi et al., 2022). In the Krka River estuary, this fractionation behavior was close to 100% (Nasrabadi et al., 2022). Combined with the phenomenon of this study, the sedimentation of Pb mainly occurred in the small molecule organic phase (Figure 5). In addition, the increase in salinity promoted the migration of Pb to macromolecular colloids (Figures 5, 6). This suggests that macromolecular colloids matter will be the main dissolution state of Pb from rivers to the ocean.

TABLE 4 The concentration of lead (Pb_3) in the truly dissolved and colloidal phases in different river flows into the sea.

	River or estuary	Colloidal Pb	Truly dissolved Pb	References
Freshwater	Guandang River estuary	13%	87%	Lu et al., 2020
	Athabasca River	≈40%	≈60%	Javed et al., 2017
	Taihu Lake	≈34%	≈76%	Zhang et al., 2022
	Blackwater river	22%	78%	Gandois et al., 2020
	In this study	31–40%	60–69%	
Brackish water	Po River Estuary	≈70%	≈30%	Illuminati et al., 2019
	Guandang River estuary	58%	42%	Lu et al., 2020
	Pearl River Estuary	82%	18%	Fang et al., 2021
	Isonzo/Soča River mouth	84–95%	6%–15%	Pavoni et al., 2020
	Krka River estuary	99.00%	1.00%	Nasrabadi et al., 2022
	In this study	50–80%	20–50%	

4.4 Potential ecological effects of Pb

From the concentration change of Pb observed in this study, we could find that, excluding the influence of industrial pollution input, most Pb was precipitated in the estuary (Figure 7). This indicates that the ecological risk of Pb in the river water was relatively low. However, the disturbance by anthropogenic factors increases the risk of Pb migrating to the sea (Wang et al., 2022). As the winter passes, the strong hydrodynamic force caused by Yellow River flows will induce scouring of the trunk channel riverbed (Mistri et al., 2019). Pb deposited in surface sediments in winter will be carried into the sea by later floods. Furthermore, the water body replacement of the urban water system and river dredging works will periodically bring urban sedimentary Pb into the offshore environments. Meanwhile, these rivers do not have a strong hydrodynamic force and vast estuary areas like the natural Xiaoqing River and the Yellow River. Hence, trunk canals (Yongfenghe River and Xiaodaohe River) and urban water systems (Guanglihe River and Shenxiangou River) may be more likely to transport sedimentary Pb to the sea.

There will still a large amount of Pb transported into the sea with the river in the Yellow River Delta. Free Pb ions were easily precipitated in the water with multiple geochemical factors. However, the colloidal Pb after salinity selection at the estuary was more stable in seawater (Chambari et al., 2018). Colloidal Pb is also more easily taken up by organisms in the water because of its organic characteristics. The ecological risk of colloidal Pb was higher than Pb ions because of the easier enrichment of this speciation in the food chain (Lintner et al., 2019). In addition, mariculture, ports, and coastal factories have become the main sources of colloidal Pb. The wastewater discharged from these areas has high salinity. Colloidal Pb in that wastewater will go through a long time of salinity selection. For this, the sedimentation of colloidal Pb will become reduced at the estuary (Lee et al., 2014). A large amount of active Pb will directly input into the seawater, increasing ecological risks. Hence, the pollution by mariculture, ports, and coastal factories should require further attention to reduce ecological impacts.

5 Conclusions

Distribution and migration behavior of toxic metal Pb in the seaward river in the Yellow River Delta in winter was studied. The results showed that the discharge from factories and residential locations are important sources of Pb because the higher concentration of Pb in the reaches crossing urban areas. The migration of Pb in the river water phase was mainly dominated by the biogeochemical factors and the characteristics of COC. The rapidly increasing salinity and higher pH values, especially the low temperature, dominated the removal of Pb from the river water. Increasing salinity and pH induced the removal of truly dissolved Pb from the river. By the combined effect, 80% of Pb present precipitated and settled into the estuary, making this area a sink for Pb in winter. The fractionation results indicated that the specific components of colloidal organic matter were the key factor to driver the migration of Pb in colloidal phase. The drastic migration of Pb in different sizes of colloidal matter accompanied by obvious fluorescence and UV absorption intensity of CDOM increases and decreases. It is worth noting that colloidal Pb inputs from ports and mariculture are not prone to precipitate in the estuary area, which will enhance the ecological risks of this metal in near-shore environments.

In summary, the study results suggest that the change of pH and salinity stores a large amount of Pb in the trunk channel and estuary sediments in winter. Colloidal matter prevented this removal behavior and different sizes of colloids play different inhibitory roles. However, unfortunately, there is still a significant amount of information lacking. Further studies are needed to examine the interaction between Pb and the different sizes or chemical composition of COC.

Data availability statement

The original contributions presented in the study are included in the article/Supplementary Material. Further inquiries can be directed to the corresponding author.

Author contributions

PR and KL contributed to the conception, design, and investigation of the study; BS organized the database and performed the statistical analysis; and QL, SW, XL, and DS wrote sections of the manuscript. All authors contributed to manuscript revision, and read and approved the submitted version.

Funding

This study was funded by the National Key R&D Program of China under contract 2020YFD0900604; and the Conservation and restoration of bio-resources and habitats in typical coastal zones in Shandong province project under contract CF-MEEC/ER/2016–03.

Acknowledgments

We would like to thank Wen Chang and Bingchen Wang for their field and laboratory assistance, helpful advice, and in-depth discussion.

Conflict of interest

The authors declare that the research was conducted in the absence of any commercial or financial relationships that could be construed as a potential conflict of interest.

Publisher's note

All claims expressed in this article are solely those of the authors and do not necessarily represent those of their affiliated organizations, or those of the publisher, the editors and the reviewers. Any product that may be evaluated in this article, or claim that may be made by its manufacturer, is not guaranteed or endorsed by the publisher.

Supplementary material

The Supplementary Material for this article can be found online at: https://www.frontiersin.org/articles/10.3389/fmars.2022.1085142/full#supplementary-material

References

Abdelrady, A., Bachwenkizi, J., Sharma, S., Sefelnasr, A., and Kennedy, M. (2021). The fate of heavy metals during bank filtration: Effect of dissolved organic matter. *J. Water. Process. Eng.* 38, 101563. doi: 10.1016/j.jwpe.2020.101563

Cantwell, M. G., and Burgess, R. M. (2001). Metal-colloid partitioning in artificial interstitial waters of marine sediments: Influences of salinity, pH, and colloidal organic carbon concentration. *Environ. Toxicol. Chem.* 20, 2420–2427. doi: 10.1002/etc.5620201104

Cao, Q. Q., Wang, H., Li, Y. R., Zhang, Y. R., Zheng, P. M., Wang, R. Q., et al. (2018). The national distribution pattern and factors affecting heavy metals in sediments of water systems in china. *Soil. Sediment. Contam.* 27, 79–97. doi: 10.1080/15320383.2018.1424113

Chambari, S., Karbassi, A., Monavari, S. M., Sabzalipour, S., and Moattar, F. (2018). The role of estuarine natural flocculation process in the removal of heavy metals. *Fresen. Environ. Bull.* 27, 2468–2475.

Cheng, X. Y., Zhu, J. R., and Chen, S. L. (2021). Extensions of the river plume under various yellow river courses into the bohai Sea at different times. *Estuar. Coast. Shelf. S.* 249, 107092. doi: 10.1016/j.ecss.2020.107092

Chen, T., Wen, X. C., Zhang, L. J., Tu, S. C., Zhang, J. H., Sun, R. N., et al. (2022). The geochemical and mineralogical controls on the release characteristics of potentially toxic elements from lead/zinc (Pb/Zn) mine tailings. *Environ. pollut.* 315, 120328. doi: 10.1016/j.envpol.2022.120328

Dallas, L. J., Cheung, V. V., Fisher, A. S., and Jha, A. N. (2013). Relative sensitivity of two marine bivalves for detection of genotoxic and cytotoxic effects: a field assessment in the Tamar estuary, south West England. *Environ. Monit. Assess.* 185, 3397–3412. doi: 10.1007/s10661-012-2800-0

Deng, J. C., Zhang, J., Yin, H. B., Hu, W. P., Zhu, J. G., and Wang, X. L. (2020). Ecological risk assessment and source apportionment of metals in the surface sediments of river systems in lake taihu basin, China. *Environ. Sci. pollut. R.* 27, 25943–25955. doi: 10.1007/s11356-019-05719-5

Dong, W. P., Ci, M. W., Yan, X. S., Wang, Y. Q., Zhang, G. D., Xu, W. F., et al. (2022). Antibiotics in the surface water and sediment from the tributaries of the xiaoqing river, China: occurrence, distribution and risk assessment. *Desalin. Water. Treat.* 247, 229–243. doi: 10.5004/dwt.2022.28003

Du, X. K., Wang, K. R., Pei, H. Y., Dou, S. T., Bi, N. S., Zhang, X., et al. (2022). Geomorphic characteristics of the qingshuigou flow path in the yellow river estuary. *Mar. Sci.* 45, 77–85. doi: 10.11759/hykx20201213001

Fang, Q. S., Chen, Z. H., Zheng, J. P., and Zhu, Z. H. (2021). Comparison of Pb (II) and Cd(II) micro-interfacial adsorption on fine sediment in the pearl river basin, china. *Int. J. Sediment. Res.* 36, 401–418.

Feng, W. H., Wang, Z. F., Zhu, W. Z., Zheng, F. Q., Zhang, D. R., and Xu, H. T. (2022). Evaluation of the bioavailability of metals in sediment from the southern coastal wetland of the qiantang estuary by using diffusive gradients in thin films technique. *J. Ocean. U. China.* 21, 375–387.

Furukawa, Y., Reed, A. H., and Zhang, G. P. (2014). Effect of organic matter on estuarine flocculation: a laboratory study using montmorillonite, humic acid, xanthan gum, guar gum and natural estuarine floc. *Geochem. T.* 15, 1. doi: 10.1186/1467-4866-15-1

Fytianos, K. (2001). Speciation analysis of heavy metals in natural waters: A review. *J. Aoac. Int.* 84, 1763–1769. doi: 10.1093/jaoac/84.6.1763

Gandois, L., Hoyt, A. M., Mounier, S., Le Roux, G., Harvey, C. F., Claustres, A., et al. (2020). From canals to the coast: dissolved organic matter and trace metal composition in rivers draining degraded tropical peatlands in indonesia. *Biogeosciences* 17, 1897–1909.

Gao, X. L., Zhou, F. X., Chen, C. T. A., and Xing, Q. G. (2015). Trace metals in the suspended particulate matter of the yellow river (Huanghe) estuary: Concentrations, potential mobility, contamination assessment and the fluxes into the bohai Sea. *Cont. Shelf. Res.* 104, 25–36. doi: 10.1016/j.csr.2015.05.005

Gong, Y. Y., Bai, Y., Zhao, D. Y., and Wang, Q. L. (2022). Aggregation of carboxyl-modified polystyrene nanoplastics in water with aluminum chloride: Structural characterization and theoretical calculation. *Water. Res.* 208, 117884. doi: 10.1016/j.watres.2021.117884

Gu, X., Xin, M., Wang, J., Lu, S., Lian, M. S., Lin, C. Y., et al. (2022). Quantitative source identification and environmental assessment of trace elements in the water and sediment of rivers flowing into laizhou bay, bohai Sea. *Mar. pollut. Bull.* 174, 113313. doi: 10.1016/j.marpolbul.2021.113313

Guzman, E., Santini, E., Benedetti, A., Ravera, F., Ferrari, M., and Liggieri, L. (2014). Surfactant induced complex formation and their effects on the interfacial properties of seawater. *Colloid. Surface. B.* 123, 701–709.

Hargreaves, A. J., Vale, P., Whelan, J., Alibardi, L., Constantino, C., Dotro, G., et al. (2018). Impacts of coagulation–flocculation treatment on the size distribution and bioavailability of trace metals (Cu, Pb, Ni, zn) in municipal wastewater. *Water. Res.* 128, 120–128. doi: 10.1016/j.watres.2017.10.050

Herzog, S. D., Gentile, L., Olsson, U., Persson, P., and Kritzberg, E. S. (2019). Characterization of iron and organic carbon colloids in boreal rivers and their fate at high salinity. *J. Geophys. Res-Biogeo.* 125, e2019JG005517. doi: 10.1029/2019JG005517

He, D., Shi, X. M., and Wu, D. Y. (2016). Particle–size distribution characteristics and pollution of heavy metals in the surface sediments of kuitun river in xinjiang, China. *Environ. Earth. Sci.* 75, 104. doi: 10.1007/s12665-015-4882-9

Huang, H. J., Yuan, X. Z., Zeng, G. M., Zhu, H. N., Li, H., Liu, Z. F., et al. (2011). Quantitative evaluation of heavy metals' pollution hazards in liquefaction residues of sewage sludge. *Bioresource. Technol.* 102, 10346–10351. doi: 10.1016/j.biortech.2011.08.117

Illuminati, S., Annibaldi, A., Truzzi, C., Tercier–Waeber, M. L., Noel, S., Braungardt, C. B., et al. (2019). Scarponi, G in–situ trace metal (Cd, Pb, Cu) speciation along the po river plume (Northern Adriatic Sea) using submersible systems. *Mar. Chem.* 212, 47–63. doi: 10.1016/j.marchem.2019.04.001

Javed, M. B., Cuss, C. W., Grant-Weaver, I., and Shotyk, W. (2017). Size-resolved pb distribution in the athabasca river shows snowmelt in the bituminous sands region an insignificant source of dissolved pb. *Sci. Rep-UK.* 7, 43622.

Klun, K., Falnoga, I., Mazej, D., Sket, P., and Faganeli, J. (2019). Colloidal organic matter and metal(loid)s in coastal waters (Gulf of Trieste, northern Adriatic Sea). *Aquat. Geochem.* 25, 179–194. doi: 10.1007/s10498-019-09359-6

Lasareva, E. V., Parfenova, A. M., Romankevich, E. A., Lobus, N. V., and Drozdova, A. N. (2019). Organic matter and mineral interactions modulate flocculation across Arctic river mixing zones. *J. Geophys. Res-Biogeo.* 124, 1651–1664. doi: 10.1029/2019JG005026

Latosinska, J., and Czapik, P. (2020). The ecological risk assessment and the chemical speciation of heavy metals in ash after the incineration of municipal sewage sludge. *Sustainability.* 12, 6517. doi: 10.3390/su12166517

Lao, Q. B., Cai, S. J., Huang, P., Chen, F. J., Su, Q. Z., Lei, X. T., et al. (2022). Contaminant characteristics and influencing factors of heavy metals in seawater and sediments in a typical mariculture bay in south china. *Front. Mar. Sci.* 9, 923494.

Lao, Q. B., Su, Q. Z., Liu, G. Q., Shen, Y. L., Chen, F. J., Lei, X. T., et al. (2019). Spatial distribution of and historical changes in heavy metals in the surface seawater and sediments of the beibu gulf, china. *Mar. pollut. Bull.* 146, 427–434.

Lee, G. J., Son, H. A., Cho, J. W., Choi, S. K., Kim, H. T., Kim, J. W., et al. (2014). Stabilization of pickering emulsions by generating complex colloidal layers at liquid-liquid interfaces. *J. Colloid. Interf. Sci.* 413, 100–105. doi: 10.1016/j.jcis.2013.09.015

Liang, M. Q., Shao, M. L., Cao, C. L., Zong, Y. N., and Tang, J. F. (2018). Characteristics of dissolved organic matter (DOM) and relationship with dissolved heavy metals in a peri–urban and an urban river. *Environ. Sci.* 39, 2095–2103. doi: 10.13227/j.hjkx.201710089

Li, L., Liu, J., Wang, X., and Shi, X. (2015). Dissolved trace metal distributions and Cu speciation in the southern bohai Sea, China. *Mar. Chem.* 172, 34–45. doi: 10.1016/j.marchem.2015.03.002

Lintner, M., Lintner, B., Wanek, W., Keul, N., von der Kammer, F., Hofmann, T., et al. (2019). Effects of heavy elements (Pb, Cu, zn) on algal food uptake by elphidium excavatum (Foraminifera). *Heliyon.* 7, e08427. doi: 10.1016/j.heliyon.2021.e08427

Lin, W. N., Wang, N., and Fu, Q. (2019). Research on the pollutant bearing capacity of bohai sea under vater exchange. *Transac. Oceanol. Limnol.* 5, 42–48. doi: 10.13984/j.cnki.cn37-1141.2019.05.005

Liu, K., and Gao, X. L. (2019). Adsorption and fractionation of pt, pd and Rh onto inorganic microparticles and the effects of macromolecular organic compounds in seawater. *Environ. pollut.* 255, 113192. doi: 10.1016/j.envpol.2019.113192

Liu, K., Gao, X. L., Li, L., Chen, C. T. A., and Xing, Q. G. (2018). Determination of ultra–trace pt, pd and Rh in seawater using an off–line pre–concentration method and inductively coupled plasma mass spectrometry. *Chemosphere.* 212, 429–437. doi: 10.1016/j.chemosphere.2018.08.098

Liu, F., Liu, X. H., Zhao, S. N., Wang, J., and Qian, X. (2019). Photochemical transformations of tetracycline antibiotics influenced by natural colloidal particles: Kinetics, factor effects and mechanisms. *Chemosphere.* 235, 867–875. doi: 10.1016/j.chemosphere.2019.06.201

Liu, W. H., Ma, T., Du, Y., Wu, X. C., Chen, L. Z., Li, J. Q., et al. (2022). Characteristics of dissolved organic matter in surface water and sediment and its ecological indication in a typical mining–affected river–le'an river, China. *Environ. Sci. pollut. R.* 29, 37115–37128. doi: 10.1007/s11356-021-18478-z

Lu, Y. X., Gao, X. L., and Chen, C. T. A. (2019). Separation and determination of colloidal trace metals in seawater by cross–flow ultrafiltration, liquid–liquid extraction and ICP–MS. *Mar. Chem.* 215, 103685. doi: 10.1016/j.marchem.2019.103685

Lu, Y. X., Gao, X. L., Song, J. M., Chen, C. T. A., and Chu, J. L. (2020). Colloidal toxic trace metals in urban riverine and estuarine waters of yantai city, southern coast of north yellow Sea. *Sci. Total. Environ.* 717, 135265. doi: 10.1016/j.scitotenv.2019.135265

Lu, Y. X., Pan, D. W., Yang, T. T., and Wang, C. C. (2021). Spatial and environmental characteristics of colloidal trace Cu in the surface water of the yellow river estuary, China. *Mar. pollut. Bull.* 168, 112401. doi: 10.1016/j.marpolbul.2021.112401

Ma, T. T., Li, X. W., Bai, J. H., and Cui, B. S. (2019). Tracking three decades of land use and land cover transformation trajectories in china's large river deltas. *Land. Degrad. Dev.* 30, 799–810. doi: 10.1002/ldr.3268

Marcinek, S., Cindric, A. M., Padan, J., and Omanovic, D. (2022). Trace metal partitioning in the salinity gradient of the highly stratified estuary: A case study in the krka river estuary (Croatia). *Appl. Sci-Basel.* 12, 12.

Men, C., Liu, R. M., Xu, L. B., Wang, Q. R., Guo, L. J., Miao, Y. X., et al. (2020). Source–specific ecological risk analysis and critical source identification of heavy metals in road dust in Beijing, China. *J. Hazard. Mater.* 388, 121763. doi: 10.1016/j.jhazmat.2019.121763

Mistri, M., Pitacco, V., Granata, T., Moruzzi, L., and Munari, C. (2019). When the levee breaks: Effects of flood on offshore water contamination and benthic community in the Mediterranean (Ionian Sea). *Mar. pollut. Bull.* 140, 588–596. doi: 10.1016/j.marpolbul.2019.02.005

Moore, W. S., DeMaster, D. J., Smoak, J. M., McKee, B. A., and Swarzenski, P. W.. (1996). Radionuclide tracers of sediment–water interactions on the Amazon shelf. *Cont. Shelf. Res.* 16, 645–665. doi: 10.1016/0278-4343(95)00049-6

Mudge, M. C., Nunn, B. L., Firth, E., Ewert, M., Hales, K., et al. (2021). Subzero, saline incubations of colwellia psychrerythraea reveal strategies and biomarkers for sustained life in extreme icy environments. *Environ. Microbiol.* 23, 3840–3866. doi: 10.1111/1462-2920.15485

Nadella, S. R., Tellis, M., Diamond, R., Smith, S., Bianchini, A., Wood, C. M., et al. (2013). Toxicity of lead and zinc to developing mussel and sea urchin embryos: Critical tissue residues and effects of dissolved organic matter and salinity. *Comp. Biochem. Phys. C.* 158, 72–83. doi: 10.1016/j.cbpc.2013.04.004

Nghiem, J. A., Fischer, W. W., Li, G. K., Lamb, M. P., et al. (2022). A mechanistic model for mud flocculation in freshwater rivers. *J. Geophys. Res–earth.* 127, e2021JF006392. doi: 10.1029/2021JF006392

Nasrabadi, T., Soodarjani, A. E., Karbassi, A., and Baghdadi, M. (2022). Role of salinity and aeration on flocculation and remobilization of metals during estuarine mixing. *Environ. Earth. Sci.* 81, 277.

Pavoni, E., Crosera, M., Petranich, E., Oliveri, P., Klun, K., Faganeli, J., et al. (2020). Trace elements in the estuarine systems of the gulf of Trieste (northern Adriatic sea): A chemometric approach to depict partitioning and behavior of particulate, colloidal and truly dissolved fractions. *Chemosphere.* 252, 126517. doi: 10.1016/j.chemosphere.2020.126517

Peuravuori, J., and Pihlaja, K. (1997). Molecular size distribution and spectroscopic properties of aquatic humic substances. *Anal. Chim. Acta* 337, 133–149. doi: 10.1016/S0003-2670(96)00412-6

Powell, K. J., Brown, P. L., Byrne, R. H., Gajda, T., Hefter, G., Leuz, A. K., et al. (2009). Chemical speciation of environmentally significant metals with inorganic ligands. part 3: The Pb^{2+}, OH^-, cl^-, CO_3^{2-}, SO_4^{2-}, and PO_4^{3-} systems (IUPAC technical report). *Pure. Appl. Chem.* 81, 2425–2476. doi: 10.1351/PAC-REP-09-03-05

Raudina, T. V., Loiko, S. V., Kuzmina, D. M., Shirokova, L. S., Kulizhskiy, S. P., Golovatskaya, E. A., et al (1997). Colloidal organic carbon and trace elements in peat porewaters across a permafrost gradient in Western Siberia. *Geoderma* 390, 114971.

Savenko, A. V., and Savenko, V. S. (2019). Effect of natural organic acids on mobilization of macro– and microelements from rocks. *Dokl. Earth. Sci.* 485, 331–335. doi: 10.1134/S1028334X19030334

Silva, D. S., Cerqueira, U. M. F. M., Aguiar, R. M., Carneiro, P. L. S., and Bezerra, M. A. (2020). Characterization, fractionation and mobility of trace elements in surface sediments of the jequiezinho river, bahia, brazi. *An. Acad. Bras. Cienc.* 92, e20190558. doi: 10.1590/0001-3765202020190558

Stolpe, B., and Hassellov, M. (2010). Nanofibrils and other colloidal biopolymers binding trace elements in coastal seawater: Significance for variations in element size distributions. *Limnol. Oceanogr.* 55, 187–202. doi: 10.4319/lo.2010.55.1.0187

Teien, H. C., Salbu, B., Kroglund, F., and Rosseland, B. O. (2004). Transformation of positively charged aluminium–species in unstable mixing zones following liming. *Sci. Total. Environ.* 330, 217–232. doi: 10.1016/j.scitotenv.2004.03.040

Wang, X., Ren, L. J., Jiao, F. C., and Liu, W. J. (2017). The ecological risk assessment and suggestions on heavy metals in river sediments of jinan. *Water. Sci. Technol.* 76, 2177–2187. doi: 10.2166/wst.2017.380

Wang, L. F., Wang, X. F., Chen, H. G., Wang, Z. H., and Jia, X. P. (2022). Oyster arsenic, cadmium, copper, mercury, lead and zinc levels in the northern south China Sea: long-term spatiotemporal distributions, combined effects, and risk assessment to human health. *Environ. Sci. pollut. R.* 29, 12706–12719. doi: 10.1007/s11356-021-18150-6

Wang, S. S., Zhang, L., Yan, B., Xu, H. L., Liu, Q. X., and Zeng, H. B. (2015). Molecular and surface interactions between polymer flocculant chitosan-g-polyacrylamide and kaolinite particles: impact of salinity. *J. Phys. Chem. C.* 119, 7327–7339. doi: 10.1021/acs.jpcc.5b00739

Weng, H. X., Ma, X. W., Fu, F. X., Zhang, J. J., Liu, Z., Tian, L. X., et al. (2014). Transformation of heavy metal speciation during sludge drying: Mechanistic insights. *J. Hazard. Mater.* 265, 96–103. doi: 10.1016/j.jhazmat.2013.11.051

Wood, C. M., Al-Reasi, H. A., and Smith, D. S. (2011). The two faces of DOC. *Aquat. Toxicol.* 105, 3–8. doi: 10.1016/j.aquatox.2011.03.007

Worms, I. A. M., Slaveykova, V. I., and Wilkinson, K. J. (2015). Lead bioavailability to freshwater microalgae in the presence of dissolved organic matter: Contrasting effect of model humic substances and marsh water fractions obtained by ultrafiltration. *Aquat. Geochem.* 21, 217–230. doi: 10.1007/s10498-015-9256-0

Wu, J., Lu, J., Zhang, C., Zhang, Y. X., Lin, Y. C., and Xu, J. (2020). Pollution, sources, and risks of heavy metals in coastal waters of China. *Hum. Ecol. Risk. Assess.* 26, 2011–2026. doi: 10.1080/10807039.2019.1634466

Wu, G. H., Pan, L., Wei, Q., and Guo, L. (2015). Decreased mobility of heavy metals in haihe river sediments: The possible role of tide gate. *J. Geochem. Explor.* 157, 92–99. doi: 10.1016/j.gexplo.2015.06.002

Wu, W. G., Zhang, J. H., Liu, Y., Wang, X. M., Yang, J., and Feng, X. (2022) Spectral and distribution characteristics of colored dissolved organic matter (CDOM) in sanggou bay in spring. *J. Fish. China.*. doi: 10.11964/jfc. 20210813009

Xiang, M. T., Li, Y., Yang, J. Y., Lei, K. G., Li, Y., Li, F., et al. (2021). Heavy metal contamination risk assessment and correlation analysis of heavy metal contents in soil and crops. *Environ. pollut.* 278, 116911. doi: 10.1016/j.envpol.2021.116911

Xie, X. F., Pu, L. J., Zhu, M., Xu, Y., and Wang, X. H. (2019). Linkage between soil salinization indicators and physicochemical properties in a long-term intensive agricultural coastal reclamation area, Eastern China. *J. Soil Sediment.* 19 (11), 3699–3707. doi: 10.1007/s11368-019-02333-3

Xu, W., Gao, Q., He, C., Shi, Q., Hou, Z. Q., and Zhao, H. Z. (2020). Using ESI FT–ICR MS to characterize dissolved organic matter in salt lakes with different salinity. *Environ. Sci. Technol.* 54, 12929–12937. doi: 10.1021/acs.est.0c01681

Xu, H. C., Yan, M. Q., Li, W. T., Jiang, H. L., and Guo, L. D. (2018). Dissolved organic matter binding with Pb(II) as characterized by differential spectra and 2D UV-FTIR heterospectral correlation analysis. *Water Res.* 144, 435–443. doi: 10.1016/j.watres.2018.07.062

Zang, Z. F., Li, Y. H., Li, H. R., Guo, Z. H., and Zhang, R. (2020). Spatiotemporal variation and pollution assessment of Pb/Zn from smelting activities in China. *Environ. pollut.* 6, 1986. doi: 10.3390/ijerph17061968

Zhang, W. G., Feng, H., Qu, J. N., and Yu, L. Z. (2008). Lead (Pb) isotopes as a tracer of Pb origin in Yangtze river intertidal zone. *Chem. Geol.* 257, 260–266. doi: 10.1016/j.chemgeo.2008.10.012

Zhang, J., Wang, K., Yi, Q. T., Zhang, T., Shi, W. Q., and Zhou, X. F. (2022). Transport and partitioning of metals in river networks of a plain area with sedimentary resuspension and implications for downstream lakes. *Environ. pollut.* 294, 11868. doi: 10.1016/j.envpol.2021.118668

Zhang, J. F., Zhang, Q. H., and Qiao, G. Q. (2015). Effects of salinity on the flocculation of illite due to differential settling. *J. Hydrau. Engin.* 46, 1305–1311. doi: 10.13243/j.cnki.slxb.20150012

Zhi, L. H., Li, X. W., Bai, J. H., and Guan, Y. N. (2020). Integrating ecological and socioeconomic networks using nitrogen metabolism in the yellow river delta, China. *Resour. Conserv. Recy.* 162, 105012. doi: 10.1016/j.resconrec.2020.105012

frontiers | Frontiers in Marine Science

TYPE Original Research
PUBLISHED 16 March 2023
DOI 10.3389/fmars.2023.1135113

OPEN ACCESS

EDITED BY
Wen Zhuang,
Shandong University, China

REVIEWED BY
Shuhan Tian,
Qingdao University, China
Fengxia Zhou,
Guangdong Ocean University, China

*CORRESPONDENCE
Jing Zhang
jzhang@sci.u-toyama.ac.jp
Qian Liu
liuqian@ouc.edu.cn

SPECIALTY SECTION
This article was submitted to Marine Biogeochemistry, a section of the journal Frontiers in Marine Science

RECEIVED 31 December 2022
ACCEPTED 06 March 2023
PUBLISHED 16 March 2023

CITATION
Cao A, Zhang J, Zhang H, Chen Z, Cui G, Liu Z, Li Y and Liu Q (2023) Dissolved rare earth elements in the Northwest Pacific: Sources, water mass tracing, and cross-shelf fluxes.
Front. Mar. Sci. 10:1135113.
doi: 10.3389/fmars.2023.1135113

Dissolved rare earth elements in the Northwest Pacific: Sources, water mass tracing, and cross-shelf fluxes

Axiang Cao[1,2], Jing Zhang[1,3,4]*, Honghai Zhang[1,2], Zhaohui Chen[5], Guanghao Cui[1,2], Zhensong Liu[1,2], Yanbin Li[1] and Qian Liu[1]*

[1]Frontiers Science Center for Deep Ocean Multispheres and Earth System, and Key Laboratory of Marine Chemistry Theory and Technology, Ministry of Education, Ocean University of China, Qingdao, China, [2]College of Chemistry and Chemical Engineering, Ocean University of China, Qingdao, China, [3]Faculty of Science, Academic Assembly, University of Toyama, Toyama, Japan, [4]Laboratory for Marine Ecology and Environmental Science, Qingdao National Laboratory for Marine Science and Technology, Qingdao, China, [5]Frontier Science Center for Deep Ocean Multispheres and Earth System, and Physical Oceanography Laboratory, Ocean University of China, Qingdao, China

In the Northwest Pacific, a key area for understanding the sources and transport of materials in the ocean, knowledge of the sources, transport, and biogeochemical cycling of trace elements is limited. Trace elements such as the rare earth elements (REEs) can trace the sources and transport of water masses. Here we present dissolved REE concentrations along a longitudinal transect (150 °E) from 13°N to 40°N in the Northwest Pacific (≤2000 m). We divided the transect into two subregions: a mixed water region (MWR; 37~40 °N, where the Oyashio and Kuroshio currents mix) and a subtropical region (13~34 °N). In the MWR, REEs were strongly positively correlated with apparent oxygen utilization in subsurface water (depth > the chlorophyll maximum layer, potential density <26.6 kg/m^3), with about a 4-fold higher slope (0.15±0.06) than in the subtropical region in subsurface and intermediate waters (0.04±0.003, potential density <27.5 kg/m^3). This suggests that REEs are released by organic matter remineralization at a higher efficiency in the MWR vs. in the subtropical region, which can be explained by different water masses and plankton community structures. In addition, we observed a lithogenic input signal of REEs from the Aleutian Islands based on the high La/Yb ratio (>0.35). This ratio was controlled by lateral transport and showed a good agreement with salinity, indicating that it is a useful tracer of low salinity water originating from the subarctic region. Furthermore, we estimated the cross-shelf fluxes of Nd in the Northwest Pacific. The estimated Nd fluxes from the Sea of Okhotsk, the Sea of Japan,

the East China Sea, and the South China Sea into the Northwest Pacific were 29~32 t/y, 159~302 t/y, 142~616 t/y, and -298~34 t/y, respectively. This study highlights the importance of considering the cross-shelf REE fluxes in the Northwest Pacific when constructing the oceanic REE budgets.

KEYWORDS

Northwest Pacific, rare earth elements, remineralization, water mass tracing, cross-shelf fluxes

1 Introduction

The Northwest Pacific, which mainly includes the Northwest Pacific subarctic region and the Northwest Pacific subtropical region, is adjacent to a large area of marginal seas and is a key area that receives trace element inputs from terrigenous sources (Nishioka et al., 2013 ; Kim et al., 2017; Yang et al., 2018; Morton et al., 2019). The Kuroshio (including Kuroshio Extension) and Oyashio are the two most important surface currents in the Northwest Pacific. They carry large quantities of trace elements (Fe/Mn/Cd/Zn, etc.) from the marginal seas (Sea of Okhotsk and East China Sea, etc.) and islands (Kuril and Aleutian Islands, etc.) into the Northwest Pacific (Nishioka et al., 2013 ; Kim et al., 2017; Yang et al., 2018; Morton et al., 2019). Rare earth elements (REEs, the lanthanide family) are important marine process tracers with coherent chemical properties and similar chemical behaviors (Elderfield, 1988). They are commonly used to trace lithogenic input sources and water mixing , which are in turn very important for understanding the behavior of trace elements in the oceans (Zhang et al., 2008; Zheng et al., 2016; Behrens et al., 2018a; Garcia-Solsona et al., 2020; Behrens et al., 2020). For instance, La/Yb ratios (the ratio of La to Yb after normalization) reflected the recent dissolution of lithogenic material from the Kerguelen and/or Heard islands in the Southern Ocean (Zhang et al., 2008). The REE anomaly (the anomaly refers to the deviation of the measured value of one element to the value predicted from two adjacent elements after normalization) in the Northwest Pacific was used to trace inputs from the Philippine Islands (Behrens et al., 2018a). In addition, heavy rare earth elements (HREEs; Gd, Td, Dy, Ho, Er, Tm, Yb, Lu), which generally behave conservatively, have been utilized to identify water mass mixing (Zhang et al., 2018; Garcia-Solsona et al., 2020; Liu et al., 2022).

The concentrations of REEs in the ocean generally increase with depth, which can be explained by the scavenging of REEs at the surface and the release of REEs by remineralization at depth (Elderfield and Greaves, 1982; de Baar et al., 1985; Elderfield, 1988; Bertram and Elderfield, 1993). Numerous studies have investigated the effect of organic matter remineralization on REEs using the relationship between REEs and apparent oxygen utilization (AOU; a reliable measure of remineralization) (e.g., Stichel et al., 2015; Lambelet et al., 2016; Behrens et al., 2018b; Seo and Kim, 2020). For example, in the eastern Atlantic, organic matter remineralization releases more Nd than in the western Atlantic (Stichel et al., 2015; Lambelet et al., 2016). However, at present, REE data is sparse in the Northwest Pacific (Piepgras and Jacobsen, 1992; Alibo and Nozaki, 1999; Behrens et al., 2018a), and thus our knowledge of the regional differences in the effects of remineralization on REEs is limited.

The mass balance of dissolved REEs in the oceans is not well constrained (Tachikawa et al., 2003; Johannesson and Burdige, 2007). Marginal seas may be a major source of material to the open oceans, and typically have high concentrations of REEs due to excessive inputs from the atmosphere, rivers, groundwater, and land-sea boundary exchanges (Amakawa et al., 2004a; Amakawa et al., 2004b; Hatta and Zhang, 2006; Wu et al., 2015; Zhang et al., 2018). The Northwest Pacific Ocean interacts with a large continental shelf area (~6×10^6 km^2), which accounts for about 20 % of the total area of global marginal seas. Therefore, marginal seas may play a key role in the supply and mass balance of REEs throughout the Pacific. However, quantitative evaluations of cross-shelf fluxes of REEs from marginal seas to the open ocean are lacking. The influence of marginal seas on oceanic REE budgets is still poorly understood.

To better understand the influencing factors and sources of REEs in the Northwest Pacific, we measured the dissolved REEs in seawater above 2000 m in the region from 13°N to 40°N along a 150°E longitudinal transect. We found regional differences in the release of REEs by organic matter remineralization. In addition, we identified the sources of REEs and suggest that REE ratios can be good tracers of water masses originating from the subarctic region. Furthermore, we estimated the cross-shelf fluxes of REEs between the marginal seas and the Northwest Pacific. Our results indicate that the marginal seas have a very important role in the REE budgets of the Northwest Pacific.

2 Materials and methods

2.1 Study area

The Northwest Pacific, from the subarctic to the subtropical region, interacts with the Sea of Okhotsk, Sea of Japan, East China Sea, South China Sea, and the Bering Sea.

The Kuroshio Current and Oyashio Current are the most important currents in the Northwest Pacific (Figure 1). The Kuroshio originates from the western boundary current to the east

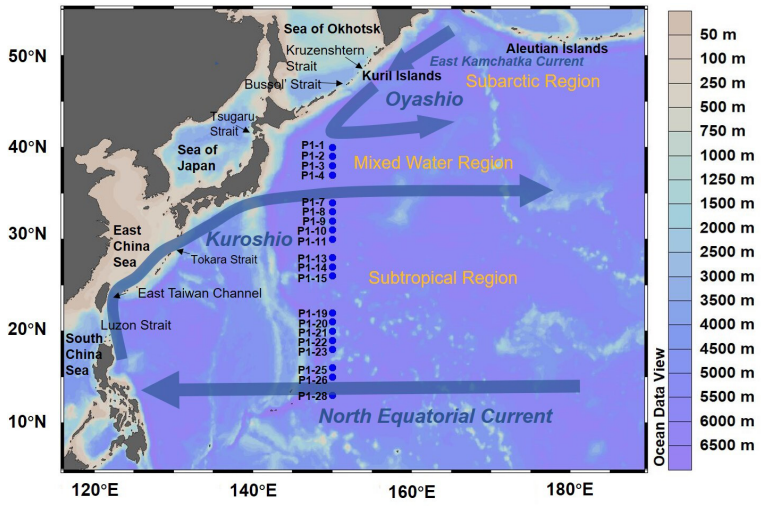

FIGURE 1
Map of stations sampled during the transect P1 cruise (blue dots) in the northwest Pacific, and generalized circulation patterns in the region. Solid arrows represent flow patterns of major surface currents (the North Equatorial Current, the Kuroshio Current, the Oyashio Current, the East Kamchatka Current). The map was created using Ocean Data View (ODV) software (Schlitzer, 2015).

of the Philippine Islands, and is characterized by high temperature, high salinity oligotrophic water (Nitani, 1972). It flows northward along Taiwan Island, passes through the East China Sea continental shelf, then flows into the Pacific Ocean through the Tokara Strait, and turns eastward at about 35°N. The Oyashio is formed by mixing of the East Kamchatka Current and Okhotsk water, which is characterized by low temperature and low salinity water, rich in oxygen and nutrients (Rogachev et al., 2000). As the Oyashio front intrudes southward, it interacts with warm and saline Kuroshio waters to form North Pacific Intermediate Water (NPIW). This region is defined as the Mixed Water Region (MWR) (stations P1-1~P1-4; Talley et al., 1995; Yasuda et al., 1996; Yasuda, 2004; Qiu and Chen, 2011; Hu et al., 2015).

At stations P1-7~P1-28 (Figure 1), North Pacific Tropical Water (NPTW) is the dominant North Pacific subsurface water mass, and is characterized by a salinity maximum (S>34.60, Suga et al., 2000). NPIW is formed in the MWR and flows cyclonically in the North Pacific. It is usually defined by a potential density of 26.6-27.5 kg/m^3 and features a vertical salinity minimum in the subtropical Pacific (Yasuda et al., 2001; Nishioka et al., 2007; Kim et al., 2017).

2.2 Sample collection and ancillary data

Seawater samples shallower than 2000 m were collected along a longitudinal transect P1 (13°N ~ 40°N, 150°E) during a cruise on the *R/V* Dongfanghong 3 (October 31st – December 1st, 2019) in the Northwest Pacific. The stations are shown in Figure 1. Stations P1-1~P1-4 are located in the MWR and stations P1-7~P1-28 are located in the subtropical region.

Seawater was sampled from 12 L Niskin-X bottles and filtered immediately through 0.45 μm membrane filters (polyether sulfone) into pre-cleaned low-density polyethylene (LDPE) bottles (500 mL). The filtering process was conducted in a clean bench onboard. Samples were then acidified to pH≤ 2 using 6 M ultra-pure hydrochloric acid (Optima grade, Fisher Chemical), and stored in double bags.

Water temperature and salinity profiles were measured using conductivity-temperature-depth sensors (CTD, Sea-Bird 911 plus). The dissolved oxygen (DO) concentration was determined *via* Winkler titration (Bryan et al., 1976). AOU was calculated by the equation below,

$$AOU = DO^s - DO \quad (1)$$

where, DO^s and DO represent the saturated oxygen concentration at the given pressure/depth and the observed oxygen concentration, respectively. Chlorophyll was measured using a HITACHI F-4700 fluorometer (Parsons et al., 1984; Li et al., 2022). Nitrate and nitrite concentrations were measured using an autoanalyzer (Seal analytical AA3) (Li et al., 2022).

2.3 Rare earth element analysis

Seawater samples were pre-concentrated with NOBIAS PA1 resin in a Class 1000 clean room and the REE concentrations were determined by inductively coupled plasma mass spectrometry (ICP-MS; Takata et al., 2009; Persson et al., 2011; Hatje et al., 2014; Liu et al., 2022). The results were corrected using a Lu (lutecium) internal standard. The recoveries of the internal standard were greater than 90%. The concentration of REEs in blank samples was within 3% of that measured in surface seawater, which usually has the lowest concentration in the ocean. Relative standard deviations (RSDs) of REEs were determined on replicate measurements of

surface (n=4) and 4000 m deep (n=11) seawater, which were both less than 5%. The sample measurement errors are reported in Supplementary Table S1.

The Ce anomaly (Ce/Ce*) was calculated as (Zhang and Nozaki, 1998; Lacan and Jeandel, 2001):

$$Ce/Ce^{*} = 2 \times (Ce)_N/((La)_N + (Pr)_N) \quad (2)$$

where $(Ce)_N$, $(La)_N$,and $(Pr)_N$ represent the Post Archean Australian Shale (PAAS) (Taylor and McLennan, 1985) normalized Ce, La, and Pr, respectively. The RSD of Ce/Ce* in Pacific deep water (4000 m, n=11) is 3.5%. By convention, an anomaly value >1 (or <1) is referred to as a positive (or negative) anomaly.

The La/Yb ratio was calculated as (Zhang et al., 2008):

$$La/Yb = (La)_N/(Yb)_N \quad (3)$$

where $(Yb)_N$ represents the PAAS normalized Yb. The RSD of the La/Yb ratio in Pacific deep water is 2.4% (4000 m, n=11).

The location of station P1-15 (26°N, 150°E) in this study is close to station TPS 24 271-1 (24.29°N, 150.45°E) from previous trans-Pacific sections (Piepgras and Jacobsen, 1992). The REE concentrations were comparable between the two stations (1000 m and 2000 m) with RSDs <10 % except for Ce (Supplementary Table S2). Considering that Ce is susceptible to contamination and has a relationship with latitude (see section 4.2), the Ce concentration RSDs of 18 % and 19 % are acceptable. The intercalibration reported here basically follows GEOTRACES protocols (https://geotracesold.sedoo.fr/Cookbook.pdf).

2.4 Isopycnal mixing model

To evaluate the quasi-conservative behavior of REEs from NPIW (26.6~27.5 kg/m^3) in the MWR (stations P1-1~P1-4), we used a mixing model to determine the Oyashio and Kuroshio mixing ratios at three isopycnal surfaces: 26.6, 27.0 and, 27.5 kg/m^3 (Du et al., 2013; Wu et al., 2015; Li et al., 2021). The equations are as follows:

$$f_{OC} + f_{KC} = 1 \quad (4)$$

$$f_{OC} \times \theta_{OC} + f_{KC} \times \theta_{KC} = \theta_M \quad (5)$$

$$f_{OC} \times S_{OC} + f_{KC} \times S_{KC} = S_M \quad (6)$$

$$\Delta Nd = Nd_M - f_{OC} \times Nd_{OC} - f_{KC} \times Nd_{KC} \quad (7)$$

where, f_{OC} and f_{KC} represent the fractions of the Oyashio and the Kuroshio waters, respectively, and the θ_{OC} (θ_{KC}), S_{OC}(S_{KC}),and Nd_{OC}(Nd_{KC}) terms are the potential temperatures (θ), salinities, and Nd concentrations of Oyashio (Kuroshio) end-members, respectively. We selected stations located in regions before the end-member currents enter the MWR since water mass properties may change after formation during transport to the study area. End-member characteristics of the Oyashio and the Kuroshio and their uncertainties are listed in Table 1. The subscript "$_M$" represents measured values. Calculated results were fitted by least-squares optimization. Non-conservative Nd (ΔNd) is defined as the difference between the observed concentrations and calculated values due to water mass mixing; ΔNd values greater than 0 or less than 0 represent additions or removals from our defined endmember region to the study region, respectively.

3 Results

3.1 Hydrographic setting

The potential temperature-salinity diagram (Figure 2) shows a potential temperature range from 1.7 to 29.5°C. At low latitudes, the surface water (≤5 m) has higher potential temperatures than that at high latitudes (Figure 3A). Potential temperature in surface water at stations P1-1~P1-4 (MWR, 37°N-40°N) ranges from 14.5 to 22.3°C. At stations P1-7~P1-28 (subtropical region, 13°N-34°N), the potential temperature in surface water ranges from 22.3 to 29.4°C. Vertically, the potential temperature decreases rapidly to <5°C from the surface to 1000 m and then remains constant below 1000 m (Figure 3A).

TABLE 1 End-member characteristics of the Oyashio and the Kuroshio currents and their uncertainties.

Water mass	Oyashio			Kuroshio		
Potential density (kg/m^3)	26.6	27	27.5	26.6	27	27.5
θ (°C)	2.18±1.16 (n=15)[a]	2.95±0.22 (n=14)[a]	2.78±0.15 (n=13)[a]	8.26±0.45 (n=10)[b]	5.03±0.46 (n=10) [b]	3.14±0.13 (n=9)[b]
Salinity	33.31±0.14 (n=15)[a]	33.88±0.03 (n=14)[a]	34.34±0.01 (n=13)[a]	34.19±0.09 (n=10)[b]	34.14±0.07 (n=10)[b]	34.40±0.02 (n=9)[b]
Location	40.0~43°N 145~153°E	40.0~43°N 146~153°E	40.0~43°N 146~153°E	32~35°N 142~146°E	32~35°N 142~146°E	32~34°N 142~146°E
Nd (pmol/kg)	17.50 (n=1)[c]	20.10 (n=1)[c]	23.00 (n=1)[c]	10.29 (n=1)[d]	14.41 (n=1)[d]	18.40 (n=1)[d]
Location	40.5°N, 144.5° E			34.7°N, 139.9° E		

[a]Mean values from the P01 transect (stations 2-30) with potential densities of 26.6, 27, and 27.5 kg/m^3 (WOCE dataset, http://www.ewoce.org).
[b]Mean values from the P10 transect (stations 79-86) and PR3N (stations 6021 and 6023) with potential densities of 26.6, 27, and 27.5 kg/m^3 (WOCE dataset, http://www.ewoce.org).
[c]Amakawa et al., 2004a.
[d]Alibo and Nozaki, 1999.

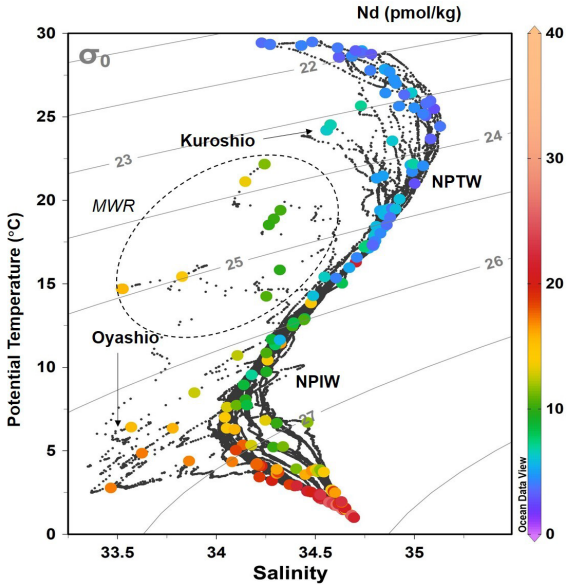

FIGURE 2
Potential temperature (°C)-salinity diagram with potential density (kg/m^3) contours as solid grey lines. The general location of major currents (Oyashio and Kuroshio) and water masses (NPTW: North Pacific Tropical Water, NPIW: North Pacific Intermediate Water) are marked based on their hydrographic properties. Colored symbols represent the Nd concentration (pmol/kg) of individual water samples. The shallow water (<100 m) in MWR was marked by a dotted ellipse.

Salinity ranges from 33.39 to 35.12. In the upper water column (≤300 m), stations P1-1 ~P1-4 have low salinities, 33.39 to 34.55, which is mainly influenced by the Oyashio. In contrast, the other stations have high salinities (34.12 to 35.12), where the NPTW forms (Figure 3B). Below 300 m, the salinities at stations P1-1 and P1-2 gradually increase with depth. However, the salinities of the other stations reach their minimum values (<34.3) between 300 m and 1000 m, which indicates the core area of NPIW (26.6-27.5 kg/m^3, Figures 3B, 4A). The salinities at all stations are constant at 34.20-34.63 in deeper water (1000 m-2000 m).

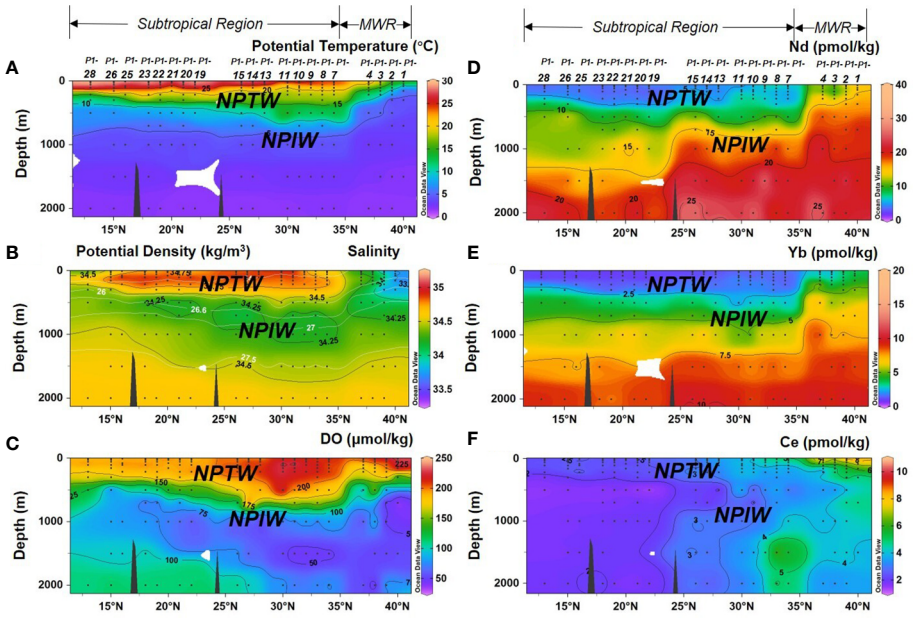

FIGURE 3
Distributions of **(A)** potential temperature (°C), **(B)** salinity with potential density contours in white, **(C)** DO (µmol/kg), **(D)** Nd (pmol/kg), **(E)** Yb (pmol/kg), and **(F)** Ce (pmol/kg) along the P1 transect.

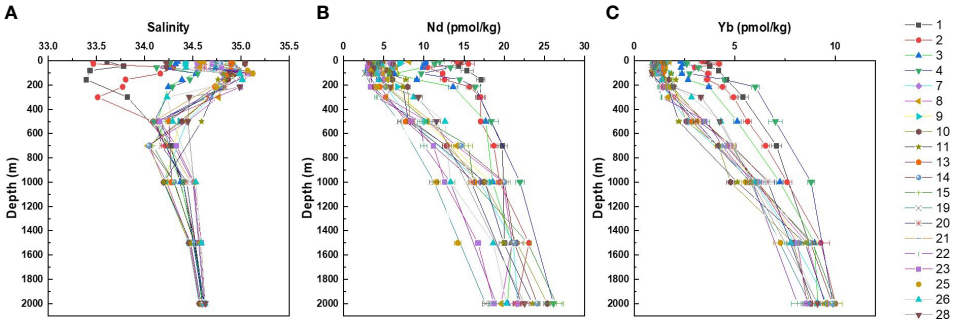

FIGURE 4
Vertical profiles of **(A)** Salinity, **(B)** Nd (pmol/kg), and **(C)** Yb (pmol/kg) with error bars from all stations.

3.2 REEs concentrations

Detailed REE concentration data is shown in Supplementary Table S1. Similar distributions were observed for Nd and the sum of LREEs (Light rare earth elements ; La , Ce, Pr, Nd, Sm, and Eu; except for Ce, which has significant redox-related behavior that other LREEs do not; R^2=0.98), and Yb and the sum of HREEs (R^2=0.98) (Supplementary Figures S1,S2), Therefore, we use Nd as a representative element for LREEs and Yb as a representative element for the HREEs (e.g., Zheng et al., 2016; de Baar et al., 2018) in this study.

The concentrations of Nd and Yb for all stations along the P1 transect are shown in Figures 3D, E. Concentrations of Nd and Yb ranged from 2.62 ~ 26.66 pmol/kg and 0.83 ~ 10.02 pmol/kg, respectively. In general, REE concentrations in the MWR were higher than those in the subtropical region. In the MWR (37-40°N, stations P1-1~P1-4), the water samples from less than 300 m depth (<26.6 kg/m^3) were characterized by high REE concentrations (Nd=13.02±2.91 pmol/kg, Yb=3.60±1.03 pmol/kg), which may indicate significant influence by the Oyashio with low salinity and high REEs. Below 300 m, the REEs increased with depth (Figures 3D, E, 4B, C). At 2000 m, the concentrations of Nd and Yb were 22.70 ±5.39 pmol/kg and 9.68±2.91 pmol/kg, respectively. In the subtropical region (13-34°N, stations P1-7~P1-28), the lowest REEs concentrations were found in surface and subsurface water (≤105 m, Nd=4.45±1.20 pmol/kg, Yb=1.18±0.26 pmol/kg), which may be due to particle scavenging (Stichel et al., 2015; Fröllje et al., 2016). Below 105 m, the REE concentrations increased with depth (Figures 3D, E, 4B, C). At 2000 m, the concentrations of Nd and Yb reached up to 21.44±2.92 pmol/kg and 9.04±0.68 pmol/kg, respectively.

Due to its significant redox behavior, Ce concentration distributions differed from other REEs (Figure 3F). The highest Ce concentration (6.29±1.94 pmol/kg) was found at a water depth less than 300 m in the MWR. The lowest Ce concentration was found in water samples from 500 m to 2000 m depths at stations P1-19~P1-28 (1.77±0.22 pmol/kg). Overall, at the same depth, Ce concentrations were higher at high latitudes than at low latitudes (except for ~1500 m at stations P1-7~P1-9). At ~1500 m of stations P1-7~P1-9, Ce concentrations (5.49 ±1.12 pmol/kg, Figure 3F) were slightly higher than the surrounding seawater and the oxygen was the lowest (46.69±1.50 μmol/kg, Figure 3C) as well.

4 Discussion

4.1 Processes controlling the vertical distributions of REEs: remineralization

REE concentrations were strongly positively correlated with AOU below the depth of the chlorophyll maximum (DCM) layer (Figure 5A, the DCM in each station is shown in Supplementary Table S1), suggesting that the remineralization of sinking organic

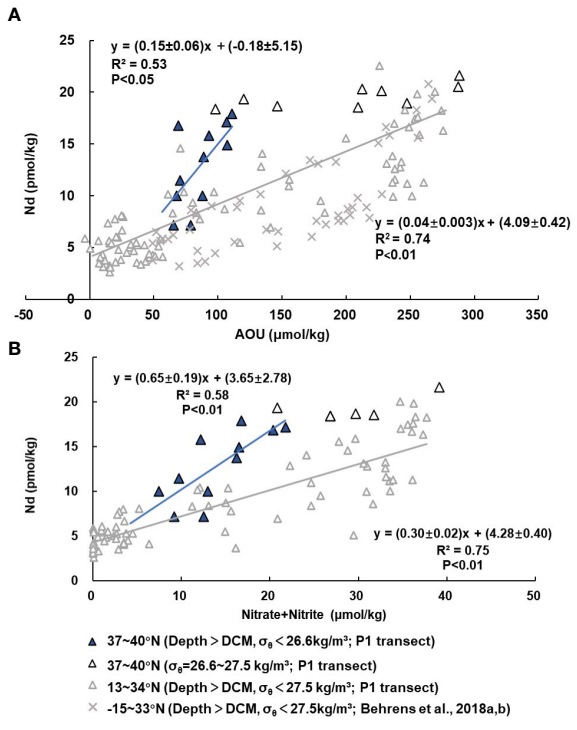

FIGURE 5
(A) Nd (pmol/kg) vs. AOU (μmol/kg) from P1 transect (triangles) and Behrens et al. (2018a,b) (crosses) within subsurface and intermediate water (Depth >DCM and σ_θ< 27.5 kg/m^3); **(B)** Nd (pmol/kg) vs. Nitrate +Nitrite (μmol/kg) from P1 transect (triangles). The colored symbols represent data from water less dense than 26.6 kg/m^3 in the MWR (stations P1-1~P1-4, 37~40°N). The linear regressions and corresponding equations are shown for water samples with densities less than 26.6 kg/m^3 in the MWR (blue line) and south of the MWR (gray line).

matter contributes to the increase of REEs (except for Ce). This is consistent with findings in the central and intermediate waters of the West Pacific by Behrens et al, (2018a, b). To systematically understand the influence of remineralization on REEs, we summarize the relationship between Nd and AOU in the subsurface and intermediate water (σ_θ< 27.5 kg/m^3, depth >DCM), where the remineralization processes are usually pronounced, based on our observations and data from the literature (Behrens et al., 2018a; Behrens et al., 2018b). The results show that Nd increased rapidly as AOU increased in subsurface water (σ_θ< 26.6 kg/m^3, depth >DCM) with the relationship yielding about a 4-fold higher slope (0.15±0.06) in the MWR (stations P1-1~P1-4, 37~40°N) vs. south of the MWR (0.04±0.003) (-15~34°N; Figure 5A). However, Nd remained almost constant with increasing AOU in the intermediate water (26.6-27.5 kg/m^3) of the MWR (stations P1-1~P1-4, 37~40°N; Figure 5A). Therefore, in the MWR remineralization processes mainly influenced the REEs in subsurface water, rather than in intermediate water. This may indicate the rapid decomposition of organic matter in the subsurface water, with few organic particles sinking to intermediate water depths in the MWR. Similarly, Nd is positively correlated with nitrate + nitrite in subsurface and intermediate water (σ_θ<27.5 kg/m^3, depth >DCM) to the south of the MWR as well as in subsurface water (σ_θ< 26.6 kg/m^3, depth >DCM) of the MWR (Figure 5B). This also suggests that the remineralization of sinking organic particles plays a critical role in the production of REEs. We also estimated the addition or removal of Nd in the intermediate water of the MWR (stations P1-1~P1-4, 26.6~27.5 kg/m^3) by using the isopycnal mixing model (section 2.4). The results show that, at 26.6 kg/m^3, the proportion of Nd added to the observed Nd (ΔNd/Nd) was 21±16%. At 27.5 kg/m^3, there was almost no addition or removal of Nd (ΔNd/Nd=-6 ±12%), which is consistent with the above conclusion that remineralization contributes negligible Nd to the intermediate water of the MWR. Overall, our results suggest that the influence of remineralization on REEs varies regionally.

Remineralization processes are related to the ambient environmental context, such as microbial community structure, nutrient supply and exogenous labile organic matter inputs (Church et al., 2000; Carlson et al., 2004; Mills et al., 2008; Carlson et al., 2009; Li et al., 2021). In the MWR, the intrusion front of the Oyashio mainly exists at σ_θ < 26.7 kg/m^3 (Zhu et al., 2019), which is almost consistent with the depth (σ_θ < 26.6 kg/m^3) where REEs appear to be significantly released by remineralization. The intrusion of the Oyashio into the Kuroshio, with distinct environmental contexts (e.g., temperature, salinity, nutrient supply, and organic matter inputs), may enhance the remineralization in the MWR subsurface water (<26.6 kg/m^3). Enhanced remineralization due to strong mixing is also found in the Luzon Strait near the Kuroshio intrusion (Li et al., 2021). In addition, the regional differences in remineralization might be associated with the plankton community structure. For instance, in the MWR, the phytoplankton are dominated by haptophytes, while in the oligotrophic subtropical region, dinoflagellates are dominant (Suzuki et al., 1997; Lin et al., 2020; Wang et al., 2021; Wang et al., 2022). We suggest that organic detritus from different organisms may have distinct ratios of consumed oxygen and released REEs during the remineralization process. This supposition requires more evidence, such as the ratio of REE concentrations to organic matter in haptophytes vs dinoflagellates. Thus, the water masses mixing and/or the plankton community structure could be responsible for the regional differences of the influence of remineralization on REEs.

Overall, our results emphasize regional differences in the release efficiency of REEs by remineralization. For other trace elements, like iron, the efficiency of organic remineralization is speculated to be one of the reasons for the difference in dissolved iron concentrations between the western and eastern subarctic Pacific (Nishioka et al., 2013). Our results may provide evidence for regional differences in trace elements caused by organic matter remineralization.

4.2 Shelf inputs and lateral transport of REEs

Figure 6 shows the distribution of LREEs (La, Ce, Pr) and La/Yb ratios in surface water (<10 m) in the Northwest Pacific. REE (La, Ce, Pr) concentrations near the margin are higher than those farther away. We suggest that the high REEs in the surface water of the MWR and Oyashio likely originate from the Kuril Islands (Morton et al., 2019). In addition, high La/Yb ratios (>0.35) (Figures 6E and 7A) were observed in northern stations (stations TPS 47 39-1 and SEEDS-II; Piepgras and Jacobsen, 1992; Hara et al., 2009), which reflects the effect of lithogenic material dissolution (Zhang et al., 2008; Pearce et al., 2013). The La/Yb ratio could be the Aleutian Islands signal caught up in the East Kamchatka Current since the elevated La/Yb ratios (0.51±0.51, Supplementary Figure S3A) have been observed in the Aleutian Islands. Furthermore, the high Nd isotopic composition (-2.2 at station CM-S-3 and -2.0 at station TPS 47 39-1) of surface water in the Oyashio also verifies the input of REEs from islands (the Kuril and Aleutian Islands), as volcanic islands usually have more radiogenic Nd (Piepgras and Jacobsen, 1988; Amakawa et al., 2004a, Amakawa et al., 2004b; Fuhr et al., 2021). Therefore, islands are important lithogenic sources of REEs to surface waters of the Northwest Pacific subarctic region and the MWR.

In addition, the Sea of Okhotsk is an important source of materials to the Oyashio and NPIW in the Northwest Pacific, such as Fe (Nishioka et al., 2013), Zn (Kim et al., 2017), Cd (Yang et al., 2018) and anthropogenic CO_2 (Yasuda, 2004). Based on the fact that the Sea of Okhotsk receives a large number of trace elements from rivers and sediments, we believe that Okhotsk seawater may also be an important source of REEs to the Oyashio (Shulkin and Bogdanova, 2003; Nishioka et al., 2007; Nishioka et al., 2013; Nishioka et al., 2014; Kim et al., 2015).

As discussed above, the REEs in the Oyashio Current are sourced from the islands and the Sea of Okhotsk and then supplied to the NPIW in the subtropical region. In the study area, REE concentrations (except for Ce) are mainly influenced by remineralization processes during NPIW transport (see above section 4.1), and their concentration changes vertically, increasing

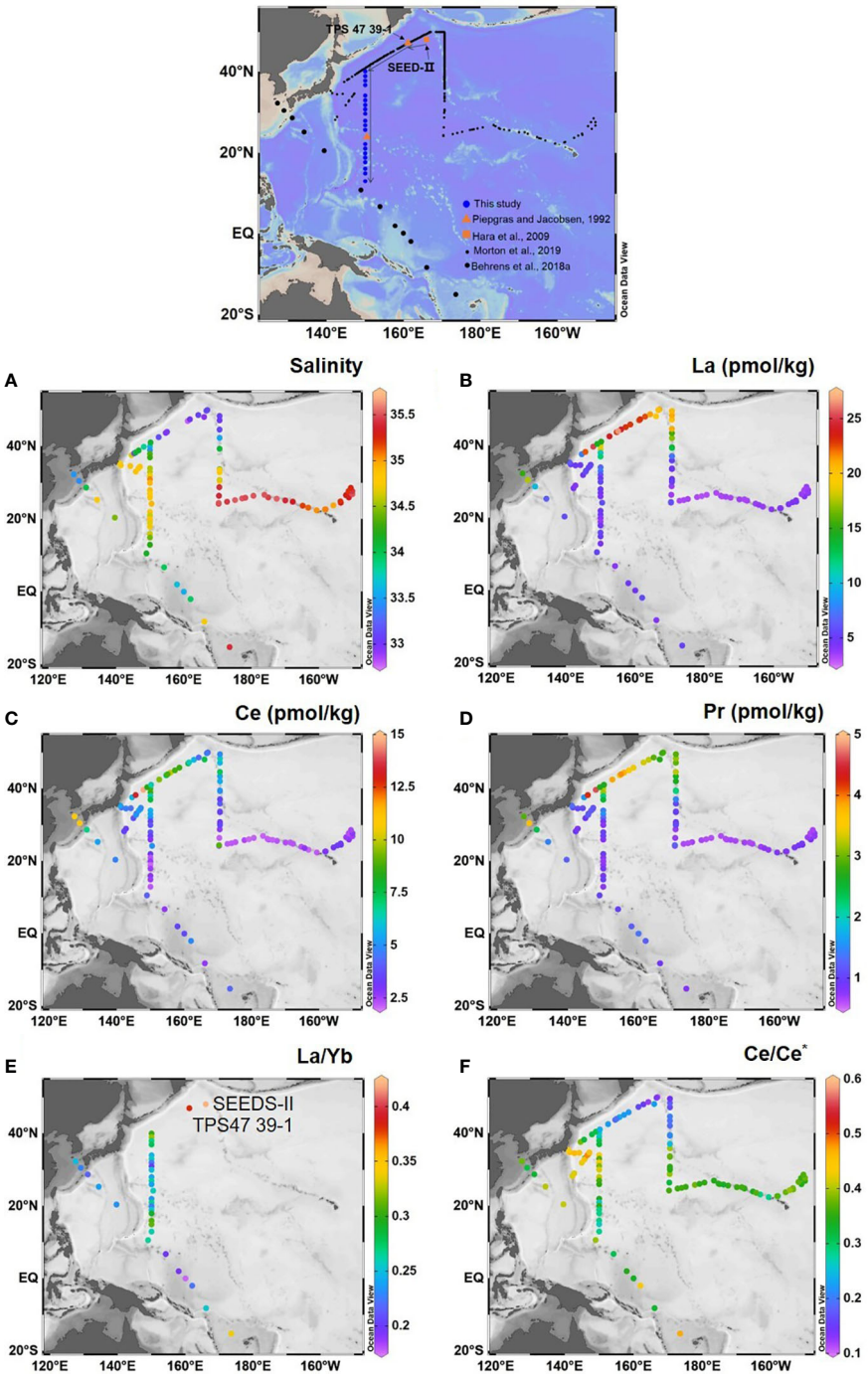

FIGURE 6
Maps showing surface sampling stations. Color bar represents **(A)** Salinity, **(B)** La (pmol/kg), **(C)** Ce (pmol/kg), **(D)** Pr (pmol/kg), **(E)** La/Yb and **(F)** Ce/Ce* (data from this study, Piepgras and Jacobsen (1992); Hara et al. (2009); Behrens et al. (2018a), and Morton et al. (2019)) in surface water (<10 m). The north-south transect is marked with arrows on the map.

with depth (Figures 3D, E, 4B, C). However, unlike other trivalent REEs, dissolved Ce is easily removed by particles in seawater. This is because Ce (III) is easily oxidized to the tetravalent state (Ce(IV)) in seawater and subsequently precipitated as CeO_2 or $Ce(OH)_4$, resulting in the depletion of dissolved Ce and negative Ce anomalies in seawater (Alibo and Nozaki, 1999; Tazoe et al., 2011). Following Morton et al. (2019), in the subarctic region, the Ce concentration was high but Ce/Ce* showed an extremely negative anomaly (<0.2) in surface water (Figures 6C, F), which suggests Ce inputs from the shelf as well as preferential removal of Ce relative to La and Pr by Mn-oxides (Morton et al., 2019). In this study area (transect P1), Ce concentrations were higher at high latitudes than at low latitudes (except for ~1500 m depth at stations P1-7 ~P1-9, Figures 3F): that is, the Ce concentration decreased

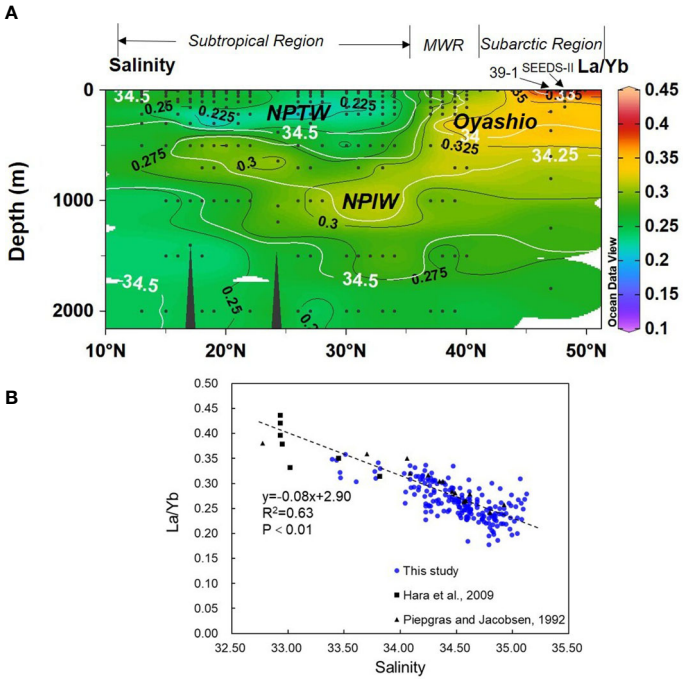

FIGURE 7
(A) Distributions of La/Yb with salinity contours in white along the south-north transect shown on the map in Figure 6, and **(B)** plots of La/Yb versus salinity (data from this study, Piepgras and Jacobsen (1992), and Hara et al. (2009)). La/Yb is significantly negatively correlated with salinity (R^2=0.63, P<0.01).

with distance from the shelf, due to the rapid oxidation and removal of Ce from seawater. At ~1500 m depth at stations P1-7~P1-9, Ce concentrations were slightly higher than in the surrounding seawater (Figure 3F), and the oxygen concentration was the lowest (Figure 3C). This might be explained by fewer oxide particles in the water column or the effect of lateral transport from a low oxygen region, and needs further research. In addition, a strong particulate negative Ce anomaly was observed in the subarctic region (station 2, 155°E, 44°N) by Morton et al. (2019), which may rule out the possibility of supply from an atmospheric source because aerosols generally have no Ce negative anomaly (Morton et al., 2019).

The Oyashio Current acquires the imprints of high La/Yb ratios from the islands through the East Kamchatka Current. As shown in Figure 7A, the highest La/Yb ratios (>0.35) were observed at stations TPS 47 39-1 (Piepgras and Jacobsen, 1992) and SEEDS-II (Hara et al., 2009) (< 100 m) in the East Kamchatka Current. In the low salinity water (<34.25, mainly the Oyashio and NPIW), the high value signature is gradually diluted as the water mass flows southward. It should be noted that because of the lack of REE data in the Sea of Okhotsk, we cannot determine whether the water masses from the Sea of Okhotsk also provided elevated La/Yb ratios to the Oyashio and NPIW. At all stations (≤2000 m), La/Yb is significantly negatively correlated with salinity (R^2=0.63, P<0.01) (Figure 7B). This indicates that the La/Yb ratios are mainly affected by water mass mixing even though it is generally accepted that the particulate process should cause a fractionation of LREEs and HREEs due to their different particle adsorption affinities (Byrne and Kim, 1990; Sholkovitz et al., 1994). Similarly, the Oyashio may also have acquired the signals of Pr/Yb and Nd/Yb ratios from nearby islands (Aleutian and Kamchatka Islands; Figures 8A, B). The islands' Pr/Yb and Nd/Yb signals are more significant than the La/Yb signal (Supplementary Figures S3B, C). NPIW has shown elevated ratios of Pr/Yb and Nd/Yb (Figures 8C, D); however, there is no correlation between Pr/Yb (or Nd/Yb) and salinity (R^2 values were 0.06 and 0.01, respectively). This indicates that La/Yb more faithfully retains the original signature of an end-member than Pr/Yb and Nd/Yb in seawater. This may be related to the fact that La is the only lanthanide element that lacks a 4f electron, resulting in a solution stability that differs from other LREEs in seawater. Otherwise, in seawater, the longer residence time of La compared to other LREEs (Li, 1991; Alibo and Nozaki, 1999; Nozaki, 2001) might also contribute to the water masses tracing values of La/Yb. In summary, the La/Yb ratio provides a useful proxy for studying the flow paths of the Oyashio and NPIW in the North Pacific, and the NPIW is critical for transporting substances that affect marine ecosystems and climate, such as Fe and CO_2 (Yasuda, 2004; Nishioka et al., 2007; Nishioka et al., 2013; Nishioka et al., 2014; Nishioka and Obata, 2017).

REEs ratios have also been used for tracing Southern Ocean water masses (Zhang and Nozaki, 1996; Osborne et al., 2015; Behrens et al., 2018a). For instance, the Ho/Dy ratio may be used to differentiate intermediate/deep water in the Southwest Pacific from Antarctic Bottom Water (Zhang and Nozaki, 1996). The low Dy/Er and high HREE/LREE ratios formed in the East Pacific Rise hydrothermal plume trace the Upper Circumpolar Deep Water

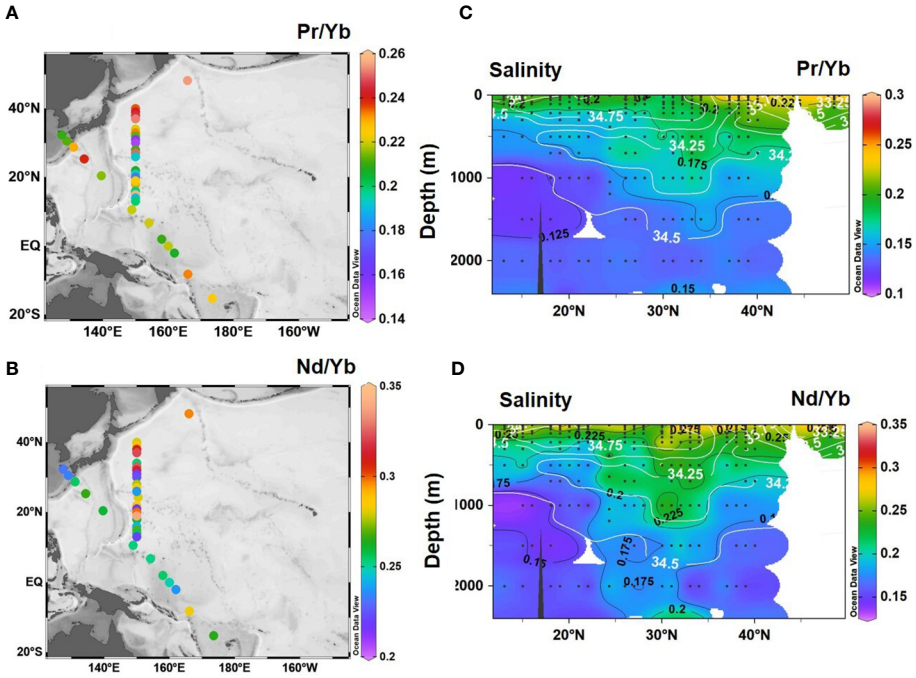

FIGURE 8
Distributions of **(A)** Pr/Yb ratio and **(B)** Nd/Yb ratio in the surface water (<10 m). Vertical distributions of **(C)** Pr/Yb ratio and **(D)** Nd/Yb ratio with salinity contours in white along the south-north transect (data from this study, Piepgras and Jacobsen (1992); Hara et al. (2009), and Behrens et al. (2018a)).

(Osborne et al., 2015; Behrens et al., 2018a). These examples indicate that the ratios of REEs in the oceans are valuable water mass tracers and should be widely focused on in future studies.

Taken together, lithogenic material input from islands (including the Kuril Islands and the Aleutian Islands) and the Sea of Okhotsk are the important sources of REEs and other trace elements (Fe, Zn, Cd, etc.) to the Oyashio current. It is also an important source for NPIW due to the supply of Oyashio water. The La/Yb ratio is mainly affected by water mass mixing and therefore is a very good tool for tracing the Oyashio and NPIW.

4.3 Estimating cross-shelf Nd fluxes

The marginal seas (including the Sea of Okhotsk, Sea of Japan, East China Sea, South China Sea, and the Bering Sea) may be important REE sources to the Northwest Pacific. We estimated the net Nd fluxes (F_{Nd}^{net}) between the marginal seas and Northwest Pacific based on the following equation:

$$F_{Nd}^{net} = F_w^{inflow} \times Nd^m - F_w^{outflow} \times Nd^p \quad (8)$$

Where, F_w^{inflow}(or $F_w^{outfolw}$) represents the water flux from the marginal sea to the Northwest Pacific (or from the Northwest Pacific to the marginal sea). Nd^m (or Nd^p) represents the end-member values of Nd concentration in the marginal seas (or the Northwest Pacific). The water fluxes and Nd concentrations are shown in Table 2. The net Nd flux from the Bering Sea was not estimated due to a lack of REE data.

A portion of the East Kamchatka Current flows into the Sea of Okhotsk through the Northern Kuril Islands Strait (mainly in the Kruzenshtern Strait) and then flows out to the Pacific Ocean through the South Kuril Islands Strait (mainly through the Bussol' Strait, water depth ~2300 m) (Figure 1; Hill et al., 2003; Shu et al., 2021). Because the water flow flux into the Sea of Okhotsk through the Kruzenshtern Strait is thought to be nearly equal to the outflow flux from the Bussol' Strait (Ohshima et al., 2010), we assume that both the inflow and outflow water fluxes are 8.2~8.8 Sv (Katsumata, 2004) (excluding the water exchange caused by tidal processes). Due to the lack of a vertical profile of REEs in the Sea of Okhotsk, the Nd concentration of Okhotsk surface water (Amakawa et al., 2004a) was used to represent the average Nd concentration of the full water column. The net input flux of Nd from the Sea of Okhotsk to the Pacific Ocean was estimated to be 29~32 tNd/y (Table 2 and Figure 9), which is comparable to the input from the Yangtze and Korean rivers combined (20~24 and 7 tNd/y, respectively; Behrens et al., 2018b; Che et al., 2022).

The Tsugaru Strait is the only pathway directly connecting the Sea of Japan and the North Pacific, at a depth of <200 m (Figure 1; Ito et al., 2003). The Tsugaru Warm Current originates from the Sea of Japan and flows into the North Pacific through the Tsugaru Strait with a water flux of 1.1~2.1Sv (Ito et al., 2003). Using above water flux and the weighted average value of Nd in the Sea of Japan (<200 m, Seo and Kim, 2020), we calculated the net Nd input flux to be 159~302 tNd/y (Table 2 and Figure 9). This Nd input flux from the Sea of Japan is of the same order of magnitude as the atmospheric and riverine contributions of Nd to the global oceans (400-630 tNd/

TABLE 2 Estimates of the cross-shelf Nd fluxes from marginal seas.

Marginal Seas	Location	Flow Depth (m)	Flow Magnitude ($10^6 m^3 s^{-1}$)*	Nd (pmol/kg)	Nd Fluxes in straits or channels (t/y)*	Cross-shelf Nd Fluxes from the Marginal Seas to the Northwest Pacific (t/y)*
Sea of Okhotsk	Bussol' Strait	Full depth	8.2~8.8[a]	25.6[b#]	953~1023	29~32 (full depth)
	Kruzenshtern Strait	Full depth	-8.2~-8.8[a]	24.82[c%]	-924~-991	
Sea of Japan	Tsugaru Strait	Full depth	1.1~2.1[d]	31.79[e#]	159~302	159~302 (full depth)
East China Sea	Tokara Strait	<200m	13.3~15.3[f]	4.84[g#]	293~336	4~47 (<200m) 142~616 (full depth)
		Full depth	19.9~27.8[f]	13.21[g#]	1194~1668	
	East Taiwan Channel	<200m	-13.8[h]	4.63[i%]	-289	
		Full depth	-22.0[h]	10.55[i%]	-1052	
South China Sea	Luzon Strait	0m~500m	-9~-4.3[j]	7.02[k%]	-287~-137	-298~34 (full depth)**
		500~1500m	1.1~5.0[j]	24.54[k#]	125~557	
		1500m~bottom	-3.4~-2[j]	25.93[k%]	-400~-236	

[a]Katsumata, 2004.
[b]Amakawa et al., 2004a.
[c]Fuhr et al., 2021.
[d]Ito et al., 2003.
[e]Seo and Kim, 2020.
[f]Guo et al., 2013; Liu et al., 2019.
[g]Liu et al., 2022 and our unpublished data.
[h]Johns et al., 2001.
[i]Wu et al., 2015 and unpublished data.
[j]Xu and Oey, 2014 and references therein.
[k]Wu et al., 2015 and unpublished data in the Philippine Sea.
* Positive and negative numbers represent inflow from and outflow to the Northwest Pacific, respectively.
** The Nd fluxes representing the full depth range include results calculated from the water fluxes provided by different literature sources (Xu and Oey, 2014 and references therein), rather than the sum of the maximum and minimum values of Nd fluxes in the three water layers in the table.
[#]End-member values of Nd (pmol/kg) in the marginal seas (Nd^m)
[%] End-member values of Nd (pmol/kg) in the Northwest Pacific (Nd^P).

y and 260-660 tNd/y, respectively ; Greaves et al., 1994; Tachikawa et al., 2003; Arsouze et al., 2009), which are considered important sources of REEs in the oceans (Lacan and Jeandel, 2001; Flierdt et al., 2004; Arsouze et al., 2009).

In the East China Sea, the channels in the Ryukyu Island chain are important links to the Northwest Pacific. The East Taiwan Channel and the Tokara Strait are the main pathways connecting the East China Sea and the Northwest Pacific (Johns et al., 2001; Isobe et al., 2002; Teague et al., 2002; Takikawa et al., 2005; Isobe, 2008). Therefore, we only focus on the fluxes across these two straits. The results show that the net Nd flux from the East China Sea is 142~616 tNd/y, which is relatively large and similar to or greater than the input from the Sea of Japan (159~302 tNd/y, Table 2 and Figure 9). On the other hand, the net Nd input to the Pacific Ocean from the East China Sea shelf at depths of <250 m was estimated to be 113 t/y using Nd isotopes and a box model (Lacan and Jeandel, 2005), which is higher than our result for depths of <200 m (4~47 tNd/y, Table 2). This indicates that our result might be an underestimate, probably due to the fact that we selected a lower average Nd endmember concentration in the Northwest Pacific for our estimation than that used by Lacan and Jeandel (2005).

The water exchange between the Northwest Pacific and the South China Sea occurs mainly through the Luzon Strait. In the Luzon Strait, the surface and deep waters flow from the Pacific to the South China Sea. At intermediate depths, the flow direction is reversed (Chao et al., 1996; Gan et al., 2006; Qu et al., 2006). The Nd fluxes between the Northwest Pacific and the South China Sea at different water layer depths are shown in Table 2. The calculated Nd fluxes for 0-500 m, 500-1500 m, and 1500 m-bottom are -287~-137, 125~557, and -400~-236 t/y (negative values represent input from the Northwest Pacific to the South China Sea), respectively. The net Nd input fluxes for the full water column are -298~34 t/y (Table 2 and Figure 9). This indicates that the South China Sea is a sink of Nd from the Northwest Pacific at 0-500 m and 1500 m-bottom, and a source of Nd in the 500-1500 m water layer. Overall, the South China Sea may be either a net source or a net sink of Nd to the Northwest Pacific depending on the selection of the endmembers in the present estimation. For instance, when the estimated water fluxes at 0-500 m, 500-1500 m, and 1500m-bottom are -9.0, 5.0, and

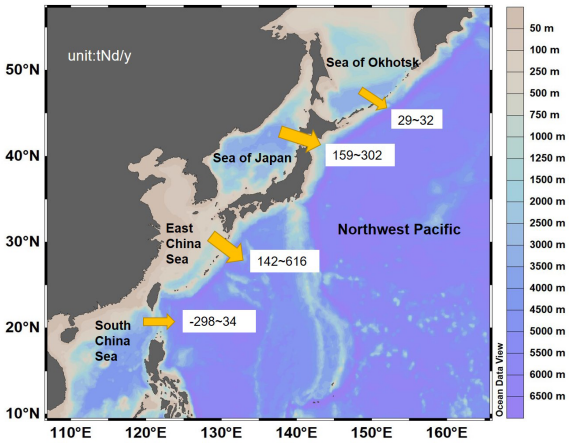

FIGURE 9
The cross-shelf Nd fluxes (tNd/y) from marginal seas to the Northwest Pacific. Negative values represent input from the Northwest Pacific to the marginal seas.

-2.0 Sv, respectively (Tian et al., 2006), the South China Sea is a source of REEs to the Northwest Pacific with net Nd flux of 34 t/y. When the water fluxes in 0-500 m, 500-1500 m, and 1500 m-bottom are estimated to be -5.1, 2.8, and -3.8 Sv, respectively (Xu and Oey, 2014), the South China Sea is a sink of REEs in the Northwest Pacific with net Nd flux of -298 t/y. It should be noted that there are large uncertainties in the estimated net fluxes of Nd. In particular, the complex water structure (Chen and Wang, 1998; Wang et al., 2010; Zhang et al., 2015) and seasonal variations of water exchange in the Luzon Strait (Xu and Oey, 2014 and references therein) lead to a wide range of water fluxes (Table 2). In addition, there may be seasonal variations in Nd concentrations, which introduce uncertainties in Nd net flux estimates.

In summary, the Sea of Okhotsk, the Sea of Japan and the East China Sea are Nd sources to the Northwest Pacific, with a relatively low net flux of Nd from the Sea of Okhotsk (29~32 t/y) but high fluxes from the Sea of Japan (159~302 t/y) and the East China Sea (142~616 t/y). In contrast, the Nd exchange flux between the South China Sea and the Pacific is subject to water exchange occurring at different water layer depths in the Luzon Strait. The South China Sea is a sink of Nd from the Northwest Pacific at the water layers of 0-500 m (-287~-137 t/y) and 1500m-bottom (-400~-236 t/y), and a source of Nd at 500-1500 m (125~557 t/y), with a net Nd flux range of -298~34 t/y.

5 Conclusions

To study the sources, transport, and biogeochemical cycling of REEs in the Northwest Pacific, we measured dissolved REE concentrations along the P1 transect at 150°E (≤ 2000 m) from 13°N to 40°N. The main findings are as follows:

(1) There are regional differences in the release of REEs by organic matter remineralization. The larger release efficiency of REEs in the MWR (σ_θ<26.6 kg/m ^{3}, depth > DCM) compared with that in the subtropical region (σ_θ<27.5 kg/m^3, depth > DCM) might be related to stronger water mass mixing and the plankton community structure.

(2) Based on our REE data and previously published trace element data, we suggest that islands in the subarctic region (including the Kuril Islands and Aleutian Islands) and the Sea of Okhotsk are important REE sources to the Northwest Pacific. The La/Yb ratio is a signal of lithogenic dissolution from the Aleutian Islands and can be used as a water mass tracer for the Oyashio Current and NPIW.

(3) The marginal seas usually receive large amounts of REEs, and typically have higher REE concentrations than the open ocean. The estimated net Nd fluxes from the Sea of Okhotsk, Sea of Japan, East China Sea, and the South China Sea were 29~32 t/y, 159~302 t/y, 142~616 t/y, and -298~34 t/y, respectively. Our estimates indicate that the Nd exchange fluxes between the marginal seas and the Northwest Pacific are not negligible.

Overall, our systematic analysis of the source, transport, and biogeochemical cycling of dissolved REEs in the Northwest Pacific provides useful proxy information for tracing regional water masses and estimating cross-shelf REE fluxes. However, the influences of particulate processes (such as the remineralization of organic matter) on REE ratio (e.g., La/Yb) distributions in seawater need further study.

Data availability statement

The original contributions presented in the study are included in the article/Supplementary Material. Further inquiries can be directed to the corresponding authors.

Author contributions

AC: Conceptualization, Investigation, Formal Analysis, Data curation, Writing - original draft. JZ: Conceptualization, Writing-review & editing, Supervision, Project administration. HZ: Data Curation. ZC: Investigation, Data Curation. GC: Formal Analysis, Visualization. ZL: Formal Analysis. YL: Writing – review & editing. QL: Conceptualization, Writing – review & editing, Supervision, Project administration. All authors contributed to the article and approved the submitted version.

Funding

This research was supported by the National Natural Science Foundation of China (Grant 41890801), Fundamental Research Funds for the Central Universities (Grant 202072001), JSPS KAKENHI (Grants JP20H04319, JP22H05206), and Laoshan Laboratory Special Fund of Shandong Province (Grant 2022QNLM010103-1).

Acknowledgments

We thank the captain and crew of the R/V Dongfanghong 3 for their help with sampling. We further thank Wenkai Guan for assisting in the sample collection. Special thanks to Dr. Huijun He for his important guidance during the data analysis. We would like to thank Dr. Richard Smith and Dr. Stella Woodard at Global Aquatic Research LLC for English language editing. We are grateful to Frontiers Science Center for Deep Ocean Multispheres and Earth System, Ocean University of China for providing frozen warehouse space for nutrient sample storage.

Conflict of interest

The authors declare that the research was conducted in the absence of any commercial or financial relationships that could be construed as a potential conflict of interest.

Publisher's note

Supplementary material

The Supplementary Material for this article can be found online at: https://www.frontiersin.org/articles/10.3389/fmars.2023.1135113/full#supplementary-material

SUPPLEMENTARY FIGURE 1
Distributions of **(A)** the sum of LREEs (pmol/kg) and **(B)** the sum of HREEs (pmol/kg) along the P1 transect.

SUPPLEMENTARY FIGURE 2
Vertical profiles of **(A)** the sum of LREEs (pmol/kg) and **(B)** the sum of HREEs (pmol/kg) with error bars from all stations.

SUPPLEMENTARY FIGURE 3
The ratios of **(A)** La/Yb, **(B)** Pr/Yb, and **(C)** Nd/Yb in rocks from the Aleutian Islands, the Kuril Islands, and Kamchatka Peninsula, including average values and their uncertainties (EarthChem- Access Geochemical Data)

References

Alibo, D. S., and Nozaki, Y. (1999). Rare earth elements in seawater: particle association, shale-normalization, and ce oxidation. *Geochim. Cosmochim. Acta* 63, 363–372. doi: 10.1016/S0016-7037(98)00279-8

Amakawa, H., Alibo, D. S., and Nozaki, Y. (2004a). Nd Concentration and isotopic composition distributions in surface waters of Northwest pacific ocean and its adjacent seas. *Geochem. J.* 38, 493–504. doi: 10.2343/geochemj.38.493

Amakawa, H., Nozaki, Y., Alibo, D. S., Zhang, J., Fukugawa, K., and Nagai, H. (2004b). Neodymium isotopic variations in Northwest pacific waters. *Geochim. Cosmochim. Acta* 68, 715–727. doi: 10.1016/S0016-7037(03)00501-5

Arsouze, T., Dutay, J. C., Lacan, F., and Jeandel, C. (2009). Reconstructing the Nd oceanic cycle using a coupled dynamical – biogeochemical model. *Biogeosciences* 6, 2829–2846. doi: 10.5194/BG-6-2829-2009

Behrens, M. K., Pahnke, K., Cravatte, S., Marin, F., and Jeandel, C. (2020). Rare earth element input and transport in the near-surface zonal current system of the tropical Western pacific. *Earth Planet. Sci. Lett.* 549, 116496. doi: 10.1016/j.epsl.2020.116496

Behrens, M. K., Pahnke, K., Paffrath, R., Schnetger, B., and Brumsack, H.-J. (2018a). Rare earth element distributions in the West pacific: Trace element sources and conservative vs. non-conservative behavior. *Earth Planet. Sci. Lett.* 486, 166–177. doi: 10.1016/j.epsl.2018.01.016

Behrens, M. K., Pahnke, K., Schnetger, B., and Brumsack, H.-J. (2018b). Sources and processes affecting the distribution of dissolved Nd isotopes and concentrations in the West pacific. *Geochim. Cosmochim. Acta* 222, 508–534. doi: 10.1016/j.gca.2017.11.008

Bertram, C. J., and Elderfield, H. (1993). The geochemical balance of the rare earth elements and neodymium isotopes in the oceans. *Geochim. Cosmochim. Acta* 57, 1957–1986. doi: 10.1016/0016-7037(93)90087-D

Bryan, J. R., Rlley, J. P., and Williams, P. L. (1976). A winkler procedure for making precise measurements of oxygen concentration for productivity and related studies. *J.Exp. Mar. Biol. Ecol.* 21 (3), 191–197. doi: 10.1016/0022-0981(76)90114-3

Byrne, R. H., and Kim, K.-H. (1990). Rare earth element scavenging in seawater. *Geochim. Cosmochim. Acta* 54, 2645–2656. doi: 10.1016/0016-7037(90)90002-3

Carlson, C. A., Giovannoni, S. J., Hansell, D. A., Goldberg, S. J., Parsons, R., and Vergin, K. (2004). Interactions among dissolved organic carbon, microbial processes, and community structure in the mesopelagic zone of the northwestern Sargasso Sea. *Limnol. Oceanogr.* 49 (4), 1073–1083. doi: 10.4319/lo.2004.49.4.1073

Carlson, C. A., Morris, R., Parsons, R., Treusch, A. H., Giovannoni, S. J., and Vergin, K. (2009). Seasonal dynamics of SAR11 populations in the euphotic and mesopelagic zones of the northwestern Sargasso Sea. *ISME J.* 3 (3), 283–295. doi: 10.1038/ismej.2008.117

Chao, S. Y., Shaw, P. T., and Wu, S. Y. (1996). Deep water ventilation in the south China Sea. *Deep Sea Res. Part I Oceanogr. Res. Pap.* 43, 445–466. doi: 10.1016/0967-0637(96)00025-8

Che, H., Zhang, J., Liu, Q., He, H., and Zhao, Z.-Q. (2022). Refining the contribution of riverine particulate release to the global marine Nd budget. *Prog. Earth Planet Sci.* 9, 22. doi: 10.1186/s40645-022-00479-2

Chen, C. T. A., and Wang, S. L. (1998). Influence of intermediate water in the western Okinawa trough by the outflow from the south China Sea. *J. Geophys. Res.* 103, 12683–12688. doi: 10.1029/98JC00366

Church, M. J., Hutchins, D. A., and Ducklow, H. W. (2000). Limitation of bacterial growth by dissolved organic matter and iron in the southern ocean. *Appl. Environ. Microbiol.* 66 (2), 455–466. doi: 10.1128/AEM.66.2.455-466.2000

de Baar, H. J. W., Bacon, M. P., Brewer, P. G., and Bruland, K. W. (1985). Rare earth elements in the pacific and Atlantic oceans. *Geochim. Cosmochim. Acta* 49, 1943–1959. doi: 10.1016/0016-7037(85)90089-4

de Baar, H. J. W., Bruland, K. W., Schijf, J., van Heuven, S. M. A. C., and Behrens, M. K. (2018). Low cerium among the dissolved rare earth elements in the central north pacific ocean. *Geochim. Cosmochim. Acta* 2365-, 40. doi: 10.1016/j.gca.2018.03.003

Du, C., Liu, Z., Dai, M., Kao, S. J., Cao, Z., Zhang, Y., et al. (2013). Impact of the kuroshio intrusion on the nutrient inventory in the upper northern south China Sea: Insights from an isopycnal mixing model. *Biogeosciences* 10 (10), 6419–6432. doi: 10.5194/bg-10-6419-2013

Elderfield, H. (1988). The oceanic chemistry of the rare-earth elements. *Phil. Trans. R. Soc Lond. A* 325, 105–126. doi: 10.1098/rsta.1988.0046

Elderfield, H., and Greaves, M. J. (1982). The rare earth elements in seawater. *Nature* 296, 214–219. doi: 10.1038/296214a0

Flierdt, T., Frank, M., Lee, D.-C., Halliday, A. N., Reynolds, B. C., and Hein, J. R. (2004). New constraints on the sources and behavior of neodymium and hafnium in seawater from pacific ocean ferromanganese crusts. *Geochim. Cosmochim. Acta* 68, 3827–3843. doi: 10.1016/j.gca.2004.03.009

Fröllje, H., Pahnke, K., Schnetger, B., Brumsack, H. J., Dulai, H., and Fitzsimmons, J. N. (2016). Hawaiian Imprint on dissolved Nd and Ra isotopes and rare earth elements in the central north pacific: Local survey and seasonal variability. *Geochim. Cosmochim. Acta* 189, 110–131. doi: 10.1016/j.gca.2016.06.001

Fuhr, M., Laukert, G., Yu, Y., Nürnberg, D., and Frank, M. (2021). Tracing water mass mixing from the equatorial to the north pacific ocean with dissolved neodymium isotopes and concentrations. *Front. Mar. Sci.* 7. doi: 10.3389/fmars.2020.603761

Gan, J., Li, H., Curchitser, E. N., and Haidvogel, D. B. (2006). Modeling south China Sea circulation: Response to seasonal forcing regimes. *J. Geophys. Res.* 111, C06034. doi: 10.1029/2005JC003298

Garcia-Solsona, E., Pena, L. D., Paredes, E., Pérez-Asensio, J. N., Quirós-Collazos, L., Lirer, F., et al. (2020). Rare earth elements and Nd isotopes as tracers of modern ocean circulation in the central Mediterranean Sea. *Prog. Oceanogr.* 185, 102340. doi: 10.1016/j.pocean.2020.102340

Greaves, M. J., Statham, P. J., and Elderfield, H. (1994). Rare earth element mobilization from marine atmospheric dust into seawater. *Mar. Chem.* 46, 255–260. doi: 10.1016/0304-4203(94)90081-7

Guo, X. Y., Zhu, X.-H., Long, Y., and Huang, D. J. (2013). Spatial variations in the kuroshio nutrient transport from the East China Sea to south of Japan. *Biogeosciences* 10, 6403–6417. doi: 10.5194/bg-10-6403-2013

Hara, Y., Obata, H., Doi, T., Hongo, Y., Gamo, T., Takeda, S., et al. (2009). Rare earth elements in seawater during an iron-induced phytoplankton bloom of the western subarctic pacific (SEEDS-II). *Deep Sea Res. Part II Top. Stud. Oceanogr.* 56, 2839–2851. doi: 10.1016/j.dsr2.2009.06.009

Hatje, V., Bruland, K. W., and Flegal, A. R. (2014). Determination of rare earth elements after pre-concentration using NOBIAS-chelate PA-1®resin: Method development and application in the San Francisco bay plume. *Mar. Chem.* 160, 34–41. doi: 10.1016/j.marchem.2014.01.006

Hatta, M., and Zhang, J. (2006). Possible source of advected water mass and residence times in the multi-structured Sea of Japan using rare earth elements. *Geophys. Res. Lett.* 33, L16606. doi: 10.1029/2006GL026537

Hill, K. L., Weaver, A. J., Freeland, H. J., and Bychkov, A. (2003). Evidence of change in the sea of Okhotsk: Implications for the north pacific. *Atmos. -Ocean* 41, 49–63. doi: 10.3137/ao.410104

Hu, D., Wu, L., Cai, W., Gupta, A. S., Ganachaud, A., Qiu, B., et al. (2015). Pacific western boundary currents and their roles in climate. *Nature* 522 (7556), 299–308. doi: 10.1038/nature14504

Isobe, A. (2008). Recent advances in ocean-circulation research on the yellow Sea and East China Sea shelves. *J. Phys. Oceanogr.* 64 (4), 569–584. doi: 10.1007/s10872-008-0048-7

Isobe, A., Ando, M., Watanabe, T., Senjyu, T., Sugihara, S., and Manda, A. (2002). Freshwater and temperature transports through the tsushima-Korea straits. *J. Geophys. Res.* 107 (7), 2-1–2-20. doi: 10.1029/2000JC000702

Ito, T., Togawa, O., Ohnishi, M., Isoda, Y., Nakayama, T., Shima, S., et al. (2003). Variation of velocity and volume transport of the tsugaru warm current in the winter of 1999-2000. *Geophys. Res. Lett.* 30(13), 11-1-11-4. doi: 10.1029/2003GL017522

Johannesson, K. H., and Burdige, D. J. (2007). Balancing the global oceanic neodymium budget: Evaluating the role of groundwater. *Earth Planet. Sci. Lett.* 253, 129–142. doi: 10.1016/j.epsl.2006.10.021

Johns, W. E., Lee, T. N., Zhang, D., Zantopp, R., Liu, C.-T., and Yang, Y. (2001). The kuroshio East of Taiwan: Moored transport observations from the WOCE PCM-1 array. *J. Phys. Oceanogr.* 31, 1031–1053. doi: 10.1175/1520-0485(2001)031<1031:TKEOTM>2.0.CO;2

Katsumata, K. (2004). Water exchange and tidal currents through the bussol' strait revealed by direct current measurements. *J. Geophys. Res.* 109, C09S06. doi: 10.1029/2003JC001864

Kim, T., Obata, H., Kondo, Y., Ogawa, H., and Gamo, T. (2015). Distribution and speciation of dissolved zinc in the western north pacific and its adjacent seas. *Mar. Chem.* 173, 330–341. doi: 10.1016/j.marchem.2014.10.016

Kim, T., Obata, H., Nishioka, J., and Gamo, T. (2017). Distribution of dissolved zinc in the Western and central subarctic north pacific: Zinc in the subarctic north pacific. *Global Biogeochem. Cycles* 31, 1454–1468. doi: 10.1002/2017GB005711

Lacan, F., and Jeandel, C. (2001). Tracing Papua new Guinea imprint on the central equatorial pacific ocean using neodymium isotopic compositions and rare earth element patterns. *Earth Planet. Sci. Lett.* 186, 497–512. doi: 10.1016/S0012-821X(01)00263-1

Lacan, F., and Jeandel, C. (2005). Neodymium isotopes as a new tool for quantifying exchange fluxes at the continent–ocean interface. *Earth Planet. Sci. Lett.* 232, 245–257. doi: 10.1016/j.epsl.2005.01.004

Lambelet, M., van de Flierdt, T., Crocket, K., Rehkämper, M., Kreissig, K., Coles, B., et al. (2016). Neodymium isotopic composition and concentration in the western north Atlantic ocean: Results from the GEOTRACES GA02 section. *Geochim. Cosmochim. Acta* 177, 1–29. doi: 10.1016/j.gca.2015.12.019

Li, Y. H. (1991). Distribution patterns of the elements in the ocean: A synthesis. *Geochim. Cosmochim. Acta* 55 (11), 3223–3240. doi: 10.1016/0016-7037(91)90485-N

Li, X., Liang, H., Zhuang, G., Wu, Y., Li, S., Zhang, H., et al. (2022). Annual variations of isoprene and other non-methane hydrocarbons in the jiaozhou bay on the East coast of north China. *JGR Biogeosciences* 127. doi: 10.1029/2021JG006531

Li, X., Wu, K., Gu, S., Jiang, P., Li, H., Liu, Z., et al. (2021). Enhanced biodegradation of dissolved organic carbon in the western boundary kuroshio current when intruded to the marginal south China Sea. *JGR Oceans* 126. doi: 10.1029/2021JC017585

Lin, G., Chen, Y., Huang, J., Wang, Y., Ye, Y., and Yang, Q. (2020). Regional disparities of phytoplankton in relation to different water masses in the Northwest pacific ocean during the spring and summer of 2017. *Acta Oceanol. Sin.* 39, 107–118. doi: 10.1007/s13131-019-1511-6

Liu, Z., Nakamura, H., Zhu, X., Nishina, A., Guo, X., and Dong, M. (2019). Tempo-spatial variations of the kuroshio current in the tokara strait based on long-term ferryboat ADCP data. *J. Geophys. Res. Oceans* 124, 6030–6049. doi: 10.1029/2018JC014771

Liu, Q., Zhang, J., He, H., Ma, L., Li, H., Zhu, S., et al. (2022). Significance of nutrients in oxygen-depleted bottom waters *via* various origins on the mid-outer shelf of the East China Sea during summer. *Sci. Total Environ.* 826, 154083. doi: 10.1016/j.scitotenv.2022.154083

Mills, M. M., Moore, C. M., Langlois, R., Milne, A., Achterberg, E., Nachtigall, K., et al. (2008). Nitrogen and phosphorus co-limitation of bacterial productivity and growth in the oligotrophic subtropical north Atlantic. *Limnol. Oceanogr.* 53 (2), 824–834. doi: 10.4319/lo.2008.53.2.0824

Morton, P. L., Landing, W. M., Shiller, A. M., Moody, A., Kelly, T. D., Bizimis, M., et al. (2019). Shelf inputs and lateral transport of Mn, Co, and ce in the Western north pacific ocean. *Front. Mar. Sci.* 6. doi: 10.3389/fmars.2019.00591

Nishioka, J., Mitsudera, H., Yasuda, I., Liu, H., Nakatsuka, T., and Volkov, Y. N. (2014). Biogeochemical and physical processes in the Sea of Okhotsk and the linkage to the pacific ocean. *Prog. Oceanogr.* 126, 1–7. doi: 10.1016/j.pocean.2014.04.027

Nishioka, J., Nakatsuka, T., Watanabe, Y. W., Yasuda, I., Kuma, K., Ogawa, H., et al. (2013). Intensive mixing along an island chain controls oceanic biogeochemical cycles. *Global Biogeochem. Cycles.* 27, 920–929. doi: 10.1002/gbc.20088

Nishioka, J., and Obata, H. (2017). Dissolved iron distribution in the western and central subarctic pacific: HNLC water formation and biogeochemical processes: Dissolved fe distribution in the western and central subarctic pacific. *Limnol. Oceanogr.* 62, 2004–2022. doi: 10.1002/lno.10548

Nishioka, J., Ono, T., Saito, H., Nakatsuka, T., Takeda, S., Yoshimura, T., et al. (2007). Iron supply to the western subarctic pacific: Importance of iron export from the Sea of Okhotsk. *J. Geophys. Res.* 112, C10012. doi: 10.1029/2006JC004055

Nitani, H. (1972). "Beginning of the kuroshio," in *Kuroshio, physical aspect of the Japan current*. Eds. H. Stommel and K. Yoshida (Tokyo, Japan: University of Tokyo Press), 129–163.

Nozaki, Y. (2001). "Rare earth elements and their isotopes in the ocean," in *Encyclopedia of ocean sciences* (New York: Elsevier), 2354–2366. doi: 10.1006/rwos.2001.0284

Ohshima, K. I., Nakanowatari, T., Riser, S., and Wakatsuchi, M. (2010). Seasonal variation in the in- and outflow of the Okhotsk Sea with the north pacific. *Deep Sea Res. Part II Top. Stud. Oceanogr.* 57, 1247–1256. doi: 10.1016/j.dsr2.2009.12.012

Osborne, A. H., Haley, B. A., Hathorne, E. C., Plancherel, Y., and Frank, M. (2015). Rare earth element distribution in Caribbean seawater: Continental inputs versus lateral transport of distinct REE compositions in subsurface water masses. *Mar. Chem.* 177, 172–183. doi: 10.1016/j.marchem.2015.03.013

Parsons, T. R., Maita, Y., and Lalli, C. M. (1984). *A manual of chemical and biological methods for seawater analysis* (New York: Pergamon Press, 99-112).

Pearce, C. R., Jones, M. T., Oelkers, E. H., Pradoux, C., and Jeandel, C. (2013). The effect of particulate dissolution on the neodymium (Nd) isotope and rare earth element (REE) composition of seawater. *Earth Planet. Sci. Lett.* 369-370, 138–147. doi: 10.1016/j.epsl.2013.03.023

Persson, P.-O., Andersson, P. S., Zhang, J., and Porcelli, D. (2011). Determination of Nd isotopes in water: A chemical separation technique for extracting Nd from seawater using a chelating resin. *Anal. Chem.* 83, 1336–1341. doi: 10.1021/ac102559k

Piepgras, D. J., and Jacobsen, S. B. (1988). The isotopic composition of neodymium in the north pacific. *Geochim. Cosmochim. Acta* 52869, 1373–1381. doi: 10.1016/0016-7037(88)90208-6

Piepgras, D. J., and Jacobsen, S. B. (1992). The behavior of rare earth elements in seawater: Precise determination of variations in the north pacific water column. *Geochim. Cosmochim. Acta* 56 (5), 1852–1861. doi: 10.1016/0016-7037(92)90315-A

Qiu, B. O., and Chen, S. (2011). Effect of decadal kuroshio extension jet and eddy variability on the modification of north pacific intermediate water. *J. Phys. Oceanogr.* 41 (3), 503–515. doi: 10.1175/2010JPO4575.1

Qu, T., Girton, J. B., and Whitehead, J. A. (2006). Deepwater overflow through Luzon strait. *J. Geophys. Res.* 111, C01002. doi: 10.1029/2005JC003139

Rogachev, K. A., Carmack, E. C., and Salomatin, A. S. (2000). Recent thermohaline transition in the pacific western subarctic boundary currents and their fresh core eddies: The response of sound-scattering layers. *J. Mar. Syst.* 26 (3), 239–258. doi: 10.1016/S0924-7963(00)00036-1

Schlitzer, R. (2015) *Ocean data view*. Available at: http://odv.awi.de.

Seo, H., and Kim, G. (2020). Rare earth elements in the East Sea (Japan sea): Distributions, behaviors, and applications. *Geochim. Cosmochim. Acta* 286, 19–28. doi: 10.1016/j.gca.2020.07.016

Sholkovitz, E. R., Landing, W. M., and Lewis, B. L. (1994). Ocean particle chemistry: The fractionation of rare earth elements between suspended particles and seawater. *Geochim. Cosmochim. Acta* 58, 1567–1579. doi: 10.1016/0016-7037(94)90559-2

Shu, H. W., Mitsudera, H., Yamazaki, K., Nakamura, T., Kawasaki, T., Nakanowatari, T., et al. (2021). Tidally modified western boundary current drives interbasin exchange between the Sea of Okhotsk and the north pacific. *Sci. Rep.* 11, 12037. doi: 10.1038/s41598-021-91412-y

Shulkin, V. M., and Bogdanova, N. N. (2003). Mobilization of metals from riverine suspended matter in seawater. *Mar. Chem.* 83, 157–167. doi: 10.1016/S0304-4203(03)00109-9

Stichel, T., Hartman, A. E., Duggan, B., Goldstein, S. L., Scher, H., and Pahnke, K. (2015). Separating biogeochemical cycling of neodymium from water mass mixing in the Eastern north Atlantic. *Earth Planet. Sci. Lett.* 412, 245–260. doi: 10.1016/j.epsl.2014.12.008

Suga, T., Kato, A., and Hanawa, K. (2000). North pacific tropical water: its climatology and temporal changes associated with the climate regime shift in the 1970s. *Prog. Oceanogr.* 47, 223–256. doi: 10.1016/S0079-6611(00)00037-9

Suzuki, K., Handa, N., Kiyosawa, H., and Ishizaka, J. (1997). Temporal and spatial distribution of phytoplankton pigments in the central pacific ocean along 175°E during the Boreal summers of 1992 and 1993. *J. Oceanogr.* 53, 383–396.

Tachikawa, K., Athias, V., and Jeandel, C. (2003). Neodymium budget in the modern ocean and paleo-oceanographic implications. *J. Geophys. Res.* 108, 10-1-10-13. doi: 10.1029/1999JC000285

Takata, H., Tagami, K., Aono, T., and Uchida, S. (2009). Determination of trace levels of yttrium and rare earth elements in estuarine and coastal waters by inductively coupled plasma mass spectrometry following preconcentration with NOBIAS-CHELATE resin. *Atomic Spectrosc.* 30, 10–19.

Takikawa, T., Yoon, J. H., and Cho, K. D. (2005). The tsushima warm current through tsushima straits estimated from ferryboat ADCP data. *J. Phys. Oceanogr* 35 (6), 1154–1168. doi: 10.1175/JPO2742.1

Talley, L. D., Nagata, Y., Fujimura, M., Iwao, T., Kono, T., Inagake, D., et al. (1995). North pacific intermediate water in the Kuroshio/Oyashio mixed water region. *J. Phys. Oceanogr.* 25, 475–501. doi: 10.1175/1520-0485(1995)025<0475:NPIWIT>2.0.CO;2

Taylor, S. R., and McLennan, S. M. (1985). *The continental crust, its composition and evolution: An examination of the geochemical record preserved in sedimentary rocks* (Oxford: Blackwell Scientific).

Tazoe, H., Obata, H., and Gamo, T. (2011). Coupled isotopic systematics of surface cerium and neodymium in the pacific ocean. *Geochem. Geophys. Geosyst.* 12, Q04004. doi: 10.1029/2010GC003342

Teague, W. J., Jacobs, G. A., Perkins, H. T., Book, J. W., Chang, K. I., and Suk, M. S. (2002). Low-frequency current observations in the Korea/Tsushima strait. *J. Phys. Oceanogr.* 32, 1621–1641. doi: 10.1175/1520-0485(2002)032<1621:LFCOIT>2.0.CO;2

Tian, J., Yang, Q., Liang, X., Xie, L., Hu, D., Wang, F., et al. (2006). Observation of Luzon strait transport. *Geophys. Res. Lett.* 33, L19607. doi: 10.1029/2006GL026272

Wang, Y., Bi, R., Zhang, J., Gao, J., Takeda, S., Kondo, Y., et al. (2022). Phytoplankton distributions in the kuroshio-oyashio region of the Northwest pacific ocean: Implications for marine ecology and carbon cycle. *Front. Mar. Sci.* 9. doi: 10.3389/fmars.2022.865142

Wang, Y., Kang, J., Sun, X., Huang, J., Lin, Y., and Xiang, P. (2021). Spatial patterns of phytoplankton community and biomass along the kuroshio extension and adjacent waters in late spring. *Mar. Biol.* 168, 40. doi: 10.1007/s00227-021-03846-7

Wang, Z., Yuan, D. L., and Hou, Y. J. (2010). Effect of meridional wind on gap-leaping western boundary current. *Chin. J. Oceanol. Limnol.* 28 (2), 354–358. doi: 10.1007/s00343-010-9281-1

Wu, Q., Colin, C., Liu, Z., Douville, E., Dubois-Dauphin, Q., and Frank, N. (2015). New insights into hydrological exchange between the south China Sea and the Western pacific ocean based on the Nd isotopic composition of seawater. *Deep Sea res. part II. Top. Stud. Oceanogr.* 122, 25–40. doi: 10.1016/j.dsr2.2015.11.005

Xu, F. H., and Oey, L. Y. (2014). State analysis using the local ensemble transform kalman filter (LETKF) and the three-layer circulation structure of the Luzon strait and the south China Sea. *Ocean Dyn.* 64, 905–923. doi: 10.1007/s10236-014-0720-y

Yang, S. C., Zhang, J., Sohrin, Y., and Ho, T. Y. (2018). Cadmium cycling in the water column of the kuroshio-oyashio extension region: Insights from dissolved and particulate isotopic composition. *Geochim. Cosmochim. Acta* 233, 66–80. doi: 10.1016/j.gca.2018.05.001

Yasuda, I. (2004). North pacific intermediate water: Progress in sage (subarctic gyre experiment) and related projects. *J. Phys. Oceanogr.* 60 (2), 385–395. doi: 10.1023/B:JOCE.0000038344.25081.42

Yasuda, I., Hiroe, Y., Komatsu, K., Kawasaki, K., Joyce, T. M., Bahr, F., et al. (2001). Hydrographic structure and transport of the oyashio south of Hokkaido and the formation of north pacific intermediate water. *J. Geophys. Res.* 106, 6931–6942. doi: 10.1029/1999JC000154

Yasuda, I., Okuda, K., and Shimizu, Y. (1996). Distribution and modification of north pacific intermediate water in the kuroshio-oyashio interfrontal zone. *J. Phys. Oceanogr.* 26, 448–465. doi: 10.1175/1520-0485(1996)026<0448:DAMONP>2.0.CO;2

Zhang, Y., Lacan, F., and Jeandel, C. (2008). Dissolved rare earth elements tracing lithogenic inputs over the kerguelen plateau (Southern ocean). *Deep Sea Res. Part II: Topical Stud. Oceanography* 55, 638–652. doi: 10.1016/j.dsr2.2007.12.029

Zhang, J., Liu, Q., Bai, L., and Matsuno, T. (2018). Water mass analysis and contribution estimation using heavy rare earth elements: Significance of kuroshio intermediate water to central East China Sea shelf water. *Mar. Chem.* 204, 172–180. doi: 10.1016/j.marchem.2018.07.011

Zhang, J., and Nozaki, Y. (1996). Rare earth elements and yttrium in seawater: ICP-MS determinations in the East Caroline, coral Sea, and south Fiji basins of the western south pacific ocean. *Geochim. Cosmochim. Acta* 60, 4631–4644. doi: 10.1016/S0016-7037(96)00276-1

Zhang, J., and Nozaki, Y. (1998). Behavior of rare earth elements in seawater at the ocean margin: a study along the slopes of the sagami and nankai troughs near Japan. *Geochim. Cosmochim. Acta* 62, 1307–1317. doi: 10.1016/S0016-7037(98)00073-8

Zhang, Z., Zhao, W., Tian, J., Yang, Q., and Qu, T. (2015). Spatial structure and temporal variability of the zonal flow in the Luzon strait. *J. Geophys. Res. Oceans* 120, 759–776. doi: 10.1002/2014JC010308

Zheng, X. Y., Plancherel, Y., Saito, M. A., and Scott, P. M. (2016). And Henderson, G Rare earth elements (REEs) in the tropical south Atlantic and quantitative deconvolution of their non-conservative behavior. *M.Geochim. Cosmochim. Acta* 177, 217–237. doi: 10.1016/j.gca.2016.01.018

Zhu, K. L., Chen, X., Mao, K. F., Hu, D., Hong, S., and Li, Y. (2019). Mixing characteristics of the subarctic front in the kuroshio-oyashio confluence region. *Oceanologia* 61, 103–113. doi: 10.1016/j.oceano.2018.07.004

frontiers | Frontiers in Marine Science

TYPE Original Research
PUBLISHED 17 March 2023
DOI 10.3389/fmars.2023.1128657

OPEN ACCESS

EDITED BY
Wen Zhuang,
Shandong University, China

REVIEWED BY
Liqin Duan,
Institute of Oceanology Chinese Academy of Sciences, China
Ruifeng Zhang,
Shanghai Jiao Tong University, China

*CORRESPONDENCE
Jingling Ren
renjingl@ouc.edu.cn

SPECIALTY SECTION
This article was submitted to Marine Biogeochemistry, a section of the journal Frontiers in Marine Science

RECEIVED 21 December 2022
ACCEPTED 01 March 2023
PUBLISHED 17 March 2023

CITATION
Yang Y, Li L, Ren J, Jiang S and Zhang J (2023) Processes controlling the distributions and cycling of dissolved aluminum and manganese in the northeastern Indian Ocean.
Front. Mar. Sci. 10:1128657.
doi: 10.3389/fmars.2023.1128657

Processes controlling the distributions and cycling of dissolved aluminum and manganese in the northeastern Indian Ocean

Yichao Yang[1], Lei Li[1], Jingling Ren[1,2]*, Shuo Jiang[3] and Jing Zhang[3,4]

[1]Frontiers Science Centre for Deep Ocean Multispheres and Earth System, and Key Laboratory of Marine Chemistry Theory and Technology, Ministry of Education, Ocean University of China, Qingdao, China, [2]Laboratory for Marine Ecology and Environmental Science, Qingdao National Laboratory for Marine Science and Technology, Qingdao, China, [3]State Key Laboratory of Estuarine and Coastal Research, East China Normal University, Shanghai, China, [4]School of Oceanography, Shanghai Jiao Tong University, Shanghai, China

Aluminum and manganese are both key parameters in the GEOTRACES program. Data on dissolved aluminum (dAl) and dissolved manganese (dMn) relative to their geochemical behavior remain limited in the northeastern Indian Ocean (IO; including the Bay of Bengal (BoB) and equatorial Indian Ocean (Eq. IO)). Seawater samples collected in the BoB and Eq. IO during the spring inter-monsoon period (7 March to 9 April) of 2017 were analyzed to investigate the behavior and main processes controlling the distributions of dAl and dMn in the northeastern IO. The average concentrations of dAl and dMn in the mixed layer of the BoB were 16.6 and 6.7 nM, respectively. A modified 1-D box-model equation was utilized to estimate the contributions of different sources to dAl and dMn in the mixed layer. Al released from the desorption of and/or dissolution of the lithogenic sediments discharged by the Ganga–Brahmaputra (G-B) river system predominantly controlled the dAl distributions in the mixed layer of the BoB, while the desorption from the lithogenic sediments only contributed approximately 13%–21% dMn. Additional dMn input from the advection of Andaman Sea water and photo-reduction–dissolution of particulate Mn(IV) contributed more than 60% dMn in the mixed layer of the BoB. dAl and dMn in the surface mixed layer of the Eq. IO were mainly affected by the mixing of dAl- and dMn-enriched BoB surface water and low-dAl, low-dMn southern Arabian Sea surface water. Considering water mass properties and dAl concentrations, the distributions of dAl in the intermediate water (750–1,500 m) of northeastern IO were controlled by the mixing of Red Sea Intermediate Water, Indonesian Intermediate Water, and intermediate water of the BoB. Different from dAl, the apparent oxygen utilization relationship with dMn concentrations indicated that the regeneration

of lithogenic particles under hypoxic conditions played a more important role than the remineralization of settling organic particles in controlling dMn distributions in the subsurface and intermediate water body (100–1,000 m) of the BoB and that remineralization of biogenic particles mattered to dMn in the subsurface of the Eq. IO.

KEYWORDS

dissolved aluminium, dissolved manganese, Indian Ocean, Bay of Bengal, influencing factors

Introduction

Aluminum (Al) and manganese (Mn) are considered key parameters in the GEOTRACES program (GEOTRACES Planning Group, 2006). Al is widely used as a tracer of atmospheric deposition to the ocean (Measures and Brown, 1996; Grand et al., 2015a). Mn is an essential micronutrient for photosynthesis and the normal function of enzymes in cells of phytoplankton (Gerringa et al., 2020). Furthermore, both Al and Mn can be used for tracing water masses mixing (Measures and Edmond, 1990; Statham et al., 1998; Zheng et al., 2022) and external sources, e.g., continental inputs (Slemons et al., 2010; Menzel Barraqueta et al., 2018; Kandel and Aguilar-Islas, 2021) and hydrothermal inputs (Resing et al., 2015; Lee et al., 2018). Mn is also used as a chemical tracer for understanding changes in the redox environment (Lenstra et al., 2020) in the ocean due to its variable valence.

Dissolved Al (dAl) is particle reactive, and its vertical profile typically presents a scavenged type in many ocean regions (Bruland et al., 2014), i.e., elevated concentrations in the surface and decreasing and keeping uniform concentrations in the deep ocean. Dissolved Mn (dMn) generally behaves as a scavenged type (Landing and Bruland, 1980; Colombo et al., 2020) but sometimes increases its concentration below the surface where dissolved oxygen is low (Thi Dieu Vu and Sohrin, 2013; Lenstra et al., 2020). Different from dAl, the elevated concentration of dMn in the surface layer mainly results from the photo-reduction–dissolution of Mn oxides (Sunda and Huntsman, 1994; Hood et al., 2009). Atmospheric deposition (Baker et al., 2006; Hsu et al., 2010; Kadko et al., 2020), hydrothermal venting (Resing et al., 2015; Chen and Wu, 2019), sediment resuspension (Wang et al., 2018; Colombo et al., 2022), and fluvial input (dissolved species and lithogenic release; Aguilar-Islas and Bruland, 2006; Singh et al., 2020) are all the main sources of dAl and dMn in the ocean. Moreover, Mn can transfer its valence from particle Mn(IV) to dissoluble Mn(II) by reductive dissolution and enter the water body below the surface layer (Lee et al., 2018; Lenstra et al., 2020; Colombo et al., 2022). Both dAl and dMn concentrations have shown huge inter-oceanic distinctions due to different biogeochemical behavior and external sources in different oceanic basins (Obata et al., 2004; Thi Dieu Vu and Sohrin, 2013; Rolison et al., 2015; Grand et al., 2015b; Häusler et al., 2018; Menzel Barraqueta et al., 2018; Wang et al., 2018; Nakaguchi et al., 2021; Singh and Singh, 2022). The concentration of dAl varies in a large range (0.05 to 673.4 nM; Menzel Barraqueta et al., 2020) in the global ocean, while dMn shows a relatively small concentration range (0.1 to 25 nM; Shiller, 1997).

The Indian Ocean (IO) occupies approximately one-fifth of the world's ocean net primary production (Behrenfeld and Falkowski, 1997) and is characterized by seasonal reversal of monsoonal winds and surface currents (Shankar et al., 2002). The IO is one of the least understood oceans due to its physical and biogeochemical dynamics (Hood et al., 2009). Obata et al. (2004) determined the vertical profiles of dAl and other elements in several stations in eastern IO. Thi Dieu Vu and Sohrin (2013) reported the basin-scale distribution of dAl, dMn, and other trace elements in the IO. Singh and Singh (2022) studied dAl distributions over the full vertical water column profiles in the Arabian Sea and the western equatorial IO. Data on dAl and dMn relative to their biogeochemical behavior remain limited in the northeastern IO. Grand et al. (2015b) conducted a meridional study from the Indian sector of the Southern Ocean to the Bay of Bengal (BoB) spaced at approximately 1° intervals, focusing on the distribution of dAl and dissolved Fe. The atmospheric dry deposition was investigated simultaneously (Grand et al., 2015a). Singh et al. (2020) measured dAl from the subtropical gyre region to the northern IO, including the BoB, the Andaman Sea, and the Arabian Sea. The huge continental input, in the form of freshwater, suspended sediments, and atmospheric deposition, deeply influence the biogeochemistry of lithogenic trace metals (e.g., Al and Mn) in the BoB and equatorial IO (Sengupta et al., 2006; Srinivas and Sarin, 2013). Moreover, due to the large riverine freshwater input, excessive rainfall, and strong stratification, along with the oldest central water in the north IO, the BoB is one of the four anoxic areas in the global ocean (Kamykowski and Zentara, 1990; You and Tomczak, 1993). Therefore, to better understand and assess the effect of different processes on the biogeochemistry of northeastern IO, we report the continental input and redox tracer, i.e., dAl and dMn concentrations in the BoB and equatorial IO during the spring inter-monsoon period (7 March to 9 April) in 2017. In this study, a modified 1-D model equation, T-S diagram, and correlations between dAl, dMn, and relevant hydrographic parameters are used to figure out the principal sources and processes governing dAl and dMn distributions in the northeastern Indian Ocean and

add to the comprehensive understanding of dAl and dMn behavior in the anoxic ocean.

Materials and methods

Study area and sampling

The BoB covers an area of 2.2 × 10^6 km^2, with an average depth of 3 km (Singh et al., 2012). The Ganga and Brahmaputra rivers together discharge 1,050 km^3/year of water, which could extend to 8°S (Nath et al., 1989), and approximately one billion tons of sediments (Galy and France-Lanord, 2001) to the BoB. Unger et al. (2003) conducted sediment trap experiments in the BoB and found obvious seasonal and interannual variations in fluxes of river sediments. The surface water of the northeastern IO receives dust input from the Indian plains, Southeast Asia, combined with possible long-range inputs from the Thar Desert (Srinivas et al., 2012; Srinivas and Sarin, 2013). Moreover, the Indonesian Throughflow (ITF) carries warm and low-salinity surface water from the west Pacific Ocean into the east IO (Gordon, 2005), and the South Equatorial Current (SEC) carries the ITF westward (You, 1998).

Seawater samples were collected aboard the *R/V ShiYan 3* in the northeastern IO during the spring inter-monsoon period (7 March to 9 April) of 2017. The dataset encompassed a total of 50 stations (Figure 1), including 37 surface stations (~10 m), eight stations of upper 500 m, and five full vertical profiles. The layer number of vertical profiles was determined as 7-8 for stations of upper 500 m and as 14–20 for the full ones, according to the water mass properties obtained from the down cast reading of temperature and salinity from the conductivity, temperature, and depth (CTD) sensor at each station. All samples were obtained through an X-Vane sampler, which consisted of a 5-L Niskin-X sampling bottle attached to a titanium and polyvinyl chloride (PVC) polymer supporting frame ("II-style" secure assembly) (Zhang et al., 2015b). The X-Vane sampler controls the Niskin-X bottle upstream of the hydrowire, away from the contaminations of the hydrowire and ship. Once the sampling bottle arrives at the desired depth, the Teflon-coated messenger is used to strike the "II-style" assembly and close the Niskin-X bottle to obtain a clean seawater sample. Five-liter Niskin-X bottles were washed rigorously according to the GEOTRACES cookbook (using Citranox (Alconox, White Plains, NY, USA), Milli-Q water (Advantage 10, Millipore, Burlington, MA, USA), 10% HCl (purified by quadruple sub-boiling point distillation in a quartz glass still) leaching solution, and Milli-Q water in sequence) and sealed using double plastic bags according to Zhang et al. (2015b). The low-density polyethylene (LDPE) and high-density polyethylene (HDPE) bottles (Nalgene, Rochester, NY, USA) and perfluoroalkoxy alkane (Savillex, Eden Prairie, MN, USA) filtration assemblies were cleaned using 2 M of purified HCl, ~1 M of Purified HCl, and Milli-Q water in sequence in a class-1000 clean lab at East China Normal University according to Zhang et al. (2015a). Samples for dissolved measurements once recovered were then taken directly to a class-100 portable clean bench (Air Control) using the filtration system and washed using the same procedures. Filtration was immediately carried out through a 0.4-µm, acid-washed, 47-mm polycarbonate membrane (Whatman, Kent, UK) in a class-100 clean bench. Subsamples were collected in 250-ml Nalgene LDPE bottles, double bagged, and quickly frozen at −20°C. Blank experiments were also carried out using Milli-Q water that was filtrated under the same conditions for the investigation of the contamination.

Analysis of dissolved Al and Mn

Frozen samples were sufficiently thawed and then acidified to pH 1.7 using purified HCl. dAl and dMn concentrations were determined at approximately 1 h after acidification. The dissolved Al was determined using the online preconcentration flow injection analysis (FIA) method modified from Brown and Bruland (2008). Briefly, the main modification was loading the buffered sample onto the column directly without conditioning the column buffer. The determining blank with its variation and the result of reference sample determination were satisfying (see below). The dissolved Mn samples were analyzed using the FIA method developed by Aguilar-Islas and Bruland (2006) in the lab. The detection limit, defined as three times the standard deviation of the blank, was 0.18 nM for Al (n = 9) and 0.21 nM for Mn (n = 9). The precision of the measurements of dAl and dMn was below 2% when concentration was high (dAl, 20 nM; dMn, 8 nM; n = 11) and below 5% for low concentration (dAl, 5 nM; dMn, 1 nM; n = 11). The column-cleaned low background seawater was made by passing buffered South China Sea seawater through the preconcentration column (Nobias Chelate PA-1, Hitachi, Japan) for estimation of the procedural blank during the sample analysis.

Multiple reference seawater samples, including Canada Standard Reference Seawater (NASS-6), North Atlantic GEOTRACES reference standards (GEOTRACES GS and GEOTRACES GD), and North Pacific reference standards (SAFe-S), were analyzed for dAl and dMn concentrations. Results of dAl and dMn measurements for the abovementioned reference seawater samples had no significant difference with consensus value (Table 1, *t*-test, $p > 0.01$).

A 1-D box-model equation to estimate external source contribution

A modified version of the 1-D box-model equation proposed by Grand et al. (2015a) was utilized to estimate the dAl and dMn input to the mixed layer, originating from atmospheric deposition and/or fluvial sediment discharge to the BoB and the equatorial Indian Ocean (Eq. IO). The 1-D box-model equation is given as follows:

$$dM = \frac{G \times MRT \times f_M \times Sol.}{M_{wt} \times MLD_c} \times 10^6, \quad (1)$$

where *dM* is the concentration of dissolved trace metals (in nM), *G* represents the lithogenic sediment flux (in g/(m^2·year)), *MRT* is the mean residence time (in years) of trace metals in the mixed layer, f_M is the fraction of trace metals in the particles (including sediments and aerosols), *Sol.* is the fractional solubility of trace metals from the lithogenic sediments or atmospheric dust,

TABLE 1 Comparison of measured dAl (nM) and dMn (nM) concentrations (this study) and consensus values in SAFe and GEOTRACES reference samples (n = 3).

Reference sample	Al		Mn	
	Consensus value	This study	Consensus value	This study
NASS-6	–	–	9.4 ± 0.5	9.6 ± 0.9
GEOTRACES GS	27.5 ± 0.2	27.2 ± 0.3	1.62 ± 0.15	1.50 ± 0.11
GEOTRACES GD	17.7 ± 0.2	18.0 ± 0.7	–	0.21 ± 0.03
SAFe-S	1.67 ± 0.1	1.60 ± 0.2	0.82 ± 0.08	0.79 ± 0.06

dAl, dissolved aluminum; dMn, dissolved manganese. -, No available data.

M_{wt} is the atomic weight of trace metals (in g/mol), *MLDc* (in m) is the depth of mixed layer retrieved from a density based on our own CTD calculated density of the sampling locations (data in accordance with Holte et al. (2017)), and 10^6 is the factor of conversions of units.

Results

The hydrographical setting

Several studies have discussed the circulation and the structure of water masses in the IO (Shankar et al., 2002; Schott et al., 2009; Singh et al., 2012). The study area (Figure 1) is separated into two sub-basins for the convenience of discussion: 1) the BoB (north of 5°N, 80–92°E) and 2) Eq. IO [5°S–5°N, including station I507 (6.5° S, 98.3°E)]. From the data obtained, salinity on the surface was higher in the south and west and lower in the north and east (Figure 2B). Station I201, which was influenced by not only South Asian Subcontinent fluvial input but also the outflow of the Andaman Sea, possessed the lowest salinity (32.43) with a relatively low temperature (29.6°C). Relatively low salinity (33.52) and temperature (28.6°C) were observed at the southeastmost station I507 compared to nearby stations. The abnormally high salinity was also found at station I103. In section E, the zonal distribution of salinity showed a decreasing trend from west to east, and a high-salinity (~35.5) water tongue appeared in the subsurface (60–120 m) (Figure 3A). Dissolved oxygen (DO) was in the range of 47 to 78 µM under the subsurface of section E (except for station I415). In the whole section L, DO was lower than 63 µM in the depth range from 200 to 1,250 m (Figure 4B). In the BoB, DO reached its minimum (<16 µM) below the pycnocline, while DO was below the surface of the Eq. IO was in the range of 31 to 78 µM, slightly higher than that in the BoB.

The T-S diagram (Figure 5) suggested major source water masses in this study. The tremendous Ganga–Brahmaputra (G-B) River System freshwater and local excess of precipitation over evaporation leads to the formation of Bay of Bengal Water (BBW), which was characterized by low salinity (32.43–33.48, observed in this study) and high dAl and dMn (12.3–19.9 and 5.1–8.7 nM, respectively). In addition, the Andaman Sea is also characterized by the low salinity for receiving freshwater from Irrawaddy and Salween rivers. Low-salinity surface water of the Andaman Sea may be transported to the BoB as well (Singh et al., 2020). The Equatorial Counter Current (ECC) carries Arabian Sea High-Salinity Water (ASHSW), which was characterized by high salinity and relatively low dAl and dMn (I401, salinity = 34.96, dAl = 4.3 nM, and dMn = 1.0 nM, this study; ER-8, salinity = 35.48, dAl = 3.0 nM, and dMn = 1.4 nM, Thi Dieu Vu and Sohrin, 2013) eastward to the east Eq. IO. Meanwhile, the BBW is able to spread southward to the east Eq. IO (I407–I415, salinity ~ 34.00, Figures 2B, 3A; Sandeep et al., 2018) as well. The existence of BBW leads to strong stratification and inhibits vertical mixing in the BoB. The low-salinity BBW overlies North Indian Central Water (NICW), which is aged from Indian Central Water (ICW) and occupies a major subsurface water body in the north IO (You, 1997). NICW is the oldest central water of the north IO (You and Tomczak, 1993) and becomes depleted in oxygen (<25 µM, Figure 4B). The concentrations of dAl and dMn were relatively high (dAl = 6.7 ± 4.3 (1SD) nM, dMn = 2.7 ± 1.7 (1SD) nM) in ICW and NICW. The potential temperature and

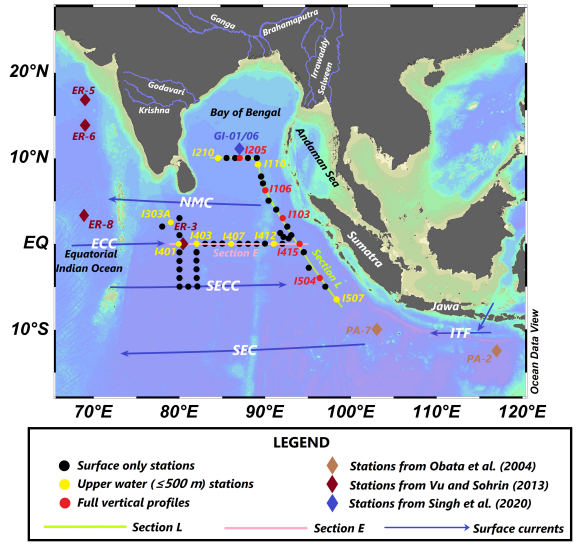

FIGURE 1
Maps presenting sampling stations during the cruise carried out in the spring inter-monsoon period of 2017. Maps also show schematic surface water circulation (blue arrow, deduced using the Ocean Surface Current Analysis Real-time (OSCAR) third-degree (1/3 × 1/3 degree) resolution ocean surface current data (ESR, 2009) during the sampling in the study region. NMC, Northeast Monsoon Current; SECC, Southern Equatorial Counter Current; SEC, Southern Equatorial Current; ECC, Equatorial Counter Current; ITF, Indonesian Throughflow.

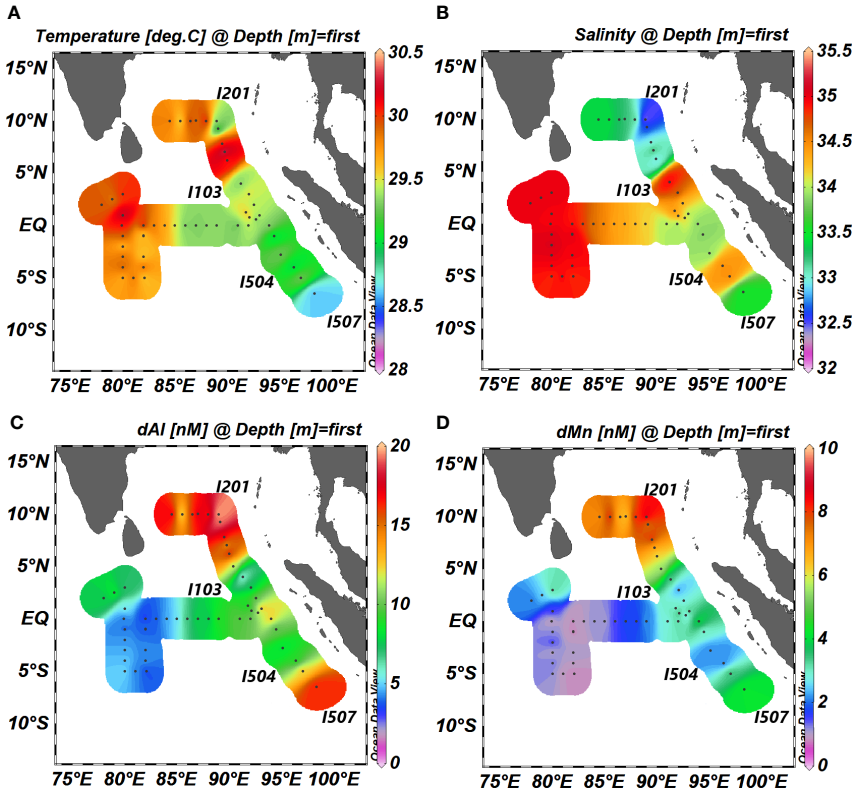

FIGURE 2
Horizontal distributions of **(A)** temperature, **(B)** salinity, **(C)** dAl, and **(D)** dMn in the surface of the northeastern IO. dAl, dissolved aluminum; dMn, dissolved manganese; IO, Indian Ocean.

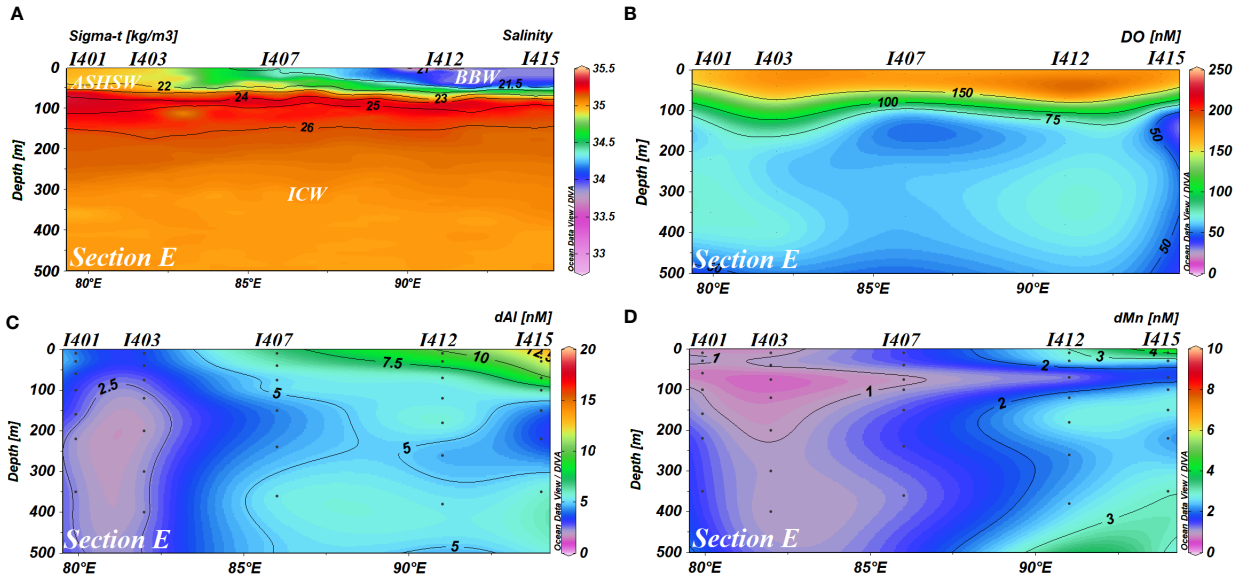

FIGURE 3
(A) Salinity, **(B)** DO, **(C)** dAl concentrations, and **(D)** dMn concentrations in the water column of section E DO, dissolved oxygen; dAl, dissolved aluminum; dMn, dissolved manganese.

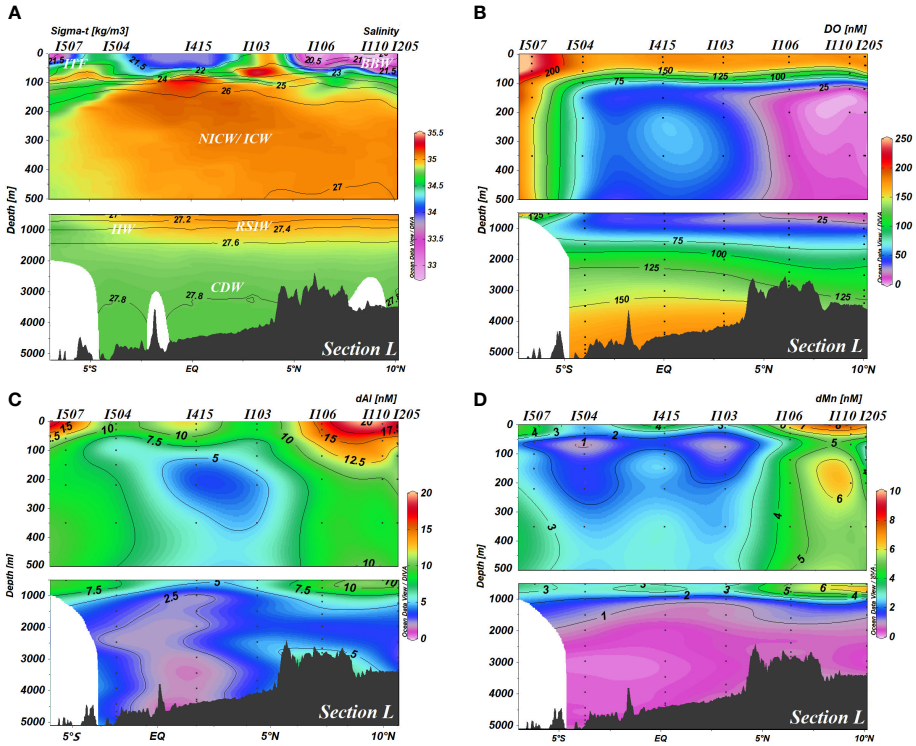

FIGURE 4
(A) Salinity, **(B)** DO, **(C)** dAl concentrations, and **(D)** dMn concentrations in the water column of section L. For better visualization of data, these four parameters' distributions are shown separately for the upper 500-m water column and the remaining water column (>500 m). DO, dissolved oxygen; dAl, dissolved aluminum; dMn, dissolved manganese.

salinity of intermediate water body in this study (σ_0 in the range of 27.1–27.6 kg/m^3, depth within 750–1,500 m) are ~6.1°C–6.7°C and ~34.87–34.95, respectively. The intermediate water body of the study area is mainly from two water masses, i.e., Red Sea Intermediate Water (RSIW; θ ~ 8.2–12.0°C, salinity ~ 35.37–35.63, You, 1998) and Indonesian Intermediate Water (IIW; θ ~ 4.7–8.2°C, salinity ~ 34.63–34.69, You, 1998) through T-S diagram.

Horizontal distributions of dissolved Al and Mn in the northeastern IO

The differences between the average value of concentrations in the mixed layer (20–30 m in the BoB, 30–35 m in the Eq. IO; dAl = 9.7 ± 5.0 (1SD) nM, dMn = 3.2 ± 2.3 (1SD) nM, n = 62) and surface layer (10 m; dAl = 9.2 ± 4.8 (1SD) nM, dMn = 3.2 ± 2.4 (1SD) nM, n = 50)

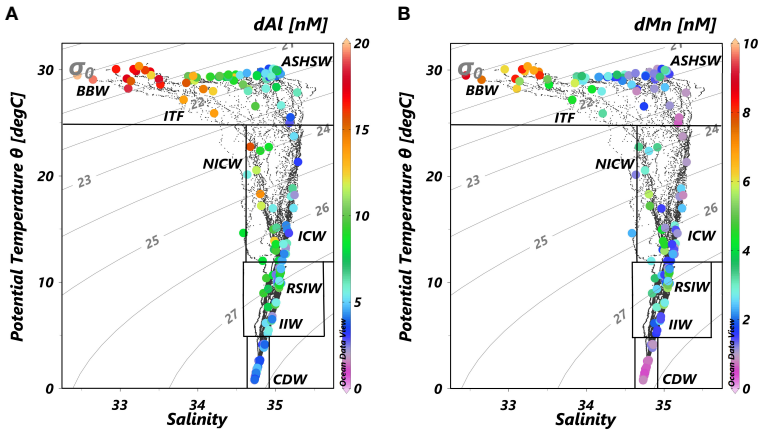

FIGURE 5
T-S diagrams of **(A)** dissolved Al and **(B)** dissolved Mn concentrations from stations in the northeastern IO. The gray solid curves were isopycnals with σ_0 values (kg/m^3) denoted. The definitions of different water masses were based on You (1997); You (1998), You (2000), Lewis and Luther III (2000), Sardessai et al. (2010), and Grand et al. (2015b). BBW, Bay of Bengal Water; ASHSW, Arabian Sea High Salinity Water; ICW, Indian Central Water; NICW, North Indian Central Water; IIW, Indonesia Intermediate Water; RSIW, Red Sea Intermediate Water; CDW, Circumpolar Deep Water.

were both within 10% for dAl and dMn in this study, indicating that the differences of concentrations of dAl and dMn were not significant between the surface layer and mixed layer in the study area. The distributions of dAl and dMn in the northern IO showed an increase from south to north and from west to east (Figures 2C, D). Station I201 possessed the highest dAl and dMn concentrations (19.9 and 8.7 nM, respectively) in the whole study area. Relatively high values of dAl and dMn (16.4 and 4.2 nM, respectively) were observed at the southeastmost station I507 compared to nearby stations. The abnormal low dAl and dMn were found at station I103, which will be discussed in the following section.

The dAl and dMn concentrations in the surface layer of the BoB were in the range of 12.3–19.9 and 6.1–8.7 nM, respectively. The mean dAl (16.7 ± 2.2 nM, n = 10) in the surface layer of the BoB in this study was comparable to that of PA-9 (14.7 nM, 8.00°N, 89.00° E, Obata et al., 2004) and was one- to twofold lower than the results from Singh et al. (9.2–48.3 nM, 2020). The northernmost station of Singh et al. (2020) was located at 20°N, 10° north of our station, indicating that the relatively high dAl concentration may come from the influence of freshwater input from the G-B River System. The ranges of dAl and dMn concentrations observed in the surface layer of the Eq. IO were 3.5–13.2 and 0.8–5.6 nM, respectively. The results of dAl and dMn were comparable to those of Singh et al. (2.5–15.4 nM, 2020) and Twining et al. (2.0–3.2 nM, 2019), respectively.

Vertical distributions of dissolved Al and Mn in the northern Indian Ocean

In section E, zonal distributions of dAl and dMn showed an increasing trend along with a decrease in salinity from west to east (Figure 3). A water tongue characterized by low dAl and dMn concentrations (<7.5 and<2 nM, respectively) appeared in the subsurface of section E, where dMn met its minimum value (<1 nM) at ~75 m. Both dAl and dMn in section E normally showed scavenging-type vertical profiles, i.e., enrichment in the surface water and decreasing with increasing depth. dMn in station I415 showed subsurface enrichment (~3 nM) at depths of 350 and 500 m.

In whole section L, distributions of dAl and dMn were regional discrepancies with DO (Figure 4). In the BoB, dAl exceeded 7.5 nM, even up to 12, and dMn could reach 6 nM, approaching the surface value. dAl and dMn concentrations were lower than 7.5 and 3 nM, respectively, in the Eq. IO. A similar distribution pattern between dAl and dMn was evident in the range of 500 to 1,000 m in section L, namely, maximum (dAl and dMn reaching up to ~10 and ~6 nM, respectively) in the BoB and minimum (dAl ~ 5 nM, dMn ~ 3 nM) in the Eq. IO. Both dAl and dMn concentrations showed remarkably uniform distributions below 1,000 m, which were consistent with the results of Singh et al. (2020) and Obata et al. (2004). The mean dAl concentration in the BoB was 4.7 nM, and an increasing dAl concentration (5.7 nM in station I106) toward the seafloor was observed. Simultaneously, in the Eq. IO, the mean dAl concentration was 3 nM below 1,000 m, lower than that in the BoB. dMn concentration was lower than 2 nM below 1,000 m, and the mean values were 0.9 and 0.5 nM in the BoB and the Eq. IO, respectively.

Discussion

Validation of dAl and dMn data with published results

Indian GEOTRACES station, GI-01/06 (11.01°N, 87.00°E, sampled in March 2014, Singh et al., 2020) in the BoB, was 112 km north of station I205 (10.00°N, 87.00°E, sampled in March 2017) in this study (Figure 1). Both stations were sampled during the spring inter-monsoon period. The dAl concentrations had significant differences (t-test, $p< 0.05$) in the upper 1,000 m but mostly overlapped in the deeper water (>1,000 m) (Figure 6A). Considering the long time span (3 years) between occupations of two stations, these differences may be attributed to variations of G-B River System freshwater discharge and lithogenic sediment fluxes to the BoB (Unger et al., 2003), which predominantly control the dissolved Fe (Chinni et al., 2019) and dAl (Singh et al., 2020) distributions, and will be discussed later in Section 4.2.

Japanese GEOTRACES station, ER-3 (0°, 80°E, sampled in November 2011, Thi Dieu Vu and Sohrin, 2013), almost overlaps station I401 (0.01°S, 79.92°E) (Figure 1). Salinity at two stations had significant differences (t-test, $p< 0.05$) in the upper water column (<200 m), and Mn distributions showed a significant difference in the upper 500 m water body (t-test, $p< 0.05$, Figure 6B). The northeastern IO is characterized by the seasonal reversal of monsoonal winds and surface currents (Shankar et al., 2002). ER-3 was sampled in November 2009, while I401 was in March 2017. March is the first month of the end of the Northeast Monsoon. The Northeast Monsoon Current carries fresher BoB water into the Arabian Sea. November is the first month of the start of the Northeast Monsoon, and the currents still exist but feature the Southwest Monsoon Current, which flows eastward from the Arabian Sea to the BoB (Shankar et al., 2002; Schott et al., 2009). Currents flowing differently and interannual differences contributed to significant differences in salinity and dMn concentrations in the depth of upper 500 m. Such difference was also observed above 1,000 m when full vertical profile station I415 was compared with station ER-3. dMn showed more sensitivity toward seasonal variations than dAl because dMn was not only seriously affected by riverine inputs (Aguilar-Islas and Bruland, 2006) but also influenced by ambient oxidation conditions (Lenstra et al., 2020). High dMn concentration in the BoB subsurface layer caused by regeneration under a low oxygen environment and the water mass mixing resulted in a relatively high dMn value in station I415 than that of ER-3 in the upper 1,000 m water body. Although the two stations were 12 longitudes apart, dMn concentrations showed comparable results in the deeper waters (>1,500 m). In general, dAl and dMn concentrations showed variations on account of different sampling seasons and years in the upper water column (<1,000 m) at nearby stations and were comparable in the deep water. The factors that may influence dAl and dMn distributions in different areas and water depths are discussed in the following section.

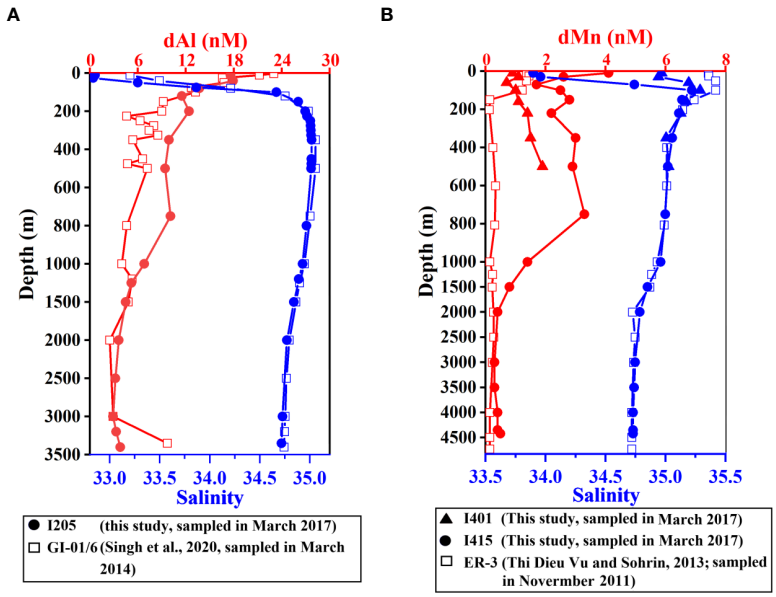

FIGURE 6
(A) Comparisons of salinity (blue) and dAl (red) at the full vertical profile of dAl of Indian GEOTRACES stations GI-01/06 (hollow square, Singh et al., 2020) and I205 (dot, this study). **(B)** Comparisons of salinity (blue) and dMn (red) at Japanese GEOTRACES stations ER-3 (hollow square, Thi Dieu Vu and Sohrin, 2013), I401 (triangle, this study), and I415 (dot, this study). dAl, dissolved aluminum; dMn, dissolved manganese.

Potential external sources of the mixed layer of BoB

Tremendous fluvial input (including freshwater and lithogenic sediments), along with atmospheric deposition and its subsequent dissolution, plays significant roles in regulating the dAl and dMn distributions in the BoB. Therefore, the 1-D box-model Equation 1 was used to estimate potential sources of dAl and dMn in the mixed layer of the BoB. As shown in Table 2; Grand et al. (2015a) calculated the residence time of dAl in the surface mixed layer to be 1.1 years in the northeastern IO (north of 5°S), while 0.01–0.47 years in the Arabian Sea was given by Singh and Singh (2022). The residence time of dMn varies in different areas (Table 2). For consistency, the same Al residence time (i.e., 1.1 years) and the mean value of Mn residence time of other studies (i.e., 1.0 years) were used to calculate different source contributions.

Mn was categorized as a crustal-derived element, same as Al (Hsu et al., 2010), while the solubility of the two elements differed (Table 2). The solubility of dAl used in the study was chosen as 3.6%, the same as that of Grand et al. (2015a) and Singh et al. (2020). The solubility of Mn from atmospheric dust was all relatively high in different areas and was chosen as 50%. Atmospheric Al dry deposition flux (0.3 mg $Al{\cdot}m^{-2}{\cdot}day^{-1}$; Srinivas and Sarin, 2013) over the south BoB was chosen to calculate the atmospheric deposition of Al. After substituting all parameters above into Equation (1), the estimate of dust input supported dAl in the south BoB was found to be 1.8–2.7 nM. Similarly, 7.8 μg $Mn{\cdot}m^{-2}{\cdot}day^{-1}$ (Srinivas and Sarin, 2013) was used, and the results showed that approximately 0.3–0.4 nM of dMn was contributed by atmospheric deposition to the mixed layer of the BoB.

The average concentration of dAl of the G-B River System was taken as 57 nM (salinity ≈ 29.4, Singh et al., 2020). Grand et al. (2015a) and Singh et al. (2020) both found that mixed layer dAl and salinity were negatively correlated in the BoB where salinity > 31. Based on the riverine freshwater charge (1,300 km^3/year, Sengupta et al., 2006), the area of the BoB (2.2×10^{12} m^2, Singh et al., 2020), and an average depth of mixed layer (20–30 m, this study), 1.3–1.9 nM enrichment of dAl in the mixed layer of the BoB was calculated due to discharge of the G-B River System. Relatively few studies focused on the distribution of dMn in the BoB nowadays. The value of 20 nM was chosen as the endmember of riverine freshwater input for dMn (unpublished data, measured at the G-B river estuary), and 0.2–0.4 nM of dMn was calculated from the G-B river system contributing to the BoB.

Singh et al. (2020) estimated the Al fraction in the sediment input to the BoB to be 8% by weight, which was similar to the Al composition in the upper continental crust (8.04%, Taylor and Mclennan, 1985) and the suspended sediments of Brahmaputra River (7.9%, Singh and France-Lanord, 2002). The Mn composition by weight was 673 ppm in the suspended sediments of the Brahmaputra River (Singh and France-Lanord, 2002) and 600 ppm in the upper crust (Taylor and Mclennan, 1985). The same Al concentration (8%) and Mn (650 ppm by weight) were used to calculate sediment input to the BoB. The solubility of Al from lithogenic sediments was chosen as 2.4% referring to Singh et al. (2020). Considering the atmospheric mineral dust to be originating from the upper crust and the results from Tessier et al. (1979) that labile particulate species occupied the percentage of total particulate concentration through five fractions processed, the solubility of Mn in the lithogenic sediments was assumed to be 50%. Substituting lithogenic sediment load (sediment trap in the south BoB, 4.3

TABLE 2 Values of each parameter chosen in the BoB.

Area		Pacific Ocean	East China Sea	Atlantic Ocean	South Pacific Ocean*	Bay of Bengal	South China Sea**	North Pacific Ocean***	Arabian Sea	Value chosen in this study
Sol. (%)	Al	3.7	5–10	4.1 ± 3.9		3.6				3.6
	Mn	45.1	50	52.9 ± 31.1	35.9 ± 11.9					50
MRT (year)	Al					1.1 ± 0.8			0.01–0.47	1.1
	Mn				0.73 ± 0.1		1.4–5.2	0.22–1.8		1.0
Reference		Buck et al., 2013	Hsu et al., 2010	López-García et al., 2017	Kadko et al., 2020	Grand et al., 2015a	Wang et al., 2018	Martin and Knauer, 1980	Singh and Singh, 2022	

* From coast to open ocean in the south Pacific Ocean.
** The mixed layer of the South China Sea.
*** The depth of 1–150 m of the central north Pacific Ocean.-

$g{\cdot}m^{-2}{\cdot}year^{-1}$, Unger et al., 2003) into Equation (1), dAl released in the mixed water of the south BoB from the sediments was estimated to be 11.2–16.8 nM. This estimated Al release from suspended sediment was an order magnitude larger than that from G-B river freshwater (1.3–1.9 nM). dMn from lithogenic sediment release was in the range of 0.9 to 1.4 nM.

Al released from lithogenic sediments predominately controlled the concentration of dAl (16.6 nM, average value), accounting for more than 67% of bulk inventory, and freshwater discharge played a secondary role in intense scavenging at the estuary. Atmospheric Al dry deposition contributed approximately 14% dAl in the mixed layer of the south BoB. There was no correlation between dAl and dMn (r = 0.02, Figure 7, right) in the mixed layer of the south BoB, indicating different controlling processes of dAl and dMn. Each source accounted for dMn (6.7 nM, average value) differed from that of dAl. Lithogenic sediments release supported only approximately 13%–21% dMn. Both freshwater input and atmospheric Mn dry deposition input contributed ~5% dMn. The three aforementioned sources sustained ~33% dMn in the mixed layer of the BoB at most. Additional dMn input from the advection of dMn-rich, low-salinity surface waters from the Andaman Sea may be another significant source (Singh et al., 2020). Moreover, numerous insoluble Mn(IV) oxides could be converted into dissolved Mn(II) for photo-reduction (Sunda and Huntsman, 1994). Meanwhile, a high dissolution efficiency of dust-derived Mn resulting from photochemical reduction was also observed by Sunda and Huntsman (1988) and Thi Dieu Vu and Sohrin (2013), indicating another important source for dMn in the surface seawater.

The range of different source contributions above was mainly from the indeterminacy of mixed layer depth. Other variable parameters could also cause uncertainties in the contribution calculation. For example, the G-B River System discharge used in this study was 1,300 km^3/year and had existing 13% interannual

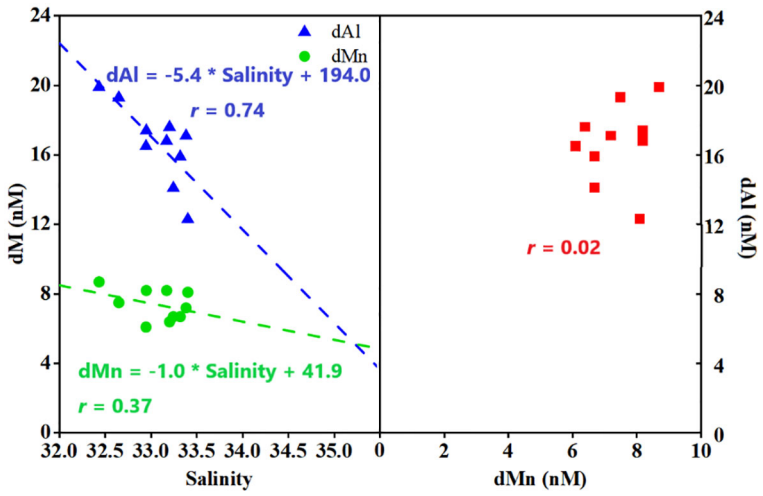

FIGURE 7
dAl and dMn variations with salinity in the mixed layer for stations in BoB (left). dMn variation with dAl in the mixed layer of BoB (right). dAl, dissolved aluminum; dMn, dissolved manganese; BoB, Bay of Bengal.

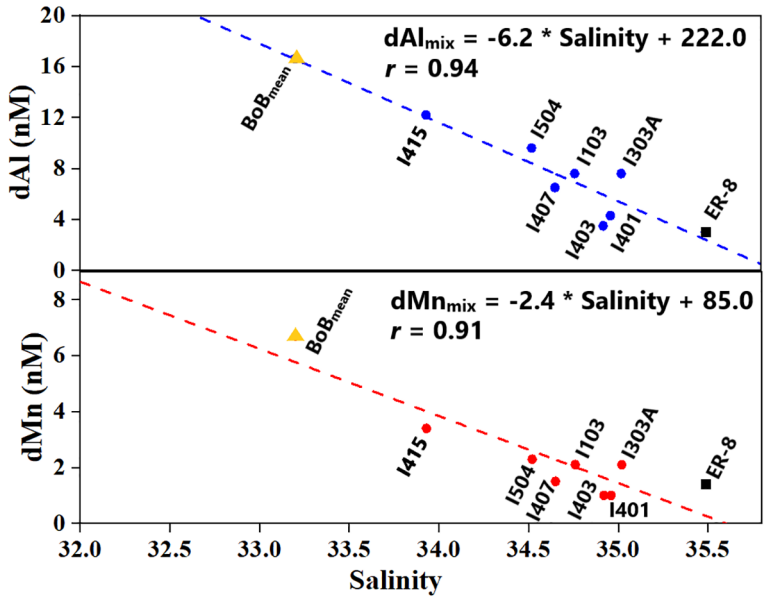

FIGURE 8
dAl (up) and dMn (down) variations with salinity for the mixed layer of stations in the Eq. IO (all stations located in 5°S–5°N). Data point for BoB_{mean} was the average value in the mixed layer of south BoB. Data point for station ER-8 (4.02°N, 69.00°W, Thi Dieu Vu and Sohrin, 2013) in the southern Arabian Sea was also plotted as an endmember. dAl, dissolved aluminum; dMn, dissolved manganese; Eq. IO, equatorial Indian Ocean; BoB, Bay of Bengal.

variations (Dai and Trenberth, 2002; Jian et al., 2009), bringing 13% contribution calculation result uncertainty. Nevertheless, even if considering this uncertainty, lithogenic sediment release may still play a predominant role in dAl distributions in the mixed layer of the BoB. Unlike dAl, sources other than lithogenic sediments were of great importance in controlling dMn contributions.

Water mass mixing in the northeastern IO

Significant low dAl and dMn concentrations compared to the nearby stations were observed at stations I103 and I504, accompanied by high salinity and low temperature (Figure 2). An upwelling isopycnal, which the two stations possessed (Figure 4A),

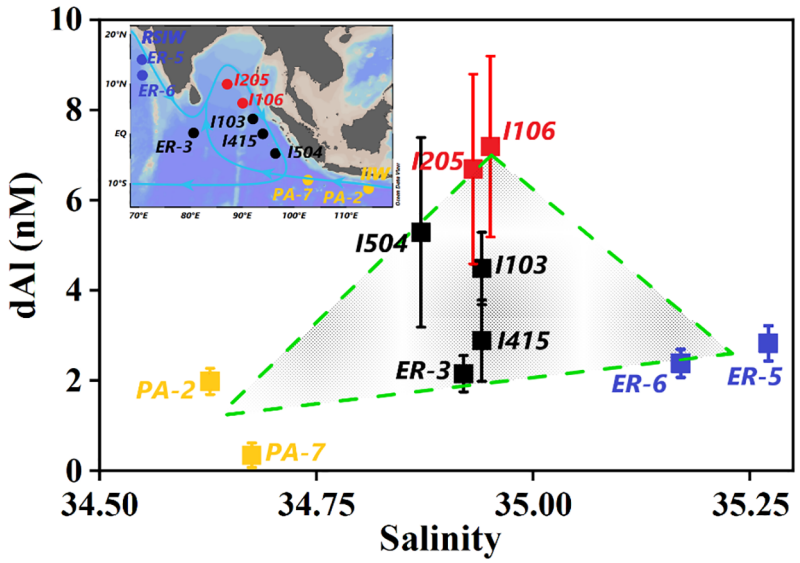

FIGURE 9
dAl variation with salinity for σ_0 within 27.1–27.6 kg/m^3 from stations in this study. ER-3, ER-5, and ER-6 from Thi Dieu Vu and Sohrin (2013) and PA-2 and PA-7 from Obata et al. (2004). The error bar means the range of dAl concentration. The inset map shows the locations of stations ahead, and the light blue line represents intermediate water (σ_0 within 27.1–27.6 kg/m^3) circulation pattern in the northeastern IO (adapted from You, 1998). dAl, dissolved aluminum; BoB, Bay of Bengal.

was significant for a cold-core eddy. The decrease in dAl and dMn concentrations with an increase in salinity of these two stations could be attributed to cold-core eddies pumping sub-surface water into the surface.

The Eq. IO was relatively far from the continent, where the atmospheric deposition was the main external source of dAl and dMn in the mixed layer. Substituting solubility, residence time, atmospheric dry deposition flux (36.0 mg Al·m^{-2}·$year^{-1}$ and 936.0 μg Mn·m^{-2}·$year^{-1}$; Srinivas and Sarin, 2013), and depth of mixed layer (30–35 m, this study) into Equation 1, atmospheric Al and Mn dry deposition to the mixed layer of the Eq. IO was calculated as 1.5–1.8 and 0.2–0.3 nM, respectively, accounting for 20%–24% dAl and 10%–14% dMn concentrations (7.4 and 2.1 nM, respectively) in the mixed layer of the Eq. IO. Atmospheric dust deposition may not play a significant role. Nevertheless, zonal distributions of dAl and dMn showed an increasing trend from west to east in section E (Figures 3C, D). Meanwhile, significantly correlated variations (Figure 8) were found between dAl, dMn, and salinity in the mixed layer of the Eq. IO (stations located in 5°S–5°N). Average values in two locations, i.e., the south BoB of this study (salinity = 33.20, dAl = 16.6 nM, dMn = 6.7 nM) and ER-8 (4.02°N, 69.00°W, salinity = 35.49, dAl = 3.0 nM, dMn = 1.4 nM, Thi Dieu Vu and Sohrin, 2013), apparently bounded the upper and lower ends of linear dAl and dMn variations with salinity in the Eq. IO region, suggesting that the dAl and dMn distributions in the surface water of the Eq. IO were predominantly controlled by the advective mixing of low-salinity, dAl-rich, and dMn-rich south BBW and relatively high-salinity, dAl-poor, and dMn-poor ASHSW.

Station I507 (6.49°S, 98.33°N) in the southeast of the study area was influenced by the ITF (5°S-15°S, You and Tomczak, 1993; Makarim et al., 2019) and possessed relatively high dAl concentrations in the upper water column (<500 m). The ITF carries 10 Sv (1 Sv = 10^6 m^3/s) low-temperature, low-salinity, oxygen-rich, and Al-rich water westward into the IO (Gordon, 2005) and can be transported to the west IO by the SEC (Grand et al., 2015a). The ITF played significant roles in governing the dAl and dMn concentrations in the surface water, especially below the surface mixed layer, where the Al and Mn release from the settling mineral particles was deemed negligible (Measures et al., 2010; Grand et al., 2015b). Elevated ^{228}Ra activities (>100 dpm/m^3; Nozaki and Yamamoto, 2001) were observed in the surface waters at PA-7 (Figure 1, 10.01°S, 103.00°E, Obata et al., 2004), where high dAl concentrations (10.0 and 9.8 nM) appeared in the mixed layer and upper water column (100–500 m), respectively, suggested that the ITF, carrying coastal and shelf sources of trace elements, may have a significant contribution to dAl and dMn in the surface waters of the east IO.

The T-S diagram (Figure 5) indicated that intermediate water (σ_0 within 27.1–27.6 kg/m^3, depth in the range of 750–1,500 m) in the study area was mainly mixed by IIW and RSIW. IIW, characterized by relatively low salinity and high oxygen, largely contributes approximately 30%–50% of its water into the BoB. On the contrary, RSIW is characterized by high salinity and low oxygen and contributes approximately 40% of its water into the BoB. The main component of the intermediate water body of stations ER-5 and ER-6 from Thi Dieu Vu and Sohrin (2013) was hypothesized as the RSIW. Stations PA-2 and PA-7 from Obata et al. (2004) were on the pathway of IIW spreading northward. Both IIW and RSIW were characterized by low dAl (Obata et al., 2004; Thi Dieu Vu and Sohrin, 2013), and when moving into the BoB as a western boundary current through the east of Sri Lanka and flowed clockwise, they exited the bay, carrying high dAl and dMn concentrations (Figure 9, I205 and I106) of intermediate water of the BoB southward along Sumatra and Java (Figure 9; You, 1998). The intermediate water body of stations I103, I415, and I504 from this study and ER-3 from Thi Dieu Vu and Sohrin (2013) were considered the results of IIW and RSIW, together with BoB intermediate water body mixing, and therefore, plots for salinity

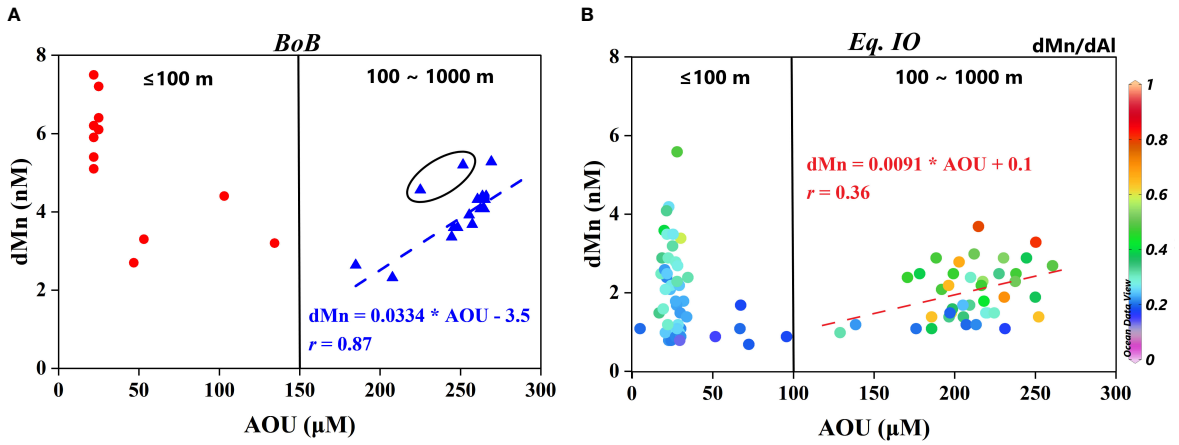

FIGURE 10
(A) dMn variation with AOU in the BoB. Red dots represent layers above (including) 100 m. Blue triangles represent layers from 100 to 1,000 m; the two triangle dots in the ellipse come from 120 and 200 m of station I110, where the advection of dMn-rich Andaman Sea was obvious. Blue dash is the linear line of AOU and dMn between 100 and 1,000 m, and blue font is its fitting equation. **(B)** dMn variation with AOU in the Eq. IO, with value of dMn:dAl on each dot (showing as a color bar). The dots on the left of black solid line represent layers above (including) 100 m, while on the right are in the range of 100–1,000 m. Red dash is the linear line of AOU and dMn between 100 and 1,000 m, and red font is its fitting equation. dMn, dissolved manganese; AOU, apparent oxygen utilization; BoB, Bay of Bengal; dAl, dissolved aluminum.

and dAl concentrations of these stations located in the dashed triangle constituted IIW, RSIW, and BoB intermediate water body (Figure 9). Based on the fact that northeastern IO is with low oxygen and that the BoB is anoxic (Figure 4B), remineralization and/or regeneration under a low-oxygen environment also mattered during the transporting of IIW and RSIW and in the subsurface water of the BoB, which will be discussed in the following section.

Remineralization versus reduction regeneration in anoxic zone

The poor ventilation of waters associated with the existence of NICW resulted in hypoxic conditions (DO below 32 µM, Figure 4B) in the subsurface and intermediate waters body of the BoB, along with high dAl and dMn concentrations simultaneously (Figures 4C, D). High or increased dAl concentration in the subsurface (100–1,000 m) was observed (Figure 4C). dAl in the depth of 100–1,000 m behaved non-conservatively with a poor relationship between dAl and salinity (r< 0.22, figure not shown), while dAl showed no correlation (r< 0.24, figure not shown) with apparent oxygen utilization (AOU) either. Singh et al. (2020) also observed the increase in dAl levels in the subsurface water and that dAl concentrations showed an overall decrease with increasing nutrients in the thermocline waters (100–800 m), and they concluded as regards the supply from the continental margin.

A tight correlation (Figure 10A, blue triangle dots, r = 0.87) between dMn and AOU in the subsurface water depth (100–1,000 m) of the BoB indicated that remineralization and/or regeneration mattered in regulating the biogeochemical behavior of dMn in a hypoxic environment. Two triangle dots in the ellipse came from 120 and 200 m of station I110, which could be attributed to the advection of dMn-rich Andaman Sea (Figures 2B, D), along with resuspended sediments from the margin shelf (Singh et al., 2020). AOU has been used to quantify the remineralized part of nutrients for its function as a tracer of organic matter remineralization (Anderson and Sarmiento, 1995; Chen and Wu, 2019). The slope achieved from the dMn : AOU linear relationship in this study was 0.0334 nM/µM, which could be converted to Mn:P = 5.01 nM/µM and Mn:C = 47.3 µM/M by applying the most commonly used Redfield ratio AOU:P:C = 150:1:106 (Redfield, 1958; Tyrrell, 2019). These two ratios far exceed the range in phytoplankton Mn:P = 0.16–0.81 nM/µM and Mn:C = 0.6–1.8 in µM/M reported and summarized in Twining et al. (2010) and Twining et al. (2019), respectively. This indicated that remineralization of biogenic particulate, compared to a reduction of Mn(IV) from lithogenic particles and/or resuspended sediments from the margin in hypoxic conditions, could be deemed as negligible for the distribution of dMn in the BoB while ignoring the effects of vertical mixing.

The low DO in the subsurface of the Eq. IO was the result of NICW expanding southward and eastward and suppressed by the ITF near 5°S–10°S (Grand et al., 2015b). The relatively tight correlation (r = 0.79, figure not shown) between dAl and salinity in the subsurface (100–1,000 m) of the Eq. IO suggested inconspicuous regeneration of dAl. On the contrary, the value of dMn:dAl (Figure 10B) increased nearly up to ~0.8 at some layers of the Eq. IO, indicating the existence of regeneration of dMn. However, a poor relationship (Figure 10B, r = 0.36) between dMn and AOU indicated a vague contribution of AOU under a low oxygen environment to the distribution of dMn. Similarly, no subsurface Mn maximum was observed in the oxygen minimum zone (OMZ;<100 µM, somewhere< 10 µM) layer in the tropical and equatorial Pacific Ocean (Chen and Wu, 2019). The average AOU value in the depth of 100–500 m of the Eq. IO was 203.3 µM. Therefore, 0.2–1.1 nM of Mn was calculated by remineralization through the Redfield ratio AOU:P = 150:1 (Tyrrell, 2019) and Mn:P = 0.16–0.81 nM/µM in the cell (Twining et al., 2010). The mean value of dMn in the subsurface (100–500 m) water of Section E in the Eq. IO was 1.8 nM (ranging from 0.8 to 3.7 nM). Therefore, the remineralization of settling organic particles contributed 11%–61% dMn in the subsurface water of the Eq. IO, which was different from that in the subsurface water of the BoB. The macronutrients and dissolved Fe were extremely low on the surface of IO tropical water, resulting in low production in the region (Wiggert et al., 2006; Grand et al., 2015b; Chinni et al., 2019). Low production in the upper water body (POC export flux (^{234}Th based): 1.0 mmol C·m^{2}·day^{-1}; Station 10, 3.5°S, 84.0°E, Anand et al., 2017) resulted in less particle settlement and *in situ* reduction of Mn(IV) from settling, and suspended particles did not likely occur in the subsurface water body.

Conclusions

This study provided a comprehensive dataset on the distributions and sources of dissolved aluminum and manganese in the northeastern Indian Ocean in the spring inter-monsoon period of 2017. The mean values of dAl and dMn in the mixed layer of the BoB were 16.6 and 6.7 nM, respectively. The release of lithogenic sediments predominately controlled the concentration of dAl and was of great importance in dMn distributions in the mixed layer of the BoB. Additional dMn input from the advection of Andaman Sea water and photo-reduction–dissolution of particulate Mn also played significant roles. Different from that in the BoB, dAl and dMn distributions in the mixed layer of the Eq. IO were predominantly controlled by the advective mixing of low-salinity, dAl-rich, and dMn-rich south BBW and high-salinity, dAl-poor, and dMn-poor ASHSW. The intermediate water (750–1,500 m) of northeastern IO was mainly formed by the migration and mixing of low-dAl, low-dMn RSIW and IIW and BoB intermediate water characterized with high dAl and dMn concentrations. Regeneration of lithogenic particles under hypoxic conditions controlled the distribution of dMn in the subsurface (100–1,000 m) of the BoB. On the contrary, the remineralization of settling organic particles mattered in the subsurface (100–500 m) water of the Eq. IO. The influence of low salinity, dAl-rich, and dMn-rich ITF was also observed in the southernmost area of the study.

Data availability statement

The raw data supporting the conclusions of this article will be made available by the authors, without undue reservation.

Author contributions

SJ and JZ were in charge of the sampling. LL was in charge of the measurements. YY was in charge of writing/original draft preparation. JZ and JR acquired the funding for the cruise and supervised the research cruise. All authors have read and agreed to the published version of the manuscript. The manuscript was written through the contributions of all authors. All authors contributed to the article and approved the submitted version.

Funding

This study was funded by the National Natural Science Foundation of China (42176042), the High-end users Program of "Kexue" (No. KEXUE2019GZ01), and the Taishan Scholars Programme of Shandong Province. The Oceanographic Research Vessel Sharing Plan (NORC2017-10) supported by the National Natural Science Foundation of China provided precious onboard opportunities.

Acknowledgments

Crews and captains of *R/V ShiYan 3* are acknowledged for their help during the fieldwork. R. Schlitzer and colleagues from the Alfred Wegener Institute for Polar and Marine Research (AWI) provided free use of the software Ocean Data View (ODV), which was used for data processing. The data for this study are available from the corresponding author *via* email: renjingl@ouc.edu.cn.

Conflict of interest

The authors declare that the research was conducted in the absence of any commercial or financial relationships that could be construed as a potential conflict of interest.

Publisher's note

References

Aguilar-Islas, A. M., and Bruland, K. W. (2006). Dissolved manganese and silicic acid in the Columbia river plume: A major source to the California current and coastal waters off Washington and Oregon. *Mar. Chem.* 101, 233–247. doi: 10.1016/j.marchem.2006.03.005

Anand, S. S., Rengarajan, R., Sarma, V., Sudheer, A. K., Bhushan, R., and Singh, S. K. (2017). Spatial variability of upper ocean POC export in the bay of Bengal and the Indian ocean determined using particle-reactive 234Th. *J. Geophys. Res* 122, 3753-3770. doi: 10.1002/2016JC012639

Anderson, L. A., and Sarmiento, J. L. (1995). Global ocean phosphate and oxygen simulations. *Glob. Biogeochem. Cycle* 9, 621–636. doi: 10.1029/95GB01902

Baker, A. R., Jickells, T. D., Witt, M., and Linge, K. L. (2006). Trends in the solubility of iron, aluminium, manganese and phosphorus in aerosol collected over the Atlantic ocean. *Mar. Chem.* 98, 43–58. doi: 10.1016/j.marchem.2005.06.004

Behrenfeld, M. J., and Falkowski, P. G. (1997). Photosynthetic rates derived from satellite-based chlorophyll concentration. *Limnol. Oceanogr.* 42, 1–20. doi: 10.4319/lo.1997.42.1.0001

Brown, M. T., and Bruland, K. W. (2008). An improved flow injection analysis method for the determination of dissolved aluminum in seawater. *Limnol. Oceanogr. Methods* 6, 87–95. doi: 10.4319/lom.2008.6.87

Bruland, K. W., Middag, R., and Lohan, M. C. (2014). "Controls of trace metals in seawater," in *Treatise on geochemistry*, *2nd ed.*, (Oxford: Elsevier) vol. 8. , 19–51.

Buck, C. S., Landing, W. M., and Resing, J. (2013). Pacific ocean aerosols: Deposition and solubility of iron, aluminum, and other trace elements. *Mar. Chem.* 157, 117–130. doi: 10.1016/j.marchem.2013.09.005

Chen, G., and Wu, J. (2019). Meridional distribution of dissolved manganese in the tropical and equatorial pacific. *Geochim. Cosmochim. Acta* 263, 50–67. doi: 10.1016/j.gca.2019.06.048

Chinni, V., Singh, S. K., Bhushan, R., Rengarajan, R., and Sarma, V. V.S. S. (2019). Spatial variability in dissolved iron concentrations in the marginal and open waters of the Indian ocean.*Mar. Chem.* 208, 11–28. doi: 10.1016/j.marchem.2018.11.007

Colombo, M., Jackson, S. L., Cullen, J. T., and Orians, K. J. (2020). Dissolved iron and manganese in the Canadian Arctic ocean: On the biogeochemical processes controlling their distributions. *Geochim. Cosmochim. Acta* 277, 150–174. doi: 10.1016/j.gca.2020.03.012

Colombo, M., Li, J., Rogalla, B., Allen, S. E., and Maldonado, M. T. (2022). Particulate trace element distributions along the Canadian Arctic GEOTRACES section: Shelf-water interactions, advective transport and contrasting biological production. *Geochim. Cosmochim. Acta* 323, 183–201. doi: 10.1016/j.gca.2022.02.013

Dai, A., and Trenberth, K. (2002). Estimates of freshwater discharge from continents: Latitudinal and seasonal variations. J. *Hydrometeorol.* 3, 660–685. doi: 10.1175/1525-7541(2002)003<0660:EOFDFC>2.0.CO;2

ESR (2009). OSCAR third degree resolution ocean surface currents. *Ver. 1. PO.DAAC, CA, USA*. Dataset accessed [2021-04-20] at . doi: 10.5067/OSCAR-03D01

Galy, A., and France-Lanord, C. (2001). Higher erosion rates in the himalaya: Geochemical constraints on riverine fluxes. *Geology (Boulder)* 29, 23. doi: 10.1130/0091-7613(2001)029<0023:HERITH>2.0.CO;2

GEOTRACES Planning Group (2006). *GEOTRACES science plan* (Baltimore, Maryland: Scientific Committee on Oceanic Research).

Gerringa, L. J. A., Alderkamp, A., van Dijken, G., Laan, P., Middag, R., and Arrigo, K. R. (2020). Dissolved trace metals in the Ross Sea. *Front. Mar. Sci.* 7. doi: 10.3389/fmars.2020.577098

Gordon, A. (2005). Oceanography of the Indonesian seas and their throughflow. *Oceanography (Washington D.C.)* 18, 14–27. doi: 10.5670/oceanog.2005.01

Grand, M. M., Measures, C. I., Hatta, M., Hiscock, W. T., Buck, C. S., and Landing, W. M. (2015a). Dust deposition in the eastern Indian ocean: The ocean perspective from Antarctica to the bay of Bengal. *Glob. Biogeochem. Cycle* 29, 357–374. doi: 10.1002/2014GB004898

Grand, M. M., Measures, C. I., Hatta, M., Hiscock, W. T., Landing, W. M., Morton, P. L., et al. (2015b). Dissolved fe and Al in the upper 1000 m of the eastern Indian ocean: A high-resolution transect along 95°E from the Antarctic margin to the bay of Bengal. *Glob. Biogeochem. Cycle* 29, 375–396. doi: 10.1002/2014GB004920

Häusler, K., Dellwig, O., Schnetger, B., Feldens, P., Leipe, T., Moros, M., et al. (2018). Massive Mn carbonate formation in the landsort deep (Baltic sea): Hydrographic conditions, temporal succession, and Mn budget calculations. *Mar. Geol.* 395, 260–270. doi: 10.1016/j.margeo.2017.10.010

Holte, J., Talley, L. D., Gilson, J., and Roemmich, D. (2017). An argo mixed layer climatology and database. *Geophys. Res. Lett.* 44, 5618–5626. doi: 10.1002/2017GL073426

Hood, R. R., Wiggert, J. D., and Naqvi, S. W. A. (2009). Indian Ocean research: Opportunities and challenges. *Geophysical Monograph Ser.* 185, 409–429. doi: 10.1029/2007GM000714

Hsu, S., Wong, G. T. F., Gong, G., Shiah, F., Huang, Y., Kao, S., et al. (2010). Sources, solubility, and dry deposition of aerosol trace elements over the East China Sea. *Mar. Chem.* 120, 116–127. doi: 10.1016/j.marchem.2008.10.003

Jian, J., Webster, P. J., and Hoyos, C. D. (2009). Large-Scale controls on Ganges and Brahmaputra river discharge on intraseasonal and seasonal time-scales. *Q. J. R. Meteorol. Soc* 135, 353–370. doi: 10.1002/qj.384

Kadko, D., Aguilar-Islas, A., Buck, C. S., Fitzsimmons, J. N., Landing, W. M., Shiller, A., et al. (2020). Sources, fluxes and residence times of trace elements measured during the U.S. GEOTRACES East pacific zonal transect. *Mar. Chem.* 222, 103781. doi: 10.1016/j.marchem.2020.103781

Kamykowski, D., and Zentara, S. (1990). Hypoxia in the world ocean as recorded in the historical data set. *Deep Sea Res. Part I* 37, 1861–1874. doi: 10.1016/0198-0149(90)90082-7

Kandel, A., and Aguilar-Islas, A. (2021). Spatial and temporal variability of dissolved aluminum and manganese in surface waters of the northern gulf of Alaska. *Deep Sea Res. Part II* 189-190, 104952. doi: 10.1016/j.dsr2.2021.104952

Landing, W. M., and Bruland, K. W. (1980). Manganese in the north pacific. *Earth Planet. Sci. Lett.* 49, 45–56. doi: 10.1016/0012-821X(80)90149-1

Lee, J., Heller, M. I., and Lam, P. J. (2018). Size distribution of particulate trace elements in the U.S. GEOTRACES Eastern pacific zonal transect (GP16). *Mar. Chem.* 201, 108–123. doi: 10.1016/j.marchem.2017.09.006

Lenstra, W. K., Séguret, M. J. M., Behrends, T., Groeneveld, R. K., Hermans, M., Witbaard, R., et al. (2020). Controls on the shuttling of manganese over the northwestern black Sea shelf and its fate in the euxinic deep basin. *Geochim. Cosmochim. Acta* 273, 177–204. doi: 10.1016/j.gca.2020.01.031

Lewis, B. L., and Luther III, G. W. (2000). Processes controlling the distribution and cycling of manganese in the oxygen minimum zone of the Arabian Sea. *Deep-sea research. Part II, Tropical studies in oceanography* 47, 1541–1561 . doi: 10.1016/S0967-0645(99)00153-8

López-García, P., Gelado-Caballero, M. D., Collado-Sánchez, C., and Hernández-Brito, J. J. (2017). Solubility of aerosol trace elements: Sources and deposition fluxes in the canary region. *Atmos. Environ.* 148, 167–174. doi: 10.1016/j.atmosenv.2016.10.035

Makarim, S., Sprintall, J., Liu, Z., Yu, W., Santoso, A., Yan, X., et al. (2019). Previously unidentified Indonesian throughflow pathways and freshening in the Indian ocean during recent decades. *Sci. Rep.* 9, 7364. doi: 10.1038/s41598-019-43841-z

Martin, J. H., and Knauer, G. A. (1980). Manganese cycling in northeast pacific waters. *Earth Planet. Sci. Lett.* 51, 266–274. doi: 10.1016/0012-821X(80)90209-5

Measures, C. I., and Brown, E. T. (1996). "Estimating dust input to the Atlantic ocean using surface water aluminium concentrations," in *The impact of desert dust across the Mediterranean*. Eds. S. Guerzoni and R. Chester (Dordrecht: Springer Netherlands), 301–311.

Measures, C. I., and Edmond, J. M. (1990). Aluminium in the south Atlantic: Steady state distribution of a short residence time element. *J. Geophys. Res. Oceans.* 95, 5331–5340. doi: 10.1029/JC095iC04p05331

Measures, C. I., Sato, T., Vink, S., Howell, S., and Li, Y. H. (2010). The fractional solubility of aluminium from mineral aerosols collected in Hawaii and implications for atmospheric deposition of biogeochemically important trace elements. *Mar. Chem.* 120, 144–153. doi: 10.1016/j.marchem.2009.01.014

Menzel Barraqueta, J., Samanta, S., Achterberg, E. P., Bowie, A. R., Croot, P., Cloete, R., et al. (2020). A first global oceanic compilation of observational dissolved aluminum data with regional statistical data treatment. *Front. Mar. Sci.* 7. doi: 10.3389/fmars.2020.00468

Menzel Barraqueta, J., Schlosser, C., Planquette, H., Gourain, A., Cheize, M., Boutorh, J., et al. (2018). Aluminium in the north Atlantic ocean and the Labrador Sea (GEOTRACES GA01 section): Roles of continental inputs and biogenic particle removal. *Biogeosciences* 15, 5271–5286. doi: 10.5194/bg-15-5271-2018

Nakaguchi, Y., Ikeda, Y., Sakamoto, A., Zheng, L., Minami, T., and Sohrin, Y. (2021). Distribution and stoichiometry of Al, Mn, fe, Co, Ni, Cu, zn, cd, and Pb in the East China Sea. *J. Oceanogr.* 77, 463–485. doi: 10.1007/s10872-020-00577-z

Nath, B. N., Rao, V. P., and Becker, K. P. (1989). Geochemical evidence of terrigenous influence in deep-sea sediments up to 8°S in the central Indian basin. *Mar. Geol.* 87, 301–313. doi: 10.1016/0025-3227(89)90067-4

Nozaki, Y., and Yamamoto, Y. (2001). Radium 228 based nitrate fluxes in the eastern Indian ocean and the south China Sea and a silicon-induced "alkalinity pump" hypothesis. *Glob. Biogeochem. Cycle* 15, 555–567. doi: 10.1029/2000GB001309

Obata, H., Nozaki, Y., Alibo, D. S., and Yamamoto, Y. (2004). Dissolved Al, in, and ce in the eastern Indian ocean and the southeast Asian seas in comparison with the radionuclides 210Pb and 210Po. *Geochim. Cosmochim. Acta* 68, 1035–1048. doi: 10.1016/j.gca.2003.07.021

Redfield, A. C. (1958). The biological control of chemical factors in the environment. *Am. Sci.* 46, 221A–230A. Available at: http://www.jstor.org/stable/27827150

Resing, J. A., Sedwick, P. N., German, C. R., Jenkins, W. J., Moffett, J. W., Sohst, B. M., et al. (2015). Basin-scale transport of hydrothermal dissolved metals across the south pacific ocean. *Nature* 523, 200–203. doi: 10.1038/nature14577

Rolison, J. M., Middag, R., Stirling, C. H., Rijkenberg, M. J. A., and de Baar, H. J. W. (2015). Zonal distribution of dissolved aluminium in the Mediterranean Sea. *Mar. Chem.* 177, 87–100. doi: 10.1016/j.marchem.2015.05.001

Sandeep, K. K., Pant, V., Girishkumar, M. S., and Rao, A. D. (2018). Impact of riverine freshwater forcing on the sea surface salinity simulations in the Indian ocean. *J. Mar. Syst.* 185, 40–58. doi: 10.1016/j.jmarsys.2018.05.002

Sardessai, S., Shetye, S., Maya, M. V., Mangala, K. R., and Prasanna Kumar, S. (2010). Nutrient characteristics of water masses and their seasonal variability in the eastern equatorial Indian Ocean. *Mar. Environ. Res.* 70, 272–282 . doi: 10.1016/j.marenvres.2010.05.009

Schott, F. A., Xie, S., and Julian, P. M. J. (2009). Indian Ocean circulation and climate variability. *Rev.Geophy.* 1985) 47, G1002. doi: 10.1029/2007RG000245

Sengupta, D., Bharath Raj, G. N., and Shenoi, S. S. C. (2006). Surface freshwater from bay of Bengal runoff and Indonesian throughflow in the tropical Indian ocean. *Geophys. Res. Lett.* 33. doi: 10.1029/2006GL027573

Shankar, D., Vinayachandran, P. N., and Unnikrishnan, A. S. (2002). The monsoon currents in the north Indian ocean. *Prog. Oceanogr.* 52, 63–120. doi: 10.1016/s0079-6611(02)00024-1

Shiller, A. M. (1997). Manganese in surface waters of the Atlantic ocean. *Geophys. Res. Lett.* 24, 1495–1498. doi: 10.1029/97GL01456

Singh, N. D., Chinni, V., and Singh, S. K. (2020). Dissolved aluminium cycling in the northern, equatorial and subtropical gyre region of the Indian ocean. *Geochim. Cosmochim. Acta* 268, 160–185. doi: 10.1016/j.gca.2019.09.028

Singh, S. K., and France-Lanord, C. (2002). Tracing the distribution of erosion in the Brahmaputra watershed from isotopic compositions of stream sediments. *Earth Planet. Sci. Lett.* 202, 645–662. doi: 10.1016/s0012-821x(02)00822-1

Singh, N. D., and Singh, S. K. (2022). Distribution and cycling of dissolved aluminium in the Arabian Sea and the Western equatorial Indian ocean. *Mar. Chem.* 243, 104122. doi: 10.1016/j.marchem.2022.104122

Singh, S. P., Singh, S. K., Goswami, V., Bhushan, R., and Rai, V. K. (2012). Spatial distribution of dissolved neodymium and εNd in the bay of Bengal: Role of particulate matter and mixing of water masses. *Geochim. Cosmochim. Acta* 94, 38–56. doi: 10.1016/j.gca.2012.07.017

Slemons, L. O., Murray, J. W., Resing, J., Paul, B., and Dutrieux, P. (2010). Western Pacific coastal sources of iron, manganese, and aluminum to the equatorial undercurrent. glob. *Biogeochem. Cycle* 24, GB3024-1–GB3024-16. doi: 10.1029/2009GB003693

Srinivas, B., and Sarin, M. M. (2013). Atmospheric dry-deposition of mineral dust and anthropogenic trace metals to the bay of Bengal. *J. Mar. Syst.* 126, 56–68. doi: 10.1016/j.jmarsys.2012.11.004

Srinivas, B., Sarin, M. M., and Kumar, A. (2012). Impact of anthropogenic sources on aerosol iron solubility over the bay of Bengal and the Arabian Sea. *Biogeochemistry* 110, 257–268. doi: 10.1007/s10533-011-9680-1

Statham, P. J., Yeats, P. A., and Landing, W. M. (1998). Manganese in the eastern Atlantic ocean: Processes influencing deep and surface water distributions. *Mar. Chem.* 61, 55–68. doi: 10.1016/S0304-4203(98)00007-3

Sunda, W. G., and Huntsman, S. A. (1988). Effect of sunlight on redox cycles of manganese in the southwestern Sargasso Sea. *Deep Sea Res. Part I* 35, 1297–1317. doi: 10.1016/0198-0149(88)90084-2

Sunda, W. G., and Huntsman, S. A. (1994). Photoreduction of manganese oxides in seawater. *Mar. Chem.* 46, 133–152. doi: 10.1016/0304-4203(94)90051-5

Taylor, S. R., and Mclennan, S. M. (1985). *The continental crust: Its composition and evolution, an examination of the geochemical record preserved in sedimentary rocks* (Oxford: Blackwell Scientific Pub).

Tessier, A., Campbell, P. G. C., and Bisson, M. (1979). Sequential extraction procedure for the speciation of particulate trace metals. *Analytical Chem. (Washington)* 51, 844–851. doi: 10.1021/ac50043a017

Thi Dieu Vu, H., and Sohrin, Y. (2013). Diverse stoichiometry of dissolved trace metals in the Indian ocean. *Sci. Rep.* 3, 1745. doi: 10.1038/srep01745

Twining, B. S., Nuez-Milland, D., Vogt, S., Johnson, R. S., and Sedwick, P. N. (2010). Variations in synechococcus cell quotas of phosphorus, sulfur, manganese, iron, nickel, and zinc within mesoscale eddies in the Sargasso Sea. *Limnol. Oceanogr.* 55, 492–506. doi: 10.4319/lo.2010.55.2.0492

Twining, B. S., Rauschenberg, S., Baer, S. E., Lomas, M. W., Martiny, A. C., and Antipova, O. (2019). A nutrient limitation mosaic in the eastern tropical Indian ocean. *Deep Sea Res. Part II* 166, 125–140. doi: 10.1016/j.dsr2.2019.05.001

Tyrrell, T. (2019). "Redfield ratio," in *Encyclopedia of ocean sciences (Third edition)*, (Oxford: Elsevier) vol. 1. , 461–472.

Unger, D., Ittekkot, V., Schäfer, P., Tiemann, J., and Reschke, S. (2003). Seasonality and interannual variability of particle fluxes to the deep bay of Bengal: Influence of riverine input and oceanographic processes. *Deep Sea Res. Part II* 50, 897–923. doi: 10.1016/s0967-0645(02)00612-4

Wang, Z., Ren, J., Xuan, J., Li, F., Yang, T., and Guo, Y. (2018). Processes controlling the distribution and cycling of dissolved manganese in the northern south China Sea. *Mar. Chem.* 204, 152–162. doi: 10.1016/j.marchem.2018.07.003

Wiggert, J. D., Murtugudde, R. G., and Christian, J. R. (2006). Annual ecosystem variability in the tropical Indian ocean: Results of a coupled bio-physical ocean general circulation model. *Deep Sea Res. Part II* 53, 644–676. doi: 10.1016/j.dsr2.2006.01.027

You,, Y. (2000). Implications of the deep circulation and ventilation of the Indian Ocean on the renewal mechanism of North Atlantic Deep Water. *Journal of Geophysical Research: Ocean* 105, 23895–23926 . doi: 10.1029/2000JC900105

You, Y. (1997). Seasonal variations of thermocline circulation and ventilation in the Indian ocean. *J. Geophys. Res. Oceans.* 102, 10391–10422. doi: 10.1029/96JC03600

You, Y. (1998). Intermediate water circulation and ventilation of the Indian ocean derived from water-mass contributions. *J. Mar. Res.* 56, 1029–1067. doi: 10.1357/002224098765173455

You, Y., and Tomczak, M. (1993). Thermocline circulation and ventilation in the Indian ocean derived from water mass analysis. *Deep Sea Res. Part I* 40, 13–56. doi: 10.1016/0967-0637(93)90052-5

Zhang, R., John, S. G., Zhang, J., Ren, J., Wu, Y., Zhu, Z., et al. (2015a). Transport and reaction of iron and iron stable isotopes in glacial meltwaters on Svalbard near kongsfjorden: From rivers to estuary to ocean. *Earth Planet. Sci. Lett.* 424, 201–211. doi: 10.1016/j.epsl.2015.05.031

Zhang, R., Zhang, J., Ren, J., Li, J., Li, F., Wang, Z., et al. (2015b). X-Vane: A sampling assembly combining a niskin-X bottle and titanium frame vane for trace metal analysis of sea water. *Mar. Chem.* 177, 653–661. doi: 10.1016/j.marchem.2015.10.006

Zheng, L., Minami, T., Takano, S., and Sohrin, Y. (2022). Distributions of aluminum, manganese, cobalt, and lead in the western south pacific: Interplay between the south and north pacific. *Geochim. Cosmochim. Acta* 338, 105–120. doi: 10.1016/j.gca.2022.10.022

frontiers | Frontiers in Marine Science

TYPE Original Research
PUBLISHED 17 April 2023
DOI 10.3389/fmars.2023.1143982

OPEN ACCESS

EDITED BY
Hermano Melo Queiroz,
University of São Paulo, Brazil

REVIEWED BY
Laís Jimenez,
University of São Paulo, Brazil
Ruifeng Zhang,
Shanghai Jiao Tong University, China

*CORRESPONDENCE
Lei Gao
gaolei2009605@163.com
Xiancai Lu
xcljun@nju.edu.cn

†These authors have contributed equally to this work and share first authorship

SPECIALTY SECTION
This article was submitted to Marine Biogeochemistry, a section of the journal Frontiers in Marine Science

RECEIVED 13 January 2023
ACCEPTED 30 March 2023
PUBLISHED 17 April 2023

CITATION
Qi Z, Gao L, Chen D, Wang X, Liu H, Yang Y, Zhao Y and Lu X (2023) Vertical distribution of Fe, P and correlation with organic carbon in coastal sediments of Yellow Sea, Eastern China. *Front. Mar. Sci.* 10:1143982. doi: 10.3389/fmars.2023.1143982

Vertical distribution of Fe, P and correlation with organic carbon in coastal sediments of Yellow Sea, Eastern China

Zizhen Qi[1†], Lei Gao[1*†], Daixing Chen[1], Xuhao Wang[1], Huan Liu[2], Yang Yang[1], Yulian Zhao[3] and Xiancai Lu[2*]

[1]School of Marine Science and Engineering, Nanjing Normal University, Nanjing, Jiangsu, China, [2]Key Laboratory of Surficial Geochemistry, Ministry of Education, School of Earth Science and Engineering, Nanjing University, Nanjing, Jiangsu, China, [3]Key Laboratory of Solid Waste Treatment and Resource Recycling, Ministry of Education, Mianyang, Sichuan, China

The coastal zone is considered as a major carbon pool. Iron minerals and phosphates are vital factors affecting the amounts and occurrence of total organic carbon (TOC) in sediments. However, coupling mechanisms of iron (Fe) and phosphorous (P) in the source-sink transition of TOC in coastal sediments is poorly understood. This study characterized the distribution of Fe, P and TOC contents of three independent 170 cm sediment cores sampled from a coastal aquaculture area in the eastern Jiangsu Province, and quantified the correlations among Fe, P, median grain diameter (Dx(50)), and TOC. The results showed total phosphorus (TP) content ranges in a scope of 337.4-578.0 mg/kg, and many depths recorded moderate P eutrophication. Inorganic phosphorus (DA + IP) and biogenic apatite were the primary components of TP, accounting for 25.19–55.00 and 26.71–49.62%, respectively. The Fe contents varied from 987.9 mg/kg to 2900.7 mg/kg, in which oxidized iron (Fe_{ox}) accounted for about 62.2–79.4%. In the vertical profile, the TOC was positively correlated with the contents of low-crystallinity Fe-bearing carbonates (Fe_{carb}), high crystallinity pyrite (Fe_{Py}), iron-bound phosphorus (P_{CDB}), manganeses (Mn), and nitrogen (N), while it was negatively correlated with DA + IP, organic phosphorus (OP), and Dx(50). Based on the the partial least squares (PLS) model, we proposed that the higher Fe_{Py}, Mn, magnetite (Fe_{Mag}), Fe_{carb}, P_{CDB}, amorphous exchangeable Fe (Ex-Fe), and authigenic apatite phosphorus (Bio-P) in sediments represent the high capacity for TOC sink, whereas, higher DA + IP, and OP indicate a TOC conversion to the source. The non-siginificat indication of Fe_{ox} on TOC source-sink is due to its surplus and strong reactivity relative to TOC content. These revealed correlations provide a theoretical reference for understanding and regulating the burial rate and storage of TOC by changing the input of Fe minerals and P components into coastal sediments.

KEYWORDS

phosphorus, iron minerals, total organic carbon, correlation, coastal sediments

Highlights

(1) Characterized the vertical speciations of Fe and P in coastal sediments

(2) Established the indicated relationship between different Fe and P speciations and TOC source-sink

(3) Higher content of Fe_{carb}, Fe_{Py}, Fe_{Mag}, Ex-Fe, Mn, P_{CDB}, and Bio-P represent TOC sink.

(4) Higher content of DA + IP, and OP indicate TOC source.

(5) Non-siginificat indication of Fe_{ox} on TOC source-sink is due to its surplus and strong reactivity.

1 Introduction

Marine "blue carbon" refers to the carbon sequestrated and stored in biomass and sediments by the oceans and coastal ecosystems (Tang et al., 2018; Macreadie et al., 2019; Macreadie et al., 2021). The contribution made by the coastal carbon pool accounts for ~99% of the final blue carbon sink (Tang et al., 2018). Some of the organic carbon is re-released or converted into CO_2 as a carbon source again through microbial metabolic activities (Zhang et al., 2017). The storage of organic carbon and inert carbon in the sediment is an important contributor to the carbon sink (Jiao et al., 2014). The "source-sink" of the coastal zone carbon pool fluctuates with the change of redox conditions due to hydrodynamics (Xu et al., 2021), terrigenous input, mineral conversion, and eutrophication. Various minerals have been widely believed to be important to promote the persistence and sink of organic carbon in sediments (Hemingway et al., 2019; Kleber et al., 2021). In particular, most of the iron and manganese minerals in sediments have large specific surface areas and high redox sensitivity, which can permanently preserve organic carbon through adsorption and surface complexation (Giannetta et al., 2020; Bao et al., 2022), as well as surface precipitation (Du et al., 2018). There is also a significant correlation between the sequestration and release of TOC with phosphorous (Huang et al., 2016; Fang and Wang, 2021). Phosphorous can accelerate TOC degradation directly or indirectly by enhancing microbial activities (Jiao et al., 2010). Meanwhile, phosphorus addition can directly improve TOC stability by increasing aggregate particle size and indirectly affect TOC stability by increasing Fe oxide form conversion in sediments (Du et al., 2022). The redox conditions of the coastal sediments commonly fluctuate greatly, different Fe oxide and phosphorus forms are very sensitive to it, and phosphorus eutrophication is serious due to terrestrial input (Singh et al., 2021). Therefore, phosphorous and Fe oxides and their special transformation are the key factors affecting TOC sequestration in coastal sediments.

In sediments, the interaction between minerals and organic matter occurs preferentially on specific minerals; therefore, the mineral composition is a crucial factor for the sequestration of organic matter (Hedges and Keil, 1995; Kleber et al., 2021). Many studies have proven that Fe minerals are important carriers of organic carbon in terrestrial soil (Sarkar et al., 2018; Kleber et al., 2021), and in the ocean sediment (Zhao et al., 2023). Fine-grained components in coastal sediments positively correlated with the contents of unstable minerals (Cao et al., 2018), especially the contents of Ca/Mg-rich carbonates with poor stability (Fookes and Higginbottom, 1975; Yalcin et al., 2022). Although the abundance of Fe minerals in coastal sediments is not as high as that of carbonates, the promotion by Fe oxides on the storage of organic matter through surface precipitation and adsorption has been well recognized (Canfield, 1994). An onion-like structure with encapsulated organic matter in iron minerals formed due to the diffusion and aggregation of iron and carbon, which weakens the decomposition of organic matters by microorganisms (Lalonde et al., 2012). Recently, scientists have proposed that the current hypothesis that the mineral matrix has a protective mechanism for TOC is simplistic, and the spatial and functional complexity of the mineral-organic matter should be considered (Yalcin et al., 2022). And study pointed that mineral–organic preservation is an important missing process in current assessments of Earth's long-term carbon cycle (Zhao et al., 2023). Hence, analyzing the correlation between the occurrence of organic carbon in the sedimentary profile of coastal zone and the occurrence of iron and manganese minerals is crucial to determine their contribution to the "carbon sink" of "blue carbon".

Phosphorus is also a key player in the geochemical cycle of TOC (Arif et al., 2021) and is easily fixed or affected by Fe minerals (März et al., 2018). The leading states of phosphorus nutrients in marine sediments include exchangeable, organic, iron-bound, autoecological apatite, detrital, and refractory organic (Fang and Wang, 2021), two-thirds of which are related to poorly crystalline iron and manganese oxides (Hermans et al., 2021). In aquatic and terrestrial systems, the interaction between phosphate and ferric oxides typically involves adsorption/desorption (Boujelben et al., 2008; Yoon et al., 2014), precipitation/dissolution of surface Fe-phosphate phases (Weng et al., 2012), and precipitation of phosphate in iron (III) oxides (Cheng et al., 2015; März et al., 2018). On the one hand, several iron minerals were found capable of promoting the hydrolysis of phosphate (Li et al., 2020). Significantly, Ca-bearing iron minerals could enhance the hydrolysis of phosphate by promoting the precipitation of calcium phosphate minerals (Wan et al., 2021). In turn, the interaction between phosphate and Fe(III) oxide significantly affects the mineralization pathway of the Fe phase, e.g., the presence of phosphate is a crucial factor for the formation of green rust during the reduction of hematite by iron-reducing bacteria (IRB) (O'loughlin et al., 2015). According to a statistic of iron minerals with different genesises, approximately 10% of phosphate in sediments remobilized into the pore fluids due to IRB activities (Schad et al., 2021). Hence, reactive P phases are therefore invoked as regulatory factor for Fe mineral transition and bounded with carbon source-sink under the driving effect of microbial remineralization.

In this study, we analyzed the total organic carbon, geochemical characteristics, and different forms of Fe oxides/minerals and phosphorus of sediment cores sampled from a coastal site of the Yellow Sea, Jiangsu Province, Eastern China. Based on Spearman's

multi-element correlation analysis, cluster analysis, and partial least squares (PLS) model, this study quantifies the correlation between median particle size (Dx(50)), Fe/Mn, P, and TOC in the profile. After that, the significant impact of human activities on the mechanisms of carbon sequestration by inducing the transformation of Fe minerals is discussed. Compared with previous studies, this paper presents the following contributions: (1) Characterized the distribution of Fe, P speciations and TOC contents in a sedimental of 170 cm core to further refine the occurrence of iron minerals and phosphorus in profile coastal; (2) Established correlation between TOC and Fe, P speciations based on Spearman's multi-element correlation analysis to deeply understand the complicated relationships between TOC and different Fe, P speciations; (3) Predicted the primary and secondary factors on affecting TOC source-sink transition based on the partial least squares (PLS) model to catch on carbon source-sink mechanism in coastal sediments.

2 Materials and methods

2.1 Sampling of sediments

In October 2021, sediments were collected from a marine mudflat in Bencha Town, Rudong, Nantong, Jiangsu Province (32°35'19.0422' N, 120°54'47.2608' E) (Figure 1). Bencha town is an important coastal aquaculture area. The sampling area was transition zone for aquaculture discharge from terrigenous to sea. Three profiles of 1.7 m in depth were excavated at adjacent three points. The samples were split every 10 cm in the profiles and were immediately put into sterile sealing bags, and there were 51 sample in total (17 samples/profiles sediment core). After emptying the air, the samples were quickly put into a foam box and frozen with dry ice. The boxes were transported back to the laboratory on the same day for cryopreservation at –80°C. In the lab, the sealing bags containing sediment were melted at 4°C, a certain amount of samples were divided into 50 ml centrifuge tubes in an anaerobic glove box, and then freeze-dried, grounded with an agate mortar and passed through a 200-mesh sieve for further analysis, including the sequential extraction of iron and phosphorus, measurement of total organic carbon (TOC) and nitrogen (N), and analysis related geochemical indexes. Meanwhile, 100 g wet sample was divided into in 250 ml centrifugal cup and centrifuged at high speed refrigerated centrifuge (6000 r/min, 20 min) to extract pore water, the supernatant liquid was filtered through a 0.45 μm microporous membrane. The chemical pH of the extract pore water were measured using a pH meter (Thermo Fisher, Star A2110). Other samples were used for analysis of grain size and microscopic observation.

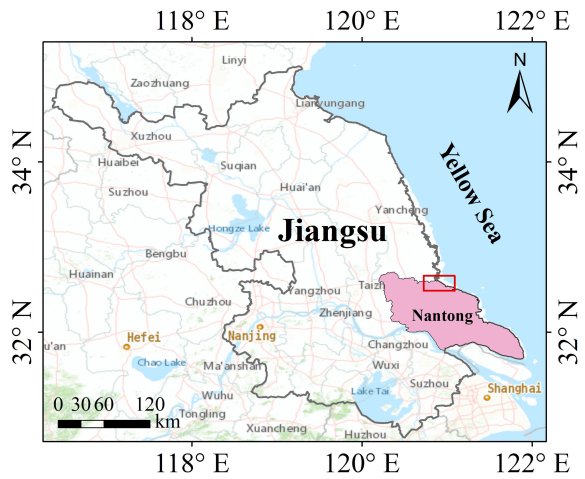

FIGURE 1
Map of the location of the study area.

2.2 Analysis of grain size of sediments

The grain size distribution of sediments was analyzed by using a Mastersizer 3000 laser grain-size analyzer (Shanghai, China). The measurement range was 0.02–2000 μm, and the relative error was less than 2%. The specific steps were as follows: 0.5 g of samples were placed in a 100 ml beaker, and 10 ml of mass fraction 10% of hydrogen peroxide (H_2O_2,CAS, 7722-84-1) was added to remove the organic matter in the sediment sample, and then 10 ml of mass fraction 10% hydrochloric acid (HCl, CAS, 7647-01-0) was added to remove the calcium cements. Next, the samples were sufficiently washed to neutralize them. Subsequently, 10 ml of 1 M sodium hexametaphosphate ($Na(PO_3)_6$, CAS, 68915-31-1) was added and placed in an ultrasonic oscillator to disperse the samples for grain size distribution analysis. The grain size ranges of clay, silt and sand were followed previous study by < 4 μm, 4–63 μm, and > 63 μm, respectively. Dx(50) was used to represent the median grain diameter of the sediment samples (Trefethen, 1950). All above chemical reagents were analytical reagent which purchased from Merck Limited Company (Shanghai, China).

2.3 X-ray fluorescence spectrometer (XRF) analysis

The abundance of major and trace elements was measured using a X-ray fluorescence analysis (Epsilon 3, PANalytical). The freeze-dried samples were pressed into pieces mixed with boric acid. And the pieces were scanned for 30 s with a step of 5 mm to acquire XRF spectra. The relative abundances of 8 significant and 26 trace elements were then calculated based on the collected spectra.

2.4 Analysis of carbon/nitrogen contents of sediments

The CN model of the Vario Max elemental analyzer (Elementar Analysensysteme GmbH) was used to test total carbon (TC), TOC, and nitrogen with an analysis error of less than 0.03%. Here 3 g pre-treated samples were placed in the sealed bags to measure the total content of carbon (TC), which includes the carbon in organic and inorganic states. Meanwhile, another 3 g pretreated samples was added with appropriate amount of 2 M HCl and shook for 48 h to

fully remove the inorganic carbon. Then, the samples with the additives were centrifuged at 3500 g, and the filter cakes were washed with ultrapure water five times, and finally freeze-dried. The acid-treated samples were placed in the sealed bags to measure the total content of carbon, which represents TOC. Therefore, the total inorganic carbon content (TIC) can be calculated by subtracting TOC from TC (TIC = TC-TOC). Calculated carbon ratio to nitrogen (C/N) by TC/N which was used to track source of organic matter.

2.5 Extraction and analysis of different speciations of iron in sediments

The five-step sequential extraction of different forms of iron was completed with little modified according to methods described in the literature (Poulton and Canfield, 2005). 0.1 g freeze-dried samples were weighted for the extraction. First, exchangeable Fe (Ex-Fe) was extracted by using 1 M $MgCl_2$. Second, low-crystallinity Fe-bearing minerals, such as iron sulfide, ferrous carbonate (calcite and dolomite), and easily reducible Fe oxides (ferrihydrite and lepidocrocite), were dissolved by using 1 M HCl to extract Fe_{carb}. Third, 0.35 M acetic acid, 0.2 M sodium citrate, and 50 $g{\cdot}L^{-1}$ sodium dithionite were mixed to the selective extraction of reducible oxides (goethite, hematite and akagane´ite) and reducible iron oxide (Fe_{ox}), including goethite, hematite, ferrihydrite or lepidocrocite. Fourth, magnetite (Fe_{Mag}) with high crystallinity was extracted by using 0.2 M oxalic acid or 0.17 M ammonium oxalate. Finally, the ferrous species in Fe-bearing minerals with high crystallinity include pyrite, iron (oxyhydr) oxides, siderite, ankerite, and certain sheet silicate minerals (e.g. nontronite, chlorite, glauconite, biotite). The concentrated HNO_3 was used to extract the Fe accommodated in these minerals, which is denoted by Fe_{Py}. The extraction of manganese hosted in iron minerals was carried out synchronously, and the final manganese content was the sum of the manganese content in five steps. The extract was diluted with 2% HNO_3 to make the Fe and Mn contents less than 2%, and was analyzed by inductively coupled plasma optical emission spectrometry (ICP-OES).

2.6 Extraction of different forms of phosphorus in sediments

0.1 g freeze-dried samples were placed in a centrifuge tube. According to the method described by Ruttenberg (1992), different forms of phosphorus were extracted in five steps. First, exchangeable or loosely sorbed phosphorus (Ex-P) was extracted by using 1M magnesium chloride. Second, iron-bound phosphorus (P_{CDB}) was extracted with CDB solution (0.30 M sodium citrate, 1.0 M $NaHCO_3$, pH 7.6, 1.125 $g{\cdot}L^{-1}$ sodium dithionite). Third, authigenic apatite, $CaCO_3$-bound P and biogenic apatite (Bio-P) were extracted by using sodium acetate solution. Fourth, 1M HCl was used to extract detrital apatite and other inorganic phosphorus (DA + IP). Finally, the samples were sintered at 550°C, and 1M HCl was used to extract the phosphorus, which represents organic phosphorus (OP). All of the final extracts were diluted to a salt content of less than 2% and then analyzed by using ICP-OES.

2.7 Scanning electron microscope (SEM) observation of iron minerals in sediments

Samples of freeze-dried sediments were dropped onto silicon wafers, and sputtered coating with Pt. A field emission-scanning electron microscope (SEM) (Carl Zeiss, Oberkochen, Germany) was used to observe Fe-Mn minerals. The energy dispersive spectrometer (EDS) (AZtecOne X-Max 150; Oxford Instruments, Abingdon, United Kingdom) equipped with SEM was used to measure the chemical composition of the minerals.

2.8 Correlation analysis of Fe-P-TOC

Spearman's correlation coefficient (one tail) analysis was performed using IBM SPSS Statistics 25 software to analyze the correlation between the mean grain size Dx (50) of iron, manganese, phosphorus, nitrogen, and total TOC. $P < 0.05$ was considered statistically significant. The K-means clustering classification principle divides similar samples into as many classes as possible (Nakamura et al., 2009). The R Core Team, 2022 (https://www.R-project.org/) was used to perform K-means clustering analysis on iron, manganese, phosphorus, nitrogen, Dx (50), and TOC to compare and analyze the factors in the same group as the TOC changes. The partial least squares (PLS) model associates two data matrices, X and Y, through a linear multivariate model, providing quantitative modeling of the complex relationship between the predictor variable X and response variable Y (Wold et al., 2001). For each PLS, the cumulative explained variation of Y (R^2) was calculated to evaluate whether the correlation was significant or not. The predictive squared correlation coefficient (Q^2) was used as the measure of robustness, and higher predictability was marked when it was larger than 0.50 (Golbraikh and Tropsha, 2002). SIMCA 14.1 was used to predict the partial least squares model to explore the relative importance of potential influencing factors of OC in Jiangsu coastal sediments. The ability of the independent variable to predict TOC and its importance to the dependent variable (Shi et al., 2014) rely on the variable importance of projection (VIP). Commonly, VIP > 1 indicates that the variables are able to predict the response variable. In contrast, VIP < 0.5 indicates that the relationship is less significant and should be removed from the model (Wold, 1995). Images were drawn using Origin 2018, R 4.1.3, CorelDRAW 2021 and online software available at https://www.chiplot.online/. All the data and standard deviations of each layer were obtained from the average of the three cores.

3 Results

3.1 Geochemical profile of sedimental components and TOC

The sediments are primarily composed by fine silt. With increasing depth, the median particle size overall decreased (Figure 2A). In the profile, the contents of sand, silt, and clay ranged from 5.05%–19.43%, 76.89%–89.86%, and 2.61%–6.37%. The silt content at most depths

exceeded 80% (Figure 2A), while the sand content was generally less than 17%. The pH of the pore water ranged from 7.45–8.48, with an average of 7.83. At depths of 40–50, 80–90, and 100–110 cm, the pH of the adjacent layers fluctuated (Figure 2B).

The TOC of sediments ranged from 1.03-2.10 g/kg, with an average of 1.44 g/kg (n = 51), a maximum at 100–110 cm, and a minimum at 120–130 cm. Its content is similar to that of most coastal zones(Fang and Wang, 2021; Xia et al., 2022), but it's significantly lower than that of terrestrial soil environment (Yan et al., 2021; Shi et al., 2022). The N was 0.20-0.44 g/kg, with a maximum at 160–170 cm and a minimum at 120–130 cm. The TOC/N ratio ranged from 3.32–6.32 with an average of 4.45 (n = 51). The TC/N ratio ranged from 22.04–46.27 with an average of 31.61 (n = 51), a maximum at 130–140 cm, and a minimum at 160–170 cm. The TOC/N ratio fluctuated significantly compared with the TC/N ratio, especially in the facultative anaerobic layer (30 cm) where redox conditions change greatly (Figure 2C). A TC/N ratio >12 indicates that the main source of organic matter is terrigenous organic matter, while a TC/N ratio between 6–9 indicates that the main source is the sea (Cifuentes et al., 1996). Therefore, the organic matter in the sediments here was mainly derived from terrestrial sources.

3.2 Vertical distribution of iron speciation

According to the sequential extraction of iron, the total iron content in the profile was scopes from 987.9 mg/kg to 2900.7 mg/kg. The reducible oxides Fe_{ox} was predominant (62.2%–79.4%), while the Fe_{carb}, Fe_{Mag}, and Fe_{Py} were 6.9%–17.9%, 6.6%–11.5%, and 4.1%–9.0%, respectively. The Ex-Fe content was the lowest, accounting for 0.5%–1.4%. Despite being low, the Ex-Fe content fluctuated the most with the depth (Figure 3). The Fe_{carb} content decreased with increasing depth, whereas Fe_{ox}, Fe_{Mag}, and Fe_{Py} accumulated gradually (Figure 3). Meanwhile, Mn content existed with extractable iron minerals increased with increasing depth, which might indicate that manganese was firstly dissolved and released into pore water, and then fixed by iron oxides as the iron minerals was reduced. At the profile bottom of 160–170 cm, iron oxide contents still were the highest, which may be due to microbial mineralization (Figure 3).

Based on SEM observation, Fe-rich or Mn-rich carbonate, iron oxides, and pyrite framboids were observed at the redox interface of 40–50 (Figure 4A) and 70–100 cm (Figures 4B–F), while Fe-rich clay minerals were the primary carrier minerals at depths of 130–140 (Figure 4G) and 160–170 cm (Figure 4H). At the redox interface at a depth of 40–50 cm, flaky iron-rich carbonates occurred along the edge of the sand matrix, such as the observed cubic regular crystalline iron-rich carbonates (Figure 4A), which is consistent with the observation of Kontny et al. (2021). However, at this depth, little manganese was detected in these iron carbonates (Figure S2-1). At depths of 70–80 cm, iron mineral species were abundant, including granular iron carbonates with high Mg and Mn adhered to the edge of the sand matrix (Figures 4B, C; Figure S2-4), pyrite framboids with diameter of about 5–20 μm (Figure 4D). Iron carbonates with higher Mg were also found at 80–90 cm (Figure 4E). At depths of 90–100 cm, the Fe-carbonate changed into plate-shape (Figure 4F) and contained much higher Mn content (Figure S2-6), the EDS analysis indicated the formation of siderite (Liu et al., 2019). We found there were Mg-rich siderite, Mg-Mn-rich siderite and Mn-rich siderite. The Mn-rich siderite likely formed at deep. Meanwhile, the SiO_2 particles became finer with increasing depth. At depths of 160–170 cm, various Fe-containing clays mainly occurred on the surface of the sandy matrix (Figure 4H). According to the XRF analysis (Figure 4I), the relatively high Mn contents were observed at the depths of 70–80, 110–110, and 160–170 cm.

3.3 Vertical distribution of phosphorus

The total phosphorus (TP) content in sediments ranged from 337.4–578.0 mg/kg, with an average of 454.4 mg/kg. Inorganic phosphorus was dominated (98.42%–99.99%), and organophosphorus content was relatively low (0.3–7.3 mg/kg). The Ex-P content was 3.3–3.7 mg/kg, only accounting for a very low proportion (0.58%–1.02%). With the increase of depth (<100 cm), Ex-P was released. The P_{CDB} content was 22.6–249.6 mg/kg, Bio-P content was 128.9–286.8 mg/kg, and detrital apatite plus other inorganic phosphorus (DA+IP) was 133.0–224.1 mg/kg, which accounted for 5.36%–47.28%, 26.71%–49.62%, and 25.19%–55.00% of TP content, respectively. The Bio-P and DA+IP were the main forms of phosphorus. The OP mainly distributed below 50 cm (Figure 5).

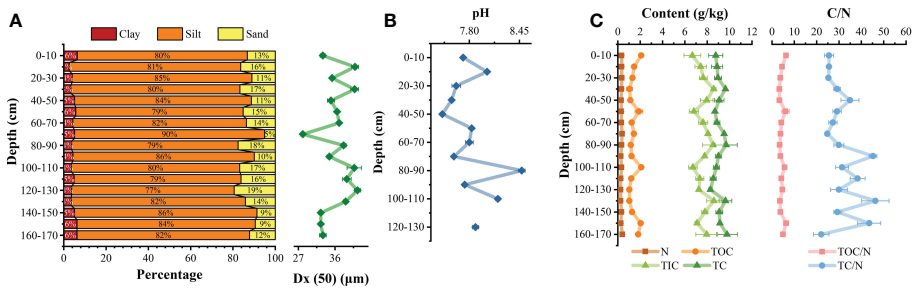

FIGURE 2
Vertical profile distribution of particle size of sediment **(A)**; vertical pH changes of pore water **(B)**; Changes of total organic carbon (TOC) and carbon ratio to nitrogen (C/N) **(C)**.

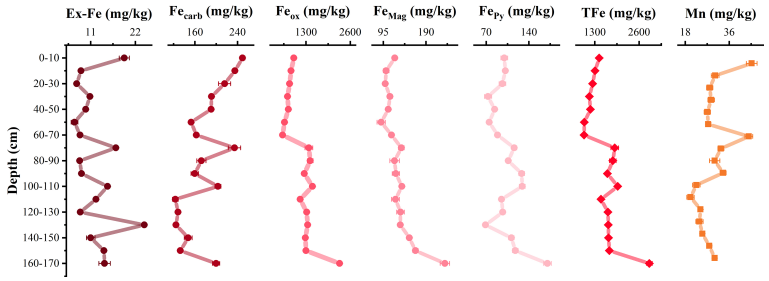

FIGURE 3
Distribution of different speciations of iron minerals at vertical profile. Ex-Fe represents exchangeable iron, Fe_{carb} represents low-crystallinity Fe-bearing carbonates, Fe_{ox} represents easy-reduced iron oxide, Fe_{Mag} represents high-crystallinity magnetite, Fe_{Py} represents high crystallinity. Non-reactive pyrite, TFe represents the total content of iron minerals, and Mn represents the occurrence of manganese hosted in iron minerals.

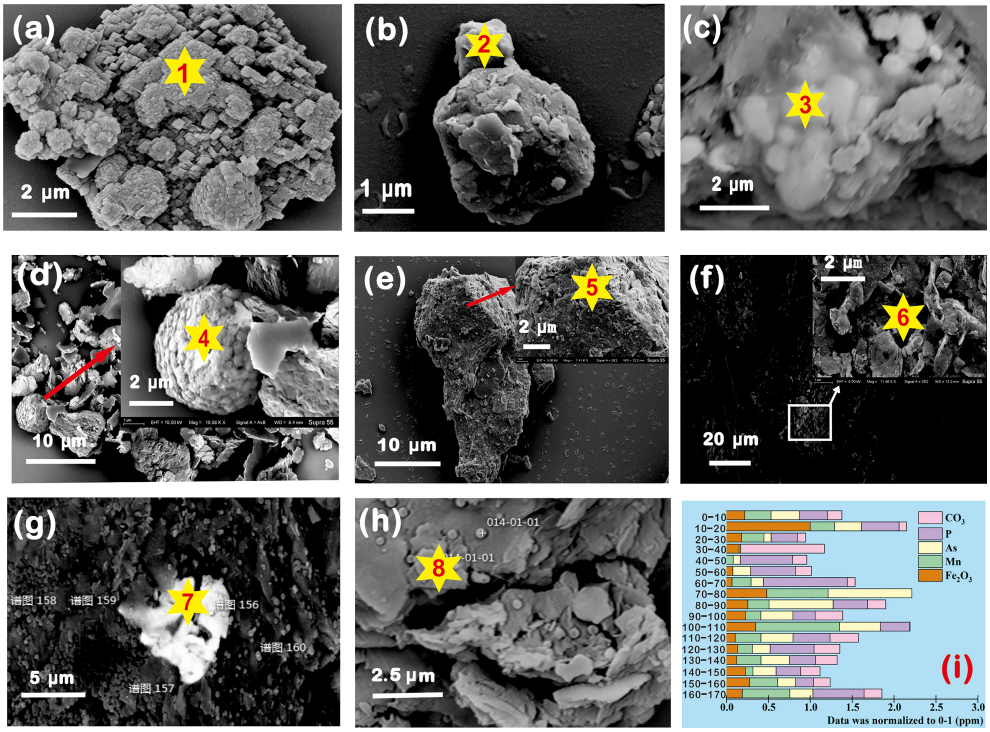

FIGURE 4
Emission-scanning electron microscope (SEM) images of different iron speciations in vertical profile. **(A)** : 40-50 cm; **(B–D)**: 70-80 cm; **(E)**: 80-90 cm; **(F)**: 90-100 cm; **(G)**: 130-140 cm; **(H)**: 160-170 cm and **(I)**: Normalized relative abundance of partial major elements based on X-ray Fluorescence Spectrometer data.

3.4 Correlation of TOC and clustering of the parameters

Using SPSS bivariate Spearman test results, TOC was positively correlated with Fe_{carb} (r = 0.495, P = 0.022), Fe_{Py} (r = 0.542, P = 0.012), Mn (r = 0.419, P = 0.047), P_{CDB} (r = 0.471, P = 0.028), and N (r = 0.554, P = 0.011) and negatively correlated with DA+IP (r = –0.427, P = 0.044) and Dx (50) (r = –0.418, P = 0.047) (Figure 6A; Table S2).

According to the K-means clustering analysis and TOC occurrence correlation index, the final clustering of relevant indicators produced three clusters. Ex-Fe, Mn, Ex-P, OP, N, Dx (50), Fe_{Py}, Fe_{Mag}, and P_{CDB} were in the same cluster as TOC (Figure 6B). Additionally, Fe_{carb}, DA+IP, and Bio-P were in the same cluster, TFe and Fe_{ox} were in the other cluster (Figure 6B).

4 Discussion

4.1 Correlation between TOC and iron states

Most studies have discussed the mechanism for stabilizing TOC by iron minerals in continent soil and in the lakes, salt marsh

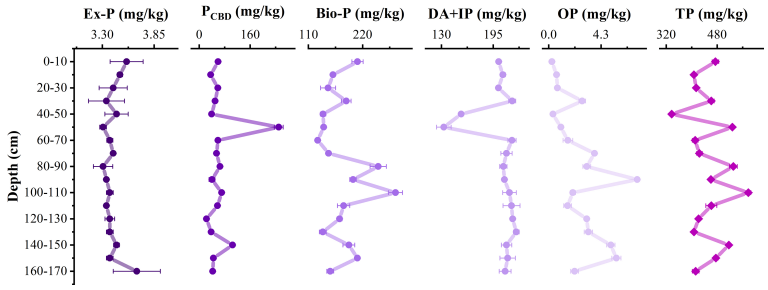

FIGURE 5
Distribution of different forms of phosphorus at vertical profile. Ex-P represents exchangeable or loosely sorbed phosphorus, P_{CDB} represents iron-bound phosphorus, Bio-P represents authigenic apatite, $CaCO_3$-bound P and biogenic apatite, DA+IP represents detrital apatite plus other inorganic phosphorus, OP represents organic phosphorus, and TP represents total phosphorus.

wetlands, or ocean sediments (Lalonde et al., 2012; Ma et al., 2018; Reichenbach et al., 2023; Zhao et al., 2023). The TOC sequestration controlled by iron minerals is complicated and strongly related to the redox conditions of sediments (Hartnett et al., 1998; Hemingway et al., 2019). While study pointed that mineral–organic preservation is an important missing process in current assessments of Earth's long-term carbon cycle (Zhao et al., 2023). Redox conditions of coastal sediments vary greatly in vertical profiles as terrigenous input (Anschutz et al., 2019), and Fe-carbonates are enriched commonly due to dynamic drive of the tide (Lapointe et al., 1992). Therefore, the correlation between different speciations of iron minerals (TFe, Ex-Fe, Fe_{carb}, Fe_{ox}, Fe_{Mag}, and Fe_{Py}) and TOC in the coastal sedimental profile is crucial for understanding the carbon sequestration and sink.

In our study, the spearman test indicates that TOC is positively correlated with Fe_{carb} and Fe_{Py} at 0.01 and 0.05 levels (Figure 6A). We observed Mn-Fe-rich carbonate minerals from the depth of 40–50 cm (Figure 4A, Figure S2-1), and Fe-carbonate with high Ca and Mg contents occurred at 80–90 cm (Figure 4C, Figure S2-4), which may be ferrodolomite (Wen et al., 2007). Fe-carbonate is generally formed in anaerobic sediments mediated by microbial dissimilatory and chemical reduction of Fe(III), accompanied by the transformation of organic matter (Lovley, 1991; Thamdrup, 2000). And high concentrations of goethite, limonite and sulfide, and small amounts of hematite and ferromanganese oxides are formed in the carbonate sediments (Ferguson et al., 1983). Recent studies suggested that the stability of TOC fixed by Fe_{carb} may be transformed due to Fe(III) reduction and Fe(II) oxidation, which will further affect the stability of TOC-Fe_{carb} (Ma et al., 2022). Therefore, we hold the opinion that the formation and occurrence of Fe_{carb} in sediments indicate TOC sink associated with symbiosis with more iron hydroxide.

The chemical zones in the sediment are named the top aerobic oxidation zone, nitrate reduction zone, manganese reduction zone, iron reduction zone, sulfate reduction zone, and methanogenesis zone in sequence (Treude et al., 2014). The type of some authigenic minerals (minerals formed after the detritus has sunk) can indicate REDOX conditions and pH (Kerr et al., 2018). At depths more than 60 cm, the extent of transformation of amorphous iron minerals to high crystalline minerals gradually increased. Pyrite framboids presented at a depth of 70–100 cm (Figure 4D) in the sulfate reduction zone and methanogenesis zone, and TOC content reached a peak of 2.10 g/kg at depths of 100–110 cm (Figure 2). Formation of pyrite occurred in the anoxic environment due to sulfate reduction (Sweeney and Kaplan, 1973; Canfield, 1989) and in methanogenesis zone coupled with sulfur to form pyrite (Wang et al., 2022). Earlier studies have

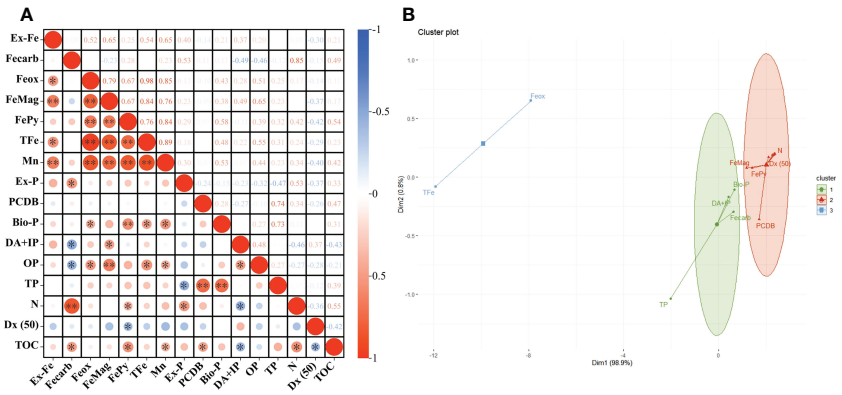

FIGURE 6
Correlation between TOC and different parameters of sediments. "*" and "**" indicated significant correlations at $P < 0.05$ level and $P < 0.01$ level respectively **(A)**. K-means clustering analysis results of different parameters **(B)**.

demonstrated that an increase in TOC inhibits the Formation of Fe exchange by decaying sulfate reduction in sediments (Raiswell and Canfield, 1998). So we suggested that Fe_{Py} indicates TOC sink in a redox range in which the accumulation of TOC is favored due to the low energy efficiency for its mineralization.

Recent reported that 25–62% of total reactive iron, which generally refers to exchangeable, low-crystallinity Fe-bearing minerals, reducible iron oxides (Canfield, 1989; Krom et al., 2002), are responsible for transferring a large quantity of TOC to the carbon sink (Barber et al., 2017). However, our study found that Fe_{ox} was not significantly correlated with TOC at 0.01 and 0.05 levels (Figure 6A), although the reducible oxides Fe_{ox} predominated 62.2%–79.4% in TFe (Figure 6A). The content of Fe_{ox} (0.98–2.99 g/kg) was surplus compared with TOC transition consumption (1.03-2.10 g/kg) and our analysis is that only part of Fe_{ox} participates in the oxidation transformation and stable preservation of TOC, so the indication absence of Fe_{ox} on TOC source-sink due to its abundance relative to TOC content. During coprecipitation of TOC with Fe_{ox}, TOC is sequestered *via* adsorption and incorporation with mineral particle (Lalonde et al., 2012). Multilayers of TOC or macromolecular OC-Fe complexes to preserve TOC when particle surfaces become saturated (Chen et al., 2014; Li et al., 2023). Previous study also reported that there was no correlation between TOC fractions and pH, Fe_{ox}(1.7-4.2 g/Kg), or Al oxides Al_{ox} (1.7-4.2 g/kg) in topsoils (0–20 cm) in subtropical China, while effects of Fe_{ox} on soil properties was significant (Mao et al., 2020), and the specific mineralogical properties and reactivity determine TOC stocks in tropical forest and cropland and was constrained by soil mineralogy (Reichenbach et al., 2023). In additional, recent study found that maybe only carboxyl-rich TOC coprecipitated with ferrihydrite becomes more stable in the solid phase (Zhao et al., 2022), and in turn TOC occurrence can delay the conversion of Fe (hydroxyl) oxide to iron minerals with higher crystallity (Pasakarnis et al., 2014). The content of Fe_{ox} (0.98–2.99 g/Kg) is not very surplus compared with TOC transition consumption (1.03-2.10 g/kg) (Figures 2, 3). Our analysis is that Fe_{ox} is very reactive, and only part of Fe_{ox} participates needed in the oxidation transformation and stable preservation of TOC. We suggested that the non-significant contribution of Fe_{ox} to on carbon sink–source in coastal sediments mainly related to surplus and strong reactivity.

For exchangeable iron (Ex-Fe) is metastable on geological time scales and is a crucial factor for long-term organic carbon storage (Lalonde et al., 2012). Large amounts of TOC in seafloor sediments have been shown to bind to Ex-Fe rather than be controlled by autogenic minerals (Faust et al., 2021). In this study, the Ex-Fe was only 0.5%–1.4% (Figure 3). However, TOC occurrence can delay the conversion of Fe(hydroxyl) oxide to iron minerals with higher crystallite and inhibits the electron transfer between the Ex-Fe in the liquid phase and Fe(III) in solid phase (Zhao et al., 2022). A previous report also suggested that carbon in the minerals may be more mobile and less stable than we previously thought due to iron minerals remaining dynamic and mixed with Ex-Fe in the surrounding liquid phase (Pasakarnis et al., 2014). So we maintained that Ex-Fe was also a vital TOC sink favor factor due to its conducive to the crystallization of iron minerals. Moreover, the low active iron Fe_{Mag}, Ex-Fe were grouped into the same category with Fe_{Py} and TOC in K-means cluster analysis (Figure 6B). So we suggested that Fe_{Mag} may be correlated with TOC sink as for its low activity.

In addition to Fe(III), Mn(III/IV) minerals strongly interact with organic matter in marine sediments (Johnson et al., 2015; Fang and Wang, 2021). The Mn content associated with extractable iron (987.9–2900.7 mg/kg) was about 20.8–46.2 mg/kg (Figure 3), and was positively correlated with TOC (Figure 6). K-means cluster analysis further shows that manganese and TOC were similar (Figure 6B), indicating that this occurrence of manganese contributed to the TOC deposition. Therefore, we propose that Ex-Fe, Fe_{carb}, Fe_{Py}, and manganese are favorable for organic carbon sink in coastal sediments. The correlation between TFe, Fe_{Mag}, Fe_{ox}, and TOC cannot be directly determined at the *P* value of 0.05 to 0.01 level (Figure 7).

4.2 Different forms of phosphorus correlated with TOC

Over the past 30 years, coastal aquaculture industries and terrestrial inputs have contributed to the eutrophication or over-eutrophication of the coastal environment (Smith and Schindler, 2009). According to Berbel et al. (2015), TP between 495–1300 mg/kg in estuarine sediments indicates moderate pollution. The TP extracted from the sediments in the studied area was 337.4–578.0 mg/kg, therefore, the TP status can be classified as moderate eutrophication. We found that Bio-P and DA+IP were the main contributors to sediment TP (Figure 5). DA+IP is predominantly from terrestrial weathering, whereas Bio-P is derived from fluorapatite phosphorus formed by biological metabolism, bioclastic mineralization, and early diagenesis (Gong and Fan, 2010). This indicates that the main sources of phosphorus eutrophication in this area were caused by terrestrial and likely aquaculture input. In addition, active phosphorus (P_{CDB}+OP) is used to characterize the potential phosphorus release from the sediments (Ruban et al., 2001b), the terrestrial sourced P_{CDB} in this study is mostly as high as 50 mg/Kg. Meanwhile, Ex-P is the most active form of phosphorus in sediments as it can easily enter the overlying water (Slomp et al., 1996; Ranjan et al., 2011). The measured bioavailable phosphorus in the sediments was 25.7–

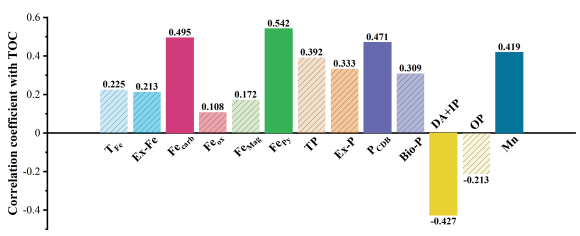

FIGURE 7
Correlation coefficients between different forms of Fe/P/Mn and TOC. The solid bar chart indicated that the variable was significantly correlated with TOC, and the shaded bar chart was not significantly correlated with TOC.

250.6 mg/kg which accounted for 6.10%–47.5% of the TP and indicated significant phosphorus release potential.

It has been revealed that the phosphorus load along the coastal estuaries of China is an important factor for decreasing TOC stability in sediments (Dan et al., 2021). Therefore, investigating the phosphorus load in coastal zones is crucial for accurately assessing the source and sink trend of marine "blue carbon". In the studied coastal sediments, different forms of phosphorus in coastal aquaculture areas correlate differently with TOC. TP and P_{CDB} are positively correlated with TOC, which is consistent with the result reported by Jiang et al. (2014), and the K-means clustering results confirmed that Ex-P, P_{CDB}, and OP can change in the same category as the TOC (Figure 6B). P_{CDB} and OP exhibit high activity and bioavailability (Ruban et al., 2001a; Ruban et al., 2001b; Xie et al., 2011). Previous studies have also confirmed that P_{CDB} has some impact on the eutrophication of overlying water with the alienation of iron oxides (Ruttenberg, 1992), and iron oxides are the main carrier in sediments (Hyacinthe et al., 2006; Fang and Wang, 2021). The phosphorus adsorption capacity gradually decreases with an increase in pH (Shang et al., 1992). In this study, the pH of pore water ranged in 7.45~8.48, P_{CDB} content was thus low in the layers at 10–20, 80–90, and 100–110 cm, where the pH of pore water was higher than 8.00 (Table S1; Figure 5). When the P_{CDB} content is high, the TOC tends to be retained, and vice versa. And P_{CDB}, and Bio-P favored TOC sink due to their high activity and bioavailability on Fe mineral formation.

TOC is negatively correlated with DA+IP (Figure 6A). Studies indicate that DA+IP shares a slight influence of the terrestrial in coastal sediment (Zhou et al., 2016), and it is a crucial P sink refractory in ocean sediment (Ni et al., 2015), which may have a lower tendency to participate in ferric oxyhydroxides transformation than high activity and bioavailability release and re-adsorption P (Chacon et al., 2006; Wen et al., 2023). So we suggested that higher content of DA + IP, and OP indicated TOC source could contribute to sharing the terrestrial's slight influence and a lower tendency to participate in ferric oxyhydroxides transformation.

4.3 Main factors influencing transition from source to sink of TOC

Controlling the TOC sequestration process in sediments is complex. Different speciations of Fe, Mn, P, grain size, and redox conditions are key regulating factors for TOC sequestration (Kothawala et al., 2021; Ma et al., 2022). Most studies have proposed controlling mechanism, which mainly focused on one or a few factors. However, the mechanism coupled with several factors have been hardly discussed. The PLS model is a typical prediction model for the primary and secondary effects of multiple factors on dependent variable changes (Wold et al., 2001). The results showed that PLS had a good predictive fit for TOC (Figure 8B), with a cumulative explanatory variation ratio of TOC as high as 84.5% (Table S3). The factors affecting TOC were ranked according to importance as follows: TIC > clay > Mn > Fe_{Py} > TP >P_{CDB} > TFe> Ex-P >Fe_{Mag} > Bio-P > Fe_{ox}> N > Fe_{carb} > DA+IP > Ex-Fe > OP. Among them, the VIP values of TIC, clay, Mn, P_{CDB}, Fe_{Py}, and TP are all greater than 1, indicating that they are all important factors affecting the occurrence of TOC (Figure 8A). In addition, the PLS model shows a significant negative relationship between Dx(50) and TOC. Clay content has a significant positive relationship with TOC (VIP > 1) (Figure 8), which is consistent with previous studies showing that clay enrichment favors a higher TOC (Gao et al., 2008; Wang et al., 2009). N is significantly positively correlated with TOC, probably due to the direct condensation reaction with TOC, making it difficult for microbe to consume TOC (Janssens et al., 2010).

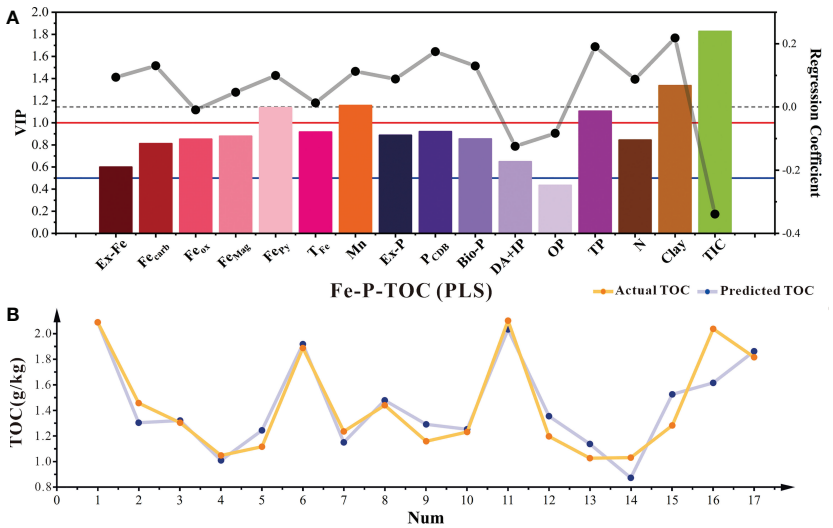

FIGURE 8
PLS model of TOC with different influencing factors in sediments **(A)**. The histogram showed the variable importance of projection (VIP) for each predictive variable; The dot plot showed the regression coefficients of each influence factor. The red solid line, blue solid line, and black dashed line represented different thresholds (VIP=1, VIP=0.5, and RC=0). And the comparison between the predicted results of the PLS model and the actual results **(B)**.

So combining correlation and PLS model prediction results, we suggested that the high contents of Fe_{Py}, Mn, Fe_{Mag}, and Fe_{carb} indicate the conversion of TOC to the sink, which is in accordance with previous studies (Tian et al., 2011; Chalmers and Bustin, 2012; Reithmaier et al., 2020; Li et al., 2021; Zhang et al., 2022). The high Fe_{ox} is also consistent with the conversion of TOC to the source, but the non-siginificant indication of Fe_{ox} on TOC source-sink is due to its abundance relative to TOC content, because only part of Fe_{ox} participates in the oxidation transformation and stable preservation of TOC. For different forms of phosphorus, the high contents of P_{CDB}, Ex-P, and Bio-P represent the transformation of TOC from source to the sink, while the high DA+IP and OP represent the reverse transformation. However, the TP load will lead to the increase of DA+IP and Bio-P simultaneously, the source and sink conversion of TOC could not be directly evaluated here. In addition, Fe_{ox} and P_{CDB} have opposite implications for the source-sink nature of TOC. In the anaerobic iron oxide dissimilated reduction layer, P_{CDB} adsorbed on iron oxides will be released into pore water (Jansson, 1987; Parker and Beck, 2003), and TP eutrophication increases. So, the TOC in the redox transition layer with high Fe_{ox} would convert into the sink. Meanwhile, larger Dx(50) indicates the transformation of TOC to the source, while higher N promote the transformation of TOC to the sink.

5 Conclusions

Iron minerals and phosphates are sensitive factors affecting TOC preservation, but the mechanisms to explain how to effect TOC source-sink transformation still need to be improved. We obtained the following findings. The TFe content was 987.9–2900.7 mg/kg, and Fe_{ox} accounted for 62.2%–79.4%. The TP of the coastal sediments ranged from 337.4–578.0 mg/kg with moderate phosphorus load-release potential, and DA+IP and Bio-P were the leading phosphorus components. Our study suggested that Fe_{carb}, Fe_{Py}, Ex-Fe, Fe_{Mag} have the positive indication for TOC sink mainly associated with symbiosis more iron hydroxide, efficient mineralization, conducive crystallization, and low activity, respectively. While non-significant presentation of Fe_{ox} on TOC source-sink is due to its surplus and strong reactivity. The occurrence of manganese contributed to the TOC deposition due to the strong interaction between Mn(III/IV) minerals and TOC. And P_{CDB}, and Bio-P favored to indicate TOC sink due to their high activity and bioavailability on Fe mineral formation. But higher content of DA+IP, and OP indicated TOC source could be attributed to the slight influence of the terrestrial and lower tendency to participate in ferric oxyhydroxides transformation. Information gained here has important implications for understanding mechanisms and reveals that the control mechanism of TOC environmental occurrence involves the transformation of iron oxide minerals and phosphorus, which forms under the disturbance of human activities.

Data availability statement

The original contributions presented in the study are included in the article/Supplementary Material. Further inquiries can be directed to the corresponding authors.

Author contributions

LG and XL designed the experiments. ZQ, LG, and DC performed all the geochemical experiments and analyzed all the results. ZQ performed the correlation analysis of the Fe-P-TOC model. ZQ and LG prepared the manuscript. XW assisted with the XRF results analysis and part of the language calibration. HL focused on assisting with the SEM experiment and analysis. LG, XL, and YY helped to revise the manuscript. All authors contributed to the article and approved the final submitted version.

Funding

We appreciate the financial support from the National Natural Science Foundation of China (Nos. 41730316, 41902032, 41807351), Key Laboratory of Solid Waste Treatment and Resource Recycling of Ministry of Education (21kfjk04), Interdisciplinary Research Project of Nanjing Normal University (164320H1847), and Nanjing Normal University Talent Training Program (1812200047).

Conflict of interest

The authors declare that the research was conducted in the absence of any commercial or financial relationships that could be construed as a potential conflict of interest.

Publisher's note

Supplementary material

The Supplementary Material for this article can be found online at: https://www.frontiersin.org/articles/10.3389/fmars.2023.1143982/full#supplementary-material

References

Anschutz, P., Bouchet, S., Abril, G., Bridou, R., Tessier, E., and Amouroux, D. (2019). *In vitro* simulation of oscillatory redox conditions in intertidal sediments: N, Mn, fe, and p coupling. *Continental Shelf Res.* 177, 33–41. doi: 10.1016/j.csr.2019.03.007

Arif, M., Ali, S., Ilyas, M., Riaz, M., Akhtar, K., Ali, K., et al. (2021). Enhancing phosphorus availability, soil organic carbon, maize productivity and farm profitability through biochar and organic–inorganic fertilizers in an irrigated maize agroecosystem under semi-arid climate. *Soil Use Management.* 37, 104–119. doi: 10.1111/sum.12661

Bao, Y., Bolan, N. S., Lai, J., Wang, Y., Jin, X., Kirkham, M., et al. (2022). Interactions between organic matter and fe (hydr) oxides and their influences on immobilization and remobilization of metal (loid) s: A review. *Crit. Rev. Environ. Sci. Technol.* 52, 4016–4037. doi: 10.1080/10643389.2021.1974766

Barber, A., Brandes, J., Leri, A., Lalonde, K., Balind, K., Wirick, S., et al. (2017). Preservation of organic matter in marine sediments by inner-sphere interactions with reactive iron. *Sci. Rep.* 7, 1–10. doi: 10.1038/s41598-017-00494-0

Berbel, G. B., Favaro, D. I., and Braga, E. S. (2015). Impact of harbour, industry and sewage on the phosphorus geochemistry of a subtropical estuary in Brazil. *Mar. pollut. bulletin.* 93, 44–52. doi: 10.1016/j.marpolbul.2015.02.016

Boujelben, N., Bouzid, J., Elouear, Z., Feki, M., Jamoussi, F., and Montiel, A. (2008). Phosphorus removal from aqueous solution using iron coated natural and engineered sorbents. *J. hazardous materials.* 151, 103–110. doi: 10.1016/j.jhazmat.2007.05.057

Canfield, D. E. (1989). Reactive iron in marine sediments. *Geochimica Cosmochimica Acta* 53, 619–632. doi: 10.1016/0016-7037(89)90005-7

Canfield, D. E. (1994). Factors influencing organic carbon preservation in marine sediments. *Chem. geology.* 114, 315–329. doi: 10.1016/0009-2541(94)90061-2

Cao, C., Cai, F., Zheng, Y., Wu, C., Lu, H., Bao, J., et al. (2018). Temporal and spatial characteristics of sediment sources on the southern Yangtze shoal over the Holocene. *Sci. Rep.* 8, 1–12. doi: 10.1038/s41598-018-33757-5

Chacon, N., Silver, W. L., Dubinsky, E. A., and Cusack, D. F. (2006). Iron reduction and soil phosphorus solubilization in humid tropical forests soils: The roles of labile carbon pools and an electron shuttle compound. *Biogeochemistry* 78, 67–84. doi: 10.1007/s10533-005-2343-3

Chalmers, G. R. L., and Bustin, R. M. (2012). Geological evaluation of halfway–Doig–Montney hybrid gas shale–tight gas reservoir, northeastern British Columbia. *Mar. Petroleum Geology.* 38, 53–72. doi: 10.1016/j.marpetgeo.2012.08.004

Chen, C., Dynes, J. J., Wang, J., and Sparks, D. L. (2014). Properties of fe-organic matter associations *via* coprecipitation versus adsorption. *Environ. Sci. technology.* 48, 13751–13759. doi: 10.1021/es503669u

Cheng, X., Chen, B., Cui, Y., Sun, D., and Wang, X. (2015). Iron (III) reduction-induced phosphate precipitation during anaerobic digestion of waste activated sludge. *Separation Purification Technol.* 143, 6–11. doi: 10.1016/j.seppur.2015.01.002

Cifuentes, L., Coffin, R., Solorzano, L., Cardenas, W., Espinoza, J., and Twilley, R. (1996). Isotopic and elemental variations of carbon and nitrogen in a mangrove estuary. *Estuarine Coast. Shelf Science.* 43, 781–800. doi: 10.1006/ecss.1996.0103

Dan, S. F., Li, S., Yang, B., Cui, D., Ning, Z., Huang, H., et al. (2021). Influence of sedimentary organic matter sources on the distribution characteristics and preservation status of organic carbon, nitrogen, phosphorus, and biogenic silica in the daya bay, northern south China Sea. *Sci. Total Environment.* 783, 146899. doi: 10.1016/j.scitotenv.2021.146899

Du, J., Liu, K., Huang, J., Han, T., Zhang, L., Anthonio, C. K., et al. (2022). Organic carbon distribution and soil aggregate stability in response to long-term phosphorus addition in different land-use types. *Soil Tillage Res.* 215, 105195. doi: 10.1016/j.still.2021.105195

Du, Y., Ramirez, C. E., and Jaffé, R. (2018). Fractionation of dissolved organic matter by co-precipitation with iron: Effects of composition. *Environ. Processes.* 5, 5–21. doi: 10.1007/s40710-017-0281-4

Fang, T.-H., and Wang, C.-W. (2021). Distribution of geochemical species of p, fe and Mn in surface sediments in the eutrophic estuary, northern Taiwan. *Water* 13, 3075. doi: 10.3390/w13213075

Faust, J. C., Tessin, A., Fisher, B. J., Zindorf, M., Papadaki, S., Hendry, K. R., et al. (2021). Millennial scale persistence of organic carbon bound to iron in Arctic marine sediments. *Nat. Commun.* 12, 1–9. doi: 10.1038/s41467-020-20550-0

Ferguson, J., Burne, R. V., and Chambers, L. A.. (1983). Iron mineralization of peritidal carbonate sediments by continental groundwaters, fisherman bay, South Australia. *Sedimentary Geology* 34 (1), 41–57. doi: 10.1016/0037-0738(83)90034-9

Fookes, P., and Higginbottom, I. (1975). The classification and description of near-shore carbonate sediments for engineering purposes. *Geotechnique* 25, 406–411. doi: 10.1680/geot.1975.25.2.406

Gao, J., Wang, Y., Pan, S., Zhang, R., Li, J., and Bai, F. (2008). Spatial distributions of organic carbon and nitrogen and their isotopic compositions in sediments of the changjiang estuary and its adjacent sea area. *J. Geograph. Sci.* 18, 46–58. doi: 10.1007/s11442-008-0046-0

Giannetta, B., Balint, R., Said-Pullicino, D., Plaza, C., Martin, M., and Zaccone, C. (2020). Fe (II)-catalyzed transformation of fe (oxyhydr) oxides across organic matter fractions in organically amended soils. *Sci. Total Environment.* 748, 141125. doi: 10.1016/j.scitotenv.2020.141125

Golbraikh, A., and Tropsha, A. (2002). Predictive QSAR modeling based on diversity sampling of experimental datasets for the training and test set selection. *J. Computer-Aided Mol. Design.* 16, 357–369. doi: 10.1023/A:1020869118689

Gong, C. S., and Fan, C. X. (2010). Effect factors analysis of phosphorus exchange across lake sediment-water interface under different dissolved oxygen concentration (in Chinese). *Journal of Lake Sciences* 22, 430–436. doi: 10.18307/2010.0317

Hartnett, H. E., Keil, R. G., Hedges, J. I., and Devol, A. H. (1998). Influence of oxygen exposure time on organic carbon preservation in continental margin sediments. *Nature* 391, 572–575. doi: 10.1038/35351

Hedges, J. I., and Keil, R. G. (1995). Sedimentary organic matter preservation: An assessment and speculative synthesis. *Mar. Chem.* 49, 81–115. doi: 10.1016/0304-4203(95)00008-F

Hemingway, J. D., Rothman, D. H., Grant, K. E., Rosengard, S. Z., Eglinton, T. I., Derry, L. A., et al. (2019). Mineral protection regulates long-term global preservation of natural organic carbon. *Nature* 570, 228–231. doi: 10.1038/s41586-019-1280-6

Hermans, M., Astudillo Pascual, M., Behrends, T., Lenstra, W. K., Conley, D. J., and Slomp, C. P. (2021). Coupled dynamics of iron, manganese, and phosphorus in brackish coastal sediments populated by cable bacteria. *Limnol. Oceanogr.* 66, 2611–2631. doi: 10.1002/lno.11776

Huang, J., Hu, B., Qi, K., Chen, W., Pang, X., Bao, W., et al. (2016). Effects of phosphorus addition on soil microbial biomass and community composition in a subalpine spruce plantation. *Eur. J. Soil Biol.* 72, 35–41. doi: 10.1016/j.ejsobi.2015.12.007

Hyacinthe, C., Bonneville, S., and Cappellen, P. V. (2006). Reactive iron(III) in sediments: Chemical versus microbial extractions. *Geochimica Cosmochimica Acta* 70, 4166–4180. doi: 10.1016/j.gca.2006.05.018

Janssens, I. A., Dieleman, W. I. J., Luyssaert, S., Subke, J. A., Reichstein, M., Ceulemans, R., et al. (2010). Reduction of forest soil respiration in response to nitrogen deposition. *Nat. Geosci.* 3, 315–322. doi: 10.1038/ngeo844

Jansson, M. (1987). Anaerobic dissolution of iron-phosphorus complexes in sediment due to the activity of nitrate-reducing bacteria. *Microbial Ecol.* 14, 81–89. doi: 10.1007/BF02011573

Jiang, S., Lin, P., Lin, J., Cai, J., Xu, Y., and Zheng, L. (2014). Distribution characteristics of phosphorus and its environmental significance in the surface sediments of xiamen gulf (in Chinese). *J. Of Trop. Oceanogr.* 33, 72–78. doi: 10.11978/j.issn.1009-5470.2014.03.011

Jiao, N., Herndl, G. J., Hansell, D. A., Benner, R., Kattner, G., Wilhelm, S. W., et al. (2010). Microbial production of recalcitrant dissolved organic matter: Long-term carbon storage in the global ocean. *Nat. Rev. Microbiol.* 8, 593–599. doi: 10.1038/nrmicro2386

Jiao, N., Robinson, C., Azam, F., Thomas, H., Baltar, F., Dang, H., et al. (2014). Mechanisms of microbial carbon sequestration in the ocean–future research directions. *Biogeosciences* 11, 5285–5306. doi: 10.5194/bg-11-5285-2014

Johnson, K., Purvis, G., Lopez-Capel, E., Peacock, C., Gray, N., Wagner, T., et al. (2015). Towards a mechanistic understanding of carbon stabilization in manganese oxides. *Nat. Commun.* 6, 1–11. doi: 10.1038/ncomms8628

Kerr, G., Craw, D., Trumm, D., and Pope, J. (2018). Authigenic realgar and gold in dynamic redox gradients developed on historic mine wastes, new Zealand. *Appl. Geochemistry.* 97, 123–133. doi: 10.1016/j.apgeochem.2018.08.009

Kleber, M., Bourg, I. C., Coward, E. K., Hansel, C. M., Myneni, S. C., and Nunan, N. (2021). Dynamic interactions at the mineral–organic matter interface. *Nat. Rev. Earth Environment.* 2, 402–421. doi: 10.1038/s43017-021-00162-y

Kontny, A., Schneider, M., Eiche, E., Stopelli, E., Glodowska, M., Rathi, B., et al. (2021). Iron mineral transformations and their impact on as (im)mobilization at redox interfaces in as-contaminated aquifers. *Geochimica Et Cosmochimica Acta* 296, 189–209. doi: 10.1016/j.gca.2020.12.029

Kothawala, D. N., Kellerman, A. M., Catalán, N., and Tranvik, L. J. (2021). Organic matter degradation across ecosystem boundaries: The need for a unified conceptualization. *Trends Ecol. Evolution.* 36, 113–122. doi: 10.1016/j.tree.2020.10.006

Krom, M. D., Mortimer, R. J., Poulton, S. W., Hayes, P., Davies, I. M., Davison, W., et al. (2002). In-situ determination of dissolved iron production in recent marine sediments. *Aquat. Sci.* 64, 282. doi: 10.1007/s00027-002-8072-y

Lalonde, K., Mucci, A., Ouellet, A., and Gélinas, Y. (2012). Preservation of organic matter in sediments promoted by iron. *Nature* 483, 198–200. doi: 10.1038/nature10855

Lapointe, B. E., Littler, M. M., and Littler, D. S. (1992). Nutrient availability to marine macroalgae in siliciclastic versus carbonate-rich coastal waters. *Estuaries* 15, 75–82. doi: 10.2307/1352712

Li, Q., Hu, W., Li, L., and Li, Y. (2023). Interactions between organic matter and fe oxides at soil micro-interfaces: Quantification, associations, and influencing factors. *Sci. Total Environ.* 855, 158710. doi: 10.1016/j.scitotenv.2022.158710

Li, H., Santos, F., Butler, K., and Herndon, E. (2021). A critical review on the multiple roles of manganese in stabilizing and destabilizing soil organic matter. *Environ. Sci. Technol.* 55, 12136–12152. doi: 10.1021/acs.est.1c00299

Li, T., Zhong, W., Jing, C., Li, X., Zhang, T., Jiang, C., et al. (2020). Enhanced hydrolysis of p-nitrophenyl phosphate by iron (hydr) oxide nanoparticles: Roles of exposed facets. *Environ. Sci. Technol.* 54, 8658–8667. doi: 10.1021/acs.est.9b07473

Liu, H., Shu, D., Sun, F., Li, Q., Chen, T., Xing, B., et al. (2019). Effect of manganese substitution on the crystal structure and decomposition kinetics of siderite. *J. Thermal Anal. Calorimetry.* 136, 1315–1322. doi: 10.1007/s10973-018-7767-9

Lovley, D. R. (1991). Dissimilatory Fe(III) and Mn(IV) reduction. *Microbiol. Rev.* 55, 259–287. doi: 10.1128/mr.55.2.259-287.1991

Ma, W.-W., Zhu, M.-X., Yang, G.-P., and Li, T. (2018). Iron geochemistry and organic carbon preservation by iron (oxyhydr) oxides in surface sediments of the East China Sea and the south yellow Sea. *J. Mar. Syst.* 178, 62–74. doi: 10.1016/j.jmarsys.2017.10.009

Ma, W.-W., Zhu, M.-X., Yang, G.-P., Li, T., Li, Q.-Q., Liu, S.-H., et al. (2022). Stability and molecular fractionation of ferrihydrite-bound organic carbon during iron reduction by dissolved sulfide. *Chem. Geology.* 594, 120774. doi: 10.1016/j.chemgeo.2022.120774

Macreadie, P. I., Anton, A., Raven, J. A., Beaumont, N., Connolly, R. M., Friess, D. A., et al. (2019). The future of blue carbon science. *Nat. Commun.* 10, 3998. doi: 10.1038/s41467-019-11693-w

Macreadie, P. I., Costa, M. D., Atwood, T. B., Friess, D. A., Kelleway, J. J., Kennedy, H., et al. (2021). Blue carbon as a natural climate solution. *Nat. Rev. Earth Environment.* 2, 826–839. doi: 10.1038/s43017-021-00224-1

Mao, X., Van Zwieten, L., Zhang, M., Qiu, Z., Yao, Y., and Wang, H. (2020). Soil parent material controls organic matter stocks and retention patterns in subtropical China. *J. Soils Sediments.* 20, 2426–2438. doi: 10.1007/s11368-020-02578-3

März, C., Riedinger, N., Sena, C., and Kasten, S. (2018). Phosphorus dynamics around the sulphate-methane transition in continental margin sediments: Authigenic apatite and fe (II) phosphates. *Mar. Geology.* 404, 84–96. doi: 10.1016/j.margeo.2018.07.010

Nakamura, J., Lall, U., Kushnir, Y., and Camargo, S. J. (2009). Classifying north Atlantic tropical cyclone tracks by mass moments. *J. Climate.* 22, 5481–5494. doi: 10.1175/2009JCLI2828.1

Ni, J., Lin, P., Zhen, Y., Yao, X., and Guo, L. (2015). Distribution, source and chemical speciation of phosphorus in surface sediments of the central pacific ocean. *Deep Sea Res. Part I: Oceanograph. Res. Pap.* 105, 74–82. doi: 10.1016/j.dsr.2015.08.008

O'loughlin, E. J., Gorski, C. A., and Scherer, M. (2015). Effects of phosphate on secondary mineral formation during the bioreduction of akaganeite (β-FeOOH): Green rust versus framboidal magnetite. *Curr. Inorganic Chem.* 5, 214–224. doi: 10.2174/1877944105666150421001126

Parker, A. K., and Beck, M. B. (2003). Iron reduction and phosphorus release from lake sediments and bt horizon soil: Incubation studies to explore phosphorus cycling. Georia Tech. Available at: http://hdl.handle.net/1853/48363.

Pasakarnis, T., Mccormick, M. L., Parkin, G. F., Thompson, A., and Scherer, M. M. (2014). FeIIaq–FeIIIoxide electron transfer and fe exchange: Effect of organic carbon. *Environ. Chem.* 12, 52–63. doi: 10.1071/EN14035

Poulton, S. W., and Canfield, D. E. (2005). Development of a sequential extraction procedure for iron: Implications for iron partitioning in continentally derived particulates. *Chem. Geology.* 214, 209–221. doi: 10.1016/j.chemgeo.2004.09.003

R Core Team. (2022). *R: A language and environment for statistical computing*. R Foundation for Statistical Computing, Vienna, Austria. Available at: https://www.R-project.org/.

Raiswell, R., and Canfield, D. E. (1998). Sources of iron for pyrite formation in marine sediments. *Am. J. Science.* 298, 219–245. doi: 10.2475/ajs.298.3.219

Ranjan, R. K., Ramanathan, A., Chauhan, R., and Singh, G. (2011). Phosphorus fractionation in sediments of the pichavaram mangrove ecosystem, south-eastern coast of India. *Environ. Earth Sci.* 62, 1779–1787. doi: 10.1007/s12665-010-0659-3

Reichenbach, M., Fiener, P., Hoyt, A., Trumbore, S., Six, J., and Doetterl, S. (2023). Soil carbon stocks in stable tropical landforms are dominated by geochemical controls and not by land use. *Global Change Biol.* 00, 1–17. doi: 10.1111/gcb.16622

Reithmaier, G. M. S., Johnston, S. G., Junginger, T., Goddard, M. M., Sanders, C. J., Hutley, L. B., et al. (2021). Alkalinity production coupled to pyrite formation represents an unaccounted blue carbon sink. *Global Biogeochem. Cycles* 35, e2020GB006785. doi: 10.1029/2020GB006785

Ruban, V., Lopez-Sanchez, J. F., Pardo, P., Rauret, G., Muntau, H., and Quevauviller, P. (2001a). Development of a harmonised phosphorus extraction procedure and certification of a sediment reference material. *J. Environ. Monitoring.* 3, 121–125. doi: 10.1039/b005672n

Ruban, V., Lopez-Sanchez, J. F., Pardo, P., Rauret, G., Muntau, H., and Quevauviller, P. (2001b). Harmonized protocol and certified reference material for the determination of extractable contents of phosphorus in freshwater sediments - a synthesis of recent works. *Fresenius J. Analytical Chem.* 370, 224–228. doi: 10.1007/s002160100753

Ruttenberg, K. C. (1992). Development of a sequential extraction method for different forms of phosphorus in marine sediments. *Limnol. Oceanogr.* 37, 1460–1482. doi: 10.4319/lo.1992.37.7.1460

Sarkar, B., Singh, M., Mandal, S., Churchman, G. J., and Bolan, N. S. (2018). Clay minerals–organic matter interactions in relation to carbon stabilization in soils. *Future Soil carbon.* 4, 71–86. doi: 10.1016/B978-0-12-811687-6.00003-1

Schad, M., Halama, M., Jakus, N., Robbins, L. J., Warchola, T. J., Tejada, J., et al. (2021). Phosphate remobilization from banded iron formations during metamorphic mineral transformations. *Chem. Geology.* 584, 120489. doi: 10.1016/j.chemgeo.2021.120489

Shang, C., Stewart, J. W. B., and Huang, P. M. (1992). pH effect on kinetics of adsorption of organic and inorganic phosphates by short-range ordered aluminum and iron precipitates. *Geoderma* 53, 1–14. doi: 10.1016/0016-7061(92)90017-2

Shi, J., Gong, J., Li, X., Zhang, Z., Zhang, W., Li, Y., et al. (2022). Plant–microbial linkages regulate soil organic carbon dynamics under phosphorus application in a typical temperate grassland in northern China. *Agriculture Ecosyst. Environment.* 335, 108006. doi: 10.1016/j.agee.2022.108006

Shi, Z., Huang, X. D., Ai, L., Fang, N., and Wu, G. (2014). Quantitative analysis of factors controlling sediment yield in mountainous watersheds. *Geomorphology* 226, 193–201. doi: 10.1016/j.geomorph.2014.08.012

Singh, P., Udayana, S. K., Mukherjee, S., Jaison, M., Das, B. P., and Mehjabeen, (2021). Nutrient biogeochemistry of coastal soils. *Pharma Innovation.* 10, 972–976. Available at: https://www.thepharmajournal.com/archives/?year=2021&vol=10&issue=7&ArticleId=6983.

Slomp, C. P., Epping, E. H. G., Helder, W., and Raaphorst, W. V. (1996). A key role for iron-bound phosphorus in authigenic apatite formation in north Atlantic continental platform sediments. *J. Mar. Res.* 54, 1179–1205. doi: 10.1357/0022240963213745

Smith, V. H., and Schindler, D. W. (2009). Eutrophication science: Where do we go from here? *Trends Ecol. evolution.* 24, 201–207. doi: 10.1016/j.tree.2008.11.009

Sweeney, R., and Kaplan, I. (1973). Pyrite framboid formation; laboratory synthesis and marine sediments. *Economic Geology.* 68, 618–634. doi: 10.2113/gsecongeo.68.5.618

Tang, J., Ye, S., Chen, X., Yang, H., Sun, X., Wang, F., et al. (2018). Coastal blue carbon: Concept, study method, and the application to ecological restoration. *Sci. China Earth Sci.* 61, 637–646. doi: 10.1007/s11430-017-9181-x

Thamdrup, B. (2000). Bacterial manganese and iron reduction in aquatic sediments. *Adv. Microbial Ecol.* 16, 41–84. doi: 10.1007/978-1-4615-4187-5_2

Tian, Q., Yang, T., Zhang, S., Shi, P., Zhang, J., and Fan, Z. (2011). Magnetic susceptibility and its environmental significance of lake sediments in Tibet plateau (in Chinese). *Acta Sedimentol. Sinica.* 29, 143–150. doi: 10.14027/j.cnki.cjxb.2011.01.011

Trefethen, J. M. (1950). Classification of sediments. *Am. J. Science.* 248, (1) 55–(1) 62. doi: 10.2475/ajs.248.1.55

Treude, T., Krause, S., Maltby, J., Dale, A. W., Coffin, R., and Hamdan, L. J. (2014). Sulfate reduction and methane oxidation activity below the sulfate-methane transition zone in alaskan Beaufort Sea continental margin sediments: Implications for deep sulfur cycling. *Geochimica Cosmochimica Acta* 144, 217–237. doi: 10.1016/j.gca.2014.08.018

Wan, B., Yang, P., Jung, H., Zhu, M., Diaz, J. M., and Tang, Y. (2021). Iron oxides catalyze the hydrolysis of polyphosphate and precipitation of calcium phosphate minerals. *Geochimica Cosmochimica Acta* 305, 49–65. doi: 10.1016/j.gca.2021.04.031

Wang, B., Lei, H., and Huang, F. (2022). Impacts of sulfate-driven anaerobic oxidation of methane on the morphology, sulfur isotope, and trace element content of authigenic pyrite in marine sediments of the northern south China Sea. *Mar. Petroleum Geology.* 139, 105578. doi: 10.1016/j.marpetgeo.2022.105578

Wang, H., Xiao, C., Li, C., Li, Y., Zhang, W., Fu, X., et al. (2009). Spatial variability of organic carbon in the soil of wetlands in chongming dongtan and its influential factors (in Chinese). *J. Agro-Environment Science.* 28, 1522–1528. Available at: https://kns.cnki.net/kcms2/article/abstract?v=pbgqCeizVJPi8XOORhwDuKDIU5yDlOn4vsQkmJn_xC6GeIEDVS8lTPFaVSG2cfBfjFaOUOmMtHVfN0oWDzHJ_FJ9_Fih_AyP0vaJ9D3wce4AKweHvlYBg==&uniplatform=NZKPT&language=CHS.

Wen, S., Lu, Y., Dai, J., Huang, X., An, S., Liu, J., et al. (2023). Stability of organic matter-iron-phosphate associations during abiotic reduction of iron. *J. Hazardous Materials* 449, 131016. doi: 10.1016/j.jhazmat.2023.131016

Wen, H., Zheng, R., Geng, W., Fan, M., and Wang, M. (2007). Characteristics of rare earth elements of lacustrine exhalative rock in the xiagou formation of lower Cretaceous in qingxi sag, jiuxi basin. *Front. Earth Sci. China.* 1, 333–340. doi: 10.1007/s11707-007-0040-3

Weng, L., Van Riemsdijk, W. H., and Hiemstra, T. (2012). Factors controlling phosphate interaction with iron oxides. *J. Environ. quality.* 41, 628–635. doi: 10.2134/jeq2011.0250

Wold, S. (1995). PLS for multivariate linear modeling. In *Chemometric Methods Mol. Design, Methods and Principles in Medicinal Chemistry* 2, 195–218. doi: 10.1002/9783527615452.ch4

Wold, S., Sjöström, M., and Eriksson, L. (2001). PLS-regression: A basic tool of chemometrics. *Chemometrics Intelligent Lab. Syst.* 58, 109–130. doi: 10.1016/S0169-7439(01)00155-1

Xia, S., Song, Z., Van Zwieten, L., Guo, L., Yu, C., Wang, W., et al. (2022). Storage, patterns and influencing factors for soil organic carbon in coastal wetlands of China. *Global Change Biol.* 28, 6065–6085. doi: 10.1111/gcb.16325

Xie, C., Tang, J., Zhao, J., Wu, D., and Xu, X. (2011). Comparison of phosphorus fractions and alkaline phosphatase activity in sludge, soils, and sediments. *J. Soils Sediments.* 11, 1432–1439. doi: 10.1007/s11368-011-0429-1

Xu, X., Shi, R., Lv, C.-Y., Liu, H., Yang, W., Qian, S., et al. (2021). Hydrodynamic-driven changes in the source and composition of sedimentary organic matter *via* grain size distribution in shallow lakes. *J. Geophys. Res.: Biogeosci.* 126, e2021JG006502. doi: 10.1029/2021JG006502

Yalcin, M. G., Nyamsari, D., Ozer Atakoglu, O., and Yalcin, F. (2022). Chemical and statistical characterization of beach sand sediments: Implication for natural and anthropogenic origin and paleo-environment. *Int. J. Environ. Sci. Technol.* 19, 1335–1356. doi: 10.1007/s13762-021-03280-8

Yan, X., Yang, W., Muneer, M. A., Zhang, S., Wang, M., and Wu, L. (2021). Land-use change affects stoichiometric patterns of soil organic carbon, nitrogen, and phosphorus in the red soil of southeast China. *J. Soils Sediments.* 21, 2639–2649. doi: 10.1007/s11368-021-02953-8

Yoon, S.-Y., Lee, C.-G., Park, J.-A., Kim, J.-H., Kim, S.-B., Lee, S.-H., et al. (2014). Kinetic, equilibrium and thermodynamic studies for phosphate adsorption to magnetic iron oxide nanoparticles. *Chem. Eng. J.* 236, 341–347. doi: 10.1016/j.cej.2013.09.053

Zhang, C., Xiao, Q., Sun, P. A., Gao, X., Guo, Y., Miao, Y., et al. (2022). Progress on karst carbon cycle and carbon sink effect study and perspective. *Bull. Geol. Sci. Technol.* 41, 190–198. doi: 10.19509/j.cnki.dzkq.2022.0193

Zhang, Y., Zhao, M., Cui, Q., Fan, W., Qi, J., Chen, Y., et al. (2017). Processes of coastal ecosystem carbon sequestration and approaches for increasing carbon sink. *Sci. China Earth Sci.* 60, 809–820. doi: 10.1007/s11430-016-9010-9

Zhao, M., Mills, B. J., Homoky, W. B., and Peacock, C. L. (2023). Oxygenation of the earth aided by mineral–organic carbon preservation. *Nat. Geosci.* 16, 262–267. doi: 10.1038/s41561-023-01133-2

Zhao, Y., Moore, O. W., Xiao, K.-Q., Curti, L., Fariña, A. O., Banwart, S. A., et al. (2022). The role and fate of organic carbon during aging of ferrihydrite. *Geochimica Cosmochimica Acta* 335, 339–355. doi: 10.1016/j.gca.2022.07.003

Zhou, F., Gao, X., Yuan, H., Song, J., Chen, C.-T. A., Lui, H.-K., et al. (2016). Geochemical forms and seasonal variations of phosphorus in surface sediments of the East China Sea shelf. *J. Mar. Syst.* 159, 41–54. doi: 10.1016/j.jmarsys.2016.03.005

frontiers | Frontiers in Marine Science

TYPE Original Research
PUBLISHED 20 April 2023
DOI 10.3389/fmars.2023.1182668

OPEN ACCESS

EDITED BY
Hermano Melo Queiroz,
University of São Paulo, Brazil

REVIEWED BY
Yanbin Li,
Ocean University of China, China
Chen-Feng You,
National Cheng Kung University, Taiwan

*CORRESPONDENCE
Kohei Matsuoka
matsuoka.kouhei.56s@st.kyoto-u.ac.jp

SPECIALTY SECTION
This article was submitted to Marine Biogeochemistry, a section of the journal Frontiers in Marine Science

RECEIVED 09 March 2023
ACCEPTED 03 April 2023
PUBLISHED 20 April 2023

CITATION
Matsuoka K, Tatsuyama T, Takano S and Sohrin Y (2023) Distribution of stable isotopes of Mo and W from a river to the ocean: signatures of anthropogenic pollution. *Front. Mar. Sci.* 10:1182668. doi: 10.3389/fmars.2023.1182668

Distribution of stable isotopes of Mo and W from a river to the ocean: signatures of anthropogenic pollution

Kohei Matsuoka*, Tomomichi Tatsuyama, Shotaro Takano and Yoshiki Sohrin

Institute for Chemical Research, Kyoto University, Uji, Japan

Molybdenum and tungsten are redox-sensitive elements, and their stable isotope ratios have attracted attention as paleoceanographic proxies. However, our knowledge of the distribution of stable Mo and W isotopes in the modern hydrosphere remains limited. In this study, we provided the concentrations and isotope ratios of dissolved Mo and W in the oceans (the North Pacific and Indian Oceans), marginal seas (the East China Sea and Sea of Japan), and a river-estuary system in Japan (from the Uji-Yodo rivers to Osaka Bay). In the North Pacific and Indian Oceans, the W concentration was 48.2 ± 6.2 pmol/kg (ave ± 2sd, n = 109), $\delta^{186/184}$W was 0.52 ± 0.06 ‰, the Mo concentration was 105.1 ± 8.0 nmol/kg, and $\delta^{98/95}$Mo was 2.40 ± 0.06 ‰. The results indicate that W has the constant concentration and isotopic composition in the modern ocean as well as Mo. In the East China Sea and the Sea of Japan, the W concentration and $\delta^{186/184}$W in the upper water (< 1000 m depth) were different from those in the ocean (W = 56 ± 18 pmol/kg, $\delta^{186/184}$W = 0.45 ± 0.06 ‰, n = 24). However, the concentrations in deeper water were congruent with those in the oceans (W = 49.9 ± 7.6 pmol/kg, $\delta^{186/184}$W = 0.50 ± 0.02 ‰, n = 7). The Mo concentration was 105.4 ± 3.1 nmol/kg and $\delta^{98/95}$Mo was 2.36 ± 0.03 ‰ (n = 31) throughout the water column, congruent with those in the ocean. In the Uji River-Yodo River-Osaka Bay system, the W concentration reached 1074 pmol/kg and $\delta^{186/184}$W reached 0.20 ‰. We propose that the enrichment of W with a low $\delta^{186/184}$W in the river-estuary system and marginal seas is caused by anthropogenic pollution. Anthropogenic Mo pollution was not detected in marginal seas. However, the Mo concentration and $\delta^{98/95}$Mo showed high anomalies above the mixing line of river water and seawater in the lower Yodo River and Osaka Bay, implying possible anthropogenic pollution of Mo in the metropolitan area.

KEYWORDS

molybdenum, tungsten, isotopic composition, anthropogenic pollution, GEOTRACES

1 Introduction

The chemical species of dissolved molybdenum and tungsten depend on the concentrations of oxygen and sulfide in the aquatic environment (Emerson and Huested, 1991; Helz et al., 1996; Cui et al., 2021), which in turn change their concentrations and stable isotope ratios in the sediments (Tsujisaka et al., 2019), making them useful redox proxies for paleoceanography. In modern aquatic environments, the concentrations and stable isotope ratios of Mo and W are of interest as tracers of oceanic cycles because the stable isotope ratios of Mo and W change owing to sources and chemical processes, such as adsorption on particles (Goldberg et al., 2009; Kashiwabara et al., 2017).

Mo has seven stable isotopes: ^{92}Mo (14.84%), ^{94}Mo (9.25%), ^{95}Mo (15.92%), ^{96}Mo (16.68%), ^{97}Mo (9.55%), ^{98}Mo (24.13%), and ^{100}Mo (9.63%) (De Laeter et al., 2003). Among Mo isotope ratios, the ^{98}Mo/^{95}Mo ratio is conventionally used as a tracer. The isotope ratio of Mo is presented as the delta value (‰) relative to that of the NIST SRM 3134 standard, which is defined as +0.25 ‰ for easy comparison with literature (Nagler et al., 2014):

$$\delta^{98/95}\mathrm{Mo} = \left(\frac{(^{98}\mathrm{Mo}/^{95}\mathrm{Mo})_{\mathrm{sample}}}{(^{98}\mathrm{Mo}/^{95}\mathrm{Mo})_{\mathrm{NIST\ SRM\ 3134}}} - 1\right) \times 1000 + 0.25 \quad (1)$$

Mo is the most abundant transition metal in the modern oxic ocean, with a concentration of ~ 107 nmol/kg (Nakagawa et al., 2012), where it exists as a hexavalent oxoacid ion (MoO_4^{2-}). Mo shows a conservative vertical profile because MoO_4^{2-} is hardly scavenged, and its amount in the surface water is much higher than that assimilated by phytoplankton. Its concentration is globally constant because the residence time of 740,000 years in the ocean (Firdaus et al., 2008) is sufficiently longer than the time required for oceanic general circulation. The isotopic composition of Mo is also homogeneous in the ocean; $\delta^{98/95}$Mo = 2.34 ± 0.10‰ (Nakagawa et al., 2012), which is higher than $\delta^{98/95}$Mo = –0.08 ± 0.46‰ in the continental crust (Nagler et al., 2014; Willbold and Elliott, 2017). Mo is adsorbed onto oxide minerals, such as manganese oxides and iron hydroxides (Bertine and Turekian, 1973; Shimmield and Price, 1986; Kashiwabara et al., 2017). Lighter isotopes of Mo tend to be adsorbed more readily, resulting in higher $\delta^{98/95}$Mo values in the oxic seawater than those found in the continental crust (Barling et al., 2001; Siebert et al., 2003). It has been experimentally confirmed that Mo adsorption on manganese oxides results in a positive isotope fractionation of +2.0–3.0 ‰ for dissolved species (Barling and Anbar, 2004). However, it has been experimentally confirmed that Mo adsorption on iron oxides and hydroxides causes a positive isotope fractionation of dissolved species of +1.0–2.0 ‰ (Goldberg et al., 2009). In general, river water has lower Mo concentrations than seawater, and the concentrations and isotopic ratios of Mo are affected by the geology, ecosystem, and chemical reactions, resulting in a wide range of values (Mo = 0.7–139 nM, $\delta^{98/95}$Mo = 0.2–1.4 ‰) (Anbar and Rouxel, 2007; Neubert et al., 2011). The impact of anthropogenic Mo pollution on river water and seawater has also been suggested (Wong et al., 2021). Under a strong reducing environment, Mo reacts with H_2S to form thiomolybdate ion $MoO_xS_{4-x}^{2-}$ ($0 \le x \le 3$). When the concentration of H_2S exceeds 11 µmol/kg, MoO_4^{2-} is quantitatively converted to MoS_4^{2-} (Cui et al., 2021), which is readily adsorbed on iron sulfides and organic matters in sediments and is removed from the water column. In addition, molybdenum sulfides are formed by reduction to Mo(IV), which causes the depletion of Mo in submarine high-temperature hydrothermal fluids (Ishibashi and Urabe, 1995). Under euxinic conditions, the most of Mo is removed from the water to the sediments, resulting in small isotope fractionation (Anbar and Rouxel, 2007). Therefore, the Mo concentration and $\delta^{98/95}$Mo in sediments vary greatly depending on redox conditions, being useful proxies for paleoceanographic studies (Rimmer, 2004; Tribovillard et al., 2006; Pattan and Pearce, 2009). In the modern euxinic water columns of the Black Sea and the Baltic Sea, dissolved Mo is depleted in concentration and enriched in the heavy isotope ($\delta^{98/95}$Mo values up to+2.9‰) (Nägler et al., 2011).

W has five stable isotopes: ^{180}W (0.12%), ^{182}W (26.50%), ^{183}W (14.31%), ^{184}W (30.64%), and ^{186}W (28.43%) (De Laeter et al., 2003). Among W isotope ratios, the ^{186}W/^{184}W ratio is conventionally used as a tracer. The isotope ratio of W is presented as the delta value (‰) relative to the NIST SRM 3163 standard (Tsujisaka et al., 2019):

$$\delta^{186/184}\mathrm{W} = \left(\frac{(^{186}\mathrm{W}/^{184}\mathrm{W})_{\mathrm{sample}}}{(^{186}\mathrm{W}/^{184}\mathrm{W})_{\mathrm{NIST\ SRM\ 3163}}} - 1\right) \times 1000 \quad (2)$$

In modern oxic seawater, W exists as a hexavalent oxoacid (WO_4^{2-}) and exhibits a conserved vertical profile similar to that of MoO_4^{2-}. However, in modern oxic ocean, the W concentration was approximately 49 pmol/kg (Sohrin et al., 1987; Sohrin et al., 1999), which is only 1/2000 of the Mo concentration. This was due to the high partitioning ratio of WO_4^{2-} to iron hydroxides and manganese oxides (Sohrin et al., 1987; Kashiwabara et al., 2013). Consequently, the oceanic residence time of W ranges from 14,000 to 61,000 years, which is shorter than that of Mo but longer than the oceanic circulation time (Sohrin et al., 1987; Sohrin et al., 1999). In modern rivers, the W concentration varies in the range of 26–1000 pmol/kg (Firdaus et al., 2008), and the average W concentration has been reported to be 160 pmol/kg (Li, 2000). W adsorption on manganese oxides has been experimentally confirmed to cause a positive isotope fractionation of dissolved species of +0.7–1.0 ‰, and iron oxides and hydroxides cause a positive isotope fractionation of +0.7–0.8 ‰ (Kashiwabara et al., 2017). The isotopic ratios of W in seawater have been reported at several stations in the North Pacific Ocean, Atlantic Ocean, and South China Sea (Fujiwara et al., 2020; Kurzweil et al., 2021). According to these results, $\delta^{186/184}$W is 0.55 ± 0.12 ‰ in the North Pacific Ocean, 0.55 ± 0.06 ‰ in the Atlantic Ocean, and 0.51 ± 0.05 ‰ in the South China Sea. Only one study reported a stable isotopic ratio of W in river water (Yang et al., 2022). Under strongly reducing conditions, W forms thiotungstate ions but requires a higher H_2S concentration than Mo (Cui et al., 2021). Thiotungstate ions cannot be easily removed by adsorption onto solids. In addition, W is hardly reduced to W(IV) and does not precipitate as sulfides. These factors result in high W concentrations in submarine hydrothermal fluids (Kishida et al., 2004). However, there is no data on the stable isotope ratios of W in hydrothermal fluids. W is also expected to be a proxy for paleoceanography.

However, further data collection from the modern hydrosphere is required to better understand the circulation of W.

We recently developed a method for determining the stable isotope ratios of Mo and W in seawater (Fujiwara et al., 2020). In this method, Mo and W are pre-concentrated by solid-phase extraction using an 8-hydroxyquinoline resin (TSK-8HQ) and chromatography using an AG1-X8 anion exchange resin. In the present study, we improved this method and applied it to seawater and river water samples. A total of 150 samples collected from the open ocean (Pacific and Indian Oceans), marginal seas (East China Sea and Sea of Japan), and Yodo River system, including Osaka Bay in a metropolitan area, were analyzed. We discuss the features of the distribution of Mo and W in the modern hydrosphere and suggest the anthropogenic pollution of Mo and W in aquatic environments.

2 Material and methods

2.1 Reagents and materials

Reagent-grade HF, HCl, HNO_3, H_2O_2, tetramethylammonium hydroxide (TMAH), and NH_3 (FUJIFILM Wako Pure Chemical, Japan) were used for cleaning and analysis. The NIST SRM 3134 and NIST SRM 3163 standards (National Institute of Standards and Technology, USA) were used to prepare standard solutions for the determination of the isotopic compositions and concentrations of Mo and W, respectively (Irisawa and Hirata, 2006). Standard solutions of Ru and Re (AccuStandard, USA) were diluted and added to the preconcentrated sample solutions as external element standards for Mo and W, respectively. Ultrapure water (UW) prepared using a Milli-Q Gradient-A10 system (Merck Millipore, Germany) was used for cleaning and analysis. Standard solutions of Mo and W were prepared by diluting 1000 ppm standard solutions for atomic absorption spectrometry (FUJIFILM Wako Pure Chemical) and were used for preliminary experiments.

We used perfluoroalkoxy alkane (PFA) vials (Savillex, USA) for chemical separation and low-density polyethylene (LDPE) bottles (Nalgene Nunc Inc., USA) for solution storage and preparation. All the vials and bottles were soaked in 5% SCAT (Nacalai Tesque, Japan) overnight and rinsed with UW at least five times. Next, they were soaked in 4 mol/kg HCl overnight and rinsed with UW 5 times. Finally, the samples were soaked in 2 mol/kg NH_3 overnight and rinsed with MQW 5 times. Other materials such as micropipette tips, columns, and tubes were cleaned similarly.

We synthesized the TSK-8HQ resin following previous studies (Firdaus et al., 2007; Fujiwara et al., 2020). The TSK-8HQ resin (dry weight ~200 mg, adsorption capacity of W 1.6 mmol/g) was packed in a polypropylene column (Type L, Tomoe Works, Japan) with an inner diameter of 12 mm and a bed height of 6.5 mm and stopped with polyethylene frits.

Anion exchange resin AG1-X8 (200–400 mesh, Bio-Rad, USA) was cleaned with five aliquots of ethanol until the cleaning solvent became colorless. The resin was rinsed with UW. Approximately 400 mg of AG1 X8 resin was charged in a polypropylene column (Mini-column S, Muromachi Chemicals, Japan) with an internal diameter of 5 mm and a bed height of 30 mm.

2.2 Sampling

Samples were collected from the Pacific Ocean, Indian Ocean, East China Sea, Sea of Japan, Osaka Bay, and the Uji and Yodo Rivers (Figure 1). Seawater samples from the Pacific Ocean were collected during cruises KH-10-2, KH-14-6, and KH-17-3 of the Hakuho Maru scientific research vessel. Seawater samples from the Indian Ocean were collected during cruise KH-09-5; those from the East China Sea were collected during cruise KH-15-3; and those from the Sea of Japan were collected during the KH-10-2 cruise. These stations are shown in Figure 1A. Sampling was conducted using a clean system (Sohrin and Bruland, 2011). A portion of seawater for the determination of dissolved species was filtered through a 0.8/0.2 µm pore size AcroPak capsule filter (PALL, USA), collected in a 5 l polyethylene container (SEKISUI SEIKEI, Japan), added with HCl up to 40 mmol/kg, and stored at room temperature.

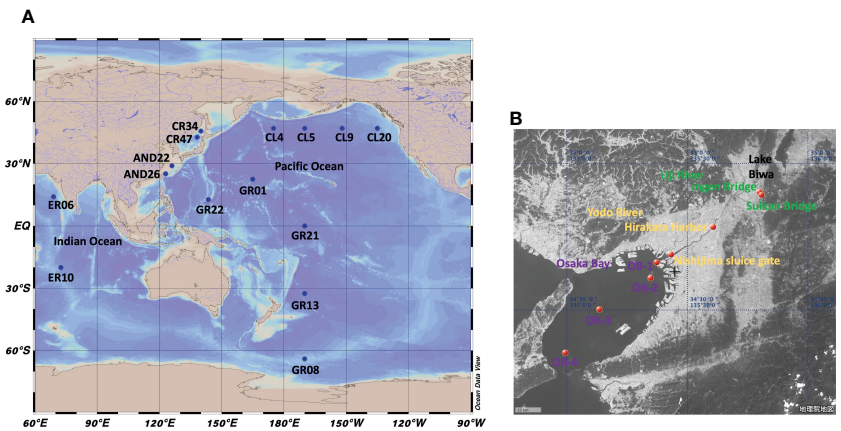

FIGURE 1
Maps showing sampling points of this study. **(A)**: Global map. **(B)**: Map of the Uji River-Yodo River-Osaka Bay system.

The sampling points in the Yodo River system are shown in Figure 1B. In the Yodo River system, water flows from Lake Biwa, the largest lake in Japan, through the Uji and Yodo Rivers, to Osaka Bay. The Yodo River flows in the Osaka metropolitan area. River water samples were simultaneously collected and filtered on-site using a MasterFlex peristaltic pump (Cole-Parmer, USA). PharMed tube (06508-13, SAINT-GOBAIN, France) was used for the flow path, one end was inserted into the river and the other was connected to a Millex-HP 0.45 μm filter (Merck Millipore, Germany). The filtered sample was collected in a 5 l polyethylene container, brought back to our laboratory, and HCl was added up to 40 mmol/kg (pH 1.4).

Samples from Osaka Bay were collected using a clean 5 l Niskin-X water sampler from the fishing boat Kaiko Maru. Within a week after sampling, samples were filtered through a Millex-HP 0.45 μm filter and added with HCl up to 40 mmol/kg (pH 1.4).

2.3 Chemical separation

2.3.1 Solid-phase extraction using the chelating resin TSK-8HQ

The solid-phase extraction procedure was almost identical to that described in a previous study (Fujiwara et al., 2020). The preconcentration system of solid-phase extraction is shown in Figure S1, which was constructed with serially connected two columns of TSK-8HQ, PFA tubes with a 2 mm internal diameter, PharMed tubes with a 1.6 mm internal diameter, Tygon tubes with a 4 mm internal diameter, and a MasterFlex pump. Each step of the chemical analysis was performed in a clean hood. This procedure is summarized in Table 1. The chelating resin columns were cleaned by flowing 100 ml 2 mol/kg NH_3, 10 ml UW, 100 ml 3 mol/kg HNO_3, and 10 ml UW. The columns were then conditioned using a flow of 20 ml 0.04 mol/kg HCl (pH 1.4). Flow rates were maintained at 1 ml/min. Approximately 3 kg of a sample (pH 1.4) was introduced into the columns at 4 ml/min, and 50 ml 0.04 mol/kg HCl (pH 1.4) was flowed into the columns to remove the remaining matrices. The chelating resin columns were detached from the preconcentration system and connected to a polypropylene syringe for elution. Compared with the previous study (Fujiwara et al., 2020) we reduced the volume of an eluent to improve an efficiency. Thirty eluents of 30 ml 5 mol/kg HF were passed through the columns in the direction opposite to that for sample loading by gravity flow at a flow rate of 0.3 ml/min. The eluates were collected in a PFA vial. The chelating resin columns were mounted on the preconcentration system and cleaned with 20 ml UW for subsequent use. One cycle of the solid-phase extraction required approximately 15 h for completion.

The eluate in a PFA vial was heated to complete dryness at 170 °C for 6 h on a hot plate (Analab, France). The residual organic matter from the chelating resin was decomposed by adding 2 ml 13 mol/kg HNO_3, 0.2 ml 10 mol/kg H_2O_2, and 0.1 ml 0.3 mol/kg H_2SO_4. The vial was loosely capped and heated at 160 °C for 12 h on a hot plate. Then the cap was removed, and the solution was heated at 170 °C, leaving H_2SO_4 in the vial. The sample was added with a 2 ml mixture of 0.5 mol/kg HF and 0.4 mol/kg HCl and heated at 80 °C for 3 h.

2.3.2 Chromatography using the anion exchange resin AG1 X8

Compared to a previous study (Fujiwara et al., 2020), we reduced the size of the anion exchange resin column and modified the procedure (Table 2) to improve efficiency. Each solution was passed through the column by gravity at a flow rate of 0.15 ml/min. The column was first cleaned by flowing 2.5 ml 6 mol/kg HNO_3 twice, 1 ml UW, and 0.3 ml 0.5 mol/kg HF–0.4 mol/kg HCl 3 times. The sample solution was loaded onto the resin. Matrix elements were eluted using a flow of 0.2 ml 0.05 mol/kg HF–9 mol/kg HCl 4 times. Tungsten was eluted thrice with 2 ml 5 mol/kg HCl and collected in a PFA vial. Mo was eluted with 1 ml 1 mol/kg HNO_3 three times and collected in another PFA vial. One cycle

TABLE 1 Procedure of chelating solid-phase extraction with TSK-8HQ.

Step	Solution	Volume (ml)	Flow rate (ml/min)
Cleaning	2 mol/kg NH_3	100	1
	UW	10	1
	3 mol/kg HNO_3	100	1
	UW	10	1
Conditioning	0.04 mol/kg HCl	20	1
Sample loading	0.04 mol/kg HCl	3000	4
Matrix removal	0.04 mol/kg HCl	50	1
Elution	5 mol/kg HF	30	0.3
Cleaning	UW	20	0.5

UW, Ultrapure water produced with a Milli-Q IQ7005

TABLE 2 Procedure of anion exchange chromatography with AG1-X8.

Step	Solution	Volume (ml)	Number of cycles
Cleaning	6 mol/kg HNO_3	2.5	2
	UW	1	1
Conditioning	0.5 mol/kg HF-0.4 mol/kg HCl	0.3	3
Sample loading	0.5 mol/kg HF-0.4 mol/kg HCl	2	1
Matrix removal	0.05 mol/kg HF-9 mol/kg HCl	0.2	4
Elution of W	3 mol/kg HCl	2	3
Elution of Mo	1 mol/kg HNO_3	1	3
Cleaning	6 mol/kg HNO_3	3	1
	UW	1	1

of anion-exchange separation required approximately 4 h for completion.

The eluates of Mo and W in PFA vials were evaporated at 170°C on a hot plate. The residual organic materials from the anion-exchange resin decomposed like that described in the previous section but without the addition of H_2SO_4. After evaporation of the acids, the Mo sample was redissolved with 20 g 0.15 mol/kg HNO_3, and the W sample was redissolved with 0.5 g 5.5 mmol/kg TMAH by heating at 80 °C for 3 h. An accurate concentration factor was calculated on a weight basis.

2.4 Measurement

The external standard solutions of Ru and Re were added to the Mo and W sample solutions obtained using the procedures described in 2.3 respectively. A Ru standard solution diluted with 0.15 mol/kg HNO_3 was added to the Mo sample solution to produce a mole ratio of Mo: Ru = 1:1. The Re standard solution diluted with 5.6 mmol/kg TMAH was added to the W sample solution such that the molar ratio of W: Re = 1:2. The obtained sample solutions were introduced into a Neptune Plus MC-ICP-MS (Thermo Fisher Scientific, USA) at the Research Institute for Humans and Nature (RIHN) to determine the concentrations and stable isotope ratios of Mo and W. Major conditions of the measurement are shown in Tables 3 and 4. The instrumental mass bias was corrected by standard-sample bracketing combined with external mass bias correction using Ru and Re. The measurements and data processing were performed as previously described (Tsujisaka et al., 2019; Fujiwara et al., 2020).

For preliminary experiments, the concentrations of Mo and W were measured using an Element 2 HR-ICP-MS (Thermo Fisher Scientific, USA). The major measurement conditions are listed in Table S1.

2.5 Verification of the analytical method

To determine the operational blanks of Mo and W, chelating solid-phase extraction and anion-exchange chromatography were performed using 3 kg of UW as the sample. The concentrations of Mo and W in the pre-concentrated solutions were measured using Element 2 HR-ICP-MS. The results are summarized in Table S2. The operational blank was 0.01 ± 0.02 nmol/kg (average (ave) ± 2 standard deviation (sd), n = 4) for Mo and 0.7 ± 0.8 pmol/kg (n = 4) for W.

Furthermore, a recovery experiment was conducted using UW as the sample. Mo and W from the NIST SRM 3134 and NIST SRM 3163 standards were added to 3 kg of UW at 100 nmol/kg and 50 pmol/kg, respectively. The results are summarized in Table S3. The recovery was 104.7 ± 2.8% (n = 4) for Mo and 101.6 ± 1.9% (n = 4) for W, indicating that both elements were quantitatively recovered. The isotope ratios of Mo and W in the pre-concentrated solutions were measured using MC-ICP-MS. $\delta^{98/95}$Mo was 0.26 ± 0.09 ‰ (n = 4) and $\delta^{186/184}$W was –0.02 ± 0.02 ‰ (n = 4), which was congruent with the isotope ratio of added Mo and W. This is indicating that significant isotope fractionation did not occur during the analytical method.

The concentrations and isotope ratios of Mo and W were measured using a large volume of mixed seawater as samples, originally collected from at some depths of station TR-16 during the KH-11-7 cruise. The experimental results are listed in Table S4. The Mo concentration was 104 ± 9 nmol/kg (n = 8), $\delta^{98/95}$Mo was 2.37 ± 0.07 ‰ (n = 8), the W concentration was 50 ± 5 pmol/kg (n = 9), and $\delta^{186/184}$W was 0.53 ± 0.05 ‰ (n = 9). These values agree with those observed at a station in the western North Pacific within a range of errors (Fujiwara et al., 2020).

TABLE 3 Major conditions of MC-ICP-MS measurement.

Item	Condition
RF power	1300 W
Cooling gas flow rate	15 l/min
Auxiliary gas flow rate	0.7 l/min
Nebulizer gas flow rate	1.1–1.2 l/min
Sampling cone	Ni sampler cone
Skimmer cone	Ni X-skimmer cone
Nebulizer	PFA-ST 100 µl/min Microflow Nebulizer
Integration time	4.2 s
Number of cycles	Mo: 15–21, W: 15–24

3 Results

3.1 Concentrations and isotope ratios of Mo and W in water samples

All Mo and W data in this study are summarized in Table S5. Vertical profiles of the concentrations and stable isotope ratios of Mo at nine stations in the Pacific Ocean and two stations in the Indian Ocean are shown in Figures 2A, C, respectively. The Mo

TABLE 4 Cup configurations of Neptune plus for Mo and W measurement.

Configuration for Mo	L4	L3	L2	L1	Center	H1	H2	H3	H4
Monitored isotopes	^{91}Zr	^{92}Mo	^{94}Mo	^{95}Mo	^{97}Mo	^{98}Mo	^{99}Ru	^{101}Ru	^{102}Ru
Interfering isotopes		^{92}Zr	^{94}Zr			^{98}Ru			^{102}Pd
Configuration for W	**L4**	**L3**	**L2**	**L1**	**Center**	**H1**	**H2**	**H3**	**H4**
Monitored isotopes		^{182}W	^{183}W	^{184}W	^{185}Re	^{186}W	^{187}Re	^{188}Os	
Interfering isotopes				^{184}Os		^{186}Os	^{187}Os		

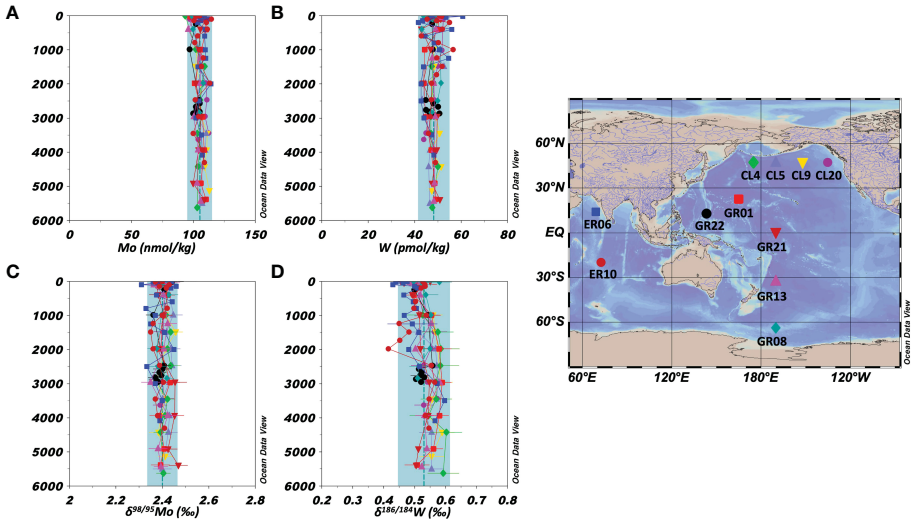

FIGURE 2
Vertical profiles of the concentrations and isotope ratios of Mo and W in the open oceans (the Pacific and Indian Oceans). The data symbols are consistent with the sampling point symbols on the map. The error bar shows a standard deviation (± 1sd). The blue columns show ranges of ave ± 2sd for all oceanic samples. **(A)**: Mo concentration. **(B)**: W concentration. **(C)**: $\delta^{98/95}$Mo. **(D)**: $\delta^{186/184}$W.

concentration was 93.6–114.7 nmol/kg and $\delta^{98/95}$Mo was 2.31–2.47 ‰ (n = 109). The average and standard deviation values at each station and for all oceanic samples are listed in Table 5. These results are consistent with previously reported Mo concentration and $\delta^{98/95}$Mo (Mo = 106 ± 7 nmol/kg, $\delta^{98/95}$Mo = 2.41 ± 0.15 ‰, n = 168) in the Pacific, Atlantic, and Antarctic Oceans (Collier, 1985; Nakagawa et al., 2012; Fujiwara et al., 2020).

The vertical profiles of the concentrations and stable isotope ratios of W at the nine stations in the Pacific Ocean and two stations in the Indian Ocean are shown in Figures 2B, D, respectively. The W concentration was 41.6–60.7 pmol/kg and $\delta^{186/184}$W was 0.41–0.60 ‰ (n = 109). The average and standard deviation values at each station and for all oceanic samples are listed in Table 5. Although significantly higher W concentration and significantly lower $\delta^{186/184}$W were found at 2 stations, the other data were within the range of ave ± 2sd of the 11 stations. The total averages of the 11 stations are congruent with recently reported W concentration and $\delta^{186/184}$W (W = 52 ± 4 pmol/kg, $\delta^{186/184}$W = 0.50 ± 0.05 ‰, n = 19) in the North Pacific and Atlantic Oceans (Fujiwara et al., 2020; Kurzweil et al., 2021).

Vertical profiles of the concentrations and stable isotope ratios of Mo at two stations in the East China Sea and two stations in the Sea of Japan are shown in Figures 3A, C, respectively. The Mo concentration was 98.6–111.3 nmol/kg and $\delta^{98/95}$Mo was 2.29–2.45 ‰ (n = 31). The average values in marginal sea water (Mo = 106 ± 3 nmol/kg, $\delta^{98/95}$Mo = 2.37 ± 0.03 ‰, n = 31) agreed with those in the open ocean water within an error range.

Vertical profiles of the concentrations and stable isotope ratios of W at two stations in the East China Sea and two stations in the Sea of Japan are shown in Figures 3B, D, respectively. There was a significant difference between data from depths above 1000 m (upper layer) and those from depths below 1000 m (deeper layer). In the depths below 1000 m, the W concentration was 56 ± 18 pmol/kg (n = 24), being significantly higher than that in the open ocean water, and $\delta^{186/184}$W was 0.45 ± 0.06 ‰ (n = 24), being significantly lower than that in the open ocean water. However, at depths below 1000 m, the W concentration was 50 ± 8 pmol/kg and $\delta^{186/184}$W was 0.49 ± 0.02 ‰ (n = 7), which were congruent with those in the open ocean water.

The range of Mo concentration in the Uji River water in this study (Table 5) included the previously reported value of 4.4 nmol/kg (Firdaus et al., 2008), and the range of Mo concentration in the Yodo River water was within the previously reported range of 2.0–68.6 nmol/kg (Sohrin et al., 1989). The $\delta^{98/95}$Mo values in the Uji and Yodo Rivers water are reported for the first time in this study. The W concentration in the Uji River water in this study was lower than that of 171 pmol/kg reported in the past (Firdaus et al., 2008). The range of W concentrations in the Yodo River water was within the previously reported range of 26–3290 pmol/kg (Sohrin et al., 1989). The $\delta^{186/184}$W values in the Uji and Yodo Rivers water are reported for the first time in this study. Figure 4 compares the Mo and W concentrations in river water between this study and previous studies(Archer and Vance, 2008; Firdaus et al., 2008; Neubert et al., 2011; Yang et al., 2022). The concentrations and isotope ratios of Mo and W in the Uji and Yodo Rivers were slightly higher than those in rivers worldwide.

4 Discussion

4.1 The Pacific and Indian Oceans

In a previous study (Nakagawa et al., 2012), we reported that $\delta^{98/95}$Mo and Mo concentration in the modern open ocean are uniform, also supported by the data obtained in this study. So far, $\delta^{186/184}$W in the open ocean water has been reported from only two

10.3389/fmars.2023.1182668

TABLE 5 Mo and W data in this study (ave ± 2sd).

	n	salinity	Mo (nmol/kg)	W (pmol/kg)	$\delta^{98/95}$Mo	$\delta^{186/184}$W
Pacific Ocean						
CL04	9	35.3 ± 1.2	104.1 ± 8.6	47.9 ± 2.4	2.39 ± 0.02	0.56 ± 0.05
CL05	10	34.0 ± 0.2	105.7 ± 6.1	46.9 ± 4.9	2.38 ± 0.03	0.55 ± 0.04
CL20	8	34.0 ± 0.1	105.4 ± 3.9	49.2 ± 5.7	2.39 ± 0.02	0.53 ± 0.05
GR01	11	34.8 ± 0.9	105.3 ± 9.3	47.5 ± 4.8	2.41 ± 0.03	0.53 ± 0.09
GR08	9	34.2 ± 1.1	103.5 ± 5.7	47.5 ± 6.3	2.40 ± 0.03	0.53 ± 0.05
GR13	11	34.9 ± 0.9	103.3 ± 7.3	48.7 ± 4.1	2.39 ± 0.04	0.52 ± 0.05
GR21	10	34.8 ± 0.7	105.5 ± 6.2	48.1 ± 5.9	2.41 ± 0.06	0.51 ± 0.05
GR22	11	34.6 ± 0.2	102.2 ± 5.0	47.7 ± 3.9	2.39 ± 0.04	0.52 ± 0.03
Indian Ocean						
ER06	18	34.4 ± 0.1	106.1 ± 9.1	49.4 ± 6.7	2.38 ± 0.04	0.51 ± 0.08
ER10	17	34.6 ± 0.2	107.6 ± 6.7	48.0 ± 11	2.38 ± 0.09	0.49 ± 0.09
Open Ocean, all data	109	34.6 ± 1.0	105.1 ± 8.0	48.2 ± 6.2	2.40 ± 0.06	0.52 ± 0.06
Sea of Japan						
CR34	9	34.6 ± 1.2	105.3 ± 3.9	57 ± 17	2.34 ± 0.07	0.43 ± 0.06
CR47	14	34.4 ± 1.2	107.3 ± 4.2	55 ± 11	2.38 ± 0.05	0.45 ± 0.05
East China Sea						
AND22	6	34.4 ± 1.7	103.1 ± 6.6	46.7 ± 5.6	2.35 ± 0.01	0.50 ± 0.02
AND26	2	34.1 (n=1)	99.4 ± 2.4	65 ± 37	2.39 ± 0.07	0.46 ± 0.07
Marginal seas, depth < 1000 m	24	34.1 ± 0.2	105.5 ± 5.4	56 ± 18	2.36 ± 0.04	0.45 ± 0.06
Marginal seas, depth > 1000 m	7	34.2 ± 0.2	104.9 ± 9.0	49.9 ± 7.6	2.38 ± 0.06	0.49 ± 0.02
Uji River-Yodo River-Osaka Bay system						
Uji River[a]	2	0.10	3.3–5.2	80.2–111.3	1.30–1.41	0.50–0.64
Yodo River[a]	2	0.07–3.2	13.3–29.0	134.7–1073	1.40–1.81	0.26–0.50
Osaka Bay[a]	6	15.8–32.8	85.1–107.4	195.7–726.6	2.27–2.38	0.20–0.32

[a] Data range

stations in the North Pacific and the South Atlantic (Fujiwara et al., 2020; Kurzweil et al., 2021). The data from the Pacific and Indian Oceans water in this study are congruent with the previous data, indicating $\delta^{186/184}$W is uniform as well as the W concentration in the modern open ocean. Although the uniform distribution of $\delta^{186/184}$W was confirmed at 11 stations in the open ocean, anomalies in $\delta^{186/184}$W were observed in the surface layer at ER06 and around 2000 m depth at ER10 (Figures 2B, D). ER06 was located 530 km from the Indian coast, where high W concentrations and low $\delta^{186/184}$W were observed in the surface water, possibly due to anthropogenic pollution from India. This hypothesis is a deduction of the discussion in sections 4.2-4.3. In contrast, ER10 is located east of the Indian Ocean Central Ridge, and the maxima of Mn and Fe have been reported at depths of 1700–3000 m, which are attributed to a hydrothermal plume (Thi Dieu Vu and Sohrin, 2013). The minimum of $\delta^{186/184}$W appeared at depths of 1240–1980 m, which might be caused by the hydrothermal plume.

4.2 The Uji River-Yodo River-Osaka Bay system

The concentration of Mo varied significantly between the Uji and Yodo Rivers (Figure 5A). The concentration of Mo at Hirakata Harbor on the Yodo River was approximately six times higher than that at Ingen Bridge on the Uji River. $\delta^{98/95}$Mo varied from 1.4 ‰ of the Uji River water to 2.5 ‰ of the open ocean water (Figure S2A). The Mo concentration and $\delta^{98/95}$Mo vary depending on the geology of the river basin, chemical reactions, and biological activities in the river (Neubert et al., 2011). However, since the Uji and Yodo Rivers belong to the same river system, the variations in the Mo concentration and $\delta^{98/95}$Mo suggest the influence of non-natural local sources. As the Yodo River flows through a metropolitan area, possibly it was affected by anthropogenic pollution.

In the plot of the Mo concentration against salinity (Figure 5A), the Mo concentrations in the Yodo River (Hirakata Harbor) and

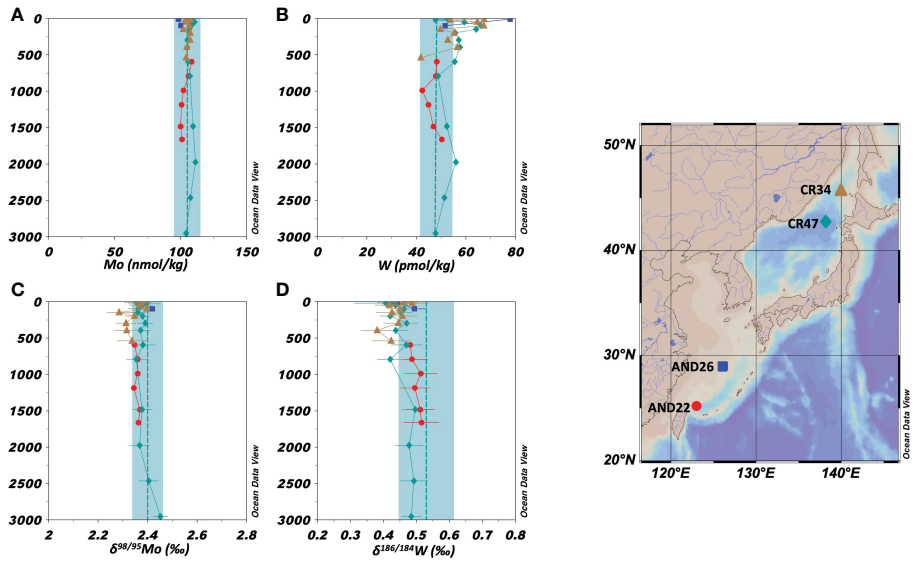

FIGURE 3
Vertical profiles of the concentrations and isotope ratios of Mo and W in the marginal seas (the East China Sea and the Sea of Japan). The data symbols are consistent with the sampling point symbols on the map. The error bar shows a standard deviation (± 1sd). **(A)**: Mo concentration. The blue columns show ranges of ave ± 2sd for all oceanic samples. **(B)**: W concentration. **(C)**: $\delta^{98/95}$Mo. **(D)**: $\delta^{186/184}$W.

Osaka Bay were significantly higher than those on the mixing line with the end members of the Uji River and open ocean waters. These anomalies may be attributed to the anthropogenic contamination of Mo. However, concentration anomalies were not observed at Nishijima Sluice Gate, Yodo River (Figure 5A). On the plot of $\delta^{98/95}$Mo against the inverse Mo concentration (Figure 5B), the data of Osaka Bay were plotted close to those of the ocean. The data from the Uji and Yodo Rivers showed

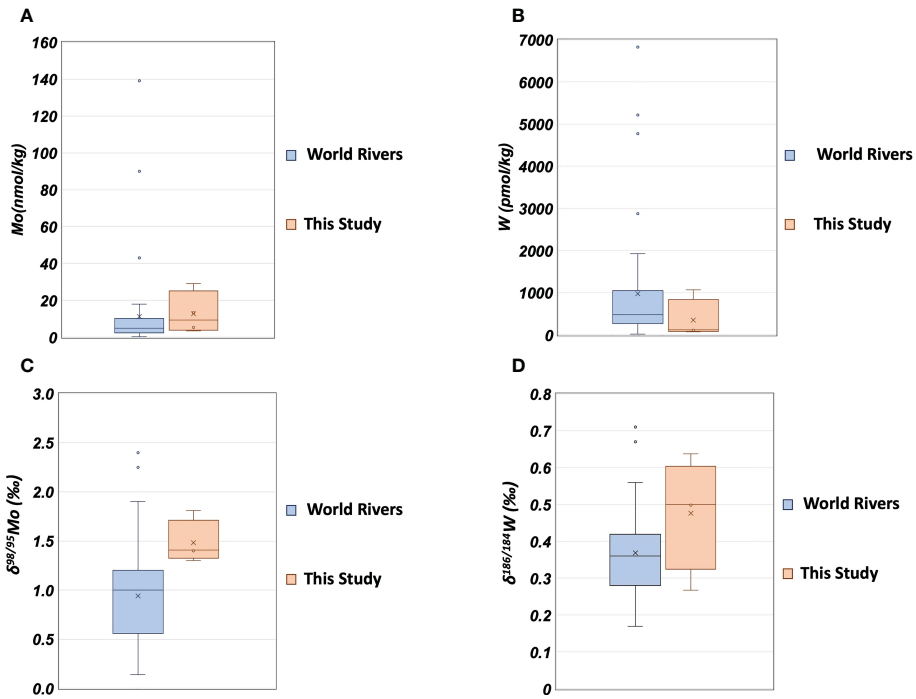

FIGURE 4
The concentrations and isotope ratios of Mo and W in river water. **(A)**: Mo concentration; blue: world rivers (Archer and Vance, 2008; Firdaus et al., 2008; Neubert et al., 2011), orange: this study. **(B)**: W concentration; blue: world rivers (Firdaus et al., 2008; Yang et al., 2022), orange: this study. **(C)**: $\delta^{98/95}$Mo; blue: world rivers (Archer and Vance, 2008; Neubert et al., 2011), orange: this study. **(D)**: $\delta^{186/184}$W; blue: world rivers (Yang et al., 2022), orange: this study.

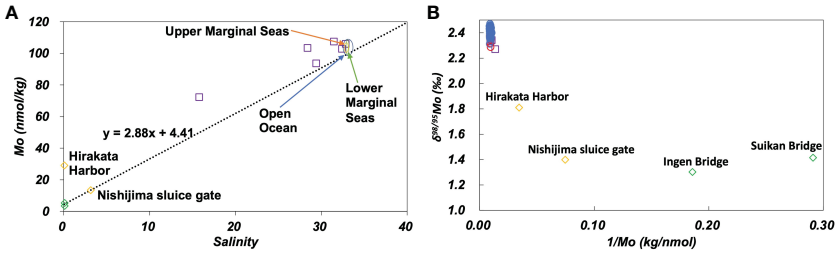

FIGURE 5
(A): Mo concentration plotted against salinity. The dotted line passes the average of the Uji River and the average of the open ocean. **(B)**: $\delta^{98/95}$Mo plotted against the inverse Mo concentration. Green diamonds: the Uji River, yellow diamonds: the Yodo River, purple squares: Osaka Bay, blue circles: the open ocean, red circles: marginal seas.

substantial variation. This plot cannot be explained by the mixing of the Uji River and Osaka Bay waters. This indicates that the distribution of the Mo concentration and $\delta^{98/95}$Mo in the Uji River-Yodo River-Osaka Bay system were affected by various factors other than simple mixing. One possibility is that multiple anthropogenic sources with different Mo concentrations and $\delta^{98/95}$Mo. Another possibility is that local anoxia occurs in the Uji River-Yodo River-Osaka Bay system, which functions as a local sink for Mo.

We compared the Mo concentration and $\delta^{98/95}$Mo in Osaka Bay with those of estuaries of the Narmada River, the Tapi River (India), and the Itchen River (UK) (Archer and Vance, 2008; Rahaman et al., 2014). The Mo concentration is plotted against salinity in Figure S3A and $\delta^{98/95}$Mo is plotted against the inverse Mo concentration in Figure S3B. For samples with the same salinity, the Mo concentrations in the Narmada and Tapi Rivers were lower than those in Osaka Bay. The Mo concentrations in the Itchen River at salinity > 30 were similar to those in Osaka Bay. The $\delta^{98/95}$Mo in Osaka Bay were congruent with those of samples with high Mo concentrations in the Narmada, Tapi, and Itchen Rivers (Figure S2B). The effect of anthropogenic pollution on Mo is not clear from these data.

The variations in the W concentration and $\delta^{186/184}$W in the Uji River-Yodo River-Osaka Bay system were substantial. As well as the case of Mo, this may be due to anthropogenic pollution. Data on $\delta^{186/184}$W from nine Asian rivers have been reported in a previous study (Yang et al., 2022) (Figure 4D). However, the effects of anthropogenic pollution on W have not been explicitly discussed.

In the plot of W concentration against salinity (Figure 6A), data from the Yodo River (Hirakata Harbor) and Osaka Bay plotted at substantially higher positions than the mixing line with end members of the Uji River and open ocean water. $\delta^{186/184}$W of the Yodo River and Osaka Bay was significantly lower than that of the Uji River and the open ocean (Figure 6B). These results are probably due to anthropogenic pollution as well as pollution of Mo. On the plot of $\delta^{186/184}$W versus the inverse W concentration (Figure 6B), all data from the Uji River, Yodo River, and Osaka Bay show a linear relationship:

$$\delta^{186/184}\mathrm{W} = 39.3(1/\mathrm{W}) + 0.145 \quad (r^2 = 0.909,\ n = 10) \qquad (3)$$

This indicates that the concentration and isotope ratio of W in the Uji River-Yodo River-Osaka Bay system can be explained by the mixing of Uji River water and an anthropogenic source. The anthropogenic source endmember is distinct from open ocean water. In previous studies, the analysis of W concentration suggested the influence of anthropogenic W pollution in the Yodo River (Sohrin et al., 1989). The analysis of stable isotope ratios in this study confirmed the possibility of anthropogenic pollution of W in the Yodo River and Osaka Bay (Figures 6 and S2B). Further observations of the river and estuarine water in the Yodo River-Osaka Bay system are needed to understand the detailed mechanism of anthropogenic pollution.

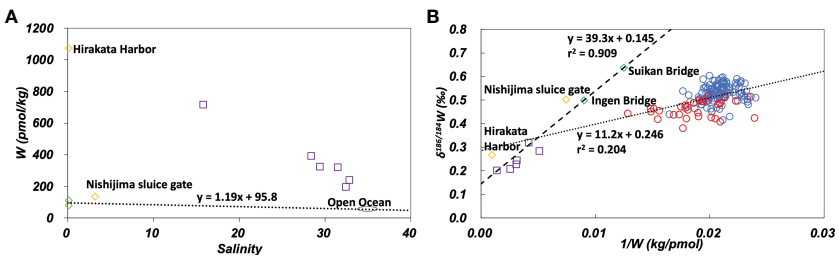

FIGURE 6
(A): W concentration plotted against salinity. The dotted line passes the average of the Uji River and the average of the open ocean. **(B)**: $\delta^{186/184}$W plotted against the inverse W concentration. The dashed line is the regression line (eq. 3) for data of the Uji River-Yodo River-Osaka Bay system. The dotted line is the regression line (eq. 4) for the open ocean and marginal seas data. Green diamonds: the Uji River, yellow diamonds: the Yodo River, purple squares: Osaka Bay, blue circles: the open ocean, red circles: marginal seas.

4.3 The East China and Japan Seas

The Mo concentration and $\delta^{98/95}$Mo in the East China Sea and the Sea of Japan were not significantly different from those in the open ocean. Therefore, it is considered that anthropogenic Mo pollution has little influence on the East China Sea and the Sea of Japan.

In contrast, the W concentration in the surface water of the marginal seas was significantly higher than that of the open ocean water (Figure 3B), and $\delta^{186/184}$W was significantly lower than that of the open ocean water (Figure 3D). At station AND 26 in the East China Sea at a depth of 11 m, the W concentration reached 78 pmol/kg and $\delta^{186/184}$W was 0.44. In the Sea of Japan, anomalies in W concentration and $\delta^{186/184}$W extended from the surface to a depth of approximately 1000 m. In the deeper layers, the W concentration and $\delta^{186/184}$W were congruent with those in the open ocean water. This indicates that anthropogenic W did not significantly reach the deep water. The vertical profile of W in the Sea of Japan is similar to that of chlorofluorocarbons, which are anthropogenic pollutants (Tsunogai et al., 2003). The surface water of the Sea of Japan is mainly formed from warm, low-density seawater carried by the Tsushima Current and mixes slowly with deep water. However, when cold water carried by the Liman Current is strongly cooled in winter once every few decades, convection reaches the bottom of the Sea of Japan. Convection was most recently observed in 2001 when chlorofluorocarbons were transported to the bottom water (Tsunogai et al., 2003). However, this convection was not sufficiently large to eliminate the differences in the concentrations of chlorofluorocarbons between the upper and lower layers. Therefore, it is likely that anthropogenic W was introduced into the Sea of Japan concurrently with chlorofluorocarbons primarily after 1950.

All the data from the open ocean and marginal seas in this study are plotted in Figure 6B. The data show weak linearity.

$$\delta^{186/184}\mathrm{W} = 11.2(1/\mathrm{W}) + 0.246 \quad (r^2 = 0.204,\ n = 140) \qquad (4)$$

One end member of this line is open ocean water. The other end member is located near Osaka Bay. This suggests that a similar anthropogenic W endmember can explain the distribution of W in the marginal seas as well as the Uji River-Yodo River-Osaka Bay system.

The data in this study are compared with data from the Yangtze River and the South China Sea (Kurzweil et al., 2021; Yang et al., 2022) on the plot of $\delta^{186/184}$W vs. 1/W in Figure 7. The dotted line in Figure 7 represents the regression line of eq. (4) in Figure 6B. Data from the South China sea are plotted along this regression line. This suggests that the influence of anthropogenic W is similar in the Sea of Japan, the East China Sea, and the South China Sea. Data from the Yangtze River estuary are plotted above the regression line. It has been suggested that the Yangtze River estuary is affected by the contribution of benthic W reflux from estuarine sediments (Yang et al., 2022). Figure 7 suggests that the anthropogenic endmember of W for the Sea of Japan, East China Sea, and South China Sea has intermediate characteristics between those of Osaka Bay and the Yangtze River estuary.

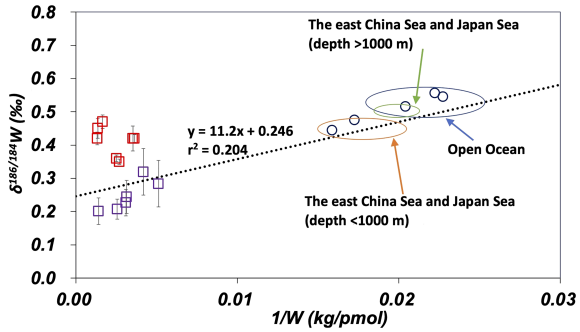

FIGURE 7
Comparison of W data of this study with literature on the plot of $\delta^{186/184}$W vs. 1/W. The dotted line is the regression line (eq. 4) for the open ocean and marginal seas data. The error bar shows a standard deviation (± 1sd). Purple squares: Osaka Bay, red squares: the Yangtze River estuary (Yang et al., 2022), and blue circles: the South China Sea (Kurzweil et al., 2021).

5 Conclusions

In the Pacific and Indian Oceans, a uniform distribution of $\delta^{186/184}$W was observed in addition to the uniformity of the concentrations of Mo and W, and $\delta^{98/95}$Mo, which has already been reported in the literature. In the Indian Ocean, some small anomalies in $\delta^{186/184}$W were observed, possibly because of the influence of anthropogenic pollution and hydrothermal plumes. The high concentrations of Mo and W observed in the Yodo River water were attributed to anthropogenic pollution, whereas the effect of anthropogenic pollution was small in the Uji River. The $\delta^{186/184}$W data are useful for understanding the sources of W in water samples. For the Uji River-Yodo River-Osaka Bay system, the $\delta^{98/95}$Mo vs. 1/Mo plot suggests multiple sources and sinks. However, the $\delta^{186/184}$W vs. 1/W plot indicates a simple mixing with the Uji River water and an anthropogenic source. Further analysis is required to understand the exact mechanisms controlling the distributions of Mo and W in this system. In the marginal seas (the East China Sea and the Sea of Japan), the Mo concentration and $\delta^{98/95}$Mo are congruent with those in the open ocean. However, significantly high W concentration and low $\delta^{186/184}$W occur in surface and upper water, which is attributed to the anthropogenic contamination of W. The extrapolated anthropogenic endmember has the W concentration and $\delta^{186/184}$W that closely resemble those in water samples from the Yangtze River estuary and Osaka Bay. As far as we know, the effects of anthropogenic pollution of W in an estuary and marginal seas are clearly shown for the first time in this study.

Data availability statement

The original contributions presented in the study are included in the article/Supplementary Material. Further inquiries can be directed to the corresponding author.

Author contributions

KM performed the analyses and drafted the original manuscript. TT improved the analytical method and performed the analyses. ST supervised the analyses. YS designed the study and reviewed the manuscript. All authors contributed to the article and approved the submitted version.

Funding

This study was supported by the KAKENHI grants (15H01727 and 19H01148 to YS) from the Japan Society for the Promotion of Science (JSPS).

Acknowledgments

The authors thank the crew, technicians, students, and scientists onboard the scientific research vessel Hakuho Maru cruises KH-09-5, KH-10-2, KH-14-6, KH-15-3, and KH-17-3 for their assistance with the sampling and analysis of routine data. Prof. Yuzuru Nakagawa is acknowledged for providing Osaka Bay samples. The Neptune Plus MC-ICP-MS (Thermo Fisher Scientific) used in this study is a joint facility at the Research Institute for Humanity and Nature (RIHN), Japan. We thank Dr. Ki-Cheol Shin who provided technical advice regarding the MC-ICP-MS measurements.

Conflict of interest

The authors declare that the research was conducted in the absence of any commercial or financial relationships that could be construed as a potential conflict of interest.

Publisher's note

Supplementary material

The Supplementary Material for this article can be found online at: https://www.frontiersin.org/articles/10.3389/fmars.2023.1182668/full#supplementary-material

References

Anbar, A. D., and Rouxel, O. (2007). Metal stable isotopes in paleoceanography. *Annu. Rev. Earth Planet Sci.* 35, 717–746. doi: 10.1146/annurev.earth.34.031405.125029

Archer, C., and Vance, D. (2008). The isotopic signature of the global riverine molybdenum flux and anoxia in the ancient oceans. *Nat. Geosci.* 1 (9), 597–600. doi: 10.1038/ngeo282

Barling, J., and Anbar, A. D. (2004). Molybdenum isotope fractionation during adsorption by manganese oxides. *Earth Planet. Sci. Lett.* 217 (3-4), 315–329. doi: 10.1016/s0012-821x(03)00608-3

Barling, J., Arnold, G. L., and Anbar, A. D. (2001). Natural mass-dependent variations in the isotopic composition of molybdenum. *Earth Planet. Sci. Lett.* 193 (3-4), 447–457. doi: 10.1016/s0012-821x(01)00514-3

Bertine, K. K., and Turekian, K. K. (1973). Molybdenum in marine deposits. *Geochim. Cosmochim. Acta* 37 (6), 1415–1434. doi: 10.1016/0016-7037(73)90080-x

Collier, R. W. (1985). Molybdenum in the northeast pacific ocean. *Limnol. Oceanogr.* 30 (6), 1351–1354. doi: 10.4319/lo.1985.30.6.1351

Cui, M. M., Luther, G. W., and Gomes, M. (2021). Cycling of W and Mo species in natural sulfidic waters and their sorption mechanisms on MnO2 and implications for paired W and Mo records as a redox proxy. *Geochim. Cosmochim. Acta* 295, 24–48. doi: 10.1016/j.gca.2020.12.007

De Laeter, J. R., Bohlke, J. K., De Bievre, P., Hidaka, H., Peiser, H. S., Rosman, K. J. R., et al. (2003). Atomic weights of the elements: review 2000 - (IUPAC technical report). *Pure Appl. Chem.* 75 (6), 683–800. doi: 10.1351/pac200375060683

Emerson, S. R., and Huested, S. S. (1991). Ocean anoxia and the concentrations of molybdenum and vanadium in seawater. *Mar. Chem.* 34 (3-4), 177–196. doi: 10.1016/0304-4203(91)90002-E

Firdaus, M. L., Norisuye, K., Nakagawa, Y., Nakatsuka, S., and Sohrin, Y. (2008). Dissolved and labile particulate zr, hf, Nb, Ta, Mo and W in the Western north pacific ocean. *J. Oceanogr.* 64 (2), 247–257. doi: 10.1007/s10872-008-0019-z

Firdaus, M. L., Norisuye, K., Sato, T., Urushihara, S., Nakagawa, Y., Umetani, S., et al. (2007). Preconcentration of zr, hf, Nb, Ta and W in seawater using solid-phase extraction on TSK-8-hydroxyquinoline resin and determination by inductively coupled plasma-mass spectrometry. *Anal. Chim. Acta* 583 (2), 296–302. doi: 10.1016/j.aca.2006.10.033

Fujiwara, Y., Tsujisaka, M., Takano, S., and Sohrin, Y. (2020). Determination of the tungsten isotope composition in seawater: the first vertical profile from the western north pacific ocean. *Chem. Geol.* 555, 1–9. doi: 10.1016/j.chemgeo.2020.119835

Goldberg, T., Archer, C., Vance, D., and Poulton, S. W. (2009). Mo Isotope fractionation during adsorption to fe (oxyhydr)oxides. *Geochim. Cosmochim. Acta* 73 (21), 6502–6516. doi: 10.1016/j.gca.2009.08.004

Helz, G. R., Miller, C. V., Charnock, J. M., Mosselmans, J. F. W., Pattrick, R. A. D., Garner, C. D., et al. (1996). Mechanism of molybdenum removal from the sea and its concentration in black shales: EXAFS evidence. *Geochim. Cosmochim. Acta* 60 (19), 3631–3642. doi: 10.1016/0016-7037(96)00195-0

Irisawa, K., and Hirata, T. (2006). Tungsten isotopic analysis on six geochemical reference materials using multiple collector-ICP-mass spectrometry coupled with a rhenium-external correction technique. *J. Anal. At. Spectrom.* 21 (12), 1387–1395. doi: 10.1039/b607945h

Ishibashi, J.-i., and Urabe, T. (1995). Hydrothermal activity related to arc-backarc magmatism in the western pacific. *Backarc basins: tectonics magmatism*, 451–495. doi: 10.1007/978-1-4615-1843-3_13

Kashiwabara, T., Kubo, S., Tanaka, M., Senda, R., Iizuka, T., Tanimizu, M., et al. (2017). Stable isotope fractionation of tungsten during adsorption on fe and Mn (oxyhydr) oxides. *Geochim. Cosmochim. Acta* 204, 52–67. doi: 10.1016/j.gca.2017.01.031

Kashiwabara, T., Takahashi, Y., Marcus, M. A., Uruga, T., Tanida, H., Terada, Y., et al. (2013). Tungsten species in natural ferromanganese oxides related to its different behavior from molybdenum in oxic ocean. *Geochim. Cosmochim. Acta* 106, 364–378. doi: 10.1016/j.gca.2012.12.026

Kishida, K., Sohrin, Y., Okamura, K., and Ishibachi, J. (2004). Tungsten enriched in submarine hydrothermal fluids. *Earth Planet. Sci. Lett.* 222 (3-4), 819–827. doi: 10.1016/j.epsl.2004.03.034

Kurzweil, F., Archer, C., Wille, M., Schoenberg, R., Munker, C., and Dellwig, O. (2021). Redox control on the tungsten isotope composition of seawater. *Proc. Natl. Acad. Sci. U.S.A.* 118 (18), 1–6. doi: 10.1073/pnas.2023544118

Li, Y.-H. (2000). *A compendium of geochemistry: from solar nebula to the human brain* (Princeton, USA:Princeton University Press).

Nagler, T. F., Anbar, A. D., Archer, C., Goldberg, T., Gordon, G. W., Greber, N. D., et al. (2014). Proposal for an international molybdenum isotope measurement standard and data representation. *Geostand. Geoanal. Res.* 38 (2), 149–151. doi: 10.1111/j.1751-908X.2013.00275.x

Nägler, T., Neubert, N., Böttcher, M., Dellwig, O., and Schnetger, B. (2011). Molybdenum isotope fractionation in pelagic euxinia: evidence from the modern black and Baltic seas. *Chem. Geol.* 289 (1-2), 1–11. doi: 10.1016/j.chemgeo.2011.07.001

Nakagawa, Y., Takano, S., Firdaus, M. L., Norisuye, K., Hirata, T., Vance, D., et al. (2012). The molybdenum isotopic composition of the modern ocean. *Geochem. J.* 46 (2), 131–141. doi: 10.2343/geochemj.1.0158

Neubert, N., Heri, A. R., Voegelin, A. R., Nagler, T. F., Schlunegger, F., and Villa, I. M. (2011). The molybdenum isotopic composition in river water: constraints from small catchments. *Earth Planet. Sci. Lett.* 304 (1-2), 180–190. doi: 10.1016/j.epsl.2011.02.001

Pattan, J., and Pearce, N. J. G. (2009). Bottom water oxygenation history in southeastern Arabian Sea during the past 140 ka: results from redox-sensitive elements. *Palaeogeogr. Palaeoclimatol. Palaeoecol.* 280 (3-4), 396–405. doi: 10.1016/j.palaeo.2009.06.027

Rahaman, W., Goswami, V., Singh, S. K., and Rai, V. K. (2014). Molybdenum isotopes in two Indian estuaries: mixing characteristics and input to oceans. *Geochim. Cosmochim. Acta* 141, 407–422. doi: 10.1016/j.gca.2014.06.027

Rimmer, S. M. (2004). Geochemical paleoredox indicators in Devonian–Mississippian black shales, central Appalachian basin (USA). *Chem. Geol.* 206 (3-4), 373–391. doi: 10.1016/j.chemgeo.2003.12.029

Shimmield, G. B., and Price, N. B. (1986). The behaviour of molybdenum and manganese during early sediment diagenesis — offshore Baja California, Mexico. *Mar. Chem.* 19 (3), 261–280. doi: 10.1016/0304-4203(86)90027-7

Siebert, C., Nagler, T. F., von Blanckenburg, F., and Kramers, J. D. (2003). Molybdenum isotope records as a potential new proxy for paleoceanography. *Earth Planet. Sci. Lett.* 211 (1-2), 159–171. doi: 10.1016/s0012-821x(03)00189-4

Sohrin, Y., and Bruland, K. W. (2011). Global status of trace elements in the ocean. *Trac-Trends Anal. Chem.* 30 (8), 1291–1307. doi: 10.1016/j.trac.2011.03.006

Sohrin, Y., Isshiki, K., Kuwamoto, T., and Nakayama, E. (1987). Tungsten in north pacific waters. *Mar. Chem.* 22 (1), 95–103. doi: 10.1016/0304-4203(87)90051-x

Sohrin, Y., Isshiki, K., Nakayama, E., Kihara, S., and Matsui, M. (1989). Simultaneous determination of tungsten and molybdenum in Sea-water by catalytic current polarography after preconcentration on a resin column. *Anal. Chim. Acta* 218 (1), 25–35. doi: 10.1016/s0003-2670(00)80279-2

Sohrin, Y., Matsui, M., and Nakayama, E. (1999). Contrasting behavior of tungsten and molybdenum in the Okinawa trough, the East China Sea and the yellow Sea. *Geochim. Cosmochim. Acta* 63 (19-20), 3457–3466. doi: 10.1016/s0016-7037(99)00273-2

Thi Dieu Vu, H., and Sohrin, Y. (2013). Diverse stoichiometry of dissolved trace metals in the Indian ocean. *Sci. Rep.* 3 (1), 1–5. doi: 10.1038/srep01745

Tribovillard, N., Algeo, T. J., Lyons, T., and Riboulleau, A. (2006). Trace metals as paleoredox and paleoproductivity proxies: an update. *Chem. Geol.* 232 (1-2), 12–32. doi: 10.1016/j.chemgeo.2006.02.012

Tsujisaka, M., Takano, S., Murayama, M., and Sohrin, Y. (2019). Precise analysis of the concentrations and isotopic compositions of molybdenum and tungsten in geochemical reference materials. *Anal. Chim. Acta* 1091, 146–159. doi: 10.1016/j.aca.2019.09.003

Tsunogai, S., Kawada, K., Watanabe, S., and Aramaki, T. (2003). CFC Indicating renewal of the Japan Sea deep water in winter 2000–2001. *J. Oceanogr.* 59 (5), 685–693. doi: 10.1023/B:JOCE.0000009597.33460.d7

Willbold, M., and Elliott, T. (2017). Molybdenum isotope variations in magmatic rocks. *Chem. Geol.* 449, 253–268. doi: 10.1016/j.chemgeo.2016.12.011

Wong, M. Y., Rathod, S. D., Marino, R., Li, L. L., Howarth, R. W., Alastuey, A., et al. (2021). Anthropogenic perturbations to the atmospheric molybdenum cycle. *Glob. Biogeochem. Cycles* 35 (2), 1–25. doi: 10.1029/2020gb006787

Yang, R. Y., Li, T., Stubbs, D., Chen, T. Y., Liu, S., Kemp, D. B., et al. (2022). Stable tungsten isotope systematics on the earth's surface. *Geochim. Cosmochim. Acta* 322, 227–243. doi: 10.1016/j.gca.2022.01.006

frontiers | Frontiers in Marine Science

TYPE Original Research
PUBLISHED 17 May 2023
DOI 10.3389/fmars.2023.1172475

OPEN ACCESS

EDITED BY
Wen Zhuang,
Shandong University, China

REVIEWED BY
Zhuo-Yi Zhu,
Shanghai Jiao Tong University, China
Xiangbin Ran,
Ministry of Natural Resources, China

*CORRESPONDENCE
Peng Yao
yaopeng@ouc.edu.cn

RECEIVED 23 February 2023
ACCEPTED 03 May 2023
PUBLISHED 17 May 2023

CITATION
Chen L, Yao P, Yang Z and Fu L (2023) Seasonal and vertical variations of nutrient cycling in the world's deepest blue hole. *Front. Mar. Sci.* 10:1172475. doi: 10.3389/fmars.2023.1172475

Seasonal and vertical variations of nutrient cycling in the world's deepest blue hole

Lin Chen[1,2], Peng Yao[1,2]*, Zuosheng Yang[3] and Liang Fu[4]

[1]Frontiers Science Center for Deep Ocean Multispheres and Earth System, and Key Laboratory of Marine Chemistry Theory and Technology, Ministry of Education, Ocean University of China, Qingdao, China, [2]Laboratory for Marine Ecology and Environmental Science, Qingdao National Laboratory for Marine Science and Technology, Qingdao, China, [3]College of Marine Geosciences, Ocean University of China, Qingdao, China, [4]Sansha Track Ocean Coral Reef Conservation Research Institute, Sansha, China

Nutrient cycling in anoxic seawaters is essential to marine ecosystem health and sustainability, yet it remains poorly understood. In this work, we analyzed dissolved inorganic nutrients as well as hydrochemical parameters in the Yongle Blue Hole (YBH) of the South China Sea in October 2019, which is the world's deepest blue hole and is characterized by anoxia below the depth of 100 m. Nutrient data collected in two sampling campaigns in 2017 were also incorporated to examine the seasonal and vertical variations of nutrient cycling across steep redox gradients in the YBH. In response to the changes in redox conditions in different seasons, nutrients in the YBH showed significant seasonal variations. The nitrate maximum rose from a depth of 90 m in March 2017 to 60-80 m in October 2019, while the primary nitrite maximum concentration decreased from 0.5 μmol/L to 0.1 μmol/L. In October 2019, the nitrite decreased to below the detection limit at about 100 m, while in March 2017, it was 140 m. The regeneration of phosphate and silicate both started from around 40 m in October 2019 and from 80 m in March 2017. Silicate shows non-conservative adding behaviors relative to phosphate and DIN, and phosphate shows a similar but weaker adding behavior relative to DIN. The nutrient ratios also varied seasonally, especially for N/P, which fluctuated greatly on the surface at 80 m, while Si/N and Si/P fluctuated above 50 m. At the oxic-anoxic interface, extreme values of nutrient ratios were observed, and below 150 m, the N/P, Si/N, and Si/P were kept constant at about 17, 1.5, and 26, respectively. Seasonal and vertical variations of nutrient concentrations and ratios in the YBH reflect the impact of redox conditions on nutrient cycling in anoxic seawaters, especially during the transition from oxic to anoxic zone. And the high-resolution distributions of nutrients and hydrochemical parameters are helpful to better understand the nutrient cycling processes in highly dynamic coastal environments that are suffering deoxygenation.

KEYWORDS

Yongle blue hole, dissolved inorganic nutrients, seasonal variation, vertical distribution, nutrient ratios

Introduction

Nutrients are the basis of primary production in the ocean, and their concentrations, structures, and distributions in seawater are directly related to biogeochemical processes in marine ecosystems (Doney et al., 2012; Hutchins and Capone, 2022). For example, nutrients can be utilized by different types of algae in water columns, and the microbial decomposition of organic matter produced by these algae may promote the regeneration of nutrients (Falkowski and Woodhead, 2013). During these processes, nutrients, especially nitrogen-containing nutrients, undergo complex transformations of forms in concert with the changes in reduction-oxidation (redox) conditions, because different nitrogen cycling processes have different oxygen requirements (Gruber, 2008). As a result, the redox conditions of water columns can be deduced to a certain extent from the concentrations and distributions of nutrients. Investigating the regeneration and transformation of nutrients during redox transitions is important to better understand the controls on nutrient biogeochemistry in seawaters, especially under the context of global oceanic deoxygenation.

There are many typical low-oxygen or anoxic marine environments in the world, of which marine blue holes are unique geomorphological features of modern reef systems that are characterized by steep redox and biogeochemical gradients, which can provide valuable information regarding karst processes, marine ecology, climate change, and paleoclimate (Bishop et al., 2015; Xie et al., 2019; Yao et al., 2020). The Sansha Yongle Blue Hole (YBH) in the South China Sea (SCS) is the deepest known marine blue hole in the world (Bi et al., 2018). It has a depth of 300 m, and the water column below 100 m is in a hypoxic or anoxic state, making it an excellent natural laboratory for studying the biogeochemical processes of nutrients during oxic-anoxic transitions (Yao et al., 2018). A few nutrient cycling studies have been carried out in the YBH previously. For example, Yao et al. (2018) collected water samples from the YBH in March 2017, analyzed dissolved inorganic nutrients in those samples, and studied the controls on vertical distributions of nutrients in the YBH. They found that in March 2017, the YBH water column was characterized by well-defined physical and chemical gradients with sharp transitions occurring at 80 m depth, and the water column changed from oxic to anoxic at 100 m depth. Nitrate and nitrite varied dramatically in the oxic layer, and ammonium accumulated in the anoxic layer (Yao et al., 2018). On the contrary, phosphate, and silicate started to accumulate after a sharp decrease of dissolved oxygen (DO) at 80 m depth. All nutrients showed relatively constant distributions below 160 m depth. Two months later, Xie et al. (2019) also collected samples from the YBH and analyzed nutrients and other hydrochemical properties. Similarly, the water column was divided into three layers: an oxic layer in the top 70 m, a chemocline at 70-100 m, and an anoxic layer below 100 m in May 2017. They found that in the oxic layer, organic matter (OM) degradation and nitrification led to the accumulation of nitrate, but within the chemocline, nitrate was depleted by the denitrification process. Within the deep anoxic layer, sulfate reduction and OM degradation resulted in accumulations of ammonium, phosphate, and silicate (Xie et al., 2019). These two studies provide preliminary knowledge about nutrient cycling and processes in the YBH. However, seasonal variations of nutrient cycling in the YBH remain poorly understood. As a semienclosed environment, the intensity of water exchange of the YBH, especially in the upper oxic layer can be influenced by tides, winds, and seasonal variations of temperature and salinity. As a result, the distributions of DO in the water column may vary among seasons, affecting the microbial composition and redox reactions and thus nutrient cycling processes.

In this study, we analyzed dissolved inorganic nutrients, including nitrate (NO_3^-), nitrite (NO_2^-) and ammonium (NH_4^+), phosphate (PO_4^{3-}), and silicate (SiO_3^{2-}), as well as hydrochemical properties, such as temperature, salinity, DO, sulfide and chlorophyll *a* (Chl *a*) in water samples collected in October 2019 in the YBH. Compared with previous work, this is the first report of such data in the autumn season. The overarching objective of this work is to build on previous studies and illuminate the seasonal and vertical variations of nutrient concentrations, distributions, and structural characteristics during oxic-anoxic transitions in the YBH, and to better understand the impacts of the changing redox conditions on the biogeochemical processes of nutrients in deoxygenated seawaters.

Materials and methods

Study area and sample collection

The YBH is located on the Yongle Atoll of the western Paracel Islands (Xisha Qundao) in the SCS (111.768° N, 16.525° E) (Figure 1). It is shaped like a ballerina's shoe, with a bottom that deviates 118 m laterally from the entrance, and the twisted structure is located between 90 and 158 meters (Figure 1) (Li et al., 2018). The sidewall of the YBH is composed of a modern coral reef above ca. 17 m, and hard limestone below that depth (Yao et al., 2020). Since the YBH is located far offshore, meteoric freshwater inputs are relatively minimal, resulting in a salinity profile not characterized by a surface freshwater lens (Bi et al., 2018), unlike many other blue hole systems located closer to shore (Schwabe and Herbert, 2004; Gischler et al., 2008; van Hengstum et al., 2011; Bishop et al., 2015) (Figure 1). The YBH water column stratification existed mostly within the depth range of 80 to 100 m, as reflected in well-defined physical/chemical and microbial gradients, resulting in metabolic pathways rapidly changing from oxic in the upper 100 m depth to anoxic, sulfidic, and methanogenic below that depth (Bi et al., 2018; Xie et al., 2019; Yao et al., 2020).

Samples were collected on October 24-25, 2019. Since the water around the YBH is very shallow, the research vessel (Qiongqionghai 03138) had to be anchored in the lagoon of the Yongle Atoll, ca. 1.7 km from the YBH. All investigators and materials were transported to a floating platform built in the center of the YBH during the spring tide period. During the survey, a buoyancy platform was set up on the surface of YBH, a winch was placed,

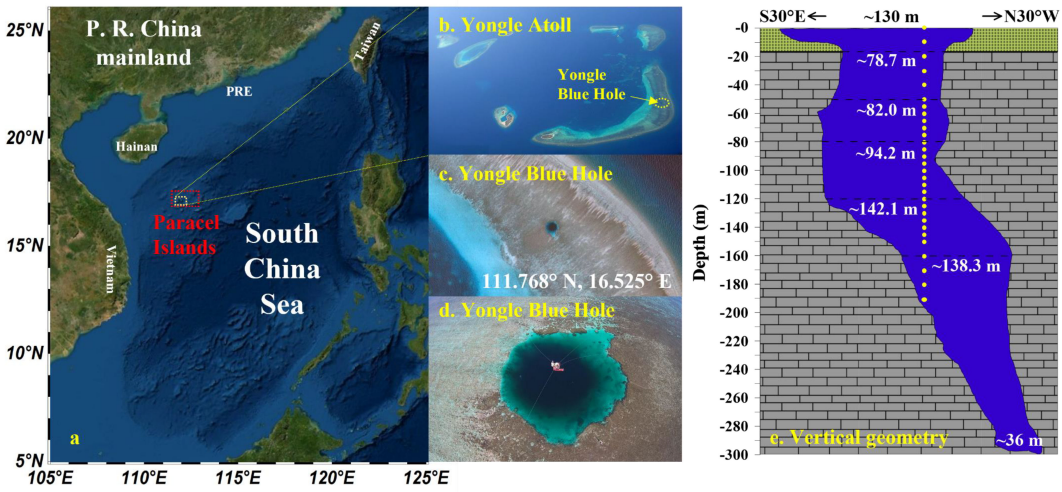

FIGURE 1
Location and vertical geometry of the Yongle Blue Hole. **(A)** Location of the Paracel Islands in the South China Sea; **(B)** Aero view of the Yongle Atoll; **(C, D)** Aero views of the Yongle Blue Hole from different altitudes and depression angles; **(E)** Vertical profile of the Yongle Blue Hole. **(E)** is modified from Li et al., 2018; Yao et al., 2020.

and Niskin samplers were mounted for water sampling. The sampling depth reached 190 m.

Hydrochemical parameters

Water samples were collected using Niskin bottles mounted on a stainless-steel wire, which is marked every five meters before the cruise, and deployed from a winch mounted on the platform. Twenty-nine samples were collected to a depth of 190 m at intervals of 5 m (50-190 m) or 10 m (surface-50 m). After recovery, DO and sulfide were sampled first from the Niskin bottles to the sample bottles. For DO, 100-mL glass stoppered bottles, which volumes were pre-determined, were carefully filled brim-full after overflowing the bottle with two times of the bottle volume of water. Reagents (1mL 2mol/L $MnCl_2$ and 1mL 1mol/L NaOH/KI) were added to fix the oxygen, following the standard procedures described by Grasshoff et al. (2007). After DO sampling, samples for sulfide analysis were collected in 25 mL colorimetric tubes and the procedural reagents (a mixture of N, N-dimethyl-p-phenylenediamine sulfate and ferric reagents) were added immediately (Cline, 1969). Duplicate samples were collected for both DO and TH_2S. DO was measured on-site using the conventional Winkler titration method (Grasshoff et al., 2007) with a digital bottle-top burette (Titrette, BrandTech Scientific Inc., USA). The detection limit of current DO measurement is about 1 µmol/L (Thamdrup et al., 2012; Ulloa et al., 2012). Sulfide was also determined on-site using a spectrophotometer at 670 nm after color development, and all necessary dilutions were made in volumetric glassware before determination (Cline, 1969). The detection limit of this measurement is about 1 µmol/L (Cline, 1969). Since this method measures the concentration of total sulfide species (H_2S, HS^-, and S_2^-) in seawaters, the result is expressed as total H_2S (TH_2S) hereafter. Average data were reported for DO and TH_2S from duplicate samples.

Dissolved inorganic nutrients

After water sampling, the samples were brought back to the supply vessel moored near the YBH. The samples were filtered through pre-soaked and washed acetic acid fiber membranes (pore size 0.45 µmol/L, diameter 47 mm) in the laboratory on board. The filtrates were frozen at -20°C for dissolved inorganic nutrient analysis (Murphy and Riley, 1962; Catalano, 1987). Nutrients were detected by standard colorimetric method on AA3 continuous flow analyzer (Seal Analytical Ltd., UK). The detection limits of NO_3^-, NO_2^-, NH_4^+, PO_4^{3-} and SiO_3^{2-} are 0.02, 0.01, 0.04, 0.02, and 0.01 µmol/L, respectively, and the analytical uncertainties of multiple replicates are less than 5-10%.

Statistical analyses

Correlation between parameters was analyzed by IBM SPSS software (V22) (two-tailed test), and statistical differences between the two groups were tested by one-way variance analysis (ANOVA). Regression analysis and Principal Component Analysis (PCA) between parameters were performed by Originpro 2022 software (OriginLab).

Results

Hydrochemical characteristics

During the investigation in October 2019, sharp transitions in salinity, temperature, and DO occurred at about 50 m depth, and most physicochemical parameters in the YBH remained relatively uniform below the depth of 140 m (Figure 2). Below 100 m depth, the YBH is characterized by both anoxic and sulfidic conditions.

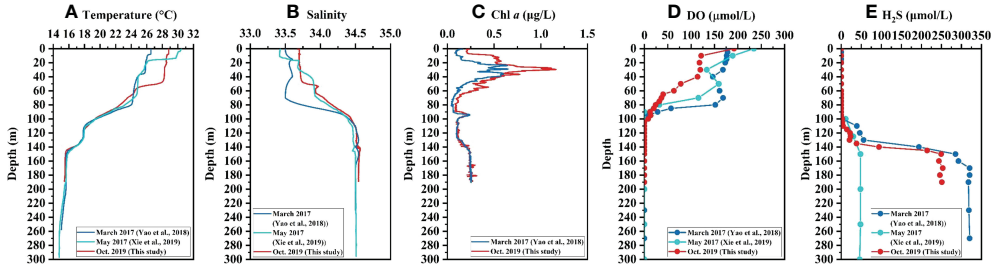

FIGURE 2
Vertical profiles of hydrochemical parameters in the Yongle Blue Hole. **(A)** Temperature, **(B)** Salinity, **(C)** Chl a, **(D)** DO, and **(E)** TH_2S.

The water temperature was roughly unchanged on the surface at 50 m but decreased sharply from 50 m to 60 m. After gradually decreasing from 60 m to 115 m, the temperature was kept at 17.6°C to 130 m, then gradually decreasing to 15.7°C at 145 m (Figure 2A). The salinity resembles the vertical distribution pattern of temperature with depth, but in a reverse way (Figure 2B). At the surface of 50 m, the salinity was kept at about 33.7, and below 140 m depth, the salinity was kept at about 34.6 (Figure 2B). The subsurface Chl *a* maximum was found at the depth of 30 m with the highest value of 1.2 μg/L and the secondary peak of Chl *a* (0.23 μg/L) appeared near 95 m (Figure 2C). The peak value of Chl *a* at 95 m is likely caused by the enrichment of cyanobacteria under anoxic conditions (He et al., 2020). The same phenomenon has been observed in the underwater anoxic layer of Rot Lake in Switzerland (Brand et al., 2016). The increase of Chl *a* concentration and its good correlation with turbidity in water below 130 m in the YBH (Bi et al., 2018) are attributed to the strong scattering of Chl *a* light source signal caused by high turbidity under the condition of extremely low Chl *a* concentration, leading to high Chl *a* fluorescence measurement value (YSI Environmental, 2006; Wang et al., 2007). The surface DO was highest and decreased sharply from 0 m (192.0 μmol/L) to 10 m depth (121.5 μmol/L), and kept at 113.8 μmol/L to 40 m depth before further decreasing (Figure 2D). With the disappearance of DO at about 100 m depth, the hydrogeochemistry of the water column in the YBH dramatically changed from oxic to strongly reductive conditions as reflected by an increase of TH_2S (Figures 2D, E). The TH_2S increased gradually from 110 m to 120m and then kept constant at 130 m, corresponding to the change of temperature at the same layer (Figures 2A, E). After that, the TH_2S increased sharply from 20.5 μmol/L to 249.4 μmol/L at 150 m depth and kept constant again below that depth (Figure 2E).

Concentration and distribution characteristics of nutrients

The nitrate concentration was very low on the surface at 40 m but increased rapidly from near 0 at 40 m to about 11 μmol/L at 60 m. From 60 m to 80 m, there has been little change in the nitrate, but from 80 m to 95 m, the nitrated decreased to near 0 (Figure 3A). The nitrite concentration was two orders of magnitude lower than the nitrate. There were two peaks of nitrite concentration at 50 m (0.12 μmol/L) and 90 m (0.16 μmol/L), respectively. The nitrite decreased to near 0 below 100 m (Figure 3B). In contrast with nitrate and nitrite, the ammonium concentration was low in the upper 90 meters of the water column, and rapidly increased below 95 m, with the trend slowing down between 110 m and 130 m, where the average concentration was 21.9 ± 2.1 μmol/L; it then increased to 83.8 μmol/L at 160 m but did not increase further, remaining at around 85 ± 2 μmol/L (Figure 3C). Therefore, the distribution of dissolved inorganic nitrogen (DIN, the sum of the concentrations of nitrate, nitrite, and ammonium) was dominated by nitrate and nitrite in the upper 100 m and by ammonium below 100 m. The phosphate and silicate had similar distribution patterns to ammonium. Like the nitrate, both phosphate and silicate

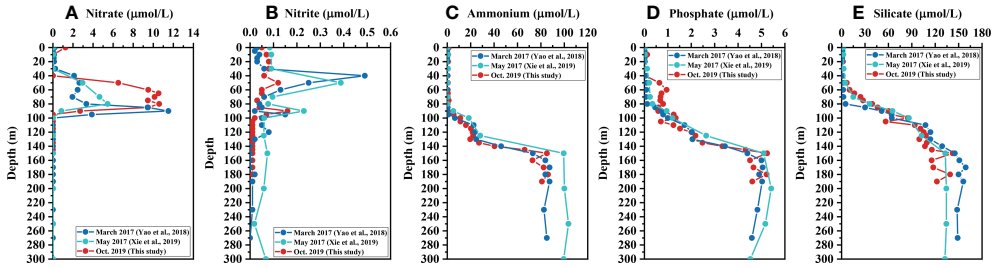

FIGURE 3
Vertical profiles of nutrients in the Yongle Blue Hole. **(A)** nitrate, **(B)** nitrite, **(C)** ammonium, **(D)** phosphate, and **(E)** silicate.

concentrations were very low on the surface at 40 m, and started to increase below that depth (Figure 3). Unlike the silicate, the phosphate concentration was kept relatively constant between 60-105 m (Figures 3D, E). Both phosphate and silicate concentrations did not increase below 160 m, remaining at around 5 µmol/L and 130 µmol/L, respectively.

Discussion

Seasonal variations of hydrochemical characteristics and nutrient distributions in the YBH

Synthetic analysis of the hydrochemical and nutrient characteristics of the YBH water column in March and May of 2017 and October 2019 indicates a significant difference in water properties between depths greater than and less than 100 m. Above 100 m, the temperature and salinity stratifications are mainly controlled by meteorological conditions and the influx of seawater, with a possible slow vertical exchange, whereas below 100 m, there is almost no exchange with the sea (Bi et al., 2018). Distributions of hydrochemical parameters and nutrients in the upper 100 m vary significantly with the season (Figures 2, 3). For example, in March 2017, the water temperature was kept constant in the upper 80 m, and in May 2017 it was about 70 m, while in October 2019, it was only 50 m (Figure 2A) (Bi et al., 2018; Xie et al., 2019; Yao et al., 2020). The seasonal variations of salinity in the upper layer were analogous to the temperature (Figure 2B), which indicated that the intensity of water exchange was higher in later winter than those in the spring and autumn seasons. This is mainly attributed to the lower atmospheric temperature and stronger wind and waves in winter than in other seasons in the SCS (Wang et al., 2008; Pan et al., 2015; Yu et al., 2019).

Under the influence of varied thermocline and halocline in different seasons, the DO showed similar stratification patterns accordingly. In March 2017, DO was kept constant in the upper 80 m, and in May 2017 the constant layer decreased to the upper 50 m, while in October 2019, it was only 40 m (Figure 2D) (Bi et al., 2018; Xie et al., 2019; Yao et al., 2020). This indicated that in October 2019, DO was consumed by aerobic OM decomposition below 40 m, and the balance between consumption and replenishment was broken due to weak water exchange in autumn, resulting in a more rapid decrease of DO concentration compared with the other two months in 2017. The distribution patterns of Chl *a* in 2017 and 2019 were basically the same, but the primary subsurface chlorophyll maximum was lower in March 2017 than that in October 2019 (Figure 2C). Previous studies have shown that the primary productivity is higher in autumn than that in later winter in the SCS, due in part to temperature and light intensity differences (Chen, 2005). The vertical distributions of TH_2S below 100 m in March 2017 and October 2019 were similar. The TH_2S concentration in October 2019 was slightly lower than that in March 2017, possibly due to the difference in upper layer OM cycling between these two months. As aforementioned, the OM decomposition in the upper aerobic layer was extensive in October 2019, as shown by the rapid depletion of DO. This should eventually result in a decrease in the supply of OM in sinking particles and/or in dissolved phase to the lower layer and thus a reduction of TH_2S. The TH_2S concentration in the bottom layer in May 2017 was only about 50 µmol/L (Xie et al., 2019), significantly lower than those in March 2017 and October 2019 ($p<0.001$) (Yao et al., 2020), which is most likely caused by oxidation of sulfides during sampling or analysis. Therefore, the TH_2S data in May 2017 are not incorporated into the later discussion.

Nutrients, especially nitrate, nitrite, and phosphate in the upper layer also varied seasonally along with the variations of hydrochemical properties. There were two peaks of nitrate concentration in March 2017, of which one peak was at 50 m and another at 90 m, with the highest concentration at the second peak, reaching 11.5 µmol/L (Figure 3A) (Yao et al., 2018). Similar to October 2019, only one peak at 80 m was found for nitrate in May 2017, but the peak value was only about 5.5 µmol/L, less than those of the other two months (Figure 2C) (Xie et al., 2019). There were three peaks of nitrite concentration in March 2017, at 40 m, 95 m, and 120 m, respectively, whereas only two peaks of nitrate were found in May 2017 and October 2019, and both were at 50 m and 90 m (Figure 3B) (Yao et al., 2018; Xie et al., 2019). Although the distribution patterns of nitrate in different seasons were similar, the maximum concentrations were significantly different ($p<0.001$). For the primary nitrite maximum at 40-50 m, both values in 2017 were higher than that in 2019, as opposed to the distributions of nitrate (Figure 3B). The third peak of nitrite at 120 m in March 2017 was the lowest compared with the other two peaks. Nevertheless, the detection of nitrite below 100 m indicated that there was a trace amount of DO undetected by the Winkler method (Ulloa et al., 2012). In fact, anoxic marine zones (AMZs) are often distinguished from oxygen minimum zones (OMZs) by the accumulation of nitrite (Ulloa et al., 2012; Vargas et al., 2021). In some AMZs, such as the Peruvian coast, the coast of Iquique, Chile, Eastern tropical South Pacific (ETSP), and the Arabian Sea, nanomolar levels of DO were detected using high-sensitivity oxygen sensors (Revsbech et al., 2009). The existence of a trace amount of DO below 100 m in March 2017 was consistent with the higher intensity of water exchange compared with the other two months, as shown by other hydrochemical parameters (Figure 2). The existence of DO, even in trace amounts, has a significant influence on microbial composition and thus biogeochemical processes. For example, at the depth of 100-120 m in March 2017, the abundance of sulfur-oxidizing bacteria (SOB) was significantly higher than that of sulfate reduction bacteria (SRB) (Yao et al., 2020; Zhou et al., 2023). The SOB is a chemolithoautotrophic microorganism living in dysoxic or suboxic conditions and deriving energy from the oxidation of thiosulfate, sulfide, or elemental sulfur to sulfate (van Vliet et al., 2021). As for the low value of nitrite below 100 m in May 2017, it is more like the background noise of the analyzing method they used (Xie et al., 2019).

In October 2019, the depth of phosphate and silicate began to increase and matched well with the decrease of DO, indicating the direct release of phosphate and silicate by aerobic decomposition of OM. Relative constant distribution of phosphate at the depth of 60-90 m in October 2019 suggests re-utilization of phosphate by microorganisms (Noffke et al., 2012), but not by phytoplankton

because of low Chl *a* at this layer (Figure 2D). While for silicate, there is no such assimilation pathway by microbial activities (Tréguer and De la Rocha, 2013), and thus it showed gradual accumulation with depth (Figure 3D).

Despite numerous studies on blue holes and/or anchialine caves over the past 30 years, there is a scarcity of continuous hydrochemical profiles for nutrients. With the exception of the YBH, there have been very few investigations into nutrient cycling in these systems, including caves in Bermuda (Maloney et al., 2011), Hospital Hole (Davis and Garey, 2018), Bundera Sinkhole (Seymour et al., 2007), caves in Croatia (Žic et al., 2011), and Amberjack Hole (Patin et al., 2021) (Figure S1). Nutrient concentrations in these blue holes are generally lower in waters above chemoclines than those in the YBH. However, below the chemoclines, nutrient concentrations vary significantly among systems, which may be related to the locations and material sources of each system (Figure S1). Overall, the depths of other blue holes are shallower, and the water column structures are more complex than those of the YBH. Some of the surface layers of these blue holes are more affected by land (e.g., caves in Bermuda (Maloney et al., 2011)), and some of their bottom layers are affected by seawater inputs (e.g., Bundera Sinkhole (Seymour et al., 2007)). Only a few of them have complete anoxic bottom waters (e.g., Hospital Hole (Davis and Garey, 2018), caves in Croatia (Žic et al., 2011), Amberjack Hole (Patin et al., 2021)). For anoxic basins in the open ocean, such as the Black Sea and Cariaco Trench, the overall variation patterns of nutrients with depth are similar to those of the YBH. However, the nutrient concentrations in deep waters are different in these systems, partly due to differences in water depth and primary productivity in the surface layer (Zhang and Millero, 1993; Murray et al., 1995; Volkov and Rozanov, 2006) (Figure S1).

The effects of hydrochemistry on nutrient cycling in the YBH

As aforementioned, seasonal differences in hydrochemical characteristics partly contribute to the seasonal changes in nutrient cycling. Despite these seasonal changes, the variety of nutrients with these environmental parameters remained somewhat consistent among different seasons, especially in the anoxic layer (Figures 2, 3). PCA analysis further proves this inference drawn from distribution characteristics. The distributions of PCA scores of samples (observation) and parameters (loading) in March 2017 were basically the same as in October 2019, and both were similar to that in May 2017 (Figure 4). Different nutrient species are greatly affected by the redox environment. Nitrate and nitrite are mainly influenced by DO and water temperature in the upper 100 m, whereas ammonium, phosphate, and silicate are more controlled by TH_2S and salinity (Figure 4).

Nevertheless, variations of nutrients with these environmental parameters differ among different nutrient species, indicating the differences in the cycling processes of these nutrient species, especially in the oxic layer (Figure 5). For example, in the oxic layer, the concentrations of nutrients increased with the decrease in

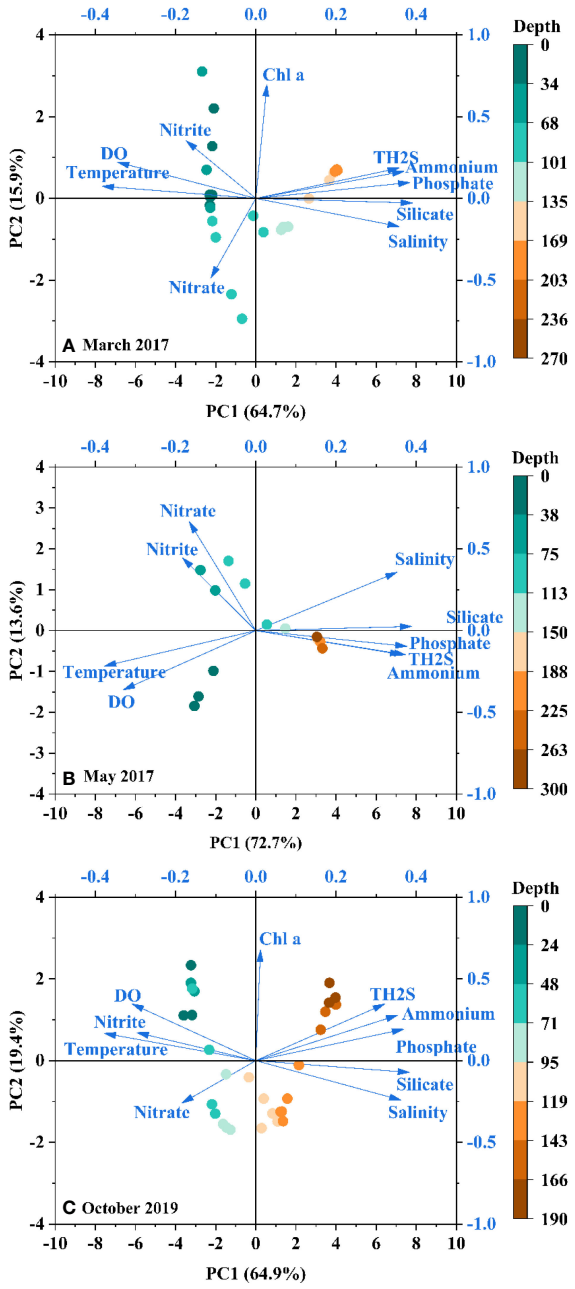

FIGURE 4
Biplots of PCA scores of observations (sampling depth) and loadings (parameters) for samples collected in the Yongle Blue Hole in **(A)** March 2017, **(B)** May 2017, and **(C)** October 2019.

temperature and Chl *a* and the increase of salinity, especially of phosphate and DIN in October 2019 (Figures 5A–I). Along with the decreasing of DO, DIN increased first and decreased rapidly when DO was below about 30 µmol/L (Figure 5J), reflecting a shift from a nitrification process to a predominantly denitrification process (Paulmier and Ruiz-Pino, 2009; He et al., 2020), the thresholds between DO and DIN were also found in other anoxic blue holes, such as the Bundera sinkhole (Seymour et al., 2007), as well as anchialine caves in Croatia (Žic et al., 2011) and the Black Sea (Murray et al., 1995), but not as obvious as in the YBH, possibly

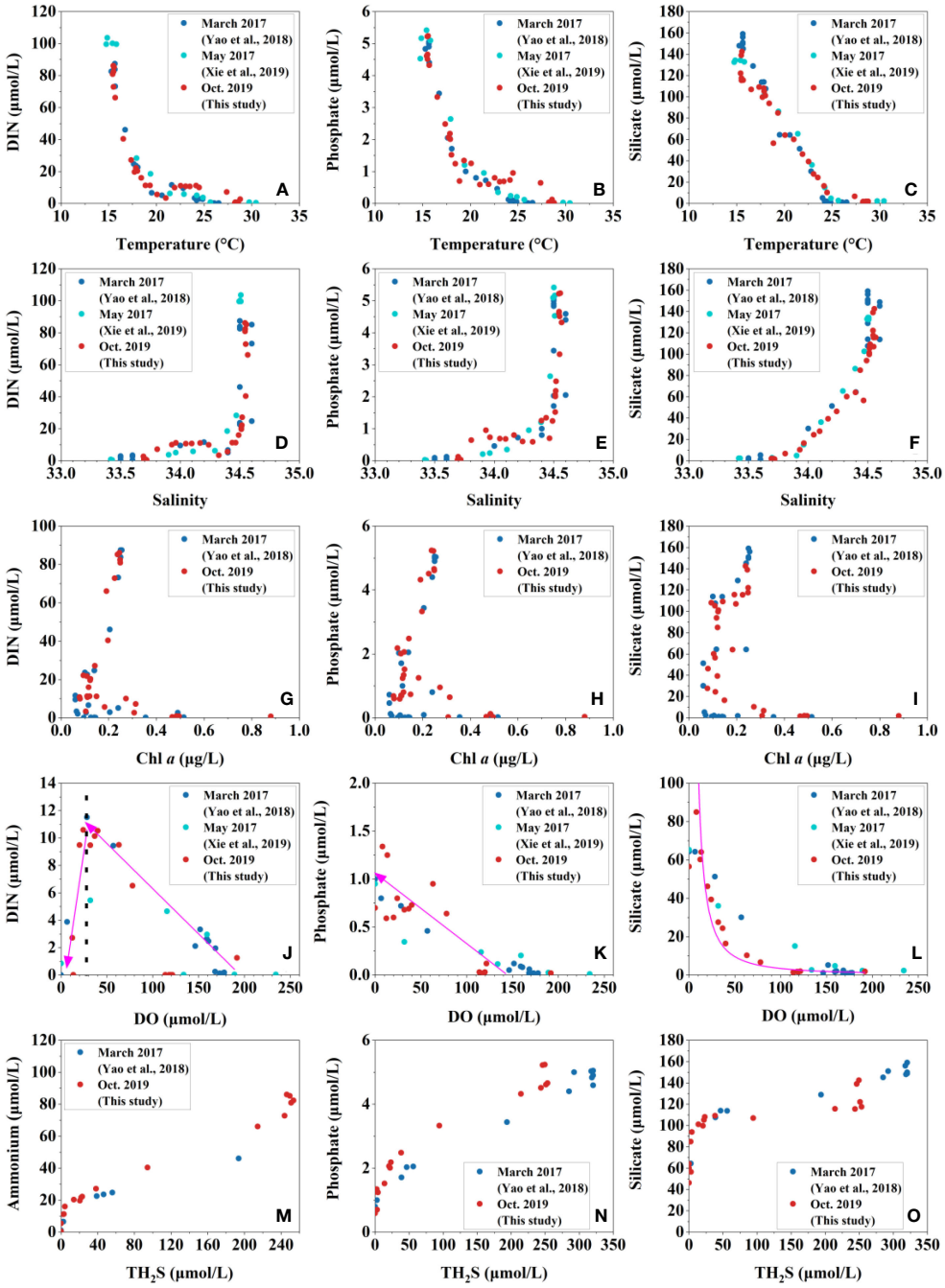

FIGURE 5
Relationships between nutrients and hydrochemical parameters in the Yongle Blue Hole. DIN, phosphate, and silicate vs. temperature **(A–C)**, salinity **(D–F)**, Chl a **(G–I)**, DO **(J–L)**, and TH_2S **(M–O)**.

because these systems have more complex hydrological structures and biogeochemical gradients and less data across oxic-anoxic interfaces (Figure S3). On the contrary, both silicate and phosphate increased with the decrease of DO, but in different manners. With the decreasing of DO, the silicate increased slowly first in a nonlinear way, and when DO was below 50 μmol/L, it increased rapidly (Figure 5L), indicating that the decreasing rate of DO (OM decomposition) is not consistent with the dissolution of silica (silicate regeneration). In general, silicate regeneration depends on the dissolution of the organism's siliceous crust in seawater, which is much slower than the phytoplankton cell lysis to release the extra- and intracellular OM (Tréguer and de la Rocha, 2013). The phosphate increased linearly with the decreasing of DO (Figure 5K), indicating that phosphate regeneration and OM decomposition were simultaneous (Redfield, 1963).

With the accumulation of TH_2S, the concentrations of ammonium, phosphate, and silicate all increased linearly, but their increasing magnitudes were different. The increasing multiple of ammonium

was much higher than those of phosphate and silicate (Figures 5M–O), probably because phosphate and silicate started to increase in the absence of TH_2S (Figures 2, 3).

Relative changes of different nutrient species in the YBH: implications for production and consumption of nutrients

As mentioned earlier, different nutrients have different sources and cycling processes, resulting in diverse response to environmental factors. For phosphate and silicate, their cycling processes in the ocean are relatively simple, mainly involving utilization by biota and organic matter decomposition and regeneration (Noffke et al., 2012; Tréguer and de la Rocha, 2013). For nitrogen-containing nutrients, their behavior is largely controlled by oxidation-reduction reactions mediated by phytoplankton and microorganisms, resulting in their presence in multiple valence states and more complex biogeochemical behavior (Gruber, 2008). In the surface layer of the YBH, phosphate and silicate were quickly utilized by primary production (Figure 3). With the decrease of DO, phosphate and silicate began to gradual accumulate (Figure 3), indicating that the regeneration of these nutrients from decomposition of organic matter exceeded the consumption. Below 100 m depth, where DO, nitrate and nitrite drop to 0, ammonium began to increase. Below 160 m, the concentrations of ammonium, phosphate and silicate, and their ratios were kept constant, indicating a balance between nutrient regeneration and consumption. The nutrient ratios are close to the Redfield ratio below 160 m, suggesting that regenerated nutrients mainly come from marine phytoplankton (Redfield, 1963).

At depths above 100 m, nitrate and nitrite are the main nitrogen nutrients, while ammonium is dominated below 100m. The distinct changes in the three nitrogen forms indicate an active nitrogen cycle in the YBH, which is mainly driven by natural processes such as changes in oxidation-reduction conditions, phytoplankton and microbial activities and organic matter decomposition (Gruber, 2008). The nitrogen cycle in marine environment mainly includes nitrification under aerobic conditions, assimilation, ammonia oxidation, aerobic ammonium oxidation and nitrification, as well as denitrification, DNRA (nitrate dissimilatory reduction to ammonium) and anaerobic ammonium oxidation (Gruber, 2008). The low DIN content in the surface water of YBH is mainly attributed to the combined effects of nitrification, assimilation, and aerobic ammonium oxidation (Yao et al., 2018; He et al., 2020). Subsequently, nitrite concentration began to increase, followed by an increase in nitrate concentration, and at 40 m, nitrite reached its first peak, which is referred to as the Primary Nitrite Maximum (PNM), and nitrate reached a relatively high value at this depth, indicating the sequential occurrence of ammonium oxidation (nitrite formation) and nitrification. PNM is a common phenomenon in oxygen-poor, nutrient-poor waters, mainly from nitrification, which has been observed in the waters near the Xisha Islands (Wu et al., 2015). Nitrite concentration quickly decreased after reaching the peak, along with the increase of nitrate, further indicating that nitrification was the main process, which converted nitrite to nitrate. Below 80 m, DO concentration decreased rapidly, and nitrate concentration increased rapidly to its highest peak, indicating that nitrification rate was at its maximum. However, below 90m, nitrate concentration quickly decreased, indicating the existence of denitrification and/or DNRA processes. Considering that ammonium did not start to accumulate until 100m, the decrease of nitrate below 90 m should be mainly attributed to denitrification, because DNRA is the direct production of NH4+ from NO3- (Gruber, 2008). At 95 m, nitrite reached its second peak, which is referred to as the Secondary Nitrite Maximum (SNM). SNM is a common phenomenon in the oxygen minimum zone of the marine environment, mainly from nitrate reduction rather than ammonium oxidation (Lam et al., 2011; Buchwald et al., 2015). Within the range of hypoxic layer, the decrease of nitrate and nitrite concentrations indicates that denitrification and nitrification occurred simultaneously. The coupling between nitrification and denitrification is a significant process of reactive nitrogen (N) removal that has been observed in many anoxic systems (Gruber, 2008). Below 100 m, nitrate and nitrite concentrations both decreased to a very low level, and ammonium began to accumulate. The massive accumulation of ammonium (concentration far higher than the maximum concentrations of nitrate and nitrite) is mainly attributed to the decomposition of organic nitrogen, as shown by the relationships between different nutrient species (Figure 6). All the relationships between DIN vs. phosphate, silicate vs. DIN and phosphate showed nonconservative trends among different seasons (Figure 6). For example, DIN increases slowly in a gentle upward concave shape

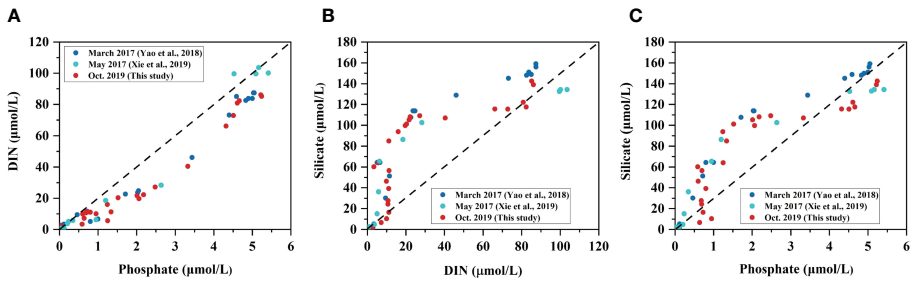

FIGURE 6
Relationships between **(A)** DIN and phosphate, **(B)** silicate and DIN, and **(C)** silicate and phosphate in the Yongle Blue Hole.

with the increase of phosphate, whereas silicate increases rapidly with the increase of DIN and phosphate, showing concave downward shapes (Figure 6). Furthermore, the increase of silicate relative to DIN is more rapid than relative to phosphate, consistent with the slow increase in DIN relative to phosphate (Figure 6). These changes may reflect the differences in the production and consumption pathways of different nutrients during cycling (Cross et al., 2007). Both nitrite and nitrate have production and consumption in the oxic layer due to complex nitrogen cycling processes, such as nitrification, denitrification, and ammonia oxidation (Paulmier and Ruiz-Pino, 2009). Whereas, silicate is not required by microbial metabolic processes except being utilized by siliceous organisms such as diatoms (Tréguer and de la Rocha, 2013). Therefore, the distribution of silicate is mainly controlled by OM decomposition and shows a net accumulation due to the lack of utilization pathways. As for phosphate, although it can also be utilized by microorganisms, e.g., to build cell membrane lipids and DNA, the amount demanded is usually lower than the amount of phytoplankton uptake (Karl, 2014). Thus, the relative constant distribution of phosphate at 60-100 m depth is most likely due to the phosphate regeneration by OM decomposition being in balance with microbial utilization (Figure 3D).

The inconsistent variations of different nutrient species also influence their proportional relationships, and the vertical variations of the nutrient ratios (e.g., DIN/Phosphate (N/P), Silicate/DIN (Si/N), and Silicate/Phosphate (Si/P)) well represent the relative changes in the production and consumption of different nutrients, which also reflecting the variations in the nutrient source and transformation. All nutrient ratios fluctuated with the season in the surface layer, especially the N/P (Figure 7). The highest N/P of different seasons occurred at different depths, and the deepest was at 40m in March 2017 (Figure 7A). The N/P reached minimum values (ca. 4~5) at about 95 m in all seasons, consistent with that this depth is the transition interface of nitrogen from oxidation status to reduction status and the DIN concentration is lowest at this depth (Figure 3). At deeper depths, the N/P was kept constant at about 16~17, which is very close to the Redfield ratio (Redfield, 1963) and the ratios in deep ocean waters (Anderson and Sarmiento, 1994). The N/P in marine environments has been extensively studied and is reported to be approximately 16:1, assuming that these nutrients are primarily derived from the decomposition of organic matter from primary production (Redfield, 1963; Hiscock and Millero, 2006). However, the N/P in deep waters varies among different anoxic systems, possibly due to the complexity of organic carbon sources in these systems. The N/P in the YBH deep water is similar to the Redfield ratio, indicating that the source of organic carbon in the YBH is relatively uniform. Similar values were observed in other permanently anoxic zones, such as the Framvaren fjord, where the N/P in deep waters is approximately 15-16 (Yao and Millero, 1995) (Figure S2). In an anoxic blue hole, the Hospital hole, the N/P in the deep water is approximately 40, which is much higher than that of the YBH, owing to the high levels of NO_3^- in the anoxic layer, which might be related to the low abundance of nitrogen reducers there (Davis and Garey, 2018). In an underwater blue hole, the Amberjack Hole in the Gulf of Mexico, the N/P in the deep water is only 7-8, probably because the depth of the anoxic layer of this blue hole is too shallow to accumulate ammonium (Patin et al., 2021). In open ocean anoxic zones, such as the Black Sea and the Cariaco Trench, the N/P is also less than 16, due to the complex water structure and allochthonous input of organic matter (Murray et al., 1995; Volkov and Rozanov, 2006). The seasonal fluctuation of Si/N occurred mainly at the surface of 50 m (Figure 7B). The Si/N also increased to the maximum near 95 m in all seasons, reaching the highest in October 2019 (~17), due in part to DIN being lowest at this depth. The Si/N at deeper depths was around 1~2, which is slightly greater than the Redfield ratio (Redfield, 1963) and the Si/N of nutrient-rich diatoms (Brzezinski et al., 1998), suggesting the accumulation of silicate and/or potential use of ammonium by anaerobic microorganisms, such as anammox bacteria (Hutchins et al., 2009). In general, the Si/P shows an S-shaped distribution from the surface to the bottom (Figure 7C). The Si/P in the surface layer was highest, up to 110, and it gradually decreased with depth, which is mainly because of the continuous regeneration of

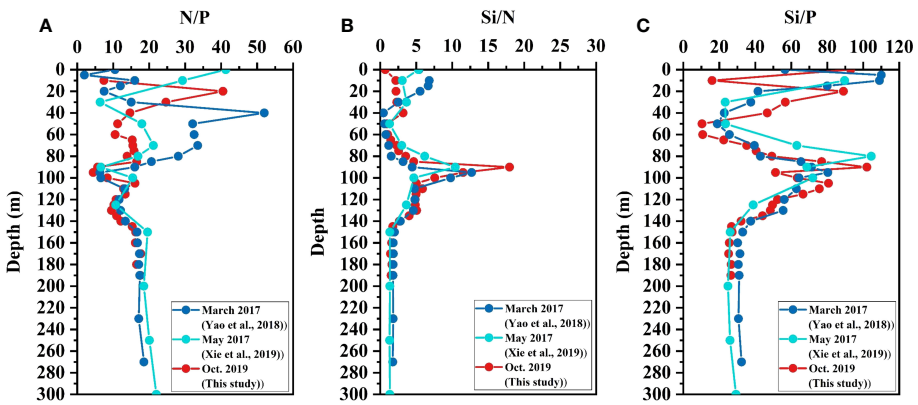

FIGURE 7
Vertical profiles of nutrient ratios in the Yongle Blue Hole. **(A)** N/P, **(B)** Si/N, and **(C)** Si/P.

phosphate from OM decomposition. The lowest Si/P was only about 10 and was found at around 50~60 m. The Si/P increased to about 100 between 80~100 m, indicating the re-utilization of phosphate by microbial activities, as mentioned earlier. Below that depth, the Si/P decreased gradually and was kept constant at around ~30 below 140 m, which is almost two times the Redfield ratio (Redfield, 1963), suggesting the continuous accumulation of silicate and further microbial utilization of phosphate (Parsons et al., 1984).

Conclusions

The YBH is a semi-enclosed marine environment, where the upper layer of the water column is actively exchanged with the outer sea, and the water exchange intensity varies seasonally. Based on the distributions of salinity and temperature, the water exchange with the outer sea for the YBH in October 2019 is weaker than those in March and May 2017. As a result, dissolved oxygen (DO) started to decrease below the depth of 40 m in October 2019, which is 30-40 m shallower than those in March and May 2017, indicating that the aerobic OM decomposition in October 2019 was more extensive than those in March and May 2017. Influenced by the hydrochemical properties, different nutrient species showed different seasonal and vertical variation patterns. The variations of nitrate, nitrite, and ammonium reflected the evolution of nitrogen cycling processes, such as nitrification, denitrification, and anammox with decreasing DO and increasing TH_2S, but the specific contribution needs to be constrained by nitrogen isotopes. It is worth noting that in March 2017, there was a small tertiary nitrite maximum at a depth of 120m, which origin needs to be further examined. The relative constant distributions of ammonium, phosphate, and silicate below the depth of 140 m indicated the depletion of decomposable OM or a balance between nutrient regeneration and reutilization. Changes in the distributions of different nutrients also affected their relationships. The non-conservative behaviors of silicate relative to phosphate and DIN and phosphate relative to DIN indicated that silicate was constantly accumulating, while the regenerated phosphate and DIN were probably re-utilized by microorganisms in addition to accumulation. As a result, nutrient ratios also varied seasonally in the surface oxic layer and had extreme values at the oxic-anoxic interfaces, indicating the relative changes in the production and consumption of different nutrient species.

In conclusion, the seasonal variations of the concentrations and ratios of nutrients in the YBH reflect the close relationships of nutrient cycling and regeneration with hydrochemical parameters, OM decomposition, and microbial activities in anoxic seawaters, and further prove that the YBH is a unique natural laboratory for studying the biogeochemical processes during the oxic-anoxic transition.

Data availability statement

The original contributions presented in the study are included in the article/Supplementary Material. Further inquiries can be directed to the corresponding author.

Author contributions

LF and ZY designed the cruise. LC, PY, and LF attended the cruise and collected the samples. LC and PY designed the experiments. LC conducted most of the experiments, analyzed the data, prepared graphs and tables, and wrote the manuscript. PY and ZY revised the manuscript. All authors contributed to the article and approved the submitted version.

Funding

This study was supported by the National Natural Science Foundation of China (NSFC) (42076034), the Research and Development Program for the South China Sea of the Sansha Track Ocean Coral Reef Conservation Research Institute (HJLD16-01, HJLD-1701), the Fundamental Research Funds for the Central Universities (201762038).

Acknowledgments

We thank the captain Yichuan Chen and the crews of the Qiongqionghai 03138, Yunyu Yuan, and Honglin Ma for logistical support and sampling assistance. We also thank Guoling Zhang for her technical assistance during laboratory analyses.

Conflict of interest

The authors declare that the research was conducted without any commercial or financial relationship that could be considered a potential conflict of interest.

Publisher's note

Supplementary material

The Supplementary Material for this article can be found online at: https://www.frontiersin.org/articles/10.3389/fmars.2023.1172475/full#supplementary-material

References

Anderson, L. A., and Sarmiento, J. L. (1994). Redfield ratios of remineralization determined by nutrient data analysis. *Global Biogeochem. Cycles* 8, 65–80. doi: 10.1029/93GB03318

Bi, N. S., Fu, L., Chen, H. J., Liu, R. Z., Chen, L., Liu, Q. Q., et al. (2018). Hydrographic features of the yongle blue hole in the south China Sea and their influential factors. *Chin. Sci. Bull.* 63, 2184–2194. doi: 10.1360/N972017-01329

Bishop, R. E., Humphreys, W. F., Cukrov, N., Žic, V., Boxshall, G. A., Cukrov, M., et al. (2015). 'Anchialine'redefined as a subterranean estuary in a crevicular or cavernous geological setting. *J. Crustacean Biol.* 35 (4), 511–514. doi: 10.1163/1937240X-00002335

Brand, A., Bruderer, H., Oswald, K., Guggenheim, C., Schubert, C. J., and Wehrli, B. (2016). Oxygenic primary production below the oxycline and its importance for redox dynamics. *Aquat. Sci.* 78, 727–741. doi: 10.1007/s00027-016-0465-4

Brzezinski, M. A., Villareal, T. A., and Lipschultz, F. (1998). Silica production and the contribution of diatoms to new and primary production in the central north pacific. *Mar. Ecol. Prog. Ser.* 167, 89–104. doi: 10.3354/meps167089

Buchwald, C., Santoro, A. E., Stanley, R. H., and Casciotti, K. L. (2015). Nitrogen cycling in the secondary nitrite maximum of the eastern tropical north pacific off Costa Rica. *Global Biogeochem Cycles* 29 (12), 2061–2081. doi: 10.1002/2015GB005187

Catalano, G. (1987). An improved method for the determination of ammonia in seawater. *Mar. Chem.* 20 (3), 289–295. doi: 10.1016/0304-4203(87)90079-X

Chen, Y. L. (2005). Spatial and seasonal variations of nitrate-based new production and primary production in the south China Sea. *Deep Sea Res. Part I: Oceanographic Res. Papers* 52 (2), 319–340. doi: 10.1016/j.dsr.2004.11.001

Cline, J. D. (1969). Spectrophotometric determination of hydrogen sulfide in natural waters. *Limnol Oceanogr.* 14 (3), 454–458. doi: 10.4319/lo.1969.14.3.0454

Cross, W. F., Wallace, J. B., and Rosemond, A. D. (2007). Nutrient enrichment reduces constraints on material flows in a detritus-based food web. *Ecology* 88 (10), 2563–2575. doi: 10.1890/06-1348.1

Davis, M. C., and Garey, J. R. (2018). Microbial function and hydrochemistry within a stratified anchialine sinkhole: a window into coastal aquifer interactions. *Water* 10 (8), 972. doi: 10.3390/w10080972

Doney, S. C., Ruckelshaus, M., Emmett Duffy, J., Barry, J. P., Chan, F., English, C. A., et al. (2012). Climate change impacts on marine ecosystems. *Annu. Rev. Mar. Sci.* 4, 11–37. doi: 10.1146/annurev-marine-041911-111611

Falkowski P. G. and Woodhead A. D. (Eds.) (2013). *Primary productivity and biogeochemical cycles in the sea* (Springer Science & Business Media), 387–405.

Gischler, E., Shinn, E. A., Oschmann, W., Fiebig, J., and Buster, N. A. (2008). A 1500-year Holocene Caribbean climate archive from the blue hole, lighthouse reef, Belize. *J. Coast. Res.* 24 (6), 1495–1505. doi: 10.2112/07-0891.1

Grasshoff, K., Kremling, K., and Ehrhardt, M. (2007). *Methods of seawater analysis (Third edition)* (Weinheim, Germany: Wiley-VCH Verlag GmbH).

Gruber, N. (2008). The marine nitrogen cycle: overview and challenges. *Nitrogen Mar. Environ.* 2, 1–50. doi: 10.1016/B978-0-12-372522-6.00001-3

He, P., Xie, L., Zhang, X., Li, J., Lin, X., Pu, X., et al. (2020). Microbial diversity and metabolic potential in the stratified sansha yongle blue hole in the south China Sea. *Sci. Rep.* 10 (1), 5949. doi: 10.1038/s41598-020-62411-2

Hiscock, W. T., and Millero, F. J. (2006). Alkalinity of the anoxic waters in the Western Black Sea. *Deep Sea Research Part II: Topical Studies in Oceanography* 53 (17–19), 1787–1801. doi: 10.1038/s41579-022-00687-z

Hutchins, D. A., and Capone, D. G. (2022). The marine nitrogen cycle: new developments and global change. *Nat. Rev. Microbiol.* 20 (7), 401–414. doi: 10.1038/s41579-022-00687-z

Hutchins, D. A., Mulholland, M. R., and Fu, F. (2009). Nutrient cycles and marine microbes in a CO_2-enriched ocean. *Oceanography* 22 (4), 128–145. doi: 10.5670/oceanog.2009.103

Karl, D. M. (2014). Microbially mediated transformations of phosphorus in the sea: new views of an old cycle. *Annu. Rev. Mar. Sci.* 6, 279–337. doi: 10.1146/annurev-marine-010213-135046

Lam, P., Jensen, M. M., Kock, A., Lettmann, K. A., Plancherel, Y., Lavik, G., et al. (2011). Origin and fate of the secondary nitrite maximum in the Arabian Sea. *Biogeosciences* 8 (6), 1565–1577. doi: 10.5194/bg-8-1565-2011

Li, T., Feng, A., Liu, Y., Li, Z., Guo, K., Jiang, W., et al. (2018). Three-dimensional (3D) morphology of sansha yongle blue hole in the south China Sea revealed by underwater remotely operated vehicle. *Sci. Rep.* 8 (1), 17122. doi: 10.1038/s41598-018-35220-x

Maloney, B., Iliffe, T. M., Gelwick, F., and Quigg, A. (2011). Effect of nutrient enrichment on naturally occurring macroalgal species in six cave pools in Bermuda. *Phycologia* 50 (2), 132–143. doi: 10.2216/09-83.1

Murphy, J., and Riley, J. P. (1962). A modified single solution method for the determination of phosphate in natural waters. *Analytica Chimica Acta* 27, 31–36. doi: 10.1016/S0003-2670(00)88444-5

Murray, J. W., Codispoti, L. A., and Friederich, G. E. (1995). Oxidation-reduction environments: the suboxic zone in the black Sea. *Aquatic Chemis.* 7, 157–176. doi: 10.1021/ba-1995-0244.ch007

Noffke, A., Hensen, C., Sommer, S., Scholz, F., Bohlen, L., Mosch, T., et al. (2012). Benthic iron and phosphorus fluxes across the Peruvian oxygen minimum zone. *Limnol Oceanogr* 57 (3), 851–867. doi: 10.4319/lo.2012.57.3.0851

Pan, X., Wong, G. T., Tai, J. H., and Ho, T. Y. (2015). Climatology of physical hydrographic and biological characteristics of the northern south China Sea shelf-sea (NoSoCS) and adjacent waters: observations from satellite remote sensing. *Deep Sea Res. Part II: Topical Stud. Oceanogr.* 117, 10–22. doi: 10.1016/j.dsr2.2015.02.022

Parsons, T. R., Takahashi, M., and Hargrave, B. (1984). *Biological Oceanographic processes. 3rd ed* (Oxford: Pergamon Press).

Patin, N. V., Dietrich, Z. A., Stancil, A., Quinan, M., Beckler, J. S., Hall, E. R., et al. (2021). Gulf of Mexico blue hole harbors high levels of novel microbial lineages. *ISME J.* 15 (8), 2206–2232. doi: 10.1038/s41396-021-00917-x

Paulmier, A., and Ruiz-Pino, D. (2009). Oxygen minimum zones (OMZs) in the modern ocean. *Prog. Oceanogr.* 80 (3-4), 113–128. doi: 10.1016/j.pocean.2008.08.001

Redfield, A. C. (1963). The influence of organisms on the composition of seawater. *Sea* 2, 26–77.

Revsbech, N. P., Larsen, L. H., Gundersen, J., Dalsgaard, T., Ulloa, O., and Thamdrup, B. (2009). Determination of ultra-low oxygen concentrations in oxygen minimum zones by the STOX sensor. *Limnol. Oceanogr.: Methods* 7 (5), 371–381. doi: 10.4319/lom.2009.7.371

Schwabe, S., and Herbert, R. A. (2004). Black holes of the Bahamas: what they are and why they are black. *Quaternary Int.* 121, 3–11. doi: 10.1016/j.quaint.2004.01.019

Seymour, J. R., Humphreys, W. F., and Mitchell, J. G. (2007). Stratification of the microbial community inhabiting an anchialine sinkhole. *Aquat. Microbial Ecol.* 50 (1), 11–24. doi: 10.3354/ame01153

Thamdrup, B., Dalsgaard, T., and Revsbech, N. P. (2012). Widespread functional anoxia in the oxygen minimum zone of the Eastern south pacific. *Deep Sea Res. Part I: Oceanographic Res. Papers* 65, 36–45. doi: 10.1016/j.dsr.2012.03.001

Tréguer, P. J., and de la Rocha, C. L. (2013). The world ocean silica cycle. *Annu. Rev. Mar. Sci.* 5, 477–501. doi: 10.1146/annurev-marine-121211-172346

Ulloa, O., Canfield, D. E., DeLong, E. F., Letelier, R. M., and Stewart, F. J. (2012). Microbial oceanography of anoxic oxygen minimum zones. *Proc. Natl. Acad. Sci.* 109 (40), 15996–16003. doi: 10.1073/pnas.1205009109

van Hengstum, P. J., Scott, D. B., Gröcke, D. R., and Charette, M. A. (2011). Sea Level controls sedimentation and environments in coastal caves and sinkholes. *Mar. Geology* 286 (1-4), 35–50. doi: 10.1016/j.margeo.2011.05.004

van Vliet, D. M., von Meijenfeldt, F. B., Dutilh, B. E., Villanueva, L., Sinninghe Damsté, J. S., Stams, A. J., et al. (2021). The bacterial sulfur cycle in expanding dysoxic and euxinic marine waters. *Environ. Microbiol.* 23 (6), 2834–2857. doi: 10.1111/1462-2920.15265

Vargas, C. A., Cantarero, S. I., Sepúlveda, J., Galán, A., De Pol-Holz, R., Walker, B., et al. (2021). A source of isotopically light organic carbon in a low-pH anoxic marine zone. *Nat. Commun.* 12 (1), 1604. doi: 10.1038/s41467-021-21871-4

Volkov, I. I., and Rozanov, A. G. (2006). Fundamentals of biohydrochemistry of anoxic basins. *Oceanology* 46 (6), 803. doi: 10.1134/S0001437006060051

Wang, H., Jin, Q., and Gao, S. (2008). A preliminary study on the response of marine primary production to monsoon variations in the south China Sea basic characteristics. *Acta Oceanologica Sin.* 5), 21–35.

Wang, Y., Zhang, J., and Sun, P. (2007). The *in-situ* chlorophyll-a fluorometer and turbidity meter for marine application. *Ocean Technol.* 26 (1), 29.

Wu, M. L., Liu, Q. Y., Dong, J. D., Wang, Y. S., and Wang, D. X. (2015). Primary nitrite maximum in the euphotic layer near the xisha islands, south China Sea. *Aquat. Ecosystem Health Manage.* 18 (4), 414–423. doi: 10.1080/14634988.2015.1115321

Xie, L., Wang, B., Pu, X., Xin, M., He, P., Li, C., et al. (2019). Hydrochemical properties and chemocline of the sansha yongle blue hole in the south China Sea. *Sci. Total Environ.* 649, 1281–1292. doi: 10.1016/j.scitotenv.2018.08.333

Yao, P., Chen, L., Fu, L., Yang, Z., Bi, N., Wang, L., et al. (2018). Controls on vertical nutrient distributions in the sansha yongle blue hole, south China Sea. *Chin. Sci. Bull.* 63 (23), 2393–2402. doi: 10.1360/N972018-00155

Yao, W., and Millero, F. J. (1995). The chemistry of the anoxic waters in the framvaren fjord, Norway. *Aquat. Geochem* 1, 53–88. doi: 10.1007/BF01025231

Yao, P., Wang, X. C., Bianchi, T. S., Yang, Z. S., Fu, L., Zhang, X. H., et al. (2020). Carbon cycling in the world's deepest blue hole. *J. Geophys Res.: Biogeosciences* 125 (2), e2019JG005307. doi: 10.1029/2019JG005307

YSI Environmental (2006). "In vivo measurement of chlorophyll and the YSI 6025 wiped chlorophyll sensor," in *YSI environmental white paper* (Ohio: Yellow Springs), 1–4.

Yu, Y., Xing, X., Liu, H., Yuan, Y., Wang, Y., and Chai, F. (2019). The variability of chlorophyll-a and its relationship with dynamic factors in the basin of the south China Sea. *J. Mar. Syst.* 200, 103230. doi: 10.1016/j.jmarsys.2019.103230

Zhang, J. Z., and Millero, F. J. (1993). The chemistry of the anoxic waters in the cariaco trench. *Deep Sea Res. Part I: Oceanographic Res. Papers* 40 (5), 1023–1041. doi: 10.1016/0967-0637(93)90088-K

Zhou, S., Liu, J., Yao, P., Fu, L., Yang, Z., Zhang, Y., et al. (2023). Unique bacterial communities and lifestyles in deep ocean blue holes: insights from the yongle blue hole (South China Sea). *Front. Mar. Sci.* 10, 104. doi: 10.3389/fmars.2023.1086117

Žic, V., Truesdale, V. W., Cuculić, V., and Cukrov, N. (2011). Nutrient speciation and hydrography in two anchialine caves in Croatia: tools to understand iodine speciation. *Hydrobiologia* 677, 129–148. doi: 10.1007/s10750-011-0686-4

frontiers | Frontiers in Marine Science

TYPE Original Research
PUBLISHED 26 May 2023
DOI 10.3389/fmars.2023.1165304

OPEN ACCESS

EDITED BY
Hermano Melo Queiroz,
University of São Paulo, Brazil

REVIEWED BY
Ruifeng Zhang,
Shanghai Jiao Tong University, China
Peter Leslie Croot,
University of Galway, Ireland

*CORRESPONDENCE
Wenhao Wang
Wenhao.Wang@soton.ac.uk

RECEIVED 13 February 2023
ACCEPTED 09 May 2023
PUBLISHED 26 May 2023

CITATION
Wang W, Goring-Harford H, Kunde K, Woodward EMS, Lohan MC, Connelly DP and James RH (2023) Biogeochemical cycling of chromium and chromium isotopes in the sub-tropical North Atlantic Ocean.
Front. Mar. Sci. 10:1165304.
doi: 10.3389/fmars.2023.1165304

Biogeochemical cycling of chromium and chromium isotopes in the sub-tropical North Atlantic Ocean

Wenhao Wang[1]*, Heather Goring-Harford[1], Korinna Kunde[1], E. Malcolm S. Woodward[2], Maeve C. Lohan[1], Douglas P. Connelly[3] and Rachael H. James[1]

[1]School of Ocean and Earth Science, University of Southampton, Southampton, United Kingdom, [2]Plymouth Marine Laboratory, Plymouth, United Kingdom, [3]National Oceanography Centre, Southampton, United Kingdom

Chromium (Cr) is a redox-sensitive element and because Cr isotopes are fractionated by redox and/or biological processes, the Cr isotopic composition of ancient marine sediments may be used to infer changes in past seawater oxygenation or biological productivity. While there appears to be a 'global correlation' between the dissolved Cr concentration and Cr isotopic composition of seawater, there is ongoing debate about the relative importance of external sources and internal cycling on shaping the distribution of dissolved Cr that needs to be resolved to validate the efficacy of using Cr isotopes as a paleo proxy. Here, we present full water column depth profiles of total dissolved Cr (Cr(VI)+Cr(III)) and dissolved Cr isotopes (δ^{53}Cr), together with ancillary data, for three stations along a transect (GEOTRACES GApr08) across the sub-tropical North Atlantic. Concentrations of dissolved Cr ranged between 1.84 and 2.63 nmol kg^{-1}, and δ^{53}Cr values varied from 1.06 to 1.42‰. Although atmospheric dust, hydrothermal vents and seabed sediments have the potential to modify the distribution of Cr in the oceans, based on our observations, there is no clear evidence for substantial input of Cr from these sources in our study region although benthic inputs of Cr may be locally important in the vicinity of hydrothermal vents. Subsurface waters (below the surface mixed layer to 700 m water depth) were very slightly depleted in Cr (by up to ~0.4 nmol kg^{-1}), and very slightly enriched in heavy Cr isotopes (by up to ~0.14‰), relative to deeper waters and the lowest Cr concentrations and highest δ^{53}Cr values coincided with lowest concentrations of colloidal (0.02 to 0.2 µm size fraction) Fe. We found no direct evidence for biological uptake of dissolved Cr in the oligotrophic euphotic zone or removal of Cr in modestly oxygen depleted waters (O_2 concentrations ~130 µmol kg^{-1}). Rather, we suggest removal of Cr (probably in the form of Cr(III)) in subsurface waters is associated with the formation of colloid aggregates of Fe-(oxyhydr)oxides. This process is likely enhanced by the high lithogenic particle load in this region, and represents a previously unrecognized export flux of Cr. Regeneration of Cr in deeper waters leads to subtly increased levels of Cr alongside decreased δ^{53}Cr values at individual sites, but this trend is more obvious at the global scale, with δ^{53}Cr values decreasing with increasing radiocarbon age of deep waters, from 1.16 ± 0.10‰ (1SD, n=11) in deep Atlantic waters to 0.77 ± 0.10‰ (1SD, n=25) in deep Pacific waters. Removal of

relatively isotopically light Cr from subsurface waters onto particulate material and regeneration of this Cr back into the dissolved phase in deep waters partly accounts for the systematic relationship between δ^{53}Cr and Cr concentrations in seawater discussed by other studies.

KEYWORDS

chromium isotopes, North Atlantic Ocean, particle scavenging, regeneration, GEOTRACES

1 Introduction

Chromium (Cr) is a transition metal, present in typical concentrations of 0.9 to 6.5 nM in seawater (e.g., Campbell and Yeats, 1981; Cranston, 1983; Jeandel and Minster, 1987; Achterberg and van den Berg, 1997; Sirinawin et al., 2000; Connelly et al., 2006; Scheiderich et al., 2015) and has a relatively long seawater residence time of ~3000 to 9500 years (Reinhard et al., 2013; McClain and Maher, 2016; Pöppelmeier et al., 2021). In some parts of the oceans, concentrations of dissolved Cr are modestly depleted in the surface layer, and Cr has been classified as intermediate between a 'conservative' and 'recycled' element (Jeandel and Minster, 1987; Sirinawin et al., 2000). In oxic seawater, Cr(VI) is predicted to be the thermodynamically stable form of Cr (Elderfield, 1970), although relatively high concentrations of dissolved Cr(III) have been reported in some studies (e.g., Achterberg and van den Berg, 1997; Connelly et al., 2006). High concentrations of Cr(III) in oxic waters are most likely due to the presence of Cr(III)-organic complexes in the colloidal fraction (Li et al., 2022) that may not be captured by some analytical techniques (Rue et al., 1997; Wang et al., 2019; Huang et al., 2021). Under oxygen deficient conditions, Cr(III) can be the dominant Cr species, accounting for up to ~64% of the total dissolved Cr (Murray et al., 1983; Rue et al., 1997; Huang et al., 2021). However, oxygen is not the sole control on Cr speciation (Goring-Harford et al., 2018; Janssen et al., 2020); field (Connelly et al., 2006; Janssen et al., 2020) and experimental (Døssing et al., 2011; Kitchen et al., 2012) studies have suggested that high levels of biological productivity, as well as the presence of Fe(II) and organic matter in surface waters, can also facilitate Cr reduction even in O_2-replete waters (Pettine et al., 1998). At the sea surface, Cr(VI) reduction most likely proceeds *via* photoreduction (Kieber and Helz, 1992; Kaczynski and Kieber, 1993). Cr(VI) is highly soluble as the chromate (CrO_4^{2-}) ion in oxic seawater, whilst Cr(III) is particle-reactive and readily adsorbed onto solid surfaces (Rai et al., 1987; Ellis et al., 2002).

Rivers are thought to be the main source of dissolved Cr to the ocean (Bonnand et al., 2013; Reinhard et al., 2013; McClain and Maher, 2016; Pöppelmeier et al., 2021). Chromium is mainly present in the form of Cr(III) in rocks; weathering reactions driven by Mn-oxides oxidise Cr(III) as it is released from silicate rocks (Eary and Rai, 1987; Frei et al., 2014; D'Arcy et al., 2016), so Cr can be in the form of both Cr(III) and Cr(VI) in river waters that are delivered to the oceans (e.g., Cranston and Murray, 1980; Goring-Harford et al., 2020). Atmospheric deposition is a major source of many trace metals to the ocean and can result in elevated concentrations of Cr in surface seawater at some locations (Achterberg and van den Berg, 1997), but not others (Goring-Harford et al., 2018; Janssen et al., 2023). Benthic Cr fluxes can be locally important (e.g., Shaw et al., 1990; Rigaud et al., 2013; Janssen et al., 2021), and may also be important for the overall oceanic Cr inventory (Pöppelmeier et al., 2021). High temperature hydrothermal fluids from the Kermadec Arc have Cr concentrations on the order of 10 to 30 nmol kg^{-1}, distinctly higher than surrounding seawater (Janssen et al., 2023). However, analyses of hydrothermal plume particles indicate that they have higher Cr/Fe ratios than predicted by mixing of vent fluids and seawater, suggesting that hydrothermal activity may be a net sink of Cr as it is scavenged from seawater onto Fe-(oxyhydr)oxides (Trocine and Trefry, 1988; German et al., 1991; Rudnicki and Elderfield, 1993; Feely et al., 1996; Bauer et al., 2019). Cr is removed from the oceanic inventory through reduction of Cr(VI), scavenging onto settling particles and burial as Cr(III) in reducing and/or anoxic sediments (Reinhard et al., 2014; Gueguen et al., 2016). Therefore, marine sediments are considered as the major sink for seawater Cr. The estimated fluxes of Cr inputs to, and outputs from, the ocean reported in the literature are summarized in Table 1.

Stable chromium isotope ratios are expressed in delta notation relative to the NBS979 standard, as:

$$\delta^{53}Cr = [(^{53}Cr/^{52}Cr)_{sample}/(^{53}Cr/^{52}Cr)_{NBS979} - 1] \times 1000 \quad (1)$$

The δ^{53}Cr values of silicate rocks show a narrow range, −0.12 ± 0.10‰ (Schoenberg et al., 2008). Groundwaters with low levels of oxygen are relatively enriched in heavy Cr isotopes (δ^{53}Cr = 0.7 to 5.8‰: Ellis et al., 2002; Izbicki et al., 2008), which is thought to reflect isotope fractionation during oxidation of Cr(III) to Cr(VI) followed by partial back reduction of the Cr(VI). Theoretical studies and laboratory experiments have shown that reduction of Cr(VI) leads to large mass-dependent fractionation, with enrichment of light Cr isotopes in the Cr(III) that forms (Ellis et al., 2002; Døssing et al., 2011; Basu and Johnson, 2012; Kitchen et al., 2012). The direction of fractionation remains the same regardless of the reductant (Fe(II), Fe(II)-bearing minerals, organic matter), but the kinetic fractionation factors are variable (δ^{53}Cr(III) – δ^{53}Cr (VI) = −1.5 to −4.2‰). To date, there have only been three reports of the Cr isotopic composition of single Cr species in seawater in the

TABLE 1 Range of concentrations and fluxes of Cr inputs and outputs to/from the ocean.

Reservoir	Cr (nM)	Cr (μmol g^{-1})	Flux Cr (mol yr^{-1})	Reference
Inputs				
Rivers	15-150		$2.5\text{-}17 \times 10^8$	Bonnand et al. (2013); McClain and Maher (2016); Pöppelmeier et al. (2021)
Low-temperature hydrothermal vents	~48		$\sim 3.4 \times 10^6$	Sander and Koschinsky (2000); Reinhard et al. (2013)
Benthic sediments	~48		$\sim 6.0 \times 10^8$	Janssen et al. (2021); Pöppelmeier et al. (2021)
Outputs				
Hydrothermal plumes		–	4.8×10^7	Rudnicki and Elderfield, 1993
Oxic sediment sink		~2	5.8×10^7	Chester and Hughes (1969); Reinhard et al. (2013)
Sub-oxic and anoxic sediment sink		~2	5.2×10^8	Reinhard et al. (2013); Gueguen et al. (2016)

peer-reviewed literature (Wang et al., 2019; Davidson et al., 2020; Huang et al., 2021). These studies all show that Cr(III) is isotopically lighter than co-existing Cr(VI), by between −0.07 to −3.1‰ (Davidson et al., 2020; Huang et al., 2021), consistent with the theoretical and laboratory studies.

There is a rapidly growing dataset on the distribution of dissolved Cr isotopes in the open ocean with δ^{53}Cr values ranging from 0.60 to 1.71‰ (Scheiderich et al., 2015; Goring-Harford et al., 2018; Moos and Boyle, 2019; Rickli et al., 2019; Janssen et al., 2020; Moos et al., 2020; Nasemann et al., 2020; Huang et al., 2021; Janssen et al., 2021). The average seawater δ^{53}Cr value yielded from the emerging dataset is 1.04 ± 0.19‰ (1SD, n=347; see Section 4.5 for more details), slightly higher than that of the global average river input (0.49 ± 0.23‰, 1SD, n=49: Frei et al., 2014; Paulukat et al., 2015; D'Arcy et al., 2016; Wu et al., 2017; Andronikov et al., 2019). Although some studies show evidence for fractionation of Cr isotopes during estuarine mixing (Roseburrough and Wang, 2021) and others do not (Goring-Harford et al., 2020), the difference between the mean river water and seawater values nevertheless suggests that the Cr isotopic signature of seawater is likely influenced by input of Cr from other sources (such as seabed sediments) and/or is modified by fractionation of Cr as it is removed from seawater (e.g., by reduction of Cr(VI) on the surface of particles that scavenge the Cr(III) that forms). The measured δ^{53}Cr values in the authigenic fractions of reducing and anoxic marine sediments are reported to be between 0.45 and 0.61‰ in Peru margin sediments (Gueguen et al., 2016; Bruggmann et al., 2019) and between 0.38 and 0.53‰ in Cariaco Basin sediments (Reinhard et al., 2014; Gueguen et al., 2016). These values are within the range of the δ^{53}Cr values of the riverine input, but are lower than most seawater values, supporting the proposition that Cr isotope fractionation occurs during reduction and scavenging of Cr (Janssen et al., 2022).

Scheiderich et al. (2015) showed that the δ^{53}Cr composition of waters in the Arctic and Pacific Ocean was highly heterogeneous (0.61 to 1.55‰) and hypothesized that this can be attributed to Cr reduction and scavenging in surface waters and oxygen minimum zones (OMZs), with subsequent release of Cr from sinking particles in deeper waters. These processes were used to explain the inverse correlation between δ^{53}Cr value and logarithmic Cr concentration in the global ocean, from which they derived an isotope fractionation factor (ϵ, the difference between the δ^{53}Cr value of Cr(III) and the δ^{53}Cr value of Cr(VI)) of ~ −0.8‰ (Scheiderich et al., 2015). More recent studies of the Cr isotopic composition of seawater from the Pacific (including oxygen-deficient zones) and the Southern Ocean (Moos and Boyle, 2019; Rickli et al., 2019; Janssen et al., 2020; Moos et al., 2020; Nasemann et al., 2020; Huang et al., 2021; Janssen et al., 2021) also follow this 'global correlation'. Whilst evidence for the roles of redox transformations (Nasemann et al., 2020; Huang et al., 2021; Wang, 2021), water mass mixing (Rickli et al., 2019) and biological uptake and regeneration (Janssen et al., 2020; Janssen et al., 2021) on seawater δ^{53}Cr is emerging, the underlying mechanisms that produce the apparent correlation between δ^{53}Cr and Cr concentration are still under debate.

Here, we report total dissolved Cr (Cr(VI) + Cr(III)) concentrations and total dissolved Cr isotope compositions (δ^{53}Cr) for full-depth water column profiles for three stations from a GEOTRACES transect along the 22°N sub-tropical Atlantic Ocean (Figure 1A). This fills an important knowledge gap, because few full-depth water column profiles of Cr isotopes, together with ancillary data (biogeochemical parameters, concentrations of other trace metals, etc.) that aid the interpretation of Cr behavior, are available for the Atlantic ocean. The potential sources of Cr to the North Atlantic Ocean as well as the effects of internal cycling are explicitly investigated, and by considering these new data together with other data from the literature, we are able to provide new insights as to the removal and regeneration processes that shape the global distributions of Cr and Cr isotopes in seawater.

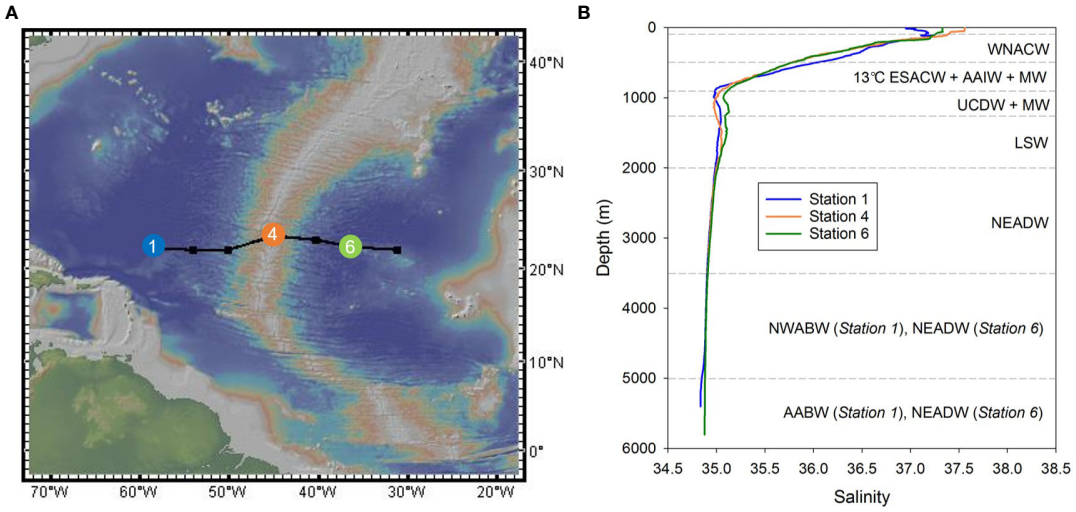

FIGURE 1
(A) Locations of sampling stations (1, 4 and 6) in the sub-tropical North Atlantic Ocean. Map courtesy of http://www.geomapapp.org **(B)** Salinity profiles for the three sampling stations. Water masses are delimited by horizontal dashed lines. WNACW, West North Atlantic Central Water; ESACW, East South Atlantic Central Water; AAIW, Antarctic Intermediate Water; MW, Mediterranean Water; UCDW, Upper Circumpolar Deep Water; LSW, Labrador Sea Water; NEADW, North East Atlantic Deep Water; NWABW, North West Atlantic Bottom Water; AABW, Antarctic Bottom Water. Water mass analysis after Artigue et al. (2020).

2 Materials and methods

2.1 Sample collection and oceanographic setting

Samples for this study were collected from Stations 1, 4, and 6 in the sub-tropical North Atlantic (Figure 1A) during RRS *James Cook* cruise JC150 (UK GEOTRACES $GA_{pr}08$ process cruise) between 26th of June and 12th of August 2017. The water depths for the three stations were 5408 m, 3505 m and 5810 m respectively. The cruise was specifically designed to investigate macro- and micro-nutrient co-limitation on nitrogen fixation in the oligotrophic gyre; thus, nutrient and trace metal distributions (e.g., Kunde et al., 2019; Artigue et al., 2021) were carefully quantified.

Seawater was collected using pre-cleaned 10 L Ocean Test Equipment (OTE) water sampling bottles that were mounted on a titanium rosette system and deployed from a Kevlar wire. On recovery, the OTE bottles were transferred into a trace metal clean container for sub-sampling. Seawater was filtered through a Sartobran 300 (Sartorius) filter capsule (0.2 µm) under gentle pressure and was collected into 2 L acid-cleaned low density polyethylene (LDPE) bottles. Filtered seawater samples were acidified with UpA-grade hydrochloric acid (HCl, Romil) to 0.024 M, and were stored for at least a year before the Cr isotope analysis, allowing complete conversion of Cr species to Cr (III) (Semeniuk et al., 2016).

Analyses of the water masses along the transect based on combined hydrographic and nutrient data are reported in Artigue et al. (2020) and summarized in Figure 1B. Briefly, surface waters were occupied by a shallow form of Eastern South Atlantic Central Water (ESACW), with a small contribution from the Amazon plume in the west. Below the surface, the waters mainly consisted of West North Atlantic Central Water (WNACW, 100-500 m) and 13°C-ESACW (500-900 m), although at approximately 700 m water depth, Antarctic Intermediate Water (AAIW) and Mediterranean Water (MW) were present, respectively, to the west and to the east of the Mid-Atlantic Ridge (MAR). Upper Circumpolar Deep Water (UCDW) was generally observed between 900-1250 m, below which Labrador Sea Water (LSW) was centered at ~1500 m. North East Atlantic Deep Water (NEADW), which includes a contribution from Iceland-Scotland Overflow Water (ISOW), was found below LSW and was centered at ~2500 m. At Station 1, to the west of the MAR, North West Atlantic Bottom Water (NWABW) was present between 3500 and 5000 m water depth, and deeper waters (>5000 m) consisted of Antarctic Bottom Water (AABW). The deep waters at Station 6 were dominated by NEADW. Note that LSW, NEADW and NWABW all contribute to North Atlantic Deep Water (NADW). Hereafter, we define waters from below the surface mixed layer to 700 m depth as subsurface waters (including the thermocline which was located between ~300 and ~700 m; Artigue et al., 2020), waters from between 700 and 2000 m depth as intermediate waters, and waters below ~2000 m water depth as deep waters (Sarmiento et al., 2007).

2.2 Cr isotope analysis

All acids used for chemical processing were thermally distilled. Milli-Q (MQ) water was used for diluting and for cleaning. LDPE bottles and Perfluoroalkoxy (PFA) vials were thoroughly cleaned for trace metal purposes. Samples were handled under laminar flow hoods, set within Class 100 clean laboratories at the National Oceanography Centre Southampton.

Dissolved Cr concentrations were initially determined using a $Mg(OH)_2$ co-precipitation method (Rickli et al., 2019; Davidson

et al., 2020). Approximately 50 mL of filtered seawater was transferred into an acid-cleaned centrifuge tube, weighed, and amended with 10 ng of a ^{53}Cr single spike. Ammonia solution (SpA-grade, Romil) was then added to the sample until $Mg(OH)_2$ formed. For 50 mL of acidified seawater (pH ~1.7), ~500 µL concentrated ammonia was required; the size of $Mg(OH)_2$ pellet was kept as small as possible to minimize the potential for matrix effects. After centrifugation and removal of the supernatant, the Cr precipitate was re-dissolved in 5 mL of 0.45 M HNO_3. The Cr concentration of the seawater sample was derived by isotope dilution, based on the ^{52}Cr/^{53}Cr ratio of the sample/spike mixture measured by inductively coupled plasma mass spectrometry (ICP-MS; Thermo Scientific Element). These Cr concentration data were used to estimate the volume of water required for pre-concentration and to optimize the amount of double spike added. The accuracy of the $Mg(OH)_2$ co-precipitation method was assessed through the analysis of (1) the NASS-6 certified reference material (*National Research Council Canada*), which gave Cr = 1.95 ± 0.23 nmol kg^{-1} (n=1; 2SE internal error), compared to certified value of 2.17 ± 0.15 nmol kg^{-1} (2SD); and (2) an OSIL Atlantic seawater salinity standard (http://www.osil.co.uk), which gave Cr = 2.96 ± 0.12 nmol kg^{-1} (n=1; 2SE internal error), consistent with a previously published value for the same OSIL batch (3.06 ± 0.04 nmol kg^{-1} (2SD, n=6); Goring-Harford et al., 2018).

The Cr isotope compositions of seawater samples were determined using a method adapted from Bonnand et al. (2013). Samples of 1-2 L volume were amended with a ^{50}Cr-^{54}Cr double spike to achieve optimal target isotope ratios (Goring-Harford et al., 2018) and were left to equilibrate for ~24 hrs. Information on our double spike technique is given in Bonnand et al. (2011). The sample pH was then adjusted to pH 8-9 to facilitate precipitation of Cr. A freshly prepared suspended precipitate of Fe(II) hydroxide, made by addition of ammonia to a fresh ammonium Fe(II) sulfate solution, was added to the samples (10 mL L^{-1} seawater), allowing oxidation of the Fe(II) hydroxide and reduction of any remaining Cr(VI). The Fe(III) hydroxide scavenges the Cr(III), resulting in quantitative precipitation of dissolved inorganic Cr (Connelly et al., 2006).

The precipitate was separated from the solution *via* vacuum filtration through pre-cleaned PTFE membrane filters (1 µm, Millipore Omnipore), and was subsequently leached from the filters using 6 M HCl before being dried down and taken up in 6 mL of 7 M HCl. The Cr was first separated from the Fe by anion exchange chromatography (~2 mL of Bio Rad AG1-X8 resin loaded in a Bio Rad Poly-Prep column). The resin was extensively cleaned with concentrated HNO_3, 0.5 M HCl and concentrated HCl, and was pre-conditioned with 7M HCl. The sample was loaded in 6 mL of 7M HCl onto the resin. The eluent was collected, dried down and then reconstituted in 6 mL of 0.5 M HCl. The column was cleaned with 0.5 M HCl to remove Fe and stored in 0.5 M HCl.

Any residual salts were removed by cation exchange chromatography (2.9 mL of BioRad AG 50W-X12 resin loaded in a 30 mL PFA Savillex column; Trinquier et al., 2008). The resin was cleaned with 10 mL of 8 M HNO_3, 30 mL of 6 M HCL and 30 mL of MQ water and was pre-conditioned with 12 mL of 0.5 M HCl. The sample was loaded in 6 mL of 0.5 M HCl and the Cr was immediately eluted and collected in a 15 mL Savillex vial. A further 4 mL of 0.5 M HCl was added to the column and collected. The resin was cleaned with 6M HCl to remove the remaining cations and stored in 0.5 M HCl. The Cr fraction was evaporated to dryness and was treated with 50 µL of concentrated H_2O_2 and HNO_3, respectively, to oxidize any remaining organic material, before being dried down once again and re-dissolved in 0.45 M HNO_3.

The isotopic composition of Cr was determined by multicollector inductively coupled plasma mass spectrometry (MC-ICP-MS; Thermo Fisher Neptune Plus) at the University of Southampton, using a method similar to that described in Goring-Harford et al. (2018). Purified samples at a concentration of ~50 ppb Cr were introduced using an Aridus 3 desolvator and signals from ^{50}Cr, ^{52}Cr, ^{53}Cr, ^{54}Cr and ^{49}Ti, ^{51}V, ^{56}Fe were quantified. Medium resolution setting was used and a mass resolution of >5000 was achieved. The NBS979 standard was analyzed after every 3 sample measurements in the analytical sequence. Each sample/standard analysis consisted of 100 individual measurements. Polyatomic interferences were avoided by making measurements on peak shoulders. The typical ion beam size was 0.15-0.24 volts per ppb for ^{52}Cr on a 10^{11} Ω amplifier. The mean signal intensity of a blank solution that was analyzed before and after each sample/standard was subtracted. Despite the large quantities of Fe added to the samples during co-precipitation, efficient removal of Fe by anion exchange chromatography ensured that the ^{56}Fe/^{54}Cr of the samples was always <0.50 and typically around 0.03, which would have no resolvable effect on δ^{53}Cr values (Bonnand et al., 2011). The raw Cr data were corrected for mass bias using an iterative deconvolution procedure (Albarède and Beard, 2004) and for the total procedural blank contribution. The final Cr isotope value is expressed in delta notation relative to the NBS979 isotope standard.

The Cr blank for the Fe(II) co-precipitation method was relatively constant, 18 ± 0.9 ng, the majority of which (~93%) came from the Fe(II) salt (Goring-Harford et al., 2018). The δ^{53}Cr value of the ammonium Fe(II) sulphate solution used in this study was –0.16 ± 0.04 ‰ (n=1; 2SE internal error), within the error of that measured previously (–0.34 ± 0.32‰, 2SD, n=6; Goring-Harford et al., 2018). The effect of the blank on the uncertainties of Cr and δ^{53}Cr is estimated to be ± 0.005 nmol kg^{-1} and ± 0.02‰ (2SD), respectively (Goring-Harford et al., 2018).

The Cr concentration of each sample was determined simultaneously with the isotope ratios using isotope dilution equations, based on the known sample volume and the quantity of added spike. The results were generally within 10% of the concentrations derived from the $Mg(OH)_2$ co-precipitation method; the reported Cr concentration data are from the MC-ICP-MS measurements because of the better precision.

Analyses of the NBS979 chromium isotope standard gave δ^{53}Cr = 0.00 ± 0.05‰ (2SD, n=43). The precision of the methods was further assessed through multiple analyses of an OSIL Atlantic seawater salinity standard that yielded Cr = 3.07 ± 0.058 nmol kg^{-1} (2SD, n=4) and δ^{53}Cr = 0.99 ± 0.04‰ (2SD, n=4) (Supplementary Info. 1; Table S1). These data are consistent with previously reported values (Cr = 3.10 ± 0.04 nmol kg^{-1}, δ^{53}Cr = 0.97 ± 0.10‰, 2SD, n=6; Goring-Harford et al., 2018) for the same batch of OSIL. By compiling the repeat analyses of the OSIL

samples from this study and Goring-Harford et al. (2018), we apply 2% and ± 0.06‰ as an estimate of external reproducibility for Cr and δ^{53}Cr, respectively, for all samples in this study.

As OSIL is a salinity standard and different batches do not have identical Cr concentrations and δ^{53}Cr values (Rickli et al., 2019), we undertook a cross-calibration exercise with the University of Saskatchewan in efforts to better assess the accuracy of our Cr and δ^{53}Cr data. Both groups measured three seawater samples collected by the University of Saskatchewan in the Beaufort Sea. δ^{53}Cr data for all samples were identical within the analytical uncertainty (Supplementary Info. 1; Table S2); Cr concentrations measured in our laboratory were 12-14% lower than those measured in Saskatchewan (Table S2). We have not been able to pinpoint the source of this difference, although we note that it is within the range of the uncertainty of Cr concentrations reported in a recent inter-laboratory comparison of the trace metal composition of NASS seawater (Yang et al., 2018).

2.3 Analysis of dissolved Fe concentrations and other ancillary parameters

Filtered (at 0.2 µm) samples of seawater for analysis of dissolved Fe (dFe) were acidified on board and analyzed using flow injection analysis with chemiluminescence detection (FIA-CL) inside a Class 1000 clean laboratory either onboard or at the University of Southampton, as discussed in Kunde et al. (2019). The accuracy of the method was assessed by repeat quantification of dFe in reference samples (SAFe; Johnson et al., 2007). Filtered (at 0.2 µm) seawater for analysis of soluble Fe (sFe, i.e., truly dissolved Fe) was additionally filtered in-line through 0.02 µm syringe filters (Anotop, Whatman) before it was acidified (Kunde et al., 2019). Concentrations of sFe were then determined using the same method as dFe. Concentrations of colloidal Fe (cFe, operationally defined as Fe in the size fraction 0.02 - 0.2 µm; e.g., Fitzsimmons et al., 2015) were derived from the difference between dFe and sFe. These dissolved and colloidal Fe data have been previously published in Kunde et al. (2019) and are given in Supplementary Info. 1 (Tables S1; S3).

A Seabird 911 plus conductivity, temperature and depth (CTD) profiler system together with additional sensors was attached to the titanium frame during the seawater sampling. Sensors were cross-calibrated with analyses of discrete seawater samples on board. Salinity was calibrated using an Autosal 8400B salinometer (Guildline). Chlorophyll-*a* (Chl-*a*) was measured by a fluorescence sensor that was calibrated using a fluorimeter (Turner Designs Trilogy). Dissolved oxygen (O_2) was measured by a Seabird SBE43 sensor, calibrated against a photometric automated Winkler titration system. Turbidity was monitored using the WETLabs BBRTD light scattering sensor.

Macronutrient concentrations were analyzed on board using a 5-channel (nitrate, nitrite, phosphate, silicic acid, and ammonium) segmented flow auto-analyzer (Woodward and Rees, 2001). The macronutrient data from this cruise are discussed in Artigue et al. (2020).

3 Results

Profiles of Chl-*a*, O_2 concentration and turbidity at Stations 1, 4 and 6 are shown in Figure 2; vertical distributions of the macronutrients phosphate (PO_4) and silicic acid (Si) at these stations are illustrated in Supplementary Info. 2 (Figure S1). Overall, there was no significant inter-site variation in these biogeochemical properties. At each station, Chl-*a* peaked at approximately 140 m water depth, with concentrations up to 0.4 µg L^{-1}. This so-called deep chlorophyll maximum (DCM) is a common feature in oligotrophic sub-tropical regions where the nutrient supply to the euphotic zone is minimal and the phytoplankton biomass and rate of primary production are low throughout the year (e.g., Pérez et al., 2006; Mignot et al., 2014). The concentrations of PO_4 and Si were the lowest within the upper ~150 m waters, and then increased with depth; PO_4 reached a concentration maximum at approximately 800 to 1000 m water depth whereas Si concentrations were highest close to the seabed. Oxygen concentrations showed minimum values of 140 µmol/kg at depths between ~700 and ~900 m. Deeper waters were well oxygenated with O_2 concentrations of >230 µmol kg^{-1} below ~2000 m water depth. Levels of turbidity were highest immediately below the surface (and above the DCM), which can be attributed to input of lithogenic particles of North African dust (Ye and Völker, 2017; Kunde et al., 2019), and gradually decreased with depth. Relatively high levels of turbidity were also found close to seafloor, which is likely due to resuspension of seabed sediments (Ohnemus and Lam, 2015). At Station 4 there was a local increase in turbidity between 3300 and 3500 m water depth that delineates the particle-rich hydrothermal plume (Kunde et al., 2019) above the Snake Pit hydrothermal vent field (Beaulieu, 2015) on the Mid-Atlantic Ridge.

Full water column depth profiles for dissolved Fe, Cr and δ^{53}Cr at the three stations are shown in Figure 3A (data given in Supplementary Info. 1). Concentrations of dissolved Cr ranged between 1.84 and 2.63 nmol kg^{-1}; the vertical distribution of Cr resembled that of dissolved Fe, notably in the euphotic (up to 200 m water depth) and mesopelagic (~200 to 1100 m water depth) zones. Measured δ^{53}Cr values varied from 1.06 to 1.42‰ and the δ^{53}Cr profiles appear to mirror the shape of the Cr concentration profiles. Lowest Cr concentrations (1.84 to 2.04 nmol kg^{-1}) and highest δ^{53}Cr values (1.36 to 1.42‰) coincided with lowest dFe concentrations (down to ~0.4 nM) between approximately 100 to 400 m water depth. Overall, subsurface waters (between the base of the surface mixed layer and 700 m water depth) were very slightly depleted in Cr and very slightly enriched in heavy Cr isotopes (average Cr = 2.14 ± 0.15 nmol kg^{-1}, δ^{53}Cr = 1.36 ± 0.04‰, 1SD, n=16), relative to intermediate (Cr = 2.31 ± 0.18 nmol kg^{-1}, δ^{53}Cr = 1.26 ± 0.06‰, 1SD, n=6) and deep (average Cr = 2.44 ± 0.18 nmol kg^{-1}, δ^{53}Cr = 1.19 ± 0.11‰, 1SD, n=9) waters.

Seawater Cr concentrations and δ^{53}Cr values measured in deep waters (>2000 m water depth) in this study are generally consistent with those reported for deep waters at a site further to the south (~12 °N) in the eastern sub-tropical north Atlantic (Cr = 2.5 to 2.9 nmol kg^{-1}, δ^{53}Cr = 1.08 to 1.20‰: Goring-Harford et al., 2018;

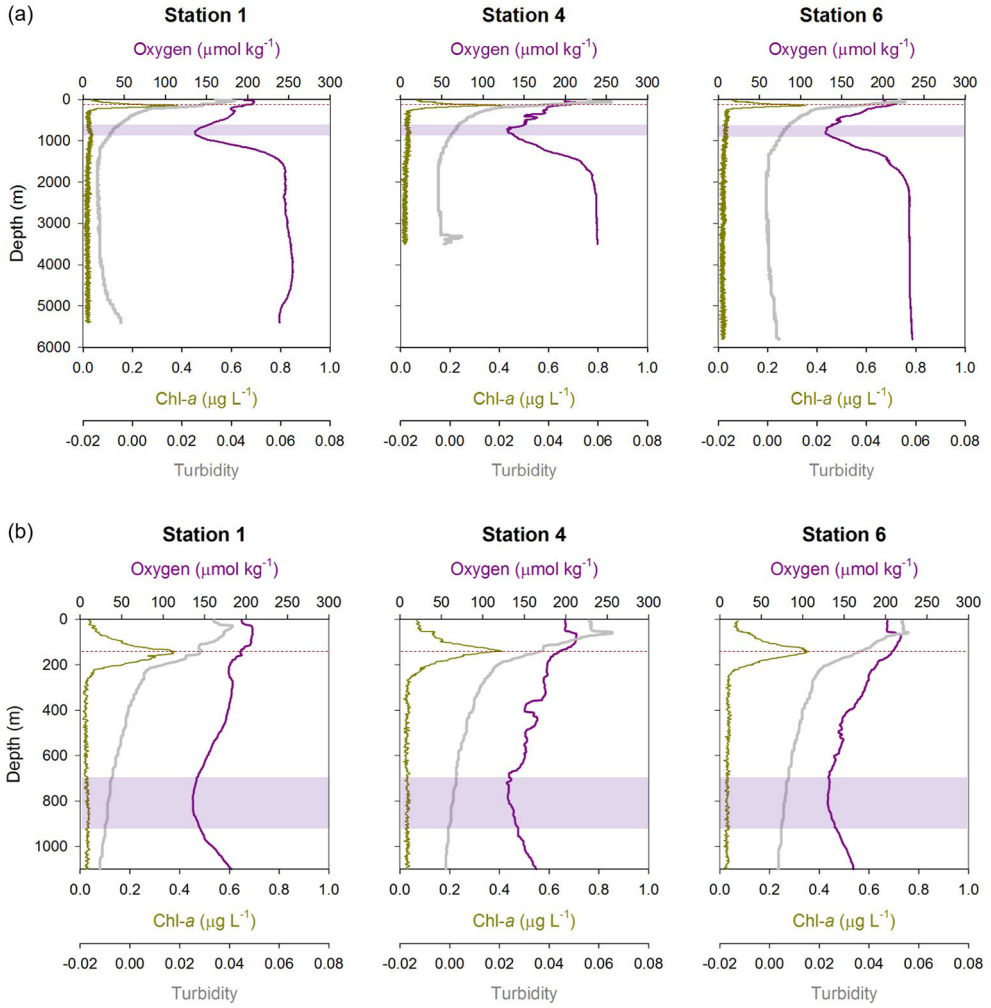

FIGURE 2
Biogeochemical properties (dissolved oxygen, Chl-*a* concentration and turbidity) at Stations 1, 4, and 6: **(A)** full water column depth profiles; **(B)** upper 1100 m of the water column. The deep Chl-*a* maximum is marked by the red horizontal dashed line, and the oxygen minimum is highlighted by the purple band at each station.

Supplementary Info. 2; Figure S2). By contrast, Cr concentrations and δ^{53}Cr values in waters between the base of the surface mixed layer and 2000 m water depth were respectively, generally lower and higher at our sites at ~22 °N than they were at ~12 °N (Figure S2).

Although no other Cr isotope data have been published to date for seawater samples collected within ± 10° latitude of our sites, Cr concentration data have been reported by a number of authors (Jeandel and Minster, 1987; Mugo and Orians, 1993; Sirinawin et al., 2000; Connelly et al., 2006) and are highly variable, ranging from ~2 nmol kg^{-1} to almost 5 nmol kg^{-1}. Our data occupy the lower end of this range (Figure S2). There are numerous potential explanations for the differences between the data sets. For example: (1) The sampling stations span almost the full width of the Atlantic Ocean, crossing many oceanographic boundaries. (2) These earlier data were obtained on samples that were not collected following GEOTRACES trace metal protocols that have been established more recently. While seawater samples collected using standard Niskin bottles from a conventional rosettes do not appear to be affected by Cr contamination (e.g., Scheiderich et al., 2015; Janssen et al., 2020; Moos et al., 2020), some types of filter can be associated with high and variable Cr blanks (e.g., Yiğiterhan et al., 2011). (3) Differences in sample treatment and analysis. Chromium concentrations were determined using various different techniques that may capture different forms of Cr. The Fe(II) co-precipitation used in this study (and also by Jeandel and Minster, 1987; Connelly et al., 2006) is unlikely to capture organically-bound dissolved Cr (Goring-Harford et al., 2020), as this fraction is thought to be resistant to reduction and adsorption (Nakayama et al., 1981). By contrast, the $Mg(OH)_2$ co-precipitation technique is expected to capture organically-bound Cr (Moos and Boyle, 2019; Davidson et al., 2020; Huang et al., 2021) and techniques that determine Cr through complexation with various ligands may capture the more labile organic-bound Cr (Mugo and Orians, 1993; Sirinawin et al., 2000). Note however that concentrations of organically-bound Cr are usually very low (e.g., Kaczynski and Kieber, 1994). In addition, most of the data reported in Jeandel and Minster (1987) were from analysis of unfiltered water samples; a handful of samples were filtered and Cr concentrations of filtered samples were between 0.15

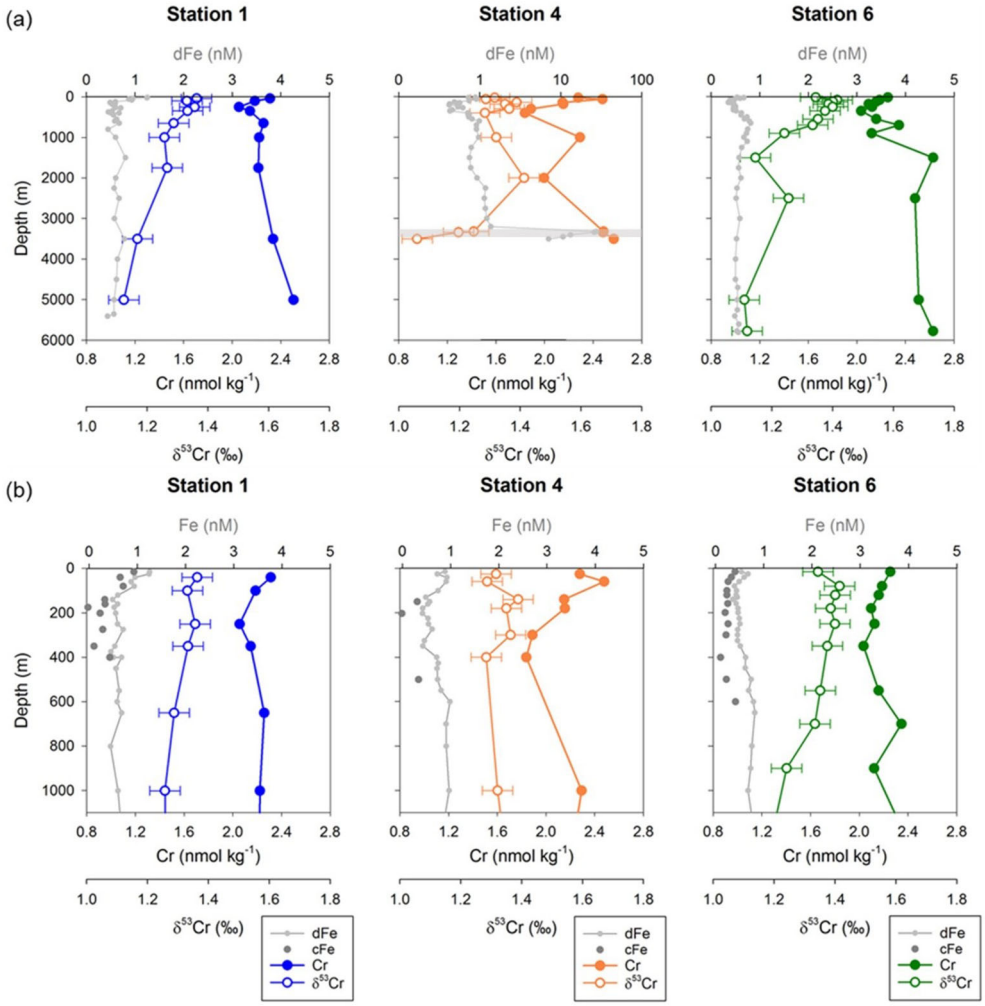

FIGURE 3
(A) Full water column depth profiles of Cr concentration, δ^{53}Cr values, and dissolved Fe concentrations at Stations 1, 4, and 6. **(B)** Profiles of Cr concentrations, δ^{53}Cr values, and dissolved and colloidal Fe concentrations for the upper 1100 m of the water column at Stations 1, 4 and 6. Location of the hydrothermal plume at Station 4 is highlighted by the grey horizontal band. Error bars on Cr and Fe concentrations are smaller than the size of symbols. Error bars on δ^{53}Cr represent the external reproducibility of the measurements (± 0.06‰, 2SD) based on the repeat analyses of OSIL Atlantic seawater salinity standard. Fe data are from Kunde et al. (2019). All Cr data are given in Supplementary Info. 1 (Table S1).

and 1.1 nmol kg^{-1} (mean 0.62 nmol kg^{-1}) lower than unfiltered samples. We also note that there are wide variations between more recent and earlier Cr concentration data from other locations. For example, Mugo and Orians (1993) reported total Cr data from 3000-4000 m water depth at Station P26 in the North Pacific of between 3.53 and 4.18 nmol kg^{-1} (data converted from reported values in nM to nmol kg^{-1} assuming salinity = 34.67; Janssen et al., 2021), whereas Janssen et al. (2021) measured values of between 4.52 and 4.54 nmol kg^{-1} for the same station over the same depth range. While there is a clear need for more concerted inter-laboratory assessments of Cr and Cr isotope data (see also Moos et al., 2020 and Huang et al., 2021), we nevertheless believe our data are analytically robust as we have carried out inter-laboratory calibration exercises as discussed in Section 2.2 together with other tests (reported in Goring-Harford et al., 2018) to validate the accuracy and precision of our data.

4 Discussion

4.1 Potential sources of Cr to the North Atlantic

Dust supply from North African deserts directly affects the subtropical North Atlantic Ocean (Jickells et al., 2005). Total (wet + dry) deposition of lithogenic particles to surface waters ranged from ~1 × 10^{-5} kg m^{-2} d^{-1} at Station 6 to ~4 × 10^{-6} kg m^{-2} d^{-1} at Station 1 (Artigue et al., 2021), which may dominate over biogenic particles (Ohnemus and Lam, 2015). Input of Fe and aluminum (Al) from dust deposition across the GEOTRACES GA$_{pr}$08 transect is evidenced by elevated concentrations of dissolved Fe and Al in the surface mixed layer (SML), which extends to 20 m, 50 m and 60 m water depth respectively, for Stations 1, 4 and 6 (Kunde et al., 2019; Artigue et al., 2021). Only two samples were collected for Cr

analysis from within the SML (at Stations 4 and 6); these had Cr concentrations of 2.28 nmol kg^{-1} (Station 4) and 2.25 nmol kg^{-1} (Station 6) (Figure 3B), similar to the Cr concentration for samples collected from the upper layer of intermediate waters at these stations (2.29 nmol kg^{-1} at 1001 m of Station 4 and 2.12-2.35 nmol kg^{-1} at 701-901 m of Station 6). The δ^{53}Cr values of dissolved Cr from the SML were 1.32‰ (Station 4) and 1.34‰ (Station 6). The δ^{53}Cr value of atmospheric dust is expected to be similar to that of crustal rocks (−0.12 ± 0.10‰; Schoenberg et al., 2008), although dissolution promoted by strong ligands may enrich heavier Cr isotopes in the dissolved phase (δ^{53}Cr up to 1.23‰; Saad et al., 2017). For total (wet + dry) deposition fluxes of ~8×10^{-6} kg m^{-2} d^{-1} (Station 4) and ~1×10^{-5} kg m^{-2} d^{-1} (Station 6; Artigue et al., 2021), with a Cr loading equivalent to average upper continental crust (~100 ppm; e.g., Rudnick and Gao, 2003), and assuming 10% of this Cr is soluble (Chester and Murphy, 1990), then the annual input of dust-derived Cr to the surface mixed layer at these stations can be expected to increase the Cr concentration by ~0.01 nM. This is within the analytical uncertainty of the measured Cr concentrations in the SML. By contrast, the expected increases in concentrations of dissolved Fe and Al due to dust deposition calculated in the same way are of the order of >1 nM, which is consistent with observations (Kunde et al., 2019; Artigue et al., 2021). It thus appears that input of dissolved Cr from atmospheric dust deposition to the surface ocean was not significant, at least at the time of sampling. In this connection, it is important to note that there can be considerable variability in dust transport and deposition in this region (Artigue et al., 2021) and potentially, variations in the Cr content of aerosol particles (Rädlein and Heumann, 1995), that may lead to increased input of dust derived Cr to surface waters at other times of the year.

The neutrally buoyant hydrothermal plume above the Snake Pit vent field was identified by a turbidity anomaly at water depths of between 3300-3500 m at Station 4 (Figure 2). Dissolved Fe concentrations reached 10.7 to 27.7 nM within the plume (Table S3), much higher than background seawater (~0.67 nM; Kunde et al., 2019), suggesting a substantial contribution of dFe from the Snake Pit vent fluids that have an end-member Fe concentration of ~3.5 mM (Findlay et al., 2015). The particulate Fe content in the plume was also high, up to ~20 nM (Kunde et al., 2019). Seawater samples from within the hydrothermal plume exhibit Cr concentrations of 2.48 to 2.57 nmol kg^{-1} and δ^{53}Cr values of 1.06 to 1.25‰ (Figure 3A). These Cr concentrations are slightly higher (by 0.14 - 0.23 nmol kg^{-1}) than a single sample collected from a similar water depth within the same water mass (3500 m, NEADW) at Station 1; the δ^{53}Cr value of the sample from Station 1 (1.17‰) is within the range of the plume samples. By contrast, seawater samples collected from a site of diffuse flow in the North Fiji basin were observed to be strongly enriched in total dissolved Cr (up to 20 nmol kg^{-1}) up to 400 m above the seabed relative to background values (~10 nmol kg^{-1}; Sander and Koschinsky, 2000). However, as discussed in Janssen et al. (2023), these results may not offer unequivocal support for hydrothermally sourced Cr. We cannot make a direct comparison between our Snakepit data and those from the North Fiji basin hydrothermal site due to differences in analytical methods, but we nevertheless assert that the hydrothermal input to the Snakepit plume can be expected to be small, for the following reasons. Firstly, reduced species of Cr in high temperature hydrothermal fluids have limited solubility (Huang et al., 2019) and recent analyses of high temperature (up to 311°C) hydrothermal fluids suggest that Cr concentrations are <30 nmol kg^{-1} (Janssen et al., 2023). Secondly, the highest Fe content (dissolved + particulate) sampled in the Snakepit plume was 47.7 nM (Kunde et al., 2019), versus a background Fe content of 0.67 nM (Kunde et al., 2019). Assuming that ~25% of the Fe in the Snakepit vent fluids precipitates immediately as Fe-sulfide as it is expelled at the seabed (James and Elderfield, 1996), then the total (dissolved + particulate) Fe data indicate that the seawater:vent fluid mixing ratio is ~56,000 at plume height. Even assuming that none of the vent fluid Cr precipitated as the fluids were expelled at the seabed (*cf.*, German et al., 1991), the expected increase in Cr in the plume due to vent fluid input would be <5×10^{-4} nmol kg^{-1}, which is smaller than the analytical uncertainty of our measurements.

At all three stations, the highest Cr concentrations (and the lowest δ^{53}Cr values) were recorded in samples taken from closest to the seabed. Slightly elevated Cr concentrations in deep waters have been reported in other studies and are generally attributed to release from sediments (e.g., Murray et al., 1983; Jeandel and Minster, 1987). In support of this, Cr concentrations in pore waters of oxic sediments can be up to an order of magnitude higher than Cr concentrations in overlying bottom waters (Shaw et al., 1990; Janssen et al., 2021). Our data suggest that Cr released by sediments is isotopically light relative to overlying bottom waters, which is consistent with release of Cr from lithogenic material (that has δ^{53}Cr = −0.12 ± 0.10 ‰; Schoenberg et al., 2008) and/or from authigenic sediment phases that have δ^{53}Cr values that range from −1.2 ‰ (Bauer et al., 2019) to 0.61 ‰ (Gueguen et al., 2016). Similarly, mass balance calculations based on bottom vs. deep water Cr concentrations and δ^{53}Cr values in the Tasman Sea have shown that oxic pore waters seem to be a source of relatively isotopically light Cr to bottom waters (δ^{53}Cr = 0.34 ± 0.25 ‰; Janssen et al., 2021).

A rough estimate of the Cr flux from sediments can be obtained from the gradient of the Cr concentration in deep waters and estimated rates of turbulent mixing above the seabed (Equation 2):

$$F_{Cr} = D\frac{\Delta[Cr]}{\Delta z} \quad (2)$$

where Δ[Cr] is change in Cr concentration between the deepest water sample and the next deepest water sample, Δz is depth interval separating the deepest from the next deepest water sample and D is diapycnal diffusivity. Discounting Station 1 (as no samples were collected within <30 m above the seabed), then the estimated Cr flux from sediments at Station 6 is ~5×10^{-3} nmol cm^{-2} yr^{-1} (for a D value of 0.1 cm^2 s^{-1}; Polzin et al., 1997), while the estimated Cr flux from sediments at Station 4 is considerably higher, ~2 nmol cm^{-2} yr^{-1}. Note for Station 4, we use a higher value for D (5 cm^2 s^{-1}), because mixing rates have been shown to be much higher above the Mid-Atlantic Ridge than they are above the seabed in the abyssal ocean (Polzin et al., 1997). If these fluxes are applied to the areal extent of all oxic oceanic sediments (*ca.* 10^8 km^2), then the estimated global benthic flux of Cr would range from 5×10^6 mol yr^{-1} (Station 6) to 3×10^9 mol yr^{-1} (Station 4),

equivalent to <0.3% to ~10 times the estimated river flux (Table 1). The value for F_{Cr} we calculate for Station 4 is comparable to that calculated based on pore water measurements in calcareous ooze in the Tasman Sea (up to ~ 3.2 nmol cm^{-2} yr^{-1}; Janssen et al., 2021), supporting the suggestion that sediment inputs of Cr can be important at the local scale (Janssen et al., 2021). In the case of Station 4, situated above the Snakepit hydrothermal vent field, loss of Cr from the sediments is likely fueled by oxidation of Cr(III) associated with metalliferous Fe-(oxyhydr)oxides derived from the hydrothermal plume, followed by diagenetic remobilization of the Cr(VI) that forms (Bauer et al., 2019).

4.2 Removal of Cr in subsurface waters

Lowest Cr concentrations were found in subsurface waters at between ~100 and ~500 m water depth (Figure 3B). The most Cr-depleted samples in subsurface waters had Cr concentrations of as low as 1.84 nmol kg^{-1}, between ~9 and 20% lower than the samples in the surface mixed layer (2.25-2.28 nmol kg^{-1}) and ~8 to 18% lower than the uppermost intermediate waters (2.25 ± 0.10 nmol kg^{-1}, 1SD, n=4). δ^{53}Cr values of the most Cr-depleted samples were also very slightly higher, by up to ~0.14‰ than the uppermost intermediate waters, which is greater than our analytical uncertainty of ± 0.06‰ (2SD). As this interval of very slightly higher δ^{53}Cr is a feature for all 3 stations, we tentatively assert that it may be real. In support of this, Jeandel and Minster (1987) also noted a weak but non-negligible subsurface Cr minimum at water depths between ~100 and 500 m in the North Atlantic Ocean (24 °N to 39 °N).

Removal of Cr does not appear to be associated with biological uptake in these oligotrophic waters. Lowest Cr concentrations occurred below the DCM (and below where macronutrient concentrations were the lowest; Figure S1), and there is no significant correlation (at $p<0.05$) between δ^{53}Cr and Chl-*a* concentration in the subsurface waters (Figure 4A). Low productivity waters in the North Pacific also showed no evidence for Cr removal (Janssen et al., 2020). Additionally, there is no significant (at $p<0.05$) correlation between δ^{53}Cr values and O_2 concentrations, or Cr and O_2 concentrations in the subsurface waters (Figure 4B), suggesting that there is no redox control on Cr isotope behavior in this slightly O_2 deficient depth interval (O_2 concentrations >130 µmol kg^{-1}). Recent studies on oxygen deficient waters (with O_2 concentrations down to ~13.2 µmol kg^{-1}) in the eastern sub-tropical Atlantic and the North Pacific have drawn the same conclusion (Goring-Harford et al., 2018; Moos and Boyle, 2019; Janssen et al., 2020) and reduction of Cr(VI) has only been demonstrated in waters with extremely low levels of oxygen (e.g., < 2 µmol kg^{-1}; Murray et al., 1983; Rue et al., 1997; Moos et al., 2020; Nasemann et al., 2020; Huang et al., 2021).

Figure 3 shows that the lowest Cr waters coincide with lowest dissolved and colloidal Fe concentrations, suggesting that cycling of Cr and Fe may be coupled in the subsurface waters. In this study area, depletion of dFe has been shown to be associated with removal of cFe from the water column and is not exclusively a result of biological uptake (Kunde et al., 2019). This is because: (1) experimental studies have indicated that sFe is biologically preferred over cFe (Chen and Wang, 2001; Hurst and Bruland, 2007); (2) lowest cFe concentrations occur below the DCM (~140 m water depth) which is, although not exclusively, an indicator of biomass maximum (Figure 3B); and (3) an enrichment of particulate Fe (pFe), which would capture the cellular Fe pool, was not observed (Kunde et al., 2019). The simultaneous minima of pFe and cFe (Kunde et al., 2019) suggests that cFe is not simply transferred from the dissolved to the particulate phase, but both phases are removed together as they sink through the DCM. The subsurface deficit of dFe may therefore be explained by active aggregation of colloidal Fe (e.g., Honeyman and Santschi, 1989), in the form of Fe-(oxyhydr)oxides, into filterable particles and/or scavenging of cFe onto settling dust-derived particles (Kunde et al., 2019). A similar Fe removal mechanism has also been proposed to explain changes in Fe size partitioning in other parts of the North Atlantic Ocean (Fitzsimmons et al., 2015; Ohnemus and Lam, 2015).

As Cr concentrations and δ^{53}Cr values only show a significant correlation ($p<0.05$) with dFe concentrations in the subsurface waters (and show no significant correlations with any of the other ancillary parameters that were measured; Figure 4), we suggest that removal of Cr proceeds *via* scavenging by newly-formed colloidal aggregates that subsequently fall out of the water column, as discussed above. This process has not been recognized previously, but is likely enhanced in this area of exceptionally high dust deposition (Section 4.1; Jickells et al., 2005), as the rate of colloidal aggregation is predicted to increase with particle loading due to so-called 'colloidal pumping' (e.g., Honeyman and Santschi, 1989). These aggregates 'shuttle' rapidly through the SML and into the sub-surface waters, where they are predicted to scavenge trace metals (Ohnemus and Lam, 2015), including presumably Cr. To date, only a handful of measurements of Cr concentrations in the colloidal and particulate fractions have been reported (Klun et al., 2019; GEOTRACES Intermediate Data Product Group, 2021), but these are clearly critical for proper assessment of the role of colloid-particulate interactions in Cr cycling.

Adsorption of Cr(VI) onto Fe-oxides (Pettine, 2000) or SiO_2-Al_2O_3 minerals (Frank et al., 2019) is limited in seawater because high concentrations of sulfate and/or chloride compete with chromate for adsorption sites (Pettine, 2000; Frank et al., 2019). However, Cr(III) species can be effectively scavenged by Fe-(oxyhydr)oxides (Frei et al., 2009), clay minerals and sand (Richard and Bourg, 1991) as well as biogenic particles (Semeniuk et al., 2016). Therefore, it seems likely that removal of Cr occurs mainly *via* scavenging of Cr(III). Cr(III) may be sourced from biologically (Connelly et al., 2006; Janssen et al., 2020; Huang et al., 2021) and/or photochemically (Kieber and Helz, 1992; Kaczynski and Kieber, 1993; Achterberg and van den Berg, 1997; Li et al., 2009) mediated reduction of seawater Cr(VI), or possibly from regeneration of Cr (III) from particles exported from the deep chlorophyll maximum (Janssen et al., 2020). If real, then the very small increase in δ^{53}Cr in the Cr-depleted waters would lend support to this idea. Cr(III) has been widely shown to be isotopically light relative to Cr(VI), hence removal of Cr(III) can be expected to leave the residual dissolved Cr pool isotopically

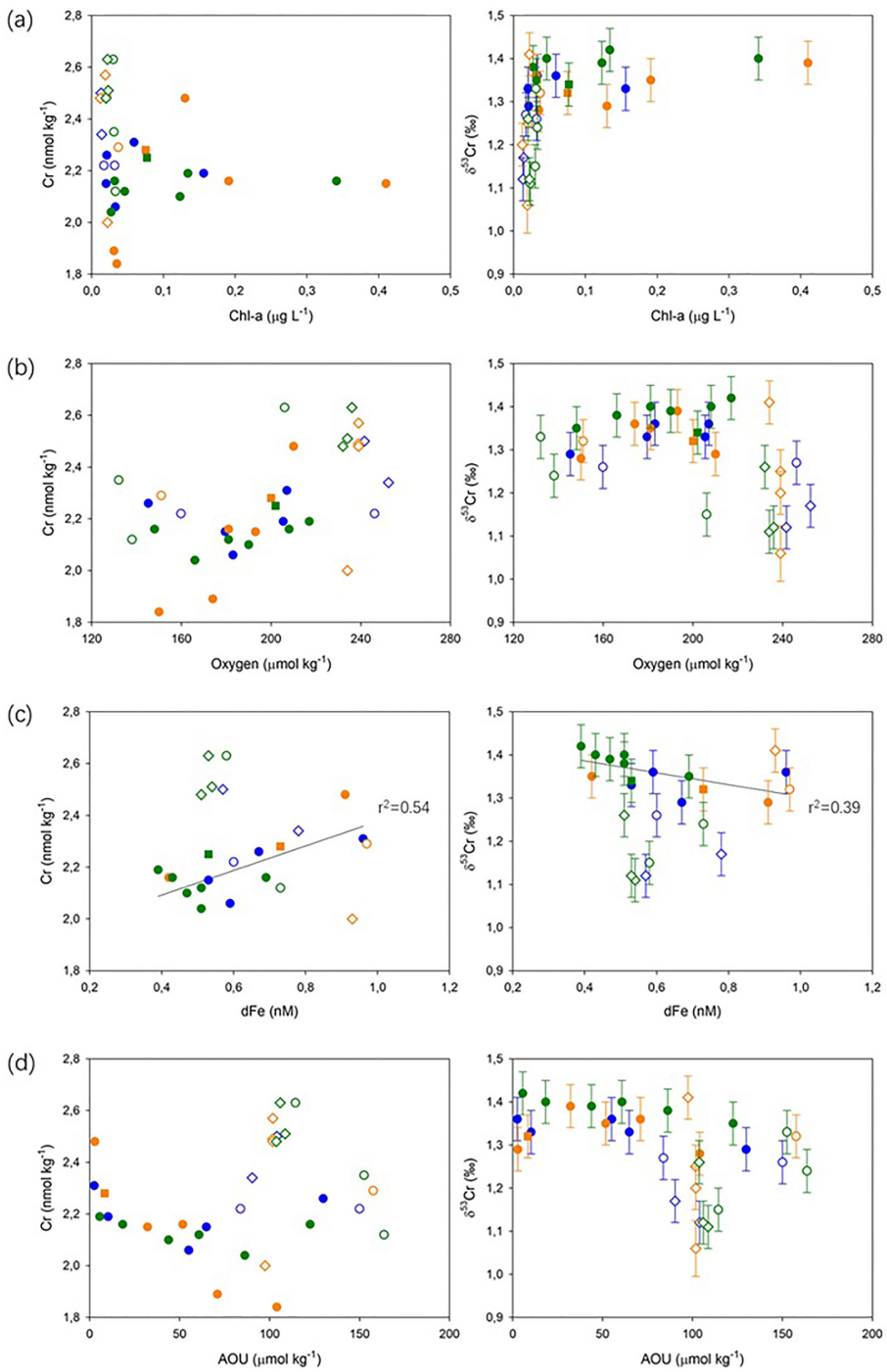

FIGURE 4
Cr and δ^{53}Cr as a function of **(A)** Chl-*a* concentration; **(B)** dissolved oxygen concentration; **(C)** dFe concentration; and **(D)** apparent oxygen utilization. SML (■), subsurface (●), intermediate (○), and deep (◊) waters are identified by the different symbols. Blue, orange, and green colors represent Stations 1, 4 and 6, respectively, as for Figure 3. Solid lines show significant correlations (p<0.05) between Cr and dFe, and δ^{53}Cr and dFe data in subsurface waters.

heavy (Ellis et al., 2002; Døssing et al., 2011; Kitchen et al., 2012; Janssen et al., 2020; Huang et al., 2021). Species-specific Cr and Cr isotope measurements of water samples, as well as the particulate phase, will be essential for validating these ideas.

4.3 Regeneration of Cr in deeper waters

While there is some evidence for scavenging of Cr in subsurface waters (Section 4.2), concentrations of total dissolved Cr were

highest in intermediate and deep waters, suggesting that Cr may be re-released. Although concentrations of Cr and Fe (and δ^{53}Cr and Fe) were correlated in the subsurface waters (Figure 4C), the cycling of Cr and Fe is apparently decoupled in intermediate and deep waters. In intermediate waters (700-2000 m water depth), there is a positive correlation between dFe concentrations and apparent oxygen utilization (AOU) respectively at Stations 4 and 6 (p<0.05; Supplementary Info. 2; Figure S3) that reflects remineralization of sinking organic material within the water column (Kunde et al., 2019), as also observed in other areas (Hatta et al., 2015). While such a correlation is not observed at Station 1, this is likely due to the small number of data points, the influence of atmospheric dust (Ye and Völker, 2017; Kunde et al., 2019), and/or other additional external Fe sources (Artigue et al., 2021). By contrast, there is no positive relationship between Cr concentrations and AOU, or δ^{53}Cr values and AOU, within the same depth interval at any of our sampling stations (Figure 4D). Consistent with our observation that there is no obvious biological control on Cr concentrations and δ^{53}Cr in subsurface waters, and recent observations of Cr behavior in intermediate and deep water masses in the Southern, Pacific and Atlantic oceans (Janssen et al., 2021), regeneration of Cr in intermediate waters *via* organic matter respiration does not appear to be an important control on Cr distributions in this part of the North Atlantic Ocean; thus, the release of Cr appears to be mechanistically different from Fe.

As removal of Cr in subsurface waters at our study sites, where lithogenic suspended particles are abundant, appears to proceed *via* scavenging of Cr(III) by colloid aggregates that consist of authigenic Fe-(oxyhydr)oxides and/or dust particles (Section 4.2), increased concentrations of dissolved Cr in intermediate waters could be due to re-oxidation of Cr(III) to the less particle reactive Cr(VI), potentially driven by reduction (and dissolution) of manganese (III, IV) oxides (MnO_x) that are present throughout the oxygenated water column (Jones et al., 2020). However, as concentrations of particulate Mn are very low (sub-nanomolar) in oceanic environments (Jones et al., 2020; Xiang et al., 2021), the predicted oxidation rate of Cr(III) is extremely slow, ~2×10^{-5} nmol kg^{-1} yr^{-1} (van der Weijden and Reith, 1982). The residence time of fine lithogenic mineral particles (~1 to 5 µm diameter) in the upper 2000 m of the North Atlantic Ocean water column is months to years (Ohnemus and Lam, 2015; Ohnemus et al., 2019), over which time oxidation of Cr(III) can be expected to increase the Cr concentration of seawater by approximately 10^{-5} to 10^{-4} nmol kg^{-1} in the intermediate waters. Clearly, this is too small to account for the observed 0.12 to 0.47 nmol kg^{-1} increase in dissolved Cr (Section 3) in intermediate waters relative to the lowest Cr subsurface waters (i.e., those between 100 and 400 m water depth).

It thus seems more likely that regeneration of Cr occurs either *via* dissolution of authigenic Fe-(oxyhydr)oxides and/or dust particles and/or desorption of Cr(III) from these particles. The latter would mean that the scavenging of Cr from subsurface waters is reversible. In deeper waters, concentrations of particulate matter are lower (Figure 2), so the equilibrium between Cr(III) in the dissolved and particulate phases will shift towards the dissolved phase (e.g., Bacon and Anderson, 1982). Reversible exchange between dissolved and particulate phases has been shown to successfully reconcile the oceanic distributions of dissolved copper and zinc whose concentrations also generally increase with depth (e.g., Little et al., 2013; John and Conway, 2014; Weber et al., 2018), although unlike Cr, copper and zinc are directly influenced by biological uptake and are strongly complexed with organic ligands in seawater (e.g., Little et al., 2013).

Regeneration of Cr is unlikely to fractionate Cr isotopes to any great extent. Cr isotope fractionation caused by oxidation of Cr(III) by MnO_x minerals is, as yet poorly constrained (Bain and Bullen, 2005; Ellis et al., 2008), but recent laboratory studies suggested that differences in δ^{53}Cr values between Cr(VI) and Cr(III) (of up to 0.39‰) cannot be sustained over time (Ansari and Johnson, 2022). Adsorption and desorption processes also do not appear to fractionate Cr isotopes due to rapid isotopic exchange on particle surfaces (Ellis et al., 2004; Wang et al., 2015); thus, the isotopic compositions of dissolved and scavenged Cr(III) are generally assumed to be identical (Huang et al., 2021). Consistent with our observations, the δ^{53}Cr value of regenerated Cr, either in the form of Cr(VI) or Cr(III), can be expected to be isotopically light compared to dissolved Cr(VI) that remains in the subsurface waters.

4.4 Accumulation of Cr in deep waters and effects of water mass mixing

Excluding samples collected from within 30 m of the seabed, deep waters (>2000 m water depth) at our stations in the sub-tropical North Atlantic have lower Cr concentrations (2.40 ± 0.19 nmol kg^{-1}; n=7) and higher δ^{53}Cr values (1.22 ± 0.10‰; n=7) than Pacific waters (average Cr = 4.75 ± 0.42 nmol kg^{-1} and δ^{53}Cr = 0.77 ± 0.10‰, 1SD, n=25; Moos and Boyle, 2019; Nasemann et al., 2020; Huang et al., 2021; Janssen et al., 2021) from >2000 m depth (including PDW, UCDW and LCDW water masses). Previous studies have suggested that Cr may accumulate in deep waters along the thermohaline flow path from the Atlantic to the Pacific Ocean (Jeandel and Minster, 1987; Janssen et al., 2021), and this behaviour has also been predicted by a model of the ocean Cr cycle (Pöppelmeier et al., 2021). Comparing our data with others from the literature (Goring-Harford et al., 2018; Moos and Boyle, 2019; Nasemann et al., 2020; Huang et al., 2021; Janssen et al., 2021), it is further apparent that Cr concentrations increase as the conventional radiocarbon (^{14}C) age of the deep waters (Supplementary Info. 1; Table S4; Supplementary Info. 2; S1) increases, whereas the δ^{53}Cr value of total dissolved Cr decreases (Figure 5). Thus, isotopically light Cr accumulates in deep waters presumably *via* release from sinking particles as the deep water masses age as they are transported laterally from the Atlantic Ocean to the Southern Ocean, the South Pacific and finally into the North Pacific Ocean (DeVries and Holzer, 2019).

The deep waters therefore act as a reservoir for Cr 'raining' down in particles descending from subsurface waters. While the close similarity between deep water Cr and macronutrient concentrations (Supplementary Info. 2; Figure S4) implies that deep water Cr concentrations are to a degree regulated by remineralization of organic material, especially in high productivity regions (Janssen et al., 2021), we show here that

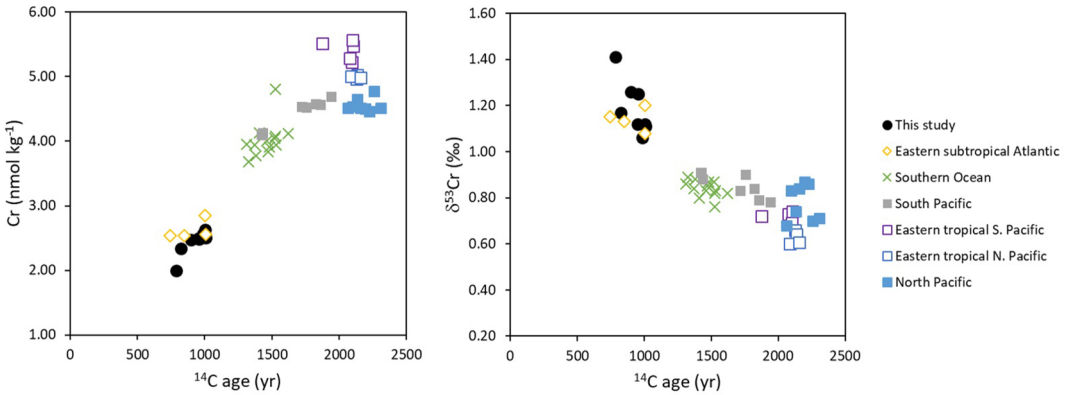

FIGURE 5
Cr and δ^{53}Cr vs radiocarbon (^{14}C) age of deep water masses (≥ 2000 m water depth). Cr data are from: this study (sub-tropical North Atlantic); Goring-Harford et al. (2018) (eastern subtropical Atlantic); Rickli et al. (2019) (Southern Ocean); Moos and Boyle (2019) (North Pacific); Janssen et al. (2021) (Southern Ocean, North Pacific, eastern tropical South Pacific and South Pacific); Nasemann et al. (2020) (eastern tropical South Pacific); Huang et al. (2021) (eastern tropical North Pacific). ^{14}C age calculated based on Δ^{14}C data extracted from de Lavergne et al. (2017), as described in Supplementary Info. 2 (S1). Note that the ^{14}C age of newly-formed North Atlantic Deep Water is ~400 years (Matsumoto, 2007). Data are provided in Supplementary Info. 1 (Table S4).

deep water Cr concentrations also reflect 'reversible scavenging' of Cr(III) taken up in subsurface waters in regions where lithogenic suspended particles are abundant (Section 4.2). Note that it is also likely that deep water Cr concentrations beneath OMZs are affected by Cr released by re-oxidation of Cr(III) (Nasemann et al., 2020; Huang et al., 2021; Janssen et al., 2021). Whilst sediments can represent an important source of Cr to the deep ocean (Janssen et al., 2021), their influence on a global scale remains uncertain (Pöppelmeier et al., 2021).

Water mass mixing can also influence the spatial distribution of Cr in deep waters at local (Rickli et al., 2019; Janssen et al., 2023) and ocean basin (Janssen et al., 2021) scales. Although there is some variation in the composition of deep water masses in our study area (Figure 1), to a first approximation they can be considered to consist of North Atlantic Deep Water (NADW) and Antarctic Bottom Water (AABW). The relative contributions of these end members can be estimated from the dissolved oxygen and phosphate concentrations of the seawater samples as follows (Broecker, 1991; Sarmiento et al., 2007):

$$f_{NADW} = \frac{1.59 - PO_4^*}{1.59 - 0.74} \quad (3)$$

where f_{NADW} is the fraction of NADW, 1.59 and 0.74 are the PO_4^* values (in µmol kg^{-1}) of, respectively, AABW and NADW (Artigue et al., 2020), and PO_4^* is given by:

$$PO_4^* = [PO_4] + \frac{[O_2]}{170} - 1.95\ \mu mol\ kg^{-1} \quad (4)$$

where $[PO_4]$ and $[O_2]$ are, respectively, the PO_4 and O_2 concentrations of a seawater sample and 170 is the stoichiometric ratio of oxygen to phosphate (Anderson and Sarmiento, 1994). Excluding one sample that has $f_{NADW} > 1$ (due to input of Mediterranean seawater; Sarmiento et al., 2007) and samples collected from within 30 m of the seabed, there is a correlation (significant at $p<0.1$) between dissolved Cr and f_{NADW} ($r^2 = 0.42$) in sub-tropical Atlantic deep waters (>2000 m) (Figure S4), suggesting that water mass mixing can, to some degree, act to homogenize distinct Cr pools. However, there is no significant correlation between δ^{53}Cr and 1/Cr for the same set of samples. From Figure S4 it appears likely that the NADW end-member has lower Cr and a higher δ^{53}Cr value relative to the AABW end-member, but as no samples of 'pure' NADW (i.e., from ~45°N in the North Atlantic at ~4000 m water depth; Sarmiento et al., 2007) or 'pure' AABW (i.e., from ~35°S in the South Atlantic at ~4000 m water depth; Sarmiento et al., 2007) have been analyzed for Cr and δ^{53}Cr to date, this cannot be confirmed.

Concentrations of dissolved Cr are also positively correlated to the ^{14}C water mass age (Supplementary Info. 1) in Atlantic deep waters (significant at $p<0.1$), supporting the accumulation of Cr, but the correlation ($r^2 = 0.32$) is weaker than it is for Cr- f_{NADW}. The Atlantic Ocean is rapidly ventilated by NADW and high-latitude source waters and has developed a relatively weaker accumulation signal of dissolved metals, such as zinc, compared to other ocean basins (Weber et al., 2018; Middag et al., 2019). This also appears to be the case for Cr.

4.5 Global correlation between seawater Cr and δ^{53}Cr

Data from this study confirm an inverse correlation between δ^{53}Cr and logarithmic Cr concentration ($r^2 = 0.53$, n=33; Figure 6A) and the slope of the linear regression is −0.79 ± 0.13‰. This is consistent with the previously proposed global δ^{53}Cr-ln[Cr] relationship for the open ocean, which was considered to reflect a Rayleigh-type fractionation of Cr isotopes as Cr is removed from seawater (Scheiderich et al., 2015; Figure 6):

$$\delta^{53}Cr = \delta^{53}Cr_0 + \varepsilon \times ln(f) \quad (5)$$

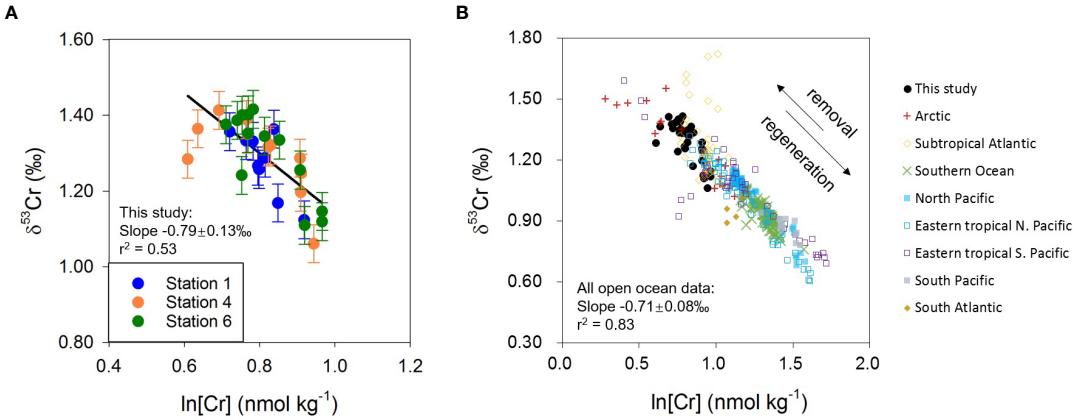

FIGURE 6
(A) Relationship between δ^{53}Cr and ln[Cr] for new data from this study. **(B)** Relationship between δ^{53}Cr and ln[Cr] for the global open ocean seawater. Literature data are from: Scheiderich et al. (2015) (Arctic); Goring-Harford et al. (2018) (eastern subtropical Atlantic); Rickli et al. (2019) (Southern Ocean); Moos and Boyle (2019) (North Pacific); Janssen et al. (2020) (North Pacific); Moos et al. (2020) (eastern tropical North Pacific); Huang et al. (2021) (eastern tropical North Pacific); Nasemann et al. (2020) (eastern tropical South Pacific); Janssen et al. (2021) (subtropical Atlantic, Southern Ocean, North Pacific, eastern tropical South Pacific, South Pacific, South Atlantic). Data sets from the South Atlantic (Bonnand et al., 2013) and the eastern Pacific OMZ (Bruggmann et al., 2019; Wang et al., 2019) are not shown as more recent studies from similar locations (Huang and Boyle, 2018; Moos et al., 2020; Nasemann et al., 2020) indicate that these data may not be representative of the true seawater signal or are likely not correct.

where $\delta^{53}Cr_0$ represents the initial Cr isotope composition, f represents the fraction of Cr remaining in seawater, and ε is the isotope fractionation factor between Cr(III) and Cr(VI). The Cr isotope fractionation factor derived from all open ocean seawater samples reported in the literature to date, including the present study, is ε = −0.71 ± 0.08‰ (r^2 = 0.83, n=347: Scheiderich et al., 2015; Goring-Harford et al., 2018; Moos and Boyle, 2019; Rickli et al., 2019; Janssen et al., 2020; Moos et al., 2020; Nasemann et al., 2020; Huang et al., 2021; Janssen et al., 2021; this study) (Table S5). This value is smaller than determined in the laboratory for Cr reduction by Fe(II) and/or organic matter (ϵ = −1.5 to −4.2‰: Døssing et al., 2011; Basu and Johnson, 2012; Kitchen et al., 2012), or biotic Cr reduction (ϵ = −1.6 to −4.3‰: Zhang et al., 2018; Zhang et al., 2019). It is now clear that although Cr is reduced in the euphotic zone due to biological and/or photochemical processes (e.g., Li et al., 2009; Janssen et al., 2020), as well as in the OMZs by organic matter, microbial activity, and possibly Fe(II) (Moos et al., 2020; Nasemann et al., 2020; Huang et al., 2021), the intrinsic Cr isotope fractionation is diminished as a portion of isotopically light Cr (III) remains in the dissolved phase (Moos et al., 2020; Nasemann et al., 2020; Huang et al., 2021; Wang, 2021). It is also possible that (1) the fractionation factor may be influenced by the rate of Cr reduction and removal (Jamieson-Hanes et al., 2014); and (2) scavenging/adsorption of Cr onto particles may cause a small (but as yet unconstrained) isotope fractionation (Ellis et al., 2004).

As discussed in Section 4.4, progressive regeneration of Cr that is removed from the upper water column in deep water causes accumulation of Cr with a lower δ^{53}Cr value along the global ocean deep water flow path (Section 4.4). In theory, the Rayleigh-type δ^{53}Cr-Cr curve requires that the δ^{53}Cr difference between regenerated Cr and total dissolved Cr in the water column is approximately equal to ϵ = −0.71‰. However, simple mass balance modelling (Figure S5) shows that incremental addition of isotopically light Cr (with δ^{53}Cr ≈ 0.08 to 0.36‰) to deep waters can partly reproduce the shape and slope of the global δ^{53}Cr-ln[Cr] relationship. Given the relatively long seawater residence time of Cr (~3000 to 9500 years: Reinhard et al., 2013; McClain and Maher, 2016; Pöppelmeier et al., 2021) compared to the time scale of ocean ventilation (~1000 years: e.g., DeVries and Holzer, 2019), this implies that, while local Cr and Cr isotope variations caused by removal of Cr fit with the global δ^{53}Cr-Cr relationship (e.g., Huang et al., 2021), regeneration of Cr from sinking particles and accumulation of isotopically light Cr as water masses age are also important processes that shape the large scale heterogeneity of Cr and Cr isotopes in the world's major ocean basins and contribute to the systematic δ^{53}Cr-Cr relationship discussed by other studies.

5 Conclusions

This study reports full water column depth profiles of dissolved Cr and δ^{53}Cr at three stations in the sub-tropical North Atlantic. Considered together with ancillary data including dissolved, and colloidal Fe concentrations, turbidity, Chl-*a*, and dissolved oxygen as well as macronutrient concentrations, we have assessed the processes that regulate the behaviour of Cr and Cr isotopes in the modern sub-tropical North Atlantic Ocean. There is no clear evidence for significant inputs of Cr from atmospheric dust and hydrothermal vents in this area, but benthic inputs of Cr may be locally important, notably in the vicinity of hydrothermal vents. The distribution of dissolved Cr and δ^{53}Cr rather appears to principally reflect internal cycling of Cr. Subsurface waters (above 700 m depth) are very slightly depleted in Cr, and very slightly enriched in heavy Cr isotopes, relative to deeper waters. Removal of Cr in subsurface waters is not directly controlled by levels of oxygen or biological uptake in this region where biological productivity is low and waters show only modest oxygen depletion, but does coincide with lowest concentrations of dFe and cFe. We suggest that Cr, most

likely in the form of relatively isotopically light Cr(III), is taken up onto colloid aggregates of Fe-(oxyhydr)oxides and/or dust particles. Despite the concurrent removal of Cr and Fe in the upper 700 m water column, the cycling of Cr and Fe is apparently decoupled in deeper waters. While regeneration of Fe occurs *via* respiration of biogenic particles (Kunde et al., 2019), we show that subtly increased levels of Cr (with relatively low δ^{53}Cr values) in intermediate waters most likely reflect reversible scavenging in this part of the North Atlantic Ocean. In deep waters, water mass mixing plays a role in controlling the Cr and δ^{53}Cr distributions, but regeneration of Cr from particles is more obvious at least at the global scale.

Data availability statement

The original contributions presented in the study are included in the article/Supplementary Material. Further inquiries can be directed to the corresponding author.

Author contributions

WW performed the chromium analyses and data interpretation and prepared the original draft of the manuscript. RJ designed the study, mentored WW and edited subsequent drafts. HG-H supported method validation, sample analysis, and data interpretation. KK collected samples in the field, performed the iron analyses, and edited the draft. EMW performed nutrient analysis in the field. ML acquired funding for the research cruise and led sample collection. DC supported the analytical work and data interpretation. All authors commented on drafts of the manuscript and have approved the submitted version.

Funding

This cruise was funded by the NERC-funded ZIPLOc project (NE/N001125/1). WW's PhD studentship was funded by the Chinese Scholarship Council and the Graduate School of the National Oceanography Centre Southampton; KK's PhD studentship was funded by the Graduate School of the National Oceanography Centre Southampton.

Acknowledgments

We thank the scientific team, captain, and crew of the RRS James Cook cruise JC150 for their invaluable help in the collection of the samples and for generously sharing ancillary data that have greatly assisted the interpretation of Cr data. We thank David Janssen for invaluable comments on a previous version of this manuscript.

Conflict of interest

The authors declare that the research was conducted in the absence of any commercial or financial relationships that could be construed as a potential conflict of interest.

Publisher's note

Supplementary material

The Supplementary Material for this article can be found online at: https://www.frontiersin.org/articles/10.3389/fmars.2023.1165304/full#supplementary-material

References

Achterberg, E. P., and van den Berg, C. M. (1997). Chemical speciation of chromium and nickel in the western Mediterranean. *Deep Sea Res. Part II: Topical Stud. Oceanography* 44 (3-4), 693–720. doi: 10.1016/S0967-0645(96)00086-0

Albarède, F., and Beard, B. (2004). Analytical methods for non-traditional isotopes. *Rev. Mineralogy Geochemistry* 55 (1), 113–152. doi: 10.2138/gsrmg.55.1.113

Anderson, L. A., and Sarmiento, J. L. (1994). Redfield ratios of remineralization determined by nutrient data analysis. *Global Biogeochemical Cycles* 8 (1), 65–80. doi: 10.1029/93GB03318

Andronikov, A. V., Novak, M., Borodulina, G. S., Efremenko, N. A., Andronikova, I. E., Chesalina, G. L., et al. (2019). One river, two streams: chemical and chromium isotopic features of the Neglinka river (Karelia, northwest Russia). *Hydrological Sci. J.* 64 (8), 974–982. doi: 10.1080/02626667.2019.1617418

Ansari, M. G., and Johnson, T. (2022). Chromium isotopic fractionation during oxidation of Cr(III)-bearing solids by manganese oxides at circum-neutral pH. *Goldschmidt Abstract*. doi: 10.46427/gold2022.11525

Artigue, L., Lacan, F., Van Gennip, S., Lohan, M. C., Wyatt, N. J., Woodward, E. M. S., et al. (2020). Water mass analysis along 22° N in the subtropical north Atlantic for the JC150 cruise (GEOTRACES, GApr08). *Deep Sea Res. Part I: Oceanographic Res. Papers* 158. doi: 10.1016/j.dsr.2020.103230

Artigue, L., Wyatt, N. J., Lacan, F., Mahaffey, C., and Lohan, M. C. (2021). The importance of water mass transport and dissolved-particle interactions on the aluminum cycle in the subtropical north Atlantic. *Global Biogeochemical Cycles* 35. doi: 10.1029/2020GB006569

Bacon, M. P., and Anderson, R. F. (1982). Distribution of thorium isotopes between dissolved and particulate forms in the deep sea. *J. Geophysical Research: Oceans* 87 (C3), 2045–2056. doi: 10.1029/JC087iC03p02045

Bain, D. J., and Bullen, T. D. (2005). Chromium isotope fractionation during oxidation of Cr(III) by manganese oxides. *Geochimica et Cosmochimica Acta Supplement* 69, A212.

Basu, A., and Johnson, T. M. (2012). Determination of hexavalent chromium reduction using Cr stable isotopes: isotopic fractionation factors for permeable

reactive barrier materials. *Environ. Sci. Technol.* 46 (10), 5353–5360. doi: 10.1021/es204086y

Bauer, K. W., Cole, D. B., Asael, D., Francois, R., Calvert, S. E., Poulton, S. W., et al. (2019). Chromium isotopes in marine hydrothermal sediments. *Chem. Geology* 529, 119286. doi: 10.1016/j.chemgeo.2019.119286

Beaulieu, S. E. (2015) *InterRidge global database of active submarine hydrothermal vent fields. prepared for InterRidge, version 3.3.* Available at: http://vents-data.interridge.org.

Bonnand, P., James, R., Parkinson, I., Connelly, D., and Fairchild, I. (2013). The chromium isotopic composition of seawater and marine carbonates. *Earth Planetary Sci. Lett.* 382, 10–20. doi: 10.1016/j.epsl.2013.09.001

Bonnand, P., Parkinson, I. J., James, R. H., Karjalainen, A. M., and Fehr, M. A. (2011). Accurate and precise determination of stable Cr isotope compositions in carbonates by double spike MC-ICP-MS. *J. Analytical Atomic Spectrometry* 26 (3), 528–535. doi: 10.1039/c0ja00167h

Broecker, W. S. (1991). The great ocean conveyor. *Oceanography* 4, 79–90. doi: 10.5670/oceanog.1991.07

Bruggmann, S., Scholz, F., Klaebe, R. M., Canfield, D. E., and Frei, R. (2019). Chromium isotope cycling in the water column and sediments of the Peruvian continental margin. *Geochimica et Cosmochimica Acta* 257, 224–242. doi: 10.1016/j.gca.2019.05.001

Campbell, J. A., and Yeats, P. A. (1981). Dissolved chromium in the northwest Atlantic ocean. *Earth Planetary Sci. Lett.* 53 (3), 427–433. doi: 10.1016/0012-821X(81)90047-9

Chen, M., and Wang, W. X. (2001). Bioavailability of natural colloid-bound iron to marine plankton: influences of colloidal size and aging. *Limnology & Oceanography* 46 (8), 1956–1967. doi: 10.4319/lo.2001.46.8.1956

Chester, R., and Hughes, M. J. (1969). The trace element geochemistry of a north Pacific pelagic clay core. *Deep Sea Res. Oceanographic Abstracts* 16 (6), 639–654. doi: 10.1016/0011-7471(69)90064-3

Chester, R., and Murphy, K. J. T. (1990). "Metals in the marine atmosphere," in *Heavy metals in the marine environment* (Boca Raton, FL: CRC Press), 27–49.

Connelly, D. P., Statham, P. J., and Knap, A. H. (2006). Seasonal changes in speciation of dissolved chromium in the surface Sargasso Sea. *Deep Sea Res. Part I: Oceanographic Res. Papers* 53 (12), 1975–1988. doi: 10.1016/j.dsr.2006.09.005

Cranston, R. E. (1983). Chromium in Cascadia Basin, northeast Pacific ocean. *Mar. Chem.* 13 (2), 109–125. doi: 10.1016/0304-4203(83)90020-8

Cranston, R. E., and Murray, J. W. (1980). Chromium species in the Columbia river and estuary 1. *Limnology & Oceanography* 25 (6), 1104–1112. doi: 10.4319/lo.1980.25.6.1104

D'Arcy, J., Babechuk, M. G., Døssing, L. N., Gaucher, C., and Frei, R. (2016). Processes controlling the chromium isotopic composition of river water: constraints from basaltic river catchments. *Geochimica et Cosmochimica Acta* 186, 296–315. doi: 10.1016/j.gca.2016.04.027

Davidson, A. B., Semeniuk, D. M., Koh, J., Holmden, C., Jaccard, S. L., Francois, R., et al. (2020). A $Mg(OH)_2$ coprecipitation method for determining chromium speciation and isotopic composition in seawater. *Limnology & Oceanography: Methods* 18 (1), 8–19. doi: 10.1002/lom3.10342

de Lavergne, C., Madec, G., Roquet, F., Holmes, R. M., and McDougall, T. J. (2017). Abyssal ocean overturning shaped by seafloor distribution. *Nature* 551, 181–186. doi: 10.1038/nature24472

DeVries, T., and Holzer, M. (2019). Radiocarbon and helium isotope constraints on deep ocean ventilation and mantle-^{3}He sources. *J. Geophysical Research: Oceans* 124 (5), 3036–3057. doi: 10.1029/2018JC014716

Døssing, L. N., Dideriksen, K., Stipp, S. L. S., and Frei, R. (2011). Reduction of hexavalent chromium by ferrous iron: a process of chromium isotope fractionation and its relevance to natural environments. *Chem. Geology* 285 (1-4), 157–166. doi: 10.1016/j.chemgeo.2011.04.005

Eary, L. E., and Rai, D. (1987). Kinetics of chromium (III) oxidation to chromium (VI) by reaction with manganese dioxide. *Environ. Sci. Technol.* 21, 1187–1193. doi: 10.1021/es00165a005

Elderfield, H. (1970). Chromium speciation in sea water. *Earth Planetary Sci. Lett.* 9 (1), 10–16. doi: 10.1016/0012-821X(70)90017-8

Ellis, A. S., Johnson, T. M., and Bullen, T. D. (2002). Chromium isotopes and the fate of hexavalent chromium in the environment. *Science* 295, 2060–2062. doi: 10.1126/science.1068368

Ellis, A. S., Johnson, T. M., and Bullen, T. D. (2004). Using chromium stable isotope ratios to quantify Cr(VI) reduction: lack of sorption effects. *Environ. Sci. Technol.* 38 (13), 3604–3607. doi: 10.1021/es0352294

Ellis, A., Johnson, T., Villalobos-Aragon, A., and Bullen, T. (2008). Environmental cycling of Cr using stable isotopes: kinetic and equilibrium effects. In *AGU Fall Meeting Abstracts* (Vol. 2008, pp. H53F–08).

Feely, R. A., Baker, E. T., Marumo, K., Urabe, T., Ishibashi, J., Gendron, J., et al. (1996). Hydrothermal plume particles and dissolved phosphate over the superfast-spreading southern East Pacific rise. *Geochimica et Cosmochimica Acta* 60 (13), 2297–2323. doi: 10.1016/0016-7037(96)00099-3

Findlay, A. J., Gartman, A., Shaw, T. J., and Luther, G. W. (2015). Trace metal concentration and partitioning in the first 1.5 m of hydrothermal vent plumes along the mid-Atlantic ridge: TAG, Snakepit, and Rainbow. *Chem. Geology* 412, 117–131. doi: 10.1016/j.chemgeo.2015.07.021

Fitzsimmons, J. N., Carrasco, G. G., Wu, J., Roshan, S., Hatta, M., Measures, C. I., et al. (2015). Partitioning of dissolved iron and iron isotopes into soluble and colloidal phases along the GA03 GEOTRACES north Atlantic transect. *Deep Sea Res. Part II: Topical Stud. Oceanography* 116, 130–151. doi: 10.1016/j.dsr2.2014.11.014

Frank, A. B., Klaebe, R. M., and Frei, R. (2019). Fractionation behavior of chromium isotopes during the sorption of Cr(VI) on kaolin and its implications for using black shales as a paleoredox archive. *Geochemistry Geophysics Geosystems* 20 (5), 2290–2302. doi: 10.1029/2019GC008284

Frei, R., Gaucher, C., Poulton, S. W., and Canfield, D. E. (2009). Fluctuations in Precambrian atmospheric oxygenation recorded by chromium isotopes. *Nature* 461, 250–253. doi: 10.1038/nature08266

Frei, R., Poiré, D., and Frei, K. M. (2014). Weathering on land and transport of chromium to the ocean in a subtropical region (Misiones, NW Argentina): a chromium stable isotope perspective. *Chem. Geology* 381, 110–124. doi: 10.1016/j.chemgeo.2014.05.015

GEOTRACES Intermediate Data Product Group (2021). *The GEOTRACES intermediate data product 2021 (IDP2021)* (NERC EDS British Oceanographic Data Centre NOC). doi: 10.5285/cf2d9ba9-d51d-3b7c-e053-8486abc0f5fd

German, C. R., Campbell, A. C., and Edmond, J. M. (1991). Hydrothermal scavenging at the mid-Atlantic ridge: modification of trace element dissolved fluxes. *Earth Planetary Sci. Lett.* 107 (1), 101–114. doi: 10.1016/0012-821X(91)90047-L

Goring-Harford, H. J., Klar, J. K., Donald, H. K., Pearce, C. R., Connelly, D. P., and James, R. H. (2020). Behaviour of chromium and chromium isotopes during estuarine mixing in the Beaulieu estuary, UK. *Earth Planetary Sci. Lett.* 536. doi: 10.1016/j.epsl.2020.116166

Goring-Harford, H. J., Klar, J. K., Pearce, C. R., Connelly, D. P., Achterberg, E. P., and James, R. H. (2018). Behaviour of chromium isotopes in the eastern sub-tropical Atlantic oxygen minimum zone. *Geochimica et Cosmochimica Acta* 236, 41–59. doi: 10.1016/j.gca.2018.03.004

Gueguen, B., Reinhard, C. T., Algeo, T. J., Peterson, L. C., Nielsen, S. G., Wang, X., et al. (2016). The chromium isotope composition of reducing and oxic marine sediments. *Geochimica et Cosmochimica Acta* 184, 1–19. doi: 10.1016/j.gca.2016.04.004

Hatta, M., Measures, C. I., Wu, J., Roshan, S., Fitzsimmons, J. N., Sedwick, P., et al. (2015). An overview of dissolved Fe and Mn distributions during the 2010–2011 US GEOTRACES north Atlantic cruises: GEOTRACES GA03. *Deep Sea Res. Part II: Topical Stud. Oceanography* 116, 117–129. doi: 10.1016/j.dsr2.2014.07.005

Honeyman, B. D., and Santschi, P. H. (1989). A Brownian-pumping model for oceanic trace metal scavenging: evidence from Th isotopes. *J. Mar. Res.* 47 (4), 951–992. doi: 10.1357/002224089785076091

Huang, T., and Boyle, E. A. (2018). Is the chromium concentration profile in the Argentine basin anomalous? *AGU Fall Meeting Abstracts*, OS21F–O1624.

Huang, J., Hao, J., Huang, F., and Sverjensky, D. A. (2019). Mobility of chromium in high temperature crustal and upper mantle fluids. *Geochemical Perspective Lett.* 12, 1–6. doi: 10.7185/geochemlet.1926

Huang, T., Moos, S. B., and Boyle, E. A. (2021). Trivalent chromium isotopes in the eastern tropical north Pacific oxygen-deficient zone. *Proc. Natl. Acad. Sci.* 118 (8). doi: 10.1073/pnas.1918605118

Hurst, M. P., and Bruland, K. W. (2007). An investigation into the exchange of iron and zinc between soluble, colloidal, and particulate size-fractions in shelf waters using low-abundance isotopes as tracers in shipboard incubation experiments. *Mar. Chem.* 103 (3-4), 211–226. doi: 10.1016/j.marchem.2006.07.001

Izbicki, J. A., Ball, J. W., Bullen, T. D., and Sutley, S. J. (2008). Chromium, chromium isotopes and selected trace elements, western Mojave desert, USA. *Appl. Geochemistry* 23 (5), 1325–1352. doi: 10.1016/j.apgeochem.2007.11.015

James, R. H., and Elderfield, H. (1996). Chemistry of ore-forming fluids and mineral formation rates in an active hydrothermal sulfide deposit on the Mid-Atlantic Ridge. *Geology* 24(12), 1147–1150. doi: 10.1130/0091-7613(1996)024<1147:COOFFA>2.3.CO;2

Jamieson-Hanes, J. H., Lentz, A. M., Amos, R. T., Ptacek, C. J., and Blowes, D. W. (2014). Examination of Cr(VI) treatment by zero-valent iron using in situ, real-time X-ray absorption spectroscopy and Cr isotope measurements. *Geochimica et Cosmochimica Acta* 142, 299–313. doi: 10.1016/j.gca.2014.07.031

Janssen, D. J., Gilliard, D., Rickli, J., Nasemann, P., Koschinsky, A., Hassler, C. S., et al. (2023). Chromium stable isotope distributions in the southwest Pacific ocean and constraints on hydrothermal input from the Kermadec Arc. *Geochimica et Cosmochimica Acta* 342, 31–44. doi: 10.1016/j.gca.2022.12.010

Janssen, D. J., Rickli, J., Abbott, A. N., Ellwood, M. J., Twining, B. S., Ohnemus, D. C., et al. (2021). Release from biogenic particles, benthic fluxes, and deep water circulation control Cr and δ^{53}Cr distributions in the ocean interior. *Earth Planetary Sci. Lett.* 574. doi: 10.1016/j.epsl.2021.117163

Janssen, D. J., Rickli, J., Quay, P. D., White, A. E., Nasemann, P., and Jaccard, S. L. (2020). Biological control of chromium redox and stable isotope composition in the surface ocean. *Global Biogeochemical Cycles*. 34, e2019GB006397. doi: 10.1029/2019GB006397

Janssen, D. J., Rickli, J., Wille, M., Sepúlveda Steiner, O., Vogel, H., Dellwig, O., et al. (2022). Chromium cycling in redox-stratified basins challenges δ^{53}Cr paleoredox proxy applications. *Geophysical Res. Lett.* 49 (21), e2022GL099154. doi: 10.1029/2022GL099154

Jeandel, C., and Minster, J. F. (1987). Chromium behavior in the ocean: global versus regional processes. *Global Biogeochemical Cycles* 1 (2), 131–154. doi: 10.1029/GB001i002p00131

Jickells, T. D., An, Z. S., Andersen, K. K., Baker, A. R., Bergametti, G., Brooks, N., et al. (2005). Global iron connections between desert dust, ocean biogeochemistry, and climate. *Science* 308 (5718), 67–71. doi: 10.1126/science.1105959

John, S. G., and Conway, T. M. (2014). A role for scavenging in the marine biogeochemical cycling of zinc and zinc isotopes. *Earth Planetary Sci. Lett.* 394, 159–167. doi: 10.1016/j.epsl.2014.02.053

Johnson, K. S., Elrod, V., Fitzwater, S., Plant, J., Boyle, E., Bergquist, B., et al. (2007). Developing standards for dissolved iron in seawater. *Eos Trans. Am. Geophysical Union* 88 (11), 131–132. doi: 10.1029/2007EO110003

Jones, M. R., Luther, G. W.III, and Tebo, B. M. (2020). Distribution and concentration of soluble manganese (II), soluble reactive Mn (III)-l, and particulate MnO_2 in the Northwest Atlantic ocean. *Mar. Chem.* 226, 103858. doi: 10.1016/j.marchem.2020.103858

Kaczynski, S. E., and Kieber, R. J. (1993). Aqueous trivalent chromium photoproduction in natural waters. *Environ. Sci. Technol.* 27, 1572–1576. doi: 10.1021/es00045a011

Kaczynski, S. E., and Kieber, R. J. (1994). Hydrophobic C18 bound organic complexes of chromium and their potential impact on the geochemistry of Cr in natural waters. *Environ. Sci. Technol.* 28 (5), 799–804. doi: 10.1021/es00054a009

Kieber, R. J., and Helz, G. R. (1992). Indirect photoreduction of aqueous chromium (VI). *Environ. Sci. Technol.* 26, 307–312. doi: 10.1021/es00026a010

Kitchen, J. W., Johnson, T. M., Bullen, T. D., Zhu, J., and Raddatz, A. (2012). Chromium isotope fractionation factors for reduction of Cr(VI) by aqueous Fe(II) and organic molecules. *Geochimica et Cosmochimica Acta* 89, 190–201. doi: 10.1016/j.gca.2012.04.049

Klun, K., Falnoga, I., Mazej, D., Šket, P., and Faganeli, J. (2019). Colloidal organic matter and metal(loid)s in coastal waters (Gulf of Trieste, northern Adriatic Sea). *Aquat. Geochemistry* 25, 179–194. doi: 10.1007/s10498-019-09359-6

Kunde, K., Wyatt, N. J., González-Santana, D., Tagliabue, A., Mahaffey, C., and Lohan, M. C. (2019). Iron distribution in the subtropical north Atlantic: the pivotal role of colloidal iron. *Global Biogeochemical Cycles*. 33, 1532–1547. doi: 10.1029/2019GB006326

Li, B., Liao, P., Liu, P., Wang, D., Ye, Z., Wang, J., et al. (2022). Formation, aggregation, and transport of NOM-Cr(III) colloids in aquatic environments. *Environ. Science: Nano* 9 (3), 1133–1145. doi: 10.1039/D1EN00861G

Li, S. X., Zheng, F. Y., Hong, H. S., Deng, N. S., and Lin, L. X. (2009). Influence of marine phytoplankton, transition metals and sunlight on the species distribution of chromium in surface seawater. *Mar. Environ. Res.* 67 (4-5), 199–206. doi: 10.1016/j.marenvres.2009.02.001

Little, S. H., Vance, D., Siddall, M., and Gasson, E. (2013). A modelling assessment of the role of reversible scavenging in controlling oceanic dissolved Cu and Zn distributions. *Global Biogeochemical Cycles* 27 (3), 780–791. doi: 10.1002/gbc.20073

Matsumoto, K. (2007). Radiocarbon-based circulation age of the world oceans. *J. Geophysical Research: Oceans* 112, C09004. doi: 10.1029/2007JC004095

McClain, C. N., and Maher, K. (2016). Chromium fluxes and speciation in ultramafic catchments and global rivers. *Chem. Geology* 426, 135–157. doi: 10.1016/j.chemgeo.2016.01.021

Middag, R., de Baar, H. J. W., and Bruland, K. W. (2019). The relationships between dissolved zinc and major nutrients phosphate and silicate along the GEOTRACES GA02 transect in the West Atlantic ocean. *Global Biogeochemical Cycles* 33, 63–84. doi: 10.1029/2018GB006034

Mignot, A., Claustre, H., Uitz, J., Poteau, A., d'Ortenzio, F., and Xing, X. (2014). Understanding the seasonal dynamics of phytoplankton biomass and the deep chlorophyll maximum in oligotrophic environments: a bio-argo float investigation. *Global Biogeochemical Cycles* 28 (8), 856–876. doi: 10.1002/2013GB00478

Moos, S. B., and Boyle, E. A. (2019). Determination of accurate and precise chromium isotope ratios in seawater samples by MC-ICP-MS illustrated by analysis of SAFe station in the north Pacific ocean. *Chem. Geology* 511, 481–493. doi: 10.1016/j.chemgeo.2018.07.027

Moos, S. B., Boyle, E. A., Altabet, M. A., and Bourbonnais, A. (2020). Investigating the cycling of chromium in the oxygen deficient waters of the Eastern tropical north Pacific ocean and the Santa Barbara basin using stable isotopes. *Mar. Chem.* 221. doi: 10.1016/j.marchem.2020.103756

Mugo, R. K., and Orians, K. J. (1993). Seagoing method for the determination of chromium (III) and total chromium in sea water by electron-capture detection gas chromatography. *Analytica Chimica Acta* 271 (1), 1–9. doi: 10.1016/0003-2670(93)80545-V

Murray, J. W., Spell, B., and Paul, B. (1983). "The contrasting geochemistry of manganese and chromium in the eastern tropical Pacific ocean," in *Trace metals in sea water* (Boston, MA: Springer), 643–669.

Nakayama, E., Kuwamoto, T., Tsurubo, S., Tokoro, H., and Fujinaga, T. (1981). Chemical speciation of chromium in sea water: part 1. Effect of naturally occurring organic materials on the complex formation of chromium (III). *Analytica Chimica Acta* 130 (2), 289–294. doi: 10.1016/S0003-2670(01)93006-5

Nasemann, P., Janssen, D. J., Rickli, J., Grasse, P., Frank, M., and Jaccard, S. L. (2020). Chromium reduction and associated stable isotope fractionation restricted to anoxic shelf waters in the Peruvian oxygen minimum zone. *Geochimica et Cosmochimica Acta*. 285, 207–224. doi: 10.1016/j.gca.2020.06.027

Ohnemus, D. C., and Lam, P. J. (2015). Cycling of lithogenic marine particles in the US GEOTRACES north Atlantic transect. *Deep Sea Res. Part II: Topical Stud. Oceanography* 116, 283–302. doi: 10.1016/j.dsr2.2014.11.019

Ohnemus, D. C., Torrie, R., and Twining, B. S. (2019). Exposing the distributions and elemental associations of scavenged particulate phases in the ocean using basin-scale multi-element data sets. *Global Biogeochemical Cycles* 33 (6), 725–748. doi: 10.1029/2018GB006145

Paulukat, C., Døssing, L. N., Mondal, S. K., Voegelin, A. R., and Frei, R. (2015). Oxidative release of chromium from Archean ultramafic rocks, its transport and environmental impact - a Cr isotope perspective on the Sukinda Valley ore district (Orissa, India). *Appl. Geochemistry* 59, 125–138. doi: 10.1016/j.apgeochem.2015.04.016

Pérez, V., Fernández, E., Marañón, E., Morán, X. A. G., and Zubkov, M. V. (2006). Vertical distribution of phytoplankton biomass, production and growth in the Atlantic subtropical gyres. *Deep-Sea Res. Part I: Oceanographic Res. Papers* 53 (10), 1616–1634. doi: 10.1016/j.dsr.2006.07.008

Pettine, M., D'Ottone, L., Campanella, L., Millero, F. J., and Passino, R. (1998). The reduction of chromium (VI) by iron (II) in aqueous solutions. *Geochimica et Cosmochimica Acta* 62, 1509–1519. doi: 10.1016/S0016-7037(98)00086-6

Pettine, M. (2000). Redox processes of chromium in sea water. *Chemical Processes in Marine Environments*, 281–296. doi: 10.1007/978-3-662-04207-6_16

Polzin, K. L., Toole, J. M., Ledwell, J. R., and Schmitt, R. W. (1997). Spatial variability of turbulent mixing in the abyssal ocean. *Science* 276 (5309), 93–96. doi: 10.1126/science.276.5309.93

Pöppelmeier, F., Janssen, D. J., Jaccard, S. L., and Stocker, T. F. (2021). Modeling the marine chromium cycle: new constraints on global-scale processes. *Biogeosciences Discussions* 18, 5447–5463. doi: 10.5194/bg-2021-106

Rädlein, N., and Heumann, K. G. (1995). Size fractionated impactor sampling of aerosol particles over the Atlantic ocean from Europe to Antarctica as a methodology for source identification of Cd, Pb, Tl, Ni, Cr, and Fe. *Fresenius' J. Analytical Chem.* 352, 748–755. doi: 10.1007/BF00323059

Rai, D., Sass, B. M., and Moore, D. A. (1987). Chromium (III) hydrolysis constants and solubility of chromium (III) hydroxide. *Inorganic Chem.* 26 (3), 345–349. doi: 10.1021/ic00250a002

Reinhard, C. T., Planavsky, N. J., Robbins, L. J., Partin, C. A., Gill, B. C., Lalonde, S. V., et al. (2013). Proterozoic ocean redox and biogeochemical stasis. *Proc. Natl. Acad. Sci.* 110 (14), 5357–5362. doi: 10.1073/pnas.1208622110

Reinhard, C. T., Planavsky, N. J., Wang, X., Fischer, W. W., Johnson, T. M., and Lyons, T. W. (2014). The isotopic composition of authigenic chromium in anoxic marine sediments: a case study from the Cariaco Basin. *Earth Planetary Sci. Lett.* 407, 9–18. doi: 10.1016/j.epsl.2014.09.024

Richard, F. C., and Bourg, A. C. (1991). Aqueous geochemistry of chromium: a review. *Water Res.* 25 (7), 807–816. doi: 10.1016/0043-1354(91)90160-R

Rickli, J., Janssen, D. J., Hassler, C., Ellwood, M. J., and Jaccard, S. L. (2019). Chromium biogeochemistry and stable isotope distribution in the Southern Ocean. *Geochimica et Cosmochimica Acta* 262, 188–206. doi: 10.1016/j.gca.2019.07.033

Rigaud, S., Radakovitch, O., Couture, R. M., Deflandre, B., Cossa, D., Garnier, C., et al. (2013). Mobility and fluxes of trace elements and nutrients at the sediment–water interface of a lagoon under contrasting water column oxygenation conditions. *Appl. Geochemistry* 31, 35–51. doi: 10.1016/j.apgeochem.2012.12.003

Roseburrough, R., and Wang, X. (2021). Chromium stable isotope geochemistry in the Mobile Bay estuary. *Chem. Geology* 584, 120530. doi: 10.1016/j.chemgeo.2021.120530

Rudnick, R. L., and Gao, S. (2003). "3.01 - composition of the continental crust," in *Treatise on geochemistry*. Eds. H. D. Holland and K. K. Turekian (Pergamon: Oxford), 1–64.

Rudnicki, M. D., and Elderfield, H. (1993). A chemical model of the buoyant and neutrally buoyant plume above the TAG vent field, 26 degrees N, mid-Atlantic ridge. *Geochimica et Cosmochimica Acta* 57 (13), 2939–2957. doi: 10.1016/0016-7037(93)90285-5

Rue, E. L., Smith, G. J., Cutter, G. A., and Bruland, K. W. (1997). The response of trace element redox couples to suboxic conditions in the water column. *Deep Sea Res. Part I: Oceanographic Res. Papers* 44 (1), 113–134. doi: 10.1016/S0967-0637(96)00088-X

Saad, E. M., Wang, X., Planavsky, N. J., Reinhard, C. T., and Tang, Y. (2017). Redox-independent chromium isotope fractionation induced by ligand-promoted dissolution. *Nat. Commun.* 8 (1), 1–10. doi: 10.1038/s41467-017-01694-y

Sander, S., and Koschinsky, A. (2000). Onboard-ship redox speciation of chromium in diffuse hydrothermal fluids from the north Fiji basin. *Mar. Chem.* 71 (1-2), 83–102. doi: 10.1016/S0304-4203(00)00042-6

Sarmiento, J. L., Simeon, J., Gnanadesikan, A., Gruber, N., Key, R. M., and Schlitzer, R. (2007). Deep ocean biogeochemistry of silicic acid and nitrate. *Global Biogeochemical Cycles* 21 (1). doi: 10.1029/2006GB002720

Scheiderich, K., Amini, M., Holmden, C., and Francois, R. (2015). Global variability of chromium isotopes in seawater demonstrated by pacific, Atlantic, and Arctic ocean samples. *Earth Planetary Sci. Lett.* 423, 87–97. doi: 10.1016/j.epsl.2015.04.030

Schoenberg, R., Zink, S., Staubwasser, M., and von Blanckenburg, F. (2008). The stable Cr isotope inventory of solid earth reservoirs determined by double spike MC-ICP-MS. *Chem. Geology* 249 (3-4), 294–306. doi: 10.1016/j.chemgeo.2008.01.009

Semeniuk, D. M., Maldonado, M. T., and Jaccard, S. L. (2016). Chromium uptake and adsorption in marine phytoplankton - implications for the marine chromium cycle. *Geochimica et Cosmochimica Acta* 184, 41–54. doi: 10.1016/j.gca.2016.04.021

Shaw, T. J., Gieskes, J. M., and Jahnke, R. A. (1990). Early diagenesis in differing depositional environments: the response of transition metals in pore water. *Geochimica et Cosmochimica Acta* 54 (5), 1233–1246. doi: 10.1016/0016-7037(90)90149-F

Sirinawin, W., Turner, D. R., and Westerlund, S. (2000). Chromium (VI) distributions in the Arctic and the Atlantic oceans and a reassessment of the oceanic Cr cycle. *Mar. Chem.* 71 (3-4), 265–282. doi: 10.1016/S0304-4203(00)00055-4

Trinquier, A., Birck, J. L., and Allègre, C. J. (2008). High-precision analysis of chromium isotopes in terrestrial and meteorite samples by thermal ionization mass spectrometry. *J. Analytical Atomic Spectrometry* 23 (12), 1565–1574. doi: 10.1039/b809755k

Trocine, R. P., and Trefry, J. H. (1988). Distribution and chemistry of suspended particles from an active hydrothermal vent site on the mid-Atlantic ridge at 26 N. *Earth Planetary Sci. Lett.* 88 (1-2), 1–15. doi: 10.1016/0012-821X(88)90041-6

van der Weijden, C. H., and Reith, M. (1982). Chromium (III)-chromium (VI) interconversions in seawater. *Mar. Chem.* 11 (6), 565–572. doi: 10.1016/0304-4203(82)90003-2

Wang, X. (2021). The chromium isotope fractionation factor in seawater. *Chem. Geology* 579. doi: 10.1016/j.chemgeo.2021.120358

Wang, X., Glass, J. B., Reinhard, C. T., and Planavsky, N. J. (2019). Species-dependent chromium isotope fractionation across the eastern tropical north Pacific oxygen minimum zone. *Geochemistry Geophysics Geosystems* 20 (5), 2499–2514. doi: 10.1029/2018GC007883

Wang, X., Johnson, T. M., and Ellis, A. S. (2015). Equilibrium isotopic fractionation and isotopic exchange kinetics between Cr(III) and Cr(VI). *Geochimica et Cosmochimica Acta* 153, 72–90. doi: 10.1016/j.gca.2015.01.003

Weber, T., John, S., Tagliabue, A., and DeVries, T. (2018). Biological uptake and reversible scavenging of zinc in the global ocean. *Science* 361 (6397), 72–76. doi: 10.1126/science.aap8532

Woodward, E. M. S., and Rees, A. P. (2001). Nutrient distributions in an anticyclonic eddy in the northeast Atlantic ocean, with reference to nanomolar ammonium concentrations. *Deep Sea Res. Part II: Topical Stud. Oceanography.* 48, 775–793. doi: 10.1016/S0967-0645(00)00097-7

Wu, W., Wang, X., Reinhard, C. T., and Planavsky, N. J. (2017). Chromium isotope systematics in the Connecticut river. *Chem. Geology* 456, 98–111. doi: 10.1016/j.chemgeo.2017.03.009

Xiang, Y., Lam, P. J., and Lee, J. M. (2021). Diel redox cycle of manganese in the surface Arctic Ocean. *Geophysical Research Letters* 48(23), e2021GL094805. doi: 10.1029/2021GL094805

Yang, L., Nadeau, K., Meija, J., Grinberg, P., Pagliano, E., Ardini, F., et al. (2018). Inter-laboratory study for the certification of trace elements in seawater certified reference materials NASS-7 and CASS-6. *Analytical Bioanalytical Chem.* 410 (18), 4469–4479. doi: 10.1007/s00216-018-1102-y

Ye, Y., and Völker, C. (2017). On the role of dust-deposited lithogenic particles for iron cycling in the tropical and subtropical Atlantic. *Global Biogeochemical Cycles* 31 (10), 1543–1558. doi: 10.1002/2017GB005663

Yiğiterhan, O., Murray, J. W., and Tuğrul, S. (2011). Trace metal composition of suspended particulate matter in the water column of the Black Sea. *Mar. Chem.* 126 (1-4), 207–228. doi: 10.1016/j.marchem.2011.05.006

Zhang, Q., Amor, K., Galer, S. J., Thompson, I., and Porcelli, D. (2018). Variations of stable isotope fractionation during bacterial chromium reduction processes and their implications. *Chem. Geology* 481, 155–164. doi: 10.1016/j.chemgeo.2018.02.004

Zhang, Q., Amor, K., Galer, S. J., Thompson, I., and Porcelli, D. (2019). Using stable isotope fractionation factors to identify Cr(VI) reduction pathways: metal-mineral-microbe interactions. *Water Res.* 151, 98–109. doi: 10.1016/j.watres.2018.11.088

frontiers | Frontiers in Marine Science

TYPE Original Research
PUBLISHED 02 June 2023
DOI 10.3389/fmars.2023.1154248

OPEN ACCESS

EDITED BY
Wen Zhuang,
Shandong University, China

REVIEWED BY
Xueyan Jiang,
Ocean University of China, China
Deli Wang,
Xiamen University, China
Liqin Duan,
Institute of Oceanology Chinese Academy of Sciences, China

*CORRESPONDENCE
Li Li
Li.Li@fio.org.cn

RECEIVED 30 January 2023
ACCEPTED 18 May 2023
PUBLISHED 02 June 2023

CITATION
Wang X, Li L, Ren Y, Cao P, Zhu A, Liu J and Shi X (2023) Early diagenesis and benthic fluxes of redox-sensitive metals in eastern China shelf sediments.
Front. Mar. Sci. 10:1154248.
doi: 10.3389/fmars.2023.1154248

Early diagenesis and benthic fluxes of redox-sensitive metals in eastern China shelf sediments

Xiaojing Wang[1,2], Li Li[1,2,3]*, Yijun Ren[1], Peng Cao[1,3], Aimei Zhu[1,2], Jihua Liu[1,2,3] and Xuefa Shi[1,2,3]

[1]Key Laboratory of Marine Geology and Metallogeny, First Institute of Oceanography, Ministry of Natural Resources, Qingdao, China, [2]Key Laboratory of Deep Sea Mineral Resources Development, Qingdao, Shandong, China, [3]Laboratory for Marine Geology, Laoshan Laboratory, Qingdao, China

Thirteen Short sediment cores (30-50 cm) were collected from Bohai Sea, Yellow Sea and Changjiang Estuary in China, and the early diagenesis of several redox sensitive metals (Fe, Mn, Mo, U and V, referring to as RSMs) in sediment were studied. The recycling process of Mo and Mn was closely correlated with each other, generating benthic fluxes diffusing upward from sediment to overlying water column, and the flux rates are related to the organic carbon oxidation rates. The recycling of U and V were more tightly coupled with Fe oxides, generating benthic fluxes going downward into the sediment in most cores. Significant authigenic accumulation of U, in contrary to little to no accumulation of Mo and V, were found in the study region, even in Changjiang Estuary where hypoxic condition was often found during summer. Benthic diffusive fluxes were compared with authigenic mass accumulate rates (MAR), which indicated that, besides the benthic diffusion process, there are other processes controlling the authigenic accumulation of the RSMs. The close relationships between authigenic accumulation of RSMs with OC_{burial} and OC_{burial} with S_{burial}, indicating the authigenic accumulation of RSMs is a consequence of redox environment in shelf sediment, which directly influencing the organic carbon degradation process. Compared with other continental margin, moderate enrichment of U was found in China continental sediment. The authigenic U accumulation in BS and NYS sediments accounted for 20 - 68% of the Yellow River input, whilst in SYS sediments accounted for ~ 64% of the Yellow River and Changjiang River input, which acting as important U sinks that cannot be ignored.

KEYWORDS

early diagenesis, redox sensitive metals, benthic flux, authigenic accumulation, eastern China marginal seas

1 Introduction

Redox sensitive metals (RSMs) such as iron (Fe), manganese (Mn), molybdenum (Mo), uranium (U), and vanadium (V) have been well-established as redox proxies in a wide range of coastal marine sediments (Mcmanus et al., 2005; Morford et al., 2005; McManus et al., 2006; Morford et al., 2009a; Abshire et al., 2020a; Abshire et al., 2020b). It is generally

accepted that RSMs are sensitive to redox conditions due to the different solubility of various species. The microbial-mediated remineralization of organic matter forms a major process that controls the redox conditions and the recycling of RSMs, often oxygen, NO_3^-, Fe/Mn oxides, $SO_4^{2-}$and CO_2 acting as electron acceptors, following certain thermodynamic order (Froelich et al., 1979; Emerson and Hedges, 2003). As a result of these early diagenetic reactions, RSMs that previously adsorbed with those biogenic/oxidized particles are released as dissolved phase, either diffused back to overlying water or accumulated into sediments by reduction (Shaw et al., 1990; Scholz et al., 2011; Li et al., 2021).

The eastern China seas are some of the most extensive shelf seas in the world, with shallow water depth and rapid sedimentation rates (Su and Yuan, 2005). Recently, studies have shown that hypoxia occurs in the bottom of the Bohai sea (BS) in summer, which is the result of stratification and the decomposition of organic matter (Zhao et al., 2017; Wei et al., 2019). The Changjiang Estuary (CJE) is one of the continental shelf areas with high primary productivity in the world. Regional and seasonal hypoxia often occurs off the Changjiang Estuary, usually begins in early June and may persist as late as October. Due to anthropogenic disturbance, excess riverine nutrient supply along with terrestrial materials has stimulated frequent coastal bottom-waters hypoxia events during summer (Chen et al., 2007; Chi et al., 2017). In recent decades, the minimum oxygen levels in the hypoxia zone did not show any decline, and the affected area has an enlarging trend (Wang, 2009; Zhu et al., 2011).

The eastern China continental shelf is reported to be an important sink for organic carbon (11- 43%), while limited studies exist on early diagenesis and reservation processes of the RSMs (Zhao et al., 2021). Previous studies in northern Okinawa Trough, where oxic and suboxic sediment environment were found, has distinct enrichment of U but little accumulation for Mo, indicating that suboxic sediments act as an important sink for U, whilst anoxic environment is needed for the accumulation of Mo in sediments (Yamada et al., 2006; Wang et al., 2019). Xu (2007) and Wu et al. (2020) presented RSMs data of the Changjiang Estuary, and highlight the impact of seasonally hypoxic settings on the enrichment of Mo and V. However, for the vast majority areas of China continental shelves, the role of sediments as sinks or sources for RSMs has not been thoroughly investigated.

In this study, we collected 13 short (30-50 cm) sediment cores along the eastern China marginal seas, including Bohai and Yellow Seas and Changjiang estuary, which are characterized by rapid sedimentation rates and intense biological activities. Dissolved concentrations in porewater, overlying seawater and bulk contents in sediments (Fe, Mn, S, Mo, U, V) were measured to systematically understand the early diagenesis processes of RSMs. Benthic fluxes were estimated from one-dimensional diagenetic transport-reaction model, and compared with the authigenic RSMs accumulation rates, to qualitative and quantitative evaluate the processes that control the RSMs' recycling at sediment-water interface. The authigenic accumulation rates are compared with other marginal areas to establish a more synthetic view of RSMs behaviors along the eastern China margin.

2 Study area

The BS and Yellow Sea (YS) are two semi-enclosed continental seas of the northwestern Pacific Ocean located in the northeast of China, with a total area of 4.6×10^5 km^2 and average depths of about 18 m and 44 m, respectively. The BS is enclosed by Liaodong and Shandong Peninsulas in northern China and connected to the YS through the narrow Bohai Strait. The YS is divided into the northern YS (NYS) and southern YS (SYS) by a boundary from Chengshanjiao of the Shandong Peninsula and Changshanchuan of the Korean Peninsula (Figure 1). Several rivers (Yellow River, Hai He and Luan He etc.) discharge along the coastal area of BS and YS, among which the Yellow River yields the largest sediment load (~1.1×10^9 tons yr^{-1}) (Wang et al., 2007; Zhang et al., 2013). As shown in Figure 1, the hydrography of the study region is dominated by several southward local coastal currents, Yellow Sea Coastal Current (YSCC) and seasonally northward Yellow Sea Warm Current (YSWC) (Su and Yuan, 2005). YSWC is strongest in winter, and disappears or becomes weak in summer (Xu et al., 2009). With the onset of water stratification when the southwest monsoon prevails in late spring, Yellow Sea Cold Water (YSCW) forms, flourishing in summer and finally depressing in autumn (Hu, 1994; Zhang et al., 2008).

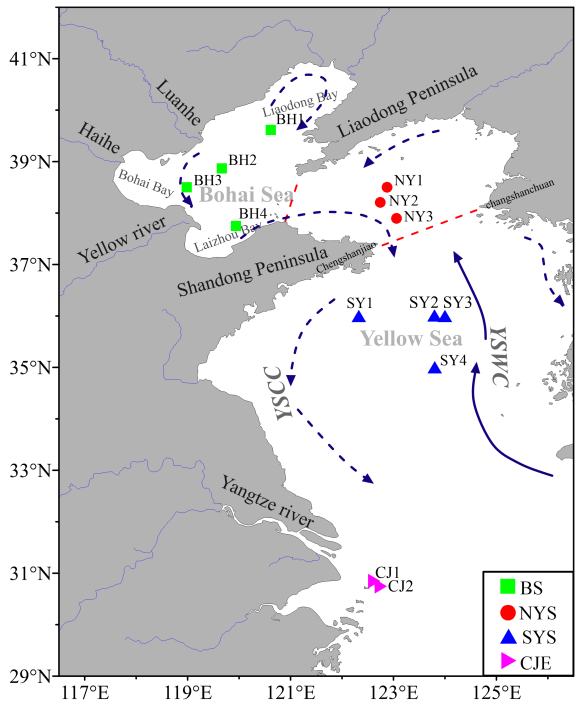

FIGURE 1
Station locations in Bohai, Yellow Seas and Changjiang Estuary of China. YSCC: Yellow Sea Coastal Current, YSWC: Yellow Sea Warm Current. The red solid lines represent the boundaries of the Bohai Sea, the North Yellow Sea and the South Yellow Sea. The blue solid lines represent the YSWC, and the blue dashed lines represent the YSCC.

3 Methods

3.1 Sample collection

Thirteen sediment cores (~ 20 - 45 cm) from the Bohai, Yellow Seas and Changjiang Estuary were collected onboard the *R/V Dongfanghong 2* (July, 2016), *R/V Zhedingyuyun* (August, 2017), *R/V Chuangxin 2* (July, 2018) and *R/V Xiangyanghong 18* (August, 2019), respectively. The sampling locations are shown in Figure 1 and the information of the sites are reported in Table 1. These cores were sampled using a box-corer at water depths of 15 to 77 m. Four cores (BH1-BH4) were located in the BS, three cores (NY1-NY3) in NYS, four cores (SY1- SY4) were in SYS and two cores (CJ1-CJ2) in CJE (Figure 1).

Upon collection, porewater was collected in a N_2-filled glove bag using Rhizon® sampler (Rhizonsphere Inc.) that was inserted into the pre-drilled holes on the cores, and Teflon lines and peristaltic pump (LongerParmer® Inc.) were coupled to form a trace-metal clean sampling system. The first mL of extracted porewater was discarded to prevent oxidation, collected samples were acidified to pH~2 with HNO_3 (Optima grade, Thermo Fisher Scientific Inc.) and stored at 4° C. Concurrently, parallel sediment cores were collected and sliced onboard the ship. Sediment samples were sealed in plastic bags and stored at 4°C until further processing. Sampling resolutions for porewater and sediment samples were 1 cm within the top 10 cm, and 2 cm for the remainder depth.

Bottom seawater samples (~ 2-5 m above the seafloor) were collected using Niskin bottles mounted on the CTD rosette. After

TABLE 1 Detailed information of the stations, and the measured TOC, $CaCO_3$, bottom water oxygen concentration ($[O_2]_{bw}$), along with the sedimentation rates, mass accumulation rates, organic carbon burial rate (OC_{burial}) used or calculated in this study.

Station	Sampling date	Water depth (m)	Bottom water temperature (°C)	$[O_2]_{bw}$ (μM)	TOC [a] (%)	$CaCO_3$ [b] (%)	Sedimentation Rates ($cm \cdot y^{-1}$)	Mass accumulation rate ($g \cdot cm^{-2} \cdot y^{-1}$)	OC_{burial} ($mmol \cdot m^{-2} \cdot d^{-1}$)
BH1	July, 2016	29	12.2	289	0.47 ± 0.03	3.57 ± 0.57	0.29[c]	0.33[c]	3.51 ± 0.24
BH2	July, 2016	25	17.6	285	0.62 ± 0.04	3.69 ± 0.58	0.31[d]	0.30[d]	4.91± 0.30
BH3	July, 2016	23	16.8	262	0.43 ± 0.02	11.2 ± 1.45	0.20[e]	0.20[j]	1.98 ± 0.11
BH4	July, 2016	16	24.3	191	0.31 ± 0.05	11.8 ± 2.09	0.31[e]	0.26[j]	1.86 ± 0.28
NY1	July, 2016	58	7.3	339	0.54 ± 0.04	2.63 ± 0.42	0.09[f]	0.07[f]	0.86 ± 0.06
NY2	July, 2016	53	6.4	296	0.38 ± 0.04	3.82 ± 0.43	0.09 [f]	0.07[f]	0.60 ± 0.07
NY3	July, 2016	61	6.7	301	0.29 ± 0.04	4.62 ± 0.54	0.08[f]	0.07[f]	0.45 ± 0.06
SY1	June, 2016	52	7.4	234	0.55 ± 0.03	5.35 ± 0.71	0.41[g]	0.33[g]	4.14 ± 0.21
SY2	August, 2019	72	7.9	182	1.02 ± 0.03	2.08 ± 0.44	0.17[g]	0.14[k]	3.16 ± 0.11
SY3	June, 2016	77	7.3	249	0.79 ± 0.04	3.82 ± 0.77	0.11[g]	0.09[g]	1.59 ± 0.09
SY4	August, 2019	76	8.3	198	0.58 ± 0.11	2.43 ± 0.69	0.06[g]	0.05[k]	0.64 ± 0.12
CJ1	July, 2018	21	27	111	0.46 ± 0.06	8.31 ± 0.45	0.34[h]	0.36[l]	3.82 ± 0.47
CJ2	August, 2017	27	21	174	0.38 ± 0.03	8.77 ± 0.43	2.40[i]	2.57[l]	22.4 ± 2.01

a: TOC contents are calculated average values from sediment samples deeper than 15 cm.
b: $CaCO_3$ contents are calculated average values of the whole sediment core.
c: Data from station B73 and BP1 in Yang et al. (1993).
d: Data from station M4-3 in Li and Shi (1995).
e: Data from station M8-4 and M8-12 in Dong et al. (1995).
f: Data from station C2 and NYS-5 in Qi et al. (2004).
g: Data from Alexander et al. (1991).
h Data from station HN108 in Xia et al. (2004).
i: Data from station CJ08-689 in Shi (2014).
j: MAR are calculated based on the Eq. (5), the ρ_{dry} data are from station M8-4 and M6-3 in Li and Shi (1995), assumed to be 1.01 $g \cdot cm^{-3}$ and 0.85 $g \cdot cm^{-3}$ for BH3 and BH4.
k: MAR are calculated based on the Eq. (5), the ρ_{dry} data is from Alexander et al. (1991), assumed to be 0.80 $g \cdot cm^{-3}$.
l: MAR are calculated based on the Eq. (5), the ρ_{dry} data is from station SC07 in Zhang et al. (2009), assumed to be 1.07 $g \cdot cm^{-3}$.

collection, seawater samples were filtered immediately through 0.2 µm AcroPak® filters (Pall Inc.) into LDPE bottles (Nalgene™, Thermo Fisher Scientific Inc.), and acidified to pH ~2 with HNO_3. Prior to the sampling, filters, bottles and other labware were thoroughly cleaned as described by Li et al. (2015).

3.2 Sample analysis

3.2.1 Seawater and porewater analysis

The seawater O_2 concentrations were determined onboard following the Winkler titration method (Grasshoff et al., 1999), the uncertainty was estimated to be ± 1 µmol·L^{-1}. Total dissolved sulfide (ΣHS^-) in porewater samples were determined on board inside a N_2-filled glove bag following the methylene-blue colorimetric method (Cline, 1969) with a UV spectrophotometer (7200 series, Shanghai Unico Inc., China). Sulfide standard solution and its dilution stabilizing solution (Beijing Aoke biotechnology Inc., China) were used to generate the calibration curves. The detection limit of the analytical method for sulfide was 1.9 µmol·L^{-1}.

Porewater and seawater samples were diluted 20-fold with 2% HNO_3 for analysis, only dissolved Mn in seawater samples were pre-concentrated using Nobias PA1® resin with a manually controlled manifold (Biller and Bruland, 2012). All samples were analyzed using ICP-MS under collision cell-mode (XII series, Thermo Fisher Scientific Inc.). Indium, Sc and Rh were added to all samples as internal standards. A random selection of 10% samples were spiked with metal standards to two increments concentrations to correct the sample matrix effects. The results showed that the recoveries for Fe, Mn, Mo, U and V were generally within 80 - 113%, and the porewater data of RSMs have been corrected by the recovery. Precision and accuracy of the method were tracked by analyzing certified reference materials (CASS-5 and NASS-6, National Research Council, Canada), and the results are shown in Table S1. The measured values were in good agreement with certified values.

3.2.2 Sediment analysis

Sediment samples (~50 mg) were freeze-dried and digested with 3 mL mixed concentration acid (HNO_3: HF =1:1) at 190°C for 48 h, then diluted to 50 ml with 2% HNO_3. Al, Fe, Mn and S were analyzed by ICP-OES (iCAP 6300, Thermo Fisher Scientific Inc.) and Mo, U and V by ICP-MS. The recoveries of all metals were within 95-106% (n = 20) using sediment reference standards (GBW07309 and GBW07305a, China). Replicate analyses showed that the relative standard deviations (RSD) were< 1% for Al, Fe, Mn and S, and< 5% for Mo, U and V.

Total carbon (TC) and total organic carbon (TOC) were measured with an Elemental Analyzer (Model EL-III, Vario), and TOC samples were treated with 4 N HCl to remove inorganic carbon (TIC) before analysis. The recovery of TOC was 95-102% (n = 10) assessed by GBW07309, and the relative errors observed in triplicate analyses were< 0.05%. Calcium carbonate content ($CaCO_3$) was calculated from TIC according to molecular ratio of $CaCO_3$:C (100:12). Grain size were determined using a laser particle size analyzer (Master sizer 2000, Malvern Instrument), and categorized as clay (<4µm), silt (4-63µm) and sand (>63µm).

3.3 Calculation of fluxes at the sediment-water interface (SWI)

Diffusive benthic fluxes of the RSMs at SWI and mass accumulation rates of authigenic metals (RSM_{AR}) in downcore sediments of coastal China were both calculated for the purpose of this study.

3.3.1 Diffusive benthic flux

The diffusive benthic fluxes across SWI were estimated using a one-dimensional transport-reaction model (Boudreau, 1997), which accounts for the effects of molecular diffusion, bioturbation and irrigation. The model takes the form:

$$\left(\frac{\partial C_{pw}}{\partial t}\right)_x = \frac{\partial}{\partial x}\left(\varphi(D_s + D_B)\frac{\partial C_{pw}}{\partial x}\right) + \varphi\alpha(C_o - C_{pw}) + R = 0 \quad (1)$$

where C_{pw} is the porewater concentration, C_0 is the bottom water concentration, x is the depth, φ is the porosity, D_s is the molecular diffusion coefficient, D_B is the bioturbation coefficient, α is the irrigation coefficient, and R is the net rate of production per unit of sediment. No available irrigation coefficient (α) was found in the study area, therefore the irrigation process was not included.

The D_s was calculated by the Stokes-Einstein diffusion coefficient temperature dependence described by Li and Gregory (1974), adjusted to the bottom water temperature of 6.4 - 27°C. As there was no published D_{sw} (25°C) value for VO_4^{3-}, we adopted the one of MoO_4^{2-} instead, because they exist in seawater as similar oxyanions (similar as in Scholz et al., 2011). Based on Eq. (2), the calculated D_s values ranged from 2.98 - 6.78×10^{-6} cm^2 s^{-1} for Mn, 4.30- 9.76×10^{-6} cm^2 s^{-1} for Mo and V, 1.85 - 4.20×10^{-6} cm^2 s^{-1} for U, respectively.

$$D_s = \frac{D_{sw}(25\,^{\circ}C)}{2.19} + \frac{T}{25} \times \left(D_{sw}(25\,^{\circ}C) - \frac{D_{sw}(25\,^{\circ}C)}{2.19}\right) \quad (2)$$

The D_B was calculated based on the formula from Tromp et al. (1995), as a function of the sedimentation rate (s), shown in Table 1:

$$log_{10}(D_B) = 1.63 - 0.05 \cdot log_{10}s \quad (3)$$

The benthic fluxes were calculated using the code PROFILE (Berg et al., 1998). The dissolved RSMs concentrations used for the bottom water (reported in Table 2) were positioned at 0.5 cm above seafloor in order to obtain the best fit between observed and modeled data. By definition, positive flux indicates diffusion upward into the overlying water, while negative flux is directed into the sediments. Strong advection flow could take place within sediments, ensuring a rapid exchange of solutes between burrows and overlying water. The calculated Peclet number are low (0.02-0.08), indicating

TABLE 2 Dissolved redox sensitive metal concentrations (*unit: nmol L^{-1}*) measured in bottom seawater in this study.

Station ID	Mn	Mo	U	V
BH1	22.0	112.7	12.6	42.1
BH2	27.1	110.8	12.7	43.2
BH3	21.1	110.8	12.7	43.2
BH4	23.3	113.1	13.8	43.8
NY3[a]	20.5	108.4	12.3	42.6
SY1	5.90	106.4	12.9	41.7
SY3	4.45	113.0	12.6	46.7
CJ1	11.5	105.8	11.9	38.2
CJ2	16.9	94.9	12.5	44.7

a. The concentrations of dissolved RSM in NY3 are applied for the NY1 and NY2.

that the advection flux can be neglected relative to diffusion (Boudreau, 1997).

3.3.2 Mass accumulation rate (MAR) of authigenic metals

MAR of authigenic metals ($[Me]_{AR}$)were calculated based on Eq. (4):

$$[Me]_{AR} = MAR_{sed} \times [Me]_{auth} \quad (4)$$

where $MAR_{sed}$is the sediment mass accumulation rate, and $[Me]_{auth}$ refers to the average authigenic metals concentration, which was calculated as follows Eq. (5):

$$[Me]_{auth} = [Me]_{sample} - \frac{[Me]_{detrital}}{[Al]_{detrital}}[Al]_{sample} \quad (5)$$

where $[Me]_{sample}$and $[Al]_{sample}$are average bulk contents below 15 cm in each sediment core. The $[Me]_{detrital}/[Al]_{detrital}$represents the ratio between detrital metal and detrital Al contents. The average metal contents of the local regional upper continental crust (UCC) values were used as the detrital values. Specifically, the UCC values of the northern margin of North China were used for BS and YS, and the UCC values of Changjiang for CJE (Gao et al., 1998). The S/Al detrital ratio in the northern margin of North China was not reported, the value in the Changjiang was adopted (7.79×10^{-3} g·g^{-1}), which is closer to the UCC value reported by Rudick and Gao (2014).

For station BH1, BH2, NYS cores, SY1 and SY3, the MAR data are chosen from the reported MAR data from nearest locations. While for other cores, only sedimentation rates were found from the nearest locations in previous studies, therefore the MAR are calculated based on Eq. (6).

$$MAR_{sed} = s \times \rho_{dry} \quad (6)$$

where s is sedimentation rate and ρ_{dry}refers to the dry sediment density. All detailed information is reported in Table 1. Organic carbon burial rates (OC_{burial}) are calculated based on Eq. 7

$$OC_{burial} = C_{org} \times \mathrm{MAR} \quad (7)$$

Where $C_{org}$is the average TOC content below 15cm in sediment core (Table 1), and the OC_{burial} results are shown in Table 1.

4 Results and discussion

4.1 Bottom water oxygen content

The bottom water oxygen concentrations ($[O_2]$) of the BS ranged from 191 μM to 289 μM (Table 1), comparable to the values previously reported in June to July in BS (average being 235 ± 30 μM; Wang et al., 2015). The bottom water $[O_2]$ in SYS (182-249 μM) were lower than that of the NYS (296-339 μM), and comparable to those reported in 35-36°N of China continental shelf during May to August (229-313 μM, averaged being 250 μM) (Sohrin et al., 1999; Chi et al., 2017). Although primary production consumed oxygen in surface water during spring to summer, seasonally northward flowing YSWC kept the bottom water oxygen concentrations still at a relatively high level in SYS (Hu, 1994; Wang, 1997).

4.2 Dissolved RSMs in porewater

4.2.1 Fe, Mn and S in porewater

The vertical distributions of Mn and Fe in porewater are shown in Figure 2. In SYS, dissolved Mn and Fe were negligible at the depth of 1-2 cm and increase to peak values by 3-10 cm, followed by a decrease downcore to constant values. Both Mn and Fe are known to be easily mobilized in reducing environment, and Fe peaks typically appear at a relatively deeper depth than Mn peaks (Figure 2), which is consistent with the expected thermodynamic order reported by Froelich et al. (1979). Similar dissolved Mn and Fe profiles were found in BH3 and NY3 cores (Figure 2). These cores indicate typical redox sequences of hemipelagic sediments, where a relatively oxidative sedimentary environment was found

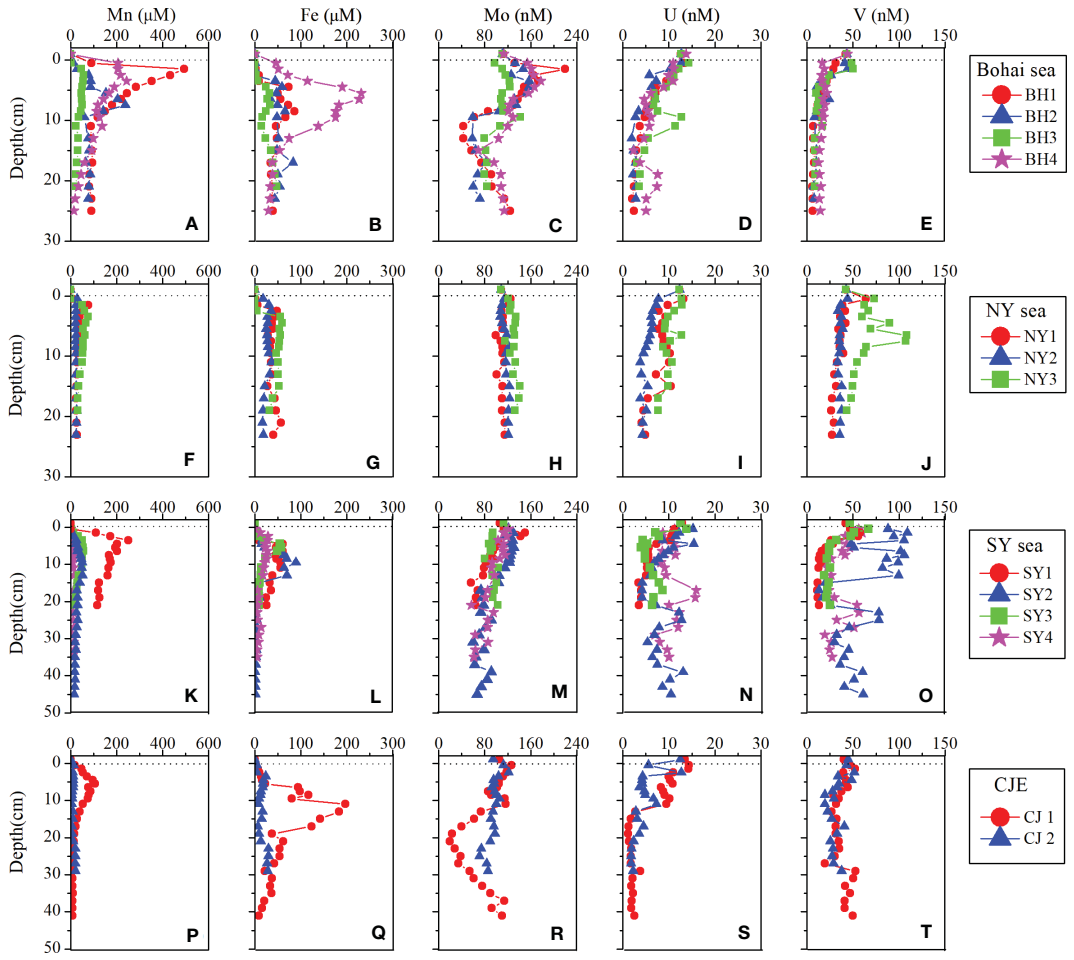

FIGURE 2
Porewater profiles for Fe, Mn, Mo, U and V for all cores. The dashed lines denote the sediment-water interface.

across the SWI (Shaw et al., 1990; Morford et al., 2005; Canfield and Thamdrup, 2009).

For other cores in the study area, dissolved Mn or Fe was measurable in surficial samples (Figure 2). Especially in cores near the coast, such as BH1, BH4 and NY2, dissolved Mn and Fe reached higher contents in the surface layer (28 - 205 μM for Mn, 18 - 46 μM for Fe). Higher dissolved Mn and Fe appear at or near-SWI, exhibiting a relatively reducing environment, especially in core BH4, consistent with the higher organic supply to the sediment and associated lower oxygen (191 μM) in the bottom waters.

According to the first appearance depth of dissolved Mn and Fe, sediments farther away from the coast were less reducible. Porewater profiles indicate that early diagenesis occurred mainly through the reduction of oxygen, Mn/Fe oxides, and no significant sulfate reduction was observed. Although no dissolved sulfide was measured (<1.9 μM) in any of the sediment cores, the formation of microsulfide environment cannot be excluded. For example, at the bottom of SY2 and SY4 cores, dissolved Fe contents is significantly reduced (1-2 μM and 5-7 μM, respectively) (Figures 2K, L), which may be affected by sulfide reduction.

4.2.2 Mo, U and V in porewater

Vertical distributions of dissolved Mo, U and V in porewater are shown in Figure 2. In most cores, dissolved Mo and V generally decrease with depth and approach constant concentrations at certain depths. Dissolved Mo and V showed one or two peaks in the Fe/Mn reduction zones (Figure 2), indicating that the recycling processes of Mo and V were coupled with Fe/Mn oxides (Morford and Emerson, 1999; Morford et al., 2005; Whitmore et al., 2019). Below the Fe/Mn oxides reduction zone, V(V) is progressively reduced to V(IV) and, if H_2S is present, to V(III) (Wehrli and Stumm, 1989; Wanty and Goldhaber, 1992). Reduced V is removed from porewater by surface adsorption of organic V(IV) complexes, formation of insoluble V(III) oxides and incorporation of V(III) into insoluble organic compounds (Wanty and Goldhaber, 1992). Reduction of Mo (VI) to Mo (IV) occurs under sulfidic conditions (H_2S > 0.1 μM), molybdate is subsequently transformed into

thiomolybdates ($Mo_4S_{4-x}^{2-}$, x=0 to 3) (Helz et al., 1996; Zheng et al., 2000) and finally scavenged as particle-reactive thiomolybdate (MoS_4^{2-}) by Fe sulfides and/or sulfur-rich organic materials (Tribovillard et al., 2004; Vorlicek et al., 2004).

Dissolved U showed significant removal from porewater, from 10-13 nM at the top to 2-6 nM below 15 cm in most cores. The prominent curvature of porewater U was coincident with the depth of the dissolved Fe peaks (Figure 2). Dissolved U exists as carbonate complex that does not adsorb to Mn/Fe oxides or any other inorganic particles in the water column. Reduction of U(VI) to U (IV), a process that usually occurs at or below the depth of Fe remobilization. Mediated by Fe and sulfate-reducing bacteria, reduced U is removed from porewater by adsorption or precipitation of U oxides (Lovley et al., 1991; Zheng et al., 2002).

For some cores, besides the subsurface peaks in Mn/Fe reduction zone, deeper peaks of dissolved Mo, U and V in BH3, NY3, SY2 and SY4 were also found (Figure 2), which may be related to the regeneration of authigenic metals caused by bioturbation or bioirrigation oxidative dissolution (Aller, 1980; Morford et al., 2009a). This is supported by the findings of shell fragments at 10 - 14 cm depths in NY3 and SY4 cores and biological burrows at the surface layer of core BH3. In BH1, BH4 and CJ1 cores, with broader Fe peaks below the Mn peaks, dissolved Mo decreased to ~ 40 nM from 2 to ~15 cm, then increased to ~120 nM by the cores bottom (Figures 2C, R). The removal of Mo from porewater in the Mn reduction zone most likely occurs when Fe (II) is oxidized by Mn (IV) (Burdige, 1993; Postma and Appelo, 2000), causing dissolved Mo released from the Mn oxides may immediately be re-adsorbed to the fresh Fe hydroxides surfaces (Gustafsson, 2003; Goldberg et al., 2009). Upon burial deeper into the Fe reduction zone, Mo is released back into the porewater as Mo-rich Fe hydroxides dissolves (Herbert et al., 2020), resulting in the porewater Mo increases gradually.

4.3 Elemental distribution in sediments

4.3.1 TOC, grain size

The sediment types varied from silty sand to clayey silt (Figure S1). Most core sediments fell into the clayey silt domain, while BH1, NY1 and NY3 were sandy silt and silty sand. The average TOC contents ranged from 0.22% to 1.08%, higher TOC contents (0.65 - 1.08%) were found in SYS (Table 1). Vertically, the TOC content decreased within the top few cm, then remained constant (Figure S2). For most cores, averaged TOC contents were correlated well with mean grain size (Mz) ($P< 0.01$), but not for BH3, BH4 and CJ2 (Figure S3). These cores have higher $CaCO_3$ contents (8 -11%) (Table 1), and the insignificant linear correlation may be caused by the source-dependent control (e.g., Yellow River and Changjiang River input) (Bigot et al., 1989; Qiao et al., 2010).

4.3.2 Solid phase RSMs

Vertical distributions of Mn, Fe, S, Mo U and V are shown in Figure 3. All data were normalized by Al to minimize the grain size effect (Roussiez et al., 2005; Hu et al., 2013). To elucidate the relationships among the RSMs, TOC, S and Mz in sediments, Spearman correlation analysis was performed, and the results are shown in Table S3. Again, all data are normalized to Al to minimize the grain size effect for the correlation analysis.

First of all, Fe exhibited a nearly invariant distribution with depth for all cores. Fe/Al in sediments were correlated well with Mz and TOC ($n = 256$, $p< 0.01$), indicating the recycling processes of Fe was associated with Mz and TOC. Unlike Fe, Mn has obvious enrichment in surface sediment in all study regions except CJE sites. The enrichment is most obvious at the sites near the Shandong Peninsula (Figure 3M), which was similar to previous reported data here (Yuan et al., 2012). Except for BH1 and BH2 cores, averaged Mn/Al for whole cores were correlated well with $CaCO_3$ ($r^2 = 0.68$, $p< 0.01$). The mechanism is probably due to the sediments dominated by high content of $CaCO_3$ originated from riverine input and biogenic $CaCO_3$, such as shell fragments (Yang et al., 2003), while dissolved Mn can be adsorbed on, or incorporated into, freshly precipitated $CaCO_3$ in seawater and settled in sediment (Aller and Rude, 1988; Kim et al., 1998). Other studies have also found that high contents of Mn in surficial sediments were related to up-diffusion Mn (II) reoxidation by the reduction of Mn oxides in deeper sediments (Nolting et al., 1996; Mouret et al., 2009; Volz et al., 2020), which is in agreement with the observation that the cores with higher surface Mn corresponding to higher dissolved Mn peaks in porewater (Figures 2, 3), indicating the influence of diagenetic process.

In surface sediments, Mo peaks often resonate with Mn peaks (Figure 3), confirming that Mo recycling process is associated with Mn in oxic layer (Morford and Emerson, 1999; Sundby et al., 2004; Li et al., 2020). The average Mo/Mn ratio is ~ 0.001 ± 0.0002 ($n = 29$) in Mn-enriched layer (≤ 5cm), comparable to the ratio for oxic sediments in North American Arctic margin (~ 0.001) (Kuzyk et al., 2017), slightly lower than the ratio observed worldwide (~ 0.002) (Shimmield and Price, 1986; Chaillou et al., 2002). While below the Mn-enriched layer (> 5cm), significant correlations were found between Mo/Al - S within most cores ($r^2 = 0.40$ - 0.92, $p< 0.01$- 0.05). It is generally accepted that Mo precipitation in reducing sediments is related to the balance between Fe and sulfate reduction (Zheng et al., 2000; Morford et al., 2009a). Kang et al. (2014) observed that S_{total} and $S_{reduced}$ gradually increased with depth in YS and CJE sediments, and pyrite -S was the predominant reduced inorganic sulfur phase. Probably, dissolved Mo removed from porewater was directly trapped by reduced S and subsequently accumulates as a Mo-Fe-S phase (Zheng et al., 2000; Helz and Vorlicek, 2019).

Solid U remains roughly detrital level (~1.23 μg/g for BH and YS, ~ 1.40 μg/g for CJE) within top 5-10 cm in most cores, with enrichment occurring at deeper depth (Figure 3). Previous studies have reported that U accumulation is sensitive to OC delivery to the seabed (Anderson et al., 1989; Zheng et al., 2002). A weak correlation between U/Al - TOC was found, while U/Al and S/Al showed a good correlation ($r^2 = 0.43$, $n = 256$, $p<0.01$) (Table S3). Normally U does not form stable sulfides, but free sulfide may promote reduction/fixation of U (Emerson and Huested, 1991). However, no vertical variation of solid U was found in CJE cores (Figure 3W), which is consistent with the results reported by Scholz et al. (2011) and Wu et al. (2020), possibly related to seasonal oxygen fluctuations in bottom water. In such settings, authigenic U precipitated during reducing periods undergoes transient re-oxidation, and correspondingly leads to the erasure of the accumulated signal.

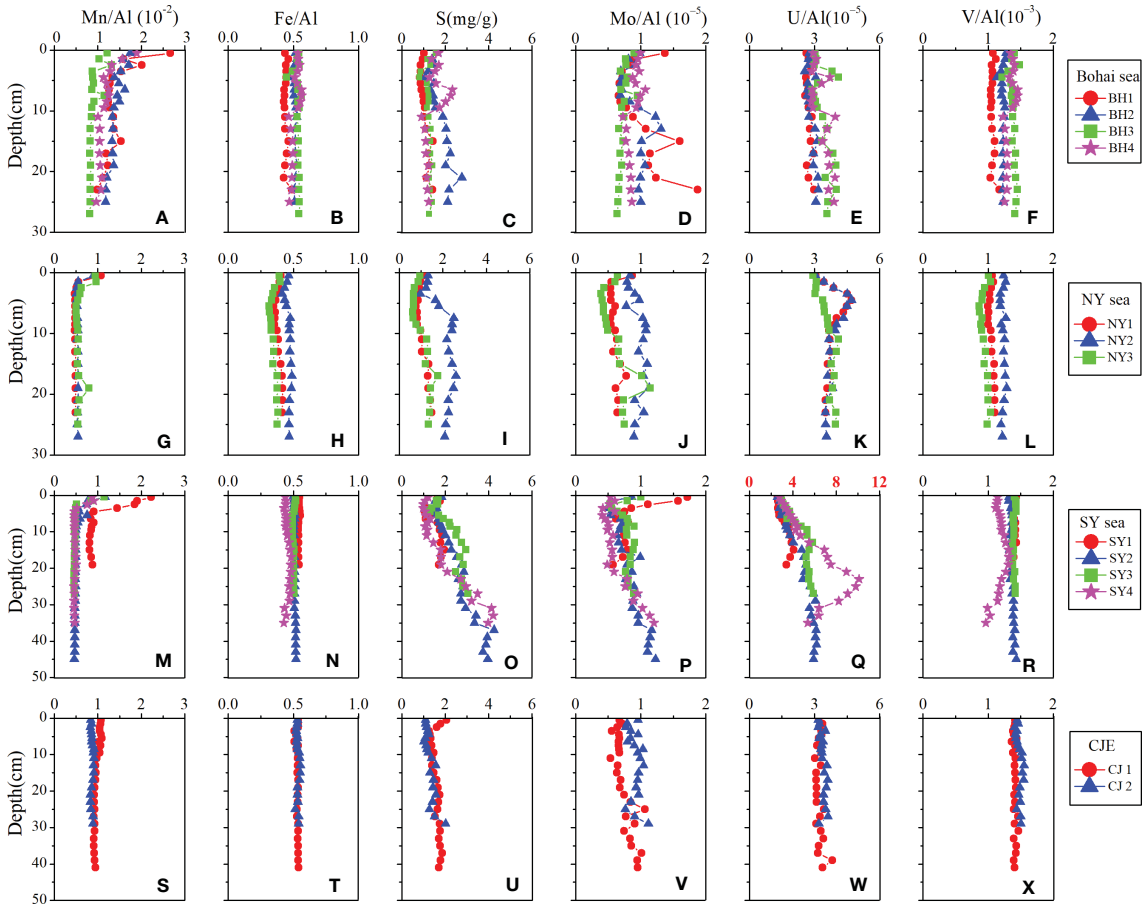

FIGURE 3
Solid phase profiles of trace metal in sediment cores.

In most cores, solid V parallel the vertical distribution of Fe (Figure 3). Various studies have well-described the scavenging of V (V) is associated with particulate Fe and Mn by either adsorbed or incorporated, and particulate Fe may have more control over V cycling than Mn in shelf sediments (Scholz et al., 2011; Whitmore et al., 2019; Li et al., 2020). Significant correlations between V/Al - Fe/Al (r^2 = 0.87, p< 0.01, Table S3) was observed, which confirmed the co-cycling of V with Fe. The close correlations were also found between V/Al, mean grain size (Mz) and TOC (n =256, p< 0.01, Table S3), which has been observed in various marine environments (Wang et al., 2019; Li et al., 2020; Wu et al., 2020). This suggests that the accumulation of V in sediments is also related to TOC and grain size, and Li et al. (2020) found that TOC may only play a role at low levels (< 1%), which is consistent with our low TOC content sediments (0.10 -1.29%).

4.4 Benthic fluxes and authigenic accumulation of RSMs

Based on the method described in section 3.3, the benthic fluxes of RSMs were calculated and compared with calculated $[RSM]_{AR}$ in sediments, and the results are shown in Figure 4 and Table S4.

4.4.1 U

As shown in Figure 4, U had benthic fluxes going into the sediments, the estimated fluxes were 0.83 - 6.36 nmol·m^{-2}·d^{-1}, with an average of 3.02 ± 1.74 nmol·m^{-2}·d^{-1}. The diffusive fluxes were comparable to that reported from the Changjiang estuary (1.10 - 2.19 nmol·m^{-2}·d^{-1}), continental shelf of central California (2.30 - 9.90 nmol·m^{-2}·d^{-1}) and central China (5.21 ± 2.74 nmol·m^{-2}·d^{-1}) (Zheng et al., 2002; Zou et al., 2010; Wang et al., 2019). U_{AR} in sediments were 8.68 - 331.7 nmol·m^{-2}·d^{-1}, with an average of 53.0 nmol·m^{-2} ·d^{-1}. NYS is the only region where benthic fluxes were in agreement with U_{AR}. In other regions, U_{AR} were 1-2 orders of magnitude higher than diffusive fluxes (Table S4).

The fraction of U_{AR} in sediment reflects not only the input from diffusion across the SWI (U_{diff}) and particulate non-lithogenic uranium (U_{PN}), but also the loss caused by U remobilization (U_{remob}) (Zheng et al., 2002). A mass budget for U is calculated as:

$$U_{AR} = U_{diff} + U_{PN} - U_{remob}$$

U_{PN} is preserved at O_2< 25 μM (Zheng et al., 2002), therefore U_{PN} was thought to be negligible for U_{AR}. The discrepancy between

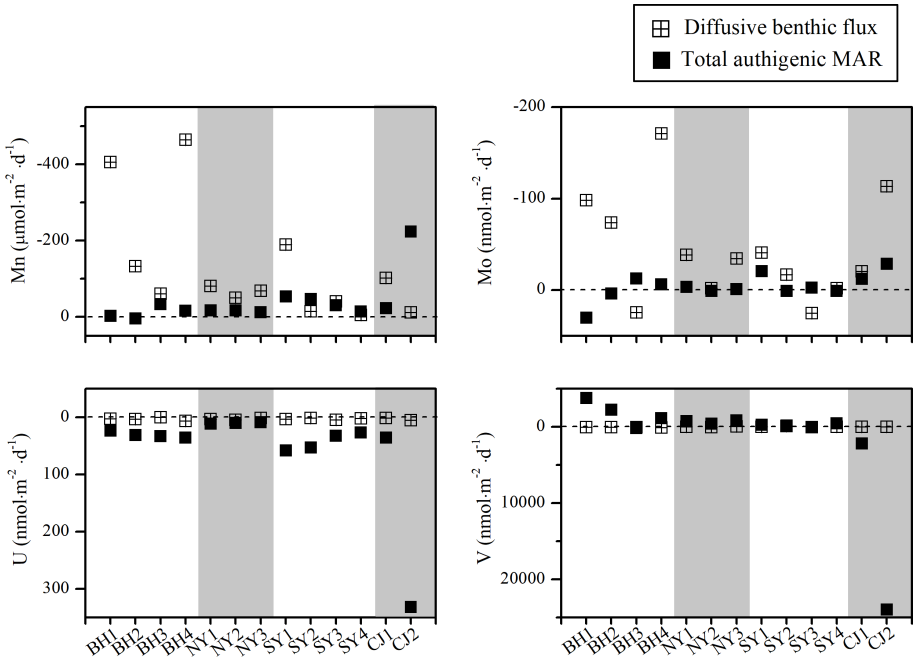

FIGURE 4
Diffusive benthic fluxes and authigenic MARs in sediment cores against stations. Horizontal dashed lines represent SWI. Grayish and whitish arrays represent BS to CJE.

U_{diff} and U_{AR} may be related to the bioturbation or bioirrigation, which can significantly influence the transport of solutes in sediments and enhance benthic flux (Morford et al., 2007; Morford et al., 2009b). Previously accumulated U can be released to bottom water or porewater by oxidation of reduced U in sediments (Zheng et al., 2002; Morford et al., 2009b), resulting in the loss of authigenic U, such as BH1 and BH2 cores with lower authigenic U (0.62 $\mu g \cdot g^{-1}$ and 0.89 $\mu g \cdot g^{-1}$, respectively). For some cores, partial remobilized U may diffuse downward into deeper and more reducing sediment, causing secondary precipitation and increasing accumulation in sediments (Morford et al., 2007; Costa et al., 2018).

Studies have found that U_{AR} is sensitive to the organic carbon flux (rain, oxidation or burial) (Zheng et al., 2002; Mcmanus et al., 2005; Kuzyk et al., 2017). Significant positive correlations were observed between the average U_{AR} with OC_{burial} and S_{AR} ($p< 0.01$) (Figures 5A, B), indicating the coastal sediment is not only an effective sink for organic carbon but also for U. Meanwhile, OC_{burial} was correlated well with S_{AR} (Figure 5C), indicating that the coupling of TS and TOC controls the accumulation of U in downcore sediments. Overall, these relationships highlight the potential utility for authigenic U as a rough proxy to reconstruct the sedimentary redox condition in marine systems.

4.4.2 Mo

At most sites, benthic Mo fluxes (-2.26 - -171.3 $nmol \cdot m^{-2} \cdot d^{-1}$) leave the sediments and enter the overlying water (Figure 4), with an average of -55.8 ± 53.2 $nmol \cdot m^{-2} \cdot d^{-1}$. The estimated average Mo benthic flux was 1-2 orders of magnitude lower than those reported in other coastal sediments overlying oxic bottom water, such as Buzzards Bay (-301 ± 225 $nmol \cdot m^{-2} \cdot d^{-1}$) and central Baltic Sea (-200 - -2000 $nmol \cdot m^{-2} \cdot d^{-1}$), with water depths less than 60 m (Morford et al., 2009a; van de Velde et al., 2020).

Previous studies have indicated the close relationship between Mo and Mn, not only in surface sediment enrichment, but also in benthic fluxes (Morford and Emerson, 1999; Sundby et al., 2004; Scholz et al., 2011). A significant correlation was found between the benthic fluxes of Mo and Mn (r = 0.86, $p< 0.01$, n = 10), which provides supplementary evidence to support coupled recycling relationship between Mo and Mn in oxic sediments. In addition, since Mn is scavenged by organic matter in seawater and settled on surface sediments (Johnson et al., 1996), organic carbon respiration exerts some primary control over the Mn flux at SWI (McManus et al., 2012; Hyun et al., 2017). Speculation thus exits that Mo fluxes may have similar behavior. Significant linear relationships between benthic fluxes of Mn and Mo and the respiration rates were found ($p< 0.01$, n = 10) (Figures 6A, B), indicating benthic Mn and Mo fluxes are associated with the organic carbon oxidation rate in coastal areas.

Few or no authigenic Mo_{AR} was found in this study (Figure 4). Authigenic Mo accumulation seems to depend on the presence of organic matter flux and sulfate reduction (Chaillou et al., 2002; Dale et al., 2012). As described by Morford et al. (2005) and Helz and Vorlicek (2019), the increase in organic carbon flux promotes the accumulation of Mo due to the coupling between organic carbon and sulfur burial. Authigenic Mo accumulation was found in core

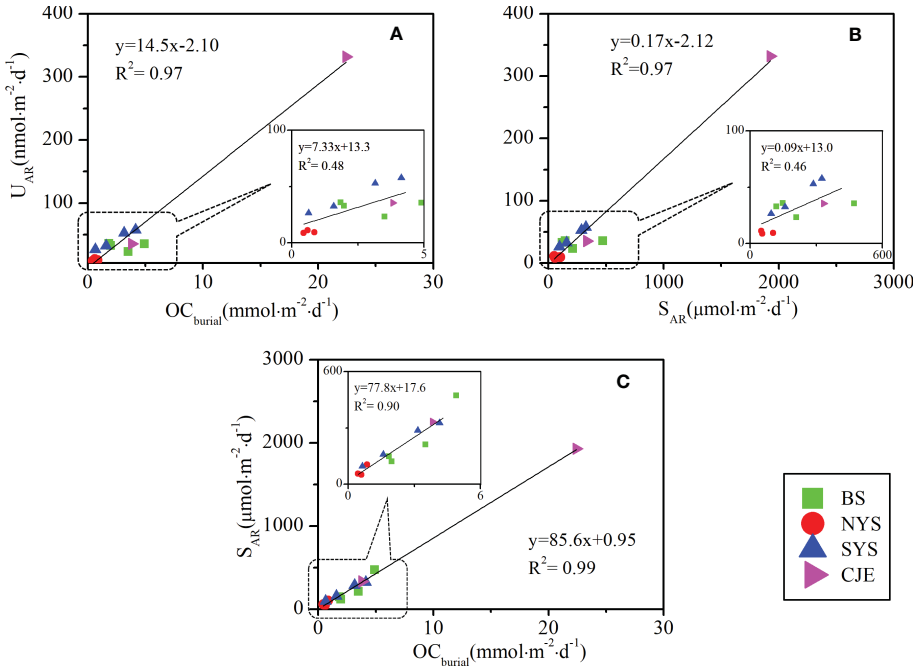

FIGURE 5
Relationship between U accumulation rates **(A)** with organic carbon burial rates; **(B)** with sulfur accumulation rates. **(C)** Sulfur accumulation rates with organic carbon burial rates. The imbedded figures are enlarged dataset without the data of station CJ2.

BH1, BH2, SY2 and SY4, accompanied by relatively high TOC burial and authigenic S (Table S4). Previous studies have reported that the amounts and reactivity of TOC were the major limiting factors for sulfate reduction in YS and CJE sites (Panutrakul et al., 2001; Kang et al., 2014), which may further limit the accumulation of authigenic Mo.

4.4.3 V

As shown in Figure 4, V diffused downward into the sediments in most cores, ranged from 2.28 to 74.2 nmol·m^{-2}·d^{-1}, with an average of 23.7 nmol·m^{-2}·d^{-1}. The downward fluxes of V were relatively low compared to those reported along the Peruvian continental sediments covered by suboxic - anoxic bottom water (169 - 256 nmol·m^{-2}·d^{-1}) (Scholz et al., 2011).

In most cores, solid V exhibited significant depletion (~ 10 - 30%) of the detrital content, which were comparable to that found in coastal-reducing sediment (Morford and Emerson, 1999). While for the cores near the estuary (BH3, CJ1 and CJ2), authigenic V accumulation were found in sediments (162 - 23977 nmol·m^{-2} ·d^{-1}), and the calculated V_{AR} were significantly higher than the benthic

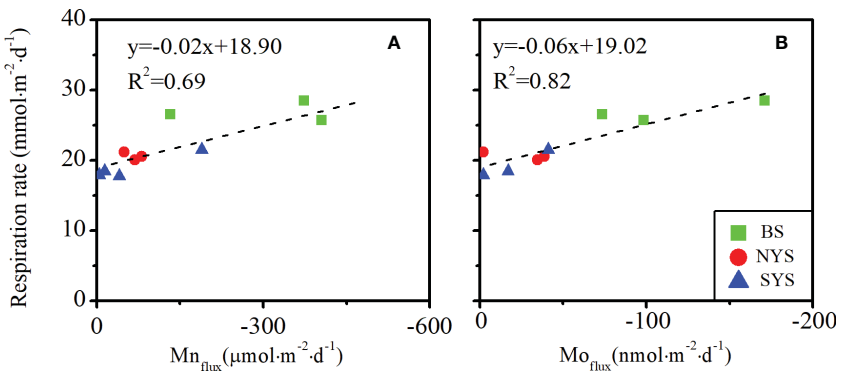

FIGURE 6
Relationship between benthic respiration rate and **(A)** benthic Mn flux; **(B)** benthic Mo flux. Core BH3, CJ1 and CJ2 are excluded from the diagrams, which are subject to strong hydrodynamic.

fluxes (Table S4), which should be caused by other processes suppling V to the sediments. As discussed in section 4.3, V adsorption onto Fe oxides may be the dominant mechanism for authigenic V accumulation in sediments, (Morford and Emerson, 1999; Whitmore et al., 2019; Li et al., 2020). Meanwhile, in reductive environment, authigenic V accumulation is primarily sensitive to the delivery and burial of organic matters (Wang and Wilhelmy, 2009; Li et al., 2020). However, most cores have no V authigenic accumulation (Figure 4), possibly due to the low TOC burial. Significant V_{AR} depletion and higher upward diffusive flux (-47.9 $nmol{\cdot}m^{-2}{\cdot}d^{-1}$ - -92.9 $nmol{\cdot}m^{-2}{\cdot}d^{-1}$) were found in NY3 and SY2 cores (Table S4), corresponding to high V concentrations above 10 cm in porewater (51.3 - 109 nM) (Figures 2J, O). Under moderate reducing conditions, V(V) is reduced and present as particle-reactive V(IV), preferentially retained in porewater and diffused upward, likely due to forming dissolved metal-organic complexes (Wehrli and Stumm, 1989; Olson et al., 2017), indicating the influence of DOC on mobilization of V from sediments.

TABLE 3 Bottom water oxygen concentration ($[O_2]_{bw}$), oxygen penetration depth ($[O_2]_{pen}$), organic carbon burial rate (OC_{burial}) and authigenic accumulation rates of RSMs in this study, compared with those data reported from other coastal sediments worldwide.

Region	$[O_2]_{bw}$ μM	$[O_2]_{pen}$ (cm)	OC_{burial} $mmol{\cdot}m^{-2}{\cdot}d^{-1}$	S_{AR} $mmol{\cdot}m^{-2}{\cdot}d^{-1}$	Mo_{AR} $nmol{\cdot}m^{-2}{\cdot}d^{-1}$	U_{AR} $nmol{\cdot}m^{-2}{\cdot}d^{-1}$	V_{AR} $nmol{\cdot}m^{-2}{\cdot}d^{-1}$	Reference
Bobai Sea	191 – 289		2.92 ± 1.20	0.22 ± 0.13		30.7 ± 5.29		*this study* Song et al., 2020
North Yellow Sea	296 - 339		0.64 ± 0.21	0.07 ± 0.03		9.76 ± 1.23		
South Yellow Sea	182 - 249		2.38 ± 1.57	0.22 ± 0.11		42.3 ± 15.2		
Changjiang Estuarine	111 - 174	0.2 - 0.3	13.1 ± 13.2	1.13 ± 1.13		183 ± 209	13084 ± 15404	
Calculated averages			3.80 ± 5.77	0.33 ± 0.50		52.9 ± 85.1	1245 ± 6964	
Northern Okinawa Trough					1.10 ± 5.48	11.2 ± 6.84		Wang et al., 2019
NE Pacific margin off Washington/ Oregon	40 - 55	0.3 - 0.5	0.3			0.58 - 0.62		Stump and Emerson, 2001; Morford et al., 2005
	81 - 124	1.5 - 5	0.01 - 0.04			0		
Pacific margin off California	3 - 27	0.2 - 0.6	1.2 - 2.6		6.0 - 22	9 - 11		Mcmanus et al., 2005; McManus et al., 2006
	65 - 132	1.3 - 2.9	0.08 - 0.9		0 - 0.6	0.4 - 6		
Mexican margin	0 - 0.2		1.7 - 8.4		30 - 134	11 - 51		
Peru margin	< LD				85 - 443	18 - 21	712 - 986	Scholz et al., 2011
	4.2 - 42				9.6 - 74	30 - 57	82 - 356	
Laurentian Trough, eastern Canadian continental margin	75 - 365	0.4 - 1.0	1.0 - 20		7.1 - 219	4.7 - 36		Sundby et al., 2004 Morford et al., 2007; Morford et al., 2009b
	247 - 271	1.4 - 4.0	0.7 - 5.5			4 - 13		
Southern margin of the Arctic					40.0 ± 24.8	6.91 ± 4.43		Kuzyk et al., 2011
North American Arctic margin				0.87 ± 0.28	202 ± 47.2	58.3 ± 23.6		Kuzyk et al., 2017
				0.07 ± 0.12	23.8 ± 36.3	18.6 ± 14.8		
East Siberian Arctic Shelves			3.50 ± 0.31	0.29 ± 0.12	58.5 ± 2.02	24.2 ± 3.26	3223 ± 76.0	Li et al., 2020

4.5 The budgetary implications of authigenic RSMs

Changes in oxygen penetration depths, OC_{burial} and S_{AR} determine the accumulation rate of authigenic RSMs, however, the extent for Chinese coastal sediments acts as a sink or source of authigenic RSMs is unclear. What is needed is a comparison with those reported in other margin sediments. As shown in Table 3, except for CJE, moderate authigenic U accumulation rates were found in sites from BS to SYS. Previous studies have found that oxygen penetration depth is relatively less important for RSMs accumulation compared to OC_{burial}, and U_{AR} can vary by over a factor of 40 in sediments with oxygen penetration depth ≤ 1 cm (Mcmanus et al., 2005; Morford et al., 2009b). However, authigenic Mo has little or no accumulation in study area, much lower than that in anoxic sediments such as Peru and North American Arctic margin. By contrast, significant authigenic accumulation of Mo and V require sufficient reducing environment and high burial of TOC and sulfur. The spatial variability of authigenic RSMs accumulation rates was revealed, providing a reference for accurately estimating the importance of the continental sediments of China in global budgets.

The amount of U_{AR} were estimated, averaged to be 2.05 ± 0.35, 0.60 ± 0.08 and 11.0 ± 3.97 $\times 10^8$ $g{\cdot}y^{-1}$ in BS, NYS and SYS (given the areas being 7.7×10^4 km^2, 7.1×10^4 km^2 and 3.0×10^5 km^2, respectively) (Qin et al., 2011; Shi, 2014). Among the rivers flowing to the coastal of eastern China, the Yellow River is the primary sources of sediment for the BS and NYS, while the SYS is mainly derived from the Yellow River and Changjiang River. Riverine input of dissolved U from the Yellow River and Changjiang River were 3.03×10^8 and 1.41×10^9 $g{\cdot}y^{-1}$, respectively (Qu et al., 1993; Dunk et al., 2002). Compared with the riverine input, the U_{AR} in BS and NYS shelf sediments accounts for ~ 67% and ~20% of the Yellow River input, while the accumulation of U_{AR} in SYS shelf sediment accounts for ~ 64% of the Yellow River and Changjiang River input combined.

In general, the results show that the costal sediments of China are important sinks for U, which play a key role in balancing the global U budget (Barnes and Cochran, 1990; Wang et al., 2019), which has never been studied before. Notably, after the impoundment of the Three Gorges reservoir and Xiaolangdi reservoir in Changjiang and Yellow River, sediment loads from rivers decreased dramatically (Wang et al., 2007), resulting in the OC burial greatly reduced (64 - 68%) in East China coastal sediments (Zhao et al., 2021). This will alter the ability of the China continental sediments to act as important sinks for OC, as well as RSMs.

5 Conclusion

This study has collected short sediment cores in Bohai Sea, Yellow Sea and Changjiang Estuary. The RSMs in porewater and solid-phase were studied, and the benthic diffusive flux and authigenic mass accumulation rate were calculated based on the observed data. First of all, the environment at sediment-water interface was found to be oxic or suboxic. Statistical analysis showed that the recycling process of Mo, U, and V was impacted by the recycling process of Fe/Mn oxides. The benthic fluxes of Mn and Mo were found to be going out of the sediments into overlying water column, while the fluxes of U and V were the opposite, going into sediments from overlying water column.

Comparison of benthic diffusive flux with MAR showed that Mo and V fluxes are independent of the authigenic accumulation rates, and U fluxes matched only in direction, indicating that there are other processes, besides the benthic diffusion, control the authigenic RSMs accumulation. Close relationship was found between the authigenic accumulation of RSMs and OC_{burial}, implying that the authigenic accumulations of RSMs is closely related with the organic carbon degradation process. Compared with other worldwide continental margins, moderate enrichment of U was found in northern China continental sediments. The estimated authigenic U fluxes in the study region accounted for approximately 20 - 68% of the Yellow River input in BS and NYS and ~ 64% of the Yellow River and Changjiang River in SYS, playing an important role in balancing the global U budget. Due to limited sampling stations, these 13 sediment cores may not be fully representative of each region's characteristic. However, they did show regional differences, and it cannot be ignored that the coastal sediments in China acts as an important sink for U globally.

Data availability statement

The original contributions presented in the study are publicly available. This data can be found here: https://dx.doi.org/10.13140/RG.2.2.26194.63681.

Author contributions

XW and LL designed the research. XW, YR, PC and AZ contributed sample collection, sample analysis, and data discussion. XW, LL and JL analyzed the data. XW, LL and XS wrote the manuscript. All authors contributed to the article and approved the submitted version.

Funding

This work is funded by the Marine S&T Fund of Laoshan Laboratory (LSKJ202204200) and the National Natural Science Foundation of China (42076046, 41776095, 41806082).

Acknowledgments

We would like to thank the captain and crew of the *R/V Dongfanghong 2*, *R/V Zhedingyuyun*, *R/V Chuangxin 2* and *R/V Xiangyanghong 18* for their support at sea. We also want to thank all the graduate students who have helped at sea or in the laboratory to make this work possible, especially Hongna Liu and Xiaotong Zhen.

Conflict of interest

The authors declare that the research was conducted in the absence of any commercial or financial relationships that could be construed as a potential conflict of interest.

Publisher's note

All claims expressed in this article are solely those of the authors and do not necessarily represent those of their affiliated organizations, or those of the publisher, the editors and the reviewers. Any product that may be evaluated in this article, or claim that may be made by its manufacturer, is not guaranteed or endorsed by the publisher.

Supplementary material

The Supplementary Material for this article can be found online at: https://www.frontiersin.org/articles/10.3389/fmars.2023.1154248/full#supplementary-material

References

Abshire, M. L., Owens, J. D., Cofrancesco, J., Inthorn, M., and Riedinger, N. (2020a). Geochemical signatures of redepositional environments: the Namibian continental margin. *Mar. Gelo.* 429, 106316. doi: 10.1016/j.margeo.2020.106316

Abshire, M. L., Romaniello, S. J., Kuzminov, A. M., Cofrancesco, J., Severmann, S., and Riedinger, N. (2020b). Uranium isotopes as a proxy for primary depositional redox conditions in organic-rich marine systems. *Earth Planet. Sci. Lett.* 529, 115878. doi: 10.1016/j.epsl.2019.115878

Alexander, C. R., Demaster, D. J., and Nittrouer, C. A. (1991). Sediment accumulation in a modern epicontinental-shelf setting: the yellow. *Sea. Mar. Gelo.* 98 (1), 51–72. doi: 10.1016/0025-3227(91)90035-3

Aller, R. C. (1980). Diagenetic processes near the sediment-water interface of long island Sound.II. fe and Mn. *Adv. Geophys* 22, 237–350. doi: 10.1016/S0065-2687(08)60067-9

Aller, R. C., and Rude, P. D. (1988). Complete oxidation of solid phase sulfides by manganese and bacteria in anoxic marine sediments. *Geochim. Cosmochim. Acta* 52 (3), 751–765. doi: 10.1016/0016-7037(88)90335-3

Anderson, R. F., Lehuray, A. P., Fleisher, M. Q., and Murray, J. W. (1989). Uranium deposition in saanich inlet sediments, vancouver island. *Geochim. Cosmochim. Acta* 53 (9), 2205–2213. doi: 10.1016/0016-7037(89)90344-X

Barnes, C. E., and Cochran, J. K. (1990). Uranium removal in oceanic sediments and the oceanic U balance. *Earth Planet. Sci. Lett.* 97 (1-2), 94–101. doi: 10.1016/0012-821X(90)90101-3

Berg, P., Risgaard-Petersen, N., and Rysgaard, S. (1998). Interpretation of measured concentration profiles in sediment pore water. *Limnol. Oceanogr.* 43 (7), 1500-1510. doi: 10.4319/lo.1998.43.7.1500

Bigot, M., Saliot, A., Cui, X., and Li, J. (1989). Organic geochemistry of surface sediments from the huanghe estuary and adjacent bohai Sea (China). *Chem. Geol.* 75 (4), 339–350. doi: 10.1016/0009-2541(89)90006-5

Biller, D. V., and Bruland, K. W. (2012). Analysis of Mn, fe, Co, Ni, Cu, zn, cd, and Pb in seawater using the nobias-chelate PA1 resin and magnetic sector inductively coupled plasma mass spectrometry (ICP-MS). *Mar. Chem.* 130-131, 12–20. doi: 10.1016/j.marchem.2011.12.001

Boudreau, B. P. (1997). *Diagenetic models and their implementation* (Berlin: Springer-Verlag).

Burdige, D. J. (1993). The biogeochemistry of manganese and iron reduction in marine sediments. *Earth - Sci. Rev.* 35 (3), 249–284. doi: 10.1016/0012-8252(93)90040-E

Canfield, D. E., and Thamdrup, B. (2009). Towards a consistent classification scheme for geochemical environments, or, why we wish the term 'suboxic' would go away. *Geobiology* 7 (4), 385–392. doi: 10.1111/j.1472-4669.2009.00214.x

Chaillou, G., Anschutz, P., Lavaux, G., Schäfer, J., and Blanc, G. (2002). The distribution of Mo, U, and cd in relation to major redox species in muddy sediments of the bay of Biscay. *Mar. Chem.* 80 (1), 41–59. doi: 10.1016/S0304-4203(02)00097-X

Chen, C. C., Gong, G. C., and Shiah, F. K. (2007). Hypoxia in the East China Sea: one of the largest coastal low-oxygen areas in the world. *Mar. Environ. Res.* 64 (4), 399–408. doi: 10.1016/j.marenvres.2007.01.007

Chi, L. B., Song, X. X., Yuan, Y. Q., Zhou, P., Cao, X. H., and Yu, Z. M. (2017). Distribution of dissolved oxygen in the yellow Sea and East China Sea in summer and winter. *Oceanol. Limnol. Sin.* 48 (6), 1337–1345. doi: 10.11693/hyhz20170500142

Cline, J. D. (1969). Spectrophotemetric determination of hydrogen sulfide in natural waters. *Limnol. Oceanogr.* 14 (3), 454–458. doi: 10.4319/lo.1969.14.3.0454

Costa, K. M., Anderson, R. F., Mcmanus, J. F., Winckler, G., Middleton, J. L., and Langmuir, C. H. (2018). Trace element (Mn, zn, Ni, V) and authigenic uranium (aU) geochemistry reveal sedimentary redox history on the Juan de fuca ridge, north pacific ocean. *Geochim. Cosmochim. Acta* 236 (1), 79–98. doi: 10.1016/j.gca.2018.02.016

Dale, A. W., Meyers, S. R., Aguilera, D. R., Arndt, S., and Wallmann, K. (2012). Controls on organic carbon and molybdenum accumulation in Cretaceous marine sediments from the cenomanian-turonian interval including oceanic anoxic event 2. *Chem. Geol.* 324-325, 28–45. doi: 10.1016/j.chemgeo.2011.10.004

Dong, T. L., Yang, G. F., and Xu, S. M. (1995). Modern sedimentary characteristics in the south of the bohai Sea. *Mar. Geol. Quaternary Geol.* 15 (4), 131–134.

Dunk, R. M., Mills, R. A., and Jenkins, W. J. (2002). A reevaluation of the oceanic uranium budget for the Holocene. *Chem. Geol.* 190 (1-4), 45–67. doi: 10.1016/S0009-2541(02)00110-9

Emerson, S., and Hedges, J. (2003). Sediment diagenesis and benthic flux. *Treatise Geochem.* 6, 293–319. doi: 10.1016/B0-08-043751-6/06112-0

Emerson, S. R., and Huested, S. S. (1991). Ocean anoxia and the concentrations of molybdenum and vanadium in seawater. *Mar. Chem.* 34 (3-4), 177–196. doi: 10.1016/0304-4203(91)90002-E

Froelich, P. N., Klinkhammer, G. P., Bender, M. L., Luedtke, N. A., Heath, G. R., Cullen, D., et al. (1979). Early oxidation of organic matter in pelagic sediments of the eastern equatorial Atlantic: suboxic diagenesis. *Geochim. Cosmochim. Acta* 43 (7), 1075–1090. doi: 10.1016/0016-7037(79)90095-4

Gao, S., Luo, T. C., Zhang, B. R., Zhang, H. F., Han, Y. W., Zhao, Z. D., et al. (1998). Chemical composition of the continental crust as revealed by studies in East China. *Geochim. Cosmochim. Acta* 62 (11), 1959–1975. doi: 10.1016/S0016-7037(98)00121-5

Goldberg, T., Poulton, S. W., Archer, C., Vance, D., and Thamdrup, B. (2009). Controls on Mo isotope fractionations in modern anoxic marine sediments - a key to paleoredox research. *Geochim. Cosmochim. Acta*, A445. doi: 10.1016/j.gca.2009.05.025

Grasshoff, K., Kremling, K., and Ehrhardt, M. (1999). *Methods of seawater analysis* (Wiley-VCH, Weinheim). doi: 10.1002/9783527613984.ch4

Gustafsson, J. P. (2003). Modelling molybdate and tungstate adsorption to ferrihydrite. *Chem. Geol.* 200 (1-2), 105–115. doi: 10.1016/S0009-2541(03)00161-X

Helz, G. R., Miller, C. V., Charnock, J. M., Mosselmans, J. F. W., Pattrick, R. A. D., Garner, C. D., et al. (1996). Mechanism of molybdenum removal from the sea and its concentration in black shales: EXAFS evidence. *Geochim. Cosmochim. Acta* 60, 3631–3642. doi: 10.1016/0016-7037(96)00195-0

Helz, G. R., and Vorlicek, T. P. (2019). Precipitation of molybdenum from euxinic waters and the role of organic matter. *Chem. Geol.* 509, 178–193. doi: 10.1016/j.chemgeo.2019.02.001

Herbert, L. C., Riedinger, N., Michaud, A. B., Laufer, K., Røy, H., and Jørgensen, B. B. (2020). Glacial controls on redox-sensitive trace element cycling in Arctic fjord sediments (Spitsbergen, Svalbard). *Geochim. Cosmochim. Acta* 271, 33–60. doi: 10.1016/j.gca.2019.12.005

Hu, D. X. (1994). Some striking fetures of circulation in huanghai Sea and East China Sea. *Oceanol. China Seas* 1, 27–38. doi: 10.1007/978-94-011-0862-1_4

Hu, B. Q., Li, J., Zhao, J. T., Yang, J., Bai, F. L., and Dou, Y. G. (2013). Heavy metal in surface sediments of the liaodong bay, bohai Sea: distribution, contamination, and sources. *Environ. Monit. Assess.* 185, 5071–5083. doi: 10.1007/s10661-012-2926-0

Hyun, J. H., Kim, S. H., Mok, J. S., Cho, H., Lee, T., Vandieken, V., et al. (2017). Manganese and iron reduction dominate organic carbon oxidation in deep continental margin sediments of the ulleung basin, East Sea. *Biogeosciences* 14, 941–958. doi: 10.5194/bg-14-941-2017

Johnson, K. S., Coale, K. H., Berelson, W. M., and Gordon, R. M. (1996). On the formation of the manganese maximum in the oxygen minimum. *Geochim. Cosmochim. Acta* 60 (8), 1291–1299. doi: 10.1016/0016-7037(96)00005-1

Kang, X. M., Liu, S. M., and Zhang, G. L. (2014). Reduced inorganic sulfur in the sediments of the yellow Sea and East China Sea. *Acta Oceanol. Sin.* 33, 100–108. doi: 10.1007/s13131-014-0499-1

Kim, G., Yang, H. S., and Kodama, Y. (1998). Distributions of transition elements in the surface sediments of the yellow Sea. *Cont. Shelf Res.* 18 (12), 1531–1542. doi: 10.1016/S0278-4343(98)00038-7

Kuzyk, Z. Z., Macdonald, R. W., Stern, G. A., and Gobeil, C. (2011). Inferences about the modern organic carbon cycle from diagenesis of redox-sensitive elements in hudson bay. *J. Mar. Syst.* 88 (3), 451–462. doi: 10.1016/j.jmarsys.2010.11.001

Kuzyk, Z. Z., Gobeil, C., Goñi, M. A., and Macdonald, R. W. (2017). Early diagenesis and trace element accumulation in north American Arctic margin sediments. *Geochim. Cosmochim. Acta* 203, 175–200. doi: 10.1016/j.gca.2016.12.015

Li, Y. H., and Gregory, S. (1974). Diffusion of ions in sea water in deep-sea sediments. geochim. *Cosmochim. Acta* 38 (5), 703–714. doi: 10.1016/0016-7037(74)90145-8

Li, L., Liu, Y. G., Wang, X. J., Hu, L. M., Yang, G., Wang, H. M., et al. (2020). Early diagenesis and accumulation of redox-sensitive elements in East Siberian Arctic shelves. *Mar. Gelo.* 429, 10639. doi: 10.1016/j.margeo.2020.106309

Li, L., Liu, J. H., Wang, X. J., and Shi, X. F. (2015). Dissolved trace metal distributions and Cu speciation in the southern bohai Sea. *China. Mar. Chem.* 172, 34–45. doi: 10.1016/j.marchem.2015.03.002

Li, F. Y., and Shi, Y. L. (1995). Accumulation rates of sediment and sedimentary environment in the south bohai Sea. *J. Oceanog. Huang Hai Bohai Sea* 13 (2), 33–37.

Li, L., Wang, X. J., Ren, Y. J., Su, H. Q., Hu, L. M., Li, Z. Q., et al. (2021). Enrichment of trace metals (V, Cu, Co, Ni, and Mo) in Arctic sediments-from Siberian Arctic shelves to the basin. *J.Geophys. Res-Oceans* 126 (4), 1–14. doi: 10.1029/2020JC016960

Lovley, D. R., Phillips, E. J. P., Gorby, Y. A., and Landa, E. R. (1991). Microbial reduction of uranium. *Nature* 350, 413–416. doi: 10.1038/350413a0

Mcmanus, J., Berelson, W. M., Klinkhammer, G. P., Hammond, D. E., and Holm, C. (2005). Authigenic uranium: relationship to oxygen penetration depth and organic carbon rain. *Geochim. Cosmochim. Acta* 69 (1), 95–108. doi: 10.1016/j.gca.2004.06.023

McManus, J., Berelson, W. M., Severmann, S., Johnson, K. S., Hammond, D. E., Roy, M., et al. (2012). Benthic manganese fluxes along the Oregon-California continental shelf and slope. *Cont. Shelf Res.* 43, 71–85. doi: 10.1016/j.csr.2012.04.016

McManus, J., Berelson, W. M., Severmann, S., Poulson, R. L., Hammond, D. E., Klinkhammer, G. P., et al. (2006). Molybdenum and uranium geochemistry in continental margin sediments: paleoproxy potential. *Geochim. Cosmochim. Acta* 70 (18), 4643–4662. doi: 10.1016/j.gca.2006.06.1564

Morford, J., and Emerson, S. (1999). The geochemistry of redox sensitive trace metals in sediments. *Geochim. Cosmochim. Acta* 63 (11-12), 1735–1750. doi: 10.1016/S0016-7037(99)00126-X

Morford, J. L., Emerson, S. R., Breckel, E. J., and Kim, S. H. (2005). Diagenesis of oxyanions (V, U, re, and Mo) in pore waters and sediments from a continental margin. *Geochim. Cosmochim. Acta* 69 (21), 5021–5032. doi: 10.1016/j.gca.2005.05.015

Morford, J. L., Martin, W. R., and Carney, C. M. (2009b). Uranium diagenesis in sediments underlying bottom waters with high oxygen content. *Geochim. Cosmochim. Acta* 73 (10), 2920–2937. doi: 10.1016/j.gca.2009.02.014

Morford, J. L., Martin, W. R., François, R., and Carney, C. M. (2009a). A model for uranium, rhenium, and molybdenum diagenesis in marine sediments based on results from coastal locations. *Geochim. Cosmochim. Acta* 73 (10), 2938–2960. doi: 10.1016/j.gca.2009.02.029

Morford, J. L., Martin, W. R., Kalnejais, L. H., François, R., Bothner, M., and Karle, I. M. (2007). Insights on geochemical cycling of U, re and Mo from seasonal sampling in Boston harbor, Massachusetts, USA. *Geochim. Cosmochim. Acta* 71 (4), 895–917. doi: 10.1016/j.gca.2006.10.016

Mouret, A., Anschutz, P., Lecroart, P., Chaillou, G., Hyacinthe, C., Deborde, J., et al. (2009). Benthic geochemistry of manganese in the bay of Biscay, and sediment mass accumulation rate. *Geo-Mar. Lett.* 29 (3), 133–149. doi: 10.1007/s00367-008-0130-6

Nolting, R. F., Dalen, M., and Helder, W. (1996). Distribution of trace and major elements in sediment and pore waters of the Lena delta and laptev Sea. *Mar. Chem.* 53 (3-4), 285–299. doi: 10.1016/0304-4203(95)00095-X

Olson, L., Quinn, K. A., Siebecker, M. G., Luther, G. W., Hastings, D., and Morford, J. L. (2017). Trace metal diagenesis in sulfidic sediments: insights from Chesapeake bay. *Chem. Geol.* 452, 47–59. doi: 10.1016/j.chemgeo.2017.01.018

Panutrakul, S., Baeyens, M. W., and Baeyens, W. (2001). Seasonal variations in sediment sulfur cycling in the ballastplaat mudflat, Belgium. *Estuaries* 24 (2), 257–265. doi: 10.2307/1352949

Postma, D., and Appelo, C. A. J. (2000). Reduction of Mn-oxides by ferrous iron in a flow system: column experiment and reactive transport modeling. *Geochim. Cosmochim. Acta* 64 (7), 1237–1247. doi: 10.1016/S0016-7037(99)00356-7

Qi, J., Li, F. Y., Song, J. M., Gao, S., Wang, G. Z., and Cheng, P. (2004). Sedimentation rate and flux of the north yellow Sea. *Mar. Geol. Quaternary Geol.* 24 (2), 9–14.

Qiao, S. Q., Shi, X. F., Zhu, A. M., Liu, Y. G., Bi, N. S., Fang, X. S., et al. (2010). Distribution and transport of suspended sediments off the yellow river (Huanghe) mouth and the nearby bohai Sea. *Estuar. Coast. Shelf* S.86 (3), 337–344. doi: 10.1016/j.ecss.2009.07.019

Qin, Y. W., Zheng, B. H., Lei, K., Lin, T., Hu, L. M., and Guo, Z. G. (2011). Distribution and mass inventory of polycyclic aromatic hydrocarbons in the sediments of the south bohai Sea, China. *Mar. pollut. Bull.* 62 (2), 371–376. doi: 10.1016/j.marpolbul.2010.09.028

Qu, C. H., Chen, C. Z., Yang, J. R., Wang, L. Z., and Lu, Y. L. (1993). Geochemistry of dissolved and particulate elements in the major rivers of China (The huanghe, changjiang, and zhunjiang rivers). *Estuaries* 16 (3), 475–487. doi: 10.2307/1352595

Roussiez, V., Ludwig, W., Probst, J. L., and Monaco, A. (2005). Background levels of heavy metals in surficial sediments of the gulf of lions (NW mediterranean): an approach based on 133Cs normalization and lead isotope measurements. *Environ. Pollut.* 138 (1), 167–177. doi: 10.1016/j.envpol.2005.02.004

Rudick, R. L., and Gao, S. (2014). Composition of the continental crust. *Treatise Geochem.* 4, 1–51. doi: 10.1016/B978-0-08-095975-7.00301-6

Scholz, F., Hensen, C., Noffke, A., Rohde, A., Liebetrau, V., and Wallmann, K. (2011). Early diagenesis of redox-sensitive trace metals in the Peru upwelling area - response to ENSO-related oxygen fluctuations in the water column. *Geochim. Cosmochim. Acta* 75 (22), 7257–7276. doi: 10.1016/j.gca.2011.08.007

Shaw, T. J., Gieskes, J. M., and Jahnke, R. A. (1990). Early diagenesis in differing depositional environments: the response of transition metals in pore water. *Geochim. Cosmochim. Acta* 54 (5), 1233–1246. doi: 10.1016/0016-7037(90)90149-F

Shi, X. F. (2014). *China Coastal seas-marine sediment* (Beijing: China ocean press).

Shimmield, G. B., and Price, N. B. (1986). The behaviour of molybdenum and manganese during early sediment diagenesis - offshore Baja California, Mexico. *Mar. Chem.* 19 (3), 261–280. doi: 10.1016/0304-4203(86)90027-7

Sohrin, Y., Matsui, M., and Nakayama, E. (1999). Contrasting behavior of tungsten and molybdenum in the Okinawa trough, the East China Sea and the yellow Sea. *Geochim. Cosmochim. Acta* 19-20, 63. doi: 10.1016/s0016-7037(99)00273-2

Song, G. D., Liu, S. M., Zhang, J., Zhu, Z. Y., Zhang, G. L., Marchant, H. K., et al. (2020). Response of benthic nitrogen cycling to estuarine hypoxia. *Limnology Oceanog.* 66, 652–666. doi: 10.1002/lno.11630

Stump, C., and Emerson, S. (2001). *Cruise report of T.G* (Seattle, WA: Thompson Cruise 131. University of Washington).

Su, J., and Yuan, Y. (2005). *Hydrology in China coastal Sea* (Beijing: Ocean Press).

Sundby, B., Martinez, P., and Gobeil, C. (2004). Comparative geochemistry of cadmium, rhenium, uranium, and molybdenum in continental margin sediments. *Geochim. Cosmochim. Acta* 68 (11), 2485–2493. doi: 10.1016/j.gca.2003.08.011

Tribovillard, N., Riboulleau, A., Lyons, T., and Baudin, F. (2004). Enhanced trapping of molybdenum by sulfurized organic matter of marine origin in mesozoic limestones and shales. *Chem. Geol.* 213, 385–401. doi: 10.1016/j.chemgeo.2004.08.011

Tromp, T., van Cappellen, P., and Key, R. (1995). A global model for the early diagenesis of organic carbon and organic phosphorus in marine sediments. *Geochim. Cosmochim. Acta* 59, 1259–1284. doi: 10.1016/0016-7037(95)00042-x

van de Velde, S. J., Hidalgo-Martinez, S., Callebaut, I., Antler, G., James, R. K., Leermakers, M., et al. (2020). Burrowing fauna mediate alternative stable states in the redox cycling of salt marsh sediments. *Geochim. Cosmochim. Acta* 276, 31–49. doi: 10.1016/j.gca.2020.02.021

Volz, J. B., Liu, B., Koster, M., Henkel, S., Koschinsky, A., and Kasten, S. (2020). Post-depositional manganese mobilization during the last glacial period in sediments of the eastern clarion-clipperton zone, pacific ocean. *Earth Planet. Sci. Lett.* 532, 116012. doi: 10.1016/j.epsl.2019.116012

Vorlicek, T. P., Kahn, M. D., Kasuya, Y., and Helz, G. R. (2004). Capture of molybdenum in pyrite-forming sediments: role of ligand-induced reduction by polysulfides. *Geochim. Cosmochim. Acta* 68, 547–556. doi: 10.1016/S0016-7037(03)00444-7

Wang, B. D. (1997). Formation mechanism of maximum value in vertical diatribution of dissolved oxygen in the yellow Sea. *J. Oceanog. Huanghai Bohai Seas* 15 (3), 10–15.

Wang, B. D. (2009). Hydromorphological mechanisms leading to hypoxia off the changjiang estuary. *Mar. Environ. Res.* 67 (1), 53–58. doi: 10.1016/j.marenvres.2008.11.001

Wang, X. J., Li, L., Liu, J. H., Wu, Y. H., Gao, J. J., Cao, P., et al. (2019). Early diagenesis of redox-sensitive trace metals in the northern Okinawa trough. *Acta Oceanol. Sin.* 38 (12), 14–25. doi: 10.1007/s13131-019-1512-5

Wang, D. L., and Wilhelmy, S. A. S. (2009). Vanadium speciation and cycling in coastal waters. *Mar. Chem.* 117 (1-4), 52–58. doi: 10.1016/j.marchem.2009.06.001

Wang, H. J., Yang, Z. S., Saito, Y., Liu, J. P., Sun, X. X., and Wang, Y. (2007). Stepwise decreases of the huanghe (Yellow river) sediment load, (1950-2005): impacts of climate change and human activities. *Global Planet. Change* 57 (3-4), 331–354. doi: 10.1016/j.gloplacha.2007.01.003

Wang, L. S., Zhang, C. S., Wang, H., and Shi, X. Y. (2015). Horizontal distribution features of biogenic elements in bohai Sea and the yellow Sea in summer. *Mar. Environ. Sci.* 34 (3), 361–366. doi: 10.13634/j.cnki.mes20150307

Wanty, R. B., and Goldhaber, M. B. (1992). Thermodynamics and kinetics of reactions involving vanadium in natural systems: accumulation of vanadium in sedimentary rocks. *Geochim. Cosmochim. Acta* 56, 1471–1483. doi: 10.1016/0016-7037(92)90217-7

Wehrli, B., and Stumm, W. (1989). Vanadyl in natural waters: adsorption and hydrolysis promote oxygenation. *Geochim. Cosmochim. Acta* 53 (1), 69–77. doi: 10.1016/0016-7037(89)90273-1

Wei, Q. S., Wang, B. D., Yao, Q. Z., Xue, L., Sun, J. C., Xin, M., et al. (2019). Spatiotemporal variations in the summer hypoxia in the bohai Sea (China) and

controlling mechanisms. *Mar. Pollut. Bull.* 138, 125–134. doi: 10.1016/j.marpolbul.2018.11.041

Whitmore, L. M., Morton, P. L., Twining, B. S., and Shiller, A. M. (2019). Vanadium cycling in the Western Arctic ocean is influenced by shelf-basin connectivity. *Mar. Chem.* 216, 103701. doi: 10.1016/j.marchem.2019.103701

Wu, Y. J., Fan, D. D., Wang, D. L., and Yin, P. (2020). Increasing hypoxia in the changjiang estuary during the last three decades deciphered from sedimentary redox-sensitive elements. *Mar. Geol.* 419, 106044. doi: 10.1016/j.margeo.2019.106044

Xia, X. M., Yang, H., Li, Y., Li, B. G., and Pan, S. M. (2004). Modern sedimentation rates in the contiguous Sea area of changjiang estuary and hangzhou bay. *Acta Sedimentol. Sin.* 22 (1), 130–135.

Xu, S. M. (2007). Distribution and environment significance of redox sensitive trace elements of the changjiang estuary hypoxia zone and its contiguous Sea area. *Acta Sedimentol. Sin.* 25 (5), 759–766. doi: 10.2514/1.26230

Xu, L. L., Wu, D. X., Lin, X. P., and Ma, C. (2009). The study of the yellow Sea warm current and its seasonal variability. *J. Hydrodynam. Ser. B* 21 (2), 159–165. doi: 10.1016/S1001-6058(08)60133-X

Yamada, M., Wang, Z. L., and Kato, Y. (2006). Precipitation of authigenic uranium in suboxic continental margin sediments from the Okinawa Trough.Estuar. *Coast. Shelf S.* 66 (3-4), 570–579. doi: 10.1016/j.ecss.2005.11.002

Yang, S. Y., Jung, H. S., Lim, D., and Li, C. X. (2003). A review on the provenance discrimination of sediments in the yellow Sea. *Earth Sci. Rev.* 63 (1-2), 93–120. doi: 10.1016/S0012-8252(03)00033-3

Yang, S. L., Liu, G. X., Du, R. Z., and Zhang, B. (1993). Study on the modern sedimentation rate through 210Pb age dating, liaodong bay. *Acta Sedimentol. Sin.* 11 (1), 128–135.

Yuan, H. M., Song, J. M., Li, X. G., Li, N., and Duan, L. Q. (2012). Distribution and contamination of heavy metals in surface sediments of the south yellow Sea. *Mar. pollut. Bull.* 64 (10), 2151–2159. doi: 10.1016/j.marpolbul.2012.07.040

Zhang, R., Pan, S. M., Wang, Y. P., and Gao, J. H. (2009). Sedimentation rates and characteristics of radionuclide 210Pb at the subaqueous delta in changjiang estuary. *Acta Sedimentol. Sin.* 27 (4), 704–713.

Zhang, L. J., Wang, L., Cai, W. J., Liu, D. M., and Yu, Z. G. (2013). Impact of human activities on organic carbon transport in the yellow river. *Biogeosciences* 10, 2513–2524. doi: 10.5194/bg-10-2513-20

Zhang, S. W., Wang, Q. Y., Lü, Y., Cui, H., and Yuan, Y. L. (2008). Observation of the seasonal evolution of the yellow Sea cold water mass in 1996-1998. *Cont. Shelf Res.* 28 (3), 442–457. doi: 10.1016/j.csr.2007.10.002

Zhao, H. D., Kao, S. J., Zhai, W. D., Zang, K. P., Zheng, N., Xu, X. M., et al. (2017). Effects of stratification, organic matter remineralization and bathymetry on summertime oxygen distribution in the bohai Sea, China. *Cont. Shelf Res.* 134, 15–25. doi: 10.1016/j.csr.2016.12.004

Zhao, B., Yao, P., Bianchi, T. S., and Yu, Z. G. (2021). Controls on organic carbon burial in the Eastern China marginal seas: a regional synthesis. *Global Biogeochem. Cy.* 35 (4), 1-27. doi: 10.1029/2020GB006608

Zheng, Y., Anderson, R. F., Geen, A. V., and Fleisher, M. Q. (2002). Remobilization of authigenic uranium in marine sediments by bioturbation. *Geochim. Cosmochim. Acta* 66 (10), 1759–1772. doi: 10.1016/S0016-7037(01)00886-9

Zheng, Y., Anderson, R. F., Geen, A. V., and Kuwabara, J. (2000). Authigenic molybdenum formation in marine sediments: a link to pore water sulfide in the Santa Barbara basin. *Geochim. Cosmochim. Acta* 64 (24), 4165–4178. doi: 10.1016/S0016-7037(00)00495-6

Zhu, Z. Y., Zhang, J., Wu, Y., Zhang, Y. Y., Lin, J., and Liu, S. M. (2011). Hypoxia off the changjiang (Yangtze river) estuary: oxygen depletion and organic matter decomposition. *Mar. Chem.* 125 (1-4), 108–116. doi: 10.1016/j.marchem.2011.03.005

Zou, J. J., Shi, X. F., Li, N. S., Liu, J. H., and Zhu, A. M. (2010). Early diagenetic processes of redox sensitive elements in Yangtze estuary. *Earth Sci. - J. China Univ. Geoscie.* 35 (1), 31–42. doi: 10.3799/dqkx.2010.004

frontiers | Frontiers in Marine Science

TYPE Correction
PUBLISHED 10 August 2023
DOI 10.3389/fmars.2023.1260014

OPEN ACCESS

APPROVED BY
Frontiers Editorial Office,
Frontiers Media SA, Switzerland

*CORRESPONDENCE
Li Li
Li.Li@fio.org.cn

RECEIVED 17 July 2023
ACCEPTED 31 July 2023
PUBLISHED 10 August 2023

CITATION
Wang X, Li L, Ren Y, Cao P, Zhu A, Liu J and Shi X (2023) Corrigendum: Early diagenesis and benthic fluxes of redox-sensitive metals in eastern China shelf sediments.
Front. Mar. Sci. 10:1260014.
doi: 10.3389/fmars.2023.1260014

Corrigendum: Early diagenesis and benthic fluxes of redox-sensitive metals in eastern China shelf sediments

Xiaojing Wang[1,2], Li Li[1,2,3]*, Yijun Ren[1], Peng Cao[1,3], Aimei Zhu[1,2], Jihua Liu[1,2,3] and Xuefa Shi[1,2,3]

[1]Key Laboratory of Marine Geology and Metallogeny, First Institute of Oceanography, Ministry of Natural Resources, Qingdao, China, [2]Key Laboratory of Deep Sea Mineral Resources Development, Qingdao, Shandong, China, [3]Laboratory for Marine Geology, Laoshan Laboratory, Qingdao, China

KEYWORDS

early diagenesis, redox sensitive metals, benthic flux, authigenic accumulation, eastern China marginal seas

A Corrigendum on

Early diagenesis and benthic fluxes of redox-sensitive metals in eastern China shelf sediments

by Wang X, Li L, Ren Y, Cao P, Zhu A, Liu J and Shi X (2023). *Front. Mar. Sci.* 10:1154248. doi: 10.3389/fmars.2023.1154248

Incorrect Funding

In the published article, there was an error in the **Funding** statement. The sentence previously stated:

"This work is funded by National Natural Science Foundation of China (LSKJ202204200, 42076046, 41776095, 41806082)".

The correct Funding statement appears below.

"This work is funded by the Marine S&T Fund of Laoshan Laboratory (LSKJ202204200) and the National Natural Science Foundation of China (42076046, 41776095, 41806082)".

The authors apologize for this error and state that this does not change the scientific conclusions of the article in any way. The original article has been updated.

Publisher's note

frontiers | Frontiers in Marine Science

TYPE Original Research
PUBLISHED 25 September 2023
DOI 10.3389/fmars.2023.1190497

OPEN ACCESS

EDITED BY
Renato S. Carreira,
Pontifical Catholic University of Rio de Janeiro, Brazil

REVIEWED BY
Yunchao Wu,
Chinese Academy of Sciences (CAS), China
Claudia Hamacher,
Rio de Janeiro State University, Brazil
Kun-Seop Lee,
Pusan National University, Republic of Korea

*CORRESPONDENCE
Tiago Osório Ferreira
toferreira@usp.br

RECEIVED 21 March 2023
ACCEPTED 05 September 2023
PUBLISHED 25 September 2023

CITATION
Nóbrega GN, de Andrade PAM, Queiroz HM, Pereira APdA, Copertino MdS, Gorman D, Zhuang W, Song J, Andreote FD, Otero XL and Ferreira TO (2023) Bridging soil biogeochemistry and microbial communities (archaea and bacteria) in tropical seagrass meadows. *Front. Mar. Sci.* 10:1190497. doi: 10.3389/fmars.2023.1190497

Bridging soil biogeochemistry and microbial communities (archaea and bacteria) in tropical seagrass meadows

Gabriel Nuto Nóbrega[1], Pedro Avelino Maia de Andrade[2], Hermano Melo Queiroz[3], Arthur Prudêncio de Araújo Pereira[1], Margareth da Silva Copertino[4], Daniel Gorman[5], Wen Zhuang[6,7,8], Jinming Song[8,9], Fernando Dini Andreote[3], Xosé Luis Otero[9,10] and Tiago Osório Ferreira[3]*

[1]Department of Soil Science, Federal University of Ceará (UFC), Fortaleza, Ceará, Brazil, [2]Agricultural Production Program, Federal University of Agreste Pernambuco (UFAPE), Garanhuns, Pernambuco, Brazil, [3]Luiz de Queiroz College of Agriculture (ESALQ), University of São Paulo (USP), Department of Soil Science, Piracicaba, São Paulo, Brazil, [4]Institute of Oceanography, Federal University of Rio Grande (FURG), Rio Grande, Rio Grande do Sul, Brazil, [5]Commonwealth Scientific and Industrial Research Organization (CSIRO), Environment, Crawley, WA, Australia, [6]Institute of Eco-environmental Forensics, Shandong University, Qingdao, Shandong, China, [7]School of Environmental Science and Engineering, Shandong University, Qingdao, Shandong, China, [8]National Laboratory for Marine Science and Technology, Qingdao, Shandong, China, [9]Key Laboratory of Marine Ecology and Environmental Science, Institute of Oceanology, Chinese Academy of Sciences, Qingdao, Shandong, China, [10]Cretus, Departamento de Edafoloxía e Química Agrícola, Facultade de Bioloxía, Universidade de Santiago de Compostela (USC), Santiago de Compostela, Spain

Introduction: Seagrass meadows are among the most valuable ecosystems, providing numerous ecosystem services and functions. Despite its importance, there is a lack of knowledge about soil's biogeochemical process variability, which can control microbiological communities. Thus, this study aimed to evaluate whether seagrass meadows in different geo-environments exhibit varying Fe and sulfate reduction intensities, shaping distinct archaea and bacteria communities.

Methods: Soil samples were collected in seagrass meadows under contrasting climatic, geological, vegetational and hydrological settings along the Brazilian coast (e.g., Semiarid Coast - SC, Southeastern Granitic Coast – GC, and Southern Quaternary Coast - QC). The soils were characterized by particle size, pH, redox potential (Eh), total organic C and total N content, acid-volatile sulfides (AVS), and simultaneously extracted Fe. Furthermore, a solid-phase Fe fractionation was performed to characterize the decomposition pathways in these soils, and the shifts in the microbial community along this spatial variation were analyzed using denaturing gradient gel electrophoresis.

Results: The studied soils presented a sandy texture (values ranging from 74 ± 11.8 to 80.5 ± 6.4%) caused by energetic hydrodynamic conditions. The pH values were circumneutral, while redox conditions presented significant distinction among the studied sites, ranging from anoxic to oxic (values ranging from -63 to +334 mV). The degree of pyritization (DOP) ranged from<

10% to values higher than 80%, highly influenced by rhizospheric oxidation, and higher AVS content was recorded for sites with lower DOP (i.e., GC and QC).

Discussions: Thus, biogeochemical processes in the seagrass soils present a wide variation in response to the geo-environmental settings. Plants influence the soil's geochemical and microbiological communities, retaining fine particles, promoting rhizosphere oxidation, and inducing anoxic conditions controlling the Fe and S forms. Moreover, the same plant species can result in distinct soil conditions and microbial communities due to geoenvironmental settings.

KEYWORDS

coastal wetlands, *Ruppia maritima*, *Halodule wrightii*, Fe fractionation, Metabolic pathways

1 Introduction

Seagrass meadows consist of a worldwide distributed ecosystem, primarily composed of plant species that typically grow fully submerged in shallow coastal areas forming extensive meadows with high productivity and biodiversity (Olsen et al., 2016; Turschwell et al., 2021). The seagrasses are a phylogenetically related plant group (order Alismatales) with low taxonomic diversity (66 known species) assigned to six families (e.g., Cymodoceaceae, Hydrocharitaceae, Posidoniaceae, Zosteraceae; Ruppiaceae and Zannichelliaceae; Zidorn, 2016). These plant species interact with a wide range of megaherbivores (e.g., dugongs, manatees, green turtles) and smaller species (e.g., fishes, molluscs, crustaceans, sponges), supporting complex and diverse communities along the coastal zone of all continents except Antarctica (Nordlund et al., 2016; Unsworth et al., 2019).

This ecosystem can be found along the coast of 163 countries, covering 160,000 to 267,000 km^2 (McKenzie et al., 2020) and, thus, widespread over contrasting climatic, geological, vegetational and hydrological settings. However, estimations suggest that it may cover up to 600,000 km^2 (Fourqurean et al., 2012), corresponding to 0.2% of the ocean areas (Charette and Smith, 2010), which equals twice the area of mangroves forests (Siikamäki et al., 2013).

Seagrass meadows provide a wide range of ecological services, e.g., support marine food webs (Cui et al., 2021; Valentine and Heck, 2021); supply raw material and food (Connolly et al., 2005; Barbier et al., 2011); provide habitat and nursery (Orth et al., 2006; Liquete et al., 2016); water purification (Fernandes et al., 2009); coastal protection (Ondiviela et al., 2014); but also educational, recreational, spiritual and touristic services (de la Torre-Castro and Rönnbäck, 2004; Nordlund et al., 2016). As a result, seagrass meadows represent one of the most valuable ecosystems on the planet with values higher than U$ 28,000.00 ha^{-1} yr^{-1} (2011 values; Barbier et al., 2011; Costanza et al., 2014).

Recently, numerous studies have been conducted to comprehend and highlight the role of seagrass meadows as globally significant carbon (C) sinks, storing significant amounts of C on their soils (Kennedy et al., 2010; Fourqurean et al., 2012; Rozaimi et al., 2016; Serrano et al., 2016; Ricart et al., 2020). The C storage in seagrass meadows results from high productivity (Duarte and Chiscano, 1999; Duarte et al., 2010), refractory plant tissues (Serrano et al., 2015; Kaal et al., 2016; Piñeiro-Juncal et al., 2020a), and the anoxic soil conditions, which may drive microbial communities and the anaerobic organic matter decomposition pathways of iron (Fe) and sulfate reduction (Fourqurean et al., 2012; Ugarelli et al., 2019; Sun et al., 2020).

In this ecosystem, due to the permanent flooding from seawater, with abundant sulfate supply, the organic matter decomposition occurs through Fe oxyhydroxides and sulfate reduction pathways since water column prevent oxygen diffusion through soil profile (Brodersen et al., 2017; Nóbrega et al., 2023). Consequently, Fe^{2+} and sulfides (including HS- and polysulfides) are produced, which can eventually form iron sulfides such as FeS and FeS_2 (Otero and Macias, 2002; Queiroz et al., 2018). In anaerobic conditions, bioauthigenic pyrite (FeS_2) emerges as the most stable product of sulfate reduction, holding diverse ecological significance (Otero et al., 2023).

In fact, the dynamics of Fe and sulfate in seagrass soils play an essential role in controlling several other processes that affect the very maintenance of this ecosystem, such as the bioavailability of nutrients (Delgard et al., 2016), trace metals (Tripathi et al., 2014), the fate of phosphorus (Brodersen et al., 2017), the geochemical control over dissolved sulfide (a highly phytotoxic compound for seagrass species (Azzoni et al., 2005; Holmer et al., 2005) and the C dynamics (Yu et al., 2021). Therefore, Fe and sulfate reduction, which are controlled by microbial processes (Brodersen et al., 2018; Piñeiro-Juncal et al., 2020b), play essential roles in the maintenance of different ecosystem services provided by seagrass meadows (e.g., carbon sequestration and pollutants immobilization) (Nordlund et al., 2016; York et al., 2017; Ramírez-Flandes et al., 2019; Ricart et al., 2020; Sun et al., 2020).

However, despite the ecological importance of Fe and sulfate biogeochemistry for seagrass meadows and other coastal wetlands (i.e., controlling pollutant, nutrient and C dynamics), there is still a global knowledge gap on its relationship with the microbial communities and how these groups are shaped in response to the

geo-environmental conditions (e.g., distinct climatic, geological conditions and vegetation), which may control the intensity of biogeochemical processes.

Because seagrass meadows colonize highly diverse environments (Gorman et al., 2020; Ricart et al., 2020; Nóbrega et al., 2023), the intensities of these geochemical processes may vary widely and shape different microbial communities. The present study tests the hypothesis that seagrass meadows at contrasting geo-environments (e.g., climate, geology, and plant species and cover) will operate under different Fe and sulfate reduction intensities and, thus, will shape different microbiological communities. This is a novel study bridging the core soil processes of coastal wetlands (i.e., Fe and sulfate reduction) and microbial communities (bacteria and archaea) in diverse tropical geo-environments. Our results provide knowledge for a better understanding of the processes related to organic C accumulation, bioavailability of nutrients, and pollutant cycling in seagrass meadows.

2 Material and methods

2.1 Study site

Soil samples were collected in seagrass meadows located in three contrasting compartments along the 9,200 km of the Brazilian coast (Figure 1), presenting distinct climate (hot semiarid, humid tropical, and humid subtropical climates), geological setting (sedimentary and magmatic rocks), coastal conditions (estuary, beach, and coastal lagoon), and different plant species (*Halodule wrightii.* and *Ruppia maritima*) aiming to assess a maximum soil variability. Thus, seagrass soils from the semiarid coast (SC), granitic coast (GC) and quaternary coast (QC) compartments were samples and analyzed (Figure 1).

The semiarid coast (SC) extends from the states of Piauí to Pernambuco (Figure 1), marked by a semiarid climate (mainly classified tropical savanna and hot semi-arid climates; i.e., Aw and BSh climate types, respectively, according to Köppen-Geiger Climate Classification; Peel et al., 2007). The SC presents an annual rainfall (approximately 800 mm) lower than the evapotranspiration; and an average water temperature ranging from 27 to 29°C during the year (average minimum water temperature: 26°C and maximum: 30°C; seatemperature.org). In addition, this compartment is marked by close contact of the *"Barreiras"* group formation to the coastline, which results in sandy beaches and coral reefs close to the estuaries favouring seagrass beds formation (Copertino et al., 2016). The *Barreiras* group is a Miocene-Pliocene (Tertiary) transitional-coastal sedimentary deposit whose upper portion is composed dominantly of poorly sorted sand (Vilas Bôas et al., 2001; Arai, 2006). The seagrass meadow soils were collected in an estuary (at Ceará state, NE-Brazil) highly densely vegetated by *H. wrightii Asch.* (Figure 1); surrounded and close to (< 100 m) mangrove forests under low anthropogenic impacts due to the low occupation of the estuary (Silva and Souza, 2006), and found at water depths ranging from 1.7 to 2.9 m (water depth corrected to the mean water level).

The granitic coast (GC) covers the area from the *Guanabara* Bay (*Rio de Janeiro* state) to the *Praia dos Sonhos* (*Santa Catarina* state). In this compartment, narrow coastal plains are interrupted by the *Serra do Mar*'s granitic-gneiss rock with small bays and beaches protected by rocky shores and almost 2,000 islands close to the shore (Schaeffer-Novelli et al., 1990). The humid tropical climate of the region (tropical rainforest climate – Af, according to Köppen-Geiger Climate Classification; Peel et al., 2007) presents an annual rainfall average higher than 1,600 mm during the entire year, with lower monthly precipitation higher than 60 mm, resulting in a hydric surplus, and the average monthly water temperature ranges from 21 and 27°C during the year (average minimum water temperature: 20°C and maximum: 28°C; seatemperature.org; Minuzzi et al., 2007). At this compartment, the representative *H. wrightii.* meadow was collected in an

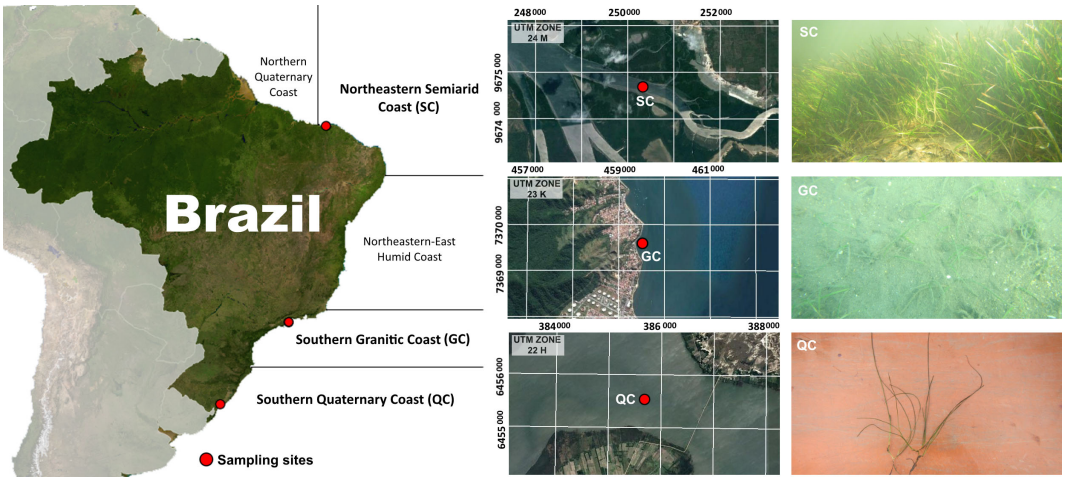

FIGURE 1
Location of sampling sites along the Brazilian coast. In detail, plant species and canopy characteristics for the three studied sites. The x and y axes in the satellite images indicate the coordinates in UTM.

urbanized beach area (at São Paulo state, Southeastern Brazil), presenting sparse vegetation with low plant density (Figure 1) at a water depth of 1.3 m (corrected to the mean water level).

The south quaternary coastal (QC) compartment extends 600 km from the Granitic coast to the border with Uruguay. This part of the coast presents a humid subtropical climate (Cfa according to Köppen-Geiger Climate Classification; Peel et al., 2007), with low annual temperature mean and a high-temperature oscillation (>10°C), annual precipitation of 1,300 mm, besides the hydric surplus (> 400 mm; Schaeffer-Novelli et al., 1990; Alvares et al., 2013). The average water temperature ranges from 13 to 24°C during the year (average minimum: 12°C and average maximum 26°C; seatemperature.org). The soil samples were collected at the *Lagoa dos Patos* (Patos Lagoon), at the *Rio Grande do Sul* State (S-Brazil), a 10,000 km^2 water body formed by sandy deposits during transgressive events during the Pleistocene (Toldo Jr. et al., 2000). The ephemeral and euryhaline *Ruppia maritima* seagrass meadow was collected at an average water depth of 1.5 m (corrected to the mean water level).

Seagrass meadows were observed and visually analyzed in each coast compartment to identify representative meadows (e.g., most frequent plant species, plant density and coverage), avoiding bare areas or seagrass meadows highly colonized with epiphytes or macroalgae.

2.2 Soil sampling procedure and physicochemical (Eh and pH) characterization

Three soil cores were randomly collected inside the representative seagrass meadows in each coast compartment using transparent polycarbonate tubes (60 mm diameter) attached to a submerged soil auger (Uwitec surface corer), which resulted in minimum sample compactation (Erich and Drohan, 2012). Soil samples were carefully extruded from the cores, partitioned into sections (0-3 cm, 3-6 cm, 6-10 cm, 10-13 cm, 13-16 cm, and 16-20 cm, with additional 5 cm increments) and, subsequently, pH and redox potential (Eh) values were promptly recorded to prevent oxidation. Following the characterization of physico-chemical conditions (Eh and pH), the samples were placed in plastic bags and transported to the laboratory under refrigeration (<4°C). In the lab, sub-samples (from the core's central region) were immediately frozen for subsequent analysis, while other sub-samples were dried (at 45°C until reaching a constant weight) and sieved through a 2 mm mesh.

The pH values were measured using a glass electrode calibrated using pH 4.0 and 7.0 buffer solution during core sectioning. The redox potential (Eh) was determined using a platinum electrode, with the final readings corrected by adding the potential of the calomel reference electrode (+ 244 mV) (Passos et al., 2016). All readings were taken after equilibrating the soil samples and the electrodes for several minutes (~2 min).

2.3 Soil characterization

The soils from each seagrass meadow were characterized by particle size composition, total organic C, and total nitrogen.

The hydrometer method was used for the particle size analysis (Gee and Bauder, 1986) by a combination of physical (overnight shaking) and chemical (1 mol L^{-1} NaOH + 0.015 mol L^{-1} $(NaPO_3)_6$) dispersion after the organic matter elimination using hydrogen peroxide (30% vol). Total nitrogen (TN) and total organic carbon (TOC) were determined in an elemental analyzer (LECO 628 series). The TOC quantification was the difference between the total C and inorganic C contents (obtained after organic matter combustion in a muffle furnace at 550 °C for two hours; Howard et al., 2014).

2.4 Fractionation of Fe and Sulfur

The partitioning of the solid phase of Fe was performed via a sequential extraction designed by the combination of methods proposed by Tessier et al. (1979); Huerta-Díaz and Morse (1990), and Fortin et al. (1993) using frozen samples, obtaining six operationally distinct fractions as follow: exchangeable Fe (Fe_{EX}), extracted with 30 mL of $MgCl_2$ 1 mol L^{-1} for 30 minutes; Fe associated with carbonates (Fe_{CA}), extracted with 30 mL of 1 mol L^{-1} sodium acetate buffer solution (pH = 5.0) for 5 hours; ferrihydrite (Fe_{FR}), extracted with 0.04 mol L^{-1} hydroxilamine + acetic acid 25% (v/v) at 30 °C for 6 hours; lepidocrocite (Fe_{LP}), extracted with 0.04 mol L^{-1} hydroxilamine + acetic acid 25% (v/v) at 96 °C for 6 hours; crystalline Fe oxyhydroxides (Fe_{CR}), extracted with 0.25 mol L^{-1} sodium citrate + 0.11 mol L^{-1} + 3 g of sodium dithionite for 30 minutes; and Fe associated with pyrite fraction (Fe_{PY}), extracted with concentrated nitric acid for 2h, after the removal of silicate fraction (10 M HF during 16 hours, then added 5 grams of boric acid and agitated during 8 hours) and organic matter (concentrated H_2SO_4 during 2 hours). For further details, please see Otero et al. (2009) and Osterrieth et al. (2016).

All solutions used for extraction were pretreatment for removing dissolved oxygen (i.e., purged with N_2 for 2 hours) to prevent possible Fe and S oxidation during the extraction steps. The extractants were collected between each step after centrifugation at 6,000 RPM (4 °C) for 30 minutes. The samples were washed with 20 mL of ultrapure water between each step and followed by centrifugation. The concentrations of Fe in each extract were quantified by flame atomic absorption spectrophotometry (Thermo Fisher Scientific, Waltham, MA, USA). Curve calibration solutions were prepared by diluting a certified standard solution (iron standard, TraceCERT®) to determine Fe concentration and a certified reference material (NIST SRM 2709a) was employed for quality control, with triplicate measurements yielding Fe concentration recovery values exceeding 92%. The results of the fractionation are presented as µmol g^{-1} (micromole per gram) of dried soil, corrected by sample water content.

The degree of Fe pyritization (DOP), which determines the percentage of reactive Fe incorporated into the pyrite fraction, was calculated as follows: DOP (%) = $100*Fe_{PY}/(Fe_{REACTIVE} + Fe_{PY})$ (Huerta-Diaz and Morse, 1992). The reactive fraction ($Fe_{REACTIVE}$) was considered the sum of the fractions exchangeable to crystalline ($\Sigma Fe_{EX} \rightarrow Fe_{CR}$), whereas the pseudo-total content was determined by the sum of the six fractions ($\Sigma Fe_{EX} \rightarrow Fe_{PY}$).

The acid-volatile sulfides (AVS) fraction was extracted from frozen wet samples by acid distillation with HCl (20 mL, 3 mol L^{-1}) in a gas-tight reaction flask after 40 minutes under continuous N_2 flow (Allen et al., 1993; Otero et al., 2009). The evolved H_2S was trapped in a Zn acetate solution (3%). The concentration of sulfides was colourimetrically determined by the method proposed by Cline (1969), and the simultaneously extracted Fe (Fe-AVS) was quantified by flame atomic absorption spectrophotometry (Allen et al., 1993).

2.5 Microbial molecular procedures

Frozen soil samples (400 mg) from different coastal compartments and depths (e.g., upper: 0-3 cm; intermediate: 16-20 cm; and deeper: 55-60 cm for SC and QC coast, and 35-40 cm for GC, due to soil depth limitation) were subjected to a total DNA extraction using the Power Soil DNA Isolation kit (MoBio Laboratories, Carlsbad, CA, USA) following the manufactory instructions. First, DNA extraction and integrity were assessed onto a 1.2% agarose gel electrophoresis with 1x TAE buffer (400 mmol L^{-1} Tris, 20 mmol L^{-1} acetic acid, and 1 mmol L^{-1} EDTA). Subsequently, the gels were stained with GelRed^{TM} (0.5 µg mL^{-1}), visualized, and photo-documented under ultraviolet light (DNR–Bio Imaging Systems/MiniBis Pro).

The amplification of the V6 region of ribosomal gene 16S rDNA for the bacterial community was performed with primers F968-GC and R1378, generating fragments of 410 bp (Heuer et al., 1997). The archaeal amplicons from *rrs* genes were obtained with primers Arch21F and Arch958R in the first reaction and Arch340FGC and Arch519R in the second nested-PCR reaction (Ovreås et al., 1997). The PCR reactions of bacterial communities were conducted in Veriti Thermal Cycler (Applied Biosystems, Waltham, USA), in a final volume of 50 µL, containing 1X Taq Buffer containing 2.50 mmol L^{-1} $MgCl_2$, 0.25 mmol L^{-1} of each dNTP, 0.4 mmol L^{-1} of each primer, 1% formamide and 1U Taq DNA Polymerase (Fermentas, Burlington, Canada). For archaea communities, 1x Taq Buffer contained 3.0 mmol L^{-1} $MgCl_2$, 0.2 mmol L^{-1} of each dNTP, 5 pmol L^{-1} of each primer, and 1U Taq DNA polymerase (Fermentas, Burlington, Canada). The amplification reactions for bacterial DNA were performed in the following conditions: initial denaturation at 94°C and then 35 cycles of denaturation for 1 minute; annealing at 56°C for 1 min and elongation at 72°C for 2 min. At the end of 35 cycles, a final extension step was conducted at 72°C for 10 min. Amplification reactions for archaea communities were performed at 95°C for 5 minutes; and 30 cycles of 1 min at 95°C, 1 min at 55°C, 1 min at 72°C, and final extension for 10 min at 72°C.

The PCR products were loaded onto 6% (16S rRNA genes) and 8% (rrs genes) (w/v) polyacrylamide gels with denaturing gradients of 45 to 65% for bacterial and 30 to 55% for archaea community, using urea 7 mol L^{-1} and 40% deionized formamide as 100% denaturing solution. The gels were run for 16 h at 100 V at 60°C using the phorU2 systems (Ingeny International, Goes, Netherlands) and stained with SYBR Green I (Invitrogen, Breda, the Netherlands). The DGGE gels were photo-documented with Storm 845 (General Electric) and analyzed using the Image Quant TL unidimensional (Amersham Biosciences, Amersham, UK, v.2003), where band patterns were converted into richness (number of bands) and abundance matrices.

2.6 Statistical analysis

Differences between soil variables were analyzed by the non-parametric Kruskal-Wallis test, followed by the Bonferonni-Dunn method for multiple pairwise comparisons (XLSTAT, Addinsoft, New York, USA, 2014). Kruskal-Wallis text was used since it was not observed a normal distribution and equal variance. Since few assumptions are required for non-parametric analysis, this test is considered more robust for environmental data (Reimann et al., 2008). Pearson's correlation coefficient (R) established the relationships between different variables. Finally, a Discriminant Analysis (DA) was performed to develop a function that yields optimal discrimination of the study sites (SC, GC, and QC coasts). Through the DA, the relative contribution of the variables could be identified to the separation of the groups, i.e., the most relevant variables for separating the study sites (Reimann et al., 2008).

The bacterial and archaeal community structure changes among sites were obtained through beta-diversity estimations. The beta-diversity analysis compares the groups of microorganisms revealed by the DGGE band patterns among the samples, relying on the microorganisms' profile structure and relationship with the environmental soil parameters (Lozupone et al., 2007). For the beta-diversity calculation, similarity matrices were produced using the Bray-Curtis algorithm on square-root transformed data, allowing the observation of the distribution of the groups between the samples on a two-dimensional scale. PERMANOVA analyses, based on two factors (i.e., coastal compartment and depth of soil sample), were followed by a Monte Carlo method with fixed effects, sums of squares type III (partial) under a reduced model, and 999 permutations. The ANOSIM test followed a one-way analysis based on one factor allowing the comparison among treatments under 999 permutations based on a p-value<0.05. Finally, we performed a redundancy detrended analysis (RDA) regarding the environmental factors correlated to the bacterial distribution and sampling depth. The statistical tests regarding microbial communities were performed using the software PAST (Hammer et al., 2001), PRIMER 6+PERMANOVA (Clarke and Gorey, 2006), and Canoco (Canoco 4.5, Biometris, Wageningen, The Netherlands).

3 Results

3.1 Characteristics of the physicochemical environments

The particle size of soils from all studied sites presented a predominance of sand, with mean ± standard deviation from 74.0 ± 11.8% at the QC to 80.5 ± 6.4% at the SC (Figure 2; Table 1). In contrast, silt content varied from 6.2 ± 4.9% at SC to 12.2 ± 5.4% at the QC coast, and clay varied from 8.1 ± 4.1% at the GC to 14.1 ±

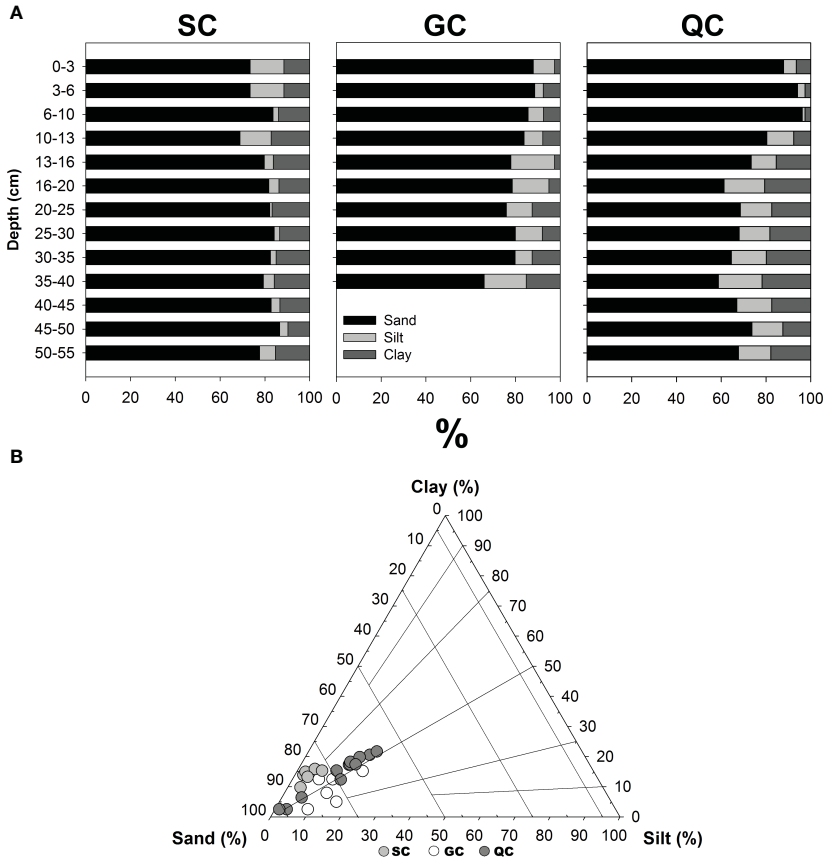

FIGURE 2
(A) Particle size distribution along seagrass meadows' soil profiles collected along the Brazilian coast. **(B)** Natural variability of particle size distribution in the seagrass meadows soils from the Brazilian coast under contrasting geo-environment conditions, according to Flemming (2000).

2.3% at the SC coast. All three particle sizes presented a statistically significant difference (Table 1). Additionally, the soils from the three studied sites presented an erratic sand distribution throughout the soil profiles (Figure 2).

Regarding the physicochemical conditions, the pH values recorded for the three sites were circumneutral, with lower pH values recorded at the SC (mean value ± standard deviation: 7.0 ± 0.2), whereas GC (7.4 ± 0.1) and QC (7.4 ± 0.4) did not differ statistically (Table 1). Additionally, whereas the pH values of the GC coast soil did not present a significant variation through soil profiles, the soils from the SC coast present higher values at the deeper soil layers (> 10 cm), and the soils from the QC coast presented oscillating values, with a decrease at the intermediate soil layers (10-30 cm) followed by an increase at deeper layers (>30 cm) (Figure 3A).

The Eh values presented a wide variation, ranging from −63 to +334 mV, evidencing significantly contrasting conditions between the studied sites (Figure 3B; Table 1). Significantly lower Eh values were recorded for the SC (mean ± standard deviation: +12 ± 134 mV), whereas the values recorded for QC (+166 ± 136 mV) and GC (+227 ± 60 mV) did not differ statistically. The redox contrasts were also evidenced in the surface soil horizons (down to 40 cm depth). While the Eh values recorded at GC and QC evidenced an oxic environment (average mean for the surface soil horizons ± standard deviation: +209 ± 113 mV), significantly lower values were recorded at SC (−22 ± 44 mV), thus, evidencing an anoxic environment. As occurred to the pH, the Eh values presented different trends in-depth among the different geoclimatic zones (Figure 3A). At the SC coast, the Eh values increased in-depth, whereas for both GC and QC coast, a decreasing trend in the recorded values (Figure 3B).

Significantly higher TOC contents were found at the SC coast (mean ± standard deviation: 2.49 ± 0.95%; Figure 3C) when compared to QC (0.53 ± 0.17%) and GC (0.41 ± 0.14%; Table 1). Similarly, significantly higher TN contents were recorded at the SC coast (0.14 ± 0.11%; Figure 3D; Table 1), while the values recorded for QC (0.07 ± 0.02%) and GC (0.05 ± 0.01%) coast did not differ significantly (Figure 3D; Table 1). When considering the variation through the soil profile, the TOC and TN values recorded for the GC and QC coast presented a slight variation. On the other hand, for the SC coast, higher values were recorded for the upper (0-10 cm) compared to deeper (>35 cm) soil layers. The C:N ratios were also significantly different among the three sites, with lower values at QC (6.8 ± 2.8), followed by GC (8.7 ± 1.8) and SC (17.8 ± 5.7; Figure 3C).

10.3389/fmars.2023.1190497

TABLE 1 Average and Kruskall-Wallis statistical results (*p*-value) for the variables in the three studied sites.

Variable	*p*-value	Site		
		Semiarid Coast (SC) (n=39)	Granitic Coast (GC) (n=30)	Quaternary Coast (QC) (n=39)
Sand (%)	0.002	79.7 ± 5.1[a]	80.5 ± 6.4[a]	74.0 ± 11.8[b]
Silt (%)	<0.01	6.2 ± 4.9[b]	11.4 ± 5.3[a]	12.2 ± 5.4[a]
Clay (%)	<0.01	14.1 ± 2.3[a]	8.1 ± 4.2[b]	13.8 ± 6.8[a]
pH	< 0.01	7.0 ± 0.2[b]	7.4 ± 0.1[a]	7.4 ± 0.4[a]
Eh (mV)	< 0.01	+12 ± 134[b]	+227 ± 60[a]	+166 ± 136[a]
TOC (%)	< 0.01	2.49 ± 0.95[a]	0.41 ± 0.14[b]	0.53 ± 0.17[b]
TN (%)	< 0.01	0.14 ± 0.11[a]	0.05 ± 0.01[b]	0.07 ± 0.02[b]
C:N ratio	< 0.01	17.8 ± 5.7[a]	8.7 ± 1.8[b]	6.8 ± 2.8[b]
Fe_T (μmol g^{-1})	0.37	78.1 ± 29.6[a]	73.3 ± 19.9[a]	63.7 ± 26.1[a]
Fe_{EX} (μmol g^{-1})	< 0.01	1.7 ± 0.3[a]	0.7 ± 0.0[b]	0.4 ± 0.1[c]
Fe_{CA} (μmol g^{-1})	0.43	0.8 ± 0.1[a]	1.0 ± 0.3[a]	0.6 ± 1.2[a]
Fe_{FR} (μmol g^{-1})	< 0.01	4.2 ± 1.5[b]	19.4 ± 15.4[a]	2.6 ± 2.5[b]
Fe_{LP} (μmol g^{-1})	< 0.01	14.7 ± 5.2[b]	24.3 ± 2.7[a]	10.0 ± 2.1[c]
Fe_{CR} (μmol g^{-1})	< 0.01	4.8 ± 1.4[b]	10.4 ± 1.9[a]	5.1 ± 1.6[b]
Fe_{OXIDES} (μmol g^{-1})	< 0.01	23.7 ± 7.9[b]	54.0 ± 16.0[a]	17.7 ± 4.4[b]
Fe_{PY} (μmol g^{-1})	< 0.01	51.9 ± 21.8[a]	17.7 ± 9.5[b]	45.0 ± 26.5[a]
DOP (%)	< 0.01	62.8 ± 4.0[a]	23.3 ± 10.6[b]	58.8 ± 27.4[a]
AVS (μmol g^{-1})	0.04	0.11 ± 0.09[b]	0.25 ± 0.22[a]	0.22 ± 0.36 [a]
Fe-AVS (μmol g^{-1})	< 0.01	11.1 ± 7.5[b]	30.2 ± 5.7[a]a	7.0 ± 3.2[b]

Mean values followed by the same letter did not present a statistically significant difference.

3.2 Fe fractionation

The values of pseudo-total Fe (Fe_T) contents were statistically similar among the three sites (means ± standard deviation for the SC:78.1 ± 29.6 μmol g^{-1}; GC: 73.3 ± 19.9 μmol g^{-1}; and QC: 63.7 ± 26.1 μmol g^{-1}; Figure 4; Table 1).

On the other hand, statistically significant differences were recorded for all Fe fractions (Figure 4; Table 1). At QC and SC, Fe_{PY} was the most important fraction (mean ± standard deviation: 51.9 ± 21.8 μmol g^{-1} for SC coast and 45.0 ± 26.5 μmol g^{-1} for QC coast) representing more than 50% of the Fe_T (DOP > 50%) whereas, for the GC, Fe_{PY} represent less than 50% of the Fe_T (DOP< 50%; Figure 4), with significantly lower contents (17.7 ± 9.5 μmol g^{-1}). Additionally, the DOP values presented a significant variation throughout the soil for GC and QC, with a lower DOP at the upper soil layers (0-10 cm; Figure 4). In contrast, the DOP at the SC did not oscillate with soil depth (Figure 4).

Both Fe_{EX} and Fe_{CA} were the fraction with a lower contribution to Fe_T, with mean ± standard deviation values of Fe_{EX} contents oscillating from 0.4 ± 0.1 to 1.7 ± 0.3 μmol g^{-1} for QC and SC coast, respectively; and mean values of Fe_{CA} varying from 0.6 ± 1.2 and 1.0 ± 0.3 μmol g^{-1} for the QC and GC coast, respectively (Figure 4).

Regarding the Fe oxides fraction (i.e., Fe_{FR} + Fe_{LP} + Fe_{CR}), significantly higher contents were quantified at GC (mean ± standard deviation: 54.0 ± 16.0 μmol g^{-1}; Table 1), followed by SC (23.7 ± 7.9 μmol g^{-1}), and QC coast (17.7 ± 9.5 μmol g^{-1}). For the three sites, the lepidocrocite (Fe_{LP}) was the most dominant oxyhydroxide fraction, with mean (± standard deviation) values ranging from 10.0 ± 2.1 to 24.3 ± 2.7 μmol g^{-1} at the QC and GC coasts (Figure 4; Table 1). Moreover, for the GC, the Fe_{CR} fraction was the less relevant oxyhydroxide fraction (10.4 ± 1.9 μmol g^{-1}), whereas the ferrihydrite (Fe_{FR}) was the less important Fe oxyhydroxide fraction for the other sites (4.2 ± 1.5 μmol g^{-1} for NE and 2.6 ± 2.5 μmol g^{-1} for QC coast; Figure 4).

3.3 Acid volatile sulfides (AVS) and simultaneously extracted Fe (AVS-Fe)

The AVS contents ranged from 0.05 to 2.03 μmol g^{-1} (Figure 3F) among the studied sites. Significantly, lower AVS contents were recorded at the SC (mean ± standard deviation: 0.11 ± 0.09 μmol g^{-1}), followed by QC (0.22 ± 0.36 μmol g^{-1}) and GC (0.25 ± 0.22 μmol g^{-1}; Figure 3F).

10.3389/fmars.2023.1190497

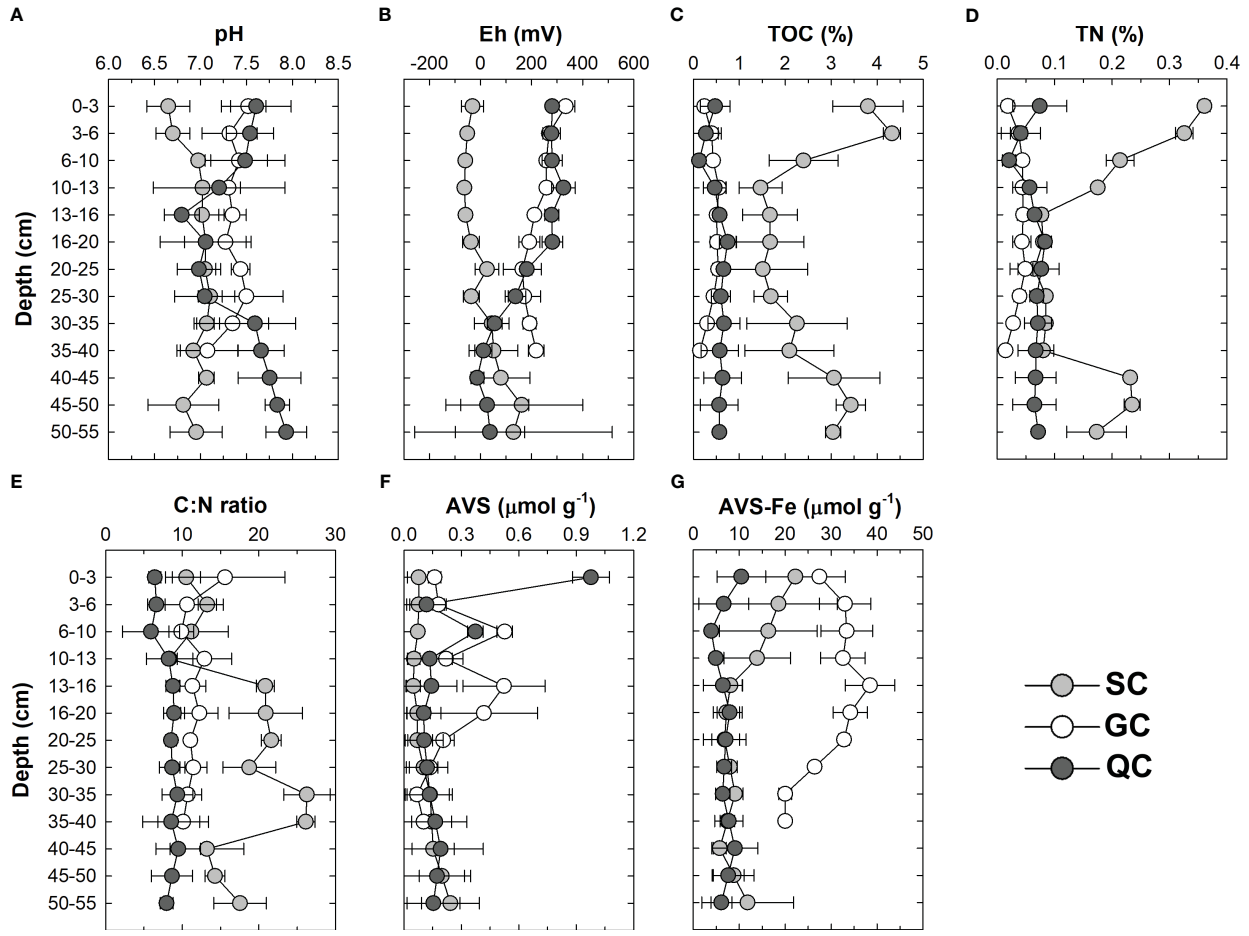

FIGURE 3
Characterization of the physico-chemical environment of the soil profiles from the three studied seagrass meadows: pH **(A)**, Eh **(B)**, total organic carbon contents, TOC **(C)**, total nitrogen contents, TN **(D)**, C:N ratio **(E)**, concentration of acid volatile sulfides, AVS **(F)** and Fe associated with AVS fraction, AVS-Fe **(G)**.

Regarding the AVS-Fe, statistically significant higher values were recorded for the GC (30.2 ± 5.7 µmol g^{-1}), whereas the values recorded for SC (5.6 ± 1.5 µmol g^{-1}) and QC (7.0 ± 3.3 µmol $g^{-1)}$ did not differ statistically (Figure 3G; Table 1).

3.4 Discriminant analysis of soils variables

The discriminant analysis indicated the most relevant variables for the differentiation of the studied sites (Figure 5). For the soils from SC, the vectors position indicates an association with higher TOC, TN, Fe_{EX} contents, higher C:N ratio values, and lower pH, Eh, and AVS contents. The GC soils were associated with higher Fe oxyhydroxides (Fe_{FR}, Fe_{LP}, $Fe_{CR,}$ and Fe_{OXIDES}) and Fe-AVS as observed by the vectors positioned in its direction and lower DOP, Fe_{PY}, and clay contents as evidenced by the vectors positioned in the opposite direction (Figure 5). On the other hand, the vector's position indicates that soils from QC differ from the SC and GC by lower sand and Fe_{EX} contents and higher silt and pH (Figure 5). Furthermore, when comparing SC and QC, it can be stated that SC presents higher values of Fe_{PY} and DOP.

3.5 Bacteria and archaea community characteristics (PCR-DGGE Results)

PCR-DGGE results evidence a clear differentiation in the bacteria and *archaea* community structure among the coastal compartments and soil depths, shown by the PERMANOVA data analysis (Table 2). In fact, the coastal compartments played a higher influence in the distribution of the *archaea* (Pseudo-F = 15.657; p = 0.001) and bacteria (Pseudo-F = 8.097; p = 0.001) communities; followed by the influence of soil depth (Pseudo-F = 4.395 and 3.519 for *archaea* and bacteria communities, respectively; p = 0.001). In addition, the results demonstrated the integration of factors (coastal compartment vs. depth) in the distribution of the bacteria (Pseudo-F = 3.745; p = 0.001) and archaea (Pseudo-F = 6.294; p = 0.001) communities (Table 2).

Moreover, the separation of the *archaea* community is also demonstrated by the ANOSIM-test (coastal compartment: Global R = 0.947; p = 0,001 and soil depth: Global R = 0.786; p = 0.001). Regarding the bacterial community, the ANOSIM-test demonstrated a clear separation among the sites (Coastal compartment: Global R = 0.967; p = 0,001). However, some

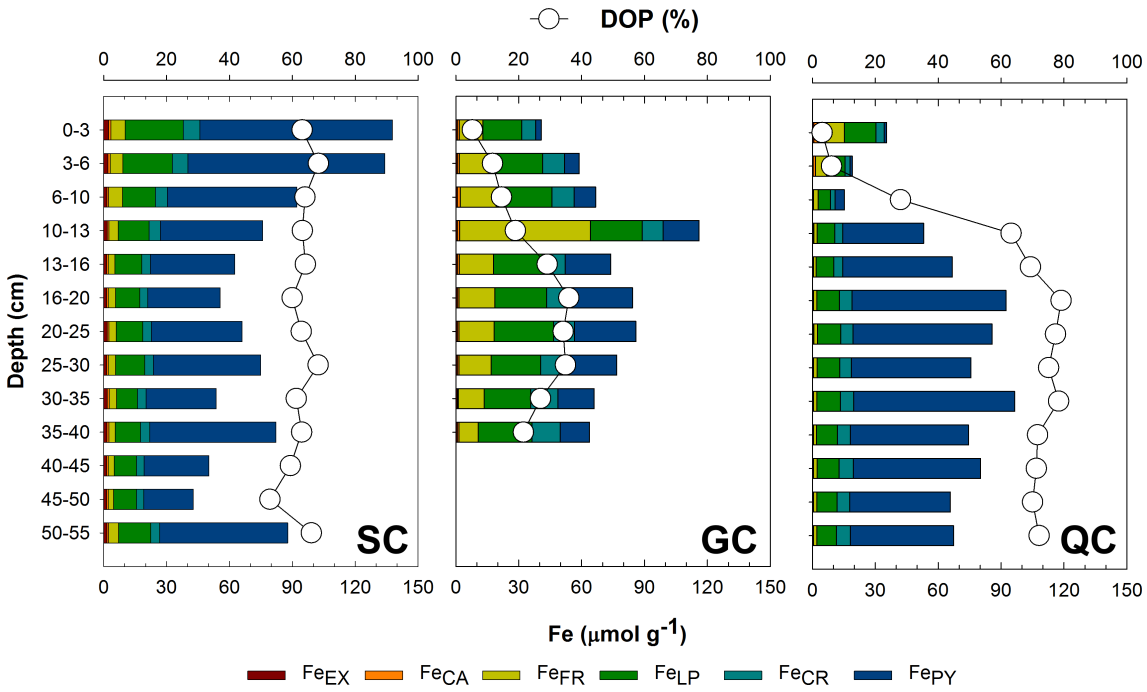

FIGURE 4
Solid-phase fractionation of Fe for the soils at the SC, GC, and QC coasts. The stacked bars indicate de fractions of soluble and exchangeable Fe (FeEX), Fe bounded to carbonates (FeCA), Fe associated with ferrihydrite (FeFR), Fe associated with lepidocrocite (FeLP), Fe associated with crystalline Fe oxyhydroxides (FeCR), and the Fe associated with pyrite (FePY). The interconnected white circles indicate the degree of Fe pyritization (DOP).

profile overlap was found regarding the soil depth (Global R = 0.58; p = 0.001), indicating some similarity among the bacterial group sampled in distinct soil depths.

According to the redundancy analysis, the soils from SC archaea communities were positively associated with TOC, Fe_T, TN, DOP, and clay, whereas the GC were associated with Fe_{OXIDES} and sand (Figure 6A). The upper horizons of the QC archaea communities were positively associated with higher Eh and pH, whereas the intermediate and deeper soil layers were negatively associated with Fe_{OXIDES} (Figure 6A). The intermediate and deeper soil layers from GC were, comparatively, more associated with the deeper layers from SC soils. The GC bacterial communities were positively associated with Fe_{OXIDES}, whereas QC communities were negatively associated with Fe_{OXIDES} (Figure 6B). The SC

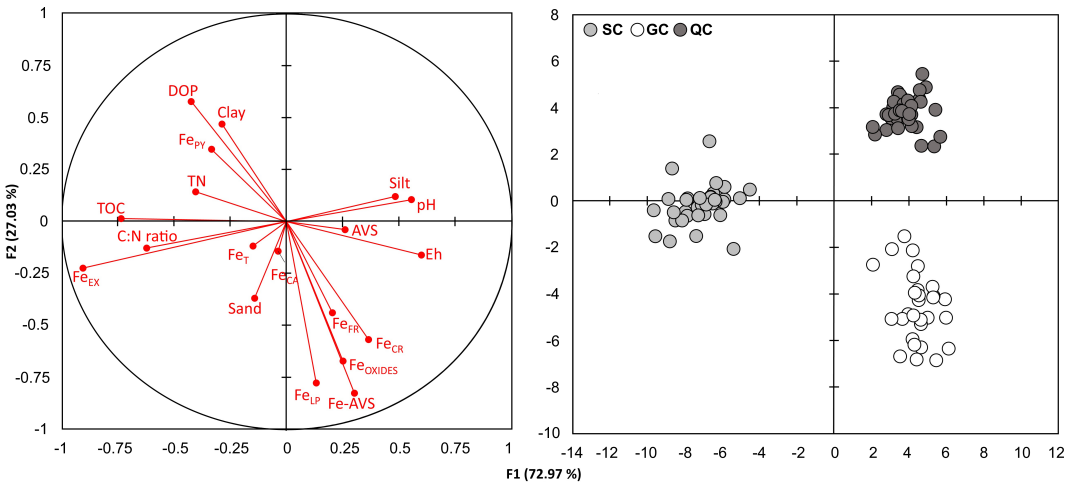

FIGURE 5
Discriminant analysis results of seagrass meadows' soils variables in the three studied geo-environment (i.e., SC, GC, and QC) along the Brazilian coast. TOC, Total organic carbon contents; TN, total nitrogen contents; AVS, acid volatile sulfides; AVS-Fe, Fe associated with AVS fraction; FeEX, soluble and exchangeable Fe; FeCA, Fe bounded to carbonates; FeFR, Fe associated with ferrihydrite; FeLP, Fe associated with lepidocrocite; FeCR, Fe associated with crystalline Fe oxyhydroxides; FePY, Fe associated with pyrite; Fe_{OXIDES}, the sum of FeFR; FeLP; and FeCR; and DOP, degree of Fe pyritization.

TABLE 2 Permanova analysis of the in a Monte Carlo test arrangement with 999 permutations, under a *p-value* MC< 0.05.

Factors	Permanova table			
	df	F test	Permutations	p-value (MC)
Archaea				
Study Sites (SS)	2	15.657	999	0.001
Soil Depth (SD)	3	4.395	997	0.002
ES x SD	3	6.294	999	0.001
Bacteria				
Study Sites (SS)	2	8.097	997	0.001
Soil Depth (SD)	3	3.519	998	0.001
SS x SD	3	3.745	999	0.001

The results evaluated the significance of the role of each factor and its combinations on the variation of the microbial community structure.

communities were positively associated with TOC, TN, Fe_T, DOP, and clay and negatively associated with Eh and pH (Figure 6B).

4 Discussion

4.1 Physicochemical diversity of seagrass meadows and its effects on soil biogeochemical processes

Diverse studies have shown that soils of coastal wetlands (e.g., mangroves, salt marshes, and hypersaline tidal flats) can be very dynamic and spatially variable, resulting from an interaction between biotic (e.g., plant species and bioturbation; Araújo Júnior et al., 2012; Cabral et al., 2020), and abiotic factors (i.e., physiographic position, flooding frequency, geological bedrocks, and climate; Seybold et al., 2002; Du Laing et al., 2009; Albuquerque et al., 2014; Ferronato et al., 2016; Ferreira et al., 2022).

Our findings indicate that the distinct geo-environments and observed vegetation characteristics (e.g., plant biomass, density, and species) resulted in differentiated soil physico-chemical conditions at the studied sites (Figures 2 and 3; Table 1). Overall, the predominance of sand in the three studied sites reflects a high hydrodynamics energy which influences the particle size distribution in the studied sites. A more energetic hydrodynamic condition favours fine particle transportation and coarse particle accumulation (Flemming, 2000; Pejrup, 1988). Accordingly, it can be stated that a more energetic condition was recorded for soils from GC, where the seagrass meadows were in a beach area with coarse soil textures, and from estuarine soils at SC. Conversely, QC seagrass meadows are located in a closed estuary, i.e., a choked lagoon (Figure 1; Toldo Jr. et al., 2000; Lanari and Copertino, 2017), and thus present characteristics of a slightly lower energetic environment according to Flemming (2000) (i.e., higher contents of fine particles such as silt and clay; Figure 2; Table 1).

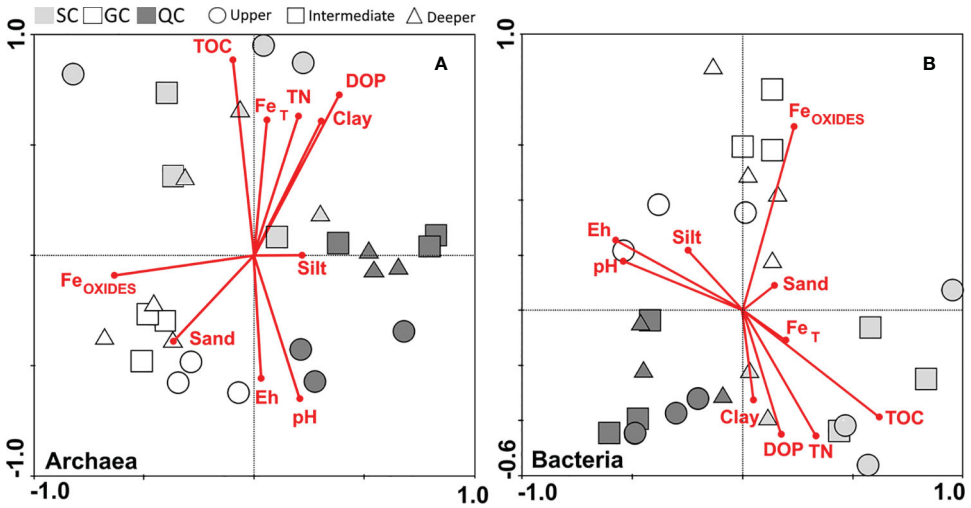

FIGURE 6
Results of redundancy detrended analysis regarding the environmental factors correlated to **(A)** archaea and **(B)** bacteria distribution and depth. TOC: Total organic carbon contents, TN: total nitrogen contents, Fe_{OXIDES}: the sum of FeFR, FeLP, and FeCR, Fe_T: pseudo total Fe, and DOP: degree of Fe pyritization.

On the other hand, SC soils present finer soil texture (mean clay content: 14.1 ± 2.3%; Table 1), mainly at the soil surface, compared to GC soils. These characteristics can be attributed to the increased plant biomass within the meadow in SC, which has developed over coarser soils (Figure 1), which attenuates the effects of turbulence and wave action, promoting sedimentation of finer suspended particles and decreasing its resuspension in the upper soil layers (Gacia et al., 1999; Ondiviela et al., 2014). On the other hand, specifically for the QC samples, the higher sand contents on the upper soil layers (down to 10 cm depth) may result from a recently enhanced erosive event that may have delivered coarse particles to the lagoon (Toldo Jr. et al., 2000).

The contrasting geo-environments reflect significantly distinct redox conditions (Figure 3). For example, at the SC coast, anoxic conditions (Eh< +100 mV; Otero et al., 2009) were predominant, whereas sub-oxic conditions (+100 mV< Eh< +350 mV; Otero et al., 2009) predominate at GC and QC, despite anoxic conditions recorded at deeper layers (deeper than 30 cm) of the QC (Figure 3). Furthermore, despite the SC and GC seagrass meadows presenting similar plant species (*H. wrightii*; Figure 1), the redox conditions recorded for the GC were closely related to the QC (vegetated by *Ruppia maritima;* Figure 3). This fact highlights that seagrass plant species do not solely drive redox conditions, since same plant species may present distinct redox conditions. Additionally, compared to seagrass meadows from other sites (Table 3), the redox potentials at GC and QC were consistently higher, indicating the importance of abiotic factors (e.g., particle size distribution, hydrodynamic) for seagrass meadows' soils characteristics.

In this sense, the different plant biomass among sites (Figure 1) and the potentially higher input of labile organic matter from the surrounding mangroves and seagrass meadows in the SC soil produced lower Eh values. This explanation corroborates the opposite association observed in the discriminant analysis (Figure 5) and the significant negative correlation between TOC and Eh (Figure 7A). As labile organic matter is produced, exuded, or trapped by seagrasses vegetation, there is an intensification of the microbial respiration processes (Kaldy, 2012; Barrón et al., 2014), depleting the dissolved oxygen concentrations, leading to the consumption of other electron acceptors substituting O_2 and resulting in lower Eh values (Canfield et al., 1993; Miller et al., 2007).

TABLE 3 Physicochemical (Eh and pH), sand, and total organic carbon (TOC) contents quantified for different seagrass meadows around the globe.

Site	Seagrass specie	Eh	pH	Sand	TOC	Reference
		(mV)		(%)		
Global data					2.5 ± 0.1	Fourqurean et al., 2012
Moreton Bay, Australia	Zostera muelleri* and others			100 ± 0	0.1 ± 0.1	Samper-Villarreal et al., 2016
				91 ± 6	0.5 ± 0.4	
Rhode Island, USA	Z. marina		7.3 to 8.5	14 to 97	0.2-30	Bradley and Stolt, 2003
Cockburn Sound, Western Australia	Posidonia sinuosa				0.4 - 1.3	Serrano et al., 2015
Port Curtis, Australia	Z. muelleri				1.5 - 2.0	Ricart et al., 2015
Slipshavn, Nyborg Fjord, Danish Baltic	Z. marina				0.2 ± 0.1	
					2.1 ± 0.1	
Sint Annaland, Eastern Scheld, The Netherland	Z. marina				0.7 ± 0.1	
Arcachon Bay, France	Z. marina				0.3 ± 0.01	
	Z. noltii				1.8 ± 0.3	
Palk Bay, India		-52 to +56	7.2 to 8.2	39-90		Thangaradjou et al., 2015
Awerange Bay, Indonesia	Halodule uninervis* and others	-300 to 0	6.4 to 7.2		1.2 ± 0.1 to 4.3 ± 0.8	Alongi et al., 2008
Leschenault Estuary, Western Australia	Ruppia megacarpa	-120 to +49		54 to 62	3.8 to 4.9	Kilminster, 2013
	Halophila ovalis	+40 to +70		42 to 61	2.5 to 3.7	
Fangan bay, Australia	Z. muelleri			72 to 93	1.7 ± 0.8	Macreadie et al., 2014
Blanes Bay, Spain		−74 to +396				Marbà and Duarte, 2001

On the other hand, it must be considered the role of seagrass plants diffusing photosynthetic-generated O_2 to protect the basal meristem from the damages arising from sulfides (Brodersen et al., 2015). This fact would explain the higher Eh values found in the uppermost soil layers from the GC and QC (Figure 3B). These roots have an oxidative effect resulting from an effective photosynthetic system (Olsen et al., 2016), and its well-developed aerenchyma enables rapid gas diffusion to roots, rhizomes, basal meristem, and soil (Koren et al., 2015). However, the oxidation of the seagrass rhizosphere can be diminished by an intense soil microbial metabolism, which rapidly consumes the diffused oxygen. As extensive mangrove forest borders the seagrass meadows at the SC sampling site, an intensification of the labile organic matter input (dissolved and particulate; Bouillon et al., 2007; Maher et al., 2013), stimulating microbial respiration, may have prevented the establishment of sub-oxic and oxic conditions at the upper-most soil layers as occurred at GC and QC coasts (Figure 3B).

The circumneutral pH values recorded for the studied sites (Figure 3A) are also related to the reductive processes of Fe and sulfate reduction in these soils. Both geochemical processes consume H^+ or produce alkalinity (Equation 1 and 2; Otero et al., 2009). Conversely, the lower pH values at the upper layers of SC (0-10 cm depth) may result from intense rhizospheric activity since the higher roots' density may result in higher organic acid exudation to increase nutrients bioavailability, especially phosphorus (Long et al., 2008).

$$4FeOOH + CH_2O + 7H^+ \rightarrow 4Fe^{2+} + HCO_3- + 6H_2O \quad (1)$$

$$SO_4^{2-} + 2CH_2O \rightarrow HS^- + H^+ + 2HCO_3- \quad (2)$$

The soils' organic C and N contents were significantly higher on the SC, presumably derived from the higher plant biomass and the input from surrounding mangroves (Figure 1). The higher C:N ratio recorded for the SC coast (Figure 3) supports a hypothesis for C inputs from mangrove forests bordering the seagrass (Kennedy et al., 2010; Garcias-Bonet et al., 2019). Furthermore, there is a significant correlation between TOC and TN for all studied sites (Figure 7B), also represented by the strong association of the TOC and TN by the discriminant analysis results (Figure 5).

This association indicates that the soil organic matter is the source of N in these areas and is possibly attributed to the N fixation and assimilation processes promoted by sulfate-reducing bacteria (Welsh, 2000; Mohr et al., 2021). Additionally, the higher TOC content in the SC results from the less energetic metabolic pathway, corroborated by the lower Eh recorded in this site (Figure 3B). Thus, the intensity of anaerobic microbial metabolism associated with primary productivity may vary and is responsible for the C accumulation in seagrass meadow soils. In this case, the lower metabolic yield (e.g., SC) promotes soil organic matter accumulation, generally with low humification and unsaturation degree but enriched in H, N, and alcoholic and methoxyl groups (Neue et al., 1997; Kristensen et al., 2008).

Compared to seagrass meadows located in other parts of the world, the TOC contents were lower than the global average (average: 2.5%, median 1.8%; Fourqurean et al., 2012; Armitage and Fourqurean, 2016) but comparable to other sites around the

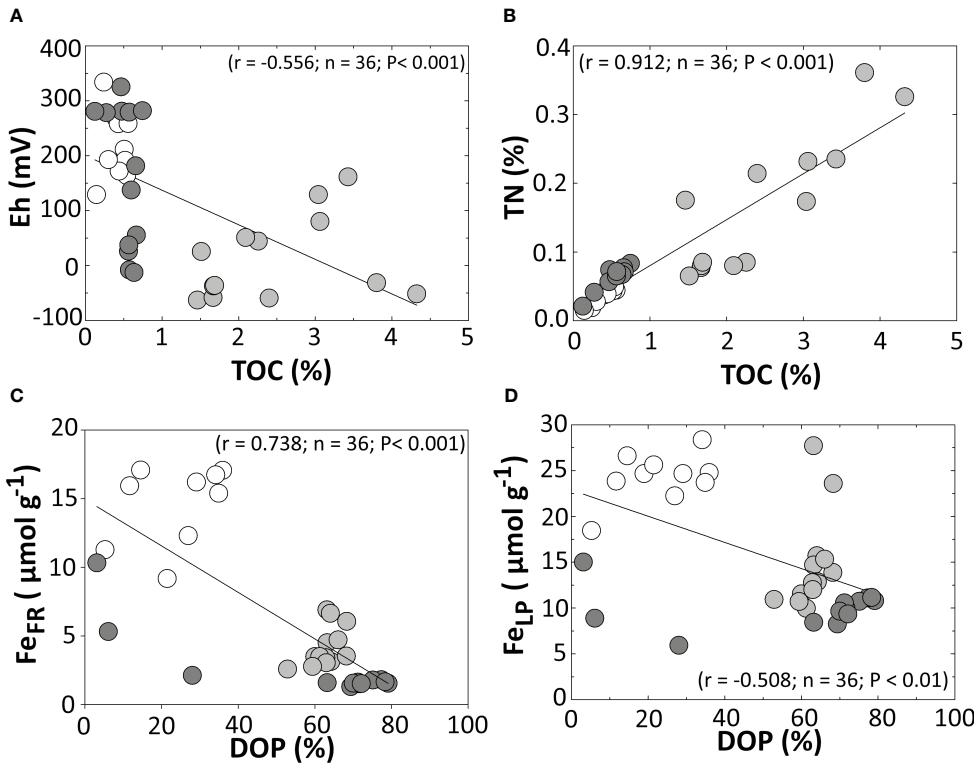

FIGURE 7
Spearman's correlations between **(A)** TOC and Eh, **(B)** and TN, and between **(C)** DOP and FeFR, and **(D)** FeLP.

globe (Table 3). However, a marked variability was observed between the studied sites, probably associated with the interaction of multiple environmental factors (e.g., seagrass species, landscape configuration, and soil redox conditions; Ricart et al., 2015; Ricart et al., 2020). However, our study evidence that geo-environmental factors controlling microbial metabolisms may be more relevant for C accumulation than plant species since the meadows formed by the same species present significant TOC contents (e.g., SC and GC). Additionally, TOC contents were a significant variable for differentiating microbial communities among studied sites (Figure 7). Thus, more studies must be conducted to improve comprehension of the spatial variability of seagrass meadows, improving the accuracy of the C stored in these ecosystems (Ricart et al., 2020), and how the effects of organic C control microbial communities.

4.2 Fe and S dynamic and metabolic pathways

Despite the differentiated geological setting of the studied sites, with the influence of granitic-gneiss rocks at the GC (Valeriano et al., 2016) and the predominance of quaternary sandy deposits at the SC and QC (Toldo Jr. et al., 2000; Vilas Bôas et al., 2001), the Fe_T contents did not differ statistically (Table 1). However, the Fe fractionating presented significant differences among the sites. Accordingly, the intensity of Fe and S metabolic pathways contrasted among the studied sites.

The seagrass meadow located at the SC differed from other sites by the significantly higher DOP values, which remained above 60% (Figure 4). Under the anoxic conditions at the SC (Table 1), microbiologically mediated Fe^{3+} reduction decreased Fe oxyhydroxide contents while increasing the soluble Fe^{2+} and Fe associated with sulfides (e.g., pyrite). On the other hand, at GC, the higher Eh values indicate an unfavourable environment for Fe reduction (i.e., oxic conditions) and the maintenance of Fe in oxyhydroxide forms (Figure 4). In such environments with redox oscillations between suboxic to oxic and circumneutral pH conditions (e.g., GC; Table 1), soluble Fe^{2+} is oxidized to Fe^{3+} and precipitated as oxyhydroxides (Ferreira et al., 2021; Ferreira et al., 2022) For the QC, fairly high DOP values occurred (>60%, especially at soil layers deeper than 10 cm; Figure 4) despite the high redox potentials (suboxic environment). In this case, the presence of pyrite could result from former (or transient) environmental conditions favourable to pyrite formation (Ferreira et al., 2015). Remnant pyrites may be protected by Fe oxyhydroxide coatings, preventing complete pyrite oxidation (Huminicki and Rimstidt, 2009). Furthermore, the presence of poorly crystalline Fe oxyhydroxides, especially Fe_{LP}, at the upper layers of GC and QC could be considered a result of the oxidation of sulfides by the rhizosphere (Azzoni et al., 2001; Brodersen et al., 2015) since lepidocrocite is the main product of Fe oxidation in saline environments (Equation 3; Otero et al., 2009).

$$FeS_2 + 3.5O_2 + H_2O \rightarrow Fe(OH)_3 + 2SO_4^{2-} + 4H^+ \quad (3)$$

The higher content of crystalline Fe oxyhydroxides (i.e., Fe_{CR}) at the GC could also explain the lower DOP registered at this site since crystalline Fe forms are less prone to reduction due to their mineralogical features such as lower surface area, reactivity, and crystal structure (i.e., rhombohedral and hexagonal or irregular plates) when compared to poorly crystalline Fe oxyhydroxides (Cornell and Schwertmann, 2003). Conversely, the higher susceptibility of poorly crystalline Fe oxyhydroxides to microbial Fe reduction could also explain the negative correlation between DOP vs. Fe_{FR} and vs. Fe_{LP} (Figures 5, 7C, D).

Moreover, the AVS and AVS-Fe contents also varied among the studied geo-environments (Figures 3F, G), corroborating its effects on Fe and S dynamics. These fractions correspond to a complex mixture of aqueous H_2S and its dissociated form, Fe-S complexes, polysulfides, and solid-phase mackinawite and greigite (Rickard et al., 2017), with significant ecological importance once it may control trace metals dynamics and bioavailability (MaChado et al., 2010). Thus, the higher AVS content in the GC compared to SC and QC reinforces the different intensities of Fe and S metabolic pathways among the studied sites. Furthermore, due to its phytotoxicity, high sulfide production has been associated with declining seagrass meadows(Holmer et al., 2005). Accordingly, the higher AVS content at the GC, especially on surface soil layers, may be related to the lower plant density at this site (Figure 1), especially compared to the SC vegetated by the same plant species, since lower plant density and lower organic C content prevents Fe oxyhydroxides reduction (and lower DOP).

Regarding microbial communities, we observed a positive correlation with higher Fe_{OXIDES} and sand contents, higher Eh values, and negatively correlated with TOC at GC site (Figure 7). This fact indicates that the low plant density and high Fe inputs from the Fe-rich geological surroundings affected the microbial structure. A recent study has reported that forming distinct Fe-cycling bacterial genera (e.g., Lewinella and Woeseia) communities in seagrass meadows positively correlates with greater Fe contents in its soils (Martin et al., 2022). On the other hand, previous studies have reported that sandy sediments (e.g., GC) with high sulfide production favour the dominance of archaea communities (Llobet-Brossa et al., 2002; Buhring et al., 2005). Specifically, high sulfide production increases genes related to sulfate reduction in a *Posidonia* spp. ecosystem (Fraser et al., 2023).

The higher plant cover in SC possibly changes microbial activity in the seagrass rhizosphere (Jankowska et al., 2015) since we observed a clear cluster in microbial communities, mainly driven by clay content, TOC, TN, and DOP (Figure 6). Accordingly, previous studies have reported that gross primary production in tropical seagrass bacteria communities increases the amount of C available for sulfate-reducing bacteria metabolism (Pollard and Moriarty, 1991; Williams et al., 2009). Moreover, Zhang et al. (2022) revealed that higher clay contents play an important role in seagrass soil biogeochemistry. For example, these authors reported that seagrass soils with a predominance of fine particles

have a higher capacity for root exudate retention, increasing its concentration around the roots and enhancing the abundance of sulfate-reducing bacteria (see DOP values in Table 1). Interestingly, in a *Thalassia hemprichii* system it was demonstrated that induced carbon addition changed the bacterial community, mainly those functional groups related to N cycle (Zhang et al., 2021). A higher TOC content in SC could increase N uptake and, consequently, boost photosynthetic performance of seagrass and modified rhizosphere microbial communities.

Changes in seagrass microbial communities seem to be context-dependent since microbial groups changed according to geographical location. More importantly, the same plant species (*H. wrightii*. at SC and GC) shapes different microbial communities in the soil (Figure 6). Thus, probably seagrass microbial communities change according to plant type, but microbial rhizosphere core strongly depends on soil geochemical properties (Cúcio et al., 2016). For example, Vogel et al. (2021) demonstrated that the main drivers of microbial community structure in *Thalassia testudinum* seagrass were local geo-environmental conditions.

Therefore, our findings reveal that seagrass meadows soils at contrasting geo-environments (e.g., climate, geology, and plant species and cover) present different intensities of Fe and sulfate reduction, ultimately shaping different microbiological communities. More importantly, we provide evidence that bacteria and archaea communities responded similarly to geo-environmental conditions, indicating that both could be equally important to microbial activity and nutrient cycling in seagrass ecosystems. These results shed light on the knowledge gap about the intensities of geochemical processes involving Fe and S dynamic and metabolic pathways in seagrass meadows' soils.

5 Conclusions

In this study, we identify that seagrass meadows are a heterogeneous ecosystem in which the variability of soil composition affects the intensities of geochemical processes due to distinct geo-environments (e.g., climate, geology, salinity, plant species and coverage, and anthropic influence). For example, in soils under higher plant cover that enhances the C contents and geology that favors higher Fe contents, there are higher contents of fine particles (e.g., clay), an abundance of sulfate-reducing bacteria, and microbial-mediated processes involving Fe and S. This environment favors metabolic pathways with low oxidation rates (e.g., sulfate reduction), Fe sulfides formation, and ultimately, high-capacity C sequestration. On the other hand, in seagrass meadow soils with higher contents of sand and low plant density, a more oxidizing environment is established that favors Fe oxyhydroxides and AVS formation. This contrasting environment presents a lower capacity for organic C accumulation and contaminants immobilization. In addition, the differentiated geo-environmental conditions markedly influenced microbial communities, even when vegetated with the same plant species. Our findings revealed novel insights into the heterogeneity of seagrass meadow soils and a better understanding of the biogeochemical processes inherent to these ecosystems.

Data availability statement

The raw data supporting the conclusions of this article will be made available by the authors, without undue reservation.

Author contributions

GN and TF: Funding acquisition, Investigation, Formal analysis, Conceptualization, Methodology, Validation, Writing original draft, review and editing. PA, HQ, AP, MC, DG, WZ, JS, FA, XO: Investigation, Formal analysis, Data validation, Writing - original draft and editing. All authors contributed to the article and approved the submitted version.

Funding

This work received financial support provided by the National Council for Scientific and Technological Development (CNPq, grants number 430010/2018-4 and 305996/2018-5 to TF), Coordination of Superior Level Staff Improvement (CAPES, Finance Code 001), São Paulo Research Foundation (FAPESP, grants number 2014/11778-5, 2016/21026-6, and 2021/00221-3), and FUNCAP research fellow (Chief Scientist Program). Furthermore, this study is part of the doctoral thesis of the author GN and is in accordance with the copyright terms of use.

Conflict of interest

The authors declare that the research was conducted in the absence of any commercial or financial relationships that could be construed as a potential conflict of interest.

Publisher's note

References

Albuquerque, A. G. B. M., Ferreira, T. O. O., Nóbrega, G. N. N., Romero, R. E. E., Júnior, V. S. S., Meireles, A. J. A., et al. (2014). Soil genesis on hypersaline tidal flats (apicum ecosystem) in a tropical semi-arid estuary (Ceará, Brazil). *Soil Res.* 52, 140. doi: 10.1071/SR13179

Allen, H. E., Fu, G., and Deng, B. (1993). Analysis of acid-volatile sulfide (AVS) and simultaneously extracted metals (SEM) for the estimation of potential toxicity in aquatic sediments. *Environ. Toxicol. Chem.* 12, 1441–1453. doi: 10.1002/etc.5620120812

Alongi, D. M. (2008). Mangrove forests: Resilience, protection from tsunamis, and responses to global climate change. *Estuarine, Coastal and Shelf Science* 76, 1–13. doi: 10.1016/j.ecss.2007.08.024.

Alvares, C. A., Stape, J. L., Sentelhas, P. C., de Moraes Gonçalves, J. L., and Sparovek, G. (2013). Köppen's climate classification map for Brazil. *Meteorol. Z.* 22, 711–728. doi: 10.1127/0941-2948/2013/0507

Arai, M. (2006). A grande elevação eustática do Mioceno e sua influência na origem do Grupo Barreiras. *Geol. USP Série Científica* 6, 01–06. doi: 10.5327/S1519-874X2006000300002

Araújo Júnior, J. M. C., Otero, X. L., Marques, A. G. B., Nóbrega, G. N., Silva, J. R. F., and Ferreira, T. O. (2012). Selective geochemistry of iron in mangrove soils in a semiarid tropical climate: effects of the burrowing activity of the crabs Ucides cordatus and Uca maracoani. *Geo-Marine Lett.* 32, 289–300. doi: 10.1007/s00367-011-0268-5

Armitage, A. R., and Fourqurean, J. W. (2016). Carbon storage in seagrass soils: long-term nutrient history exceeds the effects of near-term nutrient enrichment. *Biogeosciences* 13, 313–321. doi: 10.5194/bg-13-313-2016

Azzoni, R., Giordani, G., Bartoli, M., Welsh, D. T., and Viaroli, P. (2001). Iron, sulphur and phosphorus cycling in the rhizosphere sediments of a eutrophic Ruppia cirrhosa meadow (Valle Smarlacca, Italy). *J. Sea Res.* 45, 15–26. doi: 10.1016/S1385-1101(00)00056-3

Azzoni, R., Giordani, G., and Viaroli, P. (2005). Iron–sulphur–phosphorus interactions: implications for sediment buffering capacity in a mediterranean eutrophic lagoon (Sacca di Goro, Italy). *Hydrobiologia* 550, 131–148. doi: 10.1007/s10750-005-4369-x

Barbier, E. B., Hacker, S. D., Kennedy, C., Koch, E. W., Stier, A. C., and Silliman, B. R. (2011). The value of estuarine and coastal ecosystem services. *Ecol. Monogr.* 81, 169–193. doi: 10.1890/10-1510.1

Barrón, C., Apostolaki, E. T., and Duarte, C. M. (2014). Dissolved organic carbon fluxes by seagrass meadows and macroalgal beds. *Front. Mar. Sci.* 1. doi: 10.3389/fmars.2014.00042. Article 42.

Bouillon, S., Dehairs, F., Velimirov, B., Abril, G., and Borges, A. V. (2007). Dynamics of organic and inorganic carbon across contiguous mangrove and seagrass systems (Gazi Bay, Kenya). *J. Geophys. Res.* 112, G02018. doi: 10.1029/2006JG000325

Bradley, M. P., and Stolt, M. H. (2003). Subaqueous soil-landscape relationships in a rhode island estuary. *Soil Sci. Soc Am. J.* 67, 1487–1495. doi: 10.2136/sssaj2003.1487

Brodersen, K. E., Koren, K., Moßhammer, M., Ralph, P. J., Kühl, M., and Santner, J. (2017). Seagrass-mediated phosphorus and iron solubilization in tropical sediments. *Environ. Sci. Technol.* 51, 14155–14163. doi: 10.1021/acs.est.7b03878

Brodersen, K. E., Nielsen, D. A., Ralph, P. J., and Kühl, M. (2015). Oxic microshield and local pH enhancement protects Zostera muelleri from sediment derived hydrogen sulphide. *New Phytol.* 205, 1264–1276. doi: 10.1111/nph.13124

Brodersen, K. E., Siboni, N., Nielsen, D. A., Pernice, M., Ralph, P. J., Seymour, J., et al. (2018). Seagrass rhizosphere microenvironment alters plant-associated microbial community composition. *Environ. Microbiol.* 20, 2854–2864. doi: 10.1111/1462-2920.14245

Buhring, S. I., Elvert, M., and Witte, U. (2005). The microbial community structure of different permeable sandy sediments characterized by the investigation of bacterial fatty acids and fluorescence in *situ* hybridization. *Environ. Microbiol.* 7, 281–293. doi: 10.1111/j.1462-2920.2004.00710.x

Cabral, R. L., Ferreira, T. O., Nóbrega, G. N., Barcellos, D., Roiloa, S. R., Zandavalli, R. B., et al. (2020). How do plants and climatic conditions control soil properties in hypersaline tidal flats? *Appl. Sci.* 10, 7624. doi: 10.3390/app10217624

Canfield, D. E., Thamdrup, B., and Hansen, J. W. (1993). The anaerobic degradation of organic matter in Danish coastal sediments: Iron reduction, manganese reduction, and sulfate reduction. *Geochim. Cosmochim. Acta* 57, 3867–3883. doi: 10.1016/0016-7037(93)90340-3

Charette, M., and Smith, W. (2010). The volume of earth's ocean. *Oceanography* 23, 112–114. doi: 10.5670/oceanog.2010.51

Clarke, K. R., and Gorey, R. N. (2006). *PRIMER v6: user manual/tutorial.* (Plymouth, UK: P.-E. Ltd).

Cline, J. D. (1969). Spectrophotometric determination of hydrogen sulfide in natural waters. *Limnol. Oceanogr.* 14, 454–458. doi: 10.4319/lo.1969.14.3.0454

Connolly, R., Hindell, J., and Gorman, D. (2005). Seagrass and epiphytic algae support nutrition of a fisheries species, Sillago schomburgkii, in adjacent intertidal habitats. *Mar. Ecol. Prog. Ser.* 286, 69–79. doi: 10.3354/meps286069

Copertino, M. S., Creed, J. C., Lanari, M. O., Magalhães, K., Barros, K., Lana, P. C., et al. (2016). Seagrass and Submerged Aquatic Vegetation (VAS) Habitats off the Coast of Brazil: state of knowledge, conservation and main threats. *Braz. J. Oceanogr.* 64, 53–80. doi: 10.1590/S1679-875920161036064sp2

Cornell, R. M., and Schwertmann, U. (2003). *The Iron Oxides: Structure, Reactions, Occurences and Uses* (Weinheim, Germany: Wiley). doi: 10.1002/3527602097

Costanza, R., de Groot, R., Sutton, P., van der Ploeg, S., Anderson, S. J., Kubiszewski, I., et al. (2014). Changes in the global value of ecosystem services. *Glob. Environ. Change* 26, 152–158. doi: 10.1016/j.gloenvcha.2014.04.002

Cúcio, C., Engelen, A. H., Costa, R., and Muyzer, G. (2016). Rhizosphere microbiomes of European + seagrasses are selected by the plant, but are not species specific. *Front. Microbiol.* 7. doi: 10.3389/fmicb.2016.00440

Cui, L., Jiang, Z., Huang, X., Liu, S., Wu, Y., and Fan, M. (2021). Decade changes of the food web structure in tropical seagrass meadow: Implication of eutrophication effects. *Mar. pollut. Bull.* 173, 113122. doi: 10.1016/j.marpolbul.2021.113122

de la Torre-Castro, M., and Rönnbäck, P. (2004). Links between humans and seagrasses—an example from tropical East Africa. *Ocean Coast. Manage.* 47, 361–387. doi: 10.1016/j.ocecoaman.2004.07.005

Delgard, M. L., Deflandre, B., Kochoni, E., Avaro, J., Cesbron, F., Bichon, S., et al. (2016). Biogeochemistry of dissolved inorganic carbon and nutrients in seagrass (Zostera noltei) sediments at high and low biomass. *Estuar. Coast. Shelf Sci.* 179, 12–22. doi: 10.1016/j.ecss.2016.01.012

Duarte, C. M., and Chiscano, C. L. (1999). Seagrass biomass and production: a reassessment. *Aquat. Bot.* 65, 159–174. doi: 10.1016/S0304-3770(99)00038-8

Duarte, C. M., Marbà, N., Gacia, E., Fourqurean, J. W., Beggins, J., Barrón, C., et al. (2010). Seagrass community metabolism: Assessing the carbon sink capacity of seagrass meadows. *Global Biogeochem. Cycles* 24, n/a–n/a. doi: 10.1029/2010GB003793

Du Laing, G., Rinklebe, J., Vandecasteele, B., Meers, E., and Tack, F. M. G. (2009). Trace metal behaviour in estuarine and riverine floodplain soils and sediments: A review. *Sci. Total Environ.* 407, 3972–3985. doi: 10.1016/j.scitotenv.2008.07.025

Erich, E., and Drohan, P. J. (2012). Genesis of freshwater subaqueous soils following flooding of a subaerial landscape. *Geoderma* 179–180, 53–62. doi: 10.1016/j.geoderma.2012.02.004

Fernandes, M., Bryars, S., Mount, G., and Miller, D. (2009). Seagrasses as a sink for wastewater nitrogen: The case of the Adelaide metropolitan coast. *Mar. pollut. Bull.* 58, 303–308. doi: 10.1016/j.marpolbul.2008.10.006

Ferreira, T. O., Nóbrega, G. N., Albuquerque, A. G. B. M., Sartor, L. R., Gomes, I. S., Artur, A. G., et al. (2015). Pyrite as a proxy for the identification of former coastal lagoons in semiarid NE Brazil. *Geo-Marine Lett.* 35, 355–366. doi: 10.1007/s00367-015-0412-8

Ferreira, T. O., Nóbrega, G. N., Queiroz, H. M., de Souza Júnior, V. S., Barcellos, D., Ferreira, A. D., et al. (2021). Windsock behavior: climatic control on iron biogeochemistry in tropical mangroves. *Biogeochemistry* 156, 437–452. doi: 10.1007/s10533-021-00858-9

Ferreira, T. O., Queiroz, H. M., Nóbrega, G. N., de Souza Júnior, V. S., Barcellos, D., Ferreira, A. D., et al. (2022). Litho-climatic characteristics and its control over mangrove soil geochemistry: A macro-scale approach. *Sci. Total Environ.* 811, 152152. doi: 10.1016/j.scitotenv.2021.152152

Ferronato, C., Falsone, G., Natale, M., Zannoni, D., Buscaroli, A., Vianello, G., et al. (2016). Chemical and pedological features of subaqueous and hydromorphic soils along a hydrosequence within a coastal system (San Vitale Park, Northern Italy). *Geoderma* 265, 141–151. doi: 10.1016/j.geoderma.2015.11.018

Flemming, B. (2000). A revised textural classification of gravel-free muddy sediments on the basis of ternary diagrams. *Cont. Shelf Res.* 20, 1125–1137. doi: 10.1016/S0278-4343(00)00015-7

Fortin, D., Leppard, G. G., and Tessier, A. (1993). Characteristics of lacustrine diagenetic iron oxyhydroxides. *Geochim. Cosmochim. Acta* 57, 4391–4404. doi: 10.1016/0016-7037(93)90490-N

Fourqurean, J. W., Duarte, C. M., Kennedy, H., Marbà, N., Holmer, M., Mateo, M. A., et al. (2012). Seagrass ecosystems as a globally significant carbon stock. *Nat. Geosci.* 5, 505–509. doi: 10.1038/ngeo1477

Fraser, M. W., Martin, B. C., Wong, H. L., Burns, B. P., and Kendrick, G. A. (2023). Sulfide intrusion in a habitat forming seagrass can be predicted from relative abundance of sulfur cycling genes in sediments. *Sci. Total Environ.* 864, 161144. doi: 10.1016/j.scitotenv.2022.161144

Gacia, E., Granata, T., and Duarte, C. (1999). An approach to measurement of particle flux and sediment retention within seagrass (Posidonia oceanica) meadows. *Aquat. Bot.* 65, 255–268. doi: 10.1016/S0304-3770(99)00044-3

Garcias-Bonet, N., Delgado-Huertas, A., Carrillo-de-Albornoz, P., Anton, A., Almahasheer, H., Marbà, N., et al. (2019). Carbon and nitrogen concentrations, stocks, and isotopic compositions in red sea seagrass and mangrove sediments. *Front. Mar. Sci.* 6. doi: 10.3389/fmars.2019.00267

Gee, G. W., and Bauder, J. W. (1986). Particle-size analysis. *Methods Soil Anal. Part 1—Physical Mineral. Methods* 1, 383–411. doi: 10.2136/sssabookser5.1.2ed.c15

Gorman, D., Sumida, P. Y. G., Figueira, R. C. L., and Turra, A. (2020). Improving soil carbon estimates of mudflats in Araçá Bay using spatial models that consider riverine

input, wave exposure and biogeochemistry. *Estuar. Coast. Shelf Sci.* 238, 106734. doi: 10.1016/j.ecss.2020.106734

Hammer, Ø., Harper, D. A. T., and Ryan, P. D. (2001). Past: paleontological statistics software package for education and data analysis. *Paleontol. Electron.* 4, 9 pp.

Heuer, H., Krsek, M., Baker, P., Smalla, K., and Wellington, E. M. H. (1997). Analysis of actinomycete communities by specific amplification of genes encoding 16S rRNA and gel-electrophoretic separation in denaturing gradients. *Appl. Environ. Microbiol.* 63, 3233–3241. doi: 10.1128/aem.63.8.3233-3241.1997

Holmer, M., Duarte, C. M., and Marbá, N. (2005). Iron additions reduce sulfate reduction rates and improve seagrass growth on organic-enriched carbonate sediments. *Ecosystems* 8, 721–730. doi: 10.1007/s10021-003-0180-6

Howard, J., Hoyt, S., Isensee, K., Telszewski, M., Pidgeon, E., and Telszewski, M. (2014). *Coastal blue carbon: methods for assessing carbon stocks and emissions factors in mangroves, tidal salt marshes, and seagrasses* (Arlington, VA, USA: Conservation International, Intergovernmental Oceanographic Commission of UNESCO, International Union for Conservation of Nature, Arlington, VA, USA).

Huerta-Díaz, M. A., and Morse, J. W. (1990). A quantitative method for determination of trace metal concentrations in sedimentary pyrite. *Mar. Chem.* 29, 119–144. doi: 10.1016/0304-4203(90)90009-2

Huerta-Diaz, M. A., and Morse, J. W. (1992). Pyritization of trace metals in anoxic marine sediments. *Geochim. Cosmochim. Acta* 56, 2681–2702. doi: 10.1016/0016-7037(92)90353-K

Huminicki, D. M. C., and Rimstidt, J. D. (2009). Iron oxyhydroxide coating of pyrite for acid mine drainage control. *Appl. Geochemistry* 24, 1626–1634. doi: 10.1016/j.apgeochem.2009.04.032

Jankowska, E., Jankowska, K., and Włodarska-Kowalczuk, M. (2015). Seagrass vegetation and meiofauna enhance the bacterial abundance in the Baltic Sea sediments (Puck Bay). *Environ. Sci. pollut. Res.* 22, 14372–14378. doi: 10.1007/s11356-015-5049-7

Kaal, J., Serrano, O., Nierop, K. G. J., Schellekens, J., Martínez, A., and Mateo, M.-Á (2016). Molecular composition of plant parts and sediment organic matter in a Mediterranean seagrass (Posidonia oceanica) mat. *Aquat. Bot.* 133, 50–61. doi: 10.1016/j.aquabot.2016.05.009

Kaldy, J. (2012). Influence of light, temperature and salinity on dissolved organic carbon exudation rates in Zostera marina L. *Aquat. Biosyst.* 8, 19. doi: 10.1186/2046-9063-8-19

Kennedy, H., Beggins, J., Duarte, C. M., Fourqurean, J. W., Holmer, M., Marbà, N., et al. (2010). Seagrass sediments as a global carbon sink: Isotopic constraints. *Global Biogeochem. Cycles* 24, n/a–n/a. doi: 10.1029/2010GB003848

Kilminster, K. (2013). Trace element content of seagrasses in the Leschenault Estuary, Western Australia. *Mar. pollut. Bull.* 73, 381–388. doi: 10.1016/j.marpolbul.2013.05.030

Koren, K., Brodersen, K. E., Jakobsen, S. L., and Kühl, M. (2015). Optical sensor nanoparticles in artificial sediments–A new tool to visualize O2 dynamics around the rhizome and roots of seagrasses. *Environ. Sci. Technol.* 49, 2286–2292. doi: 10.1021/es505734b

Kristensen, E., Bouillon, S., Dittmar, T., and Marchand, C. (2008). Organic carbon dynamics in mangrove ecosystems: A review. *Aquat. Bot.* 89, 201–219. doi: 10.1016/j.aquabot.2007.12.005

Lanari, M., and Copertino, M. (2017). Drift macroalgae in the Patos Lagoon Estuary (southern Brazil): effects of climate, hydrology and wind action on the onset and magnitude of blooms. *Mar. Biol. Res.* 13, 36–47. doi: 10.1080/17451000.2016.1225957

Liquete, C., Cid, N., Lanzanova, D., Grizzetti, B., and Reynaud, A. (2016). Perspectives on the link between ecosystem services and biodiversity: The assessment of the nursery function. *Ecol. Indic.* 63, 249–257. doi: 10.1016/j.ecolind.2015.11.058

Llobet-Brossa, E., Rabus, R., Böttcher, M., Könneke, M., Finke, N., Schramm, A., et al. (2002). Community structure and activity of sulfate-reducing bacteria in an intertidal surface sediment: a multi-method approach. *Aquat. Microb. Ecol.* 29, 211–226. doi: 10.3354/ame029211

Long, M. H., McGlathery, K. J., Zieman, J. C., and Berg, P. (2008). The role of organic acid exudates in liberating phosphorus from seagrass-vegetated carbonate sediments. *Limnol. Oceanogr.* 53, 2616–2626. doi: 10.4319/lo.2008.53.6.2616

Lozupone, C. A., Hamady, M., Kelley, S. T., and Knight, R. (2007). Quantitative and qualitative β diversity measures lead to different insights into factors that structure microbial communities. *Appl. Environ. Microbiol.* 73, 1576–1585. doi: 10.1128/AEM.01996-06

MaChado, W., Villar, L. S., Monteiro, F. F., Viana, L. C. A., and Santelli, R. E. (2010). Relation of acid-volatile sulfides (AVS) with metals in sediments from eutrophicated estuaries: Is it limited by metal-to-AVS ratios? *J. Soils Sediments* 10, 1606–1610. doi: 10.1007/s11368-010-0297-0

Macreadie, P. I., Baird, M. E., Trevathan-Tackett, S. M., Larkum, A. W. D., and Ralph, P. J. (2014). Quantifying and modelling the carbon sequestration capacity of seagrass meadows – A critical assessment. *Mar. pollut. Bull.* 83, 430–439. doi: 10.1016/j.marpolbul.2013.07.038

Maher, D. T., Santos, I. R., Golsby-Smith, L., Gleeson, J., and Eyre, B. D. (2013). Groundwater-derived dissolved inorganic and organic carbon exports from a mangrove tidal creek: The missing mangrove carbon sink? *Limnol. Oceanogr.* 58, 475–488. doi: 10.4319/lo.2013.58.2.0475

Marbà, N., and Duarte, C. (2001). Growth and sediment space occupation by seagrass Cymodocea nodosa roots. *Mar. Ecol. Prog. Ser.* 224, 291–298. doi: 10.3354/meps224291

Martin, B. C., Middleton, J. A., Skrzypek, G., Kendrick, G. A., Cosgrove, J., and Fraser, M. W. (2022). Composition of seagrass root associated bacterial communities are linked to nutrients and heavy metal concentrations in an anthropogenically influenced estuary. *Front. Mar. Sci.* 8. doi: 10.3389/fmars.2021.768864

McKenzie, L. J., Nordlund, L. M., Jones, B. L., Cullen-Unsworth, L. C., Roelfsema, C., and Unsworth, R. K. F. (2020). The global distribution of seagrass meadows. *Environ. Res. Lett.* 15, 074041. doi: 10.1088/1748-9326/ab7d06

Miller, H. L., Meile, C., and Burd, A. B. (2007). A novel 2D model of internal O2 dynamics and H2S intrusion in seagrasses. *Ecol. Modell.* 205, 365–380. doi: 10.1016/j.ecolmodel.2007.03.004

Minuzzi, R. B., Sediyama, G. C., Barbosa, E., da, M., and Melo Júnior, J.C.F. de (2007). Climatologia do comportamento do período chuvoso da região sudeste do Brasil. *Rev. Bras. Meteorol.* 22, 338–344. doi: 10.1590/S0102-77862007000300007

Mohr, W., Lehnen, N., Ahmerkamp, S., Marchant, H. K., Graf, J. S., Tschitschko, B., et al. (2021). Terrestrial-type nitrogen-fixing symbiosis between seagrass and a marine bacterium. *Nature* 600, 105–109. doi: 10.1038/s41586-021-04063-4

Neue, H. U., Gaunt, J. L., Wang, Z. P., Becker-Heidmann, P., and Quijano, C. (1997). Carbon in tropical wetlands. *Geoderma* 79, 163–185. doi: 10.1016/S0016-7061(97)00041-4

Nóbrega, G. N., Otero, X. L., Romero, D. J., Queiroz, H. M., Gorman, D., Copertino, M., et al. (2023). Masked diversity and contrasting soil processes in tropical seagrass meadows: the control of environmental settings. *SOIL* 9, 189–208. doi: 10.5194/soil-9-189-2023

Nordlund, L. M., Koch, E. W., Barbier, E. B., and Creed, J. C. (2016). Seagrass ecosystem services and their variability across genera and geographical regions. *PloS One* 11, e0163091. doi: 10.1371/journal.pone.0163091

Olsen, J. L., Rouzé, P., Verhelst, B., Lin, Y.-C., Bayer, T., Collen, J., et al. (2016). The genome of the seagrass Zostera marina reveals angiosperm adaptation to the sea. *Nature* 530, 331–335. doi: 10.1038/nature16548

Ondiviela, B., Losada, I. J., Lara, J. L., Maza, M., Galván, C., Bouma, T. J., et al. (2014). The role of seagrasses in coastal protection in a changing climate. *Coast. Eng.* 87, 158–168. doi: 10.1016/j.coastaleng.2013.11.005

Orth, R. J., Carruthers, T. I. M. J. B., Dennison, W. C., Carlos, M., Fourqurean, J. W., Jr, K. L. H., et al. (2006). A global crisis for seagrass ecosystems. *Bioscience* 56, 987–996. doi: 10.1641/0006-3568(2006)56[987:AGCFSE]2.0.CO;2

Osterrieth, M., Borrelli, N., Alvarez, M. F. F., Nóbrega, G. N., MaChado, W., and Ferreira, T. O. (2016). Iron biogeochemistry in Holocene palaeo and actual salt marshes in coastal areas of the Pampean Plain, Argentina. *Environ. Earth Sci.* 75, 672. doi: 10.1007/s12665-016-5506-8

Otero, X. L., Ferreira, T. O., Huerta-Díaz, M. A., Partiti, C. S. M., Souza, V., Vidal-Torrado, P., et al. (2009). Geochemistry of iron and manganese in soils and sediments of a mangrove system, Island of Pai Matos (Cananeia — SP, Brazil). *Geoderma* 148, 318–335. doi: 10.1016/j.geoderma.2008.10.016

Otero, X. L., Guevara, P., Sánchez, M., López, I., Queiroz, H. M., Ferreira, A., et al. (2023). Pyrites in a salt marsh-ria system: Quantification, morphology, and mobilization. *Mar. Geol.* 455, 106954. doi: 10.1016/j.margeo.2022.106954

Otero, X. L., and Macias, F. (2002). Variation with depth and season in metal sulfides in salt marsh soils. *Biogeochemistry* 61, 247–268. doi: 10.1023/A:1020230213864

Ovreås, L., Forney, L., Daae, F. L., and Torsvik, V. (1997). Distribution of bacterioplankton in meromictic Lake Saelenvannet, as determined by denaturing gradient gel electrophoresis of PCR-amplified gene fragments coding for 16S rRNA. *Appl. Environ. Microbiol.* 63, 3367–3373. doi: 10.1128/aem.63.9.3367-3373.1997

Passos, T. R. G., Artur, A. G., Nóbrega, G. N., Otero, X. L., and Ferreira, T. O. (2016). Comparison of the quantitative determination of soil organic carbon in coastal wetlands containing reduced forms of Fe and S. *Geo-Marine Lett.* 36, 223–233. doi: 10.1007/s00367-016-0437-7

Peel, M. C., Finlayson, B. L., and McMahon, T. A. (2007). Updated world map of the Köppen-Geiger climate classification. *Hydrol. Earth Syst. Sci.* 11, 1633–1644. doi: 10.5194/hess-11-1633-2007

Pejrup, M. (1988). *The Triangular Diagram Used for Classification of Estuarine Sediments: A New Approach. In: Tide-Influenced Sedimentary Environments and Facies* (Dordrecht: Springer Netherlands), 289–300. doi: 10.1007/978-94-015-7762-5_21

Piñeiro-Juncal, N., Kaal, J., Moreira, J. C. F., Martínez Cortizas, A., Lambais, M. R., Otero, X. L., et al. (2020a). Cover loss in a seagrass Posidonia oceanica meadow accelerates soil organic matter turnover and alters soil prokaryotic communities. *Org. Geochem.* 151, 104140. doi: 10.1016/j.orggeochem.2020.104140

Piñeiro-Juncal, N., Leiva-Dueñas, C., Serrano, O., Mateo, M. Á., and Martínez-Cortízas, A. (2020b). Pedogenic processes in a Posidonia oceanica mat. *Soil Syst.* 4, 18. doi: 10.3390/soilsystems4020018

Pollard, P. C., and Moriarty, D. J. W. (1991). Organic carbon decomposition, primary and bacterial productivity, and sulphate reduction, in tropical seagrass beds of the Gulf of Carpentaria, Australia. *Mar. Ecol. Prog. Ser.* 69, 149–159. doi: 10.3354/meps069149

Queiroz, H. M., Nóbrega, G. N., Otero, X. L., and Ferreira, T. O. (2018). Are acid volatile sulfides (AVS) important trace metals sinks in semi-arid mangroves? *Mar. pollut. Bull.* 126, 318–322. doi: 10.1016/j.marpolbul.2017.11.020

Ramírez-Flandes, S., González, B., and Ulloa, O. (2019). Redox traits characterize the organization of global microbial communities. *Proc. Natl. Acad. Sci.* 116, 3630–3635. doi: 10.1073/pnas.1817554116

Reimann, C., Filzmoser, P., Garrett, R. G., and Dutter, R. (2008). *Statistical Data Analysis Explained* (Chichester, UK, UK: Wiley). doi: 10.1002/9780470987605

Ricart, A. M., York, P. H., Bryant, C. V., Rasheed, M. A., Ierodiaconou, D., and Macreadie, P. I. (2020). High variability of Blue Carbon storage in seagrass meadows at the estuary scale. *Sci. Rep.* 10, 1–12. doi: 10.1038/s41598-020-62639-y

Ricart, A. M., York, P. H., Rasheed, M. A., Pérez, M., Romero, J., Bryant, C. V., et al. (2015). Variability of sedimentary organic carbon in patchy seagrass landscapes. *Mar. pollut. Bull.* 100, 476–482. doi: 10.1016/j.marpolbul.2015.09.032

Rickard, D., Mussmann, M., and Steadman, J. A. (2017). Sedimentary sulfides. *Elements* 13, 117–122. doi: 10.2113/gselements.13.2.117

Rozaimi, M., Lavery, P. S., Serrano, O., and Kyrwood, D. (2016). Long-term carbon storage and its recent loss in an estuarine Posidonia australis meadow (Albany, Western Australia). *Estuar. Coast. Shelf Sci.* 171, 58–65. doi: 10.1016/j.ecss.2016.01.001

Samper-Villarreal, J., Lovelock, C. E., Saunders, M. I., Roelfsema, C., and Mumby, P. J. (2016). Organic carbon in seagrass sediments is influenced by seagrass canopy complexity, turbidity, wave height, and water depth. *Limnol. Oceanogr.* 61, 938–952. doi: 10.1002/lno.10262

Schaeffer-Novelli, Y., Cintrón-Molero, G., Adaime, R. R., de Camargo, T. M., Cintron-Molero, G., and de Camargo, T. M. (1990). Variability of mangrove ecosystems along the Brazilian coast. *Estuaries* 13, 204. doi: 10.2307/1351590

Serrano, O., Lavery, P. S., Duarte, C. M., Kendrick, G. A., Calafat, A., York, P. H., et al. (2016). Can mud (silt and clay) concentration be used to predict soil organic carbon content within seagrass ecosystems? *Biogeosciences* 13, 4915–4926. doi: 10.5194/bg-13-4915-2016

Serrano, O., Ricart, A. M., Lavery, P. S., Mateo, M. A., Arias-Ortiz, A., Masque, P., et al. (2015). Key biogeochemical factors affecting soil carbon storage in *Posidonia* meadows. *Biogeosci. Discuss.* 12, 18913–18944. doi: 10.5194/bgd-12-18913-2015

Seybold, C. A., Mersie, W., Huang, J., and Mcnamee, C. (2002). Soil redox, pH, temperature, and water-table patterns of a freshwater tidal wetland. *Wetlands* 22, 149–158. doi: 10.1672/0277-5212(2002)022[0149:SRPTAW]2.0.CO;2

Siikamäki, J., Sanchirico, J. N., Jardine, S., McLaughlin, D., and Morris, D. (2013). Blue carbon: coastal ecosystems, their carbon storage, and potential for reducing emissions. *Environ. Sci. Policy Sustain. Dev.* 55, 14–29. doi: 10.1080/00139157.2013.843981

Silva, E. V., and Souza, M.M. A. (2006). Main forms of use and occupation of the mangroves of the State of Ceará. *Cult. Sci. Period.* 1, 12–20.

Sun, Y., Song, Z., Zhang, H., Liu, P., and Hu, X. (2020). Seagrass vegetation affect the vertical organization of microbial communities in sediment. *Mar. Environ. Res.* 162, 105174. doi: 10.1016/j.marenvres.2020.105174

Thangaradjou, T., Bala Krishna Prasad, M., Subhashini, P., Raja, S., Dilipan, E., and Nobi, E. P. (2015). Biogeochemical processes in tropical seagrass beds and their role in determining the productivity of the meadows. *Geochemistry International* 53, 473–486. doi: 10.1134/S0016702915050055

Tessier, A., Campbell, P. G. C., and Bisson, M. (1979). . Biogeochemical processes in tropical seagrass beds and their role in determining the productivity of the meadows. *Anal. Chem.* 51, 844–851. doi: 10.1021/ac50043a017

Toldo, E. E. Jr., Dillenburg, S. R., Corrêa, I. C. S., and Almeida, L. E. S. B. (2000). Holocene Sedimentation in Lagoa dos Patos Lagoon, Rio Grande do Sul, Brazil. *J. Coast. Res.* 16, 816–822. doi: 10.2307/4300091

Tripathi, R. D., Tripathi, P., Dwivedi, S., Kumar, A., Mishra, A., Chauhan, P. S., et al. (2014). Roles for root iron plaque in sequestration and uptake of heavy metals and metalloids in aquatic and wetland plants. *Metallomics* 6, 1789–1800. doi: 10.1039/C4MT00111G

Turschwell, M. P., Connolly, R. M., Dunic, J. C., Sievers, M., Buelow, C. A., Pearson, R. M., et al. (2021). Anthropogenic pressures and life history predict trajectories of seagrass meadow extent at a global scale. *Proc. Natl. Acad. Sci.* 118, 1–11. doi: 10.1073/pnas.2110802118

Ugarelli, K., Laas, P., and Stingl, U. (2019). The microbial communities of leaves and roots associated with turtle grass (Thalassia testudinum) and manatee grass (syringodium filliforme) are distinct from seawater and sediment communities, but are similar between species and sampling sites. *Microorganisms* 7, 4. doi: 10.3390/microorganisms7010004

Unsworth, R. K. F., Nordlund, L. M., and Cullen-Unsworth, L. C. (2019). Seagrass meadows support global fisheries production. *Conserv. Lett.* 12, e12566. doi: 10.1111/conl.12566

Valentine, J. F., and Heck, K. L. (2021). Herbivory in seagrass meadows: an evolving paradigm. *Estuaries Coasts* 44, 491–505. doi: 10.1007/s12237-020-00849-3

Valeriano, C., de, M., Mendes, J. C., Tupinambá, M., Bongiolo, E., Heilbron, M., et al. (2016). Cambro-Ordovician post-collisional granites of the Ribeira belt, SE-Brazil: A case of terminal magmatism of a hot orogen. *J. South Am. Earth Sci.* 68, 269–281. doi: 10.1016/j.jsames.2015.12.014

Vilas Bôas, G. S., Sampaio, F. J., and Pereira, A. M. S. (2001). The Barreiras Group in the Northeastern coast of the State of Bahia, Brazil: depositional mechanisms and processes. *An. Acad. Bras. Cienc.* 73, 417–427. doi: 10.1590/S0001-37652001000300010

Vogel, M. A., Mason, O. U., and Miller, T. E. (2021). Composition of seagrass phyllosphere microbial communities suggests rapid environmental regulation of community structure. *FEMS Microbiol. Ecol.* 97, 1–13. doi: 10.1093/femsec/fiab013

Welsh, D. T. (2000). Nitrogen fixation in seagrass meadows: Regulation, plant-bacteria interactions and significance to primary productivity. *Ecol. Lett.* 3, 58–71. doi: 10.1046/j.1461-0248.2000.00111.x

Williams, C. J., Jaffé, R., Anderson, W. T., and Jochem, F. J. (2009). Importance of seagrass as a carbon source for heterotrophic bacteria in a subtropical estuary (Florida Bay). *Estuar. Coast. Shelf Sci.* 85, 507–514. doi: 10.1016/j.ecss.2009.09.019

York, P. H., Smith, T. M., Coles, R. G., McKenna, S. A., Connolly, R. M., Irving, A. D., et al. (2017). Identifying knowledge gaps in seagrass research and management: An Australian perspective. *Mar. Environ. Res.* 127, 163–172. doi: 10.1016/j.marenvres.2016.06.006

Yu, C., Xie, S., Song, Z., Xia, S., and Åström, M. E. (2021). Biogeochemical cycling of iron (hydr-)oxides and its impact on organic carbon turnover in coastal wetlands: A global synthesis and perspective. *Earth Sci. Rev.* 218, 103658. doi: 10.1016/j.earscirev.2021.103658

Zhang, J., Ling, J., Zhou, W., Zhang, W., Yang, F., Wei, Z., et al. (2021). Biochar addition altered bacterial community and improved photosynthetic rate of seagrass: A mesocosm study of seagrass Thalassia hemprichii. *Front. Microbiol.* 12. doi: 10.3389/fmicb.2021.783334

Zhang, X., Liu, S., Jiang, Z., Wu, Y., and Huang, X. (2022). Gradient of microbial communities around seagrass roots was mediated by sediment grain size. *Ecosphere* 13, 1–15. doi: 10.1002/ecs2.3942

Zidorn, C. (2016). Secondary metabolites of seagrasses (Alismatales and Potamogetonales; Alismatidae): Chemical diversity, bioactivity, and ecological function. *Phytochemistry* 124, 5–28. doi: 10.1016/j.phytochem.2016.02.004

Frontiers in Marine Science

Explores ocean-based solutions for emerging global challenges

The third most-cited marine and freshwater biology journal, advancing our understanding of marine systems and addressing global challenges including overfishing, pollution, and climate change.

Discover the latest Research Topics

See more →

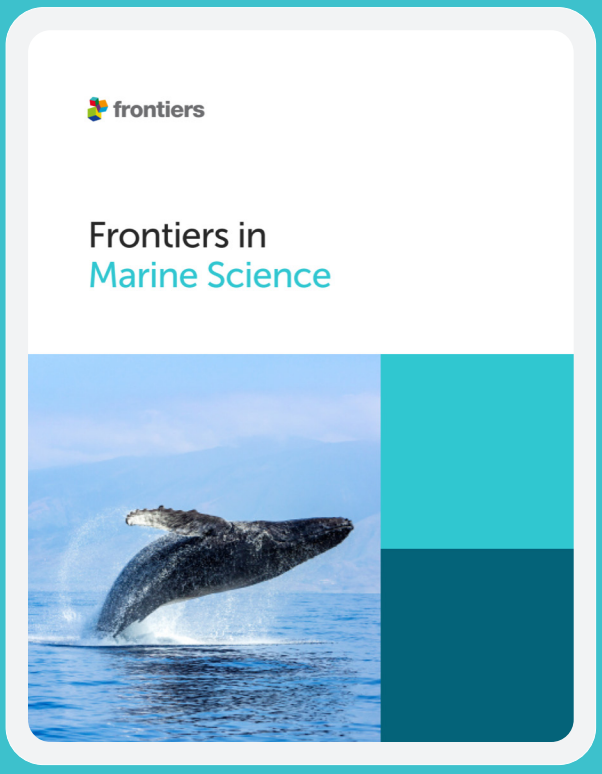

Frontiers

Avenue du Tribunal-Fédéral 34
1005 Lausanne, Switzerland
frontiersin.org

Contact us

+41 (0)21 510 17 00
frontiersin.org/about/contact